Etude de la composition chimique des particules fines et des sources d'aérosol organique sur différents sites en France à partir de jeux de données pluriannuels à haute résolution temporelle

Hasna Chebaicheb

N° d'ordre : 2023MTLD0006

THÈSE

présentée en vue d'obtenir le grade de

DOCTEURE

en

Discipline : Sciences de la terre et de l'univers, espace

Spécialité : Terre, enveloppes fluides

par

Hasna CHEBAICHEB

Doctorat de l´Université de Lille délivré par IMT Nord Europe

« Etude de la composition chimique des particules fines et des sources d'aérosol organique sur différents sites en France à partir de jeux de données pluriannuels à haute résolution temporelle »

Soutenance le 19/12/2023 devant le jury d'examen :

Présidente du jury	SARTELET Karine	DR CEREA, ENPC
Rapporteuse	D'ANNA Barbara	DR CNRS, LCE – Aix-Marseille Université
Rapporteur	JAFFREZO Jean-Luc	DR CNRS, IGE Grenoble
Examinatrice	GROS Valérie	DR CNRS, LSCE
Examinatrice	MARCHAND Caroline	Ingénieure, ASUR, Ineris
Directrice de thèse	RIFFAULT Véronique	PR, CERI EE, IMT Nord Europe
Co-encadrant	FAVEZ Olivier	Ingénieur-chercheur, ASUR, Ineris
Co-encadrant	FERREIRA DE BRITO Joel	MA, CERI EE, IMT Nord Europe

Laboratoires d'accueil :

- Centre d'Enseignement, de Recherche et d'Innovation Energie et Environnement (CERI EE), IMT Nord Europe
- Unité Accompagnement à la surveillance de la qualité de l'air et des eaux de surface (ASUR), Ineris

École doctorale Sciences de la Matière, du Rayonnement et de l'Environnement (ED SMRE)
(Université de Lille, Centrale Lille, IMT Nord Europe)

Résumé

L'étude des aérosols atmosphériques est cruciale en raison de leurs impacts climatiques et sur la santé humaine. Selon les recommandations actuelles de l'Organisation Mondiale de la Santé (OMS), les concentrations de $PM_{2,5}$ ne devraient pas dépasser 5 µg m^{-3} en moyenne annuelle. Cependant, seul 2 % de la population européenne vit dans des zones respectant cette limite, entraînant environ 238 000 décès par an. Comprendre l'exposition aux particules fines à cette échelle peut donc jouer un rôle important pour développer des mesures visant à réduire leurs effets. Dans ce contexte, cette thèse a caractérisé les particules fines sur 13 sites (péri-)urbains en France dans le cadre du programme CARA du dispositif national du Laboratoire Central de Surveillance de la Qualité de l'Air (LCSQA), en collaboration avec les associations agréées de surveillance de la qualité de l'air (AASQA), en utilisant des données de composition chimique des particules fines, à partir de spectromètres de masse (*Aerosol Chemical Speciation Monitor*, ACSM) et d'aethalomètres (AE33), collectées sur 2015-2021 à haute résolution temporelle. Leur traitement a inclus un contrôle qualité conforme aux procédures opérationnelles standard de l'infrastructure de recherche européenne ACTRIS.

Globalement, l'aérosol organique (AO) prédomine sur l'ensemble des sites, représentant entre 40 et 60 % des PM_1, et montrant une saisonnalité distincte avec des concentrations plus élevées (i) en hiver, en raison de l'augmentation des émissions du chauffage résidentiel, et (ii) en été, en raison de l'augmentation de la photochimie, ce qui favorise la formation secondaire. Le NO_3 est le deuxième contributeur le plus important de PM_1 (15-30 %), atteignent son maximum en printemps, en particulier dans le nord de la France, et jouant un rôle important lors des épisodes de pollution. Le sulfate d'ammonium et le carbone suie (eBC) complètent les espèces majeures de l'aérosol fin, avec des contributions relatives fortement influencées respectivement par l'origine des masses d'air et la stabilité météorologique.

Une méthode récemment développée de type *rolling Positive Matrix Factorization* (PMF glissante) a été utilisée pour étudier les sources et origines de l'AO. Elle a l'avantage de déceler les changements temporels potentiels dans les profils des sources au sein de jeux de données pluriannuels. Les facteurs primaires identifiés sont liés principalement aux processus de combustion. En particulier, l'AO de type hydrocarboné lié aux émissions à l'échappement du trafic (HOA) et celui provenant de la combustion de biomasse (BBOA) sont présents sur tous les

sites, avec des contributions de l'ordre de 15 % de la masse d'AO. Le BBOA présente une saisonnalité marquée avec un pic en hiver dû à l'augmentation des émissions du chauffage au bois résidentiel. D'autres sources primaires spécifiques à certains sites ont été également mises en évidence : celles liées aux activités de cuisson (10-14 %), à des émissions portuaires et/ou industrielles (4 % à Marseille) ou des activités industrielles spécifiques incluant l'utilisation d'amines (Strasbourg, Creil). Les facteurs oxygénés, distingués entre leurs fractions moins et plus oxydées (LO-OOA et MO-OOA, respectivement), dominent l'AO sur tous les sites, avec une contribution moyenne de 74 %, suggérant des processus de vieillissement et de formation secondaire importants.

L'ensemble de ces résultats éclaire les principales sources d'AO en France et permet d'orienter les politiques publiques de réduction des émissions et d'amélioration de la qualité de l'air. Ils peuvent aussi contribuer à améliorer la précision des modèles de qualité de l'air, avec l'initiation de premiers exercices de comparaison avec le modèle CHIMERE au cours de la thèse. Les résultats obtenus présentent également un fort intérêt pour une meilleure compréhension de l'impact sanitaire des PM, constituant notamment la base de futures études épidémiologiques.

Mots clés : Qualité de l'air, pollution urbaine, PM_1, aérosol organique, PMF glissante.

Abstract

The study of atmospheric aerosols is crucial due to their climatic and human health impacts. According to current recommendations from the World Health Organization (WHO), the concentrations of $PM_{2.5}$ should not exceed 5 µg m^{-3} on an annual average. However, only 2 % of the European population lives in areas below this limit, resulting in approximately 238 000 deaths per year. Understanding exposure to fine particles on this scale can play a significant role in developing measures to reduce their effects. In this context, this thesis characterized fine particles at 13 (sub)-urban sites in France as part of the CARA program of the national network of the Central Laboratory for Air Quality Monitoring (LCSQA), in collaboration with accredited air quality monitoring associations (AASQA). This was done using high-time resolution data on the chemical composition of fine particles collected from 2015 to 2021, with the use of mass spectrometers (*Aerosol Chemical Speciation Monitor*, ACSM) and aethalometers (AE33). The data processing included quality control in accordance with the standard operational procedures of the European research infrastructure ACTRIS.

Overall, organic aerosols (OA) predominate across all sites, representing between 40 and 60 % of PM_1, and showing a distinct seasonality with higher concentrations (i) in winter, due to increased emissions from residential heating, and (ii) in summer, due to increased photochemistry, which favors secondary formation. NO_3 is the second most important contributor to PM_1 (15-30 %), peaking in spring, particularly in northern France, and playing an important role during pollution episodes. Ammonium sulfate and black carbon (eBC) complement the major fine aerosol species, with their relative contributions strongly influenced by the origin of air masses and meteorological stability, respectively.

A recently developed method called *rolling Positive Matrix Factorization* (PMF) was used to study the origins of OA. This method has the advantage of treating multi-annual PMF datasets on a harmonized and well-controlled manner. The primary factors identified are mainly related to combustion processes. In particular, hydrocarbon-like OA from traffic emissions (HOA) and biomass burning OA (BBOA) are present at all sites, with contributions of around 15 % of the total OA mass. BBOA shows a marked seasonality, with a peak in winter due to increased

residential wood heating emissions. Other site-specific primary sources were also identified, including cooking activities (10-14 %), port and/or industrial emissions (4 % in Marseille), and specific industrial activities involving the use of amines (Strasbourg, Creil). Oxygenated factors, distinguished between less and more oxidized fractions (LO-OOA and MO-OOA, respectively), dominate the OA at all sites, with an average contribution of 74 %, indicating significant aging and secondary formation processes.

All these results shed light on the main sources of OA in France and help guide public policies to reduce sources and improve air quality. The results can also lead to more accurate air quality models, with the first comparison exercises with the CHIMERE model presented in this thesis. The results obtained are also of great interest for a better understanding of the health impact of PM, serving as a basis for future epidemiological studies.

Keywords: Air quality, urban pollution, PM_1, organic aerosol, rolling PMF

Remerciements

الحمد لله الذي بنعمته تتم الصالحات

Je souhaite tout d'abord exprimer ma reconnaissance envers mes organismes d'accueil, IMT Nord Europe et l'Ineris, ainsi que le laboratoire de surveillance de la qualité de l'air (LCSQA), pour le soutien financier indispensable à la réalisation de cette thèse.

Je tiens également à exprimer ma profonde gratitude aux membres du jury pour avoir accepté d'évaluer mon travail de thèse et pour avoir consacré du temps à la lecture de mon manuscrit et à leurs échanges lors de la soutenance.

Un grand merci particulièrement à mes chers encadrants Joel, Olivier, Caroline et Véronique pour leur soutien permanent, leur patience et leurs conseils attentifs tout au long de ces trois années de recherche. Leur disponibilité et leur engagement ont été essentiels à ma réussite. Merci infiniment pour votre confiance, votre gentillesse et votre expertise. Je me considère extrêmement chanceuse de vous avoir comme encadrants.

Je tiens également à exprimer mes sincères remerciements à tous les collaborateurs et personnes impliquées dans ce travail. Je remercie les AASQA pour leur collaboration dans la réalisation de ce projet, en particulier Mélodie Chatain d'Atmo Grand Est, Grégory Abbou et Alexia Baudic d'AirParif, Grégory Gille d'Atmo Sud, Shouwen Zhang d'Atmo Hauts-de-France, Romain Vidaud et Sabrina Pontet d'Atmo AURA, Raphaele Falhun d'Air Breizh, Benjamin Chazeau et Nicolas Marchand de LCE. Je remercie Ian Chen et Marta Via, ainsi que tous les collègues de Colossal, pour les échanges fructueux autour de la méthode PMF glissante. Je tiens également à remercier Anna Tobler et Francesco Canonaco pour leur aide précieuse et leurs échanges constructifs sur SoFi Pro. Je remercie également Vincent Crenn et Florian Couvidat pour leurs précieuses contributions à mes articles de thèse. Je tiens également à remercier sincèrement les membres de mon comité de thèse, Jean-Eudes Petit et Isabelle Chiapello, pour leurs commentaires et suggestions visant à améliorer mon travail.

Mes remerciements vont aussi à tous mes collègues et amis qui ont enrichi mon expérience à l'IMT et à l'Ineris, ainsi qu'à l'ensemble du personnel, des RH, des techniciens et des ingénieurs, pour leur soutien, leurs encouragements constants et leur chaleureuse compagnie.
À mes chères amies marocaines, je vous adresse toute ma gratitude pour les moments agréables partagés et votre soutien moral.

Enfin, un immense merci à ma famille pour leur soutien inconditionnel et leur présence constante tout au long de cette aventure. Vos encouragements, vos paroles et votre soutien moral ont été les piliers sur lesquels je me suis appuyée durant cette période. Encore une fois, merci du fond du cœur pour tout ce que vous avez fait pour moi.

Table des matières

Table des illustrations

Table des tableaux

Glossaire

Terme	Définition
AAE	Angström Absorption Exponent
AN	Nitrate d’ammonium
AO	Aérosol organique
AOP	Aérosols organiques primaires
AOS	Aérosols organiques secondaires
AS	Sulfate d’ammonium
ATOLL	ATmospheric Observations in liLLe
BBOA	Biomass Burning Organic Aerosol
BSOA	Biogenic secondary organic aerosols
CCOA	Coal combustion organic aerosol
CDCE	Composition-Dependent Collection Efficiency
CE	Efficacité de collecte
COA	Cooking organic aerosol
COSV	Composés organiques semi-volatils
COV	Composés organiques volatils
eBC	Equivalent Black Carbon
eBC_{ff}	eBC issues de la combustion de combustibles fossiles
eBC_{wb}	eBC issues de la combustion de biomasse
EC	Carbone élémentaire
ECMWF	European Centre for Medium-Range Weather Forecasts
HOA	Hydrocarbon-like OA
IFS	Integrated Forecasting System
IQR	InterQuartile Range

LO-OOA	Less oxydized oxygenated OA
LVOC	Composés organiques peu volatils
MAE	Mass Absorption Efficiency
MCM	Master Chemical Mechanis
MO-OOA	More oxydized oxygenated OA
NVOC	Composés organiques non volatils
OC	Carbone organique
OM	Matière organique
PM	Particulate Matter
PM_1	Particules d'un diamètre aérodynamique ≤ 1 µm
PM_{10}	Particules d'un diamètre aérodynamique ≤ 10 µm
$PM_{2,5}$	Particules d'un diamètre aérodynamique ≤ 2,5 µm
PMF	Positive Matrix Factorization
RF	Facteur de réponse
RIE	Efficacités d'ionisation relative
RIT	Relative Ion Transmission
SEM	Secondary Electron Multiplier
UFP	Particules ultrafines

Introduction générale

L'étude des aérosols atmosphériques est au cœur des discussions scientifiques et politiques sur la qualité de l'air en raison de leurs effets climatiques directs, par réchauffement ou refroidissement de la planète à travers l'absorption ou la diffusion du rayonnement solaire, ou indirects, en agissant sur la microphysique des nuages (IPCC, 2023), ainsi que leurs impacts négatifs sur la santé humaine. En effet, plusieurs études confirment notamment leur influence sur l'apparition de maladies respiratoires, cérébrovasculaires et cardiovasculaires (Kelly et Fussell 2015). L'exposition aux particules fines est parmi les causes principales de mort prématurée (Wang et al. 2020). Selon une publication récente dans la revue Neurology (Toubasi et Al-Sayegh, 2023), une exposition à court terme à la pollution atmosphérique peut augmenter le risque d'accident vasculaire cérébral. Ils montrent qu'il existe un lien solide et notable entre les polluants atmosphériques gazeux et particulaires et les taux d'incidence et de mortalité des accidents vasculaires cérébraux. Ce lien temporel immédiat souligne la nécessité cruciale d'efforts mondiaux pour formuler des politiques axées sur la réduction de la pollution atmosphérique. Un récent article publié dans The Guardian (Taylor et Duncan, 2023) révèle que près de 30 millions d'Européens vivent dans des zones où les concentrations de particules fines sont au moins quatre fois supérieures aux recommandations de l'Organisation Mondiale de la Santé (OMS). En France, on estime que 37 % de la population respire en moyenne un air dont les concentrations sont deux fois supérieures à celles recommandées par l'OMS. La circulation, l'industrie, le chauffage domestique et l'agriculture sont les principales sources de $PM_{2.5}$ (particules ayant un diamètre aérodynamique inférieur à 2,5 µm), dont l'impact est souvent ressenti de manière disproportionnée par les communautés les plus démunies. Selon les directives actuelles de l'OMS, les concentrations moyennes annuelles de $PM_{2,5}$ ne devraient pas dépasser 5 µg m^{-3}. Cependant, seuls 2 % de la population européenne vit dans des zones respectant cette limite. Selon l'Agence Environnementale Européenne (EEA, 2022), l'exposition aux particules fines entraîne environ 238 000 décès prématurés chaque année. En France, le nombre est estimé à 40 000 morts par an (Medina et al. 2021), d'où l'importance de développer des stratégies d'atténuation pour réduire les émissions et améliorer la qualité de l'air.

Au cours des deux dernières décennies, les techniques de caractérisation en ligne des aérosols, telles que l'AMS (*Aerosol Mass Spectrometer*) et l'ACSM (*Aerosol Chemical Speciation*

Monitor), ont démontré leur capacité à améliorer notre compréhension des constituants chimiques clés des particules en fournissant des données de spectres de masse hautement résolus dans le temps pour la fraction PM_1 non réfractaire (NR-PM_1). L'ACSM est mieux adapté aux applications de surveillance à long terme en raison de sa maintenance aisée et de son coût réduit. Des méthodes de répartition des sources ont été également développées au cours des dernières décennies, telles que la PMF (*Positive Matrix Factorization*) (Paatero et Tapper, 1994). Les spectres de masse obtenus par l'AMS et l'ACSM ont été intégrés dans des analyses par PMF pour quantifier les sources d'aérosols organiques (AO) (e.g., Zhang et al., 2011, Crippa et al., 2014, Srivastava et al., 2018, Sun et al., 2018, Canonaco et al., 2021, Chen et al., 2022a).

Dans ce contexte, cette thèse s'inscrit dans le cadre des travaux du Laboratoire Central de Surveillance de la Qualité de l'Air en France (LCSQA), au travers d'une collaboration entre l'IMT Nord Europe et l'Ineris, où j'ai passé 23 et 15 mois de ma thèse, respectivement. Le LCSQA est soutenu par le Ministère en charge de l'environnement, et il est l'organisme national de référence conformément aux directives nationales et européennes. Ses missions sont définies dans l'arrêté du 16 avril 2021 pour améliorer le système de surveillance de la qualité de l'air en France, en fournissant un soutien scientifique et technique au ministère et aux Associations Agréées de Surveillance de la Qualité de l'Air (AASQA). Son objectif clé est de contribuer à l'amélioration de la précision des mesures effectuées dans l'air ambiant, de la collecte et l'analyse des données issues de ces mesures.

Créé et géré par le LCSQA, le programme CARA, « caractérisation chimique des particules », a été mis en place en 2008, en réponse au besoin de compréhension et d'information sur l'origine des épisodes de pollution particulaire mis en évidence par les pics de PM_{10} du printemps 2007. Ce dispositif aujourd'hui pérenne, fonctionne en étroite collaboration avec les AASQA volontaires et des laboratoires de recherche (notamment le Laboratoire des Sciences de l'Environnement, CNRS-CEA-Université Paris Saclay, et l'Institut des Géosciences de l'Environnement, CNRS-Université Grenoble Alpes). Il repose historiquement sur l'analyse chimique au laboratoire de filtres collectés en plusieurs points du dispositif national. Néanmoins, l'utilisation exclusive de prélèvements sur filtres et leurs analyses en différé ne permettent pas de bien répondre au besoin grandissant d'une détermination en temps quasi-réel de la composition chimique des PM. Au cours de ces dernières années, le LCSQA s'est donc attaché à accompagner

les AASQA dans l'implantation d'analyseurs automatiques de la composition chimique des PM au sein du dispositif national, qui dispose aujourd'hui d'un réseau opérationnel unique en Europe.

En conséquence, treize jeux de données issus d'observations à long terme réalisées avec des ACSM et des aethalomètres (AE33) (ainsi que d'autres données PM) ont été collectés par les AASQA concernées, notamment AirParif, ATMO Grand-Est, ATMO Hauts-de-France, Air Breizh, ATMO Auvergne-Rhône-Alpes, ATMO Nouvelle-Aquitaine et ATMO Sud (en collaboration avec le LCE à Marseille). Les mesures in-situ de deux observatoires de recherche ATOLL (à Lille, IMT Nord Europe/LOA) et SIRTA (à Paris, LSCE/Ineris), membres d'ACTRIS-France et candidat à la labellisation européenne de l'infrastructure de recherche européenne ACTRIS, font également partie du programme CARA et ont été intégrées à cette étude.

La thèse s'inscrit également dans le cadre des projets CaPPA (ANR-11-LABX-0005-01), financé par l'Agence Nationale de la Recherche (ANR) au travers du PIA (Programme d'Investissement d'Avenir), et CPER CLIMIBIO (maintenant CPER ECRIN), tous deux financés par le Conseil Régional "Hauts-de-France" et le Fonds Européen de Développement Régional (ERDF). Ces projets financent notamment des études dans la région Hauts-de-France, y compris la plateforme ATOLL.

Cette thèse est structurée en 6 chapitres. Le premier chapitre traite de l'état de l'art et des objectifs de la thèse, tandis que le deuxième chapitre aborde la présentation des stations de mesure, l'instrumentation ainsi que les méthodologies mises en œuvre. Les 4 chapitres suivants sont consacrés aux résultats obtenus, présentés sous forme d'articles scientifiques en anglais précédés de résumés en français.

- Le chapitre 3 expose la phénoménologie de la composition chimique des particules fines, recueillies à partir des instruments ACSM et AE33 sur les différents sites (AASQA, ATOLL et SIRTA). Une présentation détaillée de la méthodologie et des procédures de contrôle qualité des données précède la description des variations temporelles et spatiales de l'ensemble de ces données. Une comparaison avec les résultats du modèle CHIMERE clôture ce chapitre.

- Le chapitre 4 examine spécifiquement deux stations à Strasbourg qui ont pu mener simultanément les mêmes types d'observations durant l'hiver 2019/2020, avec une évaluation de la cohérence des mesures et des résultats des analyses de répartition des sources d'aérosols carbonés.
- Le chapitre 5 présente une étude approfondie des sources et origines géographiques de l'AO sur la station ATOLL à Lille, en appliquant une méthode de PMF glissante (*Rolling PMF*) récemment développée et testée à l'échelle européenne.
- Enfin, le dernier chapitre offre une vue d'ensemble des sources d'AO en France, basée sur les différents jeux de données ACSM et l'application de la méthode *Rolling PMF* avec une harmonisation des critères utilisés. Ce chapitre se conclut par une comparaison avec les résultats du modèle CHIMERE.

A noter enfin qu'au cours de ce travail, nous avons élaboré un guide utilisateur pour le traitement des données ACSM et la répartition des sources en utilisant la PMF sous le logiciel SoFi Pro, afin de faciliter le transfert de connaissances vers les services opérationnels des AASQA (mission du LCSQA). Ce guide est présenté en annexe 3.

Chapitre I. Etat de l'art et objectifs de la thèse

Les particules fines peuvent être émises directement dans l'atmosphère sous forme d'aérosols primaires, provenant de diverses sources naturelles et anthropiques. Elles peuvent également se former dans l'atmosphère en tant qu'aérosols secondaires, par le biais de processus de conversion gaz-particules d'espèces gazeuses. De plus, les aérosols primaires et secondaires peuvent subir des transformations physico-chimiques, influencées par des processus de transport, d'incorporation dans les nuages et/ou d'élimination atmosphérique (Zhang et al., 2015). Cette variété de sources d'émission et de processus de formation et de transformation contribue à la diversité et à la complexité de la composition chimique et des propriétés physiques des aérosols atmosphériques, avec des impacts avérés sur le climat et la santé humaine (Zhang et al., 2015). Il est essentiel de décrire les caractéristiques physiques et chimiques de ces particules, et de mieux comprendre la répartition de leurs sources, l'intensité de leurs émissions et leurs origines. Ces informations sont primordiales pour mettre en place des réglementations efficaces concernant les particules fines et pour évaluer les risques sanitaires associés (Pandis et al., 2016). La Figure I.1 résume l'ensemble de ces processus qui sont décrits plus en détail dans ce chapitre.

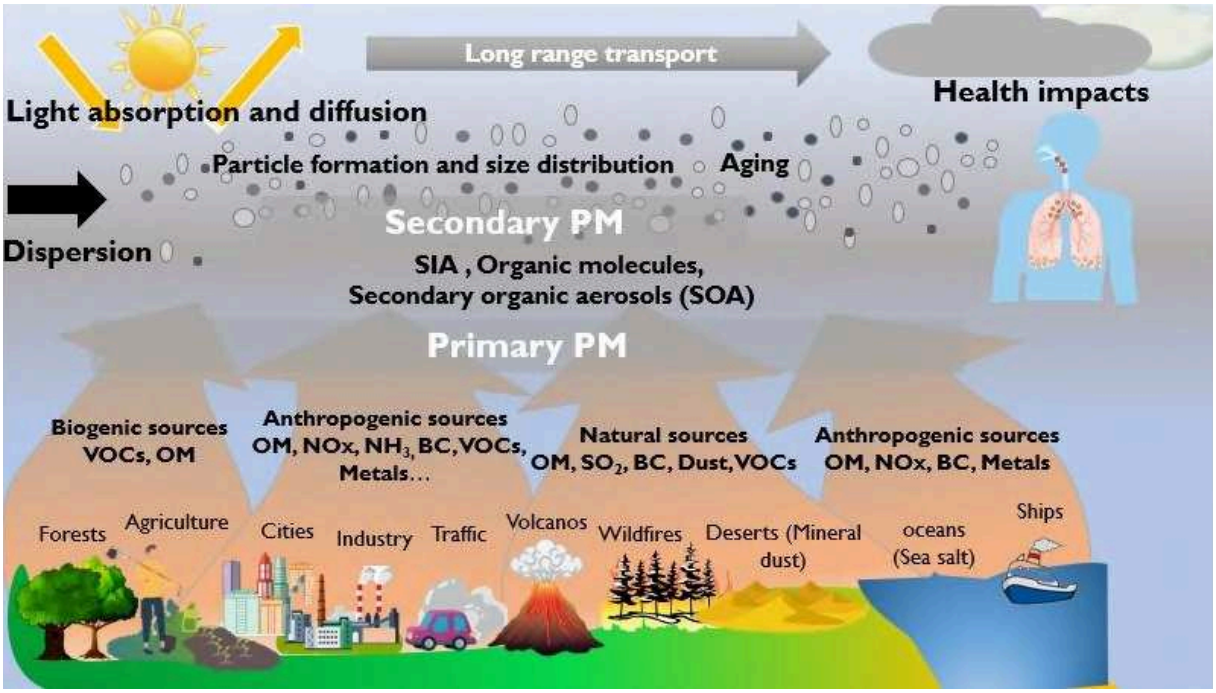

Figure I.1 : Sources et processus de formation et transformation des particules fines dans l'atmosphère et leurs divers impacts sur le climat et la santé humaine. SIA : *Secondary Inorganic Aerosol* (aérosols inorganiques secondaires) ; VOCs : *Volatile Organic Compounds* (composés organiques volatils); OM : *Organic Matter* (matière organique) ; BC: *Black Carbon* (carbone suie).

Les aérosols atmosphériques, également nommés PM (*Particulate Matter*), désignent les particules solides et/ou liquides présentes dans l'air. Leur caractéristiques distinctives comprennent leur distribution en taille et leur composition chimique, qui sont associées à la variété des sources à partir desquelles ils sont émis. Leur durée de vie dans l'atmosphère dépend de leur taille, de leurs propriétés et des conditions environnementales.

Les sources et la composition des aérosols, leurs propriétés, interactions et transformations dans l'atmosphère, ainsi que leurs effets sur le climat et la santé créent une interdépendance importante, comme illustré dans la Figure I.2. Ainsi, une meilleure compréhension des sources, des propriétés et de la transformation des particules est nécessaire pour la caractérisation, la modélisation et l'atténuation efficace des effets des aérosols naturels et anthropiques sur le climat et la santé publique.

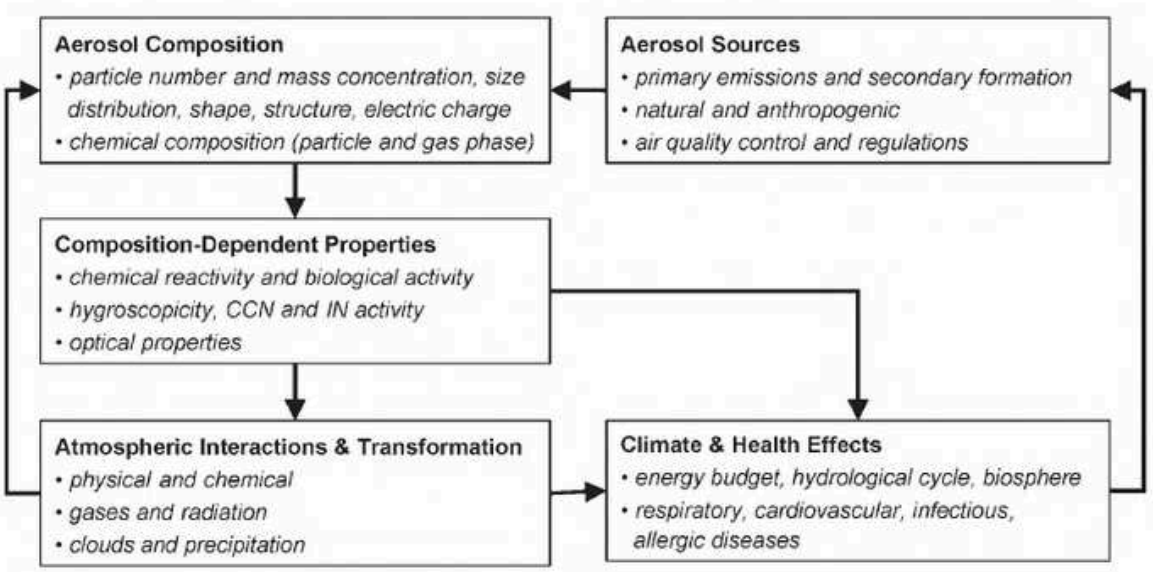

Figure I.2 : Interdépendance existant entre les différentes composantes des aérosols (source : Pöschl, 2005).

I.1 Propriétés physiques et chimiques des aérosols

I.1.1 Aérosols primaires/secondaires

Les propriétés variées des aérosols sont étroitement liées à la diversité de leurs origines et de leurs sources. On distingue les particules primaires des particules secondaires.

Les **aérosols primaires** désignent les particules émises directement dans l'atmosphère, telles que la combustion de biomasse, la combustion incomplète de combustibles fossiles, les éruptions volcaniques, ainsi que les aérosols produits par l'effet de la friction du vent sur une surface océanique ou terrestre, comme les sels marins et les poussières minérales.

Quant aux **aérosols secondaires**, ce sont des particules qui n'ont pas été émises directement dans la phase particulaire mais sont issues de processus de nucléation et de condensation des espèces en phase gazeuse ou à partir de réactions chimiques hétérogènes et multi-phasiques. Les espèces en phase gazeuse, appelées précurseurs d'aérosols, subissent un certain nombre de transformations chimiques pour former des espèces condensables.

Les aérosols secondaires occupent une part substantielle parmi les particules fines, représentant entre 50 % et 75 % de la masse totale en milieu urbain, selon Pandis et al. (2016) qui ont mené une étude dans cinq grandes villes : Athènes et Paris en Europe, Pittsburgh et Los Angeles aux États-Unis, Mexico en Amérique centrale. Parmi ces constituants secondaires figurent les sulfates (SO_4), les nitrates (NO_3) et les composés organiques oxydés, tandis que les composants primaires prédominants englobent le carbone élémentaire (EC), les oxydes métalliques ainsi que les particules organiques fraîchement émises.

I.1.2 Distribution en taille

Les particules atmosphériques sont classées en quatre modes par rapport à leur diamètre aérodynamique (qui est défini comme celui d'une sphère, dont la densité est de 1 g cm^{-3}), s'étalant sur cinq ordres de grandeur.

Les plus petites particules ayant une taille comprise entre 1 et 20 nm sont formées par des processus de conversion gaz-particules (nucléation) à partir des précurseurs en phase gazeuse. Certains processus de combustion, notamment ceux des moteurs Diesel, peuvent aussi générer des particules dans ce mode, appelé mode de nucléation.

Les particules ayant une taille comprise entre 20 et 100 nm sont produites par la condensation de gaz chauds ou de vapeur d'eau sur des nanoparticules existantes, en particulier lors des processus de combustion. En outre, des particules primaires sont émises par la combustion de biomasse ou par les moteurs. Ces particules sont associées au mode d'Aitken.

Ces deux modes, le mode de nucléation et le mode d'Aitken, rassemblent les particules ultrafines (UFP). Elles sont rapidement éliminées, soit par impaction sur les surfaces, soit par coagulation, ce qui les amène au troisième mode.

Les particules ayant une taille comprise entre 100 nm et 1 µm (ou 2,5 µm) appartiennent au mode d'accumulation. Ce sont des particules fines qui demeurent plus longtemps dans l'atmosphère en raison de la moindre efficacité des mécanismes de croissance ou d'élimination. Ce mode regroupe les UFP précédentes ayant condensé ou coagulé, ainsi que certaines émissions primaires résultant d'une combustion incomplète.

Enfin, **les particules ayant une taille supérieure à 1 (ou 2,5 µm)** : les processus de croissance des particules fines étant peu significatifs, les particules grossières sont principalement émises par

des processus mécaniques tels que l'abrasion de surface, l'érosion éolienne, la combustion, les sources marines et volcaniques. Ces particules, appartenant au mode grossier, résident peu de temps dans l'atmosphère en raison de leur sédimentation rapide.

La Figure I.3 montre quelques exemples d'espèces atmosphériques et leurs diamètres aérodynamiques correspondants.

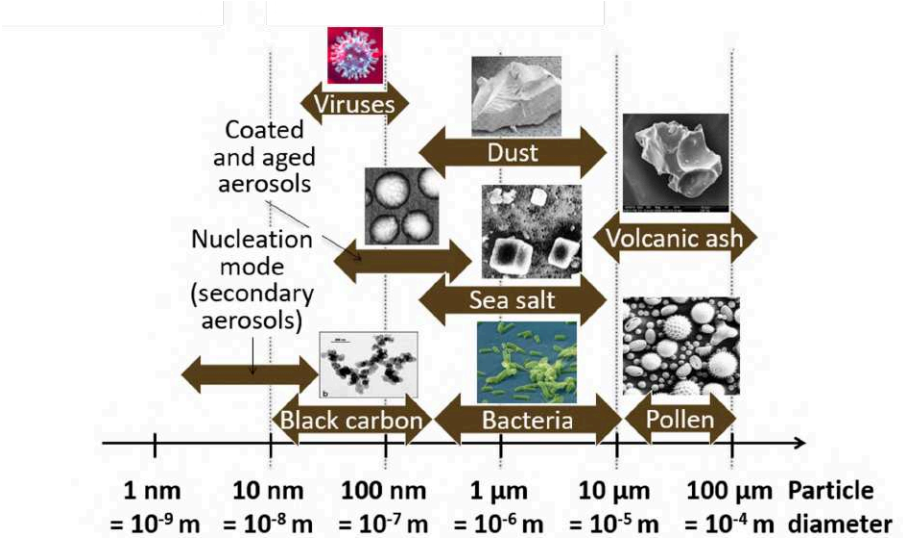

Figure I.3 : Distribution en taille de divers aérosols atmosphériques (d'après Karlen et al., 2022)

I.1.3 Composition chimique

Les impacts, climatique et sanitaire, dépendent de la composition chimique des particules. Cette composition chimique est par ailleurs un paramètre clé qui contrôle l'hygroscopicité de l'aérosol (c'est-à-dire sa capacité à absorber l'eau et à croître en taille lorsque l'humidité relative ambiante augmente), la facilité avec laquelle il peut être lessivé par la pluie, sa capacité à servir de noyau de condensation des nuages ou de noyau glaciogène, ou ses propriétés optiques.

Deux catégories fondamentales peuvent être identifiées : la matière minérale ou inorganique, ainsi que la matière carbonée principalement composée de carbone organique et élémentaire.

Composants des aérosols inorganiques ou minéraux : essentiellement sulfate SO_4^{2-}, nitrate NO_3^- et ammonium NH_4^+. D'autres substances sont présentes, généralement à des concentrations plus faibles, telles que certains métaux (plomb, arsenic, cadmium, ...) et des sels (issus des

embruns marins, ...).

Les SO_4 et les NO_3 présents dans les PM proviennent typiquement de l'oxydation du dioxyde de soufre (SO_2) et du dioxyde d'azote (NO_2), respectivement. SO_2 est émis par la combustion de combustibles fossiles contenant du soufre, comme le charbon et le pétrole résiduel, qui sont généralement brûlés dans des systèmes de combustion à grande échelle, comme les centrales électriques au charbon et les moteurs diesel des navires. NO_2 est directement émis lors des combustions ou formé à partir de monoxyde d'azote (NO) émis par la combustion à haute température de gaz, de combustibles liquides et de charbon. NO_2 et SO_2 peuvent être oxydés de manière homogène par les radicaux hydroxyles et de manière hétérogène dans les gouttelettes et à la surface des particules (Pandis et al., 2016). En général, le NO_3 formé a tendance à dominer en hiver lorsque les températures sont plus basses, ce qui favorise la formation de nitrate d'ammonium particulaire (NH_4NO_3 ; AN) ; tandis que le SO_4 atteint généralement son maximum en été, lorsque l'augmentation de l'activité photochimique permet la formation du SO_4 à partir du SO_2 émis.

Composants des aérosols carbonés : ils représentent une proportion allant de 20 à 50 % de la masse totale des $PM_{2,5}$ et PM_{10} (Putaud et al., 2010). Cette catégorie présente une variété étendue de structures moléculaires et exerce une influence significative sur les caractéristiques physico-chimiques, biologiques, climatiques et sanitaires des aérosols atmosphériques, ainsi que sur leurs effets. Les aérosols carbonés sont principalement constitués de carbone organique (OC, *Organic Carbon*) et de carbone inorganique (carbonates) ou élémentaire (EC, *Elemental Carbon*).

Le **carbone élémentaire** se compose pratiquement à 100 % d'atomes de carbone et possède une inertie chimique. Lors du processus de combustion, les particules de carbone élémentaire sont émises directement dans l'atmosphère par la combustion de biomasse à basse température et la combustion incomplète de combustibles fossiles à haute température. Il est également assimilé au carbone suie (BC).

Le **carbone organique** constitue une fraction qui englobe tous les composés organiques fonctionnalisés. Ces composés sont émis soit directement dans l'atmosphère, soit générés par la condensation ou la nucléation des produits résultant de la dégradation photochimique des composés organiques volatils (COV).

Les aérosols organiques comprennent une variété de composés chimiques (alcanes, alcènes, alcools, composés aromatiques, composés carbonylés, acides organiques, amines, composés organo-soufrés, ...), ce qui illustre leur complexité. On peut distinguer les aérosols organiques primaires et secondaires. Les aérosols organiques contenant des composés riches en oxygène sont appelés les aérosols organiques oxygénés. Le rapport O/C dans les aérosols organiques est en fait un indicateur de la composition chimique. Ce rapport est supérieur à 0,25 dans les organiques et peut atteindre des valeurs aussi élevées que 1 pour les aérosols les plus âgés (Boucher, 2015). Jimenez et al., (2009) ont montré qu'en vieillissant dans l'atmosphère, les aérosols organiques deviennent plus oxygénés, moins volatils et plus hygroscopiques.

Les composants organiques primaires des aérosols (AOP) sont directement émis en phase condensée (particules liquides ou solides) ou sous forme de vapeurs semi-volatiles, qui sont condensables dans les conditions atmosphériques. Les principales sources de ces particules sont la combustion de la biomasse naturelle et anthropique (feux de forêt, brûlages, chauffage domestique), la combustion de combustibles fossiles (domestique, industriel, trafic), la (re)suspension de poussières du sol et des routes due au vent ou au trafic, les matériaux biologiques (débris végétaux et animaux, micro-organismes, pollens, spores, etc.), les embruns marins ou provenant d'autres eaux de surface, contenant des composés organiques dissous.

Les composants des aérosols organiques secondaires (AOS) sont connus pour constituer une quantité considérable de la matière organique (MO) et des particules fines. Ils sont formés par réaction chimique et conversion de COV en particules dans l'atmosphère, selon différentes voies (Boucher, 2015) :

- Formation de nouvelles particules : formation de composés organiques semi-volatils (COSV) par des réactions en phase gazeuse et participation des COSV à la nucléation et à la croissance de nouvelles particules d'aérosol ;
- Séparation gaz-particules : formation de COSV par des réactions en phase gazeuse et absorption (ou adsorption) par des particules préexistantes d'aérosols ou de nuages ;
- Réactions hétérogènes ou multi-phasiques : formation de composés organiques peu ou non volatils (LVOC, NVOC) par réaction chimique de COV ou de COSV à la surface ou dans des particules d'aérosol ou de nuage.

I.1.4 Origines & sources

Comme indiqué précédemment, les particules d'aérosols atmosphériques proviennent d'une grande variété de sources naturelles et anthropiques.

Parmi **les sources naturelles** des aérosols, on trouve les sels marins et les poussières minérales avec des contributions de 10,2 et 18,8 % des PM_{10} au nord de l'Europe, respectivement (Hopke et al., 2020). On trouve aussi les poussières volcaniques et les particules biogéniques (dont les pollens). Ces particules primaires naturelles sont principalement dans la fraction grossière. Les sources naturelles secondaires typiques des aérosols sont la biosphère émettrice de COV précurseurs, et les volcans relarguant du soufre (DMS ou SO_2) qui s'oxyde en acide sulfurique puis en SO_4.

- **Aérosols marins :** Les particules de sel marin sont de fines particules d'eau salée éjectées par la friction du vent à la surface de l'océan. Elles sont principalement composées de Cl^-, Na^+, SO_4^{2-}, Mg^{2+} et Ca^{2+} ainsi que d'autres impuretés, et couvrent des tailles qui vont généralement de 100 nm à plusieurs dizaines de µm (Boucher, 2015). Elles peuvent être fraîches - elles contiennent dans ce cas une concentration significative de chlorure (Cl) - ou vieillies pendant le transport où Cl est remplacé par SO_4 et NO_3 dans des réactions acide-base, conduisant à un mélange de particules fraîches et âgées, où les particules âgées sont une combinaison d'émissions de sources naturelles et anthropiques (Hopke et al., 2020). À l'échelle mondiale, les sels marins sont le deuxième contributeur le plus significatif à la charge totale d'aérosols présents dans l'atmosphère, juste après les poussières minérales. Ils jouent un rôle clé dans le cycle global de l'eau et peuvent modérer le changement climatique. Des concentrations moyennes saisonnières de Na^+ allant jusqu'à 1 µg m^{-3} dans les PM_{10} sont observées le long de toutes les côtes du territoire métropolitain français, tandis que les concentrations les plus faibles sont relevées dans la partie orientale de la France et dans les vallées alpines. Un cycle saisonnier bien défini, marqué par des pics hivernaux liés aux vents dominants et aux tempêtes plus fréquentes, est observable sur tous les sites situés dans le nord de la France, tandis qu'un modèle inverse tend à se manifester dans les régions méridionales (Favez et al., 2021).

- **Poussières minérales :** Les aérosols de poussière minérale sont très majoritairement des particules naturelles désertiques mises en suspension dans l'atmosphère par la friction du vent ; ainsi que des particules de poussière en (re)suspension provenant de la circulation. Ces dernières contiennent généralement des métaux supplémentaires provenant de l'usure des freins (par exemple, Cu, Sb, Si, Fe) et des pneus (Zn), et des émissions de gaz d'échappement issues de la combustion de l'huile de lubrification (Ca, Ba, Zn). Comme pour les aérosols marins, les particules de poussière désertique ont des tailles qui varient généralement de 100 nm à des dizaines de μm. Les particules les plus grosses peuvent également être soulevées, mais elles retombent rapidement. Les émissions de poussière désertique sont de nature sporadique et dépendent beaucoup des conditions environnementales et météorologiques (Boucher, 2015). Les poussières sahariennes influencent le territoire métropolitain français (partie sud-est), ainsi que les Antilles françaises qui sont touchées régulièrement par des épisodes de poussière saharienne provenant d'Afrique de l'Ouest ou d'Afrique du Nord entre mars et octobre et qui sont transportées par les alizés à travers l'Océan Atlantique (Favez et al., 2021).
- **Aérosols volcaniques :** Les cendres volcaniques consistent en des fragments de roches et de minéraux pulvérisés provenant des volcans lors d'éruptions explosives. Ces particules ont une taille qui varie généralement entre 1 μm et 1 mm. Elles peuvent être transportées sur de longues distances de quelques centaines à quelques milliers de kilomètres mais étant des particules microniques, elles ont tendance à retomber rapidement. Par conséquent, leur effet sur le climat est limité sauf lorsque l'altitude d'émission leur permet d'atteindre la stratosphère. Les volcans émettent également des gaz riches en soufre (sous forme de SO_2 et de sulfure d'hydrogène ; H_2S) qui s'oxydent dans l'atmosphère pour former des aérosols de SO_4 submicroniques. Si ces gaz contenant du soufre sont émis dans la troposphère, le temps de séjour de ces aérosols sera court (quelques semaines). Cependant, si l'éruption est assez puissante pour injecter les gaz et les particules dans la stratosphère, les aérosols auront un temps de séjour beaucoup plus long (de l'ordre de quelques mois à plus d'un an), selon la région et l'altitude d'injection (Boucher, 2015).
- **Aérosols biogéniques :** Les aérosols biogéniques peuvent être composés de débris de plantes et d'insectes, des pollens (une fine poudre produite par les plantes à graines qui

contiennent les gamètes mâles servant à la reproduction), des spores (cellule ou organe de reproduction de nombreuses plantes et champignons), des bactéries et des virus. Leur source primaire est la biosphère terrestre. Une fois en suspension dans l'air, ces particules peuvent être transportées par le vent sur des distances variables en fonction de leur taille. Les débris sont généralement supérieurs à 100 μm, le pollen, les spores et les bactéries sont généralement de l'ordre de 1 à 100 μm, tandis que les petites bactéries et les virus sont généralement inférieurs à 1 μm. Les écosystèmes terrestres et marins jouent également un rôle important en tant que sources de précurseurs d'aérosols. Certaines espèces de phytoplancton émettent du diméthylsulfure (DMS), un gaz qui subit une oxydation dans l'atmosphère pour former des aérosols contenant du soufre. Les plantes et les algues émettent des COV qui sont oxydés dans l'atmosphère et peuvent former des aérosols organiques. Ces aérosols sont appelés aérosols secondaires biogéniques. Leurs tailles sont généralement de l'ordre de quelques dixièmes de μm (Boucher, 2015).

Les sources anthropiques sont largement dominées par les émissions provenant de la combustion de combustibles fossiles (c'est-à-dire le charbon, le gaz et le pétrole), de biocarburants (biomasse végétale, y compris le bois, les huiles végétales, les déchets animaux), d'autres combustibles (par exemple la tourbe) ou de feux de végétation causés en majorité par l'homme. Les activités industrielles, le transport, le chauffage, ou même les activités domestiques liées à la cuisine dans les pays en développement, sont également des sources importantes d'aérosols. Certains pays industriels et agricoles peuvent également émettre des aérosols primaires, appelés poussière industrielle, en quantité significative.

- **Aérosols issus de la combustion de biomasse :** La biomasse correspond à toute matière biologique (organique) provenant du monde vivant et qui peut potentiellement brûler (par exemple la végétation, le bois, les excréments d'animaux, la tourbe) tout en excluant les combustibles fossiles. La combustion de la biomasse produit des aérosols primaires provenant d'une combustion incomplète de la matière organique. Ces aérosols sont généralement submicroniques et composés de carbone organique, qui est associé aux atomes d'hydrogène et d'oxygène, et du BC, dont la teneur en carbone est très élevée (Boucher, 2015). Les sources de ces aérosols sont alors multiples, à la fois naturelles et anthropiques, y compris le brûlage agricole et le chauffage/cuisson résidentiels à l'aide de

bois ou d'autres types de biomasse (résidus de cultures, fumier, etc.). Ces sources sont généralement caractérisées par la présence de concentrations élevées en potassium (K) et parfois complétée par du lévoglucosane (issu de la pyrolyse de la cellulose) ou d'autres marqueurs moléculaires (Hopke et al., 2020). La combustion du bois est considérée comme une source majeure de pollution hivernale dans certaines des plus grandes villes françaises depuis plus de dix ans (Favez et al., 2009). Pourtant, elle reste un sujet délicat politiquement, notamment en raison d'intérêts divergents dans les stratégies politiques visant à promouvoir l'utilisation des énergies renouvelables et limiter les émissions de CO_2 fossile. La Figure I.4 résume certains résultats obtenus dans le cadre du projet SOURCES mené par Weber et al., (2019), qui visait à étudier de manière harmonisée un ensemble de données de composition chimique de PM_{10} collectées en milieu urbain pour en déterminer les sources. La combustion de biomasse se révèle être la principale source d'AO influençant la qualité générale de l'air urbain en France, avec des concentrations annuelles moyennes d'environ 2,5 ± 1,2 μg m^{-3} (représentant environ 30 ± 10 % de la masse totale de MO).

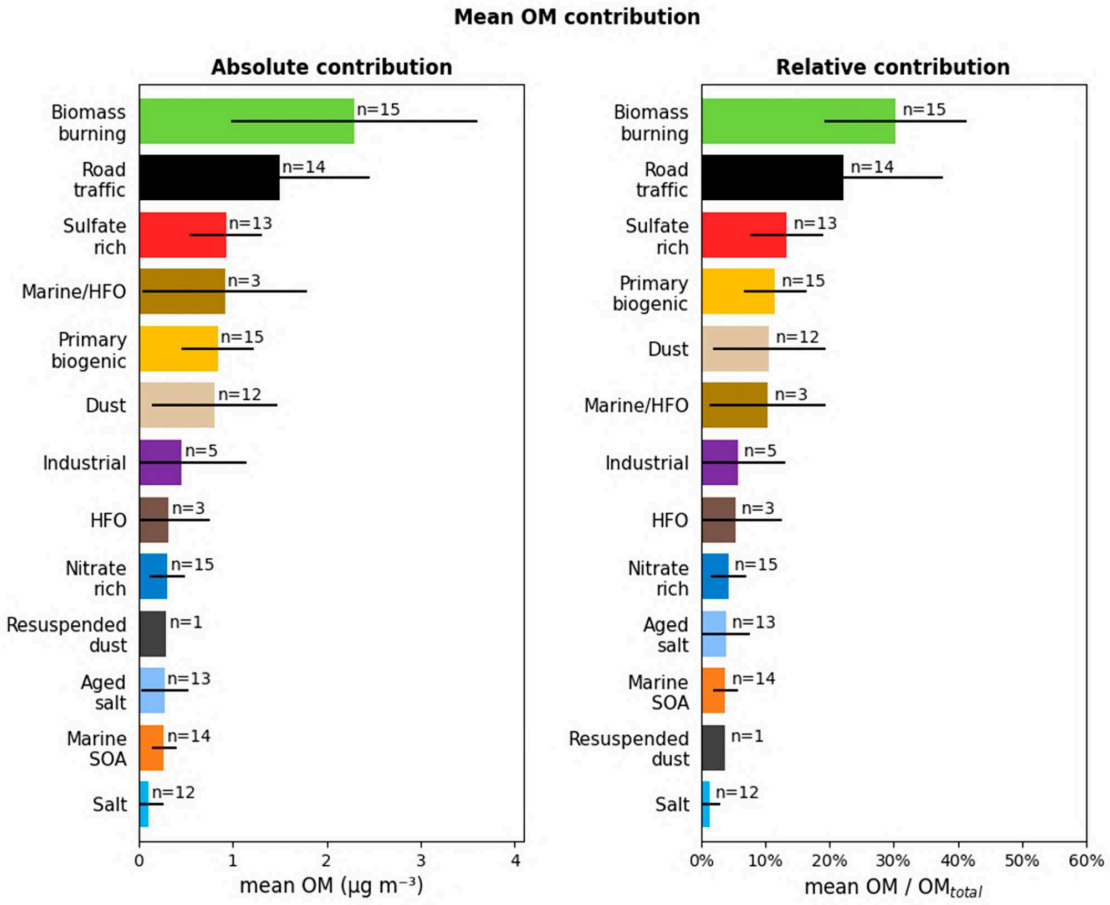

Figure I.4: Contributions des différentes sources par rapport à la masse totale de MO dans le milieu urbain en France : à gauche les concentrations moyennes et à droite les contributions relatives moyennes (n représente le nombre de sites) (source : Favez et al., 2021, adapté de Weber et al., 2019)

Selon Weber et al., (2019), la variabilité plus élevée du facteur de combustion de la biomasse d'un site urbain à l'autre peut s'expliquer, en plus des contributions homogènes du lévoglucosane (et du OC), par d'autres espèces (telles que le EC, le K, le Cl et le NO_3) en quantités variables en raison notamment du type de bois utilisé et/ou des conditions de la combustion. En outre, les émissions de la combustion de biomasse dans l'air ambiant peuvent favoriser des mécanismes nocturnes conduisant à la condensation du nitrate d'ammonium en phase particulaire (Rodelas et al., 2019), l'accumulation d'aérosols organiques secondaires (AOS) dans les aérosols humides (Gilardoni et al., 2016), et la

formation d'organo-nitrates (ou de composés organiques nitrés) et/ou d'organo-sulfates (Petit et al., 2019). Ces processus sont susceptibles de renforcer l'impact des émissions du chauffage au bois sur la qualité de l'air urbain en hiver, à des niveaux de complexité et d'étendue nécessitant une compréhension et une quantification plus approfondies. Étant donné que certains des composés secondaires formés par ces processus absorbent la lumière à des longueurs d'onde proches de l'ultraviolet (Gilardoni et al., 2016), ils sont partiellement détectés et comptabilisés avec les aérosols primaires de combustion de biomasse lorsqu'on utilise le modèle de déconvolution de l'Aéthalomètre en deux sources liées au chauffage au bois et à la combustion de combustibles fossiles (Favez et al., 2010). En ce qui concerne les mesures ACSM, la diversité des espèces émises ainsi que les processus secondaires impliqués complique la tâche d'attribuer ces éléments à un seul facteur (BBOA : *Biomass Burning Organic Aerosol* ; aérosols organiques issus de la combustion de biomasse), dérivé de l'analyse PMF classique appliquée aux spectres de masse organique (Favez et al., 2021).

- **Aérosols issus de la combustion de combustibles fossiles :** Ce sont des particules submicroniques issues de la combustion du charbon et des dérivés du pétrole qui produisent du BC et du OC, ainsi que du SO_2 qui se transforme en SO_4. Ils représentent une source importante de pollution atmosphérique dans les pays en développement et industrialisés (Boucher, 2015). La combustion de charbon peut se produire à haute température dans les centrales électriques au charbon, ou relever d'autres activités industrielles ou consister en du charbon pulvérisé injecté dans une chaudière. Beaucoup de ces sources sont équipées de dispositifs de contrôle des particules, de sorte que les principales émissions sont le SO_2 et les NO_x, même si des efforts importants ont également été réalisés pour ajouter ou améliorer les dispositifs de contrôle des polluants gazeux dans les centrales électriques au charbon. Dans de nombreuses villes, les centrales de chauffage urbain locales brûlent du charbon pulvérisé à haute température, mais sans contrôle, ce qui entraîne des émissions de particules et de polluants gazeux, mais peu ou pas de SO_4 primaire. Le profil de ce type de combustion dépend fortement de la nature et de la qualité du charbon. Enfin, il existe une combustion résidentielle du charbon pour le chauffage/la cuisson, dans laquelle sont brûlés du charbon de houille ou des briquettes, conduisant à l'émission de grandes quantités de sulfate primaire et d'OC primaire oxydé

pendant les phases de démarrage et d'extinction du cycle de combustion. Ainsi, la compréhension de la nature des sources locales est importante pour l'identification correcte des profils de sources dérivés par des méthodes d'analyse factorielle comme la PMF (Hopke et al., 2020).

Globalement, le transport routier constitue le deuxième contributeur aux charges de la MO affectant la qualité de l'air dans les milieux urbains français. On estime que les AO associés au transport routier proviennent des émissions du pot d'échappement, mais aussi d'émissions non liées aux gaz d'échappement (Favez et al., 2021). Dans la pratique, la discrimination entre les particules des gaz d'échappement des véhicules et les autres particules semble difficilement possible lorsqu'on applique l'approche classique de la PMF aux données de spéciation chimique obtenues dans des conditions urbaines. De même, les émissions d'échappement de l'essence et du diesel sont à peine séparées par les modèles récepteurs sur les sites de fond. La combinaison de ces diverses sources d'émissions en un seul facteur PMF aboutit à des profils chimiques de trafic primaire relativement disparates d'un site à un autre (Weber et al., 2019). Une étude de répartition des sources des AO a été faite à São Paulo par Brito et al., (2018) en utilisant l'éthanol comme traceur pour caractériser le facteur trafic. Quatre facteurs ont pu être obtenus à partir de cette analyse PMF. La Figure I.5 présente les contributions relatives de chacun de ces quatre facteurs HDV, LDV et OOA (la somme de OOA-I et OOA-II). Le premier, "HDV", présente les émissions primaires de véhicules lourds, tandis que le second, "LDV", correspond aux émissions primaires pour les véhicules légers. En utilisant ces facteurs comme prédicteurs dans une analyse de régression linéaire multiple d'un large éventail de polluants, ils ont quantifié le rôle des émissions primaires des HDV ou des LDV, ainsi que des processus secondaires atmosphériques, sur la dégradation de la qualité de l'air. Les résultats montrent une contribution significative des émissions des LDV, bien qu'elles ne représentent qu'environ 5 % du nombre de véhicules dans la zone. Ces derniers sont responsables de 40 % et 47 % de la concentration atmosphérique de benzène et de BC, respectivement. Ce travail décrit une utilisation innovante du biocarburant comme traceur des émissions des véhicules de tourisme, permettant de mieux séparer les facteurs "trafic" et de comprendre le rôle des sources véhiculaires sur la dégradation de la qualité de l'air.

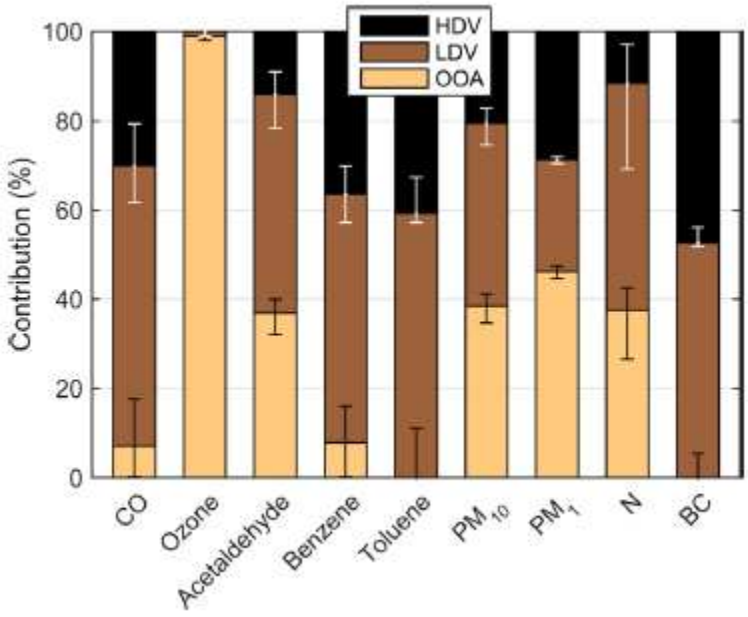

Figure I.5: Contribution relative des sources primaires (LDV: *Light-Duty Vehicles*, HDV: *Heavy-Duty Vehicles*) et secondaires (OOA : somme de OOA-I et de OOA-II) (source : Brito et al., 2018).

En France, les niveaux d'émissions de $PM_{2,5}$ ont enregistré une tendance à la baisse globale, selon le dernier rapport du Centre interprofessionnel technique d'études de la pollution atmosphérique, publié récemment (CITEPA, 2023). Ces émissions sont générées par l'ensemble des secteurs (Figure I.6). En 2021, le principal secteur responsable des émissions de $PM_{2.5}$ est le domaine « usage et activités des bâtiments », avec une contribution de 73 %, dont la principale source est la combustion de biomasse, principalement domestique, ainsi que dans une moindre mesure l'utilisation de fioul. Il est suivi par les activités d'industrie manufacturière et de construction (11 %), avec des sources majeures telles que les chantiers de construction/BTP, la sidérurgie et l'extraction de carrières. Le domaine des transports représente 9 % des émissions de $PM_{2.5}$, principalement engendrées par les gaz d'échappement des carburants brûlés, notamment le diesel et l'essence, ainsi que par l'usure des routes, des pneus et des freins. L'agriculture a une contribution de 6 %.

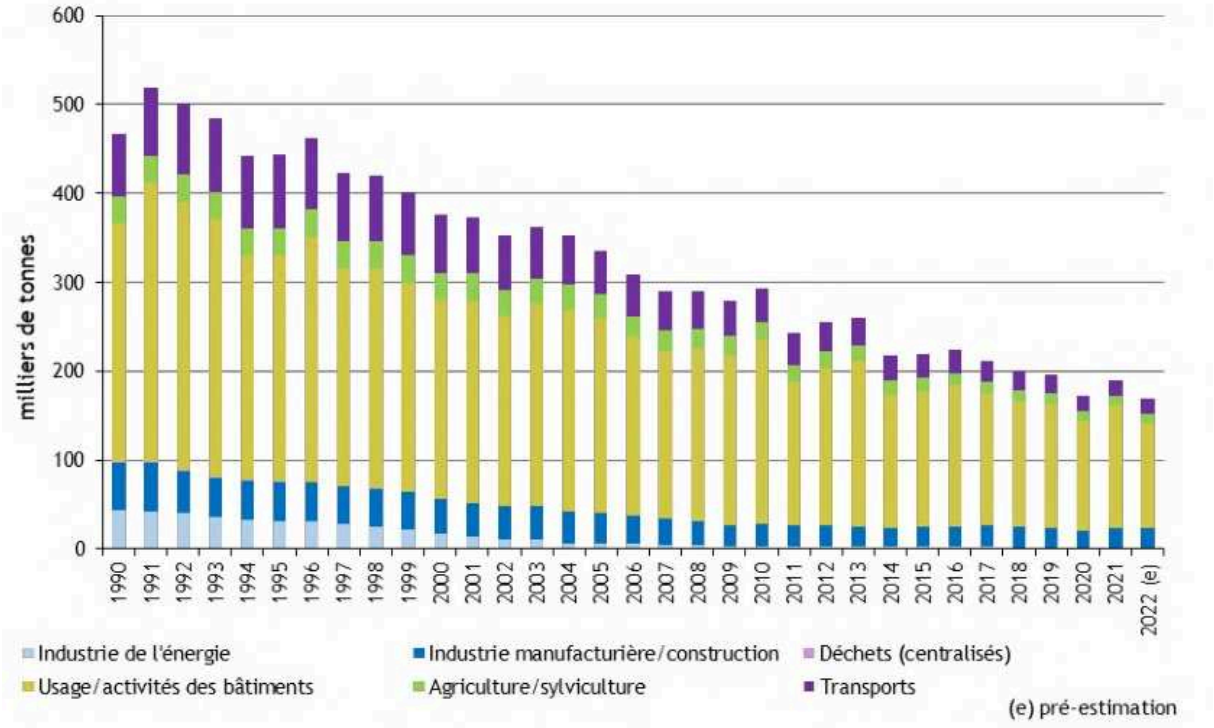

Figure I.6 : Évolution des émissions des $PM_{2.5}$ en France métropolitaine entre 1990 et 2022 (Source : CITEPA, 2023).

I.2 Distribution temporelle et géographique des particules fines et risques sanitaires associés

La concentration, la composition et la distribution en taille des particules d'aérosols atmosphériques sont très variables dans le temps et l'espace.

En termes de concentration, Southerland et al., (2022) ont calculé les tendances relatives aux concentrations de $PM_{2,5}$ ainsi que les décès associés dans différentes villes à travers le monde. L'étude a révélé que pendant la période 2000-2019, la grande majorité de la population urbaine mondiale (environ 85 %) résidait dans des régions où les niveaux de $PM_{2,5}$ dépassaient les seuils considérés comme sains par l'OMS et établis en 2005 (10 µg m^{-3} en moyenne annuelle), à la fois en 2000 (2 milliards d'habitants) et en 2019 (2,5 milliards d'habitants). Seulement 16 % de l'ensemble des régions urbaines mondiales avaient réussi à respecter cette recommandation entre

2000 et 2019. Ces 2054 zones étaient localisées dans les Amériques (988 zones, soit 48 %), en Afrique (347 zones, soit 17 %) et en Europe (269 zones, soit 13 %).

Cette situation contribue de manière significative à la prévalence des maladies non transmissibles. Elle a engendré un excédent de décès estimé entre 1 et 8 millions en 2019. Les concentrations en $PM_{2,5}$ dépassaient encore de plus de sept fois les directives établies par l'OMS en 2021 pour les moyennes annuelles de $PM_{2,5}$ (5 μg m^{-3} en moyenne annuelle) et étaient plus de trois fois supérieures au niveau de la directive de 2005, qui est désormais l'objectif intermédiaire (10 μg m^{-3}). Même si les concentrations moyennes annuelles mondiales de $PM_{2,5}$ dans les zones urbaines sont restées relativement stables au fil du temps, les tendances entre 2000 et 2019 présentent d'importantes variations d'une région à l'autre (Figure I.7B).

Le taux de mortalité urbaine moyen mondial imputable aux $PM_{2,5}$ était de 61 décès pour 100 000 habitants en 2019, avec un intervalle de confiance à 95 % de 45 à 77. En 2019, les moyennes régionales divergeaient de la moyenne urbaine mondiale. Les taux de mortalité attribuables aux $PM_{2,5}$ étaient inférieurs à la moyenne mondiale en Amérique (18, intervalle de confiance à 95 % : 10-28) ainsi qu'en Afrique (31, intervalle de confiance à 95 % : 22-40). En revanche, les moyennes urbaines dans le Pacifique occidental (86, intervalle de confiance à 95 % : 66-107) et en Asie du sud-est (84, intervalle de confiance à 95 % : 66-101) étaient supérieures (Figure I.7C). En outre, les moyennes urbaines en Europe (50, intervalle de confiance à 95 % : 32-70) et en Méditerranée orientale (50, intervalle de confiance à 95 % : 37-63) étaient proches de la moyenne urbaine mondiale. Parmi toutes les régions du monde, ce sont les villes d'Asie du sud-est (incluant l'Inde) qui ont enregistré la plus forte augmentation des taux de mortalité attribuables aux $PM_{2,5}$ au cours de cette période (33 % ; passant de 63 à 84 pour 100 000 habitants), suivies par les villes du Pacifique occidental avec une hausse de 14 % (passant de 76 à 86). En revanche, les villes d'Afrique ont connu la plus forte diminution de ces taux (-40 % ; passant de 51 à 31), suivies par les villes d'Europe (-33 % ; passant de 74 à 50) et les villes des Amériques (-29 % ; passant de 25 à 18).

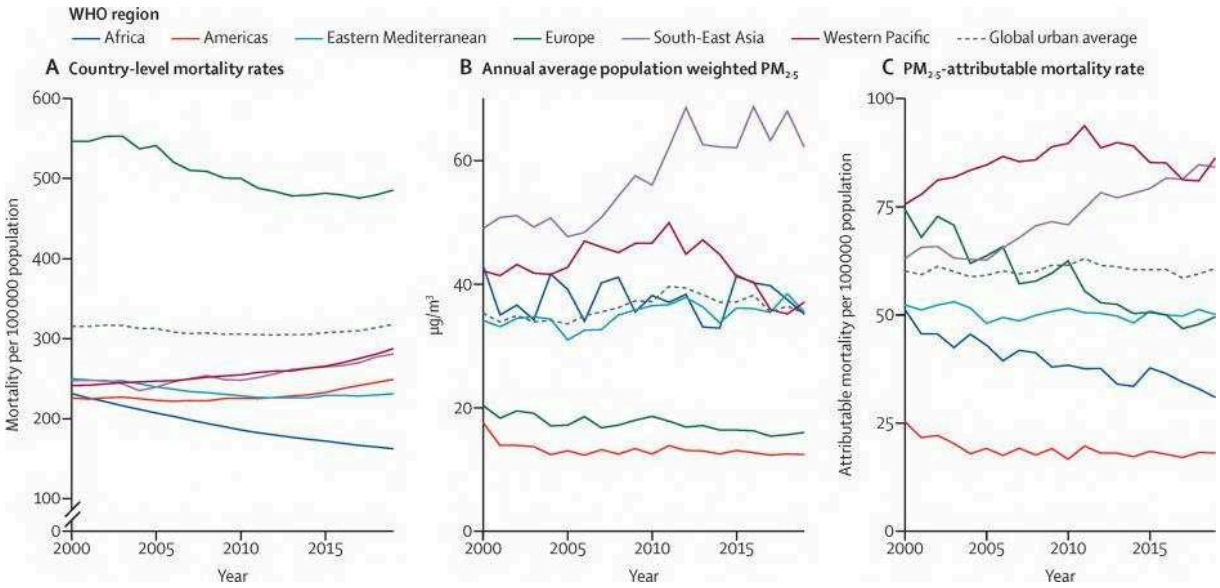

Figure I.7 : Évolutions des taux de décès en milieu urbain et des niveaux de $PM_{2,5}$ à l'échelle mondiale, de 2000 à 2019. (A) Taux de mortalité de base au niveau national. (B) Moyennes régionales des concentrations annuelles moyennes de $PM_{2,5}$ au sein des zones urbaines, ajustées en fonction de la population. (C) Moyennes régionales des taux de mortalité en milieu urbain attribuables aux $PM_{2,5}$ (source : Southerland et al., 2022).

Pour résumer, les concentrations pondérées de $PM_{2,5}$ en fonction de la population ainsi que les taux de mortalité attribuables à ces particules sont restés relativement stables entre 2000 et 2019 dans toutes les zones urbaines à travers le monde, bien que les tendances globales masquent d'importantes variations régionales. Les résultats mettent en évidence la nécessité d'adopter des stratégies visant à réduire l'impact considérable des $PM_{2,5}$ sur la santé publique en milieu urbain. Ces stratégies devraient impliquer des efforts pour réduire l'exposition en limitant les émissions, ainsi que des initiatives visant à renforcer la résistance aux effets des $PM_{2,5}$ en améliorant la santé globale de la population.

Une étude réalisée par Lim et al., (2020) a identifié les zones à risque à l'échelle globale en termes de concentrations de $PM_{2,5}$ entre 1998 et 2016 : l'Inde et la Chine, où l'augmentation de la population est fortement corrélée aux niveaux de $PM_{2,5}$, sont prédominantes, avec des zones affichant des concentrations élevées dépassant les 35 µg m^{-3}, ainsi que des concentrations exceptionnellement élevées excédant les 50 µg m^{-3} en moyenne sur la période étudiée. De plus,

des valeurs dépassant les 15 µg m^{-3} ont été relevées dans certaines régions de l'Europe de l'Est, de l'Afrique centrale et dans plusieurs pays asiatiques (Figure I.8a).

L'analyse de la tendance des $PM_{2,5}$ au cours des vingt dernières années a permis de distinguer les zones où la concentration a augmenté ou diminué. Les valeurs supérieures à 0,5 (ce qui équivaut à une augmentation de plus de 50 %) étaient particulièrement prédominantes en Inde et dans les régions avoisinantes, indiquant une hausse marquée même au niveau moyen de la concentration. Dans le nord-est de la Chine, une augmentation notable des concentrations de $PM_{2,5}$ a été observée, avec des zones sporadiques d'augmentation extrême repérées dans certaines parties de l'Afrique, de l'Amérique du Sud et de l'Asie. En contraste, de nombreuses régions aux États-Unis et en Europe occidentale ont enregistré une diminution substantielle, voire marquée, des concentrations de $PM_{2,5}$ sur la période étudiée. De manière générale, ils ont constaté une tendance à la hausse des concentrations de $PM_{2,5}$ dans la plupart des pays en développement, incluant l'Asie, l'Amérique du Sud et l'Afrique subsaharienne, tandis que des diminutions ont été observées dans les régions plus développées ou moins accessibles (comme la Sibérie et l'Amazonie ; Figure I.8b).

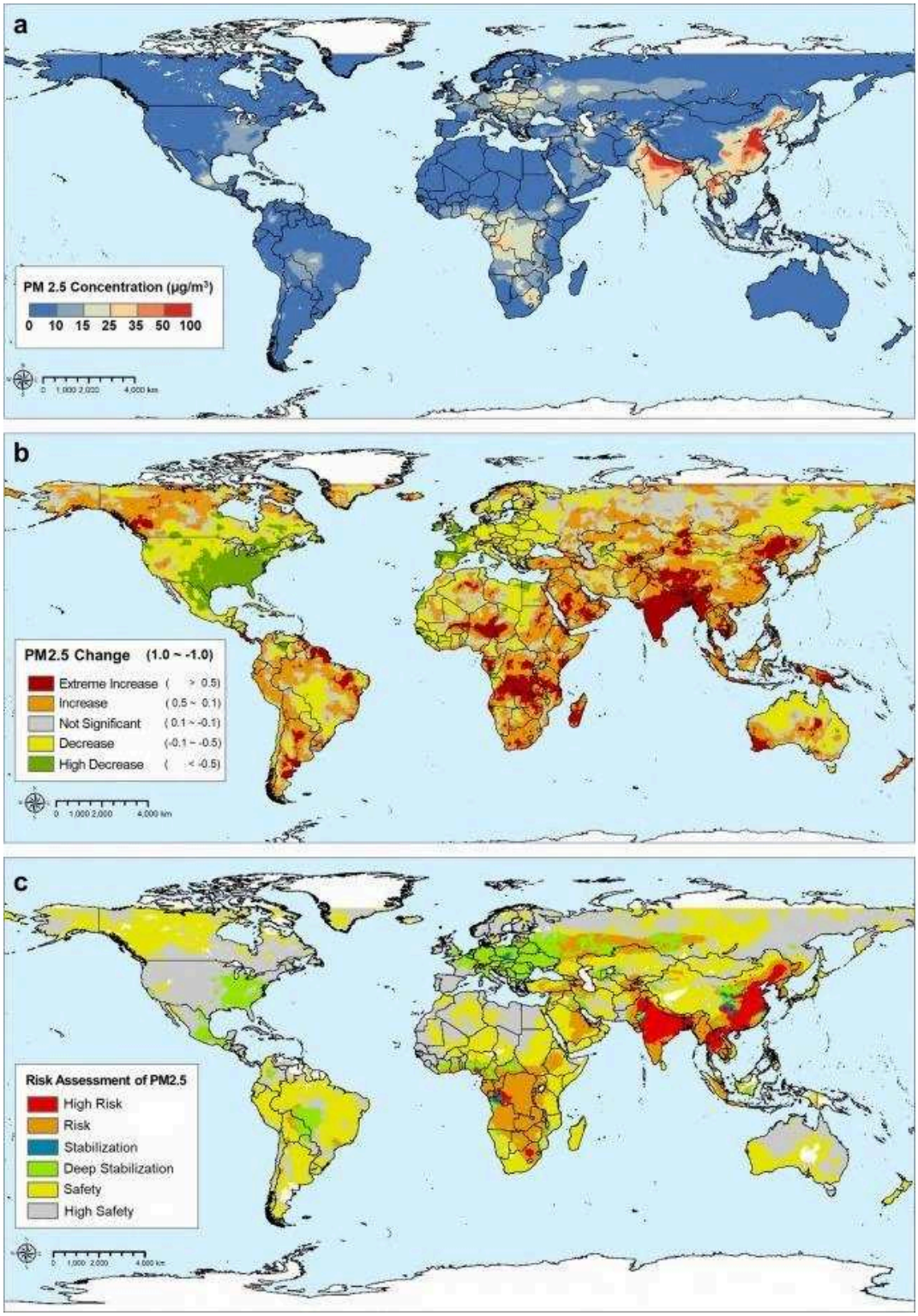

Figure I.8 : Étude spatio-temporelle comprenant (a) les moyennes annuelles des concentrations de $PM_{2,5}$ de 1998 à 2016, (b) l'analyse des tendances des $PM_{2,5}$, et (c) l'évaluation des risques liés aux concentrations et aux évolutions des $PM_{2,5}$ au cours des vingt dernières années.

En Europe, selon l'Agence Environnementale Européenne (EEA, 2023), les niveaux de $PM_{2,5}$ les plus élevés sont constatés dans le nord de l'Italie (vallée du Pô) et dans certaines régions d'Europe de l'Est (Figures I.9 et I.10). Cette situation découle de l'usage de combustibles solides et d'un parc automobile plus ancien dans les pays d'Europe centrale et orientale. Dans le nord de l'Italie, ces concentrations élevées résultent d'une combinaison de facteurs, notamment une forte densité d'émissions humaines, des conditions météorologiques et géographiques favorisant l'accumulation de polluants dans l'air, et la formation de particules secondaires.

En 2021, huit pays déclarants, dont quatre États membres de l'UE, ont enregistré des concentrations dépassant la limite annuelle de 25 $\mu g\ m^{-3}$ fixée par l'UE, tandis que les 37 pays déclarants ont observé des concentrations supérieures à la valeur guide annuelle de 5 $\mu g\ m^{-3}$ établie par l'OMS, et tous les pays déclarants ont enregistré des concentrations excédant la valeur guide journalière de 15 $\mu g\ m^{-3}$ établie par l'OMS. Des niveaux de $PM_{2,5}$ dépassant la limite annuelle fixée par l'UE ont été relevés dans 2 % des stations de surveillance, dont 72 % étaient situées en milieu urbain et 23 % en milieu péri-urbain.

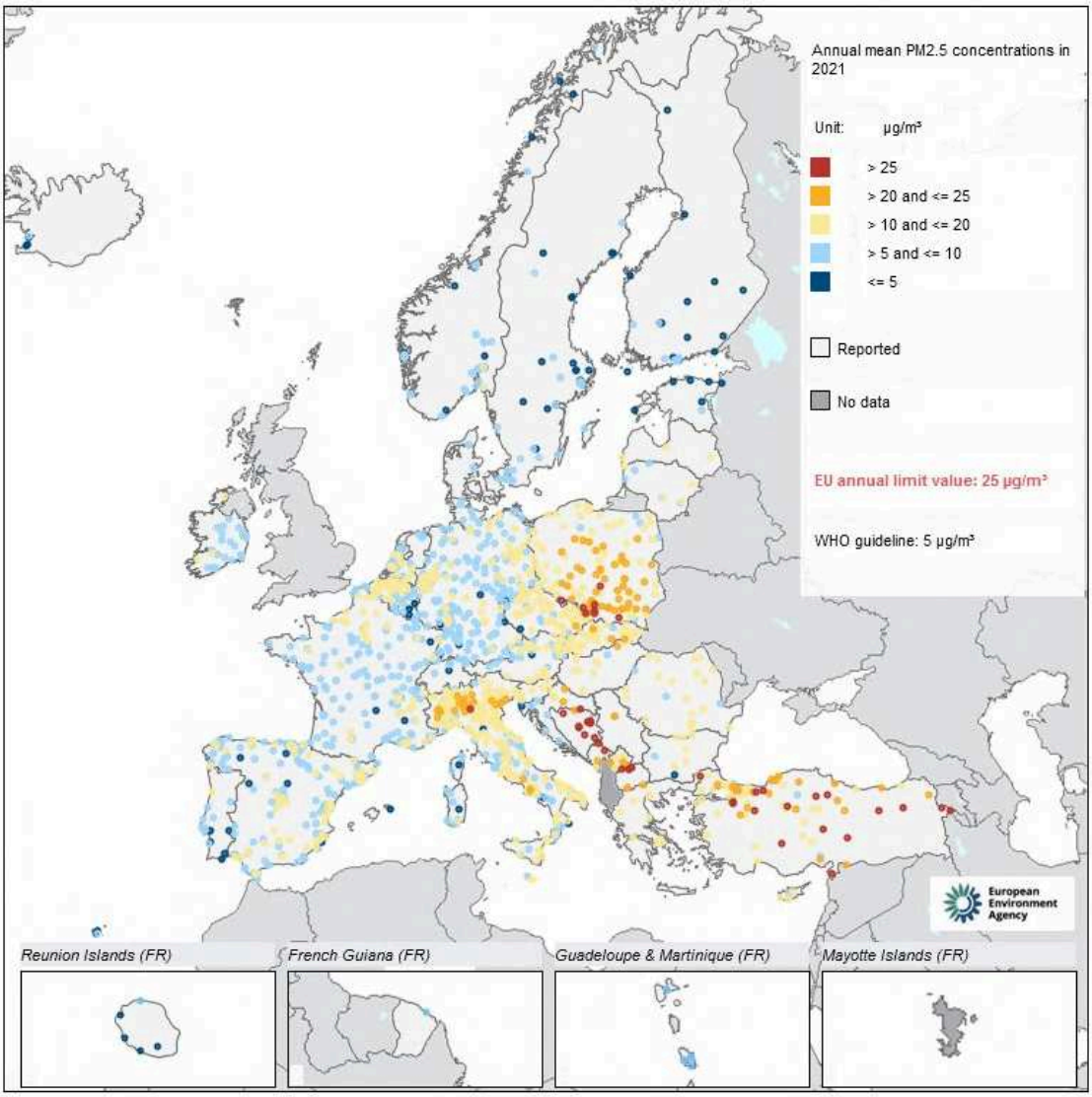

Figure I.9 : Moyennes annuelles des concentrations en $PM_{2,5}$ pour plusieurs sites de l'Union Européenne en 2021. Les points en rouge dépassent la limite annuelle de l'UE fixée à 25 µg m^{-3} ; seuls les points en bleu foncé respectent les recommandations de l'OMS (5 µg m^{-3}).

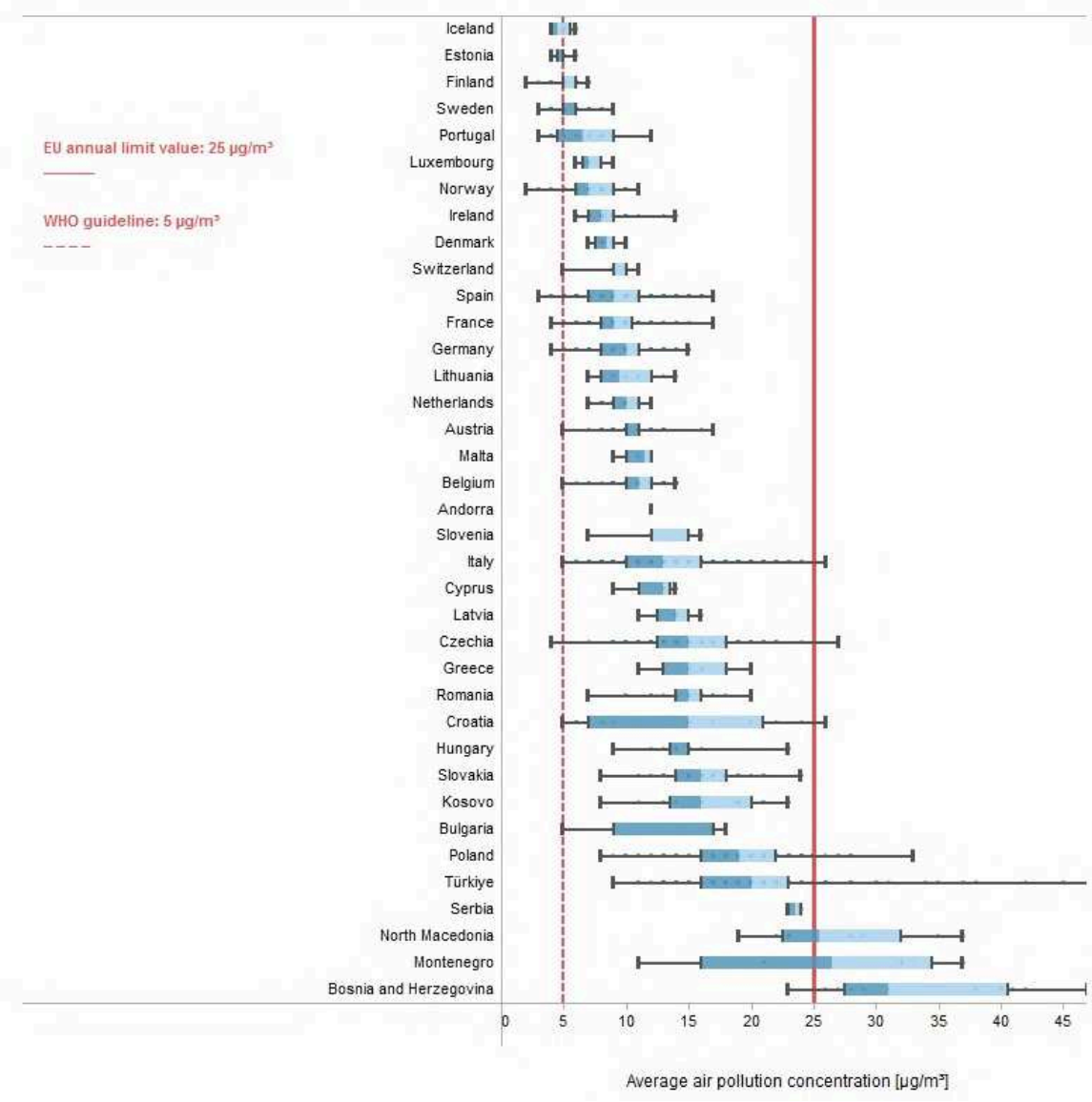

Figure I.10 : Comparaison des concentrations de $PM_{2,5}$ en 2021 par pays avec la limite annuelle de l'UE (trait plein rouge) et le niveau de référence annuel de l'OMS (trait en pointillés rouge). Pour chaque pays, les concentrations sont rapportées par chaque station, ainsi que les valeurs minimales et maximales, la médiane et les percentiles 25 et 75 de l'ensemble des mesures.

Selon un rapport récent (EMEP, 2023), les concentrations en particules fines présentent une variation géographique du nord au sud en Europe, avec des niveaux de PM_{10} inférieurs à 2-5 µg m^{-3} dans le Nord, atteignant 5-15 µg m^{-3} aux latitudes moyennes et dépassant 20 µg m^{-3} dans le Sud (Figure I.11). Cette tendance est également observée pour les $PM_{2,5}$, avec des concentrations légèrement inférieures aux PM_{10}. Les observations et les simulations du modèle EMEP

concordent quant à la répartition spatiale des particules. Les concentrations maximales annuelles de PM_{10} et de $PM_{2,5}$ se situent respectivement à Melpitz et à Agia Marina, avec des valeurs élevées également enregistrées dans d'autres sites. Le modèle EMEP simule des concentrations de PM_{10} supérieures à 20 µg m^{-3} dans certaines zones d'Europe centrale. Les concentrations annuelles maximales de $PM_{2,5}$ sont observées à Ispra et d'autres sites, tandis que les simulations du modèle EMEP montrent des niveaux généralement inférieurs à 10 µg m^{-3} dans la plupart de l'Europe, à l'exception de quelques régions. La vallée du Pô se démarque avec des niveaux plus élevés de $PM_{2,5}$ dépassant 20 µg m^{-3}.

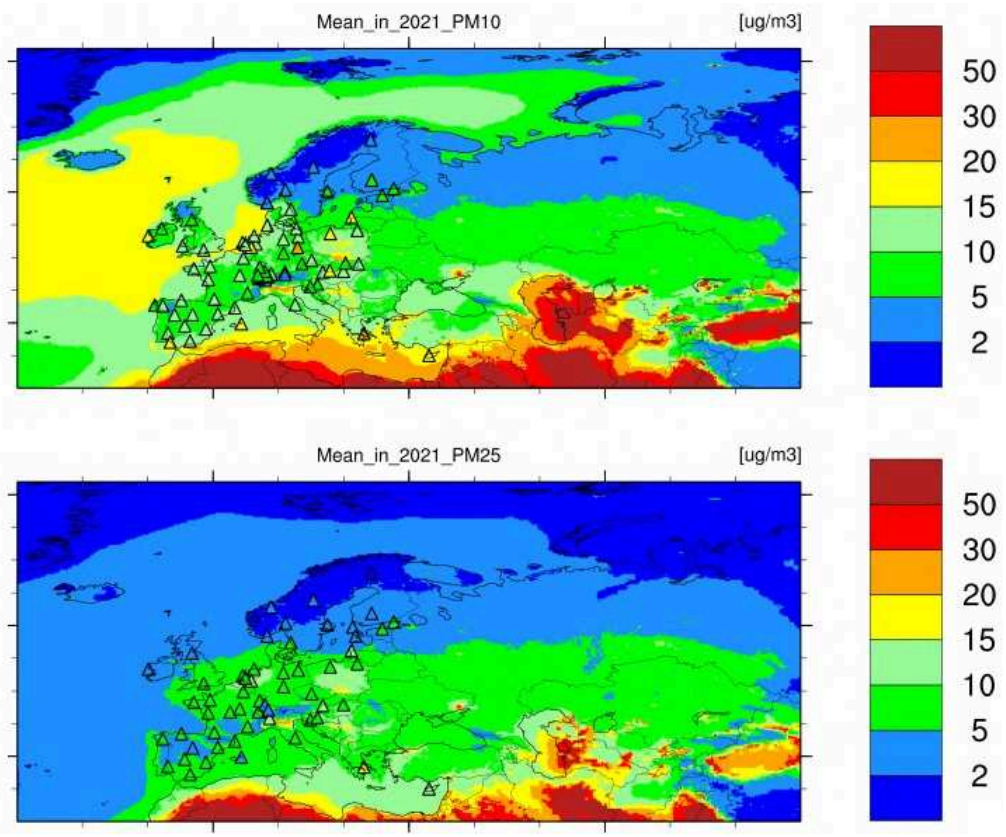

Figure I.11 : Moyennes annuelles simulées par le modèle EMEP MSC-W des concentrations de PM_{10} et $PM_{2.5}$ en 2021 (représentées par les contours colorés), comparées aux mesures observées sur les sites du réseau EMEP (triangles colorés).

En termes de distribution en taille, les aérosols du mode d'accumulation se situent de préférence près des sources industrielles et des zones où les pratiques agricoles et la déforestation entraînent d'importantes activités de combustion de la biomasse. Les aérosols grossiers proviennent

principalement de la production de sel marin par la houle dans les zones où la vitesse du vent près de la surface est élevée, ou des émissions de poussières minérales dans les régions désertiques arides, avec une variabilité spatio-temporelle élevée en raison, par exemple, des cycles saisonniers d'émissions ou de la variabilité météorologique (IPCC, 2021).

En termes de composition chimique, Putaud et al., (2010) ont synthétisé les données sur les caractéristiques physiques et chimiques des aérosols obtenues au cours de la dernière décennie dans plus de 60 sites à travers l'Europe, couvrant différents environnements tels que le fond naturel, rural, urbain et de proximité. Les données comprennent les concentrations en masse de PM_{10} et/ou $PM_{2.5}$ ainsi que celles en nombre de particules et leur composition chimique. Les principaux constituants des $PM_{2,5}$ et PM_{10} ont été analysés, avec des contributions variables de différents éléments tels que la poussière minérale, le sel marin, NH_4, les sulfates non-marins (nss-SO_4), l'EC, la matière organique. Les proportions de NO_3 dans les deux fractions ont été examinées, avec une variabilité en fonction des sites. La MO (OM = 1,4 × OC), est le principal composant des PM_{10} sur presque tous les sites où sa contribution a été mesurée. Cependant, les compositions chimiques des PM_{10}, $PM_{2,5}$ et PM grossier ($PM_{10-2,5}$) ont montré des différences régionales, avec davantage de matière carbonée dans les PM_{10} en Europe centrale, plus de NO_3 au nord-ouest de l'Europe et davantage de poussière minérale en Europe méridionale.

En ce qui concerne les $PM_{2.5}$, les comparaisons possibles entre les secteurs concernent principalement les sites urbains. Certaines conclusions établies pour les PM_{10} restent pertinentes, comme une contribution plus élevée des poussières minérales en Europe du Sud, une proportion de sel marin plus faible en Europe centrale et une proportion de matière carbonée plus faible en Europe du Nord-Ouest. Cependant, les rapports $SO_4^{2-}/PM_{2,5}$ et $NO_3^-/PM_{2,5}$ en Europe du Sud sont moins élevés que dans les autres secteurs. En ce qui concerne la composition chimique du PM grossier, l'élément distinctif du gradient géographique réside dans une contribution plus importante à la fois de SO_4^{2-} et de NO_3^- en Europe du Nord-Ouest par rapport à l'Europe méridionale et centrale.

I.3 Les impacts sanitaires et environnementaux des aérosols

Les aérosols ont de multiples répercussions, ayant des conséquences préjudiciables sur la santé humaine et les écosystèmes.

Impacts sur le climat : Les particules atmosphériques ont la capacité d'influencer le climat de manière directe ou indirecte (Figure I.12). Ces particules émises par différentes sources anthropogéniques et/ou naturelles sont en mesure d'absorber et de diffuser le rayonnement solaire entrant. Cela engendre une modification directe du bilan énergétique entre la Terre et l'atmosphère, ce qui a un impact final sur le changement climatique (Wang et al., 2018, Adam et al., 2021). En outre, les particules atmosphériques jouent un rôle en tant que noyaux de condensation (CCN) pour la formation de nuages, ce qui modifie les propriétés optiques et la durée de vie des nuages, influençant ainsi indirectement le climat (Wang et al., 2019). Dans la Figure I.13 sont exposés les coefficients de forçage associés à différentes espèces chimiques (IPCC-AR6-2021).

- **Effet direct :** aussi qualifié d'effet parasol, cet impact résulte des propriétés optiques des particules qui peuvent soit absorber soit diffuser le rayonnement solaire qu'elles reçoivent. Cet effet résultant de l'absorption et la diffusion de la lumière par les particules atmosphériques, notamment les particules fines, est la principale raison derrière la dégradation de la visibilité (Wu et al., 2018). En réalité, les composés organiques et inorganiques diffusent le rayonnement, ce qui engendre un forçage radiatif négatif (provoquant un refroidissement de la planète). D'autre part, le BC absorbe le rayonnement, induisant ainsi un forçage radiatif positif (conduisant à un réchauffement de la planète). Cet effet des aérosols influence la distribution verticale de la température, ce qui à son tour affecte la circulation atmosphérique.
- **Effet indirect :** il est démontré par la manière dont les aérosols agissent en tant que noyaux de condensation. Ces aérosols, de petite taille et hydrophiles, ne se déposent pas rapidement, ce qui leur permet de subsister suffisamment longtemps pour contribuer à la formation des nuages.

  En maintenant une quantité d'eau liquide constante, l'accroissement du nombre de noyaux de condensation entraîne une augmentation du nombre de gouttelettes (et par conséquent

de l'albédo associé aux nuages) et une diminution de leur taille, ce qui retarde leur précipitation et allonge la durée de vie des nuages.

Les AO s'oxydent au cours des processus de vieillissement, ce qui augmente les groupes fonctionnels hydrophiles à la surface des particules donc l'hygroscopicité et l'activité des noyaux de condensation des nuages (Slade et al., 2017). Pour les particules de sel marin, composante importante des particules atmosphériques dans les villes côtières, qui vieillissent rapidement dans l'environnement urbain, elles ont une influence importante sur l'hygroscopicité et la diffusion de la lumière (Adachi et Buseck, 2015). Les particules de sel marin augmentent principalement la quantité de CCN, ce qui accroît les précipitations. Pour les particules minérales, en raison de leur grande hétérogénéité, il est difficile d'estimer l'effet du forçage radiatif atmosphérique. Elles peuvent constituer une interface importante pour les réactions chimiques atmosphériques et jouent un rôle important dans les effets climatiques en raison de leur influence hygroscopique sur la circulation de l'eau dans l'atmosphère et le rayonnement des nuages.

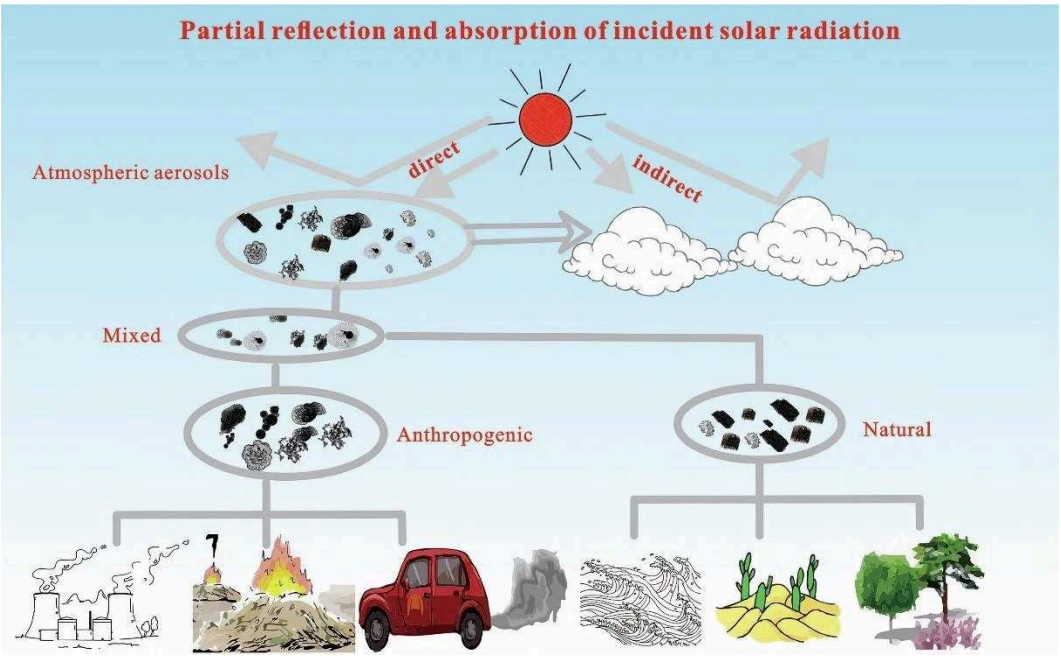

Figure I.12 : Schéma résumant les sources naturelles et anthropiques et les effets climatiques des aérosols (source: Shao et al., 2022).

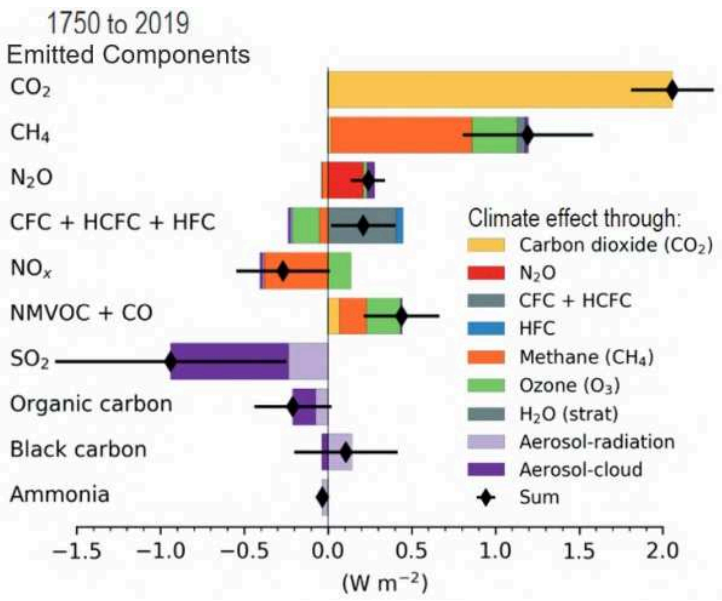

Figure I.13 : Forçage radiatif de différents composés atmosphériques gazeux et particulaires (source : IPCC, 2021).

Impacts sur la santé : Le degré de nocivité induit par les particules atmosphériques sur la santé humaine est essentiellement conditionné par la taille, le nombre et la composition de ces particules (Dockery et Pope, 1994). Plus elles sont petites, plus elles pénètrent profondément dans le système respiratoire (Figure I.14). La composition des particules constitue l'un des facteurs pathogènes majeurs et détermine la nature et le type des maladies. La concentration de particules ainsi que la durée d'exposition influent sur la quantité inhalée par l'organisme humain. À mesure que la concentration de particules s'accroît et que l'exposition se prolonge, les effets nuisibles sur le corps humain sont d'autant plus prononcés.

L'exposition à court terme à la pollution atmosphérique provoque des inflammations pulmonaires, tandis qu'une exposition à long terme accroît le risque de maladies pulmonaires chroniques et de maladies cardiovasculaires. Des études épidémiologiques et toxicologiques ont établi des liens entre une exposition chronique et à long terme aux particules présentes dans les environnements urbains, et de nombreux effets préjudiciables pour la santé ont été mis en évidence. Ces effets incluent des lésions dans les voies respiratoires ainsi que des troubles cardio-pulmonaires (Mukherjee et al., 2017). Les divers niveaux et types de ces effets nuisibles

sur la santé sont liés aux différentes propriétés physico-chimiques des particules urbaines (Molina et al., 2020).

Les recommandations concernant les niveaux de pollution de l'air ambiant établis par l'OMS servent de repères aux décideurs politiques pour établir des normes et des objectifs de gestion de la qualité de l'air. Elles ont été initialement proposés en 2005 et actualisées en 2021. Selon la plus récente, les concentrations moyennes annuelles de $PM_{2,5}$ ne devraient pas excéder 5 $\mu g\ m^{-3}$, et les expositions moyennes sur 24 heures ne devraient pas dépasser 15 $\mu g\ m^{-3}$ pendant plus de 3 à 4 jours par an. Selon l'OMS, la pollution atmosphérique est la principale menace environnementale pour le bien-être humain puisque 99 % de la population mondiale est exposée à des niveaux de pollution atmosphérique qui dépassent les niveaux recommandés pour les $PM_{2.5}$. Environ 4,2 millions de décès prématurés à l'échelle mondiale sont ainsi attribués à la pollution atmosphérique ambiante, et principalement associés à des affections telles que les maladies cardiaques, les accidents vasculaires cérébraux, les bronchopneumopathies chroniques obstructives, les cancers du poumon et les infections respiratoires aiguës (WHO, 2023). En France, on estime que près de 40 000 décès prématurés sont causés par l'exposition aux $PM_{2,5}$ (Medina et al., 2021), qui entraîne en moyenne une diminution d'environ 8 mois d'espérance de vie pour les individus âgés de 30 ans et plus (CITEPA, 2023).

Malgré la diminution des émissions, la majeure partie de la population urbaine de l'Union Européenne en 2021 se trouvait exposée à des niveaux de polluants atmosphériques clés nuisibles à la santé (Figure I.15). En particulier, 97 % de la population urbaine en Europe était exposée à des concentrations de particules fines supérieures aux niveaux recommandés par l'OMS. L'Europe centrale et orientale ainsi que l'Italie ont signalé les concentrations les plus élevées en particules, principalement en raison de la combustion de combustibles solides pour le chauffage domestique et de leur utilisation dans l'industrie (EEA, 2023).

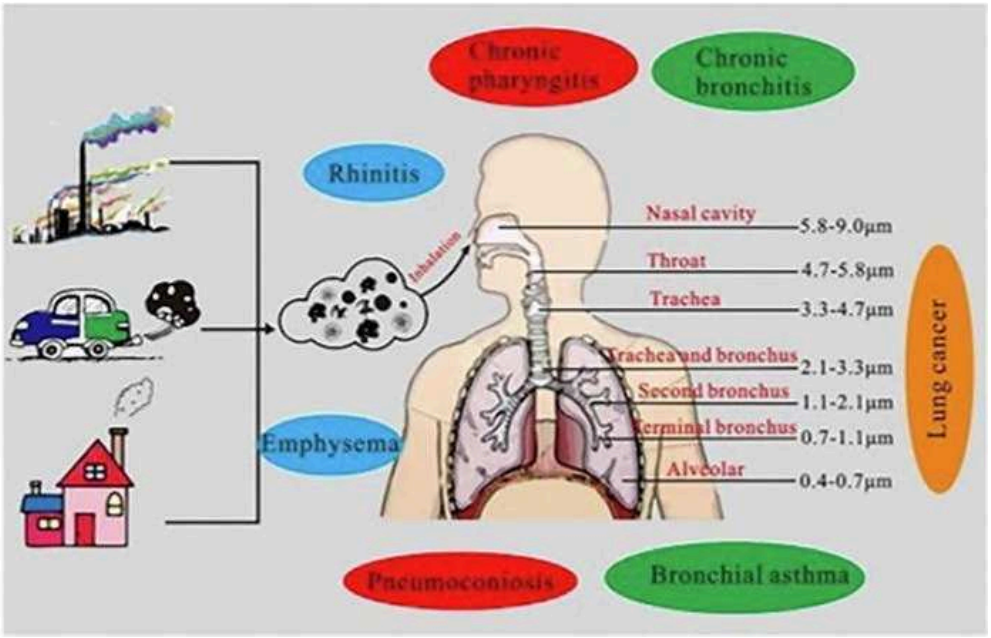

Figure I.14 : Illustration du système respiratoire et profondeur de pénétration des particules avec leurs effets sanitaires associés (source: Shao et al., 2022)

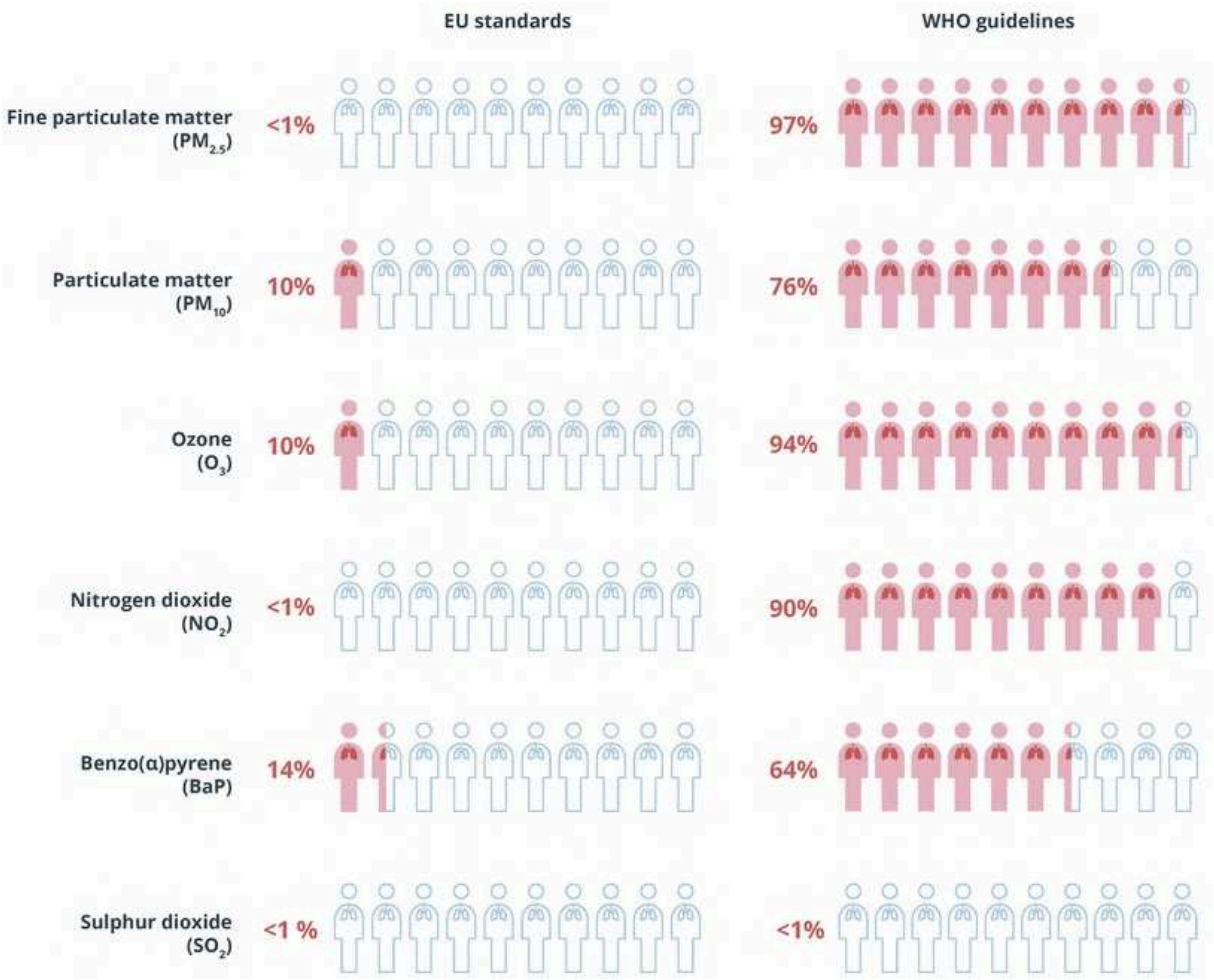

Figure I.15 : Proportion de la population urbaine de l'Union Européenne exposée à des niveaux de polluants atmosphériques dépassant les valeurs réglementaires de l'UE et les recommandations de l'OMS en 2021.

I.4 Etudes de la composition chimique et sources potentielles des particules fines en Europe et en France

La composition chimique des aérosols atmosphériques est liée à la variété de leurs sources. Dans cette section, quelques études récentes sur la composition chimique et les sources potentielles des particules fines en Europe et en France sont présentées.

En Europe

Bressi et al., (2021) ont étudié la composition chimique des aérosols submicroniques sur 21 différents sites avec différentes typologies (sites éloignés, côtiers, ruraux, industriels et urbains) à travers l'Europe pendant au moins une année de mesures. Toutes les mesures ont été collectées en temps réel avec une fréquence de 30 min à l'aide d'instruments basés sur la spectrométrie de masse, notamment l'*Aerosol Chemical Speciation Monitor* (ACSM) et l'*Aerosol Mass Spectrometer* (AMS), tout en respectant des protocoles de mesure standardisés. Les niveaux de concentrations des PM_1 non réfractaires (NR-PM_1 : AO, SO_4, NO_3, NH_4 et Cl) tendent à augmenter depuis les sites éloignés jusqu'aux sites urbains. Ces concentrations sont plus élevées dans les régions situées dans la bande des latitudes moyennes, par rapport à celles dans le Sud et le nord de l'Europe. En moyenne, l'AO constitue la composante prédominante (36-64 %) des NR-PM_1, suivies des SO_4 (12-44 %) et des NO_3 (6-35 %). En outre, la contribution des NO_3 est considérable dans les sites régionaux et urbains et présente de grandes variations saisonnières avec des minima en été. De plus, la contribution des NO_3 augmente avec la concentration massique des NR-PM_1 dans la plupart des sites. Elle devient dominante lorsque les niveaux des NR-PM_1 excèdent les 40 $\mu g\ m^{-3}$ sur la moitié des sites (Figure I.16).

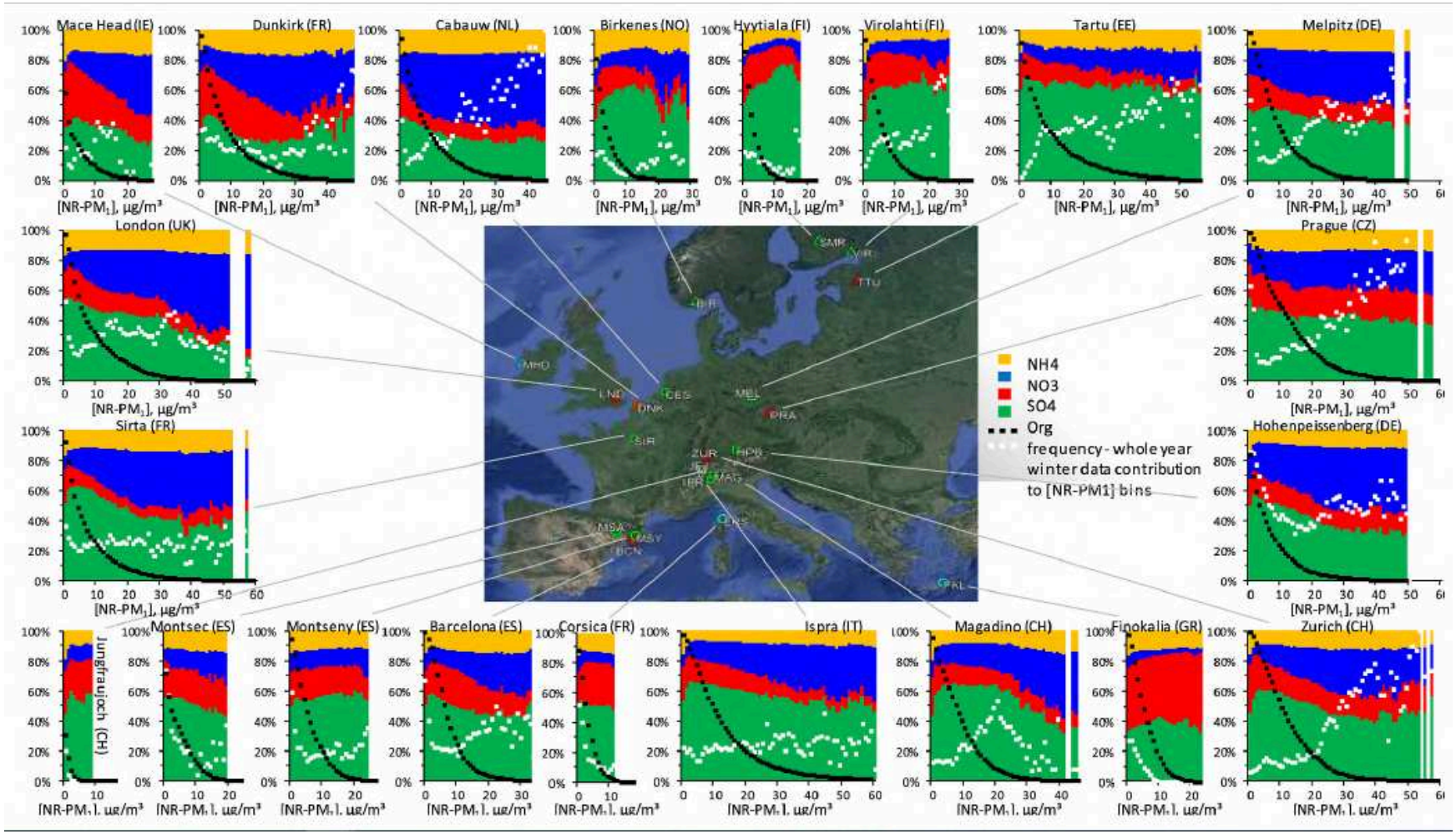

Figure I.16 : Contributions relatives des espèces chimiques en fonction des niveaux de concentrations en NR-PM_1 (source : Bressi et al., 2021).

D’autres études ont également analysé la composition chimique des aérosols atmosphériques. Lin et al., (2020) ont analysé la composition et les sources des aérosols submicroniques PM_1 sur 2 sites : un site en bordure d’axe routier dans le centre-ville de Dublin et un autre site résidentiel dans le sud de Dublin (~ à 5 km de distance), à l'aide d'un ACSM et d'un AE33 pendant les périodes de non-chauffage (début septembre) et de chauffage (fin octobre) en 2018. Cette étude a mis en évidence l'augmentation significative du BC dû aux émissions du trafic en site de proximité automobile et à l'impact important de l’AO provenant du chauffage résidentiel sur les deux sites.

De même, Jiang et al., (2019) ont étudié la contribution des composants de l'AO et leurs sources sur 9 sites européens en 2011. Ils ont constaté que la combustion de la biomasse et les sources biogéniques sont les principales sources d'AO en Europe, respectivement en hiver et en été. La combustion de la biomasse a une contribution de 70 % en hiver dans la vallée du Pô et les régions d'Europe de l'Est. Et les sources biogéniques constituent en moyenne plus de 50 % de l'AO en été (le taux le plus élevé étant de 77 % en Scandinavie).

En outre, Paglione et al., (2020) ont analysé les données issues de 8 périodes d'observation intensive réalisées sur 4 ans (de 2011 à 2014) sur deux sites différents (rural et urbain) en Italie, afin de caractériser la variabilité spatiale et la saisonnalité des sources d'AO, avec un accent particulier sur la saison froide. La combustion de la biomasse reste la source la plus importante d'AO. Cette étude a pu identifier et quantifier un rôle particulièrement essentiel de la réactivité en phase aqueuse dans la formation et la transformation des émissions primaires de la combustion de la biomasse.

Dans le tableau ci-dessous sont présentées quelques autres études de répartition des sources des particules fines en utilisant la PMF dans d’autres régions européennes.

Tableau I.1 : Exemples d'études de répartition des sources en Europe

Étude	Lieu/Période	Méthode	Sources/facteurs identifiés	Contributions % à la masse totale de $PM_{2.5}$
(Almeida et al., 2020)	16 sites urbains européens et asiatiques	EPA PMF 5.0	Combustion de biomasse Sulfates secondaires Trafic Sol (resuspension) Combustion du mazout Combustion du charbon Sel Émissions industrielles Autres	16% 15% 13% 12% 8% 5,5% 1,9% 0,8% 5,1%
(Crippa et al., 2014)	17 sites en Europe (mai-juin et septembre-octobre 2008) et (février-mars 2009)	PMF avec ME2 sur les données AMS	HOA (trafic) BBOA (combustion de biomasse) COA (cooking factor) MSA (source marine) SV-OOA LV-OOA	11 ± 6% 12 ± 5% 15% 2 - 6% 34 ± 11% 50 ± 16%
(Cesari et al., 2019)	Sud de l'Italie en période hivernale de 2018	EPA PMF5	Combustion de biomasse Sulfate secondaire Circulation automobile et nitrate secondaire Embruns marins Émissions industrielles (primaires)	32,8 ± 1,4 % 19,7 ± 2,4 % 17,0 ± 3,9 % 12,9 ± 2,3 % 5,4 ± 2,3 %
(Daellenbach et al., 2017)	9 stations d'Europe centrale pour l'année 2013	PMF, Analyse offline	HOA COA BBOA SOOA (OA oxygéné en été) WOOA (ASOA en hiver) SC-OA (Soufre)	4 - 14 % 3 - 11 % 11 - 59 % 15 - 38 % 14 - 27 % 5 - 23 %
(Seibert et al., 2020)	3 sites au Nord-Est de la République tchèque	PMF	Émissions résidentielles provenant des combustibles solides Sources régionales d'aérosols primaires et secondaires Particules minérales et biogéniques Transport longue distance Industrie lourde	50 - 60 % Jusqu'à 40 % 15 - 20 % Jusqu'à 10 % Jusqu'à 10 %

Ces résultats suggèrent l'importance d'un système de surveillance continue pour une meilleure caractérisation de la pollution due à la combustion de la biomasse dans la plupart des régions européennes, en utilisant des mesures complémentaires à la fois de façon régulière et par le biais de campagnes intensives afin d'explorer l'importance de la combustion de la biomasse pour la qualité de l'air et le climat. De fait, plusieurs programmes internationaux sont en place pour

fournir des mesures continues de différents polluants atmosphériques. Parmi elles, on compte : le réseau Global Atmosphere Watch (www.gaw-wdca.org) de l'Organisation Météorologique Mondiale ; le programme EMEP (European Monitoring and Evaluation Programme, www.emep.int) pour la surveillance et l'évaluation du transport à longue distance des polluants atmosphériques en Europe axé sur les politiques au titre de la Convention sur la pollution atmosphérique transfrontalière à longue distance (CLRTAP) ; ainsi que l'infrastructure de recherche européenne Aerosol, Clouds, and Trace Gases Research Infrastructure (ACTRIS) (www.actris.eu) qui est officiellement devenu un consortium européen pour les infrastructures de recherche (ERIC) en avril 2023 et rassemble 17 pays fondateurs dont la France.

Récemment, et dans le cadre de l'action COST *Chemical On-Line cOmpoSition and Source Apportionment of fine aerosoL* (COLOSSAL) (www.costcolossal.eu), Chen et al., (2022) ont utilisé 22 ensembles de données provenant de 14 pays différents, exploitant les mesures obtenues par l'infrastructure de recherche ACTRIS à travers les instruments ACSM/AMS de 2013 à 2019. Cette étude a englobé 9 sites non urbains et 13 sites urbains. L'objectif de cette étude était de quantifier les principales sources d'AO en Europe, composante essentielle des PM_1 (Figure I.17). L'étude a consisté à mettre au point un protocole de répartition des sources pour analyser les données d'AO à long terme, en utilisant des méthodologies (notamment PMF glissante, ME-2 et bootstrap) qui sont expliquées dans le chapitre 2. L'étude a réussi à distinguer les sources primaires d'AO, comprenant les hydrocarbures (HOA), la combustion de biomasse (BBOA), la cuisson résidentielle (COA), systématiquement identifiés sur tous les sites, ainsi que la combustion du charbon (CCOA), des combustibles solides (SFOA), la fumée de cigarette (CSOA) et bien d'autres identifiés sur des sites spécifiques. De plus, des sources d'AO secondaires ont été observées sur tous les sites, avec des états d'oxydation plus (MO-OOA) ou moins (LO-OOA) importants. Ces composants d'AO oxygénés (OOA) constituaient la majeure partie de la masse d'AO submicronique (71,1 %). Il est important de noter que les composants d'AO associés à la combustion de combustibles solides (c'est-à-dire BBOA, CCOA, SFOA) restaient significatifs, contribuant à un total annuel d'AO de 16,0 %, particulièrement durant les mois d'hiver (21,4 %).

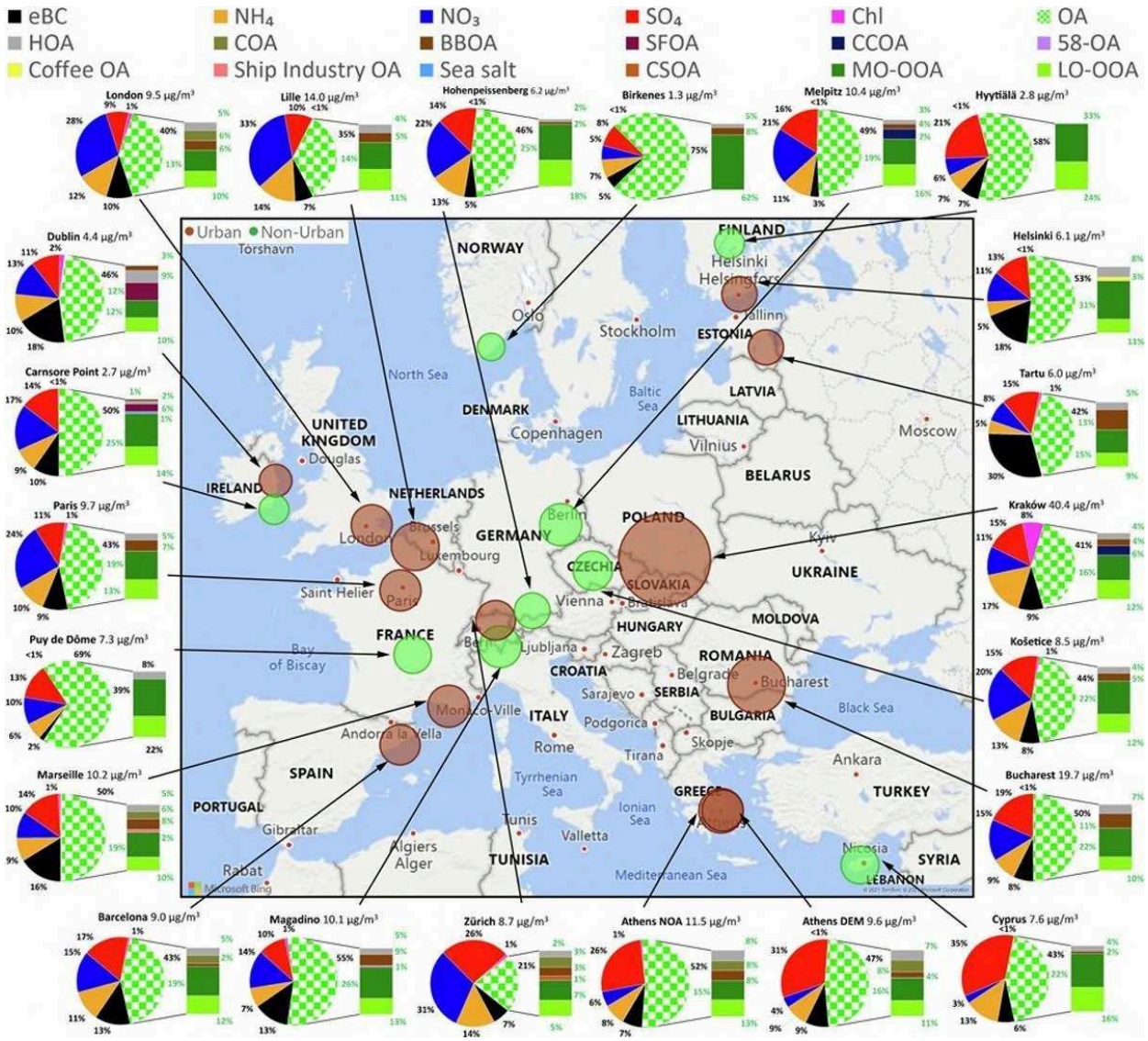

Figure I.17 : Concentrations massiques en PM_1 et contributions relatives des espèces inorganiques non réfractaires, du carbone suie eBC et de l'AO en Europe. Source : Chen et al., 2022.

En France

À partir des années 2010, un nombre grandissant d'études des sources de particules atmosphériques ont été conduites en France sous l'impulsion notamment des programmes CARA du LCSQA et MERA/EMEP, ainsi que divers projets de recherche financés à l'échelle nationale ou régionale. Favez et al., (2021) ont notamment résumé les principaux résultats obtenus dans le cadre du programme CARA au cours de la dernière décennie. Ils ont en premier lieu présenté les

principales conclusions issues des exercices de comparaison inter-laboratoires, cruciaux pour garantir la qualité et le contrôle des données. Ils ont ensuite dressé une vue d'ensemble de la composition chimique des particules, obtenue par le biais des mesures de leurs constituants principaux. Après avoir approfondi les discussions sur les principales sources primaires de particules explorées jusqu'à présent dans le contexte du programme CARA, notamment le chauffage résidentiel au bois, le transport routier, les sels marins et les poussières sahariennes, ils ont également abordé les origines prédominantes des aérosols secondaires ayant un impact sur les environnements urbains français. Cela comprend le nitrate d'ammonium (AN), le sulfate d'ammonium ($(NH_4)_2SO_4$; AS) et les aérosols organiques secondaires (AOS).

En outre, le projet SOURCES (cofinancé par l'ADEME) a permis une réanalyse homogène de jeux de données collectées lors de la première moitié de la décennie 2010 dans le cadre du programme CARA et/ou de projets de recherche nationaux/européens impliquant l'institut de géophysique de l'environnement (IGE), constituant la plus large étude de sources de PM_{10} au niveau national par application de modèle statistique sources-récepteur. Les résultats obtenus ont notamment été synthétisés par Weber et al., (2019), confirmant non seulement l'influence prédominante du chauffage au bois résidentiel en hiver et des émissions de véhicules sur la qualité globale de l'air urbain en France, mais aussi l'importance de sources supplémentaires à l'échelle locale (telles que les émissions maritimes et industrielles à Marseille) ou lors de périodes critiques de l'année (comme les émissions d'ammoniac (NH_3) issues des activités agricoles durant les périodes de conditions météorologiques stables de basse pression, en fin hiver/ début printemps). A noter que ce travail a également permis de réaliser de premières études des sources du potentiel oxydant des particules à l'échelle nationale (Calas et al., 2019; Weber et al., 2021).

En parallèle, différents travaux ont également permis de mettre en évidence les impacts significatifs de différentes sources d'émissions primaires négligées jusqu'alors, telles que les émissions hors échappement du transport routier (Amato et al., 2016; Charron et al., 2019) ou les aérosols organiques primaires d'origine biogénique (Waked et al., 2014; Golly et al., 2019; Samake et al., 2019; Samake et al., 2021).

Pour la moitié nord de la métropole, différentes études ont été réalisées en régions Ile de France et Hauts de France (Bressi et al., 2014; Beekman et al., 2015; Waked et al., 2018; He et al. 2018, Roig Rodelas et al., 2019), soulignant l'impact significatif du transport atmosphérique des masses

d'air polluées provenant d'Europe centrale et d'Europe de l'Est sur la qualité de l'air des régions voisines. La région de l'Europe centrale présente un potentiel significatif en tant que source majeure en raison de la concentration d'activités industrielles et résidentielles d'envergure. Des résultats similaires ont été mis en évidence pour le site de fond périurbain de Metz-Borny, au coeur de la région Grand-Est (Petit et al., 2019).

La forte influence de la combustion de biomasse sur la qualité de l'air dans les vallées alpines en hiver a également été documentée (Aymoz et al., 2007; Favez et al., 2010; Bonvalot et al., 2016). Plus récemment, Borlaza et al. (2021a et 2021b) ont étudié la variation spatiale de l'influence des différentes sources de PM - et de leur potentiel oxydant - à l'échelle urbaine, à partir de campagnes de mesures mises en œuvre sur 3 sites grenoblois.

À Marseille, Chazeau et al. (2020) ont analysé les données des aérosols submicroniques issus des instruments ToF-ACSM et Aéthalomètre pour une période de 14 mois (fév. 2017 à avril 2018). Les résultats obtenus indiquent de fortes contributions d'AO et de BC en hiver, en raison d'un trafic urbain intense, d'émissions élevées provenant du chauffage résidentiel, de la combustion de déchets verts, et de la faible hauteur de la couche limite. En été, les SO_4 contribuent de plus aux concentrations des PM_1, ceci étant dû aux activités anthropiques locales (émissions de navires, émissions industrielles de SO_2) et au transport méditerranéen à longue distance. Cette étude a également permis de souligner la contribution significative du transport régional des particules à la pollution atmosphérique locale qui doit être considérée par les autorités locales dans le déploiement de stratégies efficaces de réduction des polluants. En effet, des niveaux élevés d'AO oxygéné et de nitrate inorganique ont été associés aux particules transportées à moyenne/longue distance.

Tableau I.2 : Exemples d'études récentes de répartition des sources d'AO en France à partir de mesures ACSM/AMS

Étude	**Lieu/Période**	**Méthode**	**Sources/facteurs identifiés**	**Pourcentages % à la masse totale de $PM_{2.5}$**
(Zhang et al., 2019)	Site péri-urbain à Paris, 6 ans (de novembre 2011 à mars 2018)	PMF partiellement contrainte à l'aide du ME2	HOA (circulation mais facteur influencé par la combustion de la biomasse) BBOA (combustion de bois résidentielle) LO-OOA (AOS biogéniques) MO-OOA (émissions anthropiques, transport longue distance en provenance du nord-est de l'Europe)	11%-16% 14%-19% 25%-42% 30%-45%
(Roig Rodelas et al., 2019)	Site péri-urbain à Douai, 5 semaines (février - mars 2016)	PMF	HOA (de type hydrocarbures) oBBOA (BBOA oxydé) LO-OOA MO-OOA	20% 28% 17% 35%
(Chazeau et al., 2021)	Marseille Longchamps, 14 mois (février 2017-Avril 2018)	PMF glissante	HOA BBOA COA ShInd-OA LO-OOA MO-OOA	11% 12% 11% 4% 21% 40%
(Srivastava et al., 2019)	SIRTA, mars 2015	PMF-ACSM et PMF combiné	PTOA (trafic primaire) BBOA (combustion de la biomasse) OBBOA (BBOA oxydé) BSOA-1 (marine-rich) BSOA-2 (isoprene-rich) ASOA-1 (nitro-PAHs) ASOA-2 (oxy-PAHs) ASOA-3 (phenolic compounds oxidation) ASOA-4 (toluène oxydation) SOA-5 (SOA âgée)	8% 3% 14% 14% 5% 10% 4% 3% 5% 34%

Le Tableau I.2 regroupe une sélection de résultats issus d'études de répartition des sources de l'AO en France à partir de mesures ACSM ou AMS. La combustion de bois pour le chauffage résidentiel ainsi que le transport routier sont les deux principales sources primaires qui influencent fortement les charges de PM en France, tandis que les aérosols organiques oxygénés constituent une partie prédominante des aérosols organiques.

Ainsi, une grande diversité de sources ont été identifiées dans les études antérieures mentionnées ci-dessus en mettant l'accent sur l'importance de l'étude de la répartition des sources des AO pour mieux comprendre les origines de la pollution particulaire ambiante. Ceci est très utile pour les pouvoirs politiques afin de concevoir des stratégies d'atténuation visant à améliorer la qualité de l'air et réduire les impacts sanitaires et climatiques des particules submicroniques ainsi que pour les modélisateurs pour valider et améliorer les simulations de modèles.

I.5 Stratégie et objectifs scientifiques de la thèse

L'objectif d'améliorer la qualité de l'air et réduire les impacts des aérosols tant sur la santé humaine que sur le climat a poussé la communauté scientifique à renforcer les études pour mieux caractériser l'AO, en adoptant différentes méthodes de répartition des sources. La détermination des sources et origines des particules fines apporte aux décideurs les informations nécessaires pour prendre des mesures efficaces visant à réduire les émissions de polluants.

Comme c'est le cas en Europe en général et en France en particulier, des concentrations relativement élevées de particules fines ont été observées, avec plusieurs dépassements de la concentration quotidienne recommandée de $PM_{2,5}$ par l'OMS (EEA, 2021). Par conséquent, il devient impératif de déterminer les principales sources des aérosols. L'objectif principal de cette étude est d'identifier les principales familles chimiques constitutives des AO submicroniques sur divers sites français. Cela est réalisé en analysant les spectres de masse obtenus à partir des mesures réalisées avec l'ACSM.

Cette thèse repose largement sur l'utilisation de la méthode PMF glissante, mise en œuvre dans le logiciel SoFi Pro (Datalystica Ltd., Villigen, Switzerland). Le protocole adapté est basé sur les recommandations de l'action COST COLOSSAL (Chen et al., 2022) et est appliqué aux sites de fond urbain dans le cadre du programme CARA.

Cette thèse vise dans un premier temps à caractériser la composition chimique des PM fines (parties organique et inorganique ainsi que le BC) dans des sites urbains ou péri-urbains. Dans un second temps, l'objectif scientifique est d'identifier les sources de ces particules fines et de mieux comprendre leur distribution géographique.

La stratégie adoptée au cours de ce travail de thèse a été la suivante :

- Assurer le contrôle qualité des jeux de données ACSM et AE33 et leur validation, pour un export adéquat des concentrations organiques et de leurs incertitudes en vue d'appliquer des méthodes de répartition de sources, principalement la PMF.
- Examiner la composition chimique des particules fines collectées sur différents sites urbains français sur des périodes étendues (entre 2015 et 2021) et analyser leur variabilité temporelle et géographique.
- Établir la phénoménologie des sources principales de PM/AO pour chaque site, en quantifiant la contribution de chaque source et en explorant les variations temporelles et spatiales de ces sources.
- Évaluer la pertinence du protocole élaboré dans le contexte de l'action COST COLOSSAL pour les mesures effectuées par les AASQA et examiner ses éventuelles limitations.

Chapitre II. Description des sites, instruments et méthodologies suivies

Ce chapitre est consacré à la présentation des différentes stations de mesure du programme CARA, dont les données ont été exploitées dans cette thèse. Une description des instruments est également fournie, avec les différentes procédures de traitement des données relatives aux particules fines. De plus, la dernière section décrit les méthodes utilisées pour quantifier les sources des aérosols organiques.

II.1 Programmes CARA et ACTRIS

Depuis sa création en 2008, le programme CARA (CARActérisation chimique des particules), coordonné par le LCSQA (Laboratoire Central pour la Surveillance de la Qualité de l'Air) et financé par le Ministère en charge de l'environnement, a pour objectif de comprendre et de caractériser la composition chimique et les sources des particules fines à travers le réseau national de surveillance de la qualité de l'air, représenté par les AASQAs , ainsi que des partenaires issus d'organismes de recherche (INERIS, IMT Nord Europe, IGE et LSCE). CARA était initialement axé sur l'analyse chimique en laboratoire de filtres prélevés par des AASQA volontaires dans différentes stations du réseau national, principalement pour les particules PM_{10} et les sites de fond urbain, dans des situations d'urgence ou dans le cadre d'études et de projets de recherche spécifiques pour répondre à des problématiques particulières, notamment le rapport européen sur l'origine des dépassements des valeurs limites annuelles. Il dispose désormais d'analyseurs automatiques adaptés à la surveillance opérationnelle, tels que l'*Aerosol Chemical Speciation Monitor* (ACSM) et l'Aethalomètre multi-longueurs d'onde (AE33), qui permettent d'obtenir une évaluation quasi-temps réel de la composition chimique des particules. Ces instruments sont installés dans différentes grandes villes françaises (Figure II.1) également équipées de plusieurs instruments du réseau national. Ces mesures automatiques permettent notamment de :

- Documenter la composition chimique et l'origine des particules lors de périodes de pollution particulaire à grande échelle ;
- Réaliser des études de sources à long terme dans différentes grandes agglomérations françaises ;
- Produire des bases de données pour la validation des modèles chimie-transport ;

- Stimuler et soutenir d'autres activités de recherche ayant pour objectif d'approfondir les bases de connaissances concernant la qualité de l'air.

Ce réseau opérationnel d'observation quasi-temps réel de la composition chimique des particules est unique en Europe et constitue une avancée significative pour la surveillance de la qualité de l'air (https://www.lcsqa.org/fr/le-dispositif-cara). Il a été largement décrit dans un article récent (Favez et al., 2021).

Figure II.1 : Distribution spatiale des principaux sites du programme CARA équipés en 2023 avec des instruments de chimie des particules fines en temps quasi réel.

L'infrastructure de recherche européenne ACTRIS est composé de plateformes expérimentales nationales (*National Facilities*), telles que des observatoires et des chambres de simulation atmosphériques, ainsi que de centre d'expertise (*Topical Centres*) permettant la fourniture de données de haute qualité harmonisées, et des centres de données. L'Ineris (en collaboration avec

le LSCE et le LaMP) pilote l'ACMCC (*Aerosol Chemical Monitor Calibration Centre*), unité d'ECAC-CAIS, le centre européen pour la calibration et la caractérisation des mesures in situ des aérosols. L'IMT Nord Europe pilote de son côté une unité du CiGas en France pour les mesures in situ des gaz traces réactifs, tels que les composés organiques volatils (COV), les vapeurs condensables et les oxydes d'azote (NO_x). L'officialisation de l'IR ACTRIS en tant qu'*European Research Infrastructure Consortium* (ERIC) a été annoncée par la commission européenne en avril 2023. Dans ce cadre, les stations ATOLL et SIRTA sont en cours de labellisation pour la mesure in situ des aérosols, avec d'autres *National Facilities* françaises. La station Marseille-Longchamp (opérée conjointement par Atmo Sud et le Laboratoire de Chimie de l'Environnement, LCE) est également partie prenante du paysage ACTRIS, au niveau national (ACTRIS-France) et dans le cadre de divers projets de recherche européens.

II.2 Description des sites de mesure

Ainsi, ce travail de thèse exploite des mesures de la composition chimique des particules fines dans le cadre du programme CARA principalement sur 14 sites urbains ou péri-urbains. Répartis à travers toute la France (Figure II.2), ces sites d'échantillonnage offrent une vision globale de la composition chimique des particules fines et de leurs sources potentielles à l'échelle nationale. La majorité des sites sont des sites de fond urbains, excepté deux sites périurbains (ATOLL et SIRTA) et deux autres en proximité automobile (trafic) (Boulevard Périphérique Est : BPEST ; et Strasbourg Clémenceau : STR CLM). Une description détaillée de ces sites est présentée ci-après. Pour chaque site d'échantillonnage, des informations détaillées, y compris les coordonnées et les organismes associés, sont fournies dans le Tableau II.1.

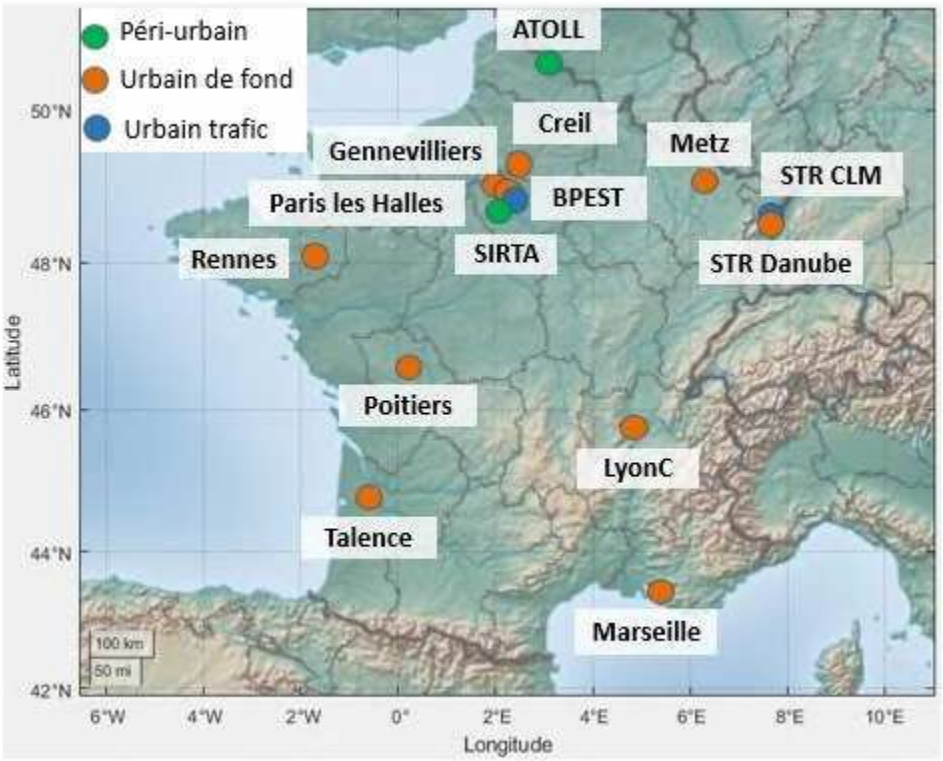

Figure II.2 : Localisation géographique des sites d'échantillonnage de ce travail (2015-2021).

Tableau II.1: Caractéristiques des stations de mesures du programme CARA dont les jeux de données ont été exploités dans le cadre de cette thèse.

AASQA ou organisme	**Nom station**	**Code station**	**Altitude (m a.s.l.)**	**Latitude**	**Longitude**	**Type de site**
IMT Nord Europe	ATOLL (Lille)	ACTRIS	70	50.6111	3.1404	Périurbain
LSCE & INERIS	SIRTA (Paris)	ACTRIS	163	48.71181	2.14818	Périurbain
AirParif	Gennevilliers	FR04002	28	48.9298083	2.2946194	Fond urbain
AirParif	Paris 1er-Les Halles	FR04055	35	48.8627083	2.3446972	Fond urbain
AirParif	Boulevard Périphérique Est	FR04329	49	48.8385167	2.4126242	Trafic
Air Breizh	Rennes Pays-Bas	FR19017	45	48.08965	-1.65911	Fond urbain
Atmo AuRA	Lyon Centre	FR20062	160	45.75779	4.85422	Fond urbain
Atmo Grand Est	Metz Borny	FR1012	204	49.1102806	6.2233361	Fond urbain
Atmo Grand Est	Strasbourg Danube	FR42010	135	48.5062222	7.7511806	Fond urbain
Atmo Grand Est	Strasbourg Clémenceau	FR16034	139	48.5902992	7.7450583	Trafic
Atmo Hauts-de-France	Creil Faïencerie	FR18043	31	49.2597222	2.4744444	Fond urbain
AtmoSud	Marseille Longchamp	FR03043	73	43.3052889	5.3947056	Fond urbain
Atmo Nouvelle-Aquitaine	Poitiers Augouard	FR09404	105	46.5839885	0.3455967	Fond urbain
Atmo Nouvelle-Aquitaine	Talence	FR31002	23	44.800442	-0.5893941	Fond urbain

II.2.1 ATOLL (Lille)

La station ATOLL (ATmospheric Observations in liLLe) est située au nord de la France et est considérée comme un site péri-urbain. Son environnement est principalement influencé par les émissions liées au transport provenant de différentes directions. Lille, la plus grande ville de la région Hauts-de-France et son chef-lieu, a une densité de population élevée (236 000 habitants en

2020 ; 6845 hab./km²). Elle est localisée au centre de la Métropole Européenne de Lille qui regroupe 95 communes et 1,2 million d'habitants.

La position géographique de la station ATOLL est un autre aspect important. Étant située à environ 4 km du centre de Lille au carrefour des grandes régions urbanisées et industrialisées du nord-ouest de l'Europe, telles que Paris, la Belgique, l'Allemagne et Londres, elle est exposée aux masses d'air provenant de ces régions, qui s'additionnent aux émissions locales, ce qui entraîne une dégradation fréquente de la qualité de l'air à Lille. En plus des influences urbaines et industrielles, la région des Hauts-de-France est également connue pour ses activités économiques et agricoles. Ces facteurs contribuent à l'environnement complexe par lequel la station ATOLL est influencée.

La station ATOLL est spécifiquement installée sur le toit du département de Physique sur le campus de l'Université de Lille à Villeneuve d'Ascq (Tableau II.1). La plateforme multi-laboratoires ATOLL, abritée depuis les années 1990 au sein du Laboratoire d'Optique Atmosphérique (LOA), est équipée pour mesurer diverses variables atmosphériques d'intérêt pour l'étude du climat, de la qualité de l'air et de la validation satellitaire. La plateforme gère deux Services Nationaux d'Observation pour l'Institut National des Sciences de l'Univers (INSU) du CNRS : PHOTONS-AERONET/EARLINET pour les mesures d'aérosols par télédétection (photomètre et LIDAR) et NDACC-UV pour le rayonnement UV. Ces services font également partie intégrante d'ACTRIS France. Les observations in situ, tout d'abord optiques et physiques, ont débuté en 2014, et ont été complétées à partir de fin 2016 par des mesures de composition chimique en collaboration avec le Centre Energie Environnement de l'IMT Nord Europe.

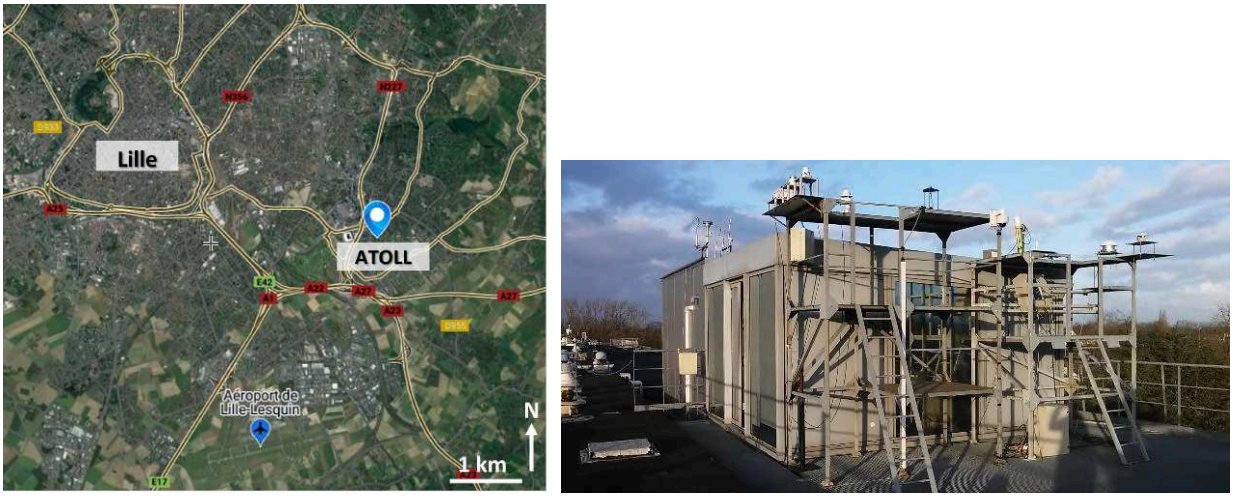

Figure II.3 : Carte précisant la localisation de la plateforme ATOLL (gauche) et photographie (crédit : IMT Nord Europe) de l'extension située sur le toit du bâtiment P5 du campus "Cité scientifique", abritant les mesures in situ (droite).

II.2.2 SIRTA (Paris)

La station de surveillance de la qualité de l'air SIRTA (Site Instrumental de Recherche par Télédétection Atmosphérique) est localisée sur le plateau de Saclay à Palaiseau, dans la région Île-de-France, à environ 20 km au sud-est du centre de Paris. Elle se structure autour de cinq zones distinctes. Les quatre premières zones sont situées sur le campus de l'École Polytechnique, tandis que la cinquième zone se trouve au LSCE. La station est équipée d'instruments de pointe qui mesurent et enregistrent en continu une variété de paramètres météorologiques atmosphériques. Elle réalise également des études sur les nuages et des mesures d'aérosols par télédétection. Par ailleurs, la station SIRTA située au LSCE (Tableau 1) fournit des mesures in situ à long terme des aérosols et des gaz réactifs, qui sont utilisées pour évaluer la qualité de l'air, surveiller les tendances de la pollution et développer des modèles de prévision. L'emplacement de la station SIRTA lui permet d'être en contact avec les masses d'air provenant de Paris et de la région environnante. Elle est principalement influencée par des vents du Sud-Ouest qui transportent des masses d'air océaniques plus propres, ainsi que par des vents du Nord-Est qui peuvent amener des masses d'air continentales potentiellement polluées. La station est considérée comme un site péri-urbain impacté par le trafic routier, l'agriculture et les résidences

environnantes. Elle permet d'obtenir des informations précieuses sur la dispersion des polluants dans la région parisienne et de mieux comprendre les variations spatiales de la qualité de l'air.

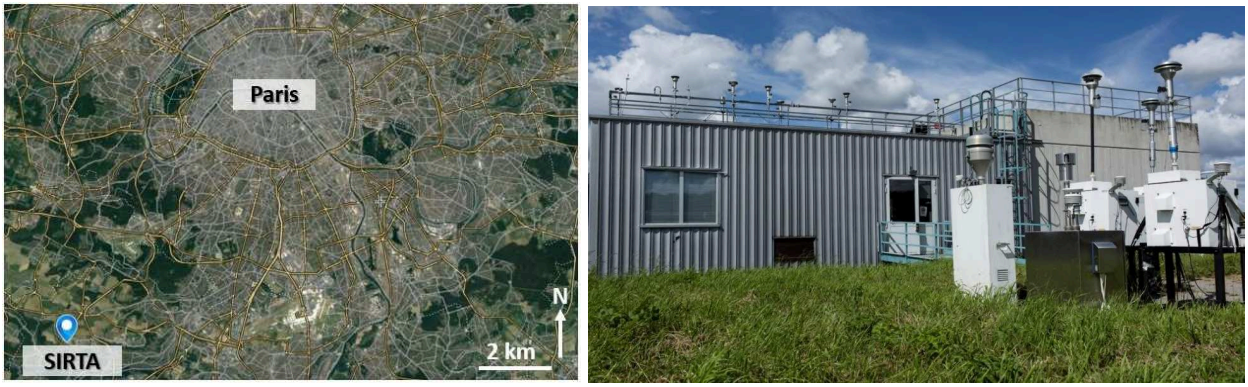

Figure II.4 : Carte précisant la localisation de la plateforme SIRTA (gauche) et photographie de la plateforme des mesures in-situ du SIRTA (droite).

II.2.3 Paris Les Halles

La station de fond urbain « Paris 1er-Les Halles » est située dans le 1er arrondissement de Paris, à 22 km du SIRTA. Les Halles, au cœur de Paris, se caractérisent par une forte activité locale, avec des espaces verts, des centres commerciaux, des restaurants et de nombreux espaces dédiés aux loisirs et à la culture, ainsi que la station de RER Châtelet - Les Halles, qui est la plus grande station souterraine et permet d'accéder à l'ensemble du réseau de la région parisienne.

La station est multi-instrumentée disposant de mesures permanentes in-situ depuis octobre 2019. Les prélèvements d'échantillons sont effectués à des hauteurs entre 1,55 et 2 m par rapport au sol, avec un dégagement de 270° pour assurer une représentativité optimale des mesures.

Figure II.5 : Carte précisant la localisation de la station Paris 1er-Les Halles d'Airparif (haut) ; photographies (crédit : AirParif) des têtes de prélèvement (bas à gauche) et de l'intérieur de la station (bas à droite).

II.2.4 Boulevard Périphérique Est (BPEst)

La station Boulevard Périphérique Est, située dans le 12ème arrondissement de Paris, est une station de trafic urbain opérationnelle depuis janvier 2013. Le boulevard périphérique entoure la ville de Paris avec une longueur de 35 km. En général, il comporte quatre voies dans chaque direction. Les flux de circulation les plus importants de la région parisienne demeurent concentrés sur le boulevard périphérique, avec un enregistrement de trafic de 180 000 à 250 000

véhicules par jour selon l'Atelier parisien d'urbanisme (APUR) en 2019. Cette route engendre des émissions importantes de gaz et de particules polluantes dans l'air.

Les prélèvements d'échantillons sont effectués à des hauteurs allant de 2,8 à 3,1 m par rapport au sol. Les distances de prélèvement sont de 5 m au bord de la voirie et de 6,5 m au centre de la première voie de circulation. L'axe de mesure couvre une largeur de 2 fois 4 voies d'une largeur totale de 34 m.

Ces mesures permettent de surveiller la qualité de l'air à proximité du Boulevard Périphérique Est de Paris, en évaluant les niveaux de polluants gazeux, de particules fines et d'aérosols. En se concentrant sur un environnement caractérisé par un trafic dense, cette station contribue à la compréhension de l'impact de la pollution liée au trafic routier sur la qualité de l'air dans cette zone urbaine.

Figure II.6 : Carte précisant la localisation de la station BPEST (gauche) et photographie (crédit: AirParif) des têtes de prélèvement en bordure du périphérique (droite).

II.2.5 Gennevilliers (Genn.)

La station de Gennevilliers est une station urbaine de fond, située à 2,1 km au nord-ouest de Paris, et qui est opérationnelle depuis janvier 1986. Gennevilliers est une commune urbaine à forte densité de population (49 880 habitants en 2020 ; 4300 habitants/km^2). Elle se situe au carrefour de deux autoroutes, l'A15 et l'A86, et s'étend sur une superficie de 1 200 hectares. Les

2/3 de sa superficie sont consacrés aux activités économiques et industrielles. La commune est située dans le département des Hauts-de-Seine, une collectivité riche en transport fluvial.

Les prélèvements d'échantillons sont effectués à une hauteur d'environ 15 m par rapport au sol, sur le toit du collège Louis Pasteur, ce qui permet d'obtenir des échantillons représentatifs de l'air ambiant. De plus, la station bénéficie d'un dégagement à 360°, assurant une prise d'échantillons sans obstruction autour du site.

Figure II.7 : Carte précisant la localisation de la station Gennevilliers (gauche) et photographie (crédit: AirParif) des têtes de prélèvement sur le toit du collège Louis Pasteur (droite).

II.2.6 Creil

La station de mesure de Creil est une station urbaine située dans le département de l'Oise, en région Hauts-de-France. Elle est spécifiquement localisée au centre de la commune de Creil, qui est le centre d'une unité urbaine composée de 22 communes et compte près de 120 000 habitants, ce qui en fait la principale agglomération de l'Oise. Creil se trouve à proximité de grandes villes telles que Paris, Beauvais et Amiens, à des distances de 45,35 et 72 km, respectivement. La ville est traversée par la rivière l'Oise et est entourée de deux forêts, la forêt d'Halatte à l'est et la forêt de Chantilly au sud-est.

La station de mesure de Creil est implantée dans un environnement urbain influencé à la fois par le trafic urbain et les émissions résidentielles. Ces mesures permettent de surveiller la qualité de l'air dans la commune de Creil et d'évaluer l'impact des émissions provenant du trafic routier, des

activités résidentielles et d'autres sources locales sur la pollution atmosphérique dans cette zone urbaine.

Figure II.8 : Carte précisant la localisation de la station de Creil (gauche) et photographie (crédit : Atmo Hauts-de-France) de l'extérieur de la station (droite).

II.2.7 Lyon

Le site de fond urbain Lyon Centre, localisé dans la zone du Bassin Lyonnais/Nord Isère, est opérationnel depuis le 5 janvier 2007. Située au cœur de la ville de Lyon, la station de surveillance joue un rôle essentiel dans la collecte de données sur la qualité de l'air dans cette agglomération densément peuplée. Elle est la troisième plus grande ville de France avec 522 969 habitants en 2019 (INSEE, 2019). Lyon est la capitale de la région Auvergne-Rhône-Alpes qui s'étend sur une superficie de 69 711 km^2. La ville est connue pour sa forte activité industrielle mais aussi pour ses activités agricoles et agroalimentaires.

Ce site est représentatif de l'exposition de la population lyonnaise à la pollution atmosphérique; il caractérise l'air respiré par tous les lyonnais. En outre, la station de surveillance est stratégiquement positionnée pour capturer les niveaux de pollution résultant des activités urbaines, telles que le trafic routier, l'industrie et les émissions domestiques. Elle fournit ainsi des informations cruciales pour évaluer l'efficacité des mesures de réduction de la pollution et soutenir la mise en place de politiques environnementales visant à améliorer la qualité de l'air dans la région.

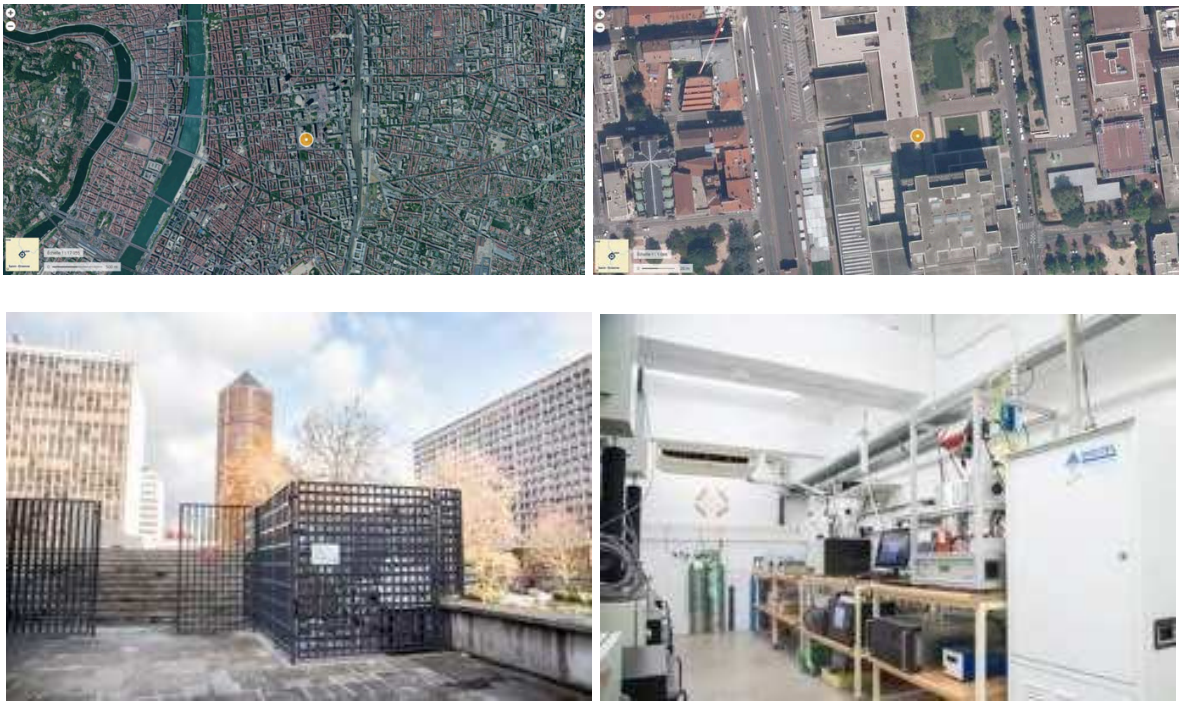

Figure II.9 : Images satellites précisant la localisation de la station de Lyon centre à grande échelle (en haut à gauche) et à petite échelle (en haut à droite) et photographies (crédit : Atmo AuRA) d'une vue extérieure (en bas à gauche) et intérieure de la station de mesure (en bas à droite).

II.2.8 Metz

La station de mesure de Metz est située dans le quartier de Borny, qui se trouve au sud-est de la ville de Metz. Metz est au cœur de trois pays européens (Allemagne, Belgique et Luxembourg). La ville se situe à mi-chemin entre Strasbourg (130 km) et Reims (155 km). Elle se trouve à 55 km du Luxembourg et à 53 km de Nancy. Sa densité de population est de 2 866,3 habitants/km^2 en 2020 (120 211 habitants). Elle est connue pour sa forte activité économique et industrielle, notamment la métallurgie, la pétrochimie, l'automobile, la logistique et le commerce.

Cette station est considérée comme un site urbain de fond, et elle se trouve dans une zone résidentielle. Dans la même rue, se trouvent principalement des maisons individuelles ainsi qu'une école maternelle, ce qui implique la présence de stationnement de bus scolaires et de parents. Au sud de la station, il y a également une zone commerciale comprenant des restaurants. Ces caractéristiques environnementales sont importantes à prendre en compte dans l'interprétation des données de mesure, car elles peuvent influencer la qualité de l'air dans cette

zone particulière. La proximité des habitations, de l'école et des activités commerciales peut contribuer à l'exposition de la population locale aux polluants atmosphériques. C'est pourquoi la surveillance de cette station urbaine de fond revêt une importance particulière pour évaluer l'impact de l'activité humaine sur la qualité de l'air dans cette zone résidentielle et commerciale de Metz.

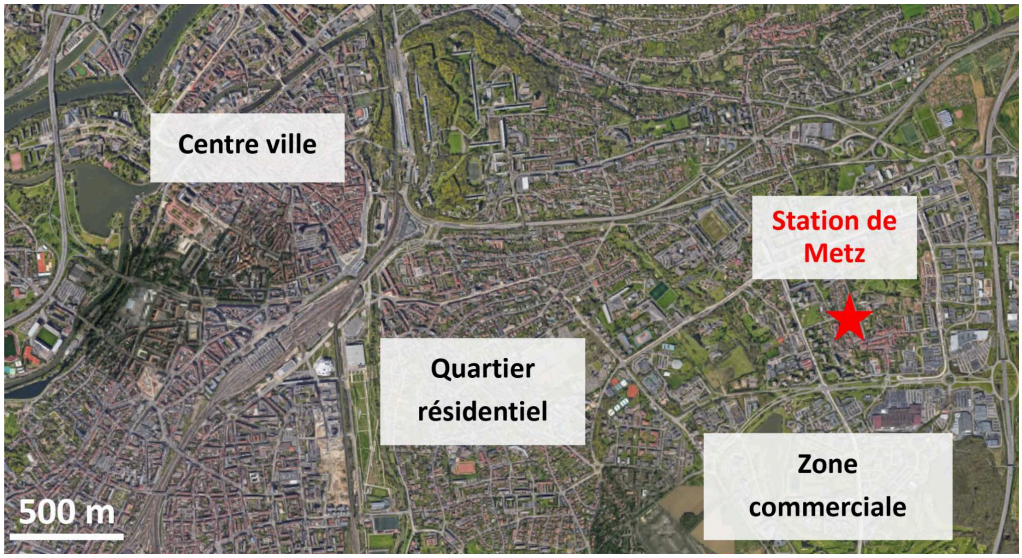

Figure II.10 : Carte précisant la localisation de la station de mesure d'Atmo Grand-Est à Metz.

II.2.9 Strasbourg

Strasbourg est une agglomération principalement urbanisée, représentant 26 % de la Communauté Urbaine de Strasbourg (CUS) avec un fort tissu agricole couvrant 40 % de la CUS. Elle compte également cinq sites industriels majeurs. La ville est desservie par deux axes routiers importants, l'autoroute A35-A4 (axe nord/sud) et la route du Rhin (axe est/ouest). Il existe également des liaisons ferroviaires, avec une gare TER et une gare TGV à Strasbourg, ainsi qu'un aéroport international à Entzheim et un port fluvial à Strasbourg.

En ce qui concerne les données météorologiques et topographiques, Strasbourg connaît un climat semi-continental, avec des précipitations faibles et un ensoleillement limité. Les directions de vent privilégiées sont le sud-sud-ouest et le nord-nord-est, et les masses d'air proviennent majoritairement selon l'axe des vents mais également une influence des masses d'air d'Europe centrale. Deux stations de mesure de Strasbourg sont utilisés ici, Danube et Clémenceau.

La station Danube est située dans le quartier Neudorf, au sud-est de Strasbourg, et est en fonction depuis décembre 2019 jusqu'à aujourd'hui. Quant à la station Clémenceau, sous l'influence du trafic urbain, elle se trouve au nord-ouest de Strasbourg et a été opérationnelle de décembre 2019 à mai 2020.

Le quartier Neudorf où se trouve la station Danube est un écoquartier en cours de construction. Il est entouré de quartiers résidentiels au sud et au nord, avec une zone d'activités commerciales comprenant notamment des restaurants. À l'est de la station, se trouvent également un port fluvial et un axe majeur (l'avenue du Rhin) à moins de 100 m.

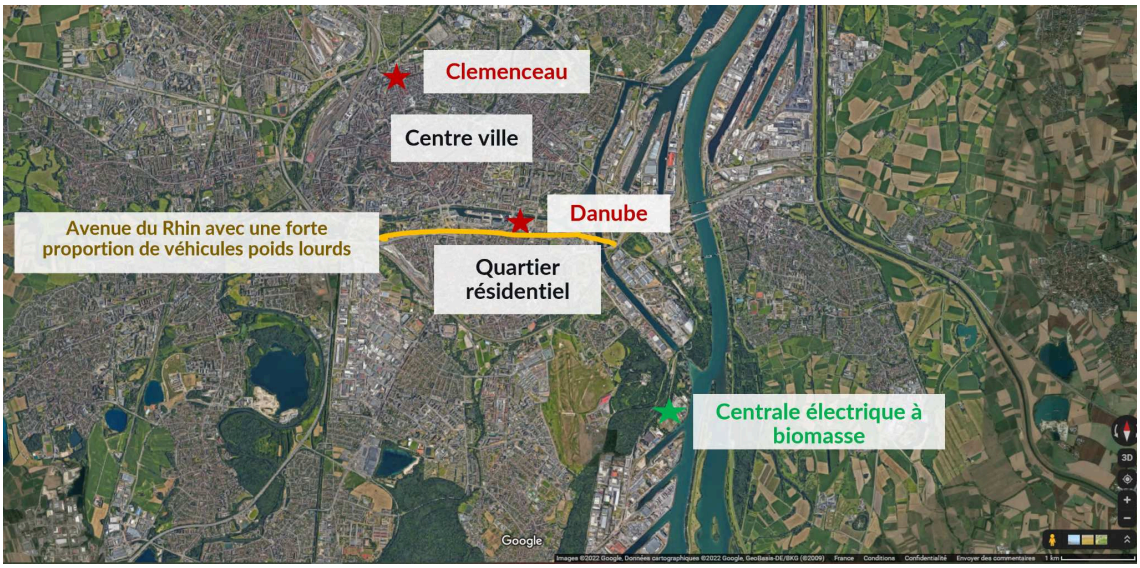

Figure II.11 : Carte précisant la localisation des deux stations de Strasbourg.

II.2.10 Talence

La station de Talence est une station de fond urbain, en retrait des axes de circulation importants. C'est une station de référence pour la surveillance des particules. Talence fait partie de l'aire métropolitaine de Bordeaux, qui comprend 73 communes. C'est l'une des communes les plus densément peuplées de la région, avec plus de 5 312,5 habitants/km² (44 359 habitants) en 2020. C'est une ville très urbanisée avec un secteur tertiaire dominant. En revanche, les activités industrielles et agricoles sont très faibles. Elle est entourée de parcs naturels régionaux, notamment la forêt des Landes de Gascogne au sud-ouest et le Parc du Médoc au nord-ouest.

Figure II.12 : Carte et image satellite précisant la localisation de la station Talence à grande échelle (gauche) et à petite échelle (droite).

II.2.11 Poitiers

La station Poitiers Augouard est une station de fond urbain située rue Augouard dans le centre-ville de Poitiers. L'agglomération de Poitiers, située à mi-chemin entre Paris et Bordeaux, est une zone urbaine densément peuplée avec 90 033 habitants en 2020. La station de mesure joue un rôle important en tant que station de référence pour la surveillance des particules fines dans la région. Elle est équipée d'un AE33 depuis 2014 et d'un ACSM depuis 2015 pour analyser en continu la composition chimique des particules fines dans l'air ambiant. En complément de ces mesures, la station effectue également des mesures de polluants gazeux.

Figure II.13 : Carte et image satellite précisant la localisation de la station Poitiers Augouard à grande échelle (gauche) et à petite échelle (droite).

II.2.12 Rennes

La station “Pays-Bas” à Rennes est une station urbaine de fond qui a été créée le 30 août 2012. Rennes est localisée au nord-ouest de la France et est le chef-lieu de la région Bretagne. C’est une commune peuplée de 354 000 habitants en 2020. Rennes se situe à la jonction de la liaison Manche-Atlantique et est caractérisée par un climat océanique. Au niveau de la métropole de Rennes, les transports routiers et de l'industrie ont des contributions moindres. En revanche, l'agriculture et le secteur résidentiel jouent un rôle plus important dans les émissions de particules PM_{10} et $PM_{2,5}$ (AASQA, 2022).

La station est située au sud de Rennes, dans un quartier résidentiel. Ce quartier est desservi par le métro et comprend des habitats collectifs, certains étant reliés au réseau de chaleur de la chaufferie biomasse. À proximité de la station, on trouve un chemin piétonnier non goudronné ainsi qu'un parking au sud-est.

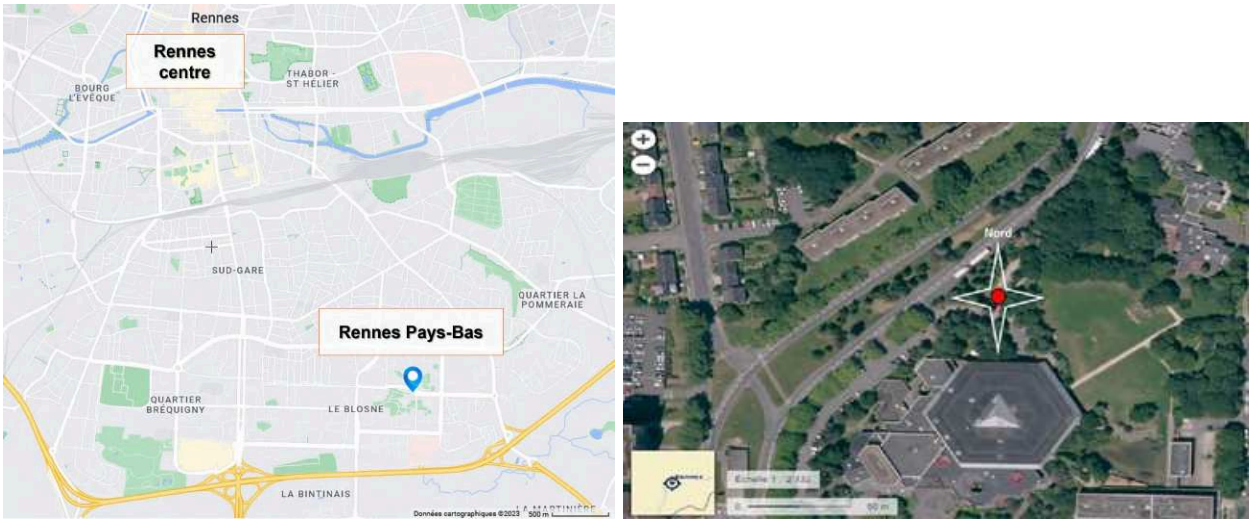

Figure II.14 : Carte (gauche) et image satellite (droite) précisant la localisation de la station Rennes Pays-Bas.

II.2.13 Marseille-Longchamp

La station de Marseille-Longchamp est un site de fond urbain clé pour l'évaluation et la surveillance de la qualité de l'air dans la ville de Marseille, située dans le sud de la France et faisant partie du réseau d'Atmo Sud. La station est opérationnelle depuis 1995 et est située au cœur du quartier urbain Longchamps, qui est caractérisé par une densité de population élevée et une activité socio-économique dynamique. En raison de sa localisation urbaine, la station est exposée à diverses sources de pollution, notamment les émissions provenant du trafic routier, de l'industrie et des activités résidentielles. Marseille est une ville portuaire importante et abrite également des infrastructures industrielles, ce qui peut contribuer à la pollution atmosphérique. C'est une station qui a émergé de la collaboration étroite entre AtmoSud et le laboratoire de Chimie de l'Environnement (LCE) d'Aix-Marseille Université.

Figure II.15 : Image satellite précisant la localisation de la station de Marseille Longchamp (en haut) et photographies (crédit : Atmo Sud) d'une vue extérieure et intérieure de la station de mesure (en bas).

II.2.14 Instrumentation déployée aux sites d'étude

Le tableau ci-dessous résume l'année de démarrage des observations ACSM correspondant aux espèces chimiques des PM_1 (particules fines de diamètre inférieur à 1 µm) non réfractaires (NR-PM_1 : organiques OA, nitrate NO_3^-, sulfate SO_4^{2-}, ammonium NH_4^+ et chlorure Cl^-), et de l'AE33 (carbone suie ou *Equivalent Black Carbon* ; eBC). Il présente aussi les mesures supplémentaires de polluants gazeux et particulaires sur chaque station. Dans cette étude, nous avons utilisé les concentrations massiques en PM_{10} et surtout $PM_{2.5}$ (dont le diamètre aérodynamique est inférieur à 10 et 2,5 µm respectivement), ainsi que les mesures d'oxydes d'azote (NOx). Les autres mesures sont mentionnées à titre indicatif mais n'ont pas été utilisées

en raison soit de leur indisponibilité sur la période de mesures ou sur un nombre de sites suffisants, soit de leur plus faible résolution temporelle.

Tableau II.2 : Données disponibles dans les stations de mesure

Site	Date de démarrage[1]	PM_{10}	$PM_{2.5}$	eBC	NR-PM_1	NO_x	O_3	Gran.	Filtres	COV
ATOLL	2016	✔	✔	✔	✔	✔[2]	✔[2]	✔	☒	☒
SIRTA	2015	✔	✔	✔	✔	✔	✔	✔	✔	☒
Paris Les Halles	2019	✔	✔	✔	✔	✔	✔	✔	✔	✔
BPEst	2020	✔	✔	✔	✔	✔	☒	✔	✔	✔
Genn.	2016	✔	✔	✔	✔	✔	☒	☒	✔	✔
Creil	2015	✔	✔	✔	✔	✔	✔	☒	✔	☒
Lyon	2015	✔	✔	✔	✔	✔	✔	☒	✔	✔
Metz	2015	✔	✔	✔	✔	✔	☒	☒	✔	☒
Strasbourg	2019	✔	✔	✔	✔	✔	☒	✔	✔	☒
Talence	2015	✔	✔	✔	✔	✔	☒	✔	✔	☒
Poitiers	2015	✔	✔	✔	✔	✔	✔	☒	✔	☒
Rennes	2020	✔	✔	✔	✔	☒	☒	☒	☒	✔
Marseillle	2017	✔	✔	✔	✔	✔	✔	✔	✔	✔

[1] pour les mesures ACSM
[2] depuis le site Lille Fives situé à environ 4,5 km

II.3 Instrumentation

Les stations présentées précédemment sont équipées de plusieurs instruments de mesure de la composition chimique en quasi temps réel. Dans cette partie, une description détaillée des instruments ayant fourni les données utilisées dans cette thèse sera présentée.

II.3.1 Aerosol Chemical Speciation Monitor (ACSM)

L'ACSM, développé par Aerodyne Research Inc., est basé sur la technologie de spectrométrie de masse à vaporisation thermique, suivie d'une ionisation des espèces par impact électronique. Il mesure en temps réel et à haute résolution temporelle (~30 minutes) la composition chimique des particules submicroniques non-réfractaires et permet des mesures à long terme avec moins de surveillance et d'intervention technique (Watson, 2017).

Toutes les stations présentées dans ce travail sont équipées d'ACSM de type 'quadrupole' (Q-ACSM, Ng et al., 2011), à l'exception du site de Marseille qui est équipé d'un ACSM de type 'temps de vol' (ToF-ACSM, Fröhlich et al., 2013). Le Q-ACSM est le plus couramment utilisé car il répond bien aux besoins de la surveillance opérationnelle pour les AASQA, et il est moins complexe que le ToF-ACSM, même si la sensibilité du ToF-ACSM est meilleure.

Le schéma de fonctionnement de l'ACSM est illustré dans la Figure II.16. L'air est introduit par un orifice critique de 100 μm, puis il passe à travers une lentille aérodynamique qui concentre l'aérosol en un faisceau d'environ 1 mm de diamètre. Ce faisceau est ensuite dirigé vers un vaporiseur maintenu à une température de 600 °C, ce qui permet de transférer une large partie des espèces contenues dans les particules en phase gazeuse. Les molécules en phase gazeuse sont ensuite ionisées par impact électronique à une énergie de 70 eV. Ce processus de vaporisation et d'ionisation entraîne la fragmentation des molécules (Watson et al., 2020). Les ions fragmentés sont guidés par des lentilles ioniques vers un filtre de masse quadrupolaire ou à temps de vol selon le modèle de l'ACSM.

Classiquement, la ligne d'échantillonnage Q-ACSM est orientée verticalement avec un tube en acier inoxydable tout au long de la ligne pour réduire les pertes de particules. Cette ligne est équipée en amont d'une tête d'échantillonnage $PM_{2,5}$ (URG-2000-30ED, URG Corp.) ainsi que d'une membrane Nafion afin de réduire l'humidité relative de l'échantillon en maintenant celle-ci en dessous de 40 %.

Les concentrations massiques sont calculées à partir d'une différence entre les signaux mesurés lorsque l'air contenant l'aérosol est échantillonné directement et les signaux mesurés lorsque le flux d'échantillon ambiant passe à travers un filtre pour éliminer l'aérosol. Cette différence

élimine du signal de l'air les composés de fond en phase gazeuse qui sont présents dans les deux modes (Watson et al., 2020). Une résolution temporelle d'environ 30 min a été utilisée pour chaque ensemble de données Q-ACSM, tandis que pour le ToF-ACSM, les données ont été acquises avec une résolution de 10 min. Tous les ACSM exploités dans le cadre du programme CARA ont été équipés d'une lentille aérodynamique PM_1 et d'un vaporisateur standard. Conformément à Ng et al. (2011), des valeurs des limites de détection de 0,284, 0,148, 0,024, 0,012 et 0,011 µg m^{-3} ont été appliquées pour NH_4, Org, SO_4, NO_3 et Cl, respectivement.

Les concentrations massiques des espèces sont obtenues selon l'équation (1) ci-dessous :

$$C_s = \frac{Q_{cal} \times G_{cal}}{Q \times G} \times \frac{CE}{T_{m/z}} \times \frac{10^{12}}{RF_{NOs} \times RIE_s} \sum_{all\ i} IC_{s,i} \qquad \text{(Eq. 1)}$$

où :

- C_s est la concentration massique des espèces (en µg m^{-3})
- Q_{cal} et Q sont les débits d'échantillonnage pendant la calibration et la mesure, respectivement
- Gcal et G sont les gains pendant la calibration et la mesure, respectivement
- CE est l'efficacité de collecte des particules par l'ACSM
- RIE_s est l'efficacité d'ionisation relative de chaque espèce
- RF est le facteur de réponse du nitrate (amps /µg m^{-3})
- $T_{m/z}$ est l'efficacité de transmission des ions

Le facteur de réponse (RF) du NO_3 et les efficacités d'ionisation relative (RIE) du NH_4 et du SO_4 sont déterminés par l'étalonnage de l'ACSM, qui se fait en injectant des aérosols de nitrate d'ammonium (NH_4NO_3) et de sulfate d'ammonium ($(NH_4)_2SO_4$) purs dans l'ACSM à une taille de 300 nm (Freney et al., 2019). Une description détaillée des procédures d'étalonnage appliquées est disponible dans un document spécifique édité au niveau national (LCSQA, 2022) et en accord également avec les procédures opérationnelles standard d'ACTRIS, disponibles en ligne (https://www.actris-ecac.eu/measurement-guidelines.html).

Les espèces mesurées par l'ACSM correspondent à une somme de fragments m/z attribués totalement ou partiellement à chaque espèce à l'aide d'un tableau de fragmentation intégré dans

le logiciel d'acquisition (Allan et al., 2004, Canagaratna et al., 2007). Les concentrations massiques quantitatives de chaque espèce chimique mesurée sont obtenues en appliquant un facteur de correction de l'efficacité de collecte (CE) pour tenir compte de la détection incomplète des espèces particulaires lors de l'utilisation d'un vaporiseur standard (Middlebrook et al., 2011).

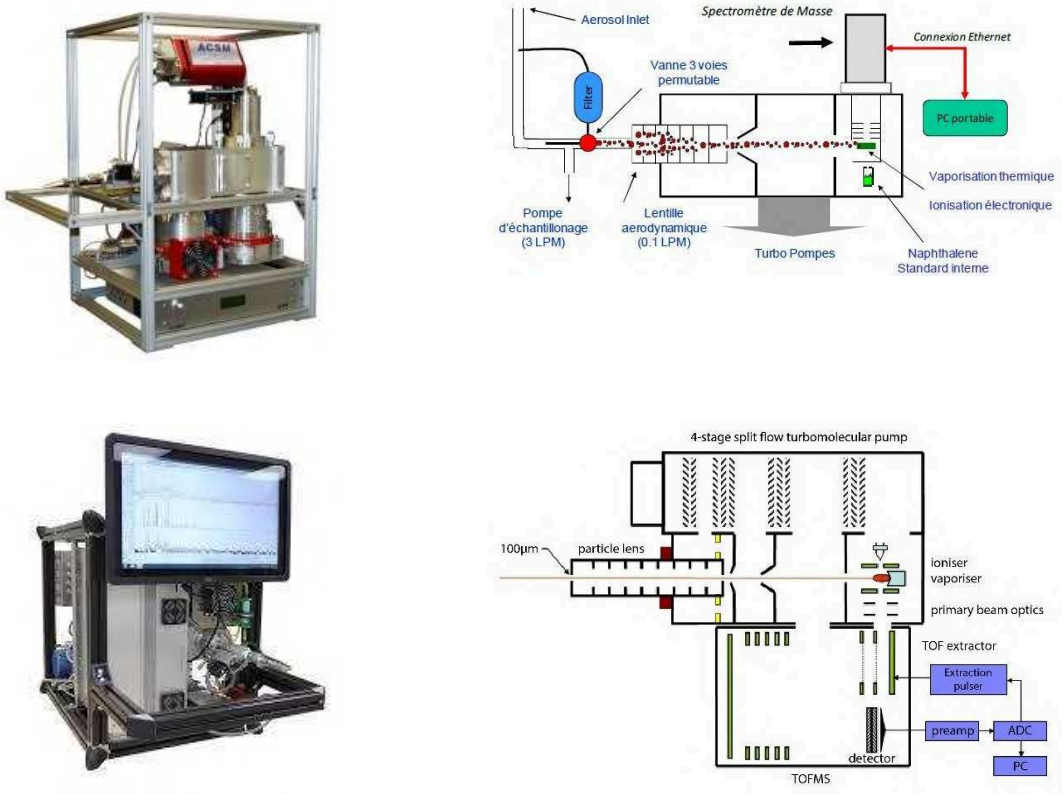

Figure II.16: Illustration à gauche et diagramme fonctionnel à droite pour le Q-ACSM en haut et le Tof-ACSM en bas.

II.3.2 L'Aethalomètre AE33

L'Aéthalomètre multi-longueurs d'onde (modèle AE33, Magee Scientific, USA) permet la quantification des concentrations du carbone suie à travers la mesure des coefficients d'absorption des aérosols, en se basant sur le taux de variation de l'atténuation de la lumière transmise à 880 nm à travers un filtre chargé en particules. Comme recommandé par Petzold et al. (2013), le

terme de carbone suie équivalent (ou eBC) est utilisé pour désigner ces concentrations dérivées de mesures d'absorption optique. Le schéma de fonctionnement de l'AE33 est illustré en Figure II.17 et le principe de mesure décrit en détail par Drinovec et al. (2015). Brièvement, l'instrument collecte les particules en continu en faisant passer le flux d'air chargé en aérosols à travers deux zones de la bande filtrante, avec deux débits différents ce qui entraîne des taux d'accumulation différents de l'échantillon. La transmission de la lumière à travers la bande filtrante contenant l'échantillon est mesurée à sept longueurs d'onde optiques allant du proche ultraviolet (UV) au proche infrarouge (IR) (370, 470, 525, 590, 660, 880 et 950 nm), par rapport à la transmission à travers une partie non chargée de la bande filtrante servant de référence. Les deux résultats sont combinés mathématiquement pour éliminer les non-linéarités et fournir une absorption lumineuse compensée des particules et une concentration massique de eBC (Drinovec et al., 2015). Les mesures AE33 ont été réalisées à une résolution temporelle d'1 min dans la fraction PM_1 pour les deux stations ATOLL et SIRTA, et dans la fraction $PM_{2.5}$ pour les autres stations du programme CARA, en accord avec les directives établies par le LCSQA (LCSQA, 2020).

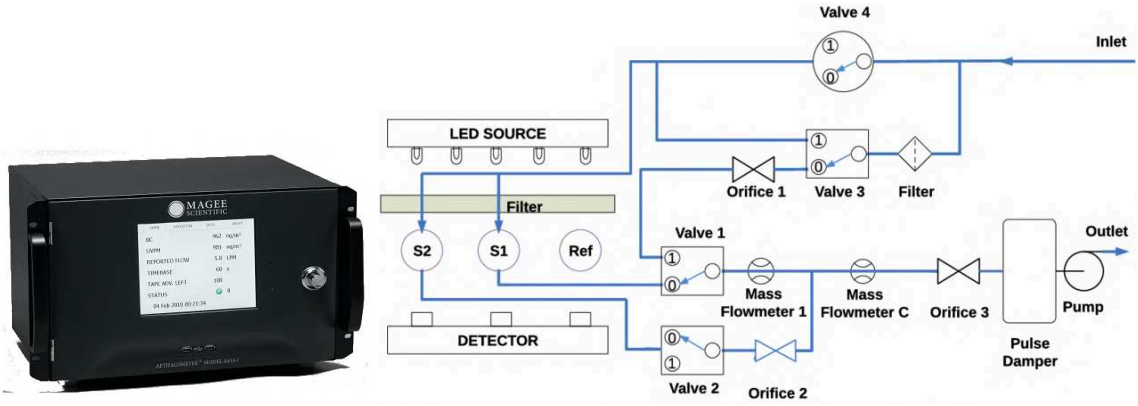

Figure II.17: Aethalomètre AE33 et schéma de fonctionnement (Drinovec et al., 2015).

Les coefficients d'absorption (b_{abs}) à chaque longueur d'onde sont calculés à partir de l'équation (2) selon les recommandations actuelles d'ACTRIS[1] :

$$b_{abs} = \frac{(eBC)_{raw} \times MAE}{H^*} \quad \text{(Eq. 2)}$$

[1] https://actris-ecac.eu/particle-light-absorption.html

où $(eBC)_{raw}$ est la valeur de concentration massique en eBC donnée par l'instrument, MAE (*Mass Absorption Efficiency*) représente le coefficient d'absorption massique spécifique correspondant à chaque longueur d'onde (déterminé empiriquement par le fabricant) (Tableau 2), et H* (sans unité) est le facteur d'harmonisation approprié pour tenir compte des effets de diffusion multiple du filtre, fixé à 1,76 pour les dispositifs AE33 utilisant le ruban filtrant M8060.

Les concentrations de eBC ont ensuite été normalisées par un coefficient d'absorption massique constant MAC_ACTRIS (Tableau II.2), récemment introduit dans le cadre du programme de recherche européen RI-URBANS (Savadkoohi et al., 2023), comme suit :

$$eBC = \frac{b_{abs}}{MAC\_ACTRIS} \quad \text{(Eq. 3)}$$

Tableau II.3 : Coefficients d'absorption massique associés à chaque longueur d'onde.

Longueur d'onde (nm)	370	470	520	590	660	**880**	950
MAE ($m^2\ g^{-1}$)	18,47	14,54	13,14	11,58	9,89	**7,77**	7,19
MAC_ACTRIS ($m^2\ g^{-1}$)	17,85	14,05	12,70	11,19	10,00	**7,50**	6,95

Les concentrations de eBC sont obtenues à une longueur d'onde de 880 nm, recommandée pour les mesures du carbone suie. En effet, cette longueur d'onde est moins sujette aux artefacts causés par d'autres composés absorbant la lumière, tels que les poussières désertiques (Rivellini et al., 2017) et certains composés organiques (notamment le carbone brun, BrC, qui absorbe la lumière à des longueurs d'onde plus courtes dans le spectre UV).

La répartition des sources d'eBC est basée sur le modèle de Sandradewi et al. (2008). Ce modèle considère le coefficient d'absorption de l'aérosol comme la somme des fractions liées à la combustion de biomasse et des combustibles fossiles, et tire parti de leur différence de dépendance d'absorption avec la longueur d'onde, avec la combustion du bois qui présente une absorption marquée dans l'UV (*Angström Absorption Exponent* ; AAE élevé) par rapport aux combustibles fossiles (faible AAE). Pour les différents sites, la séparation entre eBC_{ff} et eBC_{wb} a été déterminée en utilisant les valeurs fournies par le fabricant de l'AE33, soit $AAE_{ff} = 1$ et $AAE_{wb} = 2$ (Drinovec et al., 2015).

II.4 Procédures de traitement et validation des données ACSM

Les données ACSM collectées à partir de l'instrument ACSM nécessitent un contrôle qualité et une validation technique, suivis d'une évaluation environnementale impliquant une comparaison avec d'autres données complémentaires.

II.4.1 Contrôle qualité et validation technique

Le contrôle qualité des données ACSM a été fait via le module 'acsm local' sous Igor Pro Version 6.37. Plusieurs étapes ont été suivies pour permettre une validation des données ACSM. Certaines étapes sont également expliquées dans le Tableau 2 du guide méthodologique du LCSQA (LCSQA, 2018).

- **Vérification des paramètres techniques de l'instrument**

Cette vérification englobe plusieurs paramètres techniques de l'instrument, entre autres : la pression d'entrée (maintenue à environ 1.3 ± 0.2), la température du vaporiseur (régulée à 600 ± 30 °C), les tensions SEM (*Secondary Electron Multiplier*) et *Heater Bias*, l'émission du filament, la valeur de l'*airbeam* (alignée sur environ 10^7 ± 30% ions/s) et l'humidité relative (qui doit être inférieure à 40 %). Tout au long de ce processus, la plus grande attention a été portée à l'identification de toute variation brutale ou de tout écart pouvant résulter d'un mauvais réglage. Tous les points de données présentant de telles incohérences ont été systématiquement répertoriés en vue d'une invalidation potentielle, afin de garantir que seules des données précises et fiables soient incluses dans les exploitations de données ultérieures.

- **Vérification des paramètres d'étalonnage**

Les paramètres d'étalonnage, à savoir le RF de NO_3 et les RIE de SO_4 et de NH_4, ainsi que la CE, ont été vérifiés, notamment car sur des séries pluri-annuelles, ces paramètres sont susceptibles de changer. Cette approche a permis de s'assurer que le processus de nettoyage des données est adapté aux changements dans les valeurs de RF et RIE, améliorant ainsi la précision et la fiabilité de l'ensemble des données obtenues.

- **Nettoyage des données (suppression des pics air/eau)**

Dans cette étape, une évaluation approfondie des ions correspondant à l'eau (m/z 18, H_2O^+) et à l'air (m/z 28, N_2^+ ; 32, O_2^+ ; et 40, Ar^+) est effectuée. Dans les cas où ces signaux d'air et/ou d'eau

présentent des anomalies (pics sporadiques), ils sont identifiés et ensuite invalidés par des procédures de nettoyage automatisées dans le logiciel Igor Pro. Cette étape critique implique également une analyse critique d'autres ions, en particulier, ceux associés aux chlorures (m/z 35, Cl^+ ; et 36, HCl^+) permet de vérifier tout artefact de mesure possible pouvant être causé par les sels marins (Tobler et al., 2020).

- **Application de diverses corrections**

L'étape finale consiste en l'application de divers facteurs correctifs qui sont automatiquement calculés dans le logiciel de traitement des données. Le premier, *Time series correction* (TS), corrige la variabilité de la masse de référence (*airbeam* N_2) dont le signal doit théoriquement rester constant en air ambiant ; une période de référence est choisie, où le débit ne fluctue pas significativement et où la valeur d'*airbeam* est proche de celle attendue (~10^7 ions/s), et la série temporelle de toutes les espèces est normalisée par le signal moyenné de cette période de référence. Le deuxième, *Relative Ion Transmission (RIT)*, permet de corriger l'efficacité de transmission du spectromètre de masse de l'ACSM en se basant sur un étalon interne, le naphtalène, qui diffuse à partir d'un orifice critique situé sous la zone de vaporisation/ionisation, et ne se trouve pas dans les espèces particulaires en raison de sa forte volatilité. Le logiciel utilise les signaux de 5 pics de naphtalène (m/z 51, 62, 76, 102 et 128), dont il calcule la valeur moyenne et l'écart-type sur l'ensemble des mesures de la période considérée ; les cinq valeurs sont ensuite normalisées par la valeur obtenue à m/z 51 (RIT = 1). Une courbe de régression (typiquement exponentielle) est ensuite calculée, où les m/z inférieurs ou égaux à 51 ont un RIT de 1, et ceux supérieurs ou égaux à 148 ont un RIT de 0,05. Un souci mis en évidence dans ce travail est l'existence de périodes où les valeurs de RIT sont problématiques avec certains instruments plus récents, conduisant généralement à des écarts-types plus élevés, mais qui sont détectés tardivement en raison du moyennage des valeurs. Nous avons donc automatisé une procédure pour vérifier la variabilité des séries temporelles des 4 pics de naphtalène au-delà de m/z 51 et ainsi pouvoir exclure les données qui présentaient des valeurs aberrantes. Une fréquence trop élevée de ce type de souci n'empêche pas nécessairement l'estimation de la composition chimique des aérosols, mais limite l'analyse plus approfondie des données, comme la *Positive Matrix Factorization*, par exemple.

Enfin, les concentrations massiques sont corrigées de l'efficacité de collecte qui dépend de la composition (CDCE, *Composition-Dependent Collection Efficiency*) en se basant sur l'algorithme de Middlebrook (Middlebrook et al., 2011) mais en fixant une valeur minimale de CE à 0.5, qui a été déterminée lors de la comparaison inter-laboratoires de 2013.

II.4.2 Validation environnementale

Cette étape consiste d'un premier temps à vérifier la répartition des espèces en vérifiant l'équilibre ionique et dans un deuxième temps à comparer avec les mesures d'autres instruments disponibles dans la station (e.g. concentrations massiques en PM_1, $PM_{2.5}$).

La vérification de l'équilibre ionique est une étape très importante dans la validation des données ACSM car elle permet de confirmer la robustesse des facteurs de calibration des espèces inorganiques (RF, RIE). Ceci implique l'évaluation de la corrélation entre les concentrations de NH_4 mesurées et prédites, avec une pente cible se situant idéalement dans l'intervalle de 1 ± 10%.

Les concentrations de NH_4 mesurées et prédites font l'hypothèse d'une neutralisation complète des ions ammonium par les nitrates (NH_4NO_3), sulfates ($(NH_4)_2SO_4$) et chlorures (NH_4Cl), et sont calculées selon les équations (4) et (5) :

$$NH4_{mesuré} = \frac{[NH4]}{18} \quad \text{(Eq. 4)}$$

$$NH4_{prédit} = \frac{[NO3]}{62} + 2\frac{[SO4]}{96} + \frac{[Cl]}{35{,}45} \quad \text{(Eq. 5)}$$

Les données corrigées des espèces chimiques ACSM ont été comparées avec les mesures $PM_{2.5}$ pour vérifier la cohérence des données. Les concentrations massiques en PM_1 (NR-PM_1 + eBC) ont été recalculées en combinant les mesures ACSM (NR-PM_1) et AE33 (eBC), et comparées aux mesures de $PM_{2.5}$ pour chaque station au cours de la période d'étude.

II.5 Export des matrices de concentrations organiques et leurs incertitudes

Cette étape, exécutée dans le même logiciel 'acsm local' (onglet 'Export'), permet d'exporter les matrices de concentrations organiques et leurs incertitudes pour l'analyse ultérieure des sources

de l'aérosol organique (voir section 2.6.1) . L'incertitude e_I associée à un signal I est calculée automatiquement sur la base d'une distribution de Poisson :

$$e_I = \alpha \sqrt{I} \quad \text{(Eq. 6)}$$

avec α un facteur appliqué pour tenir compte du fait que le signal d'un seul ion n'est pas une constante mais provient d'une distribution gaussienne de l'impulsion. En combinant cette gaussienne avec la distribution de Poisson, on donne à α la valeur de 1,2 (Allan et al., 2003).

Pour l'ACSM, le signal I provient de la différence entre le signal 'open' (mode échantillon/non filtré) et 'closed' (mode filtré) et par la suite l'erreur est associée à la différence entre ces signaux plus le bruit électronique selon les équations suivantes :

$$I = I_{open} - I_{closed} \quad \text{(Eq. 7)}$$

$$e_I = \sqrt{(e^2_{I_{open}} + e^2_{I_{closed}}) + e^2_{Noise}} \quad \text{(Eq. 8)}$$

avec :

$$e_{I_{open}} = 1,2 \sqrt{I_{open}} \quad \text{(Eq. 9),}$$

$$e_{I_{closed}} = 1,2 \sqrt{I_{closed}} \quad \text{(Eq. 10)}$$

$$e_{Noise} = I_{closed,\, m/z} \text{ ; pour le Q-ACSM} \quad \text{(Eq. 11a)}$$

$$e_{Noise} = \sqrt{(I^2_{open,\, m/z} + I^2_{closed,\, m/z})} \text{ ; pour le ToF-ACSM} \quad \text{(Eq. 11b)}$$

pour un m/z sans signal réel (m/z 140 pour les Q-ACSM ; m/z 219 pour les ToF-ACSM).

Plus de détails sur cette procédure d'évaluation des incertitudes et les éventuelles corrections apportées sont données en Annexe 2.

A l'issue de cette étape, les deux matrices sont exportées (pour cette étude on considère les m/z jusqu'à 100) et le temps (en UTC et Local Time). L'étude de ces jeux de données a également permis de mettre en évidence un souci dans le paramètre 'ACSM_LocalTime' qui n'est modifié que lorsque le spectromètre de masse Prisma est arrêté/redémarré après un changement d'heure,

notamment été/hiver (donc parfois des semaines/mois plus tard). Par conséquent, nous avons systématiquement corrigé le Local Time car ce paramètre conditionne ensuite les profils journaliers calculés des espèces et des fragments organiques.

Il faut noter également que dans le logiciel 'acsm local', la correction CDCE appliquée sur les espèces chimiques ne l'est pas automatiquement sur les matrices des fragments organiques et de leurs incertitudes ; c'est pourquoi nous avons appliqué cette correction manuellement en divisant toutes les valeurs par CDCE.

Ce travail a finalement permis de détecter, pour certains instruments, des fragments avec des signaux très bruités (rapport S/N très faible ; faibles concentrations et incertitudes élevées) qui induisent par la suite une part plus forte de signal non expliqué pour ces fragments lors de la factorisation par matrice positive. Selon Paatero (2010), une variable peut être considérée comme expliquée si sa variation inexpliquée ne dépasse pas 25 %. Typiquement, dans les cas mentionnés ci-dessus, cette valeur dépasse 40 % ; néanmoins les masses concernées restant faibles, nous n'avons pas observé de différence significative dans les résultats avec ou sans ces m/z.

II.6 Etude des sources

Cette section est axée sur une introduction au principe de l'étude des sources et à la méthode PMF (*Positive Matrix Factorisation*), en présentant d'abord sa théorie, puis l'approche PMF glissante (ou *rolling PMF*).

II.6.1 Répartition des sources : Principe de la modélisation source-récepteur

Comprendre la contribution de chaque source à la pollution de l'air est essentiel pour mettre en place des politiques efficaces de contrôle de la qualité de l'air et pour évaluer les effets sur la santé humaine et l'environnement. Dans ce sens, les modèles sources-récepteur sont utilisés pour comprendre et quantifier la répartition des sources de pollution (Belis et al., 2014). Le principe de cette modélisation repose sur l'idée de démêler les contributions individuelles des différentes sources de pollution à un signal observé ou à un niveau de concentration dans un environnement donné. Elle est basée sur le principe de la conservation de masse entre les sources d'émissions et les sources des polluants identifiés (Watson et al., 1984), simplifié dans l'équation (18) :

$$X = G \times F + E \quad \text{(Eq. 18)}$$

où X est la matrice des concentrations mesurées sur un site récepteur et qui peuvent être expliquées comme le produit linéaire d'une matrice source (F) et d'une matrice contributrice (G), plus une matrice résiduelle (E). La PMF (Paatero et Tapper, 1994) est parmi les modèles sources-récepteur les plus utilisés dans la communauté.

II.6.2 La méthode PMF

La méthode PMF est une technique statistique couramment utilisée dans les études de répartition des sources pour identifier et quantifier les sources de la pollution atmosphérique. La PMF repose sur le principe selon lequel les échantillons d'air collectés sur un site (récepteur) peuvent être décomposés en une combinaison linéaire de profils de facteurs de sources statiques et de leurs contributions en fonction du temps. Ces facteurs nous renseignent sur la/les sources potentielles des polluants impactant ce site.

En utilisant des techniques d'optimisation, la PMF cherche à trouver les valeurs optimales des deux matrices, de manière à minimiser l'écart entre les valeurs mesurées et les valeurs estimées. Les facteurs identifiés par la PMF sont interprétés pour les attribuer à des sources de pollution. Cela peut impliquer l'analyse de la variabilité temporelle des profils, la connaissance des sources locales, et l'utilisation de données supplémentaires pour une interprétation plus précise.

La PMF est basée sur la même équation que précédemment :

$$x_{ij} = \sum_{k=1}^{p} g_{ik} f_{kj} + e_{ij} \quad \text{(Eq. 19)}$$

L'objectif est de déterminer le nombre de facteurs p, les profils des facteurs de chaque source f_{kj} et leurs contributions au cours du temps g_{ik}.

La PMF se base sur un algorithme interactif des moindres carrés pour l'obtention des deux matrices F et G. Cet algorithme vise à minimiser itérativement une quantité Q qui représente la somme totale des carrés des résidus e_{ij} du modèle, pondérés par les incertitudes de mesure σ_{ij} pour tous les points ij.

$$Q = \sum_{i=1}^{n}\sum_{j=1}^{m}\left(\frac{e_{ij}}{\sigma_{ij}}\right)^2 \quad \text{(Eq. 20)}$$

L'application de la PMF peut entraîner des difficultés qui sont liées à l'ambiguïté rotationnelle, car différentes combinaisons de G et F peuvent donner des valeurs similaires de Q, dont certaines peuvent contenir des facteurs mixtes et/ou des solutions incohérentes du point de vue environnemental. Pour remédier à ce problème, et si des sources sont connues a priori pour le site étudié, l'approche par "*a-value*" permet de contraindre les profils de facteurs prévus ou les séries temporelles à l'aide du solveur ME-2 dans le logiciel SoFi Pro (Canonaco et al., 2013). Cette approche permet de faire varier chaque variable d'un spectre de masse d'un certain pourcentage selon la valeur de "a" (qui est comprise entre 0 - aucune variabilité - et 1 - 100% de variabilité autorisée) par rapport à un spectre de référence, comme décrit dans les équations (21) et (22):

$$f_{solution} = f_{reference}\,(1 \pm a) \quad \text{(Eq. 21)}$$

$$g_{solution} = g_{reference}\,(1 \pm a) \quad \text{(Eq. 22)}$$

De plus, afin de déterminer des solutions PMF robustes et stables et d'évaluer les incertitudes statistiques du modèle, la méthode de rééchantillonnage "*Bootstrap*" est mise en œuvre. Cette méthode implique la création de sous-échantillons aléatoirement à partir des données d'entrée, permettant ainsi de vérifier si ces sous-échantillons conduisent aux mêmes solutions et contributions de facteurs que celles identifiées précédemment (Efron, 1979).

La méthode PMF est appliquée aux données d'aérosol organique dans le but de quantifier les sources et les origines de cette fraction. La matrice d'entrée du modèle est constituée des concentrations massiques des fragments organiques m/z et leurs incertitudes associées. Ces matrices sont obtenues dans le logiciel 'acsm local' et ont été vérifiées avant leur export (comme expliqué dans la section précédente).

La PMF a été appliquée en utilisant l'outil SoFi Pro v8, développé par Datalystica, sous Igor Pro v8 en utilisant le solveur ME-2.

II.6.3 L'approche PMF glissante

La PMF classique considère que les profils de source sont fixés et constants sur toute la période d'étude. Ceci n'est pas le cas pour les mesures des aérosols sur le long terme qui sont plutôt variables dans le temps, notamment intersaisonnier. C'est pourquoi dans cette étude, une méthode par PMF glissante récemment développée a été utilisée (Canonaco et al., 2021). Elle consiste à diviser la base de données en périodes plus courtes (par exemple des fenêtres d'un mois, décalées de sept jours, Figure II.18), ce qui présente l'avantage de permettre une certaine variabilité dans les profils des facteurs tout au long de la période d'observation, à travers les saisons et les années.

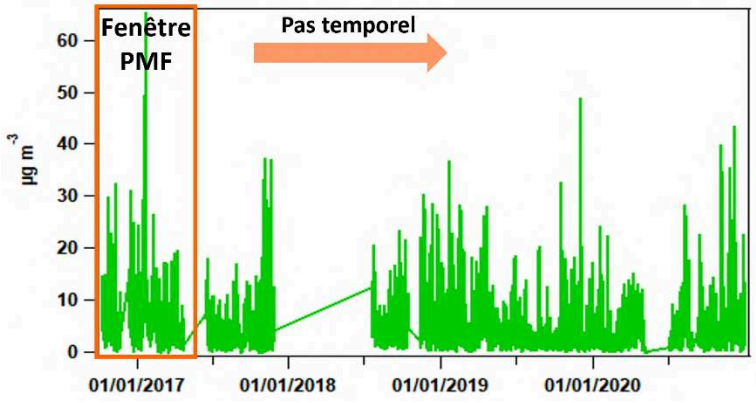

Figure II.18: Schéma de principe de la PMF glissante

Pour effectuer une analyse pluriannuelle, une PMF standard est d'abord réalisée par saison dans une année de référence pour (i) déterminer le nombre de facteurs attendus dans l'ensemble de la base de données et (ii) récupérer les spectres de référence des facteurs primaires. Ensuite, une PMF glissante est appliquée en combinant les contraintes de spectres sur les facteurs primaires et le bootstrapping. Un protocole a été défini dans le cadre de l'Action COST COLOSSAL (https://www.cost.eu/actions/CA16109/) par Chen et al. (2022) à laquelle les deux laboratoires du CERI EE et de l'Ineris ont participé. L'étude réalisée dans le cadre du *Working Group 2* a présenté une phénoménologie des sources d'aérosols organiques sur 22 sites de mesures (urbains et non urbains) à travers l'Europe, incluant 3 sites français : les deux plateformes d'observation ATOLL et SIRTA, et le site de Marseille Longchamps. La PMF glissante a été appliquée sur une année de données, généralement 2016/2017, suivant un protocole commun harmonisé. Cette méthode a été validée dans le cadre du même projet par Via et al. (2022) en comparant les deux méthodes, PMF classique par saison et PMF glissante, sur un nombre plus limité de sites

(incluant également ATOLL et SIRTA) ainsi qu'avec un jeu de données synthétiques. Cette étude a montré des résultats assez similaires pour les deux approches, bien que la PMF glissante permette d'obtenir des profils plus adaptés aux mesures en termes de degré de vieillissement des aérosols (comparaison de la différence des ratios entre les ions m/z 44 et m/z 43 des données d'entrée AO et des facteurs d'AO oxygéné). Une comparaison a également été effectuée pour les résidus et les corrélations avec les mesures externes, montrant que la PMF glissante induit de meilleures corrélations avec les mesures externes, en particulier pour les transitions entre saisons, et une minimisation des résidus, même si les résidus de type "*scaled residuals*" respectent la plage conseillée par le protocole harmonisé [-3, 3] pour les deux méthodes. Dans l'ensemble, les conclusions de cette étude confirment la robustesse des deux méthodes et démontrent l'efficacité globale de l'approche PMF glissante (plus précise et exacte, moins sujette à la subjectivité, moins coûteuse en temps de calcul et mieux adaptée aux analyses à long terme).

II.7 Organisation du travail

Ce travail a été réalisé en collaboration plus ou moins étroite avec les AASQA, en fonction des ressources dont elles disposaient ; le tableau ci-dessous résume les contributions de chacun.

Tableau II.4 : Étapes de réalisation du travail

	QA/QC des données	**PMF saisonnières**	**PMF glissante**
Genn.	Du 01/2018 au 09/2019 ✔ Hasna Chebaicheb	Du 09/2018 au 08/2019 ✔ Hasna Chebaicheb	Du 01/2018 au 09/2019 ✔ Hasna Chebaicheb
Paris Les Halles	Du 10/2019 au 12/2021 ✔ Hasna Chebaicheb	Du 10/2019 au 08/2020 ✔ Hasna Chebaicheb	Du 10/2019 au 12/2020 ✔ Hasna Chebaicheb
BPEst	Du 09/2021 au 12/2021 ✔ Hasna Chebaicheb	Du 09/2021 au 07/2022 ✔ Hasna Chebaicheb	Du 09/2021 au 07/2022 ✔ Hasna Chebaicheb
Creil	Du 01/2016 au 12/2017 ✔ Hasna Chebaicheb Du 01/2018 au 12/2021 ✔ Shouwen Zhang	Du 06/2016 au 05/2017 ✔ Hasna Chebaicheb Du 12/2019 au 11/2020 ✔ Shouwen Zhang ; échanges réguliers avec Hasna Chebaicheb	Du 01/2016 au 12/2021 ✔ Hasna Chebaicheb

Lyon	Du 03/2015 au 12/2021 ✔ Hasna Chebaicheb	Du 06/2018 au 05/2019 ✔ Hasna Chebaicheb	Du 03/2015 au 12/2021 ✔ Hasna Chebaicheb
Rennes	Du 01/2020 au 12/2021 ✔ Hasna Chebaicheb	Du 03/2020 au 02/2021 ✔ Hasna Chebaicheb	
Strasbourg Danube	Du 11/2019 au 12/2021 ✔ Mélodie Chatain	Du 12/2019 au 08/2020 ✔ Mélodie Chatain ; échanges réguliers avec Hasna Chebaicheb	Du 12/2019 au 12/2021 ✔ Hasna Chebaicheb
Strasbourg Clemenceau	Du 11/2019 au 04/2020 ✔ Mélodie Chatain	Du 11/2019 au 04/2020 ✔ Hasna Chebaicheb	
Metz	Du 01/2015 au 12/2021 ✔ Mélodie Chatain ; Vérification et export PMF ✔ Hasna Chebaicheb	Du 06/2018 au 05/2019 ✔ Hasna Chebaicheb	Du 03/2018 au 12/2021 ✔ Hasna Chebaicheb
Marseille	Du 02/2017 au 12/2021 ✔ Benjamin Chazeau	Du 02/2017 au 04/2018 ✔ Benjamin Chazeau	Du 02/2017 au 12/2021 ✔ Hasna Chebaicheb
Poitiers	Du 11/2015 au 12/2021 ✔ Hasna Chebaicheb	Du 06/2018 au 05/2019 ✔ Hasna Chebaicheb	Du 11/2015 au 12/2021 ✔ Hasna Chebaicheb
Talence	Du 11/2015 au 12/2021 ✔ Hasna Chebaicheb	Du 06/2018 au 05/2019 ✔ Hasna Chebaicheb	Du 11/2015 au 12/2021 ✔ Hasna Chebaicheb

Chapitre III. Etude de la composition chimique des particules fines à partir des données pluriannuelles à haute résolution temporelle sur 13 sites du programme CARA

III.1. Résumé de l'article 1

Le premier chapitre des résultats de cette thèse présente la phénoménologie des particules fines sur 13 sites (péri-)urbains en France, distribués dans 8 régions métropolitaines différentes. Les données présentées dans cette étude ont été obtenues à partir de mesures de l'ACSM et de l'AE33 collectées sur la période de 2015 à 2021. Ce travail a été réalisé en collaboration plus ou moins étroite avec les AASQA, en fonction des ressources dont elles disposaient ; les contributions de chacun ont été indiquées au Chapitre II, section II.7, Tableau II.3. Cet article présente un aperçu global de l'ensemble de ces données à l'échelle multi-annuelle, offrant une analyse des disparités géographiques dans la composition chimique des particules non réfractaires à savoir l'aérosol organique (AO), le nitrate (NO_3), l'ammonium (NH_4), le sulfate (SO_4), le chlorure non marin (Cl), ainsi que le carbone suie (*equivalent Black Carbon* ; eBC). Leurs principales variations saisonnières et journalières ont été également abordées.

Cet article reprend la description des stations et principes de mesure (ACSM et AE33) ainsi que des processus de traitement et de validation des données décrits en chapitre 2. Les mesures ACSM pour les espèces chimiques ont été traitées dans le logiciel "acsm local" en effectuant un traitement rigoureux de contrôle qualité, de validation technique et d'évaluation environnementale. Ce processus de traitement a été effectué conformément aux préconisations du LCSQA (LCSQA, 2018) et respecte les procédures standard d'exploitation des données fournies par ACTRIS[2] afin d'assurer la fiabilité de l'ensemble de ces données. De même, pour les données AE33, qui ont été traitées conformément aux recommandations du LCSQA (LCSQA, 2020) et en prenant en compte les récents travaux d'ACTRIS[3] et du projet recherche européen H2020 RI-Urbans[4] pour le calcul de la concentration d'eBC, en considérant un facteur d'harmonisation

[2] https://www.actris-ecac.eu/pmc-non-refractory-organics-and-inorganics.html
[3] https://actris-ecac.eu/particle-light-absorption.html
[4] https://riurbans.eu/

de 1.76 pour les dispositifs AE33 utilisant la bande filtrante M8060, pour le calcul du coefficient d'absorption, et en normalisant par une valeur de *Mass Absorption Cross-section* considérée comme représentative des conditions de fond rurale et urbaine à l'échelle européenne (MAC_{ACTRIS} d'environ 7.5 $m^2\ g^{-1}$ à la longueur d'onde de 880 nm ; Zanatta et al. (2016); Alastuey et al. (2022); Savadkoohi et al. (2023)). Les deux principales sous-familles d'eBC issues de la combustion de combustibles fossiles et de la biomasse (eBC_{ff} et eBC_{wb}), ont ensuite été obtenues en appliquant le modèle de Sandradewi et al. (2008) avec des valeurs d'exposant d'Ångström d'absorption (AAE ; *Absorption Ångström Exponent*) par défaut de 1 et 2, respectivement (Drinovec et al., 2015).

Le premier axe des résultats porte sur la distribution géographique de la composition chimique des aérosols, et le deuxième axe sur les variations saisonnières et journalières des différentes espèces chimiques. Les concentrations moyennes des PM_1 varient entre 6,8 (à Rennes) et 16,0 µg m^{-3} (à BPEst) sur les 13 sites, reflétant les caractéristiques distinctes de chaque site urbain. Ces niveaux sont comparables aux concentrations annuelles moyennes de NR-PM_1 rapportées par Bressi et al. (2021) sur 21 sites d'échantillonnage en Europe (de 2,8 à 14 µg m^{-3}). Les niveaux de PM_1 en France atteignent en moyenne 9,4 ± 8,3 µg m^{-3}, et ceux de $PM_{2,5}$ étaient en moyenne de 11,5 ± 9,2 µg m^{-3}. Ces valeurs dépassent la limite de 5 µg m^{-3} établie par l'OMS pour les $PM_{2,5}$, comme dans la plupart des sites européens (EEA, 2021).

Les AO dominent les PM_1, représentant de 43 à 60 % de la concentration massique totale en moyenne annuelle. Ils sont suivis par les NO_3 avec une contribution allant de 15 à 30 % de la masse des PM_1, le SO_4 de 8 à 14 %, le NH_4 de 7 à 13 %, et l'eBC de 5 à 11 %. Les stations situées dans le centre et le sud de la France (Lyon, Poitiers, Talence et Marseille) ont tendance à présenter des concentrations plus élevées en AO, probablement en raison de processus de formation secondaire plus prononcés. De plus, les AO contribuent de manière plus significative lors des périodes de niveaux élevés des PM_1 en hiver, principalement en raison de la combustion de biomasse, et en été, en raison de la production secondaire de composés organiques liée à l'augmentation des températures et à la photolyse. En revanche, les contributions des NO_3 sont plus importantes dans les sites du nord (ATOLL, Creil, Gennevilliers) pendant les épisodes de pollution, notamment au printemps lorsque des conditions favorables favorisent la formation de particules de nitrate d'ammonium.

Les variations temporelles mettent en évidence des schémas saisonniers distincts dans la composition chimique des PM_1. L'AO et l'eBC_{wb} présentent des niveaux de concentrations les plus élevées pendant les mois d'hiver. Cette tendance peut être attribuée à l'augmentation des émissions liées au chauffage résidentiel, en particulier la nuit. De plus, les AO ont un pic en été, ce qui indique la formation d'aérosols organiques secondaires (AOS). Les concentrations de NO_3 atteignent leur maximum en fin d'hiver et au début du printemps, surtout pendant les heures matinales. Cette augmentation est liée à des niveaux élevés d'ammoniac (NH_3) et d'oxydes d'azote (NO_x), conjugués à des conditions météorologiques favorables (températures froides, plus forte humidité, faible dispersion). Ces variations saisonnières sont influencées par divers facteurs, notamment les conditions météorologiques, les activités humaines et la proximité des sources d'émission. De plus, les variations journalières présentent également des caractéristiques spécifiques sur des sites particuliers. Par exemple, le site Paris Les Halles est caractérisé par un pic d'AO à midi, ce qui suggère une contribution substantielle des activités de cuisson. Le SO_4 présente un profil journalier relativement constant, avec un pic le matin dans certains sites (en particulier à Lyon), probablement en raison des dynamiques d'émissions des sources locales ou régionales (e.g., activités pétrochimiques en vallée du Rhône).

L'ensemble de ces données pluriannuelles collectées sur les sites urbains en France est d'un grand intérêt pour la communauté scientifique. Elles constituent une base solide pour les recherches futures, notamment celles visant à caractériser les sources de pollution, à étudier les tendances et à mener des études épidémiologiques. De plus, ces ensembles de données jouent un rôle crucial dans l'évaluation et la validation des modèles de qualité de l'air régionaux et mondiaux. Dans cet article, nous montrons - à titre d'exemple - une comparaison avec des simulations 3D issues d'une version récente du modèle CHIMERE pour l'année de référence 2018, englobant les données de neuf sites en France. Ce travail a été mené en collaboration avec l'équipe modélisation à l'Ineris (Florian Couvidat, Augustin Colette). Ces simulations ont été réalisées avec le modèle CHIMERE CTM (Menut et al., 2021) couplé au modèle SSH-aérosol v1.3 (Sartelet et al., 2020), caractérisé par le calcul de la répartition gaz-particule à l'aide du module thermodynamique SOAP (Couvidat et al., 2015). Ce modèle prend en compte les interactions entre les composés organiques et inorganiques en se basant sur la structure moléculaire. L'équilibre thermodynamique a été supposé pour la répartition gaz-particule. Le mécanisme SOA

de Wang, (2023, Chapter 4; *Modeling the response of biogenic secondary organic aerosol formation to anthropogenic NOx emission mitigation: a comparison of simplified and reduced aerosol mechanisms*)) a été utilisé. Ce mécanisme a été obtenu en utilisant l'algorithme GENOA v2.0 (Wang et al., 2022, 2023) afin de réduire les mécanismes AOS des monoterpènes et des sesquiterpènes du *Master Chemical Mechanism* (Saunders et al., 2003) couplé à PRAM (pour prendre en compte la formation d'AOS à partir des monoterpènes par auto-oxydation) (Roldin et al., 2019). Conformément à Wang, (2023), le mécanisme *Hydrophilic/Hydrophobic Organics* (Chrit et al., 2017) a été utilisé pour d'autres précurseurs et les simulations ont été réalisées sur la France à une résolution d'environ 7 km. La simulation a été imbriquée dans une simulation sur l'Europe à une résolution de 0,25°x0,4°. Les conditions aux limites ont été intégrées à partir des simulations du modèle global CAMS CIFS (Flentje et al., 2021). Les paramètres météorologiques ont été obtenus à partir de l'analyse opérationnelle du modèle du Système de Prévision Intégrée (*Integrated Forecasting System; IFS*) du Centre Européen pour les Prévisions Météorologiques à Moyen Terme (*European Centre for Medium-Range Weather Forecasts; ECMWF*) (Flentje et al., 2021). Les émissions anthropiques de gaz et de particules proviennent de l'inventaire CAMS-REG-AP (version v5.1 REF 2.1) (Kuenen et al., 2022).

En général, le modèle simule correctement les espèces inorganiques telles que le NO_3, SO_4, NH_4 et eBC. En revanche, on constate une nette tendance à la sous-estimation des concentrations d'AO, bien qu'il existe d'assez bonnes corrélations entre les simulations du modèle et les mesures. Il convient de noter que les concentrations de NO_3 semblent être surestimées par le modèle dans les sites du nord pendant les mois d'hiver, mais nettement sous-estimées dans les sites du sud, notamment pendant la saison estivale. Enfin, une analyse comparative similaire avec des mesures offline basées sur des filtres souligne la plus-value des mesures à haute résolution temporelle de l'ACSM et de l'AE33 dans une optique de validation dynamique des modèles de qualité de l'air.

III.2. Article 1

Multi-year high time resolution datasets of fine PM at 13 sites of the French Operational Network (CARA program): Data processing and chemical composition

Hasna Chebaicheb[1,2,3], Joel F. de Brito[1], Tanguy Amodeo[2,3], Florian Couvidat[2], Jean-Eudes Petit[4], Emmanuel Tison[1], Gregory Abbou[5], Alexia Baudic[5], Mélodie Chatain[6], Benjamin Chazeau[13,8], Nicolas Marchand[8], Raphaële Falhun[9], Florie Francony[10], Cyril Ratier[10], Didier Grenier[11], Romain Vidaud[11], Shouwen Zhang[12], Gregory Gille[7], Laurent Meunier[2,3], Véronique Riffault[1,3], Olivier Favez[2,3]

[1]IMT Nord Europe, Institut Mines-Télécom, Université de Lille, Centre for Energy and Environment, 59000, Lille, France
[2]Institut National de l'environnement Industriel et des Risques (INERIS), 60550 Verneuil-en-Halatte, France
[3]Laboratoire Central de Surveillance de la Qualité de l'Air (LCSQA), 60550 Verneuil-en-Halatte, France
[4]Laboratoire des Sciences du Climat et de l'Environnement (LSCE), CNRS-CEA-UVSQ (UMR 8212), 91191 Gif-sur-Yvette, France
[5]Airparif, Air Quality Monitoring Network for the Greater Paris Area,75004 Paris, France
[6]Atmo Grand Est, 67300 Schiltigheim, France
[7]AtmoSud, Regional Network for Air Quality Monitoring of Provence-Alpes-Côte-d'Azur, Marseille, France
[8]Aix Marseille Univ, CNRS, LCE, Marseille, France
[9]Air Breizh, 35200 Rennes, France
[10]Atmo Nouvelle-Aquitaine, 33692 Mérignac, France
[11]Atmo Auvergne Rhône-Alpes, 69500 Bron, France
[12]Atmo Hauts-de-France, 59800 Lille, France
[13]Laboratory of Atmospheric Chemistry, Paul Scherrer Institute, 5232 Villigen, Switzerland

Correspondence to: hasna.chebaicheb@ineris.fr

For submission in Earth System Science Data (ESSD)

Abstract. This paper presents a first comprehensive analysis of long-term measurements of atmospheric aerosol components from Aerosol Chemical Speciation Monitor (ACSM) and multi-wavelength Aethalometer (AE33) instruments collected between 2015 and 2021 at 13 (sub)-urban sites as part of the French CARA program. The datasets contain major chemical species within PM_1, including organic aerosols (OA), nitrate (NO_3), ammonium (NH_4), sulfate (SO_4), chloride (Cl), and equivalent black carbon (eBC). Rigorous quality control, technical validation, and environmental evaluation processes were applied, adhering to the guidance from the French reference laboratory for air quality monitoring and the Aerosol, Clouds, and Trace gases Research Infrastructure (ACTRIS) standard operating procedures. Key findings include geographical differences in aerosol chemical composition, seasonal variations, and diel patterns, which are influenced by meteorological conditions, anthropogenic activities, and proximity to emission sources. Overall, OA dominates PM_1 (43-60 %), showing distinct seasonality with higher concentrations (i) in winter, due to enhanced residential heating emissions, and (ii) in summer, due to increased photochemistry, enhancing secondary aerosol formation. NO_3 is the second most important contributor to PM_1 (15-30 %), peaking in late winter and early spring, especially in northern France, and playing a significant role during pollution episodes. Ammonium sulfate and eBC complement the major fine aerosol species, with their relative contributions strongly influenced by the origin of air masses and the stability of meteorological conditions, respectively.

Such chemically-speciated multi-year datasets have significant value for the scientific community, offering opportunities for future research, including source apportionment studies, trend analyses, and epidemiological investigations. They are also vital for evaluating and validating regional air quality models. In this regard, a comparison with the CHIMERE Chemical Transport Model shows good performances in simulating inorganic components but also an underestimation of OA concentrations, although with high correlations between simulations and measurements. Regional discrepancies in NO_3 concentration levels emphasize the importance of these datasets in validating air quality models.

Keywords. Urban pollution, ACSM, AE33, equivalent black carbon eBC, non-refractory submicron aerosols NR-PM_1, Chemical composition, France, chemical transport model/modeling

1 Introduction

The investigation of atmospheric aerosols holds significant importance in both the scientific and policy domains, mainly due to their substantial impacts on climate (IPCC, 2021) and human health (WHO, 2021). In Europe, for instance, it is estimated that in 2021, 97 % of the urban population experienced levels surpassing the annual concentration of 5 μg m^{-3} recommended by the World Health Organization (WHO) for particulate matter (PM) with an aerodynamic diameter smaller than 2.5 μm ($PM_{2.5}$), and exposure to these fine particles was associated in 2020 with more than 238,000 premature deaths (EEA, 2022). WHO guidelines as well as regulatory thresholds set at the national level (according to the Directive 2008/50/EC for European Member States) are mainly linked with the total mass concentration of suspended particles in a given size range. However, the elaboration and evaluation of specific action plans to improve air quality require a sound knowledge of their formation, which also allows the investigation of their emission sources and chemical processes in ambient air (Viana et al., 2008, Fuzzi et al., 2015). Moreover, forecasting systems, such as those using Chemical Transport Models (CTMs), usually use chemically-speciated emission inventories as inputs, and their validation benefits from comparisons with measurements of the PM chemical composition at representative sites (e.g., Ciarelli et al., 2016, EMEP, 2022).

Historically, PM chemical speciation was mainly based on offline laboratory analyses of aerosol samples collected on filters (e.g., Putaud et al., 2004). Such methods are nowadays well standardized and provide the opportunity for comprehensive characterization of major species as well as trace compounds (EMEP, 2022). However, they are known to be subject to various sampling artifacts (Eatough et al., 1999; Kirchstetter et al., 2001; Schaap et al., 2004; Wittmaack and Keck, 2004) and are generally applied at relatively low temporal resolution (typically 24h). They are also quite laborious and costly when used for long-term monitoring purposes. To overcome these limitations, significant efforts have been made to develop online chemical analyzers for in situ measurements of selected species in near real time. In particular, there has been a growing interest in the continuous quantification of black carbon in ambient air, especially using filter-based absorption photometers, given the significant influence of this aerosol component on climate (Jacobson et al., 2001) and its accuracy as an indicator of PM health effects (Janssen et al., 2011). In parallel, the use of mass spectrometry techniques, such as the

Aerodyne Aerosol Mass Spectrometer (AMS, Canagaratna et al., 2007), has spread worldwide in the last two decades to study non-refractory compounds within the fine aerosol mode (mainly PM_1) (Sun et al., 2010, Lanz et al., 2010, Daellenbach et al., 2016, Zhang et al., 2017). In addition to these sophisticated high-resolution instruments, which are well suited for intensive but short-term campaigns, the Aerosol Chemical Speciation Monitor (ACSM) has been specifically designed for continuous measurements of the same major chemical species (i.e., organic aerosol (OA), nitrate (NO_3^-), sulfate (SO_4^{2-}), chloride (Cl^-), and ammonium (NH_4^+)) in the PM_1 or $PM_{2.5}$ fraction over last years (Ng et al., 2011; Bressi et al., 2021; Zhang et al., 2019; Heikkinen et al., 2021). Both measurement methods (i.e., absorption photometers and ACSM) have become widely used in research monitoring, such as the Aerosol, Clouds, and Trace gases Research Infrastructure (ACTRIS, www.actris.eu) in Europe, and within the Atmospheric Science and mEasurement NeTwork (ASCENT, https://research.gatech.edu/) in the United States of America. Their robustness and relatively low operating costs also make them good candidates for deployment at air quality monitoring stations operated by environmental agencies (Petit et al., 2015).

In this context, since 2015, multi-wavelength Aethalometers (AE33 model, Drinovec et al., 2015) and ACSM instruments have been operated at an increasing number of urban sites in France as part of the CARA program within the national air quality monitoring network (Favez et al., 2021), with the following main objectives: (i) to document in near real time the chemistry (and possibly the dominant sources) of PM pollution episodes; (ii) to provide multi-year datasets of the chemical composition of the fine PM fraction, which will be available for future trend analyses and/or epidemiological studies; (iii) to provide a comprehensive overview of the temporal and spatial variability of the chemical composition of the fine PM over France, which can contribute in particular to evaluating and improving the accuracy of air quality models.

The main objective of this paper is to report on the chemically-speciated datasets and major findings obtained so far from these observations. After describing the quality control procedures applied to the corresponding measurements, we investigate the geographical specificities exhibited by the main chemical species within fine PM and then provide typical seasonal and diel variations displayed by these compounds in France during the last years (2015-2021). The datasets presented here are made fully available for complementary research activities, including

the evaluation of the accuracy of CTMs through comparison exercises, examples of which are also discussed in this article.

2 Methodology

2.1 Sites and measurement periods

The current study presents measurements of the chemical composition of fine particles within the CARA program during the period 2015-2021, mainly at 13 sites in France, including 11 stations of the regional air quality monitoring networks (AASQAs), as well as two research platforms - i.e., SIRTA (Greater Paris area) and ATOLL (Lille metropolis) - which are both also part of the ACTRIS European research infrastructure. These stations have been gradually equipped with AE33 and ACSM instruments from 2015 onwards. A detailed description of these instruments is given in the next section, and the temporal coverage of the measurements considered here for each site is presented in Figure 1. A summary of each sampling site, including coordinates and related networks, can also be found in Table S1 in the Supplementary Information. The majority of these sites are urban background sites, with the exception of two suburban sites (ATOLL and SIRTA) and one urban traffic site (Boulevard Périphérique Est; BPEst in Paris). Distributed throughout France, these sampling sites provide a global view of the chemical composition of fine particles on a national scale.

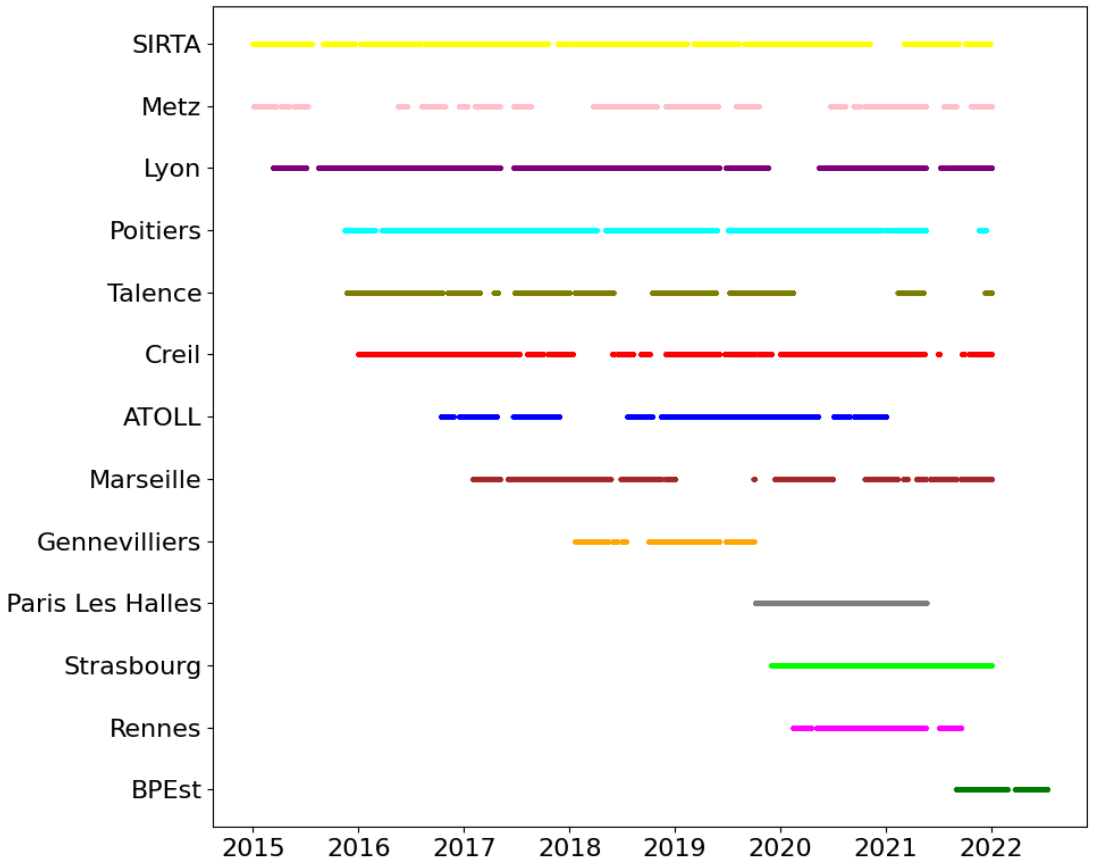

Figure 1: ACSM and AE33 measurement periods considered for each site in this study.

2.2 Non-refractory submicron aerosol measurements

2.2.1 ACSM measurement principles

The ACSM, developed by Aerodyne Research Inc., is based on mass spectrometry. It measures the chemical composition of NR-PM_1 (namely organic aerosols (OA), SO_4, NO_3, NH_4, and Cl) in real time, allowing long-term measurements with less monitoring and technical intervention, and high temporal resolution (Watson, 2017). All stations presented in this study are equipped with Quadrupole ACSMs (Q-ACSM, Ng et al., 2011), except for the Marseille-Longchamp site, which is equipped with a Time-of-flight ACSM (ToF-ACSM, Fröhlich et al., 2013). The Q-ACSM is

the most commonly used analyzer because it meets the operational monitoring needs of AASQAs and is less complex than the ToF-ACSM, although the latter usually has lower detection limits.

The operating principle of the ACSM is briefly described below. Ambient air first enters the vacuum system through a 100 μm diameter critical orifice. It then passes through an aerodynamic lens that focuses the aerosol into a concentrated beam, which is then directed onto a vaporizer heated at a temperature of about 600°C, causing the particles to transition to the gas phase. The gas phase molecules are then subjected to ionization at 70 eV, resulting in molecular fragmentation. The fragmented ions are guided by ion lenses to a quadrupole or time-of-flight mass filter, depending on the ACSM model.

In the ACSM, the atmospheric sample is analyzed alternatively by passing or through a particulate filter. The air signal can then be subtracted from the unfiltered measurements to refine the quantification of the particulate chemical species. A measurement timebase of approximately 29 min (corresponding to 28 cycles of filtered/unfiltered atmospheric samples) was used for each Q-ACSM dataset, while data were acquired with a 10 min timebase for the ToF-ACSM. All ACSMs operated under the CARA program were equipped with a PM_1 aerodynamic lens and a standard vaporizer.

In the measured mass spectra, each m/z fragment is linked to one or more species based on a fragmentation table originally developed by Allan et al. (2004) and subsequently refined by Canagaratna et al. (2007). The concentration of each chemical species is then obtained as the sum of its contribution in every corresponding m/z fragments. Moreover, the instrument-specific response factor (RF) of NO_3 and the relative ionization efficiencies (RIE) of NH_4 and SO_4 are determined by sampling pure, 300 nm ammonium nitrate (NH_4NO_3) and ammonium sulfate ($(NH_4)_2SO_4$) aerosols (Freney et al., 2019). For OA and Cl, the default RIE values of 1.4 and 1.3, respectively, are used here. Finally, to obtain quantitative mass concentrations for each measured chemical species, a collection efficiency (CE) correction factor is applied, following the protocol proposed by Middlebrook et al. (2011).

2.2.2 ACSM quality checks and data handling

The data collected from the ACSM instrument requires quality control and technical validation, followed by an environmental evaluation involving comparison with other complementary data.

ACSM measurements used for the present paper have been performed following the guidance provided by the French reference laboratory for air quality monitoring (LCSQA, 2018) and in full agreement with the ACTRIS standard operating procedures which are available online (https://www.actris-ecac.eu/pmc-non-refractory-organics-and-inorganics.html).

On-site calibrations have been achieved yearly by LCSQA personnel as well as after each sensitive maintenance by the instrument distributor in Europe (ADDAIR). A detailed description of the applied calibration procedures is available in a specific document edited at the national level (LCSQA, 2022). Moreover, each ACSM of the CARA program has routinely participated in intercomparison exercises organized by the Aerosol Chemical Monitor Calibration Centre (ACMCC) at SIRTA, to ensure proper calibration and functioning of the instruments (e.g., LCSQA, 2023).

Given the majority of instruments treated here are Q-ACSM, data processing will be detailed focusing on this model. ToF-ACSM data processing (deployed at Marseille-Longchamps) is described in Chazeau et al. (2021). The Q-ACSM data handling was carried out using the manufacturer's software in Igor Pro Version 6.37. Several steps were performed to ensure the thorough validation of ACSM data. The initial phase involved thoroughly checking the stability and continuity of various instrument technical parameters, including inlet pressure (maintained at approximately 1.3 ± 0.2 torr), vaporizer temperature (regulated from the voltage calibration curve initially defined by the manufacturer), Secondary Electron Multiplier (SEM) and Heater Bias voltages, filament emission, airbeam value (set around 10^7 ± 30% ions/s), and relative humidity (ensuring it remains below 40 % using a Nafion dryer upstream the inlet). Any data points exhibiting inconsistencies were systematically flagged for potential invalidation, ensuring that only accurate and reliable data were subjected to subsequent analyses. Secondly, the calibration results, notably the RF and RIE, were carefully analyzed. This approach ensured that the data cleaning process was attuned to changes in RF and RIE, thereby enhancing the accuracy and reliability of the resultant dataset. If the RIE/RF values from two subsequent calibrations are closed, the average of these response factors can be applied. During this data cleaning phase, the CE was maintained at a constant value of 1.

Thirdly, the data validation process involves the removal of air and water spiking peaks. To do so, a thorough evaluation of ions corresponding to water (m/z 18) and air (m/z 28, 32, and 40) was

conducted. In cases where these air and/or water signals exhibit anomalies, they were identified and subsequently invalidated through a systematic cleaning procedure executed within the Igor Pro software. This critical step also entails a comprehensive analysis of other specific main ions to capture additional insights from the data. In particular, the examination of ions associated with chlorides (m/z 35 and 36) allows for checking any possible measurement artifact that may be caused by sea salts (Tobler et al., 2020), while specific organic compounds (m/z 43, 44, and 55), including the fragment related to levoglucosan (m/z 60), serves as a crucial checkpoint for assessing the impact of distinct sources, such as biomass combustion, traffic emissions and/or secondary formation processes.

As a next step, the implementation of the TIS (*Time series*) and RIT (*Relative Ion Transmission*) corrections were performed. The TIS correction encompasses the correction of crucial time-dependent signals that exert a significant influence on the measured concentrations captured by the instrument. These include the adjustment of variables such as the inflow rate directed into the ACSM 'reference P' (inlet pressure), the 'reference N2' signal for airbeam, and the 'reference RF' for ionization efficiency. Subsequently, the RIT correction is applied to account for the mass spectrometer transmission efficiency within the ACSM, based on the naphthalene peaks used as internal standard and represented by m/z 51, 62, 76, 102, and 128 (normalized to 1 below m/z 51 and set at 0.05 for m/z 154 and beyond with an exponential fit for the interval in between). It is highly recommended to closely examine the RIT time series linked to these ions, particularly in cases where the RIT standard deviation is high. We found several instances where the mean RIT value may appear satisfactory, yet the time series could have periods of anomalous behavior. Thus, it is essential to carefully examine each time series of individual naphthalene masses, beyond the evaluation of average RIT values alone.

After these corrections, the Middlebrook algorithm (Middlebrook et al., 2011), with a minimum CE of 0.5, was applied to correct the mass concentrations for so-called composition-dependent collection efficiency (CDCE) correction.

The following step involves confirming the inorganic species calibration by examining the ion balance. This validation procedure entails evaluating the correlation between the measured and predicted NH_4 concentrations, with a target slope theoretically falling within the range of 1 ± 10

%, assuming most aerosols contain enough ammonium to be neutral as ammonium nitrate NH_4NO_3, ammonium sulfate $(NH_4)_2SO_4$ and ammonium chloride NH_4Cl. To compute the measured and predicted NH_4 concentrations, the following calculations are employed:

$$NH_{4,measured} = \frac{[NH_4]}{18} \quad \text{(Eq. 1)}$$

$$NH_{4,predicted} = \frac{[NO_3]}{62} + 2\frac{[SO_4]}{96} + \frac{[Cl]}{35.45} \quad \text{(Eq. 2)}$$

Finally, the analysis carefully accounted for the specific detection limits (DL) corresponding to various chemical species. Following Ng et al. (2011a), DL values for Q-ACSM are 0.284, 0.148, 0.024, 0.012, and 0.011 μg m^{-3} for NH_4, OA, SO_4, NO_3, and Cl, respectively. The same DL has been considered here for the ToF-ACSM instrument deployed in Marseille-Longchamp. Data levels above the DL were validated, whereas between -3×DL to DL were replaced by DL/2. Conversely, data below -3×DL were invalidated.

2.3 Equivalent Black Carbon measurements

2.3.1. Brief description of the AE33 device

Complementary to ACSM measurements, equivalent black carbon (eBC) has been monitored at all sites on the same periods using a multi-wavelength Aethalometer model AE33 (Magee Scientific). As with other filter-based absorption photometers, the AE33 primarily determines aerosol absorption coefficients (b_{abs}) at selected wavelengths, based on the rate of change in the attenuation of light transmitted through the particle-laden filter. A full description of the AE33 operating principles is given by Drinovec et al. (2015). Briefly, the instrument continuously captures aerosol particles by directing the aerosol-laden airflow onto a specific spot on the filter belt. It assesses the aerosol by gauging the amount of light transmission that passes through a part of the filter belt containing the sample, compared to the light passing through an empty part of the filter belt, which serves as a reference zone. In the AE33, this analysis is carried out at seven optical wavelengths ranging from near-ultraviolet (UV) to near-infrared (IR) (370, 470, 525, 590, 660, 880, and 950 nm).

As a significant improvement compared to previous Aethalometer versions, the AE33 benefits from the so-called dual-spot technology, which allows for minimizing the influence of sampling artifacts known as the filter-loading effect (Drinovec et al., 2015). To do so, for each measured wavelength, two measurements are obtained simultaneously from two sampling points with different sample accumulation rates. Both spots draw their samples from the same inlet air stream. By combining the two results, non-linearities are eliminated, and compensated particle light absorption and eBC mass concentration are obtained (Drinovec et al., 2015).

It should be noted that AE33 measurements used in the present paper have been performed in the PM_1 fraction at both ACTRIS national facilities (ATOLL and SIRTA) but in the $PM_{2.5}$ fraction at the other stations. It is however considered that black carbon aerosols are overwhelmingly present in submicron particle matter (Bond et al., 2013) so that eBC concentrations discussed herewith can be (i) compared together (i.e., from one site to another), and (ii) combined with ACSM NR-PM_1 measurements to describe the main chemical components of submicron PM at the studied sites.

2.3.2. AE33 quality checks and data handling

Similarly to ACSM measurements, AE33 devices have been operated following the LCSQA guidelines (LCSQA, 2020). The absorption coefficients used herewith were then calculated at each wavelength according to current ACTRIS guidelines (https://actris-ecac.eu/particle-light-absorption.html) following this equation:

$$b_{abs} = \frac{eBC \times MAE}{H} \quad \text{(Eq. 3)}$$

where MAE represents the specific mass absorption efficiency corresponding to each wavelength (empirically determined by the manufacturer), and H is the appropriate harmonization factor to account for multiple scattering effects of the filter, which is set at 1.76 for AE33 devices using the M8060 filter tape. eBC concentrations were then deduced by normalization with a constant mass absorption cross-section (MAC_{ACTRIS}) recently investigated in the frame of the H2020 RI-Urbans EU research program (Alastuey et al., 2022; Savadkoohi et al., 2023), following:

$$eBC = \frac{b_{abs}}{MAC_{ACTRIS}} \quad \text{(Eq. 4)}$$

eBC concentrations are obtained at a wavelength of 880 nm, which is recommended for soot carbon measurements. This is because it is less prone to artifacts caused by other light-absorbing compounds such as dust and organic compounds (notably iron oxides and brown carbon, BrC, which absorb light at shorter wavelengths in the UV spectrum). At 880 nm, the MAC_{ACTRIS} factor used here is equivalent to 7.5 $m^2\ g^{-1}$, also in good agreement with results previously obtained by Zanatta et al. (2016).

AE33 data qualification procedures include the inspection of the AAE value obtained from the seven wavelengths for each data point, aggregated at a 15 min timebase. Lower and higher acceptable AAE values of 0.7 and 3.0 are considered here, and the determination coefficient (r^2) of the exponential fit used to calculate this AAE value shall be higher than 0.9. Datapoints that do not meet these criteria have been discarded. The carefully validated data also underwent a thorough assessment against the instrumental detection limit (DL) set here to a value of about 100 ng m^{-3}. Data that fell within the range of -3×DL to DL was replaced by DL/2, and data below -3×DL was invalidated.

The source apportionment of ambient eBC concentrations is based on the model of Sandradewi et al., (2008). Briefly, the two-component model calculates the aerosol optical absorption coefficient by combining fractions associated with wood burning (wb) and fossil fuel (ff) combustion. It exploits the variations in absorption characteristics at different wavelengths. This method is based on the assumption that wood combustion has a marked absorption in the UV (high AAE) compared with fossil fuels (low AAE). For this study, for the different sites, the separation between eBC_{ff} and eBC_{wb} was performed using the values provided by the AE33 manufacturer: AAE_{ff}= 1 and AAE_{wb} = 2 (Drinovec et al., 2015).

2.4 Chemical mass closure

PM_1 mass was reconstructed from combining chemical species from ACSM (NR-PM_1 = OA + NO_3 + SO_4 + NH_4 + Cl) and eBC from AE33 (PM_1 = NR-PM_1 + eBC). The results obtained were compared with $PM_{2.5}$ measurements for each sampling station over the study period. For these

stations, continuous $PM_{2.5}$ measurements have been conducted using a tapered element oscillating microbalance equipped with the filter dynamic measurement system (TEOM-FDMS; Thermo Fisher Scientific) and/or a FIDAS 200 optical particle counter (Palas GmbH) and/or β gauge monitor (BAM 1020; MET ONE), according to the European standard for PM regulatory measurements (EN 16450).

Linear regressions of hourly data reveal fairly good agreement between the reconstructed PM_1 and the $PM_{2.5}$ mass concentrations measured at each specific site (Figure S1), with determination coefficients (r^2) ranging from 0.72 to 0.88 (except for the Marseille-Longchamp site which yielded an r^2 value of 0.58) and slopes varying from 0.71 to 0.99 (except for Lyon, Strasbourg, and Metz, which showed distinct lower slopes of 0.57, 0.58, and 0.61, respectively). These results suggest that $PM_{2.5}$ are predominantly made up of submicron particles and underscore the ACSM efficacy in capturing a significant proportion of that fraction at most sites. Hereafter, PM_1 (mass concentration) will be used to refer to submicron aerosol loadings estimated as the sum of eBC and NR-PM_1 species measured by the AE33 and ACSM, respectively.

2.5 The CHIMERE model

In order to compare the PM_1 species measurements and results obtained with a Chemical Transport Model (CTM), 3D simulations were performed from a recent version of the CHIMERE model (Menut et al. 2021) coupled with the SSH-aerosol v1.3 aerosol model (Sartelet et al., 2020). One important feature of SSH-aerosol consists in the computation of gas-particle partitioning with the thermodynamic module SOAP (Couvidat et al., 2015). This model accounts for the condensation of semivolatile organic compounds onto the organic and aqueous phases of particles as well as the effect on partitioning of interactions between organic and inorganic compounds based on their molecular structure. Thermodynamic equilibrium was assumed for gas-particle partitioning.

The SOA mechanism of Wang et al., (2024) was used. This mechanism was obtained by using the GENOA (*GENerator of reduced Organic Aerosol*) v2.0 algorithm (Wang et al., 2022, 2023) in order to reduce the SOA mechanisms for monoterpenes and sesquiterpenes from the Master Chemical Mechanism (Saunders et al., 2003) coupled with PRAM (in order to account for SOA

formation from monoterpenes by auto-oxidation) (Roldin et al., 2019). Following Wang, (2023), the Hydrophilic/Hydrophobic Organics (Chrit et al., 2017) mechanism was used for other precursors. Primary organic aerosols are treated as semivolatile organic compounds that partition as a function of environmental conditions and that can undergo aging (Couvidat et Bessagnet 2021).

Boundary conditions were taken from CAMS CIFS global model simulations (Flentje et al., 2021). Meteorological data were obtained from the operational analysis of the Integrated Forecasting System (IFS) model of the European Centre for Medium-Range Weather Forecasts (ECMWF) (Flentje et al., 2021). The anthropogenic emissions of gases and particles were taken from the CAMS-REG-AP inventory (version v5.1_REF2.1) (Kuenen et al., 2022).

3 Results

3.1 Geographical specificities in the chemical composition

Figure 2 summarizes the PM_1 average values, as well as their relative contributions, both globally in the form of pie charts, as well as barplots, calculated according to the PM_1 percentiles at various sites in France.

The mean PM_1 concentrations at the 13 sites range from 6.8 to 16.0 µg m^{-3}, reflecting the local specificities of each urban site. These levels are comparable with the annual average NR-PM_1 levels reported by Bressi et al., (2021) across 21 sampling sites in Europe (from 2.8 to 14 µg m^{-3}, including remote mountain sites), with the highest NR-PM_1 concentrations observed in mid-latitude Europe. In addition, Chen et al., (2022) reported an average PM_1 concentration of 12.2 ± 9.3 µg m^{-3} for 13 urban sites in Europe. In the present study, PM_1 averaged 9.4 ± 8.3 µg m^{-3} and $PM_{2.5}$ 11.5 ± 9.2 µg m^{-3}. It is important to note that this multi-year $PM_{2.5}$ level exceeds the annual WHO guideline value of 5 µg m^{-3} for $PM_{2.5}$ (WHO, 2021), as is the case at most sites in Europe (EEA, 2021).

Figure 3 further displays some key statistics on the various chemical species as well as for PM_1 and $PM_{2.5}$ mass concentrations, as a function of mean levels measured at each site. The only one site with a “Road-Traffic” site typology, - BPEst - located on the east side of the Paris ring road,

exhibits the highest mean PM_1 concentration (16.0 µg m^{-3}), standing out notably on eBC, SO_4 and OA levels (Fig. 3). On the other hand, Rennes and Strasbourg display the lowest mass concentrations of PM_1 (6.8 µg m^{-3}), both having the lowest levels of OA (around 3.5 µg m^{-3}). In addition, the site in Rennes shows a significantly lower mean eBC level (0.4 µg m^{-3}), compared to the general average (0.8 µg m^{-3}), thus depicting a lower influence of combustion aerosols at this site. The remaining sites generally exhibit a fairly homogeneous PM_1 mass concentration, ranging from about 8 to 10 µg m^{-3}. ATOLL, Creil and Talence sites have higher PM_1 concentrations (between 10 and 10.4 µg m^{-3}): the first two (located in the northern Hauts-de-France region) are influenced by higher NO_3 concentration levels of 3.1 and 2.4 µg m^{-3}, respectively, whereas Talence (near Bordeaux in the southern Nouvelle-Aquitaine region) has a strong contribution of OA (6.0 µg m^{-3}).

The NO_3 levels at these two sites in northern France are attributed to local and regional sources from road-traffic and combustion emissions (rich in nitrogen oxides; NO_x) that with ammonia (NH_3) from agricultural activities formed ammonium nitrate (NH_4NO_3; AN) under favorable meteorological conditions (Roig Rodelas et al., 2019), as well as to transboundary pollution from Eastern Europe (Chebaicheb et al., 2023). Conversely, Talence has the highest OA 95th percentile (higher than 19.0 µg m^{-3}, Fig. 3), associated with a strong biomass combustion in the Bordeaux area during the cold season (Favez et al., 2021).

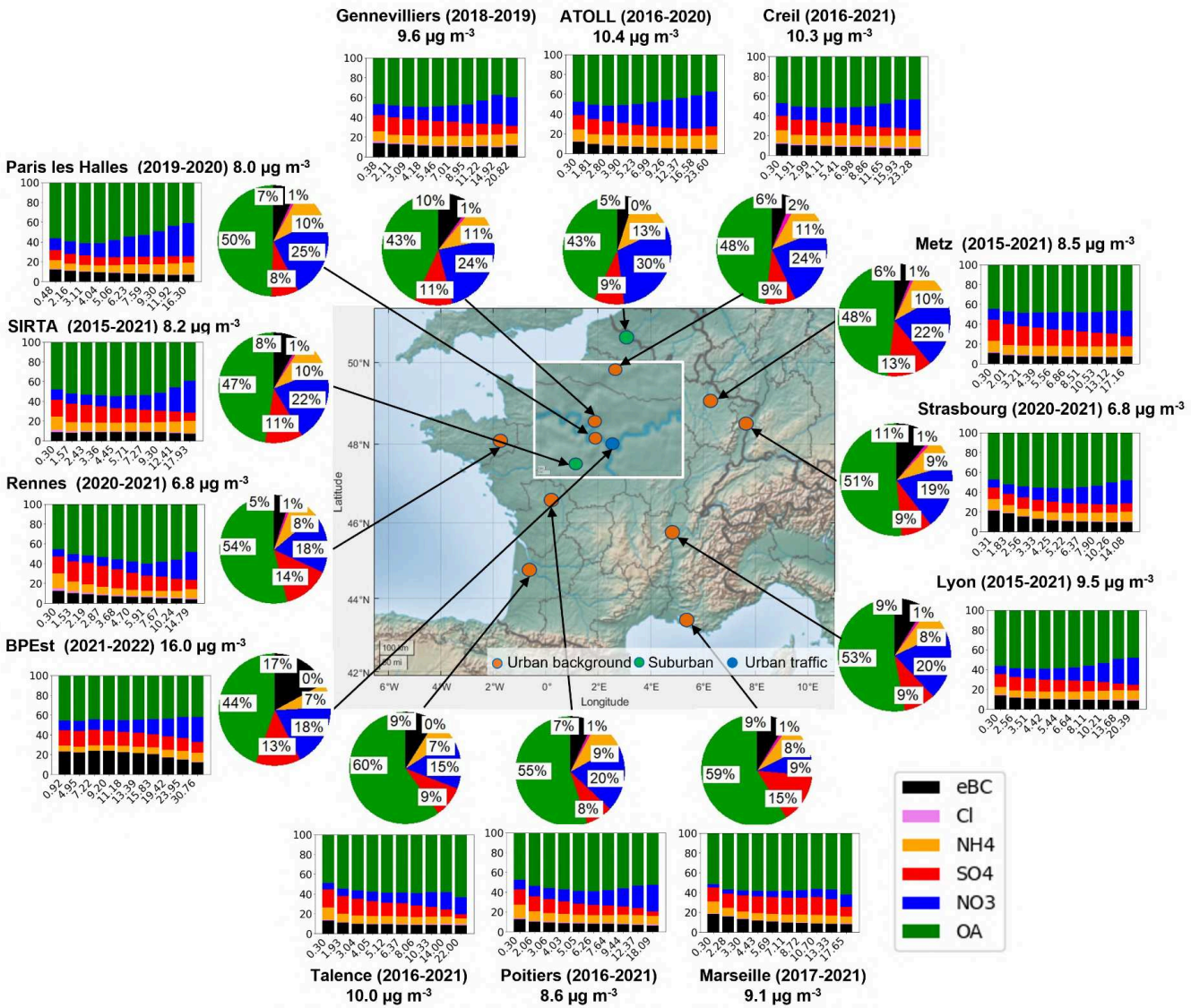

Figure 2: Multi-annual averaged PM_1 mass concentration and pie charts of average relative contributions of non-refractory species and eBC at different sites in France; the bar charts represent the relative contribution as a function of PM_1 deciles.

For the Greater Paris region, the SIRTA facility is located 22 and 25 km away from the sites representing central areas of Paris, i.e., Paris Les Halles and Gennevilliers, respectively. Logically, due to the closer proximity with intense emission sources, Gennevilliers exhibits higher PM_1 concentrations (9.6 µg m^{-3} on average over the 2018-2019 period) compared to SIRTA levels of 8.2 µg m^{-3}. The equivalence in mean PM_1 loading presented here between Paris Les Halles (8.0 µg m^{-3}) and SIRTA has to be linked with the specific measurement periods analyzed for each site. Indeed, data from Paris Les Halles presented here include the COVID-19 lockdown periods of 2020-2021, while SIRTA data are averaged over 2015-2021. When averaged over the same period as Paris Les Halles, the PM_1 level at SIRTA decreases to 6.2 µg m^{-3}. Moreover, an increased mixing layer height over Paris city center, due to the urban heat island effect which may dilute the aerosol content in a wider volume, should also be considered when comparing concentrations from inner and suburban sites within such a megapolis (e.g., Dupont et al., 2016).

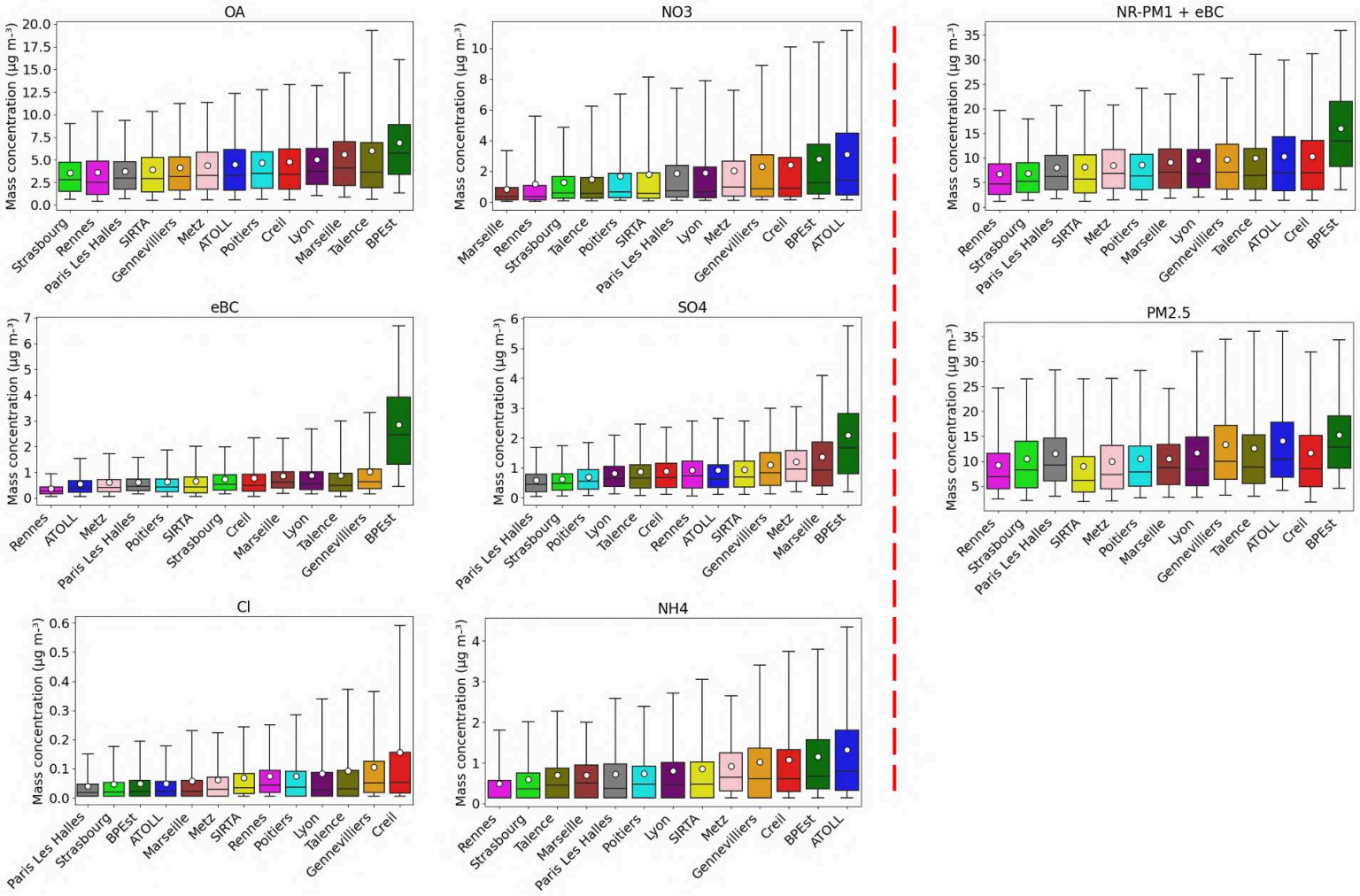

Figure 3: Box plots of the statistical distribution (5th, 25th, 50th, 75^{th,} and 95th percentiles) of each NR-PM_1 species and eBC, as well as PM_1 and $PM_{2.5}$ mass concentrations; means are indicated by the circle symbol.

The analysis of individual contributions shows that organic compounds make up about half of the PM_1 total mass across all sites, ranging from 43 to 60 %, which is comparable with the average of OA at urban sites in Europe (around 50 % of PM_1), as reported by Chen et al., (2022). It is also consistent with the OA relative contribution observed by Bressi et al., (2021) in Europe (36-64 % of NR-PM_1). The stations located in central and southern France, including Marseille-Longchamp, Poitiers, Talence, and Lyon, show higher OA mass concentrations than sites in the north, which can be partly due to more intense secondary formation processes. Conversely, NO_3 contributions are more pronounced at northern sites (22-30 % *vs* 9-20 %), due to more favorable conditions for particulate AN formation (e.g., Favez et al., 2007). Consequently, NO_3 mass concentrations in France decrease from north to south and from east to west, consistent with the findings by Favez et al., (2021). Furthermore, NO_3 constitutes the second most significant contributor, accounting for 15-30 % of PM_1 mass, except for Marseille-Longchamp, where it is less than 10 % (0.8 µg m^{-3}). Other studies have also reported the predominance of NO_3 over SO_4 at many European sites (Bressi et al. 2021, Chen et al. 2022). As Marseille is characterized by high emissions from industry and shipping activities, the Marseille-Longchamp site exhibits a higher contribution of SO_4 (15 %), making it the second major contributor to PM_1 at that site (Chazeau et al., 2021).

Overall, SO_4 is the third largest contributor in France, with contributions ranging from 8 to 14 %. Besides Marseille-Longchamp and the BPEst traffic site, significant SO_4 concentrations are also obtained for Metz and Gennevilliers (around 1 µg m^{-3} on average), probably reflecting their proximity to emission sources of gaseous precursors. Indeed, ammonium sulfate particles (AS; $(NH_4)_2SO_4$) are formed in the atmosphere from chemical reactions involving sulfur dioxide (SO_2) and NH_3. In France, CITEPA (2023) estimated for 2021 that the manufacturing industry (52 %), followed by energy transformation (28 %), and building use and activities (17 %) are the main sources of SO_2. Furthermore, SO_4 is known to be strongly influenced by long-range transport from Central Europe, which is the case for many sites in northern France, including SIRTA, ATOLL, Creil, Paris Les Halles, and Poitiers.

For the remaining compounds, mean NH_4 levels range from 0.5 to 1.3 µg m^{-3}, with a contribution fluctuating between 7 % and 13 %, showing a strong correlation with NO_3 and SO_4 levels, linked to the neutralization of sulfuric and nitric acids by NH_3. Meanwhile, the contribution of eBC

varies from 5 to 11 % at the urban background sites investigated here. Previous studies, including Chen et al. (2022), reported higher contributions of BC at different European urban sites (12 %), which can be explained by recent changes in the data processing. The recently proposed MAC_{ACTRIS}, taking into account the harmonization factor, effectively decreases eBC concentration estimates by about 42% compared to previously used data (Section 2.3.2). Finally, Cl makes a minor contribution of around 1 % at all sites, with averaged mass concentrations generally very low, remaining below 0.1 µg m^{-3}, except for Gennevilliers (0.1 µg m^{-3}) and Creil (0.15 µg m^{-3}), with a slightly higher contribution of 2 %. Ammonium chloride (AC; NH_4Cl) is formed in the atmosphere from the chemical reaction of hydrochloric acid (HCl) and NH_3. The main sources of HCl in the atmosphere are biomass combustion (Andreae et al., 1996), coal burning (Tobler et al. 2020), and waste combustion (McCulloch et al., 1999). In Creil, there is a large waste treatment plant 2 km northeast of the monitoring station, which can explain the higher concentration of Cl at this site (Fig. S3).

Figure 2 also illustrates the variations in PM_1 chemical composition as a function of PM_1 mass concentrations, divided into 10 concentration levels (corresponding to deciles) for each site. OA exhibits even higher contributions at high PM_1 mass concentrations at Talence, Marseille-Longchamp, and Poitiers especially during the coldest and warmest months of the year (Figure S4). This can generally be explained by the influence of biomass burning during winter pollution episodes as also previously described for the Paris area (Petit et al., 2015; Foret et al., 2022), and by the impact of secondary formation of organic compounds in summer (e.g., Favez et al., 2007). However, OA decreases from the 30th percentile (around 4 to 5 µg m^{-3}) of PM_1 levels with an increase in NO_3 at sites in northern France and Lyon. NO_3 plays an important role during pollution events, particularly in spring, as reported previously in France (Dupont et al., 2016; Petit et al., 2017) and in other mid-latitude European sites (Bressi et al., 2021).

The contributions of SO_4 and eBC are generally stable or show a slight decrease with increasing PM_1. Nevertheless, at BPEst and, to a lesser extent, Marseille-Longchamp, Strasbourg and Rennes sites, eBC exhibits significant contributions at lower PM_1 levels, confirming the local traffic influence at BPEst, and suggesting significant local combustion sources for the other sites. Furthermore, Marseille-Longchamp exhibits quite consistent OA, NO_3, and SO_4 contributions with PM_1 levels, showing nonetheless a significant increase of the first two during pollution

events. Globally, SO_4 is a relevant contributor for Metz, Rennes, Gennevilliers, SIRTA, Talence, and Marseille-Longchamp, while OA retains significance at all sites throughout the PM_1 percentiles.

3.2 Seasonal and diel cycles of fine aerosol chemical species

Common pictures might be obtained from the investigation of the averaged seasonal and diel cycles displayed for the different chemical species at the various sites of this study. Figure 4 shows the median and interquartile range (IQR) monthly variability for each species considered here, over the averaged cycles for the (sub)urban sites over France. The averaged monthly variabilities of the PM_1 species for individual sites are shown in Figure S5.

All chemical species exhibit significant variability in mass concentration over the months. In particular, eBC_{wb} shows a clear seasonality, with higher concentrations during winter (around an average of 0.3 µg m^{-3}) compared to summer (0.05 µg m^{-3}). This is mainly due to the high level of wood combustion for domestic heating during wintertime. Furthermore, there is substantial variability between sites in winter (represented by a larger IQR), probably as a result of different meteorological conditions, as well as the usage of wood combustion for residential heating. Conversely, eBC_{ff} shows seasonal variations relatively similar, but with smaller winter/summer differences than eBC_{wb}. It ranges from around 0.4 (in May) to 0.7 µg m^{-3} (in November). This variability is associated with variations in road-traffic intensity, compounded with meteorological conditions favoring (or not) the accumulation of atmospheric pollutants, linking to a maximum commonly observed in autumn (Petit et al., 2015). Similarly, OA displays higher levels during cold seasons (5.5 µg m^{-3}), with reasons comparable to those for eBC, and lower levels during warm periods (3.5 µg m^{-3}). Nevertheless, OA peaks (with a higher OA/eBC mass ratio) in summer, reflecting the formation of secondary organic aerosols (SOA) from biogenic and anthropogenic sources (Favez et al., 2007). Notably, SOAs are formed mainly from biogenic VOC in summer, when temperatures and sunlight are high (Canonaco et al., 2015; Cao et al., 2022). Furthermore, OA yields lower site-to-site variability (i.e. IQR) (Fig. S6), as most of the OA, even in wintertime, is associated with regional process and secondary formation (Chen et al., 2022; Chebaicheb et al., 2023).

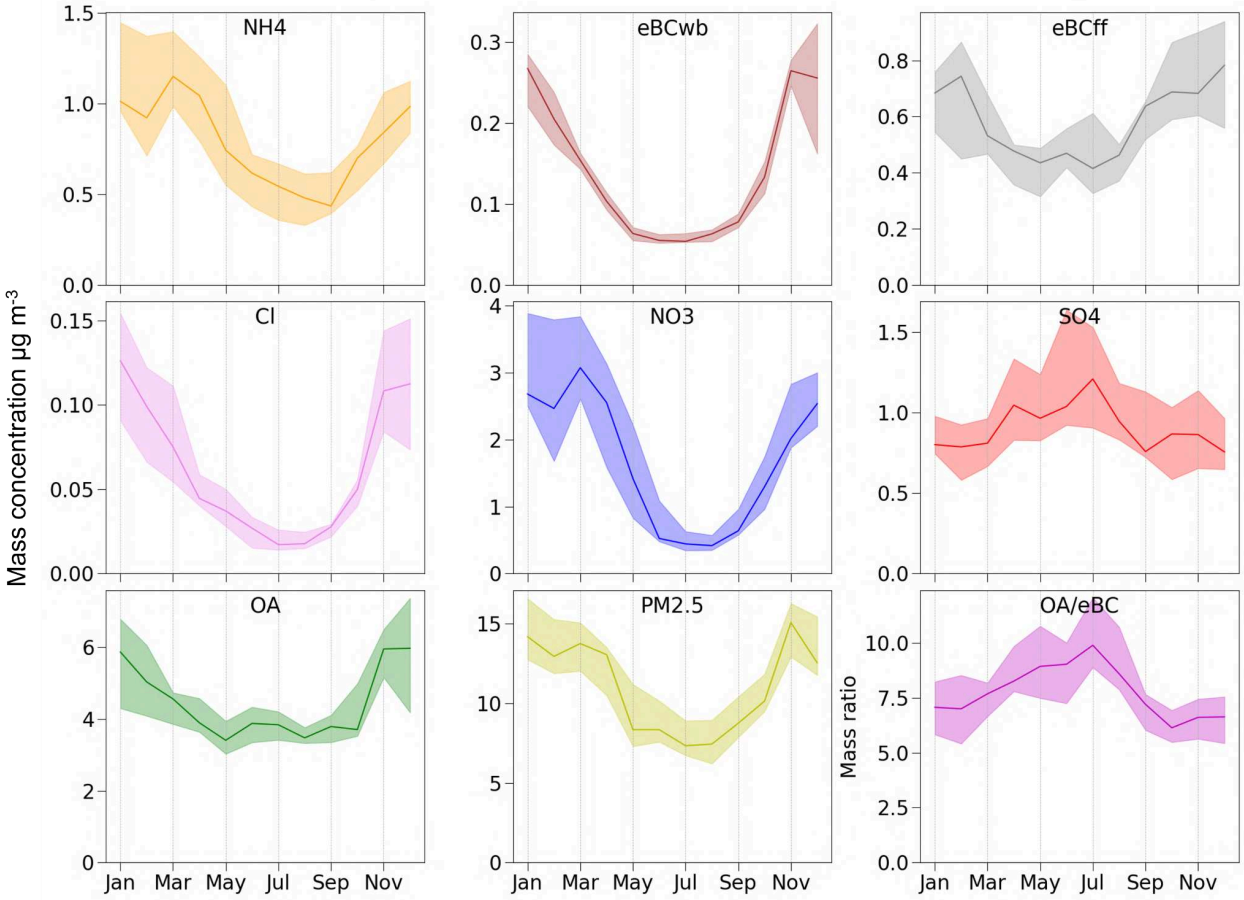

Figure 4: Monthly variability of mass concentrations of PM_1 species, $PM_{2.5}$, and OA/eBC ratio across all sites. The Figure shows the median and IQR (25th and 75th percentiles) calculated from the averaged monthly concentrations for each site. Months were considered only if data coverage was at least 75 %.

NO_3 and NH_4 concentrations display a marked seasonal pattern, peaking in late winter and early spring, and averaging around 3.0 and 1.2 µg m^{-3}, respectively. As discussed previously, AN (including NO_3 and a fraction of NH_4) is formed from the combination of NH_3 (typically highest in spring from agricultural activities) with HNO_3 formed by the oxidation of NO_x emitted mainly by vehicles or industrie. AN formation is favored by meteorological conditions during colder periods (i.e. low temperature and high humidity, Fortems-Cheney et al., 2016). Moreover, as discussed in the previous section, AN concentrations depend on site-specific factors, contributing to a greater variability between sites. In contrast, SO_4 shows a relatively stable monthly variation, with higher levels observed between April and August. Elevated summertime SO_4 concentrations could be attributed to favorable meteorological conditions. In addition, SO_4 can either be formed

"locally" from the oxidation of SO_2 or transported from emission hotspots, such as Eastern European regions (Roig Rodelas et al., 2019). Cl exhibits a strong seasonality, ranging from 0.02 (summer) to 0.14 μg m^{-3} (winter). The higher concentrations during the cold seasons can be partly attributed to its semi-volatile nature (similarly to AN, its formation should be favored by low temperatures and high humidity), as well as transport from emission hotspots areas, notably of intense coal combustion, further enhanced during wintertime (Tobler et al., 2021).

The mean diel profiles obtained for each chemical species across all (sub)urban background sites and for each season are shown in Figure 5. All species exhibit higher concentrations at night, which could be, at least partially, associated with a lower boundary layer height. Some species show variability associated with local emission sources, including road-traffic (morning and evening peaks), notably for OA and eBC_{ff}, with a consistent behavior throughout the year. OA stronger nighttime peak, notably during the colder months, mimics eBC_{wb} associated with house heating. OA enhancement during nighttime in wintertime is linked with residential heating (Chebaicheb et al., in prep.). Furthermore, at Paris Les Halles, in the city center, OA further exhibits a small peak at noon (Fig. S7), pointing to an influence of cooking emissions at this site. Overall, $PM_{2.5}$ profile aligns with OA diel cycles, with higher loadings during the morning and evening hours, due to the predominance of the organic species in the fine aerosol fraction.

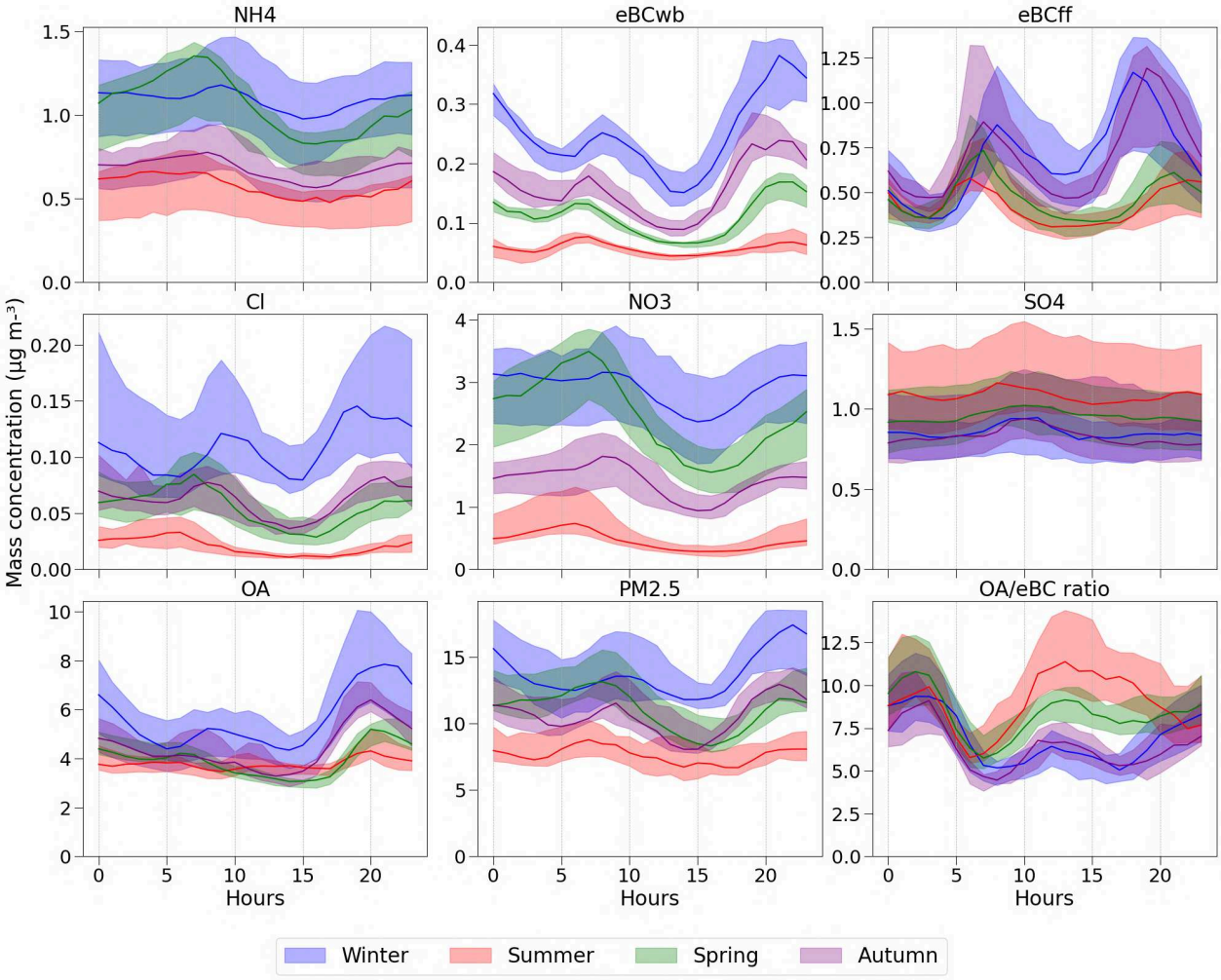

Figure 5: Seasonal median and IQR of daily profiles for all sites for each PM_1 component, $PM_{2.5}$ and OA/eBC ratio.

Both NO_3 and NH_4 display a comparable diel cycle, featuring higher mass concentrations during the morning hours in all seasons, albeit at different levels. Lower temperatures and higher relative humidity in the morning favor the formation of AN. During the day, as temperatures rise, AN evaporates into the gas phase as NH_3 and HNO_3. Consequently, AN mass concentrations are lowest in summer, due to unfavorable weather conditions and reduced NO_x levels associated with school holidays (Roig Rodelas et al., 2019). As discussed previously, AN levels are highest in spring, due to favorable meteorological conditions and intensive agricultural activities. On the other hand, the diel cycle of SO_4 shows relatively constant values during the day, with higher levels observed in summer, as discussed previously. Notably, the diel cycle of SO_4 at some sites

features morning or afternoon peaks, especially for Lyon and Marseille-Longchamp sites, which may be explained by the presence of local or regional sources (Fig. S7, S8, and S9).

Finally, the OA/eBC ratio shows an interesting diel cycle, exhibiting greater values at night in all seasons, ranging from 8 to 12. This ratio also increases during the day, which could be explained by photochemistry and SOA formation, particularly of biogenic origin during summertime (Chebaicheb et al., 2023). As expected, the ratio decreases during the morning and evening rush hours, associated with more BC-rich traffic emissions.

3.3 Examples of comparison between our observations and chemical transport model outputs

In this section, CHIMERE model results for 2018, with a spatial resolution of 7 km over France, were used to compare with PM_1 observations. The simulation results could only be compared with 9 of the sites analyzed here. BPEst, Paris Les Halles, Rennes, and Strasbourg were excluded from this analysis because measurements at these sites only started after 2018. The time series of observed and modeled concentrations are shown in the supporting material (Figure S10). Figure 6 summarizes results from the comparison between observations and simulations, typically showing good agreement. Loadings for inorganics (NO_3, SO_4, NH_4, and Cl) and eBC are fairly well-captured by the model across the sites, with some particularities. In particular, at the Marseille-Longchamp site, SO_4, NO_3, NH_4 and eBC are consistently underestimated by the model (33, 41, 45 and 65 %, respectively). This discrepancy could be due to the low resolution of the model grid (7 km over France) that may not be sufficient to capture some specificity of the site (local meteorology, proximity of the sea), as well as a potential underestimation of emissions in the Southeastern region of France. Several sites also present an underestimation of SO_4 (Metz, SIRTA, Talence) by around 35-39 %. In contrast, NO_3 is strongly overestimated by the model (57 %) in the north of France (ATOLL). Organics, on the other hand, are consistently underestimated by the model at all sites by a factor of 2-3. Other recent studies also reported underestimations of OA at 11 European sites, focusing on winter 2009 (Ciarelli et al., 2016). In the present study, OA yields a strong underestimation particularly in the warmer months (60 % vs. 41 % for the colder months), suggesting a greater contribution from SOA in summer than in winter.

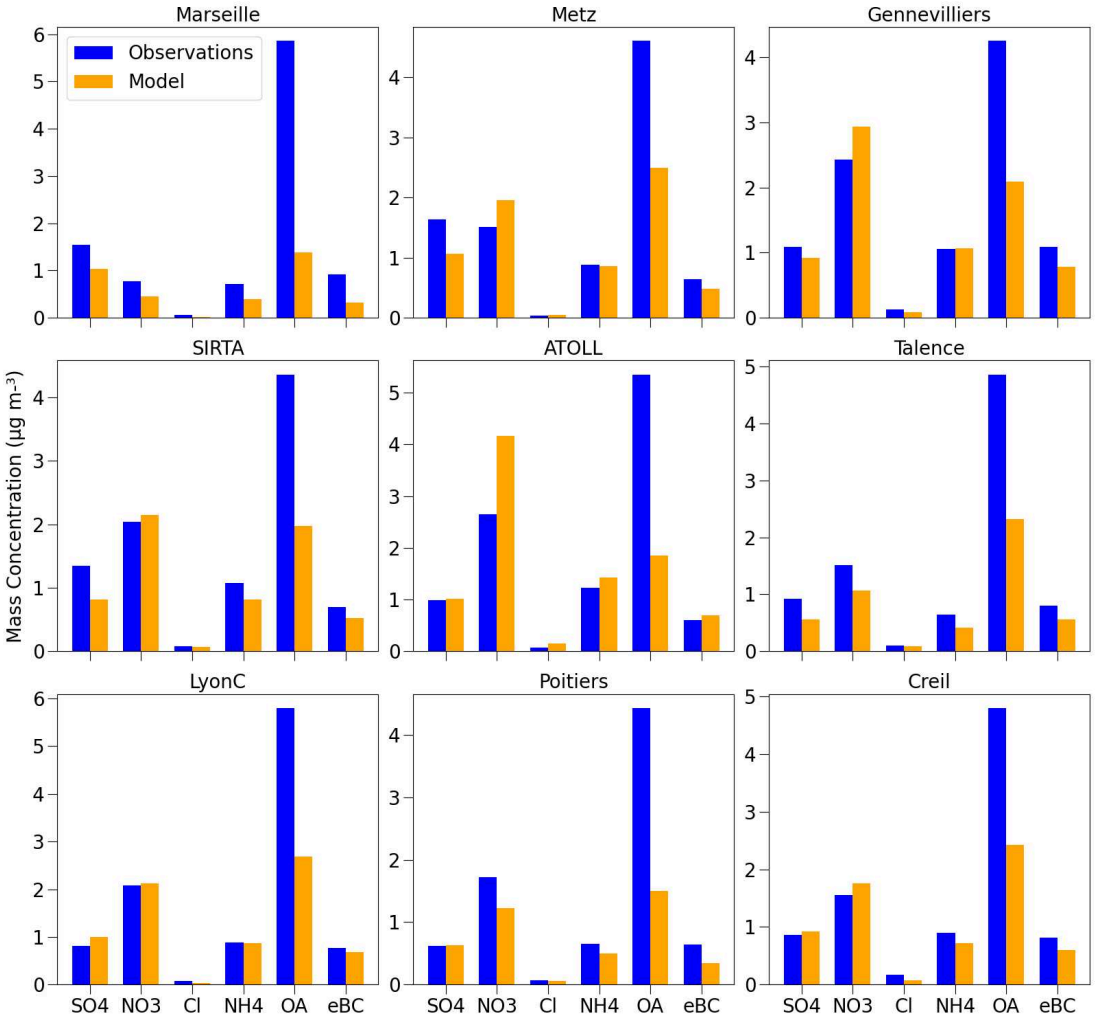

Figure 6: Mean mass concentration (in µg m^{-3}) of different chemical species for observations (in blue) and simulations (in orange) at nine French sites.

Figure 7 displays the diel profiles of each species, comparable with Figure 5, however restricted to winter and summer of 2018, allowing the comparison with model outputs. In general, the species exhibit relatively consistent model performance between winter and summer, although there is an underestimation by the model during the latter. For NO_3, during wintertime, the concentrations observed are relatively stable throughout the day, whereas the model shows a strong daytime decrease due to the modeled evaporation of ammonium nitrate. During summertime, enhancement of NO_3 in the early morning is captured by both observations and model, however as a smooth nighttime increase/decrease for the former, and a sharp peak in the latter. A similar pattern is observed for NH_4. For SO_4, the diel profile is stable for both

observations and simulations in summer. In winter, the slight increase of SO_4 during the day is not captured by the model, which instead shows a low peak at night. For eBC, both observations and model simulations show two peaks during rush hours. In winter, the night peak is more pronounced in the model, but nonetheless they display comparable levels, in contrast to summertime, when the model tends to underestimate the concentrations. These differences in daily eBC profiles may be attributed to meteorological conditions or issues in the seasonal temporality of emissions. Finally for OA, as discussed before, the model largely underestimates observations in summer. Generally the behavior is fairly well represented, however wintertime nighttime enhancement is larger than observations, similar to eBC.

Figure 8 presents some statistical parameters (mean bias, normalized *Root Mean Square Error* (RMSE), and correlation coefficient r) calculated from the daily means for each chemical species across the nine urban sites in France. Overall, the correlations between observations and model results show good agreement, with correlation coefficients (r) ranging between 0.6 and 0.8, which is consistent with the literature (Couvidat et al., 2018, Cholakian et al. 2018). The mean bias and normalized RMSE confirm the model robustness. Mean bias is nearly negligible for SO_4, NO_3, NH_4, Cl and eBC, and approximately -2 µg m^{-3} for OA, up to -4 µg m^{-3} for the Marseille Longchamp site. RMSE exhibits a slightly more scattered distribution, generally ranging between 0.5 and 2 µg m^{-3}.

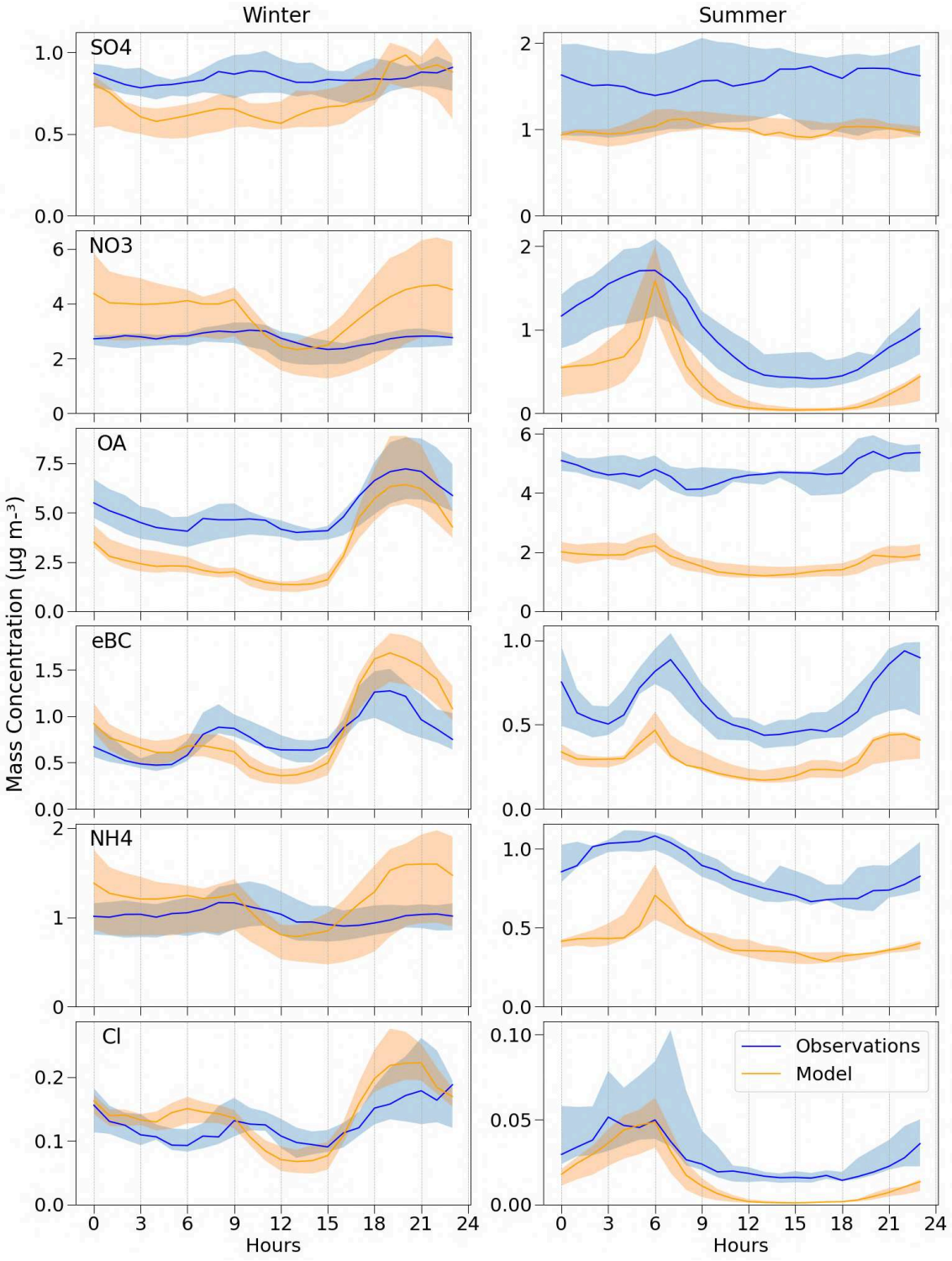

Figure 7: Observed and modeled diel profiles during winter and summer of 2018 across 9 French sites.

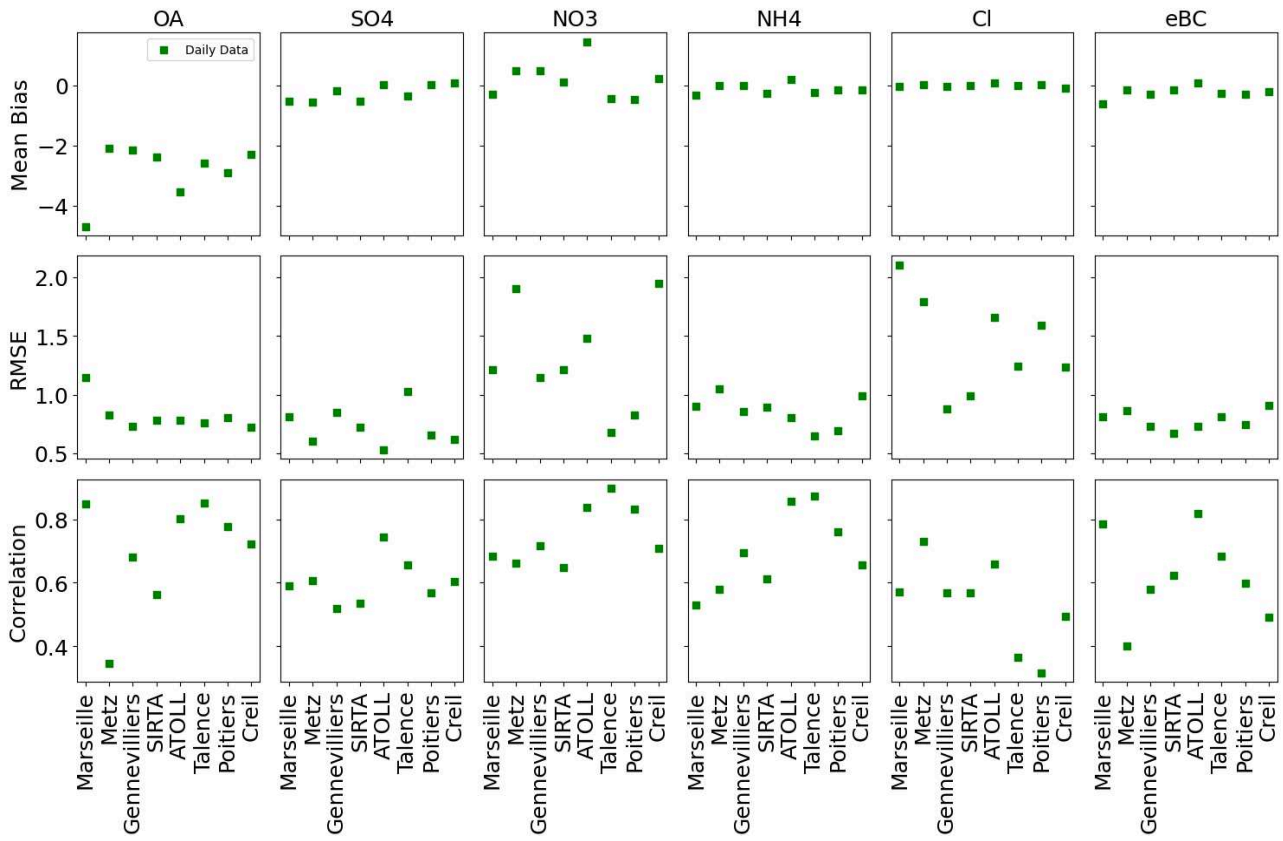

Figure 8: Statistic parameters (mean bias, normalized RMSE, and correlation coefficient r) for different species at each site, using daily averages.

Furthermore, offline chemical information from filter samples collected in the submicron aerosol fraction at four sites in 2018 has been compared with model daily results. These filter samples were collected daily from March 15th to April 29th, 2018 in Talence, from February 16th to April 1st in Poitiers, from January 1st to January 23rd, from May 13th to May 27th, and from September 19th to September 22nd in Lyon, as well as every 4 hours from July 5th to July 27th in Marseille-Longchamp. They were analyzed in the laboratory for their organic carbon (OC), elemental carbon (EC), SO_4, NO_3, and NH_4 loadings. Figure S11 illustrates the comparison between model simulations and either online or offline observations, for these four sites with respect to OA, NO_3, NH_4, SO_4, and eBC.

A higher correlation is observed between simulations and ACSM observations for OA, NO_3, and NH_4 compared to filters (with r^2 values of 0.5, 0.7, and 0.6 with ACSM, as opposed to 0.24, 0.54,

and 0.36 with filters, respectively). SO_4 and eBC show relatively similar correlations (with r^2 values of 0.44 and 0.42 with ACSM and AE33, respectively, and 0.18 and 0.11 with filters, respectively), but they exhibit different slopes (the model vs. ACSM-AE33 demonstrates higher slopes at 0.45 and 0.5 compared to 0.36 and 0.33 with filters). Overall, the comparison of model results with observations from ACSM and AE33 shows higher correlations than with filter analyses, emphasizing the importance of online measurements for validating air quality models.

4 Conclusions

This study presents multiannual measurements of ACSM and AE33 collected at 13 (sub)-urban sites which are part of the national French CARA program. The datasets ranged from 1 to 6 years, in the period between 2015 and 2021. Two of those sites are integrated into the ACTRIS European infrastructure, namely ATOLL (near Lille) and SIRTA (near Paris). The dataset contains submicron aerosol species, namely OA, NO_3, NH_4, SO_4, Cl, and eBC, with its two fractions, eBC_{ff} and eBC_{wb}. A meticulous process of quality control, technical validation, and environmental assessment were employed to validate homogeneously and rigorously the datasets. This process followed the guidelines provided by the French reference laboratory for air quality monitoring and adhered strictly to the ACTRIS standard operating procedures. This article presents a comprehensive overview of these long-term datasets, offering an analysis of the geographical disparities in PM_1 chemical composition, as well as the main seasonal and diel variations in fine particle content.

In France, OA is the predominant compound, with a mean concentration of 4.7 µg m^{-3} (43-60 %) of the PM_1, followed by NO_3 (15-30 %), SO_4 (8-14 %), NH_4 (7-13 %), and eBC (5-11 %). Stations in central and southern France exhibit higher OA mass concentrations (5.3 µg m^{-3}), likely attributed to more pronounced photochemical formation processes. Such secondary processes may also explain that OA is the predominant compound for highest concentration levels at summertime at all sites. Additionally, for other seasons, OA exhibits greater contributions (>55 %) during periods of elevated PM_1 levels in the southern half of France, while NO_3 contributions (>40 %) are more notable during pollution episodes at northern sites, illustrating the competing influences on the aerosol chemical composition of biomass burning

emissions and favorable meteorological conditions leading to the formation of ammonium nitrate, depending on the site location.

Temporal variations reveal distinct seasonality in PM_1 chemical species. eBC_{wb} and OA peak during wintertime, with values of around 0.3 and 5.5 µg m^{-3}, respectively, typically associated with increased residential heating emissions. Those values peak particularly at night, combining stronger emissions and a potentially shallower boundary layer height, facilitating pollutant accumulation. OA also peaks in summer (3.5 µg m^{-3}), typically associated there with the enhanced formation of SOA from both biogenic and anthropogenic sources. NO_3 peaks in late winter and early spring, correlated with typical increase of NH_3 and favorable meteorological conditions during cold periods. Diel variations also manifest unique characteristics at certain sites, such as the Paris Les Halles site, where an organic peak at noon suggests a significant contribution from cooking activities; similarly, a more pronounced rush hour enhancement at BPEst suggests a strong role of local traffic on OA levels.

Furthermore, the datasets presented here serve as essential tools for evaluating and validating regional and global air quality models. An illustrative comparison with CHIMERE is presented in this paper for 2018, encompassing nine French sites. Generally, the model successfully simulates inorganics (NO_3, SO_4, NH_4) and eBC but underestimates OA by about 46-76 %, although with a high correlation between simulations and measurements (r between 0.6 and 0.8). Notably, NO_3 seems to be overestimated at the ATOLL site in northern France (57 %), whereas it is substantially underestimated by 29-42 % at southern sites. Overall, these multi-year datasets from French urban background sites hold significant value for the scientific community, enabling future research endeavors, including source apportionment studies, trend analyses, and epidemiological and health-related investigations.

Data availability

ACSM and AE33 datasets for SIRTA and ATOLL are available in the EBAS database (https://ebas.nilu.no/) and the other site measurements are available on this open link (...).

Funding

This work was notably supported by the French Ministry of Environment, through direct funding of activities achieved by the AASQAs and the LCSQA in the frame of the CARA program. SIRTA observations have been partly funded by the H2020 ACTRIS-2 project under grant agreement No 654109 as well as in the frame of the CNRS-INSU long-term monitoring aerosol program SNO CLAP as a component of the ACTRIS French Research Instructure. Measurements conducted at ATOLL are also part of the Labex CaPPA project (ANR-11-LABX-0005-01), and the CLIMIBIO and ECRIN projects, both also funded by the Regional Council "Hauts-de-France" and the European Regional Development Fund (ERDF). Observations at the Marseille Longchamp supersite benefited from complementary financial support from the PACA region (PRISM project; grant n◦ 2017_08809).

Acknowledgments

The authors are very much grateful to many technicians, engineers and scientists working in the AASQAs as well as at Ineris, IMT Nord-Europe, LSCE and LCE for their precious involvement in long-term operation of the monitors and data handling at the sites investigated in the present study. Authors cannot cite each of them exhaustively but strongly hope they will all recognize themselves here.

Conflicts of Interest. The authors declare no conflict of interest.

References

Allan, J. D., Delia, A. E., Coe, H., Bower, K. N., Alfarra, M. R., Jimenez, J. L., Middlebrook, A. M., Drewnick, F., Onasch, T. B., Canagaratna, M. R., Jayne, J. T., and Worsnop, D. R.: A generalised method for the extraction of chemically resolved mass spectra from Aerodyne aerosol mass spectrometer data, J. Aerosol Sci., 35, 909–922, https://doi.org/10.1016/j.jaerosci.2004.02.007, 2004.

Alastuey, A., Querol, X., García, M., Trechera, P., Savadkoohi, M., Karanasiou, A., Minguillón, M. C., Fiebig, M., Dallënbach, K. R., Salameh, T., Sauvage, S., and Petäjä, T.: Deliverable D1 (D1.1): Guidelines, datasets of non-regulated pollutants incl. metadata, methods, 2022.

Bond, T. C., Doherty, S. J., Fahey, D. W., Forster, P. M., Berntsen, T., DeAngelo, B. J., Flanner, M. G., Ghan, S., Kärcher, B., Koch, D., Kinne, S., Kondo, Y., Quinn, P. K., Sarofim, M. C., Schultz, M. G., Schulz, M., Venkataraman, C., Zhang, H., Zhang, S., Bellouin, N., Guttikunda, S. K., Hopke, P. K., Jacobson, M. Z., Kaiser, J. W., Klimont, Z., Lohmann, U., Schwarz, J. P., Shindell, D., Storelvmo, T.,

Warren, S. G., and Zender, C. S.: Bounding the role of black carbon in the climate system: A scientific assessment, J. Geophys. Res. Atmospheres, 118, 5380–5552, https://doi.org/10.1002/jgrd.50171, 2013.

Bressi, M., Cavalli, F., Putaud, J. P., Fröhlich, R., Petit, J.-E., Aas, W., Äijälä, M., Alastuey, A., Allan, J. D., Aurela, M., Berico, M., Bougiatioti, A., Bukowiecki, N., Canonaco, F., Crenn, V., Dusanter, S., Ehn, M., Elsasser, M., Flentje, H., Graf, P., Green, D. C., Heikkinen, L., Hermann, H., Holzinger, R., Hueglin, C., Keernik, H., Kiendler-Scharr, A., Kubelová, L., Lunder, C., Maasikmets, M., Makeš, O., Malaguti, A., Mihalopoulos, N., Nicolas, J. B., O'Dowd, C., Ovadnevaite, J., Petralia, E., Poulain, L., Priestman, M., Riffault, V., Ripoll, A., Schlag, P., Schwarz, J., Sciare, J., Slowik, J., Sosedova, Y., Stavroulas, I., Teinemaa, E., Via, M., Vodička, P., Williams, P. I., Wiedensohler, A., Young, D. E., Zhang, S., Favez, O., Minguillón, M. C., and Prevot, A. S. H.: A European aerosol phenomenology - 7: High-time resolution chemical characteristics of submicron particulate matter across Europe, Atmospheric Environ. X, 10, 100108, https://doi.org/10.1016/j.aeaoa.2021.100108, 2021.

Canagaratna, M. r., Jayne, J. t., Jimenez, J. l., Allan, J. d., Alfarra, M. r., Zhang, Q., Onasch, T. b., Drewnick, F., Coe, H., Middlebrook, A., Delia, A., Williams, L. r., Trimborn, A. m., Northway, M. j., DeCarlo, P. f., Kolb, C. e., Davidovits, P., and Worsnop, D. r.: Chemical and microphysical characterization of ambient aerosols with the aerodyne aerosol mass spectrometer, Mass Spectrom. Rev., 26, 185–222, https://doi.org/10.1002/mas.20115, 2007.

Canonaco, F., Slowik, J. G., Baltensperger, U., and Prévôt, A. S. H.: Seasonal differences in oxygenated organic aerosol composition: implications for emissions sources and factor analysis, Atmospheric Chem. Phys., 15, 6993–7002, https://doi.org/10.5194/acp-15-6993-2015, 2015.

Chazeau, B., Temime-Roussel, B., Gille, G., Mesbah, B., D'Anna, B., Wortham, H., and Marchand, N.: Measurement report: Fourteen months of real-time characterisation of the submicronic aerosol and its atmospheric dynamics at the Marseille–Longchamp supersite, Atmospheric Chem. Phys., 21, 7293–7319, https://doi.org/10.5194/acp-21-7293-2021, 2021.

Chazeau et al, Organic aerosol source apportionment by using rolling positive matrix factorization: Application to a Mediterranean coastal city, Atmospheric environment: X, 2022

Chebaicheb, H., F. de Brito, J., Chen, G., Tison, E., Marchand, C., Prévôt, A. S. H., Favez, O., and Riffault, V.: Investigation of four-year chemical composition and organic aerosol sources of submicron particles at the ATOLL site in northern France, Environ. Pollut., 330, 121805, https://doi.org/10.1016/j.envpol.2023.121805, 2023.

Chebaicheb, H et al., Phenomenology of organic aerosol multi-annual source apportionment at 12 urban and peri-urban sites in France, in preparation.

Chen, G., Canonaco, F., Tobler, A., Aas, W., Alastuey, A., Allan, J., Atabakhsh, S., Aurela, M., Baltensperger, U., Bougiatioti, A., De Brito, J. F., Ceburnis, D., Chazeau, B., Chebaicheb, H., Daellenbach, K. R., Ehn, M., El Haddad, I., Eleftheriadis, K., Favez, O., Flentje, H., Font, A., Fossum, K., Freney, E., Gini, M., Green, D. C., Heikkinen, L., Herrmann, H., Kalogridis, A.-C., Keernik, H., Lhotka, R., Lin, C., Lunder, C., Maasikmets, M., Manousakas, M. I., Marchand, N., Marin, C., Marmureanu, L., Mihalopoulos, N., Močnik, G., Nęcki, J., O'Dowd, C., Ovadnevaite, J., Peter, T., Petit, J.-E., Pikridas, M., Matthew Platt, S., Pokorná, P., Poulain, L., Priestman, M., Riffault, V., Rinaldi, M., Różański, K., Schwarz, J., Sciare, J., Simon, L., Skiba, A., Slowik, J. G., Sosedova, Y., Stavroulas, I., Styszko, K., Teinemaa, E., Timonen, H., Tremper, A., Vasilescu, J., Via, M., Vodička, P., Wiedensohler, A., Zografou, O., Cruz Minguillón, M., and Prévôt, A. S. H.: European aerosol phenomenology − 8: Harmonised source

apportionment of organic aerosol using 22 Year-long ACSM/AMS datasets, Environ. Int., 166, 107325, https://doi.org/10.1016/j.envint.2022.107325, 2022.

Campagne 2021 d'étalonnage et de comparaison inter-laboratoire (CIL) des Q-ACSM | LCSQA: https://www.lcsqa.org/fr/rapport/campagne-2021-detalonnage-et-de-comparaison-inter-laboratoire-cil-des-q-acsm, last access: 24 October 2023.

Cholakian, A., Beekmann, M., Colette, A., Coll, I., Siour, G., Sciare, J., Marchand, N., Couvidat, F., Pey, J., Gros, V., Sauvage, S., Michoud, V., Sellegri, K., Colomb, A., Sartelet, K., Langley DeWitt, H., Elser, M., Prévot, A. S. H., Szidat, S., and Dulac, F.: Simulation of fine organic aerosols in the western Mediterranean area during the ChArMEx 2013 summer campaign, Atmospheric Chem. Phys., 18, 7287–7312, https://doi.org/10.5194/acp-18-7287-2018, 2018.

Chrit, M., Sartelet, K., Sciare, J., Pey, J., Marchand, N., Couvidat, F., Sellegri, K., and Beekmann, M.: Modelling organic aerosol concentrations and properties during ChArMEx summer campaigns of 2012 and 2013 in the western Mediterranean region, Atmospheric Chem. Phys., 17, 12509–12531, https://doi.org/10.5194/acp-17-12509-2017, 2017.

Ciarelli, G., Aksoyoglu, S., Crippa, M., Jimenez, J.-L., Nemitz, E., Sellegri, K., Äijälä, M., Carbone, S., Mohr, C., O'Dowd, C., Poulain, L., Baltensperger, U., and Prévôt, A. S. H.: Evaluation of European air quality modelled by CAMx including the volatility basis set scheme, Atmospheric Chem. Phys., 16, 10313–10332, https://doi.org/10.5194/acp-16-10313-2016, 2016.

Couvidat, F. and Sartelet, K.: The Secondary Organic Aerosol Processor (SOAP v1.0) model: a unified model with different ranges of complexity based on the molecular surrogate approach, Geosci. Model Dev., 8, 1111–1138, https://doi.org/10.5194/gmd-8-1111-2015, 2015.

Couvidat, Florian, et Bertrand Bessagnet. 2021. « Role of ecosystem-atmosphere exchanges of semi-volatile organic compounds in organic aerosol formation ». Atmospheric Environment 263 (octobre): 118541. https://doi.org/10.1016/j.atmosenv.2021.118541.

Couvidat, Florian, Bertrand Bessagnet, Marta Garcia-Vivanco, Elsa Real, Laurent Menut, et Augustin Colette. 2018. « Development of an Inorganic and Organic Aerosol Model (CHIMERE 2017β v1.0): Seasonal and Spatial Evaluation over Europe ». Geoscientific Model Development 11 (1): 165‑94. https://doi.org/10.5194/gmd-11-165-2018.

Daellenbach, K. R., Bozzetti, C., Křepelová, A., Canonaco, F., Wolf, R., Zotter, P., Fermo, P., Crippa, M., Slowik, J. G., Sosedova, Y., Zhang, Y., Huang, R.-J., Poulain, L., Szidat, S., Baltensperger, U., El Haddad, I., and Prévôt, A. S. H.: Characterization and source apportionment of organic aerosol using offline aerosol mass spectrometry, Atmospheric Meas. Tech., 9, 23–39, https://doi.org/10.5194/amt-9-23-2016, 2016.

Drinovec, L., Močnik, G., Zotter, P., Prévôt, A. S. H., Ruckstuhl, C., Coz, E., Rupakheti, M., Sciare, J., Müller, T., Wiedensohler, A., and Hansen, A. D. A.: The "dual-spot" Aethalometer: an improved measurement of aerosol black carbon with real-time loading compensation, Atmospheric Meas. Tech., 8, 1965–1979, https://doi.org/10.5194/amt-8-1965-2015, 2015.

Dupont, J.-C., Haeffelin, M., Badosa, J., Elias, T., Favez, O., Petit, J. E., Meleux, F., Sciare, J., Crenn, V., and Bonne, J. L.: Role of the boundary layer dynamics effects on an extreme air pollution event in Paris, Atmos. Environ., 141, 571–579, https://doi.org/10.1016/j.atmosenv.2016.06.061, 2016.

Eatough, D. J., Obeidi, F., Pang, Y., Ding, Y., Eatough, N. L., and Wilson, W. E.: Integrated and real-time diffusion denuder sample for PM2.5, Atmos. Environ., 33, 2835–2844, https://doi.org/10.1016/S1352-2310(98)00326-4, 1999.

Europe's air quality status 2023 — European Environment Agency: https://www.eea.europa.eu/publications/europes-air-quality-status-2023, last access: 22 August 2023.

Favez, O., Cachier, H., Sciare, J., and Le Moullec, Y.: Characterization and contribution to PM2.5 of semi-volatile aerosols in Paris (France), Atmos. Environ., 41, 7969–7976, https://doi.org/10.1016/j.atmosenv.2007.09.031, 2007.

Favez, O., El Haddad, I., Piot, C., Boréave, A., Abidi, E., Marchand, N., Jaffrezo, J.-L., Besombes, J.-L., Personnaz, M.-B., Sciare, J., Wortham, H., George, C., and D'Anna, B.: Inter-comparison of source apportionment models for the estimation of wood burning aerosols during wintertime in an Alpine city (Grenoble, France), Atmospheric Chem. Phys., 10, 5295–5314, https://doi.org/10.5194/acp-10-5295-2010, 2010.

Favez, O., Weber, S., Petit, J.-E., Alleman, L., Albinet, A., Riffault, V., Chazeau, B., Amodeo, T., Salameh, D., Zhang, Y., Srivastava, D., Samaké, A., Aujay, R., Papin, A., Bonnaire, N., Boullanger, C., Chatain, M., Chevrier, F., Detournay, A., and Leoz-Garziandia, E.: Overview of the French Operational Network for In Situ Observation of PM Chemical Composition and Sources in Urban Environments (CARA Program), https://doi.org/10.20944/preprints202101.0182.v1, 2021.

Flentje, H., Mattis, I., Kipling, Z., Rémy, S., and Thomas, W.: Evaluation of ECMWF IFS-AER (CAMS) operational forecasts during cycle 41r1–46r1 with calibrated ceilometer profiles over Germany, Geosci. Model Dev., 14, 1721–1751, https://doi.org/10.5194/gmd-14-1721-2021, 2021.

Foret, G., Michoud, V., Kotthaus, S., Petit, J.-E., Baudic, A., Siour, G., Kim, Y., Doussin, J.-F., Dupont, J.-C., Formenti, P., Gaimoz, C., Ghersi, V., Gratien, A., Gros, V., Jaffrezo, J.-L., Haeffelin, M., Kreitz, M., Ravetta, F., Sartelet, K., Simon, L., Té, Y., Uzu, G., Zhang, S., Favez, O., and Beekmann, M.: The December 2016 extreme weather and particulate matter pollution episode in the Paris region (France), Atmos. Environ., 291, 119386, https://doi.org/10.1016/j.atmosenv.2022.119386, 2022.

Fortems-Cheiney, A., Dufour, G., Hamaoui-Laguel, L., Foret, G., Siour, G., Van Damme, M., Meleux, F., Coheur, P.-F., Clerbaux, C., Clarisse, L., Favez, O., Wallasch, M., and Beekmann, M.: Unaccounted variability in NH3 agricultural sources detected by IASI contributing to European spring haze episode, Geophys. Res. Lett., 43, 5475–5482, https://doi.org/10.1002/2016GL069361, 2016.

Freney, E., Zhang, Y., Croteau, P., Amodeo, T., Williams, L., Truong, F., Petit, J.-E., Sciare, J., Sarda-Esteve, R., Bonnaire, N., Arumae, T., Aurela, M., Bougiatioti, A., Mihalopoulos, N., Coz, E., Artinano, B., Crenn, V., Elste, T., Heikkinen, L., Poulain, L., Wiedensohler, A., Herrmann, H., Priestman, M., Alastuey, A., Stavroulas, I., Tobler, A., Vasilescu, J., Zanca, N., Canagaratna, M., Carbone, C., Flentje, H., Green, D., Maasikmets, M., Marmureanu, L., Minguillon, M. C., Prevot, A. S. H., Gros, V., Jayne, J., and Favez, O.: The second ACTRIS inter-comparison (2016) for Aerosol Chemical Speciation Monitors (ACSM): Calibration protocols and instrument performance evaluations, Aerosol Sci. Technol., 53, 830–842, https://doi.org/10.1080/02786826.2019.1608901, 2019.

Fuzzi, S., Baltensperger, U., Carslaw, K., Decesari, S., Denier van der Gon, H., Facchini, M. C., Fowler, D., Koren, I., Langford, B., Lohmann, U., Nemitz, E., Pandis, S., Riipinen, I., Rudich, Y., Schaap, M., Slowik, J. G., Spracklen, D. V., Vignati, E., Wild, M., Williams, M., and Gilardoni, S.: Particulate matter,

air quality and climate: lessons learned and future needs, Atmospheric Chem. Phys., 15, 8217–8299, https://doi.org/10.5194/acp-15-8217-2015, 2015.

Heikkinen, L., Äijälä, M., Daellenbach, K. R., Chen, G., Garmash, O., Aliaga, D., Graeffe, F., Räty, M., Luoma, K., Aalto, P., Kulmala, M., Petäjä, T., Worsnop, D., and Ehn, M.: Eight years of sub-micrometre organic aerosol composition data from the boreal forest characterized using a machine-learning approach, Atmospheric Chem. Phys., 21, 10081–10109, https://doi.org/10.5194/acp-21-10081-2021, 2021.

Jacobson, M. Z.: Strong radiative heating due to the mixing state of black carbon in atmospheric aerosols, Nature, 409, 695–697, https://doi.org/10.1038/35055518, 2001.

Janssen, N. A. H., Hoek, G., Simic, -Lawson Milena, Fischer, P., van, B. L., ten, B. H., Keuken, M., Atkinson, R. W., Anderson, H. R., Brunekreef, B., and Cassee, F. R.: Black Carbon as an Additional Indicator of the Adverse Health Effects of Airborne Particles Compared with PM10 and PM2.5, Environ. Health Perspect., 119, 1691–1699, https://doi.org/10.1289/ehp.1003369, 2011.

Kirchstetter, T. W., Corrigan, C. E., and Novakov, T.: Laboratory and field investigation of the adsorption of gaseous organic compounds onto quartz filters, Atmos. Environ., 35, 1663–1671, https://doi.org/10.1016/S1352-2310(00)00448-9, 2001.

Kuenen, J., Dellaert, S., Visschedijk, A., Jalkanen, J.-P., Super, I., and Denier van der Gon, H.: CAMS-REG-v4: a state-of-the-art high-resolution European emission inventory for air quality modelling, Earth Syst. Sci. Data, 14, 491–515, https://doi.org/10.5194/essd-14-491-2022, 2022.

Lanz, V. A., Prévôt, A. S. H., Alfarra, M. R., Weimer, S., Mohr, C., DeCarlo, P. F., Gianini, M. F. D., Hueglin, C., Schneider, J., Favez, O., D'Anna, B., George, C., and Baltensperger, U.: Characterization of aerosol chemical composition with aerosol mass spectrometry in Central Europe: an overview, Atmospheric Chem. Phys., 10, 10453–10471, https://doi.org/10.5194/acp-10-10453-2010, 2010.

LCSQA: Guide méthodologique pour la mesure du « Black Carbon » par Aethalomètre multi longueur d'onde AE33 dans l'air ambiant (Version 2020), 2020.

LCSQA: CAHIER DES CHARGES POUR L'ETALONNAGE DES Q-ACSM, 2022.

Menut, L., Bessagnet, B., Briant, R., Cholakian, A., Couvidat, F., Mailler, S., Pennel, R., Siour, G., Tuccella, P., Turquety, S., and Valari, M.: The CHIMERE v2020r1 online chemistry-transport model, Geosci. Model Dev., 14, 6781–6811, https://doi.org/10.5194/gmd-14-6781-2021, 2021.

Middlebrook, A. M., Bahreini, R., Jimenez, J. L., and Cana-Garatna, M. R.: Evaluation of Composition-Dependent Collection Efficiencies for the Aerodyne Aerosol Mass Spectrometer using Field Data, Aerosol Sci Technol, 46, 258–271, 2011.

Ng, N. L., Herndon, S. C., Trimborn, A., Canagaratna, M. R., Croteau, P. L., Onasch, T. B., Sueper, D., Worsnop, D. R., Zhang, Q., Sun, Y. L., and Jayne, J. T.: An Aerosol Chemical Speciation Monitor (ACSM) for Routine Monitoring of the Composition and Mass Concentrations of Ambient Aerosol, Aerosol Sci. Technol., 45, 780–794, https://doi.org/10.1080/02786826.2011.560211, 2011a.

Ng, N. L., Canagaratna, M. R., Jimenez, J. L., Zhang, Q., Ulbrich, I. M., and Worsnop, D. R.: Real-Time Methods for Estimating Organic Component Mass Concentrations from Aerosol Mass Spectrometer Data, Environ. Sci. Technol., 45, 910–916, https://doi.org/10.1021/es102951k, 2011b.

Petit, J.-E., Favez, O., Sciare, J., Crenn, V., Sarda-Estève, R., Bonnaire, N., Močnik, G., Dupont, J.-C., Haeffelin, M., and Leoz-Garziandia, E.: Two years of near real-time chemical composition of submicron aerosols in the region of Paris using an Aerosol Chemical Speciation Monitor (ACSM) and a multi-wavelength Aethalometer, Atmospheric Chem. Phys., 15, 2985–3005, https://doi.org/10.5194/acp-15-2985-2015, 2015.

Petit, J.-E., Amodeo, T., Meleux, F., Bessagnet, B., Menut, L., Grenier, D., Pellan, Y., Ockler, A., Rocq, B., Gros, V., Sciare, J., and Favez, O.: Characterising an intense PM pollution episode in March 2015 in France from multi-site approach and near real time data: Climatology, variabilities, geographical origins and model evaluation, Atmos. Environ., 155, 68–84, https://doi.org/10.1016/j.atmosenv.2017.02.012, 2017.

Putaud, J.-P., Raes, F., Van Dingenen, R., Brüggemann, E., Facchini, M.-C., Decesari, S., Fuzzi, S., Gehrig, R., Hüglin, C., Laj, P., Lorbeer, G., Maenhaut, W., Mihalopoulos, N., Müller, K., Querol, X., Rodriguez, S., Schneider, J., Spindler, G., Brink, H. ten, Tørseth, K., and Wiedensohler, A.: A European aerosol phenomenology—2: chemical characteristics of particulate matter at kerbside, urban, rural and background sites in Europe, Atmos. Environ., 38, 2579–2595, https://doi.org/10.1016/j.atmosenv.2004.01.041, 2004.

Roig Rodelas, R., Perdrix, E., Herbin, B., and Riffault, V.: Characterization and variability of inorganic aerosols and their gaseous precursors at a suburban site in northern France over one year (2015–2016), Atmos. Environ., 200, 142–157, https://doi.org/10.1016/j.atmosenv.2018.11.041, 2019.

Roldin, P., Ehn, M., Kurtén, T., Olenius, T., Rissanen, M. P., Sarnela, N., Elm, J., Rantala, P., Hao, L., Hyttinen, N., Heikkinen, L., Worsnop, D. R., Pichelstorfer, L., Xavier, C., Clusius, P., Öström, E., Petäjä, T., Kulmala, M., Vehkamäki, H., Virtanen, A., Riipinen, I., and Boy, M.: The role of highly oxygenated organic molecules in the Boreal aerosol-cloud-climate system, Nat. Commun., 10, 4370, https://doi.org/10.1038/s41467-019-12338-8, 2019.

Sandradewi, J., Prévôt, A. S. H., Szidat, S., Perron, N., Alfarra, M. R., Lanz, V. A., Weingartner, E., and Baltensperger, U.: Using Aerosol Light Absorption Measurements for the Quantitative Determination of Wood Burning and Traffic Emission Contributions to Particulate Matter, Environ. Sci. Technol., 42, 3316–3323, https://doi.org/10.1021/es702253m, 2008.

Sartelet, K., Couvidat, F., Wang, Z., Flageul, C., and Kim, Y.: SSH-Aerosol v1.1: A Modular Box Model to Simulate the Evolution of Primary and Secondary Aerosols, Atmosphere, 11, 525, https://doi.org/10.3390/atmos11050525, 2020.

Saunders, S. M., Jenkin, M. E., Derwent, R. G., and Pilling, M. J.: Protocol for the development of the Master Chemical Mechanism, MCM v3 (Part A): tropospheric degradation of non-aromatic volatile organic compounds, Atmospheric Chem. Phys., 3, 161–180, https://doi.org/10.5194/acp-3-161-2003, 2003.

Savadkoohi, M., Pandolfi, M., Reche, C., Niemi, J. V., Mooibroek, D., Titos, G., Green, D. C., Tremper, A. H., Hueglin, C., Liakakou, E., Mihalopoulos, N., Stavroulas, I., Artiñano, B., Coz, E., Alados-Arboledas, L., Beddows, D., Riffault, V., De Brito, J. F., Bastian, S., Baudic, A., Colombi, C., Costabile, F., Chazeau, B., Marchand, N., Gómez-Amo, J. L., Estellés, V., Matos, V., van der Gaag, E., Gille, G., Luoma, K., Manninen, H. E., Norman, M., Silvergren, S., Petit, J.-E., Putaud, J.-P., Rattigan, O. V., Timonen, H., Tuch, T., Merkel, M., Weinhold, K., Vratolis, S., Vasilescu, J., Favez, O., Harrison, R. M., Laj, P., Wiedensohler, A., Hopke, P. K., Petäjä, T., Alastuey, A., and Querol, X.: The variability of

mass concentrations and source apportionment analysis of equivalent black carbon across urban Europe, Environ. Int., 178, 108081, https://doi.org/10.1016/j.envint.2023.108081, 2023.

Schaap, M., Spindler, G., Schulz, M., Acker, K., Maenhaut, W., Berner, A., Wieprecht, W., Streit, N., Müller, K., Brüggemann, E., Chi, X., Putaud, J.-P., Hitzenberger, R., Puxbaum, H., Baltensperger, U., and ten Brink, H.: Artefacts in the sampling of nitrate studied in the "INTERCOMP" campaigns of EUROTRAC-AEROSOL, Atmos. Environ., 38, 6487–6496, https://doi.org/10.1016/j.atmosenv.2004.08.026, 2004.

Sun, J., Zhang, Q., Canagaratna, M. R., Zhang, Y., Ng, N. L., Sun, Y., Jayne, J. T., Zhang, X., Zhang, X., and Worsnop, D. R.: Highly time- and size-resolved characterization of submicron aerosol particles in Beijing using an Aerodyne Aerosol Mass Spectrometer, Atmos. Environ., 44, 131–140, https://doi.org/10.1016/j.atmosenv.2009.03.020, 2010.

Tobler, A. K., Skiba, A., Wang, D. S., Croteau, P., Styszko, K., Nęcki, J., Baltensperger, U., Slowik, J. G., and Prévôt, A. S. H.: Improved chloride quantification in quadrupole aerosol chemical speciation monitors (Q-ACSMs), Atmospheric Meas. Tech., 13, 5293–5301, https://doi.org/10.5194/amt-13-5293-2020, 2020.

Tobler, A. K., Skiba, A., Canonaco, F., Močnik, G., Rai, P., Chen, G., Bartyzel, J., Zimnoch, M., Styszko, K., Nęcki, J., Furger, M., Różański, K., Baltensperger, U., Slowik, J. G., and Prevot, A. S. H.: Characterization of non-refractory (NR) PM_1 and source apportionment of organic aerosol in Kraków, Poland, Atmospheric Chem. Phys., 21, 14893–14906, https://doi.org/10.5194/acp-21-14893-2021, 2021.

Viana, M., Kuhlbusch, T. A. J., Querol, X., Alastuey, A., Harrison, R. M., Hopke, P. K., Winiwarter, W., Vallius, M., Szidat, S., Prévôt, A. S. H., Hueglin, C., Bloemen, H., Wåhlin, P., Vecchi, R., Miranda, A. I., Kasper-Giebl, A., Maenhaut, W., and Hitzenberger, R.: Source apportionment of particulate matter in Europe: A review of methods and results, J. Aerosol Sci., 39, 827–849, https://doi.org/10.1016/j.jaerosci.2008.05.007, 2008.

Wang, Z., Couvidat, F., and Sartelet, K.: GENerator of reduced Organic Aerosol mechanism (GENOA v1.0): an automatic generation tool of semi-explicit mechanisms, Geosci. Model Dev., 15, 8957–8982, https://doi.org/10.5194/gmd-15-8957-2022, 2022.

Wang, Z., Couvidat, F., and Sartelet, K.: Implementation of a parallel reduction algorithm in the GENerator of reduced Organic Aerosol mechanisms (GENOA v2.0): Application to multiple monoterpene aerosol precursors, J. Aerosol Sci., 174, 106248, https://doi.org/10.1016/j.jaerosci.2023.106248, 2023.

Wang, Z., Couvidat, F. and Sartelet, K. Response of biogenic secondary organic aerosol formation to anthropogenic NOx emission mitigation. Submitted to Science of The Total Environment, 2024.

Watson, T. B.: Aerosol Chemical Speciation Monitor (ACSM) Instrument Handbook, https://doi.org/10.2172/1375336, 2017.

Wittmaack, K. and Keck, L.: Thermodesorption of aerosol matter on multiple filters of different materials for a more detailed evaluation of sampling artifacts, Atmos. Environ., 38, 5205–5215, https://doi.org/10.1016/j.atmosenv.2004.05.047, 2004.

WHO Air Quality Guidelines:
https://www.c40knowledgehub.org/s/article/WHO-Air-Quality-Guidelines?language=en_US, last access: 23 January 2023.

Zanatta, M., Gysel, M., Bukowiecki, N., Müller, T., Weingartner, E., Areskoug, H., Fiebig, M., Yttri, K. E., Mihalopoulos, N., Kouvarakis, G., Beddows, D., Harrison, R. M., Cavalli, F., Putaud, J. P., Spindler, G., Wiedensohler, A., Alastuey, A., Pandolfi, M., Sellegri, K., Swietlicki, E., Jaffrezo, J. L., Baltensperger, U., and Laj, P.: A European aerosol phenomenology-5: Climatology of black carbon optical properties at 9 regional background sites across Europe, Atmos. Environ., 145, 346–364, https://doi.org/10.1016/j.atmosenv.2016.09.035, 2016.

Zhang, Y., Favez, O., Albinet, A., Canonaco, F., Truong, F., Amodeo, T., Prevot, A., Sciare, J., and Gros, V.: Long-term measurements of the chemistry and sources of submicron aerosols at SIRTA in Paris area, France, in: European Aerosol Conference (EAC 2017), Zurich, Switzerland, 2017.

Zhang, Y., Favez, O., Petit, J.-E., Canonaco, F., Truong, F., Bonnaire, N., Crenn, V., Amodeo, T., Prévôt, A. S. H., Sciare, J., Gros, V., and Albinet, A.: Six-year source apportionment of submicron organic aerosols from near-continuous highly time-resolved measurements at SIRTA (Paris area, France), Atmospheric Chem. Phys., 19, 14755–14776, https://doi.org/10.5194/acp-19-14755-2019, 2019.

III.3. Supplementary Information de l'article 1

Supplementary Information

Multi-year high time resolution datasets of fine PM at 13 sites of the French Operational Network (CARA program): Data processing and chemical composition

Hasna Chebaicheb[1,2,3], Joel F. de Brito[1], Tanguy Amodeo[2,3], Florian Couvidat[2], Jean-Eudes Petit[4], Emmanuel Tison[1], Gregory Abbou[5], Alexia Baudic[5], Mélodie Chatain[6], Benjamin Chazeau[7,8], Nicolas Marchand[8], Raphaële Falhun[9], Florie Francony[10], Cyril Ratier[10], Didier Grenier[11], Nicolas Vigier[11], Shouwen Zhang[12], Gregory Gille[7], Laurent Meunier[2,3], Véronique Riffault[1,3], Olivier Favez[2,3]

[1]IMT Nord Europe, Institut Mines-Télécom, Université de Lille, Centre for Energy and Environment, 59000, Lille, France
[2]Institut National de l'environnement Industriel et des Risques (INERIS), 60550 Verneuil-en-Halatte, France
[3]Laboratoire Central de Surveillance de la Qualité de l'Air (LCSQA), 60550 Verneuil-en-Halatte, France
[4]Laboratoire des Sciences du Climat et de l'Environnement (LSCE), CNRS-CEA-UVSQ (UMR 8212), 91191 Gif-sur-Yvette, France
[5]Airparif, Air Quality Monitoring Network for the Greater Paris Area, 75004 Paris, France
[6]Atmo Grand Est, 67300 Schiltigheim, France
[7]AtmoSud, Regional Network for Air Quality Monitoring of Provence-Alpes-Côte-d'Azur, Marseille, France
[8] Aix Marseille Univ, CNRS, LCE, Marseille, France
[9]Air Breizh, 35200 Rennes, France
[10]Atmo Nouvelle-Aquitaine, 33692 Mérignac, France
[11]Atmo Auvergne Rhône-Alpes, 69500 Bron, France
[12]Atmo Hauts de France, 59044 Lille, France

Correspondence to: hasna.chebaicheb@ineris.fr

Table S1: Description of the measurement stations from the CARA program used in this paper. A detailed description of these sites is presented at the end of SI, section “Sites description”.

Operator	**Station name**	**City**	**Airbase ID**	**Altitude (m a.s.l)**	**Latitude**	**Longitude**	**Site type**
IMT Nord Europe	ATOLL	Lille	-	70	50.6111	3.1404	Suburban
LSCE & Ineris	SIRTA	Greater Paris	-	163	48.71181	2.14818	Suburban
Airparif	Gennevilliers	Greater Paris	FR04002	28	48.9298083	2.2946194	Urban background
Airparif	Paris Les Halles	Paris	FR04055	35	48.8627083	2.3446972	Urban background
Airparif	Paris BPEst	Paris	FR04329	49	48.8385167	2.4126242	Urban Traffic
Air Breizh	Rennes Pays-Bas	Rennes	FR19017	45	48.08965	-1.65911	Urban background
Atmo AuRA	Lyon Centre	Lyon	FR20062	160	45.75779	4.85422	Urban background
Atmo Grand Est	Metz Borny	Metz	FR01012	204	49.1102806	6.2233361	Urban background
Atmo Grand Est	Strasbourg Danube	Strasbourg	FR42010	135	48.5062222	7.7511806	Urban background
Atmo Hauts-de-France	Creil Faïencerie	Creil	FR18043	31	49.2597222	2.4744444	Urban background
AtmoSud & LCE	Marseille Longchamp	Marseille	FR03043	73	43.3052889	5.3947056	Urban background
Atmo Nouvelle-Aquitaine	Poitiers Augouard	Poitiers	FR09404	105	46.5839885	0.3455967	Urban background
Atmo Nouvelle-Aquitaine	Talence	Bordeaux	FR31002	23	44.800442	-0.5893941	Urban background

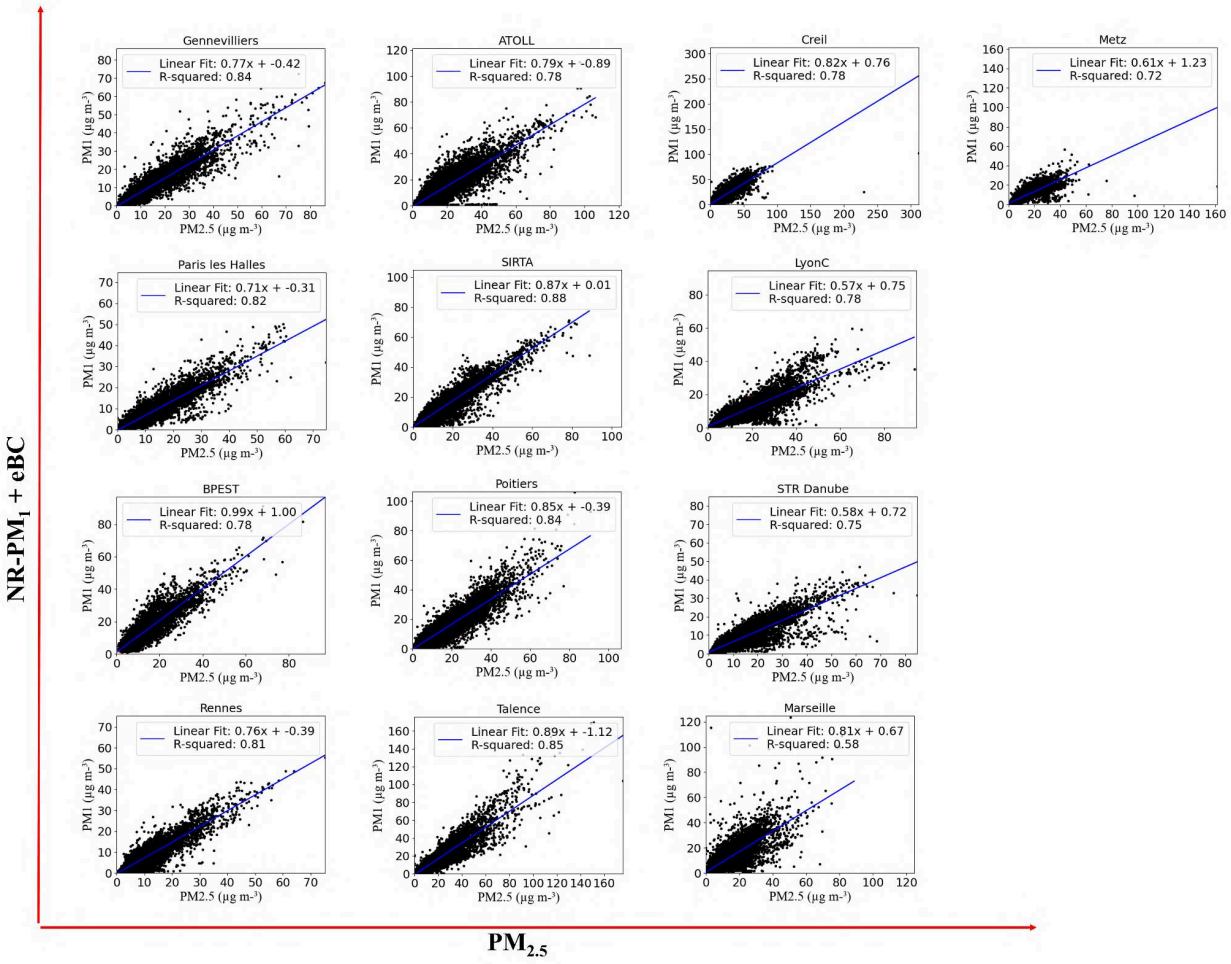

Figure S1: NR-PM_1+eBC vs. $PM_{2.5}$ for each site during the whole study period.

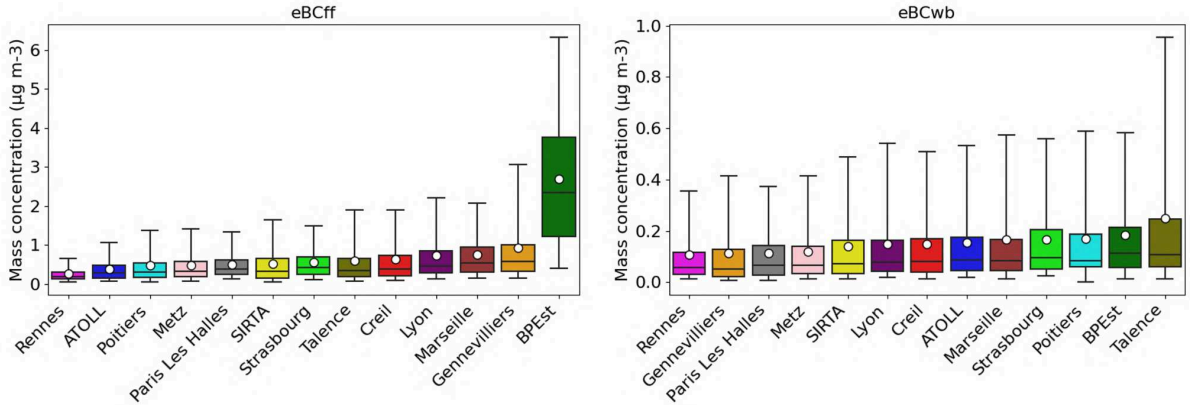

Figure S2: Box plots of statistical information (mean in circle, median, the percentiles 5, 25, 75, and 95th) of eBC_{ff} and eBC_{wb} for the 13 French sites.

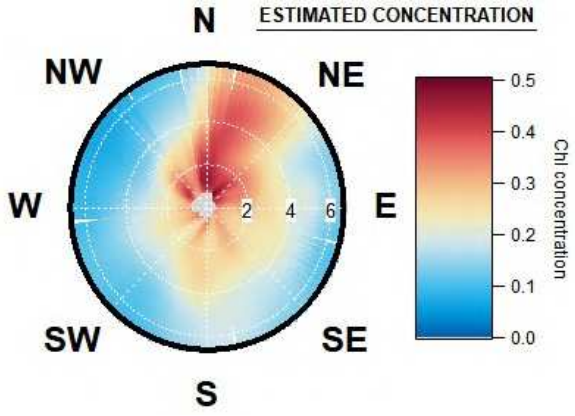

Figure S3: Pollution rose of Chloride at Creil site (Zefir).

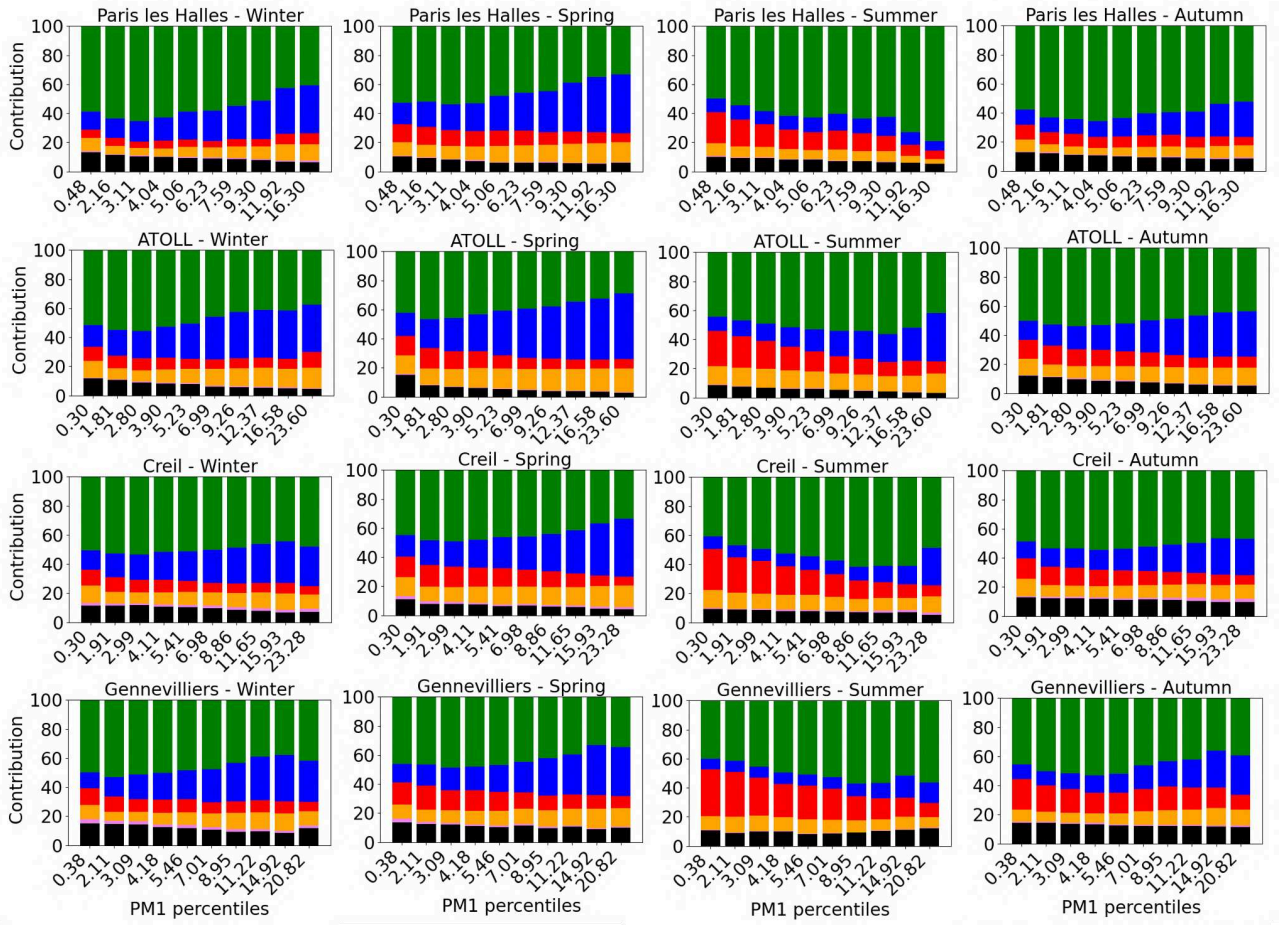

Figure S4: Relative contribution of chemical species as a function of PM_1 percentiles by season (continued)

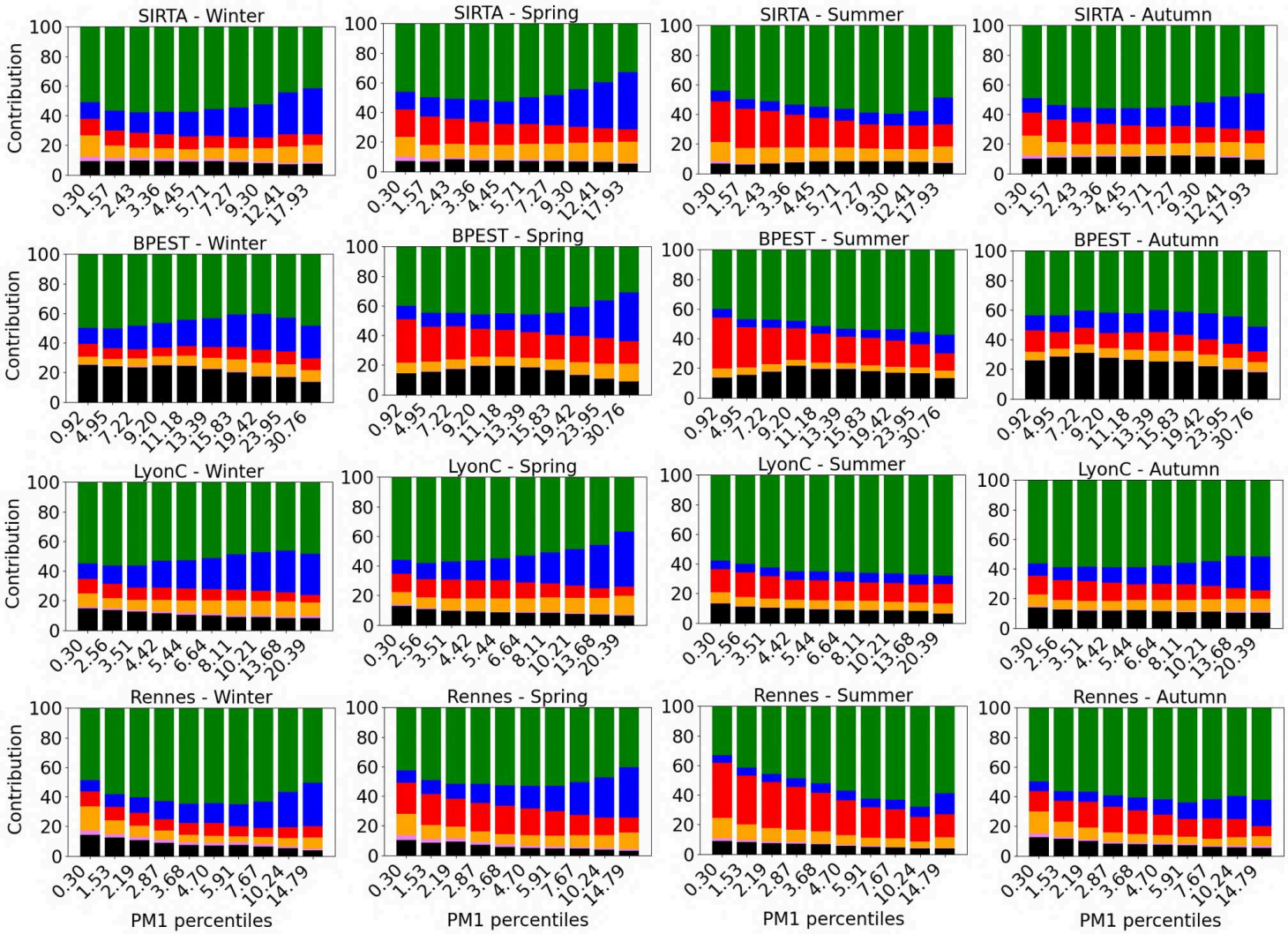

Figure S4: Relative contribution of chemical species as a function of PM_1 percentiles by season (continued).

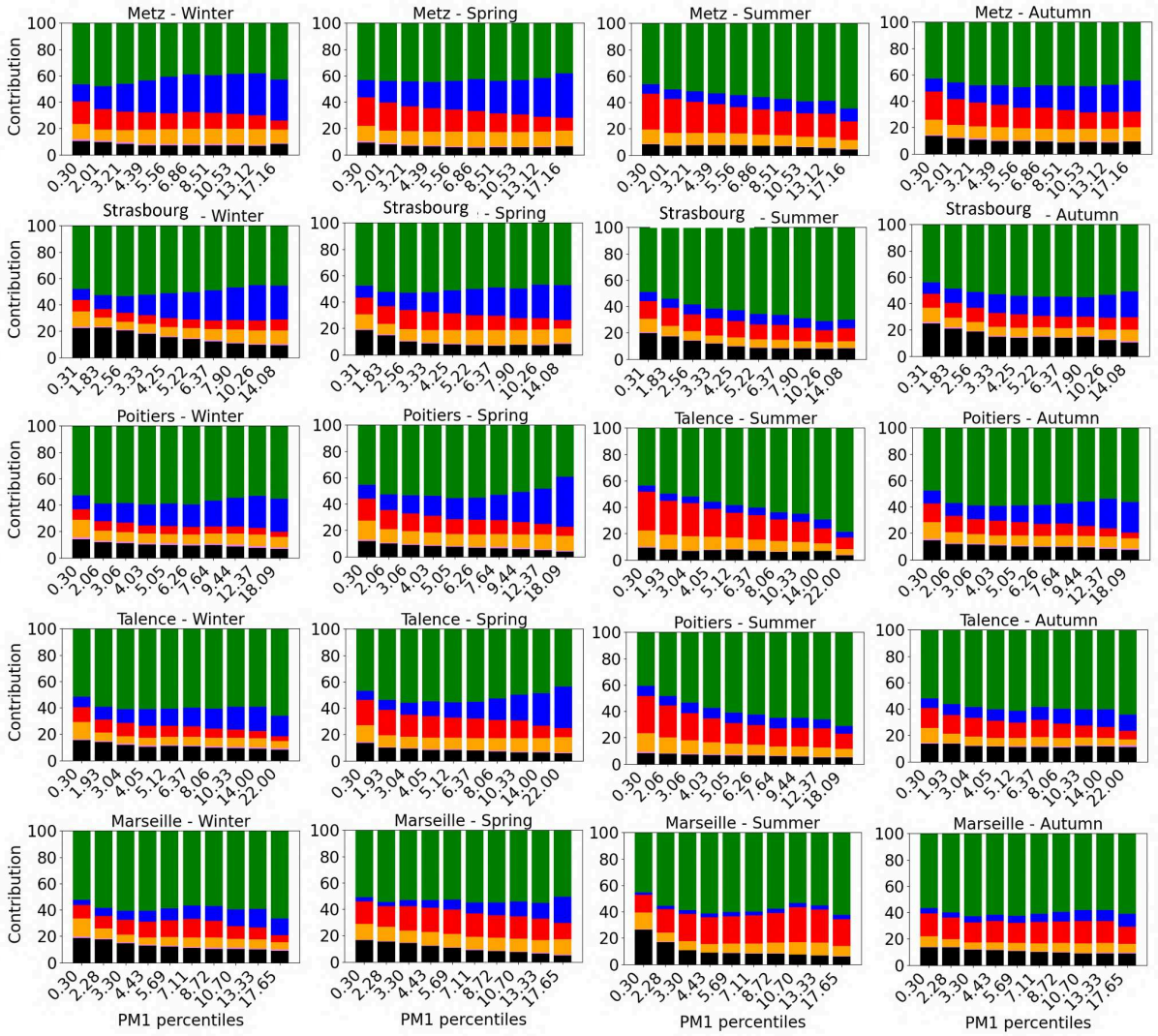

Figure S4: Relative contribution of chemical species as a function of PM_1 percentiles by season.

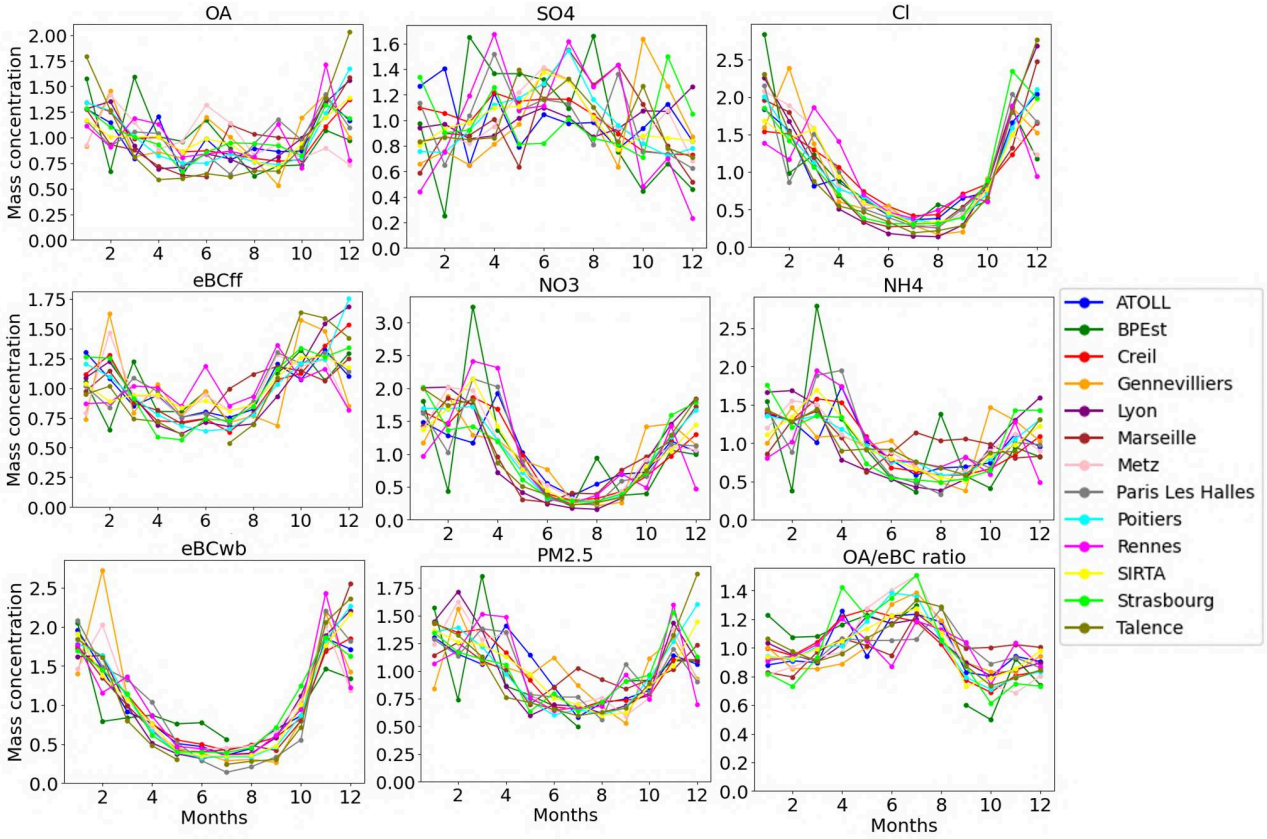

Figure S5: Monthly concentrations normalized by site-specific annual averages of the species studied here.

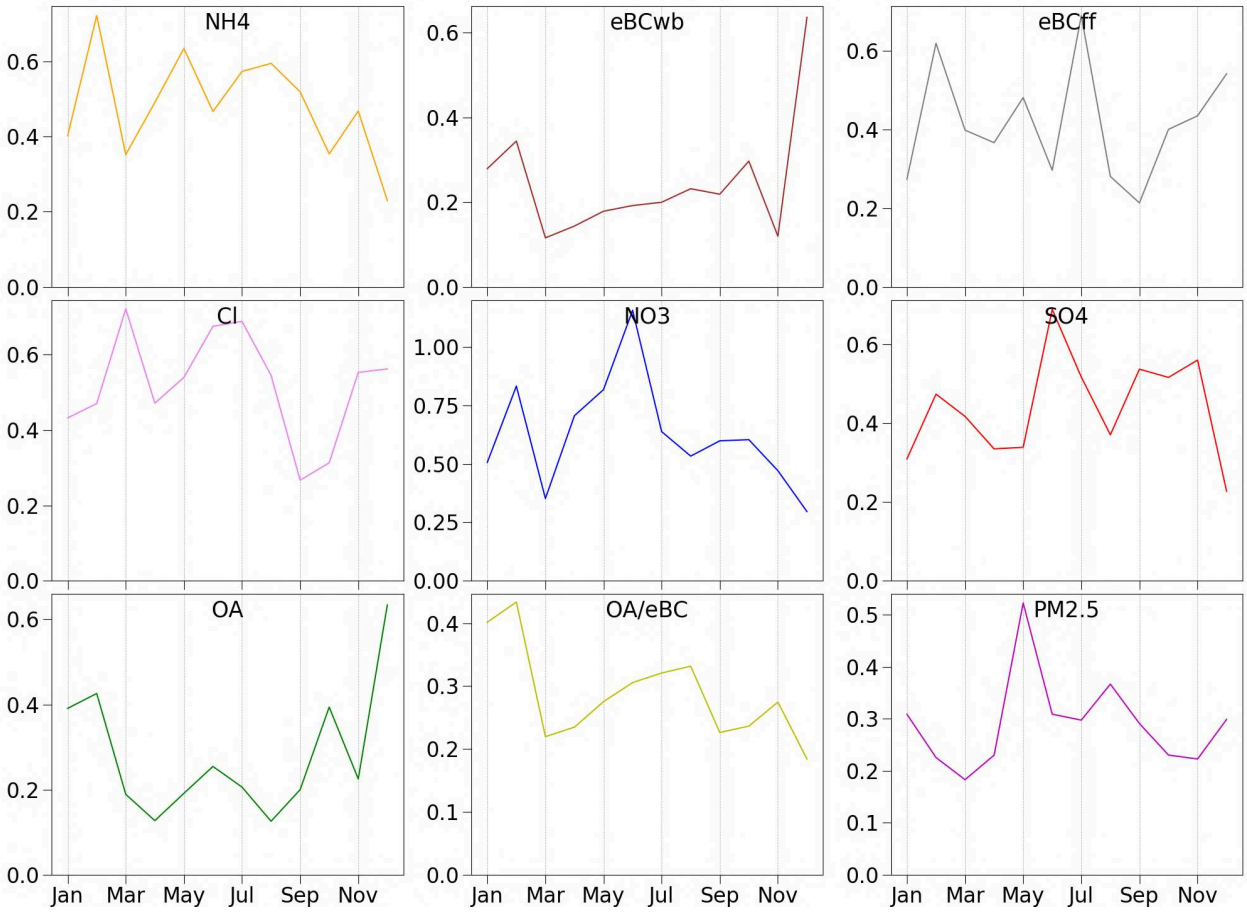

Figure S6: Monthly IQR/median ratios for each component from Fig. 4 from the main text.

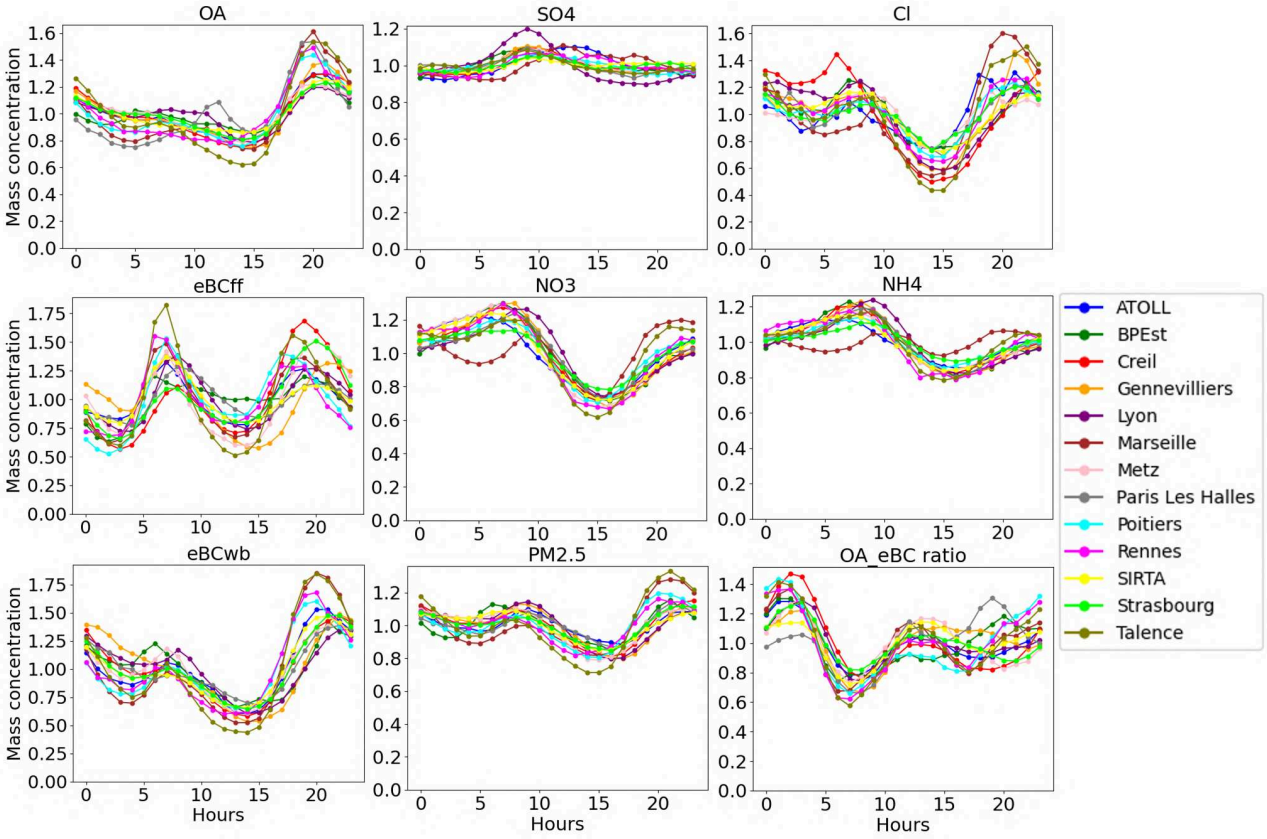

Figure S7: Diel concentration profiles, normalized by site-specific daily averages.

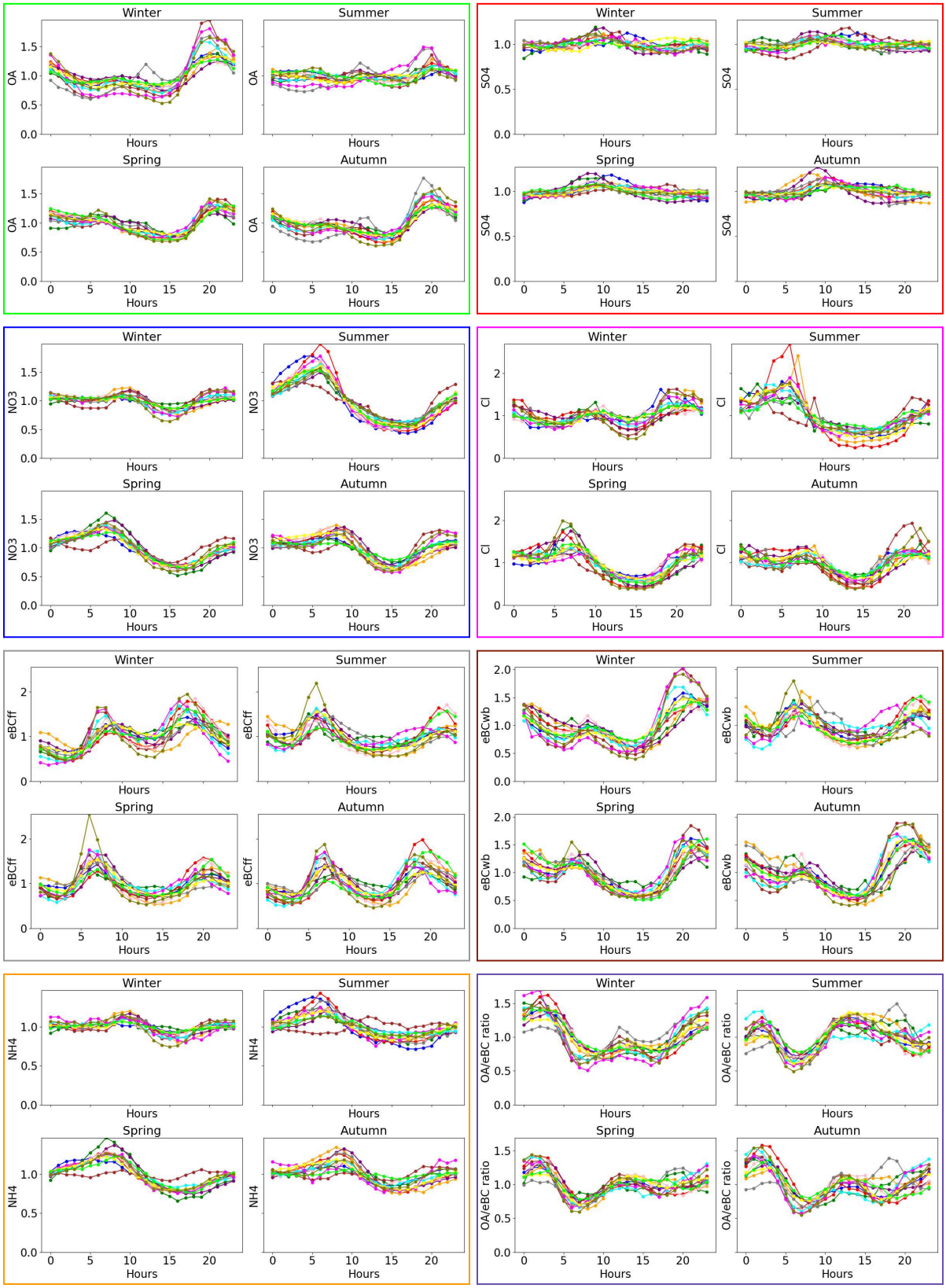

Figure S8: Seasonal diel concentration profiles, normalized by site-specific daily averages.

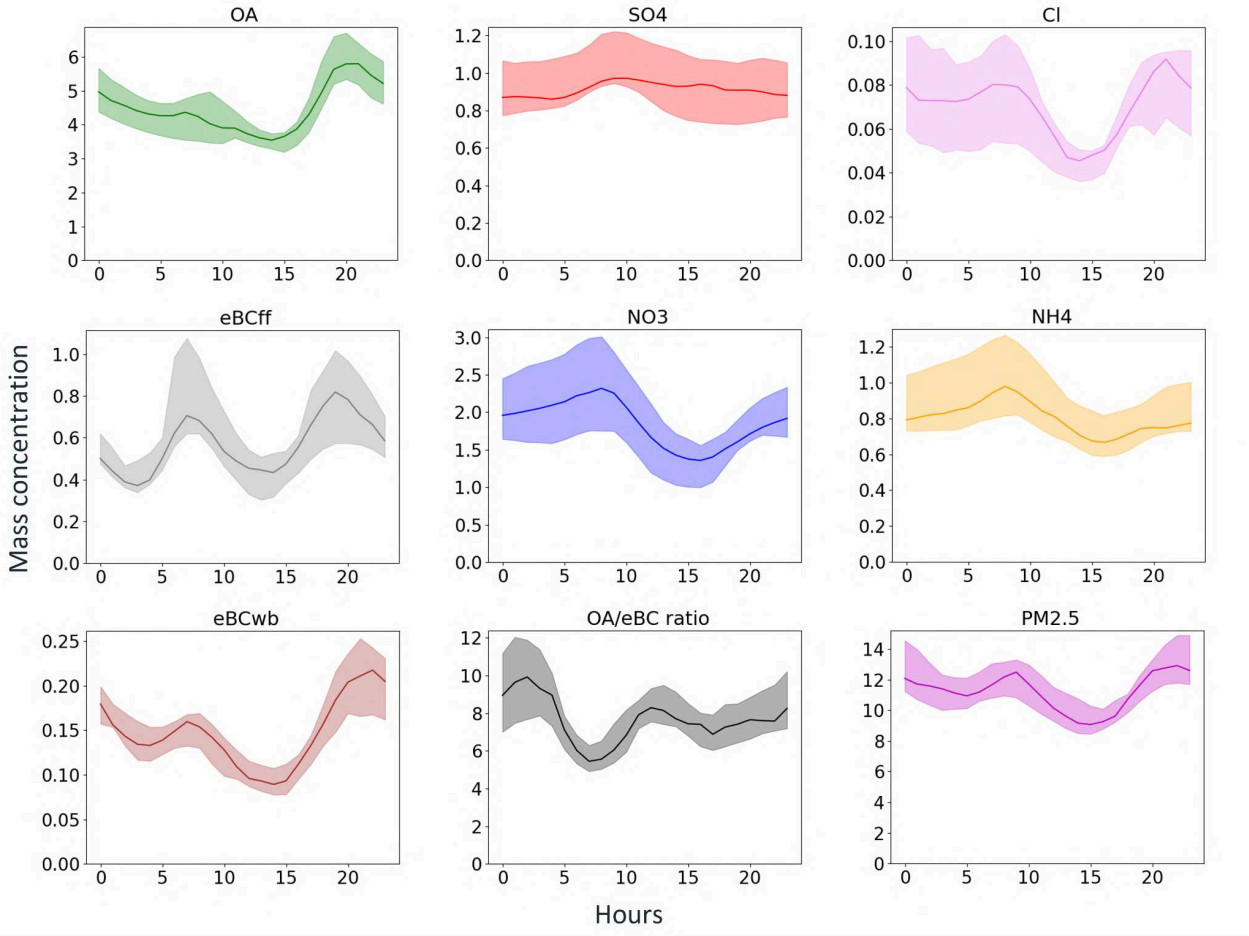

Figure S9: Diel median and IQR for each species across all sites.

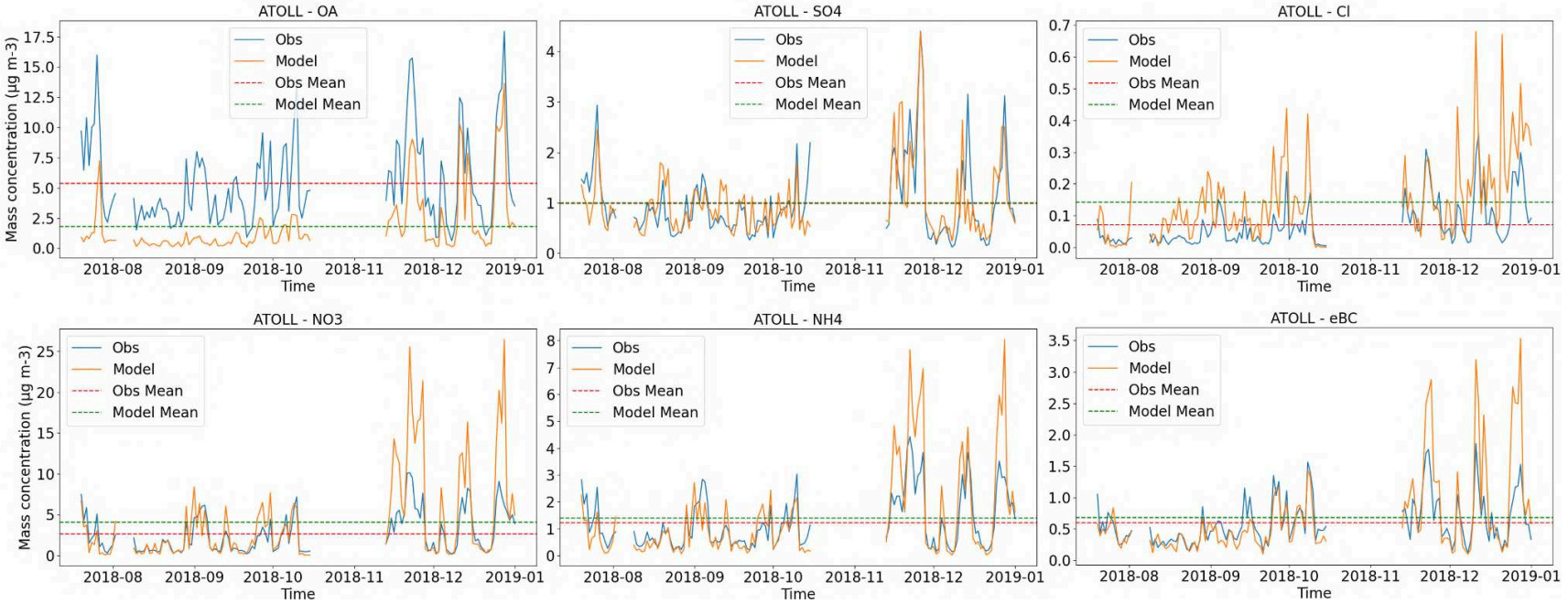
ATOLL - OA
ATOLL - SO4
ATOLL - Cl
ATOLL - NO3
ATOLL - NH4
ATOLL - eBC
Obs
Model
Obs Mean
Model Mean
Mass concentration (µg m-3)
Time
2018-08
2018-09
2018-10
2018-11
2018-12
2019-01

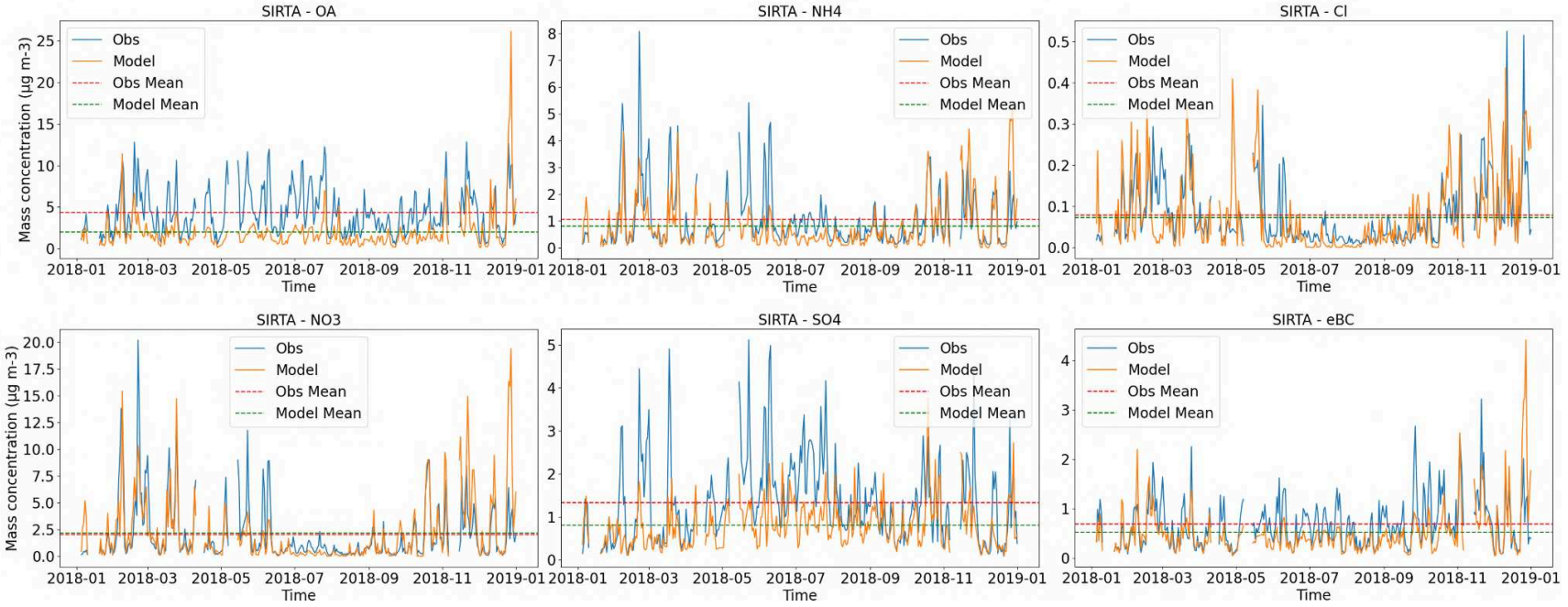
SIRTA - OA
SIRTA - NH4
SIRTA - Cl
SIRTA - NO3
SIRTA - SO4
SIRTA - eBC
Obs
Model
Obs Mean
Model Mean
Mass concentration (µg m-3)
Time
2018-01
2018-03
2018-05
2018-07
2018-09
2018-11
2019-01

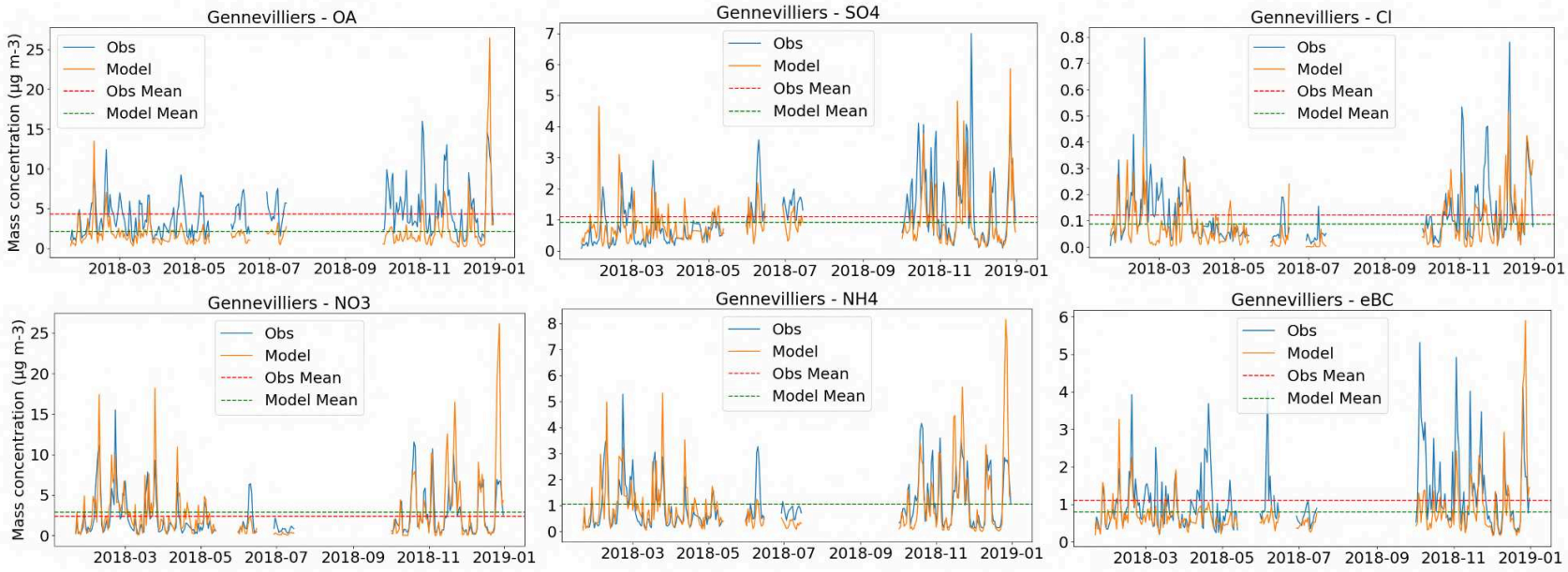
Gennevilliers - OA
Gennevilliers - SO4
Gennevilliers - Cl
Gennevilliers - NO3
Gennevilliers - NH4
Gennevilliers - eBC
Obs
Model
Obs Mean
Model Mean
Mass concentration (µg m-3)
2018-03
2018-05
2018-07
2018-09
2018-11
2019-01

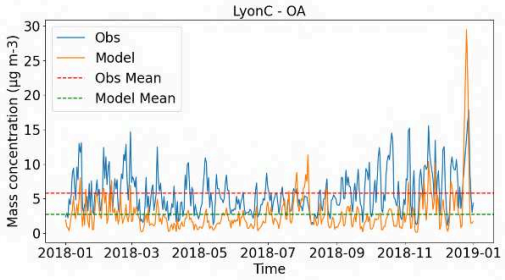
LyonC - OA
Obs
Model
Obs Mean
Model Mean
Mass concentration (µg m-3)
Time
2018-01 2018-03 2018-05 2018-07 2018-09 2018-11 2019-01

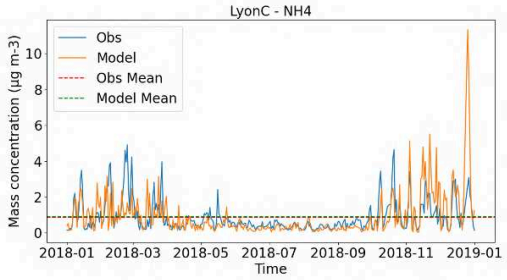
LyonC - NH4
Obs
Model
Obs Mean
Model Mean
Mass concentration (µg m-3)
Time
2018-01 2018-03 2018-05 2018-07 2018-09 2018-11 2019-01

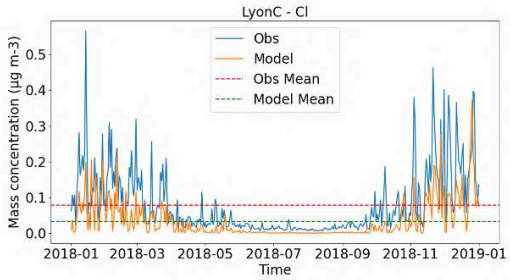
LyonC - Cl
Obs
Model
Obs Mean
Model Mean
Mass concentration (µg m-3)
Time
2018-01 2018-03 2018-05 2018-07 2018-09 2018-11 2019-01

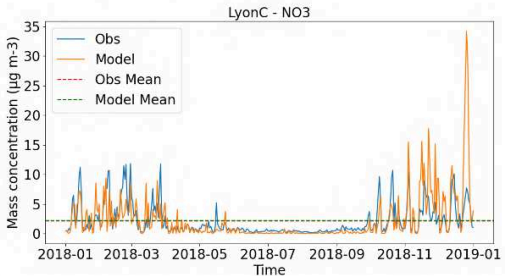
LyonC - NO3
Obs
Model
Obs Mean
Model Mean
Mass concentration (µg m-3)
Time
2018-01 2018-03 2018-05 2018-07 2018-09 2018-11 2019-01

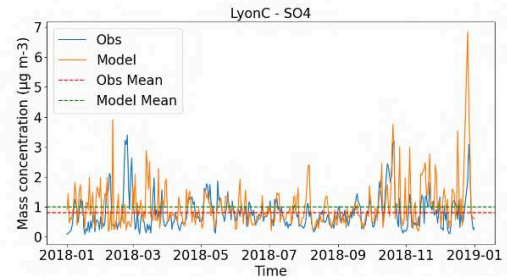
LyonC - SO4
Obs
Model
Obs Mean
Model Mean
Mass concentration (µg m-3)
Time
2018-01 2018-03 2018-05 2018-07 2018-09 2018-11 2019-01

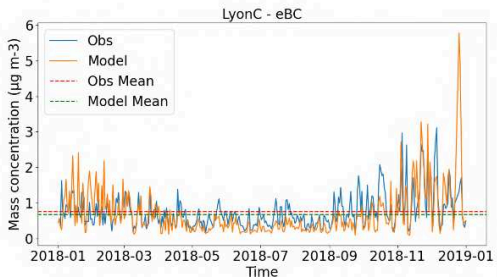
LyonC - eBC
Obs
Model
Obs Mean
Model Mean
Mass concentration (µg m-3)
Time
2018-01 2018-03 2018-05 2018-07 2018-09 2018-11 2019-01

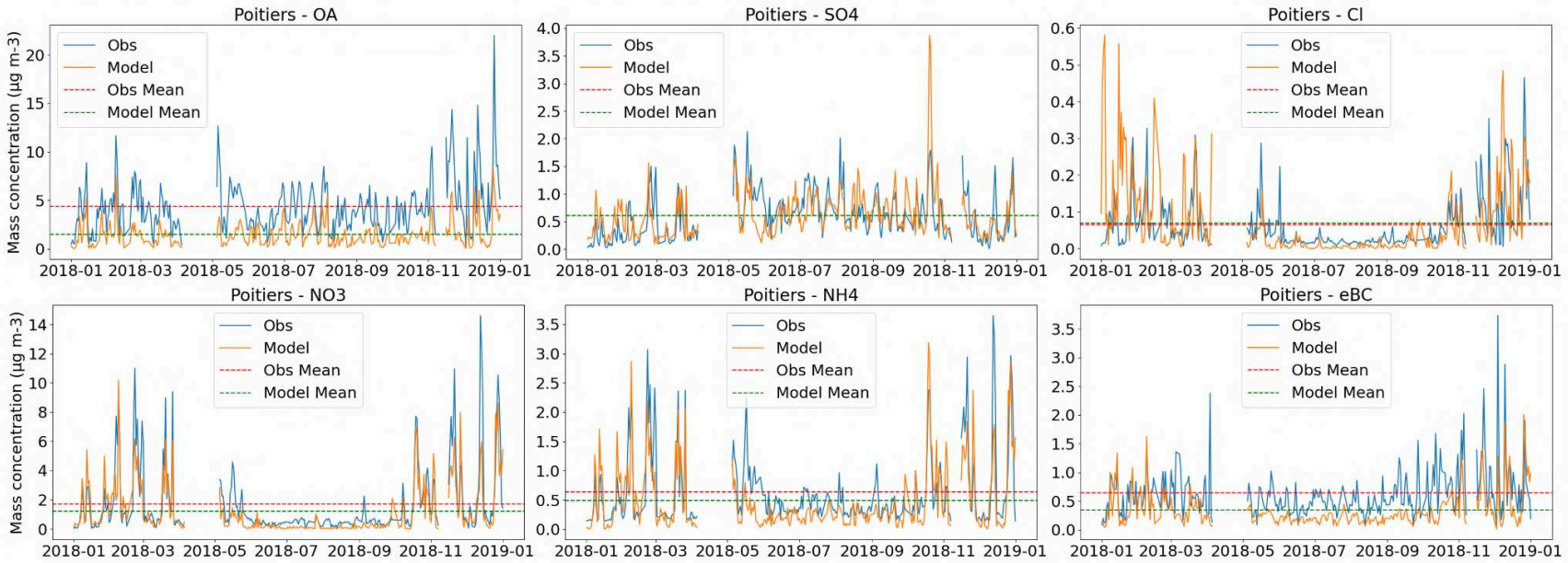
Poitiers - OA
Poitiers - SO4
Poitiers - Cl
Poitiers - NO3
Poitiers - NH4
Poitiers - eBC
Obs
Model
Obs Mean
Model Mean
Mass concentration (µg m-3)
2018-01 2018-03 2018-05 2018-07 2018-09 2018-11 2019-01

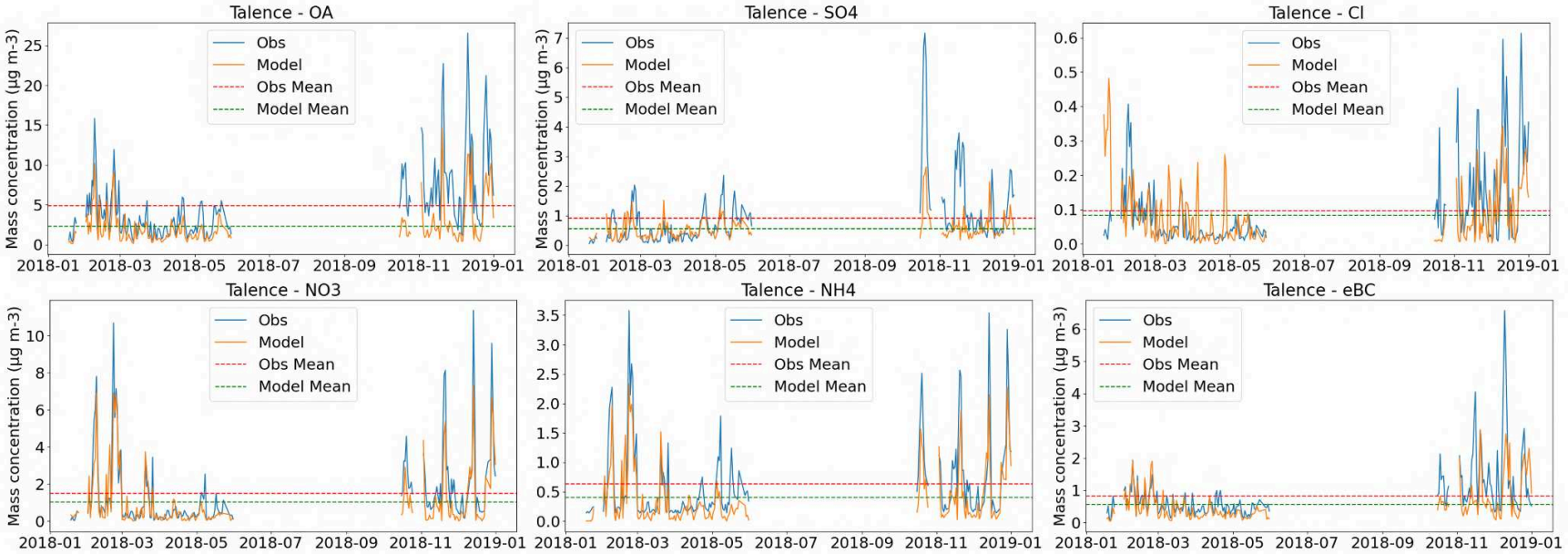
Talence - OA
Talence - SO4
Talence - Cl
Talence - NO3
Talence - NH4
Talence - eBC
Obs
Model
Obs Mean
Model Mean
Mass concentration (µg m-3)
2018-01
2018-03
2018-05
2018-07
2018-09
2018-11
2019-01

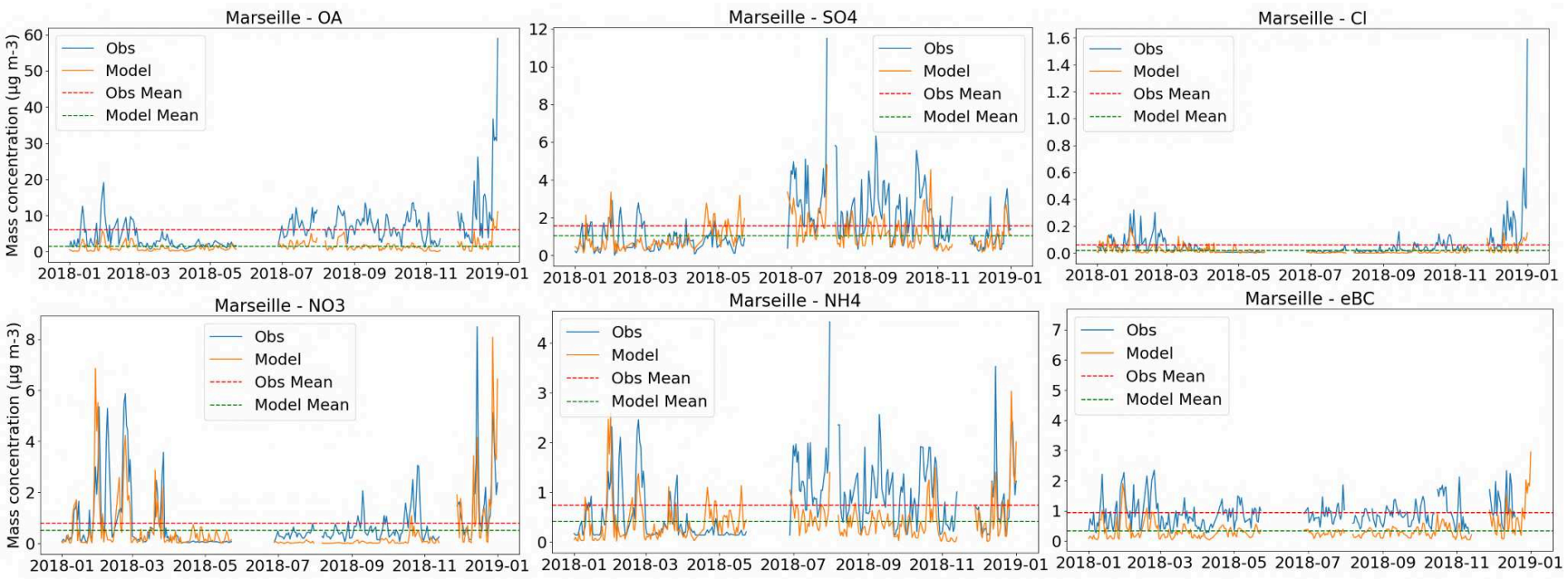
Marseille - OA
Marseille - SO4
Marseille - Cl
Marseille - NO3
Marseille - NH4
Marseille - eBC
Mass concentration (µg m-3)
Obs
Model
Obs Mean
Model Mean
2018-01 2018-03 2018-05 2018-07 2018-09 2018-11 2019-01

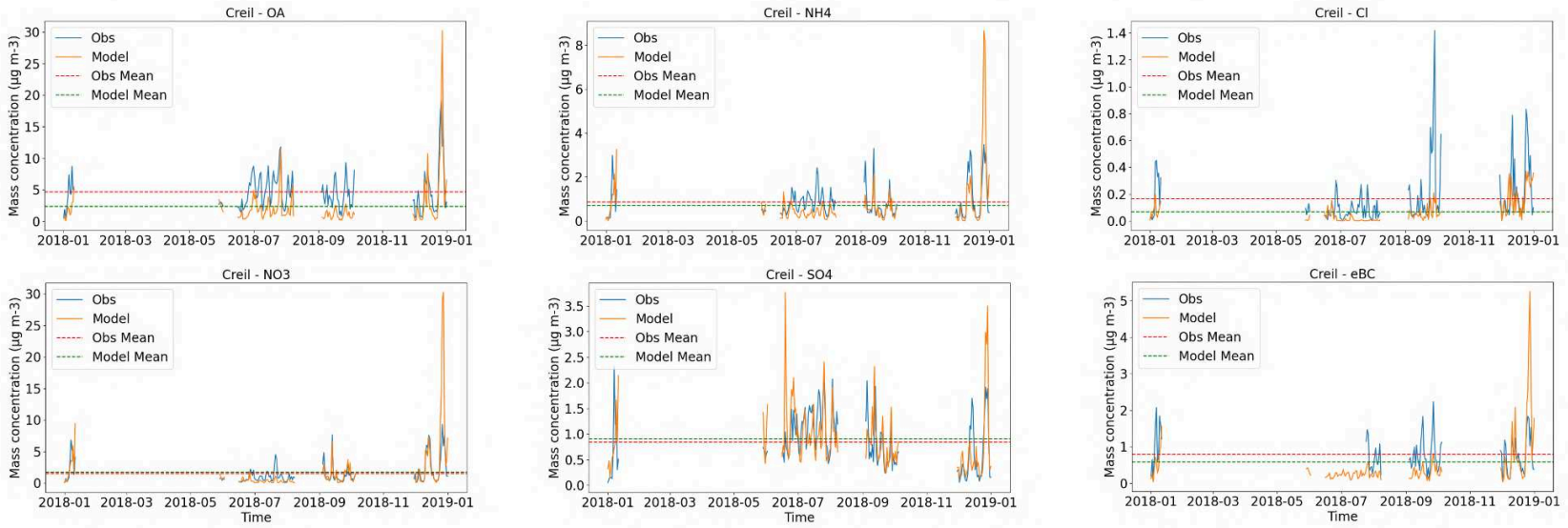

Figure S10: Temporal variability from simulations and observations for PM_1 chemical species at each site.

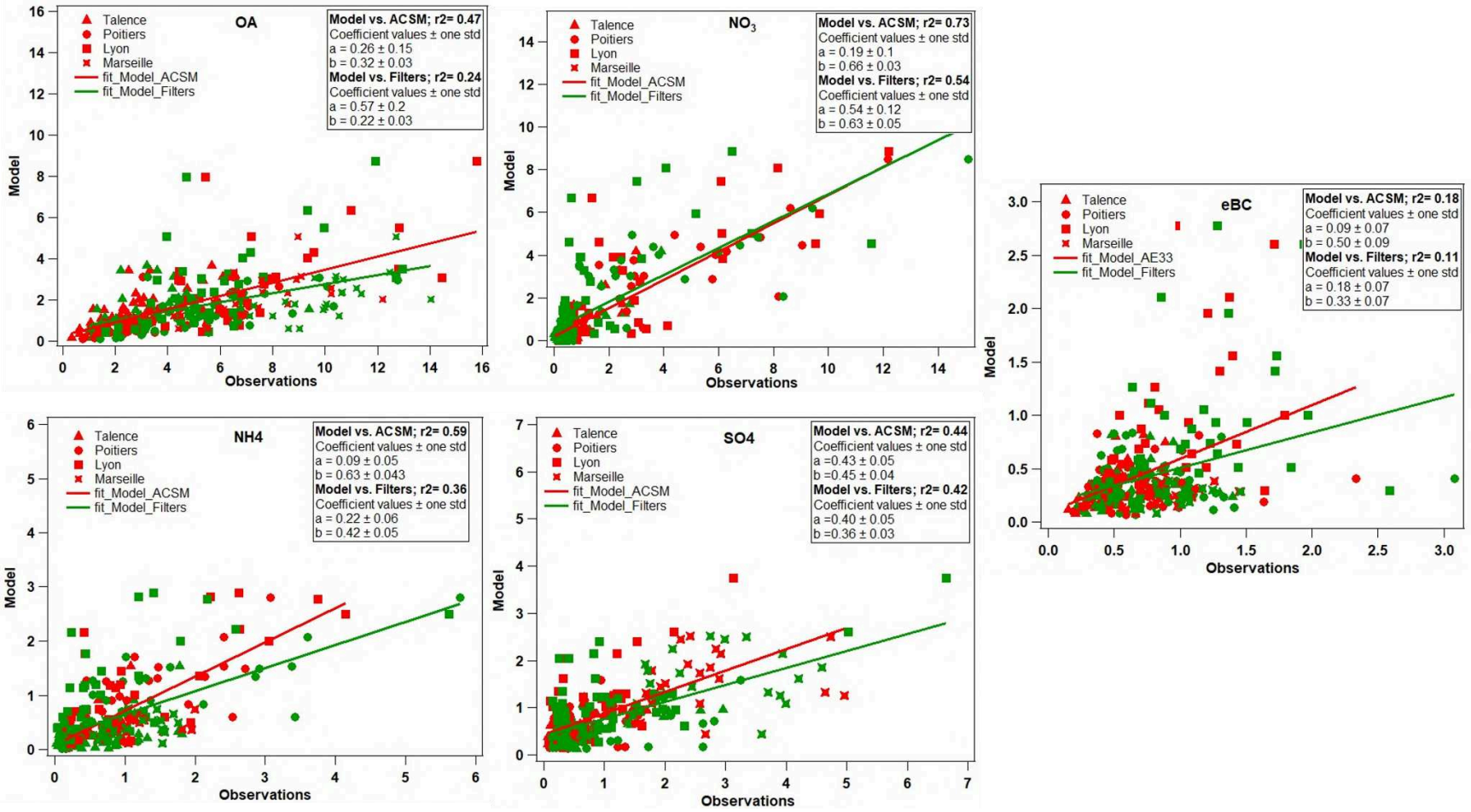

Figure S11: Scatterplots of comparison between daily averages of simulations and either online (in red; ACSM or AE33) or offline observations (in green; filter analyses) (in µg m^{-3}) for OA, NO_3, NH_4, SO_4, and eBC at four French urban sites (Talence, Poitiers, Lyon and Marseille).

Chapitre IV. Leçons tirées de la comparaison et de la combinaison des méthodes de la répartition des sources d'aérosols organiques sur deux sites à Strasbourg, France

IV.1. Résumé de l'article 2

Ce deuxième chapitre de résultats vise à comparer et évaluer la cohérence des mesures ainsi que les résultats des analyses de répartition de sources d'aérosols carbonés réalisées sur deux sites urbains voisins à Strasbourg pendant une saison hivernale 2019/2020. Ces deux sites font partie du réseau régional de surveillance de la qualité de l'air ATMO Grand Est (www.atmo-grandest.eu). Le premier site, nommé "Danube", est une station urbaine de fond dans le sud-ouest du centre-ville de Strasbourg ; le deuxième site, "Clemenceau", est une station urbaine de proximité automobile dans la partie nord du centre ville de Strasbourg et situé à 2,5 km du premier site. Les deux sites ont été équipés simultanément des mêmes types d'instruments pour les mesures in-situ des aérosols. Ce travail a été réalisé en étroite collaboration avec Mélodie Chatain d'ATMO Grand Est, et nous avons travaillé à parité à la rédaction de cet article.

L'article est divisé en trois parties principales : une section détaillée sur les mesures effectuées avec les ACSM et les AE33, suivie d'une étude de la répartition des sources d'aérosols organiques (AO) et de eBC, et enfin, une dernière section dédiée aux comparaisons, couvrant à la fois la composition chimique et les analyses PMF appliquées.

Les deux instruments ACSM utilisés dans cette étude pour caractériser les espèces chimiques submicroniques ont été initialement comparés sur un même site à Metz avant le début de la campagne hivernale. Cette comparaison a permis d'étalonner les instruments et de déterminer leurs efficacités d'ionisation. Elle a aussi démontré une excellente cohérence en ce qui concerne les concentrations de nitrate, ce qui confirme la fiabilité des données obtenues grâce à l'étalonnage des deux instruments. Néanmoins, des variations significatives d'environ 30 % ont été constatées pour les concentrations massiques d'AO (et de sulfate). La comparaison des spectres de masse des AO a révélé un comportement inattendu pour certaines masses (telles que m/z 60 et 73, traceurs de la combustion de biomasse), avec des niveaux plus élevés dans l'ACSM

qui présentait globalement des concentrations totales d'AO plus faibles. Des protocoles d'assurance qualité et de contrôle qualité ont été rigoureusement appliqués par l'AASQA, conformément aux normes recommandées, et aucune source d'erreur instrumentale spécifique n'a pu être identifiée pour expliquer ces disparités. Par conséquent, les divergences observées sont principalement attribuables aux caractéristiques techniques propres à chaque instrument.

Pour les mesures effectuées avec l'AE33, nous avons suivi les recommandations d'ACTRIS pour quantifier les concentrations de eBC. En ce qui concerne la répartition des sources d'eBC, nous avons cherché à déterminer des exposants d'Ångström d'absorption (*Absorption Ångström Exponent,* AAE) spécifiques au site, provenant des combustions fossiles α_{ff} et de la combustion du bois α_{wb}. Cette détermination a été réalisée en commençant par le calcul d'α_{ff}, en ne conservant que les mesures présentant un excellent coefficient de corrélation ($r^2 > 0,99$) pour la courbe de dépendance spectrale du coefficient d'absorption b_{abs} en fonction de la longueur d'onde λ. La valeur de α obtenue pour le premier percentile de cette sélection de données a été considérée comme représentative de la valeur de α_{ff} caractéristique du site étudié (comme proposé précédemment par Tobler et al. (2021)). Ensuite, α_{wb} a été établi à partir des résultats d'une étude de sensibilité visant à optimiser les corrélations entre eBC_{wb} et m/z 60 (ACSM), ainsi qu'entre eBC_{ff} et NO. Grâce à cette approche, nous avons obtenu des coefficients α_{ff} et α_{wb} de 1,00 et 1,70 pour le site Danube, et de 1,06 et 1,60 pour le site Clemenceau, respectivement. Ce premier résultat permet d'illustrer une tendance à des valeurs de α_{ff} et α_{wb} moins différenciées sur le site de proximité automobile, et questionne l'opportunité d'utiliser des paramètres d'ajustement du modèle aethalomètre différents à l'échelle locale, e.g., au sein d'une même agglomération (cf. ci-dessous).

La répartition des sources d'AO a été effectuée en utilisant la méthode de la *Positive Matrix Factorization* (PMF). Une analyse PMF classique a été appliquée à chacun des deux sites séparément en suivant une méthodologie identique, puis de manière combinée en utilisant les données des deux sites. Cette approche, consistant à fusionner les matrices d'AO pour créer une seule matrice d'entrée PMF, présente des avantages, notamment en intégrant les différences inexpliquées dans les empreintes spectrales observées avant le début de la campagne hivernale. De plus, elle peut être considérée comme un moyen efficace de vérifier la robustesse et la précision des solutions PMF individuelles. Pour les deux analyses PMF, seuls les facteurs HOA

et COA ont été contraints en utilisant les spectres de masse de référence de Crippa et al. (2013) obtenus lors de la campagne MEGAPOLI en Ile-de-France.

Le premier volet de résultats montre les évolutions temporelles de la composition chimique des particules fines pendant l'hiver 2019/2020 pour les deux stations de Strasbourg. En général, on observe des concentrations légèrement plus élevées sur le site trafic Clemenceau par rapport au site urbain de fond Danube, ce qui peut être attribué à des émissions primaires et/ou à des processus de transformation plus intenses. Ces observations ont pu être confirmées par les analyses des mesures sur filtres pour le mois de février 2020, qui montrent des concentrations légèrement plus élevées des espèces chimiques majeures à Clemenceau.

Le deuxième volet présente les résultats des analyses PMF individuelles et de la PMF combinée. Un premier résultat intéressant de cette étude est l'identification d'un facteur lié aux amines '*amine-related OA*' sur les 2 sites, permettant de confirmer une influence substantielle à Strasbourg. Ce facteur est caractérisé par une forte contribution des m/z 58 et 42, représentant environ 4 % de la masse totale d'AO. L'analyse combinée des concentrations de polluants et des vitesses et directions de vent met en évidence une source locale spécifique. Il se distingue des autres facteurs 58-OA observés précédemment dans la littérature, suggérant ainsi l'existence d'une source spécifique, propre à notre étude, potentiellement liée à la production de bitume. A noter qu'un facteur relativement similaire a été observé pour la station de Creil (cf. chapitre 6).

Les résultats mettent aussi en évidence des contributions plus élevées de HOA à la station Clemenceau, ce qui est en accord avec les concentrations plus élevées de eBC_{ff} et de EC et attendu vu la typologie du site. Concernant la combustion de biomasse, des contributions similaires sont obtenues pour le BBOA aux deux stations, en accord avec des concentrations équivalentes de lévoglucosane sur les deux sites (basées sur l'analyse de filtres journaliers prélevés lors du dernier mois de la campagne de mesure), et en dépit des différences observées initialement sur les spectres de masse pour les m/z 60 et 73 traceurs de biomasse. En revanche, les concentrations de eBC_{wb} - ainsi que les concentrations du signal m/z 60 mesuré par ACSM - estimées pour le site trafic de Clemenceau sont significativement plus importantes qu'à Danube. Pour eBC_{wb}, ces différences sont notamment à relier à la plus faible valeur de α_{wb} choisie pour Clemenceau dans l'application du modèle Aethalomètre. La différence des valeurs de m/z 60 peut

être liée à des spécificités instrumentales inhérentes au fonctionnement de chaque ACSM, comme observé lors de la campagne de Metz-Borny.

Par ailleurs, un facteur de type COA-like a été facilement identifié sur le site de Clemenceau, montrant un pic à midi correspondant aux heures de repas. Le facteur COA-like obtenu pour le site de Danube présente quant à lui un cycle journalier moins marqué, et relativement similaire à celui du facteur BBOA. Ce résultat met en lumière la complexité d'attribuer exclusivement une origine à ce facteur. De manière intéressante, les résultats obtenus grâce à l'analyse PMF combinée ont amélioré l'identification de ce facteur, réduisant le ratio COA/HOA pendant la nuit, en particulier à la station Clemenceau, par rapport aux sorties des analyses PMF individuelles. Cependant, ce n'était pas le cas pour les autres facteurs d'AO, probablement en raison des différences instrumentales spécifiques entraînant des disparités dans les spectres de masse d'AO obtenus par les deux instruments. En effet, les profils d'AO obtenus à l'aide de la méthode PMF combinée présentent une plus grande similitude avec les profils issus de l'analyse PMF individuelle à la station Clemenceau, par rapport à ceux obtenus par l'analyse PMF individuelle à la station Danube. Cette divergence se traduit par une diminution de la contribution des ions m/z 43 (associés à HOA) et m/z 44 (associés à BBOA) à Danube lors de l'application de l'approche PMF combinée, par rapport aux analyses PMF individuelles. En conséquence, ces facteurs (HOA et BBOA) semblent clairement sous-estimés - et donc OOA surestimé - à la station Danube dans les résultats obtenus avec la méthode PMF combinée.

Au final, cette étude révèle de potentielles divergences à la fois dans les mesures des aérosols carbonés entre deux sites urbains voisins et dans les solutions de répartition des sources, malgré l'utilisation d'instruments identiques, illustrant les précautions à prendre dans l'interprétation des résultats obtenus par l'utilisation d'outils statistiques pour la quantification de sources d'émission (plus ou moins) clairement identifiées.

IV.2. Article 2

Lessons learned from the comparison and combination of fine carbonaceous aerosol source apportionment at two locations in the city of Strasbourg, France

Hasna Chebaicheb[1,2,3], Mélodie Chatain[4], Olivier Favez[2,3], Joel F. de Brito[1], Vincent Crenn[5], Tanguy Amodeo[2,3], Mohamed Gherras[2], Emmanuel Jantzem[4], Véronique Riffault[1,3]

[1]IMT Nord Europe, Institut Mines-Télécom, Université de Lille, Centre for Energy and Environment, 59000, Lille, France
[2]Institut National de l'environnement Industriel et des Risques (INERIS), 60550 Verneuil-en-Halatte, France
[3]Laboratoire Central de Surveillance de la Qualité de l'Air (LCSQA), 60550 Verneuil-en-Halatte, France
[4]Atmo Grand Est, 67300 Schiltigheim, France
[5]ADDAIR, F-78530 Buc, France

Correspondence to: hasna.chebaicheb@ineris.fr

For submission in Atmospheric Chemistry and Physics: Measurement report

Abstract. This study qualitatively assesses the consistency of measurements and results from carbonaceous aerosol source apportionment analyses conducted at two neighboring urban sites in Strasbourg during the winter of 2019/2020 using the same type of instruments. Quality assurance and quality control procedures for both ACSMs (Aerosol Chemical Speciation Monitors) were conducted in accordance with the current recommendations, therefore the differences observed can be mainly related to the technical specificities from each device. During the campaign, the results showed moderately higher concentrations of submicron aerosol chemical species at the Clemenceau traffic site compared to the Danube urban background site. These differences were attributed to primary emissions and transformation processes at the roadside, confirmed by filter-based offline measurements during the same period.

Positive Matrix Factorization (PMF) analysis was applied at both sites using two PMF methods: one classical (individual) and the other with a combined dataset. Both methods resolved five organic aerosol (OA) factors: hydrocarbon-like OA (HOA), biomass burning OA (BBOA), cooking-like OA (COA-like), amine-related OA (58-OA), and oxygenated OA (OOA). As expected, the Clemenceau site exhibited higher contributions of HOA. The analysis also showed similar BBOA contributions at both stations, consistent with the comparison of levoglucosan measurements, but not with eBC_{wb}, which was higher at Clemenceau. This discrepancy may be attributed to the application of the Aethalometer model, confirming its sensitivity to empirical assumptions. The study also highlights the challenge of attributing a cooking-only origin to the COA-like factor, which exhibited a diel cycle similar to biomass burning OA at the Danube site. The combined PMF analysis improved the apportionment of cooking emissions at nighttime, especially for Clemenceau, compared to individual PMF, but it did not enhance the consistency of other OA factors due to instrumental specificities leading to differences in OA mass spectra between the two instruments.

Finally, the study confirmed the influence of an amine-related OA factor in Strasbourg, characterized by a high proportion of m/z 58 and accounting for approximately 4% of the total OA mass. This factor showed distinct diel profiles, suggesting a unique local source, potentially linked to industrial emissions, which requires further investigation.

Keywords. Urban pollution, combined PMF, organic aerosols, Amine-related OA

1 Introduction

Air pollution influences climate change, but has also adverse effects on human health, with increased disease and mortality rates (EEA, 2022). In particular, fine particles such as those with an aerodynamic diameter smaller than 1 µm (PM_1) are inhaled and reach the deeper respiratory system, leading to a range of health problems including respiratory and cardiovascular disorders, disruptions in reproductive and central nervous functionalities, as well as the development of cancer (WHO, 2022; Duarte et al., 2023). Identifying their chemical composition and main emission sources has become a priority for air quality agencies to build up and assess efficient abatement strategies. Improving knowledge of their geographical origins is also a major challenge to better adapt local policies in a larger regional scale context.

In France, regional air quality monitoring networks (termed 'AASQA') and the national reference laboratory (termed 'LCSQA') are operating the CARA program for in situ observation of the particulate matter (PM) chemical composition in urban environments and subsequent source apportionment studies (Favez et al., 2021). Chebaicheb et al. (ESSD, in prep.) recently analyzed and discussed long-term (> 1 year) measurements of fine particles using online instruments at a dozen of CARA sites, providing PM_1 chemical composition, with annual mean loadings ranging from 7 to 16 µg m^{-3} in French urban background environments. This concentration range is relatively low compared to other cities outside Europe but still exceeds the World Health Organization (WHO) recommended annual concentration limit of 5 µg m^{-3} for $PM_{2.5}$. Organic aerosols (OA) represent a major fraction of total PM_1 mass (40-60 %), a trend commonly observed worldwide (Chen et al., 2022; Li et al., 2022; Via et al., 2021).

Identifying the sources of this complex OA fraction is therefore crucial to develop effective mitigation strategies and improve air quality. Source apportionment (SA) approaches, including receptor models, have been widely used in urban air quality research during the last decades. In particular, Positive Matrix Factorization (PMF), as introduced by Paatero and Tapper (1994), stands out as one of the most extensively utilized tools (Hopke et al., 2020). PMF can be applied to various types of datasets, typically obtained from offline chemical analyses of filter samples or from online characterization of the aerosol chemistry and/or physical properties. Knowledge of OA chemistry and sources has greatly benefited from the development of aerosol mass

spectrometry and subsequent application of PMF-type analysis to organic mass spectra since the mid-2000s (Crippa et al., 2014). This commonly allows to feature different families of organic compounds originating from primary emissions - typically, biomass burning OA (BBOA), hydrocarbon-like OA (HOA), cooking-like OA (COA) - or from various oxidation processes, e.g., leading to less- or more-oxidized oxygenated OA (LO-OOA and MO-OOA, respectively). Chen et al. (2022) recently proposed and applied a common protocol for advanced PMF analysis on unit-mass resolution (UMR) organic mass spectra obtained from long-term measurements at 22 European sites. This protocol is based on the use of the multi-linear engine (ME-2), allowing to introduce a priori knowledge (or assumption) on the mass spectral fingerprint of some OA factors to facilitate the comparison of SA outputs obtained at different locations. Such a standard methodology might also be of particular interest when conducting a SA study at the city scale to estimate increments due to local emissions on top of regional and/or urban background air pollution. Furthermore, some previous studies proposed to combine the datasets obtained at neighboring sites in a single input matrix for PMF analysis, in order to reinforce the consistency of the comparison of SA results obtained for each site (e.g., Pandolfi et al., 2020). To our knowledge, such a combined approach has been applied mostly on filter-based offline measurements but has never been reported so far for OA measurements using aerosol mass spectrometry.

In a previous paper, Chatain et al., (2021) compared the particle size distribution and aerosol concentrations between an urban background site and a roadside site during winter 2019/2020 in Strasbourg, France, showing higher particle number concentrations and particles smaller than 100 nm at the latter site compared to the former throughout the observation period. This measurement campaign also included simultaneous monitoring of black carbon and non-refractory submicron chemical species at both sites, allowing for the investigation of major factors contributing to fine aerosols. In this context, a SA study was achieved to analyze the main origins of carbonaceous species at these two nearby sites: Danube and Clemenceau, located 2.5 km apart in Strasbourg. In order to compare the PMF results obtained for OA between these neighboring sites, a two-fold approach was undertaken. Initially, a standard PMF analysis was conducted independently for each site but in a harmonized way (i.e. using the same constraints and criteria). Subsequently, considering the geographical proximity of the sites, a combined PMF analysis was also carried

out. Thus, the present study assesses the reliability and consistency of the results obtained from the individual PMF outputs compared with the combined ones. This comparative assessment also aims at discerning the main sources of pollution at these closely related sites.

2 Methodology

2.1 Sampling sites

The city of Strasbourg is located in north-eastern France, close to the German border, along the river Rhine. It is the 13th most populous urban area in France and the largest on a regional scale. It is highly urbanized and crossed by several major roads, including the north-south axis (A35-A4 motorway) and the east-west axis (Rhine Avenue). Residential and commercial areas are adjacent to major industrial areas to the east and south, and the entire urban area is surrounded by agricultural land.

Despite significant improvements in air quality in recent decades, Strasbourg still experiences more than ten days per year with PM_{10} levels exceeding the daily limit value of 50 µg m^{-3} set by the European Directive 2008/50/CE. In addition, in 2022, 100 % of the population lived in an area exceeding the WHO guideline for the annual $PM_{2.5}$ average (ATMO Grand Est, 2023). It should also be noted that Strasbourg is one of the 12 French zones affected by the European litigation for nitrogen dioxide (NO_2). Moreover, the city can be significantly influenced by air masses from central Europe under anticyclonic conditions, as already observed for other urban areas in northern France, such as Greater Paris (MEGAPOLI, e.g., Beekmann et al. 2015; Freutel et al., 2013) and Lille (Chebaicheb et al., 2023).

A detailed description of the two sites investigated here can be found in Chatain et al. (2021). Briefly, both sites correspond to fixed stations operated by the ATMO Grand Est regional air quality monitoring network (www.atmo-grandest.eu). The first one (called Danube) corresponds to an urban background station located southwest of the city center of Strasbourg (Figure 1). This station was installed at the center of a recently built eco-district between a small canal (Bassin Dusuzeau) and the Rhine Avenue. The second site (called Clemenceau) corresponds to an urban

roadside station located at the corner of an intersection between two major roads in the north of the city center of Strasbourg.

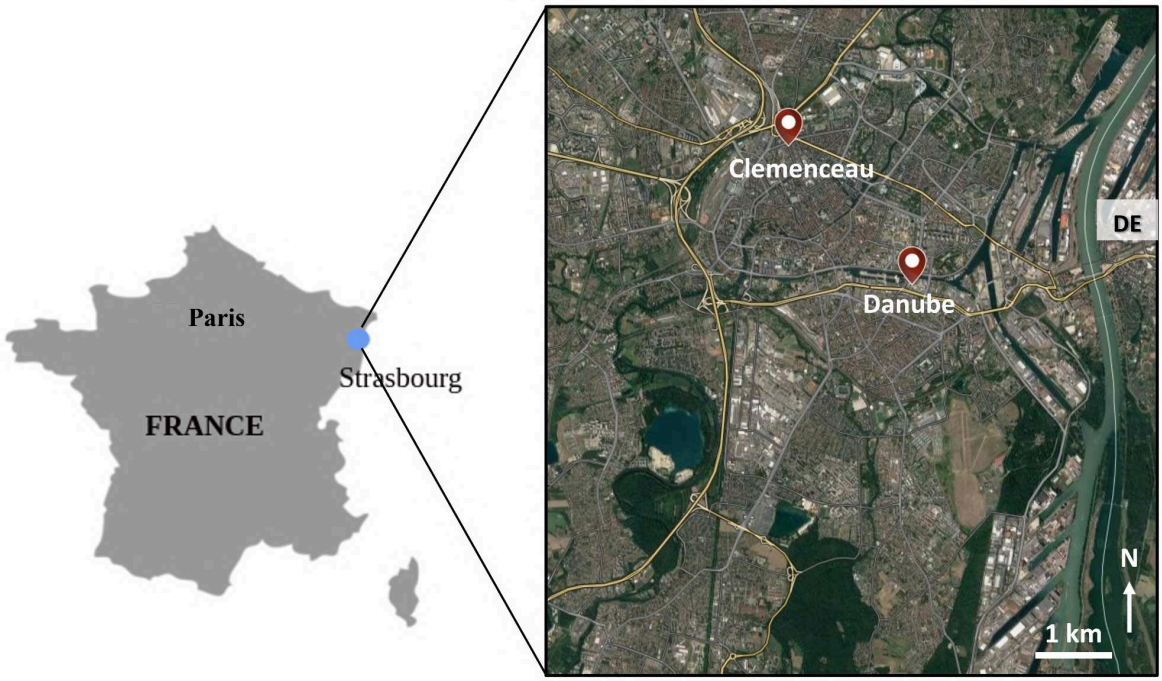

Figure 1: Location of the two sites, Strasbourg Danube, and Strasbourg Clemenceau.

2.2 Measurements

Measurements at both sites were carried out by ATMO Grand Est. These measurements include regulatory monitoring of particulate matter concentrations (PM) using an optical analyzer (FIDAS 200, Palas Gmbh) demonstrated to be equivalent to the gravimetric reference method for PM_{10} and $PM_{2.5}$ (NF EN 12341), as well as NO_x using the chemiluminescence method (APNA-370, Horiba) as recommended by the NF EN 14211 reference method.

During winter 2019/2020, the chemical composition of non-refractory submicron particles (NR-PM_1) was investigated using two quadrupole ACSM (Q-ACSM, *Aerosol Chemical Speciation Monitor*, Ng et al., (2011)) concomitantly at Danube and Clemenceau stations. In this instrument, atmospheric particles are sampled at a flow rate of 3 L/min with a cut-off at 2.5 µm using a sampling head. The submicron particles are then focused by an aerodynamic lens system

at the instrument inlet toward a tungsten vaporizer heated at 600°C under vacuum. The non-refractory constituents of particles are vaporized then electronically ionized (70 eV). The resulting fragments are separated by a quadrupole to obtain the mass spectra. The final concentrations of OA, nitrate (NO_3), sulfate (SO_4), ammonium (NH_4), and chloride (Cl) are obtained using a fragmentation table (Allan et al., 2004). Roughly, inorganic compounds are first quantified based on their fragmentation patterns and the remaining signal at each m/z is attributed to organic fragments, forming the measured organic fraction. The resulting OA mass spectra can then be used as an input matrix, along with its corresponding uncertainties matrix, for PMF analysis. A critical point for the calculation of the species' mass concentrations is the determination of their ionization efficiencies. This is basically done by taking nitrate as the reference (since it has a rather simple fragmentation pattern and few interferences at its specific m/z fragments) and then measuring or assuming specific relative ionization efficiency (RIE) value relative to NO_3 response factor (RF) for other species. In the present study, RF, $RIE_{NH4,}$ and RIE_{SO4} were determined by on-site calibrations during the measurement campaign, and the commonly-used default RIE value of 1.4 was used for OA, for both ACSM datasets.

It is also worth noting that the two used ACSMs were previously compared (August-October 2019) at a suburban station of a nearby city (Metz-Borny, France), showing very satisfactory agreement for NO_3 measurements but substantial differences - of about 30% at highest concentration ranges - in OA (and SO_4) measurements (Fig. S1). These differences did not appear to be influenced by discrepancies in relative ion transmission (RIT) as the corresponding correction curves, based on the naphthalene internal standard fingerprint, behaved as generally expected for ACSM devices (Fig. S2), and the highest differences were already observed at lowest m/z (Fig. S3). They are also unlikely to be related to differences in RIE since both instruments were sampling the same ambient air and IE values led to a satisfactory agreement for nitrate measurements (slope: 1.05; $r^2 = 0.96$, Fig. S1), except if the variations of organic RIE with the aerosol oxidation state (Xu et al., 2018) might also be instrument-specific. As a matter of fact, the few m/z ratios showing highest concentrations for the under-estimating instrument – which was further installed at the Clemenceau station during the wintertime Strasbourg campaign – includes m/z commonly attributed to biomass burning OA (in particular m/z 60 and 73, see Fig. S3). It should also be noted that no Pieber-like artifact (Pieber et al., 2016) was observed from

(R)IE calibrations using ammonium nitrate and ammonium sulfate. Moreover, the voltage applied to the vaporizers in both instruments was kept at the values determined for each of them by the manufacturer, theoretically ensuring a similar vaporizer temperature of about 600°C in the two ACSM. In this context, besides any possible difference in lens transmission efficiencies, no other instrumental bias could be suspected to explain the discrepancies observed in OA measurements during this pre-campaign intercomparison exercise.

For the winter campaign, both Strasbourg sites were also equipped with a multi-wavelength aethalometer (AE33, Magee Scientific), using a sampling head with a cut-off diameter of 2.5 µm at a flow rate of 5 L/min. A full description of the AE33 operating principles is given by Drinovec et al. (2015). Briefly, it is based on the measurement of optical attenuation in order to determine aerosol absorption coefficients (b_{abs}) at selected wavelengths. Aerosols are continuously sampled onto a filter tape, causing a decrease of light transmission through the sampled filter spot(s) which is compared to the light transmission through an unsampled area of the filter tape. In the AE33 model, optical measurements are conducted at seven optical wavelengths ranging from near-ultraviolet (UV) to near-infrared (IR) (370, 470, 525, 590, 660, 880, and 950 nm), and sampling artifacts known as filter-loading effect are corrected thanks to the dual-spot technology (Drinovec et al., 2015). By convention for multi-wavelength aethalometer, equivalent Black Carbon (eBC) is derived from measurements at 880 nm, assuming a mass absorption cross-section (MAC) value, such as:

$$eBC = b_{abs,880nm} / MAC_{880nm} \quad \text{(Eq. 1)}$$

In accordance with the current ACTRIS guidelines, $b_{abs,880nm}$ was obtained applying a filter type-dependent harmonization factor (1.76 for the MF8060 filter tape used here) to account for multiple scattering effects, and a MAC value of 7.5 $m^2\ g^{-1}$ at 880 nm was considered to estimate eBC concentrations (https://actris-ecac.eu/particle-light-absorption.html).

All these measurements underwent regular quality checks, including calibration and preventive maintenance, following the manufacturer's recommendations and guidelines provided by the LCSQA at the national level. Quality control was routinely achieved following daily and weekly technical validation procedures, supplemented by a monthly environmental validation

investigation. Finally, data handling procedures defined in Chebaicheb et al. (in prep.) data were applied to ACSM and AE33 datasets.

In addition, quartz fiber filters (TissuQuartz, Whatman, 47 mm diameter) pre-heated at 500°C during 4 hours and Leckel samplers (model SEQ 47/50) running at 2.3 m^3/h were used to collect daily samples simultaneously at both sites from 4 to 29 February for offline analyses of organic carbon (OC) and elemental carbon (EC) using a Sunset Lab instrument and following the EUSAAR-2 thermo-optical protocol (Cavalli et al., 2010). Daily mean values obtained for eBC and OA (from AE33 and ACSM, respectively) were then compared to EC and OC offline measurements, respectively. Results showed very good correlation coefficient values for both comparisons ($r^2 > 0.9$, Fig. S4) with OA-to-OC ratios (about 1.4) in the lower range of what is commonly observed in urban environments (e.g., Aitken et al., 2008). This may be linked to the predominance of primary organic aerosols (from various combustion processes), which are known as less oxidized than secondary OA (SOA). This could also be partly related to possible OC overestimations due to positive sampling artifacts - e.g., adsorption of volatile organic compounds onto the filter (e.g., Kim et al., 2001) - and/or OA underestimation from ACSM measurements, for instance due to poor lens transmission efficiency at the entrance of the ACSM for the finest and/or largest particles within the submicron aerosol fraction (e.g., Liu et al., 2007). Nevertheless, the consistency obtained for OA-to-OC ratio values with both ACSMs comforts the comparability of ACSM results.

2.3 eBC source apportionment

Following Sandradewi et al. (2008), multi-wavelength absorption measurements can be used to deconvolve eBC into two main fractions, classically identified as fossil fuel (eBC_{ff}) and wood burning (eBC_{wb}) components. To do so, it is assumed that the light absorption due to Brown Carbon (BrC) at near UV wavelengths in winter is primarily linked to wood-burning emissions, which has been recently documented by Zhang et al. (2020) at the national scale. More generally, the model allows distinguishing between highly efficient combustion processes (like traffic exhaust emissions) and poor combustion conditions.

This so-called Aethalometer model is based on the additivity of absorption coefficients from both of these source categories and on their own light absorption spectral fingerprints, such as:

$$b_{abs,\lambda} = b_{abs,ff,\lambda} + b_{abs,wb,\lambda} \quad \text{(Eq. 2)}$$

$$b_{abs,wb,470nm} / b_{abs,\ wb,950nm} = (470/950)^{-\alpha wb} \quad \text{(Eq. 3)}$$

$$b_{abs,ff,470nm} / b_{abs,ff,950nm} = (470/950)^{-\alpha ff} \quad \text{(Eq. 4)}$$

where α_{ff} and α_{wb} stand for the Absorption Ångström Exponent (AAE) of the fossil fuel and wood burning fractions, respectively. These parameters have initially been set to default values of 1 and 2, respectively (Sandradewi et al., 2008; Drinovec et al., 2015). However, further studies illustrated that the choice of these parameters is highly critical for the consistency of the Aethalometer model outputs so that site-specific set of values should preferably be determined (e.g., Favez et al., 2010; Zotter et al., 2017; Savadkoohi et al., 2023). Following Tobler et al. (2021), α_{ff} has been defined here as the first percentile of AAE values measured for ambient air particles during the campaign, applying a stringent data point selection based on the determination coefficient ($r^2 > 0.99$) obtained from the fit of the b_{abs} spectral dependence ($b_{abs,\lambda}$ vs. λ). Once α_{ff} has been set for both sites (at 1.00 and 1.06 for Danube and Clemenceau, respectively), the optimal α_{wb} values could be investigated based on the results of a sensitivity study aiming at optimizing correlation coefficients between eBC_{wb} and m/z 60 signal (commonly used as a biomass burning tracer) from ACSM measurements on the one hand, and between eBC_{ff} and NO concentration (considered as a proxy for road traffic exhaust emission) on the other hand. This led to the determination of α_{wb} values of 1.6 and 1.7 for the Clemenceau and Danube sites, respectively, during the studied period (Fig. S5).

2.4 OA source apportionment

The data derived from the Q-ACSM at both sites were analyzed using the Aerodyne software 'acsm local' version 6.37. Both organic concentrations matrices and their error matrices were exported to apply the PMF method using the Source Finder Pro software (SoFi Pro, Datalystica Ltd., Switzerland) with the ME-2 solver within the Igor Pro software environment (Wave Metrics, Inc., USA). Briefly, the PMF model allows for the separation of the measured organic concentrations matrix (x_{ij}) at a receptor site into their organic mass spectra attributed to "sources"

(profiles f_{kj}) and their contributions over time (time series g_{ik}), along with the residuals (e_{ij}), as described in this equation:

$$x_{ij} = \sum_{k=1}^{p} g_{ik} \times f_{kj} + e_{ij} \quad \text{(Eq. 5)}$$

The objective is to find the number of factors "p" while minimizing a quantity Q defined as the sum of the squares of the residuals (e_{ij}) on the measurement uncertainties (σ_{ij}):

$$Q = \sum_{i=1}^{n} \sum_{j=1}^{m} (e_{ij}/\sigma_{ij})^2 \quad \text{(Eq. 6)}$$

SoFi Pro software allows the use of the a-value approach to overcome the rotational ambiguity caused by the application of PMF. This approach helps constrain known factor profiles or time series at the site, using a scalar a-value varying from 0 to 1, as defined in these equations:

$$f_{solution} = f_{reference}(1 \pm a) \quad \text{(Eq. 7)}$$

$$g_{solution} = g_{reference}(1 \pm a) \quad \text{(Eq. 8)}$$

The PMF solutions are then evaluated using the bootstrap technique which allows estimating the uncertainties of the study.

A standard PMF was first performed for each site during winter 2019/2020 (December, January, February; DJF), as detailed in the supplementary information, section S1. Briefly, unconstrained PMF was initially applied to pre-determine the potential number of factors (2-8 factor tests with ten PMF runs for each number of factors), allowing to identify five main OA factors at each site, namely one oxygenated (OOA) and four primary OA factors (hydrocarbon-like OA (HOA), cooking-like factor (COA), biomass burning OA (BBOA), as well as a specific 58-related OA). Then, constrained PMF was conducted using the reference profiles from Crippa et al., (2013) for HOA and COA, which allowed us to obtain BBOA and 58-OA factors for each site without constraining them. After establishing a reasonable PMF solution for both sites, we applied bootstrap analysis to test the stability of the solutions. The average bootstrapped solutions obtained at both sites are presented and discussed in section 3.

An interesting experimental issue is the effect of possible instrumental biases - e.g., such as described by Pieber et al. (2016) - on the obtained source apportionment results. From the comparison of PMF analysis performed on datasets simultaneously obtained by 14 different ACSMs, Fröhlich et al. (2015) demonstrated that relatively important discrepancies in the OA mass spectra do not lead to significant differences in the PMF results from one instrument to another. An open question relies on the effect of mixing together mass spectra datasets from two (or more) distinct ACSMs in a single input PMF matrix. Such multisite PMF studies have been recently introduced for the combined analysis of filter-based chemical speciation datasets, which can be obtained from offline analyses using the same laboratory equipment (e.g., Mooibroek et al., 2011, 2016; Pandolfi et al., 2020), but have not been presented yet for online ACSM (or AMS) measurements, to the best of our best knowledge. Considering the unexplained differences in mass spectral fingerprints observed from co-located measurements during the preliminary intercomparison campaign in Metz (see above), it appeared of particular interest to test here such a multisite approach combining OA measurements at both nearby Strasbourg sites in a single PMF input matrix. This might also be considered as a good way to check the robustness and accuracy of the individual PMF solutions. This combined PMF consisted of merging the two organic and error matrices from the two sites vertically with the same number of profiles (m/z up to 100) and of averaging the two-time series over 30 min. As for standard independent PMF analyses, the HOA and COA factors were constrained using Crippa's reference mass spectra. Bootstrap analysis and selection criteria were then applied to obtain the final solution as presented in SI, section S2.

2.5 Meteorological data and wind analysis

Meteorological parameters have been measured at a background site located a few kilometers northwest of the study sites. Temperature (T) and relative humidity (RH) were measured by dedicated probes (HMP Vaisala model) and wind data (speed, WS; and direction, WD) by a wind vane (TAVID Chauvin Arnoux model). As presented in Figure 2, the investigated period was dominated by south-western and relatively warm (5-10°C) air masses, except during relatively short colder periods (e.g., around New Year and 22 Jan.) with northern winds.

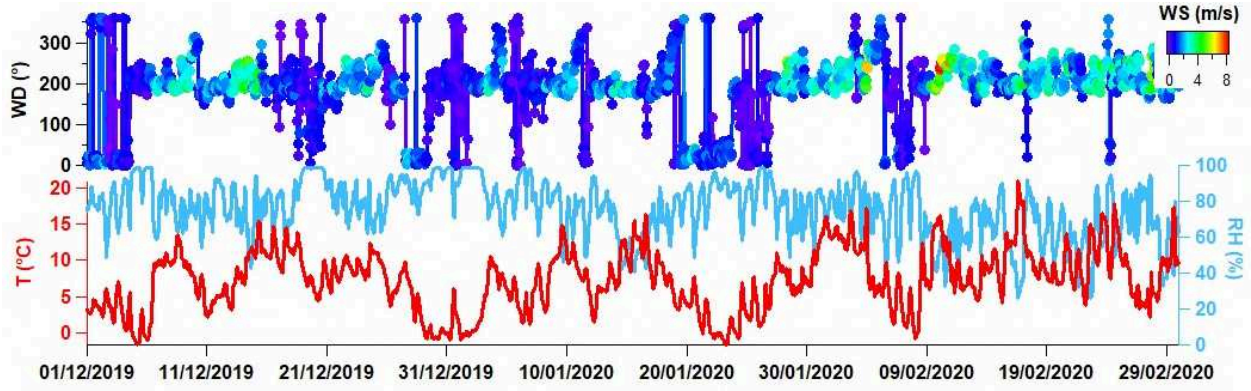

Figure 2: Meteorological parameters in Strasbourg during winter 2019/2020**.**

In order to understand the origin of air pollutants, wind and trajectory analyses were conducted, coupling pollutant concentrations with meteorological parameters (wind speed and direction) by computing the Non-parametric Wind Regression (NWR) model using the Zefir tool (Petit et al., 2017a), also allowing to qualitatively differentiate between local and regional eBC and OA origins according to wind speed.

3 Chemical composition

Online chemical measurements could be validated by comparison with co-located regulatory $PM_{2.5}$ measurements. In this chemical mass closure exercise, NR-PM_1 is first calculated as the sum of the five chemical species from ACSM: OA, NO_3, SO_4, NH_4, and Cl. The PM_1 concentration is then approximated by adding eBC to NR-PM_1 and further compared with the mass concentration of $PM_{2.5}$ measured by the FIDAS instrument at both sites. Results indicate that ACSM and AE33 measurements together account for 62 % and 75 % of $PM_{2.5}$, with coefficient of determination (r^2) values equal to 0.90 and 0.87 for the Danube and Clemenceau sites, respectively (Fig. S6).

Figure 3 displays the mass concentrations of PM_1 species and the average contribution of eBC, NR-PM_1 species, and $PM_{2.5}$ during winter 2019/2020 at the Danube and Clemenceau sites, respectively. OA dominates the average PM_1 chemical composition with 48 % and 45 % at the background and traffic sites, respectively, as already observed in previous studies at the national scale (Petit et al. (2014)). Secondary inorganic species (NO_3, SO_4, and NH_4) also contribute

significantly, accounting for around 40 % of PM_1 total mass, mainly from NO_3 (22-24 %). These observations are consistent with regional formation of ammonium nitrate (NH_4NO_3; AN) greater than ammonium sulfate ($(NH_4)_2SO_4$); AS). NH_3, mainly emitted by agriculture, is expected to react preferentially with sulfur compounds (mainly sulfuric acid (H_2SO_4) formed from sulfur dioxide (SO_2)). However, regional SO_2 concentrations have been extremely low since the late 2010s (below 1 µg m^{-3} since 2016 at regional background sites). Therefore, AS is mainly derived from long-range transport, and the remaining NH_3 is available to react with NO_x present in urban areas, notably to form AN locally. However, the balance of AN formation also depends on meteorological conditions (low temperatures, high relative humidity, high pressure), leading to higher AN concentrations in winter/early spring when these meteorological conditions are met simultaneously with higher local NH_3 emissions. Previous studies conducted in Paris (Zhang et al., 2019; Petit et al., 2014) and at the ATOLL site in Lille (Chebaicheb et al., 2023) also highlighted the high contribution of organics and nitrate in PM_1 particles, as well as the high impact of transboundary pollution advection from Eastern Europe in northern France.

Both sites showed similar high temporal variation, with PM_1 ranging from a few µg m^{-3} to over 40 µg m^{-3} at the Danube site and over 60 µg m^{-3} at the Clemenceau site. The peaks observed at both sites appear at the same time, reflecting the major influence of atmospheric conditions and common local sources. The accumulation of local primary particles is expected during the coldest periods associated with low wind speed. New Year's evening is one of the peaks associated with increased levels due to these stable atmospheric conditions, combined with the use of fireworks and firecrackers. In particular, some hours at the Danube site have been invalidated given the negative chlorine levels attributed to these particular sources, which emit chlorinated species that are potentially poorly vaporized and not accounted for in the fragmentation table (chlorates, perchlorates) (Schmid et al., 2014).

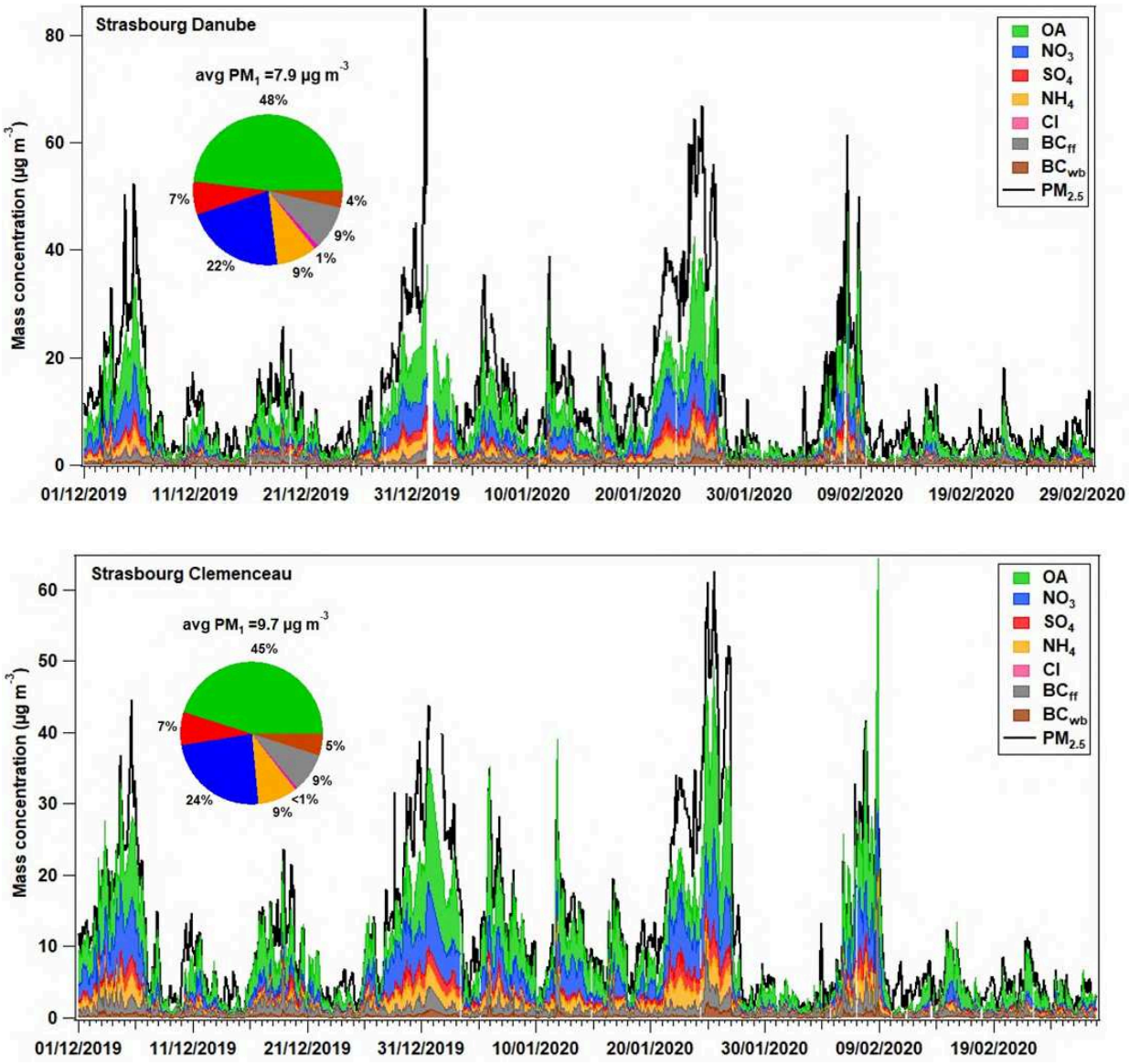

Figure 3: PM_1 species at the Danube (top) and Clemenceau (bottom) sites during the studied period.

The average mass concentrations of NR-PM_1 species and eBC presented in Table 1 revealed only slight differences between the two sites, with globally higher loadings at the Clemenceau site. This might be attributed to the proximity of primary exhaust and non-exhaust emissions from road traffic as well as more intense condensation and coagulation processes. It shall also be noted that the environment of the Clemenceau station is more urbanized (city center) compared to the Danube site, which may also partly explain these observations. OA is associated with the highest

concentrations at both sites - with values of 3.8 µg m^{-3} and 4.3 µg m^{-3} at the Danube and Clemenceau sites, respectively - reinforcing the interest of the apportionment of its major sources. The second main compound at both sites was nitrate, showing concentrations about 30% higher at Clemenceau compared to Danube. As for OA, the difference in sulfate and eBC_{ff} concentrations is of about 15 % on average (with the highest ones still observed at Clemenceau). Complementarily, results from offline analyses performed on filters collected during February 2020 indicate slightly higher concentrations for Clemenceau (Table 1). Surprisingly however, filter-based levoglucosan analyses indicate similar concentration levels at both sites while eBC_{wb} appears to be about 40 % higher at Clemenceau and the comparison of OA mass spectra averaged over the investigated period also indicates substantially higher signals for the highest m/z's, including common wood burning tracers (see Figure S3), at Clemenceau.

Table 1. Average (± standard deviation) mass concentrations of PM_1 species (in µg m^{-3}) at both Strasbourg sites during the studied period.

Species	**Danube**	**Clem.**	**Danube**	**Clem.**	**Danube**	**Clem.**
	ACSM/AE33 (DJF)		Filters (4-29 Feb.)		ACSM/AE33 (4-29 Feb.)	
OA	3.8 ± 3.6	4.3 ± 4.0			2.5 ± 3.1	3.2 ± 4.0
SO_4	0.6 ± 0.7	0.7 ± 0.8	0.4 ± 0.3	0.4 ± 0.3	0.3 ± 0.5	0.45 ± 0.6
NO_3	1.7 ± 2.1	2.3 ± 2.5	0.7 ± 1.2	0.8 ± 1.4	0.9 ± 1.5	1.3 ± 2.1
NH_4	0.7 ± 0.8	0.9 ± 0.9	0.3 ± 0.5	0.3 ± 0.5	0.4 ± 0.6	0.5 ± 0.8
eBC_{ff}	0.75 ± 0.7	0.8 ± 0.9			0.6 ± 0.7	0.7 ± 1.2
eBC_{wb}	0.3 ± 0.3	0.5 ± 0.5			0.2 ± 0.3	0.3 ± 0.5
EC			0.7 ± 0.5	0.9 ± 0.7		
OC			2.0 ± 1.7	2.2 ± 2.0		
Levo.			0.13 ± 0.13	0.13 ± 0.14		

4 OA source apportionment

Figures 4 and 5 summarize the results obtained from the individual and combined PMF analyses for the two sites, respectively providing the relative contributions of each identified OA factor and their corresponding mass spectra. These results are described in the following paragraphs, according to their nature.

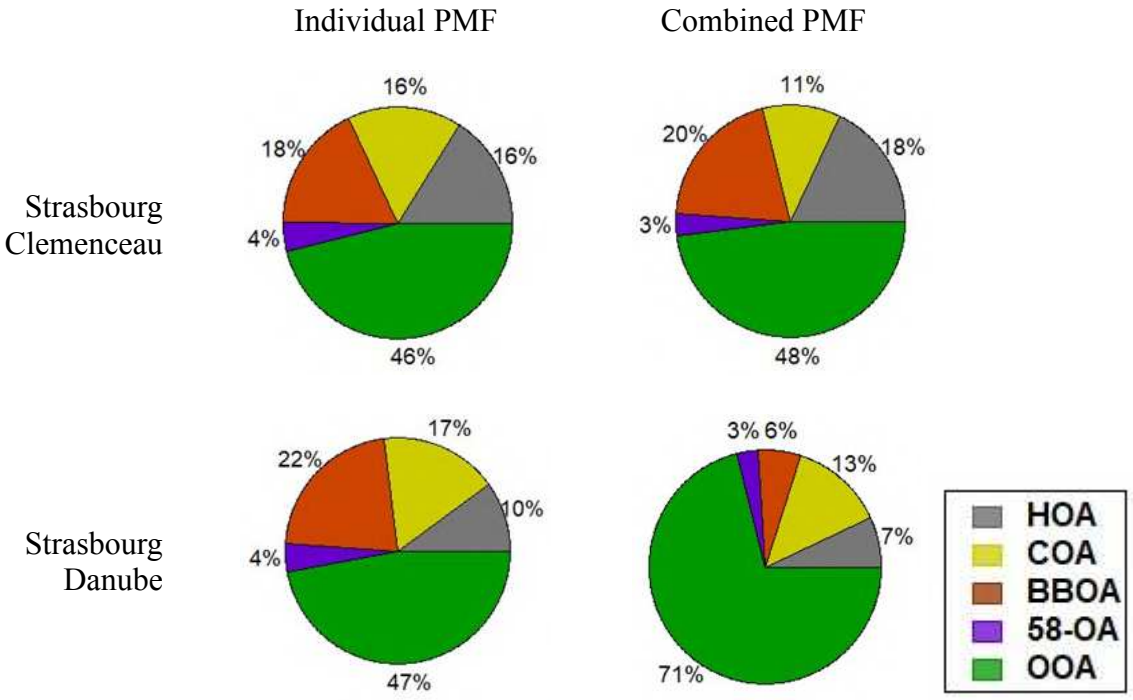

Figure 4: Contributions of OA factors at both sites from individual PMF and combined PMF.

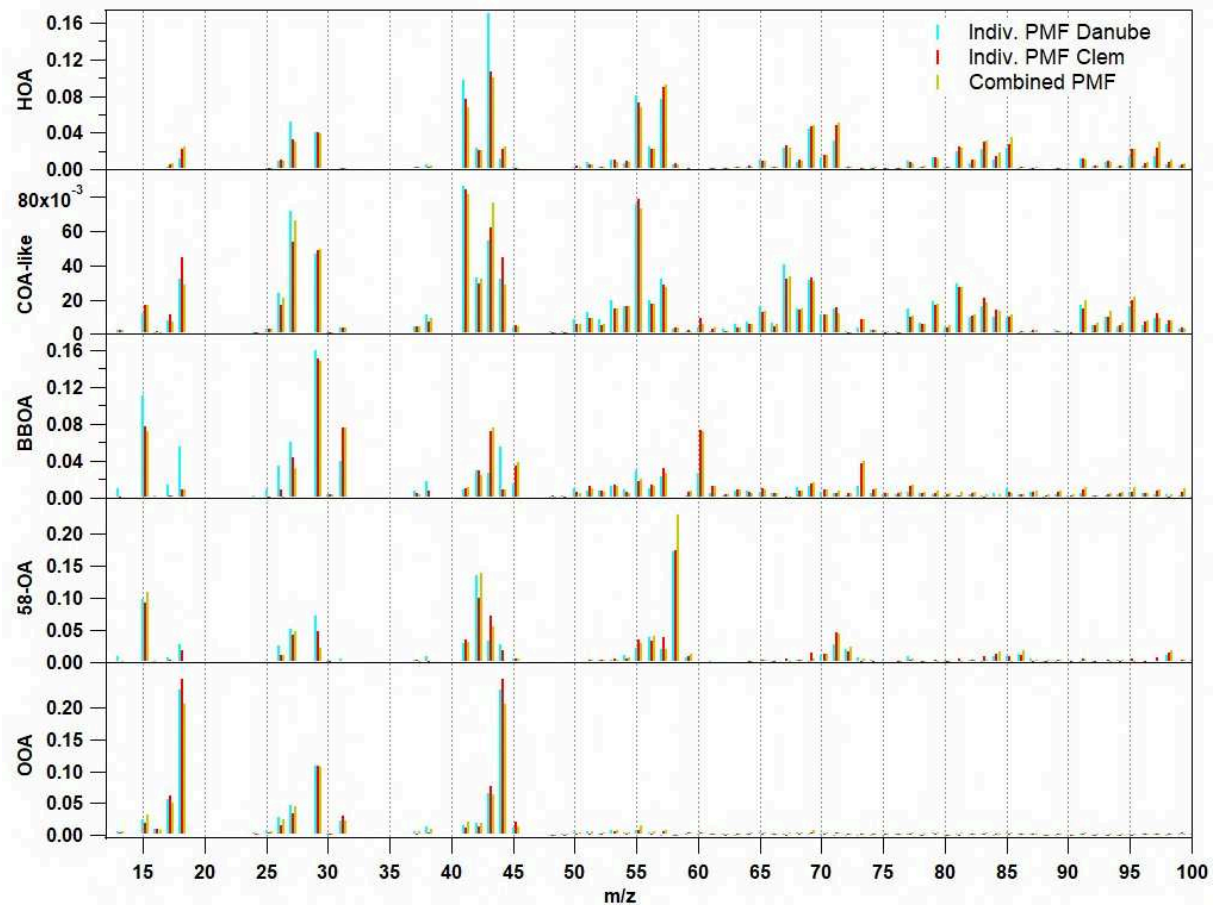

Figure 5: Mass spectra of OA factors from individual and combined PMF for both sites.

4.1 Amine-related OA

A noticeable result of the present study is the identification of a specific amine-related OA factor which could be observed at both sites. This unusual factor is characterized by a high proportion of m/z 58 (mainly $C_3H_8N^+$), with a contribution of about 4 % of the OA total mass. It was observed in both unconstrained and constrained PMF analyses and regardless of the number of factors or specific runs, the unconstrained PMF consistently revealed this factor among the 4-factor (or more) solutions. It exhibited a relatively stable profile across different PMF runs with high contributions of m/z 58 and 42 ($C_2H_4N^+$). The time series for this factor at both sites show a highly variable temporal pattern with rather sporadic and intense peaks. The diel profile for this factor is not completely flat. It displays a peak in the morning and an increase towards the end of

the day. However, associating this diel profile with a specific source proved to be challenging. Numerous tests were conducted in other seasons for continued measurements performed at the Danube site after the winter campaign presented in this paper. The 58-OA factor also emerged during an individual study conducted in summer, suggesting that it was not exclusively associated with winter sources.

The average mass spectrum for this factor is different from the few m/z 58-rich factors observed in previous studies based on AMS or ACSM measurements (Hildebrandt et al., 2011; Chen et al., 2021) where this factor was rather associated with an instrument artifact. Specifically, we observe high peaks for m/z 58 and 42, rather than the higher masses (m/z 84 and 98) observed in these previous studies. Furthermore, this factor does not appear when analyzing the data from Metz (prior to the campaign) with the same two instruments. This suggests that the factor is more closely linked to local sources in Strasbourg.

The pollution rose analysis at both Strasbourg sites reveals a specific and localized direction associated with this amine-related OA factor (Figure S16). The direction pointed to an industrial area which could explain these specific particle emissions. A factor profile associated with amine-OA and a specific daily profile are consistent with an industrial source. This factor could therefore be associated with an industrial source of OA, although further investigation is required.

4.2 Other POA factors

Besides this site-specific amine-related factor, the PMF analyses revealed the three main POA factors commonly observed in such a source apportionment analysis, namely HOA, BBOA, and a COA-like factor. For HOA, the mass spectrum fingerprint is characterized by a high contribution of hydrocarbon fragments m/z 41, 43, 55, 57, 69, and 71, and its time series displays well-marked diel variations associated with morning and evening traffic peaks corresponding to home/work commutes. The BBOA factor is marked by high contribution at m/z 29, 60, and 73 (tracers of biomass combustion) and by a diel variation showing an increase in the evening that extends into the night, associated with domestic heating in winter. Some differences were observed between the BBOA profiles at the two sites. These differences can be explained by particle aging, especially with a higher 44/60 ratio at the Danube site than at the Clemenceau site, indicating more oxidized particles from biomass burning at the Danube site. Compared to HOA and BBOA,

the COA profile is usually characterized by higher peaks at m/z 41 and 55, and by diel cycles showing mid-day (lunch) and evening (dinner) peaks associated with cooking activities. Such a clear diel profile could not be obtained for the Danube site, where it shows variations quite similar to that of BBOA, with a concentration maximum in the late evening. Consequently, we rather refer to this factor as COA-like.

For individual PMF, HOA, BBOA, and COA-like contributed 16 %, 16 %, and 18 % of organic matter, respectively, at the Clemenceau site. A lower HOA contribution (10 %) was observed for Danube, consistent with an increased influence of traffic at the Clemenceau site. The two primary factors HOA and BBOA showed a strong correlation with eBC_{ff} and eBC_{wb} (r^2 (HOA, eBC_{ff}) = 0.80 and 0.73; and r^2 (BBOA, eBC_{wb}) = 0.92 and 0.90 for the Clemenceau and Danube sites, respectively, Figure S13, SI). COA-like at Danube has a fairly similar contribution to COA-like at the Clemenceau site (around 17 %) but with a lower mass concentration of 0.6 µg m^{-3} compared to Clemenceau (0.9 µg m^{-3}) which is closer to the city center. However, BBOA shows a higher contribution at the Danube site (22 % of total OA mass) with a concentration of 0.8 µg m^{-3}, close to that of Clemenceau. A comparison of m/z 60 at Danube and Clemenceau (Figure S14 in the supplementary information) shows an m/z 60 signal twice as high at Clemenceau as at Danube.

Results from the combined PMF analysis may help gaining a deeper understanding of the variation of these POA factors between both sites. Interestingly, contributions obtained from the combined PMF differ from those obtained using the individual PMF for Danube, whereas only minor differences are obtained for Clemenceau, with slightly more HOA and BBOA and less COA-like at that site (Figure 5). For the Danube site, on the other hand, relative contributions and mass concentrations are significantly altered for these factors, especially for HOA and BBOA. The COA-like factor shows similar mass concentrations close to 0.6 µg m^{-3}, representing 17 % and 13 % of the total mass for the individual and combined PMF, respectively. HOA also decreased slightly from 10 % to 7 % between the two PMF approaches. A strong decrease is observed for BBOA, from 22 % to 6 %, in agreement with the m/z 60 comparison, which shows less BBOA at the Danube site.

4.3 Oxygenated organic aerosols (OOA)

The obtained OOA mass spectra are consistent with those reported in the literature, associated with stable diel variation, and characterized by a high contribution of m/z 44 (Figure S10). At both sites, the OOA factor showed similar profiles and diel variations. For the individual PMF, OOA dominated OA at both sites with a contribution of about 47 % but with different mass concentrations of 2.6 and 1.7 μg m^{-3} at the Clemenceau and Danube sites, respectively.

The combined PMF identified two OOA factors, named OOA1 and OOA2 (section S2, Figure S9). As the two factors are correlated, we summed them together to obtain a single OOA factor (Figure S11). At the Clemenceau site, the contribution of the OOA factor (48 %) is similar to the one obtained from the individual PMF, with a mass concentration of 2.8 μg m^{-3}. At the Danube site, the contribution of the OOA factor strongly increased from 47 % for the individual PMF to 71 % for the combined one (Figure 4), reaching a mass concentration of 2.6 μg m^{-3}, close to that of the Clemenceau site. These combined PMF results provided further insight into this factor and demonstrated its regional origin. In Clemenceau, we observed a balance between primary and secondary OA factors, while for Danube, the combined PMF outputs indicated an average OOA contribution of about 70 % of total OA.

5 Discussion and concluding remarks

The present study offers the opportunity to qualitatively assess measurement consistency and results of carbonaceous aerosol source apportionment analyses conducted using the same type of instruments at two neighboring urban sites. The two ACSMs used in this study for the characterization of non-refractory submicron chemical species were initially compared at the same location prior to the campaign. This side-by-side comparison showed a very good agreement for nitrate concentrations, validating the consistency of the response factors obtained from the calibration of both ACSMs. However, significant discrepancies - of about 30% - were obtained for OA (and sulfate) mass concentrations, and the comparison of OA mass spectra showed a surprising behavior with a few m/z's (including m/z 60 and 73, commonly used as biomass burning tracers) at higher levels in the instrument which presented overall lower

loadings in total OA concentrations. Quality assurance and quality checks have been achieved following the most advanced recommendations provided by the manufacturer as well as within the scientific community, and no specific instrumental bias could be evidenced to explain these differences. Therefore, both ACSMs may be considered as running in their usual and proper operating conditions, with discrepancies mainly due to inherent technical specificities of each apparatus.

Once installed at their respective monitoring stations in Strasbourg, the ACSMs delivered meaningful measurements of the submicron aerosol chemical species, with moderately higher concentrations at the Clemenceau traffic site compared to the urban background Danube station, which can be attributed to more intense primary emissions and/or transformation processes at roadside. Filter-based offline measurements available for the last month of the campaign tend to confirm these observations, with slightly higher concentrations of major chemical species at Clemenceau. Results from individual PMF analyses also indicated higher HOA contributions for Clemenceau, in good agreement with moderately higher eBC_{ff} and EC concentrations at this same site compared to Danube. They also pointed to similar BBOA contributions at the two stations, in agreement with the comparison of filter-based levoglucosan measurements. Less expected is the substantially higher eBC_{wb} loading obtained from the application of the so-called Aethalometer model to AE33 measurements at both sites. This might be due to the choice of site-specific sets of AAE (α_{ff} and α_{wb}) values chosen to represent the two eBC sub-fractions at each monitoring station. This finding confirms the high sensitivity of the Aethalometer model to empirical assumptions to be made for its application. In particular, this may illustrate how cautiously it should be considered for any eBC source apportionment study at a traffic site (Savadkoohi et al., 2023).

The COA-like factor showed expected peaks at lunch and dinner time for Clemenceau, but displayed a diel cycle relatively similar to BBOA (with no significant mid-day increase) for Danube, illustrating the difficulty to attribute a cooking-only origin to this factor. Interestingly, results obtained from the combined PMF analysis may improve the apportionment of these cooking emissions, reducing the COA-to-HOA ratio at nighttime - especially for Clemenceau - compared to individual PMF outputs (Fig. S12). However, such a combined PMF analysis may not be suitable to enhance the consistency of other OA factors, probably due to instrumental

specificities leading to differences in the OA mass spectra obtained by the two apparatus. More precisely, the OA profiles obtained using the combined PMF method exhibit greater similarity to the profiles obtained from the individual PMF analysis of Clemenceau compared to those from the individual PMF analysis of Danube. As a result, there is a reduced contribution of m/z 43 (associated with HOA) and m/z 44 (associated with BBOA) at Danube when applying the combined PMF approach in contrast to the individual PMF analyses. This discrepancy leads to an underestimation of these factors (HOA and BBOA) and an overestimation of OOA at the Danube site when employing the combined PMF method.

Finally, simultaneous ACSM measurements at these paired-sites allow to confirm the substantial influence of an amine-related OA factor in Strasbourg. This unique factor, characterized by a high proportion of m/z 58, represents approximately 4 % of the total OA mass and is consistently observed in both PMF analyses. The diel profile of this factor exhibits peaks in the morning and late in the day, but its specific source remains challenging to identify. It differs from previously observed m/z 58-rich factors, suggesting a distinct local source, possibly linked to industrial emissions. Further investigation is needed to pinpoint the exact source of this intriguing amine-related OA factor.

References

Äijälä, M., Heikkinen, L., Fröhlich, R., Canonaco, F., Prévôt, A. S. H., Junninen, H., Petäjä, T., Kulmala, M., Worsnop, D., and Ehn, M.: Resolving anthropogenic aerosol pollution types – deconvolution and exploratory classification of pollution events, Atmospheric Chem. Phys., 17, 3165–3197, https://doi.org/10.5194/acp-17-3165-2017, 2017.

Air quality in Europe 2022 — European Environment Agency:
https://www.eea.europa.eu/publications/air-quality-in-europe-2022, last access: 31 July 2023.

Chatain, M., Alvarez, R., Ustache, A., Rivière, E., Favez, O., and Pallares, C.: Simultaneous Roadside and Urban Background Measurements of Submicron Aerosol Number Concentration and Size Distribution (in the Range 20–800 nm), along with Chemical Composition in Strasbourg, France, Atmosphere, 12, 71, https://doi.org/10.3390/atmos12010071, 2021.

Chebaicheb, H., F. de Brito, J., Chen, G., Tison, E., Marchand, C., Prévôt, A. S. H., Favez, O., and Riffault, V.: Investigation of four-year chemical composition and organic aerosol sources of submicron

particles at the ATOLL site in northern France, Environ. Pollut., 330, 121805, https://doi.org/10.1016/j.envpol.2023.121805, 2023.

Chebaicheb, H et al., Multi-year high time resolution datasets of fine PM at 13 sites of the French Operational Network (CARA program): Data processing and chemical composition, in preparation.

Chen, G., Sosedova, Y., Canonaco, F., Fröhlich, R., Tobler, A., Vlachou, A., Daellenbach, K. R., Bozzetti, C., Hueglin, C., Graf, P., Baltensperger, U., Slowik, J. G., El Haddad, I., and Prévôt, A. S. H.: Time-dependent source apportionment of submicron organic aerosol for a rural site in an alpine valley using a rolling positive matrix factorization (PMF) window, Atmospheric Chem. Phys., 21, 15081–15101, https://doi.org/10.5194/acp-21-15081-2021, 2021.

Chen, G., Canonaco, F., Tobler, A., Aas, W., Alastuey, A., Allan, J., Atabakhsh, S., Aurela, M., Baltensperger, U., Bougiatioti, A., De Brito, J. F., Ceburnis, D., Chazeau, B., Chebaicheb, H., Daellenbach, K. R., Ehn, M., El Haddad, I., Eleftheriadis, K., Favez, O., Flentje, H., Font, A., Fossum, K., Freney, E., Gini, M., Green, D. C., Heikkinen, L., Herrmann, H., Kalogridis, A.-C., Keernik, H., Lhotka, R., Lin, C., Lunder, C., Maasikmets, M., Manousakas, M. I., Marchand, N., Marin, C., Marmureanu, L., Mihalopoulos, N., Močnik, G., Nęcki, J., O'Dowd, C., Ovadnevaite, J., Peter, T., Petit, J.-E., Pikridas, M., Matthew Platt, S., Pokorná, P., Poulain, L., Priestman, M., Riffault, V., Rinaldi, M., Różański, K., Schwarz, J., Sciare, J., Simon, L., Skiba, A., Slowik, J. G., Sosedova, Y., Stavroulas, I., Styszko, K., Teinemaa, E., Timonen, H., Tremper, A., Vasilescu, J., Via, M., Vodička, P., Wiedensohler, A., Zografou, O., Cruz Minguillón, M., and Prévôt, A. S. H.: European aerosol phenomenology − 8: Harmonised source apportionment of organic aerosol using 22 Year-long ACSM/AMS datasets, Environ. Int., 166, 107325, https://doi.org/10.1016/j.envint.2022.107325, 2022.

Crippa, M., DeCarlo, P. F., Slowik, J. G., Mohr, C., Heringa, M. F., Chirico, R., Poulain, L., Freutel, F., Sciare, J., Cozic, J., Di Marco, C. F., Elsasser, M., Nicolas, J. B., Marchand, N., Abidi, E., Wiedensohler, A., Drewnick, F., Schneider, J., Borrmann, S., Nemitz, E., Zimmermann, R., Jaffrezo, J.-L., Prévôt, A. S. H., and Baltensperger, U.: Wintertime aerosol chemical composition and source apportionment of the organic fraction in the metropolitan area of Paris, Atmospheric Chem. Phys., 13, 961–981, https://doi.org/10.5194/acp-13-961-2013, 2013.

Drinovec, L., Močnik, G., Zotter, P., Prévôt, A. S. H., Ruckstuhl, C., Coz, E., Rupakheti, M., Sciare, J., Müller, T., Wiedensohler, A., and Hansen, A. D. A.: The "dual-spot" Aethalometer: an improved measurement of aerosol black carbon with real-time loading compensation, Atmospheric Meas. Tech., 8, 1965–1979, https://doi.org/10.5194/amt-8-1965-2015, 2015.

Favez, O., Weber, S., Petit, J.-E., Alleman, L., Albinet, A., Riffault, V., Chazeau, B., Amodeo, T., Salameh, D., Zhang, Y., Srivastava, D., Samaké, A., Aujay, R., Papin, A., Bonnaire, N., Boullanger, C., Chatain, M., Chevrier, F., Detournay, A., and Leoz-Garziandia, E.: Overview of the French Operational Network for In Situ Observation of PM Chemical Composition and Sources in Urban Unvironments (CARA Program), https://doi.org/10.20944/preprints202101.0182.v1, 2021.

Guide méthodologique pour la mesure des concentrations en ammoniac dans l'air ambiant | LCSQA: https://www.lcsqa.org/fr/rapport/guide-methodologique-pour-la-mesure-des-concentrations-en-ammoniac-dans-lair-ambiant, last access: 31 July 2023.

Hildebrandt, L., Kostenidou, E., Lanz, V. A., Prevot, A. S. H., Baltensperger, U., Mihalopoulos, N., Laaksonen, A., Donahue, N. M., and Pandis, S. N.: Sources and atmospheric processing of organic aerosol in the Mediterranean: insights from aerosol mass spectrometer factor analysis, Atmospheric Chem. Phys., 11, 12499–12515, https://doi.org/10.5194/acp-11-12499-2011, 2011.

Hopke, P. K., Dai, Q., Li, L., and Feng, Y.: Global review of recent source apportionments for airborne particulate matter, Sci. Total Environ., 740, 140091, https://doi.org/10.1016/j.scitotenv.2020.140091, 2020.

Le bilan annuel 2022 de la qualité de l'air dans le Grand Est | ATMO GrandEst: https://www.atmo-grandest.eu/actualite/le-bilan-annuel-2022-de-la-qualite-de-lair-dans-le-grand-est, last access: 31 July 2023.

Masson-Delmotte, V., Zhai, P., Pirani, A., Connors, S. L., Péan, C., Berger, S., Caud, N., Chen, Y., Goldfarb, L., Gomis, M. I., Huang, M., Leitzell, K., Lonnoy, E., Matthews, J. B. R., Maycock, T. K., Waterfield, T., Yelekçi, Ö., Yu, R., and Zhou, B. (Eds.): Climate Change 2021: The Physical Science Basis. Contribution of Working Group I to the Sixth Assessment Report of the Intergovernmental Panel on Climate Change, Cambridge University Press, Cambridge, United Kingdom and New York, NY, USA, https://doi.org/10.1017/9781009157896, 2021.

Mooibroek, D., Schaap, M., Weijers, E. P., and Hoogerbrugge, R.: Source apportionment and spatial variability of PM2.5 using measurements at five sites in the Netherlands, Atmos. Environ., 45, 4180–4191, https://doi.org/10.1016/j.atmosenv.2011.05.017, 2011.

Mooibroek, D., Staelens, J., Cordell, R., Panteliadis, P., Delaunay, T., Weijers, E., Vercauteren, J., Hoogerbrugge, R., Dijkema, M., Monks, P. S., and Roekens, E.: PM10 Source Apportionment in Five North Western European Cities—Outcome of the Joaquin Project, https://doi.org/10.1039/9781782626589-00264, 2016.

Ng, N. L., Herndon, S. C., Trimborn, A., Canagaratna, M. R., Croteau, P. L., Onasch, T. B., Sueper, D., Worsnop, D. R., Zhang, Q., Sun, Y. L., and Jayne, J. T.: An Aerosol Chemical Speciation Monitor (ACSM) for Routine Monitoring of the Composition and Mass Concentrations of Ambient Aerosol, Aerosol Sci. Technol., 45, 780–794, https://doi.org/10.1080/02786826.2011.560211, 2011.

Paatero, P., Tapper, U., 1994. Positive matrix factorization: a non-negative factor model with optimal utilization of error estimates of data values. Environmetrics 5, 111–126. https://doi.org/10.1002/env.3170050203.

Petit, J.-E., Favez, O., Sciare, J., Canonaco, F., Croteau, P., Močnik, G., Jayne, J., Worsnop, D., and Leoz-Garziandia, E.: Submicron aerosol source apportionment of wintertime pollution in Paris, France by double positive matrix factorization (PMF^2) using an aerosol chemical speciation monitor (ACSM) and a

multi-wavelength Aethalometer, Atmospheric Chem. Phys., 14, 13773–13787, https://doi.org/10.5194/acp-14-13773-2014, 2014.

Petit, J.-E., Pallares, C., Favez, O., Alleman, L., Bonnaire, N., and Rivière, E.: Sources and Geographical Origins of PM 10 in Metz (France) Using Oxalate as a Marker of Secondary Organic Aerosols by Positive Matrix Factorization Analysis, Atmosphere, 10, 370, https://doi.org/10.3390/atmos10070370, 2019.

Qi, L., Bozzetti, C., Corbin, J. C., Daellenbach, K. R., El Haddad, I., Zhang, Q., Wang, J., Baltensperger, U., Prévôt, A. S. H., Chen, M., Ge, X., and Slowik, J. G.: Source identification and characterization of organic nitrogen in atmospheric aerosols at a suburban site in China, Sci. Total Environ., 818, 151800, https://doi.org/10.1016/j.scitotenv.2021.151800, 2022.

Sandradewi, J., Prevot, A., Weingartner, E., Schmidhauser, R., Gysel, M., and Baltensperger, U.: A study of wood burning and traffic aerosols in an Alpine valley using a multi-wavelength Aethalometer, Atmos. Environ., 42, 101–112, https://doi.org/10.1016/j.atmosenv.2007.09.034, 2008.

Schmid, P., Bogdal, C., Wang, Z., Azara, V., Haag, R., and von Arx, U.: Releases of chlorobenzenes, chlorophenols and dioxins during fireworks, Chemosphere, 114, 158–164, https://doi.org/10.1016/j.chemosphere.2014.03.088, 2014.

WHO Air Quality Guidelines:
https://www.c40knowledgehub.org/s/article/WHO-Air-Quality-Guidelines?language=en_US, last access: 23 January 2023.

Xu, W., Lambe, A., Silva, P., Hu, W., Onasch, T., Williams, L., Croteau, P., Zhang, X., Renbaum-Wolff, L., Fortner, E., Jimenez, J. L., Jayne, J., Worsnop, D., and Canagaratna, M.: Laboratory evaluation of species-dependent relative ionization efficiencies in the Aerodyne Aerosol Mass Spectrometer, Aerosol Sci. Technol., 52, 626–641, https://doi.org/10.1080/02786826.2018.1439570, 2018.

Zhang, Y., Favez, O., Petit, J.-E., Canonaco, F., Truong, F., Bonnaire, N., Crenn, V., Amodeo, T., Prévôt, A. S. H., Sciare, J., Gros, V., and Albinet, A.: Six-year source apportionment of submicron organic aerosols from near-continuous highly time-resolved measurements at SIRTA (Paris area, France), Atmospheric Chem. Phys., 19, 14755–14776, https://doi.org/10.5194/acp-19-14755-2019, 2019.

Zhou, S., Collier, S., Xu, J., Mei, F., Wang, J., Lee, Y.-N., Sedlacek III, A. J., Springston, S. R., Sun, Y., and Zhang, Q.: Influences of upwind emission sources and atmospheric processing on aerosol chemistry and properties at a rural location in the Northeastern U.S., J. Geophys. Res. Atmospheres, 121, 6049–6065, https://doi.org/10.1002/2015JD024568, 2016.

IV.3. Supplementary Information de l'article 2

Supplementary Information

Lessons learned from the comparison and combination of fine carbonaceous aerosol source apportionment at two locations in the city of Strasbourg, France

Hasna Chebaicheb[1,2,3], Mélodie Chatain[4], Olivier Favez[2,3], Joel F. de Brito[1], Vincent Crenn[5], Tanguy Amodeo[2,3], Mohamed Gherras[2], Emmanuel Jantzem[4], Véronique Riffault[1,3]

[1]IMT Nord Europe, Institut Mines-Télécom, Université de Lille, Centre for Energy and Environment, 59000, Lille, France
[2]Institut National de l'environnement Industriel et des Risques (INERIS), 60550 Verneuil-en-Halatte, France
[3]Laboratoire Central de Surveillance de la Qualité de l'Air (LCSQA), 60550 Verneuil-en-Halatte, France
[4]Atmo Grand Est, 67300 Schiltigheim, France
[5]ADDAIR, F-78530 Buc, France

Correspondence to: hasna.chebaicheb@ineris.fr

S0. ACSM data analysis

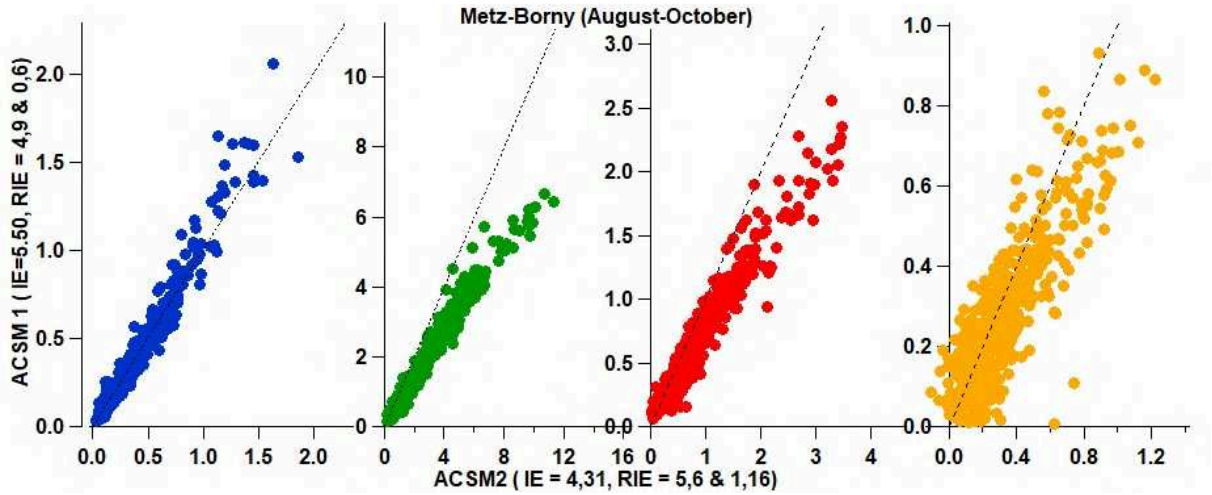

Figure S1: Scatter plots between ACSM #1 and ACSM #2 for non-refractory chemical species (OA, NO_3, NH_4, and SO_4).

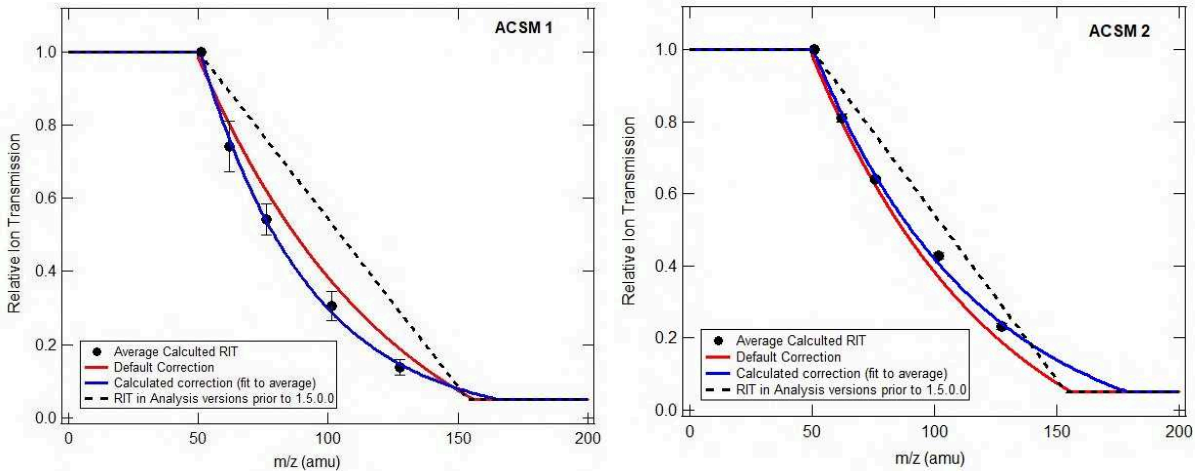

Figure S2: Relative ion transmission (RIT) graphs for ACSM #1 and ACSM #2.

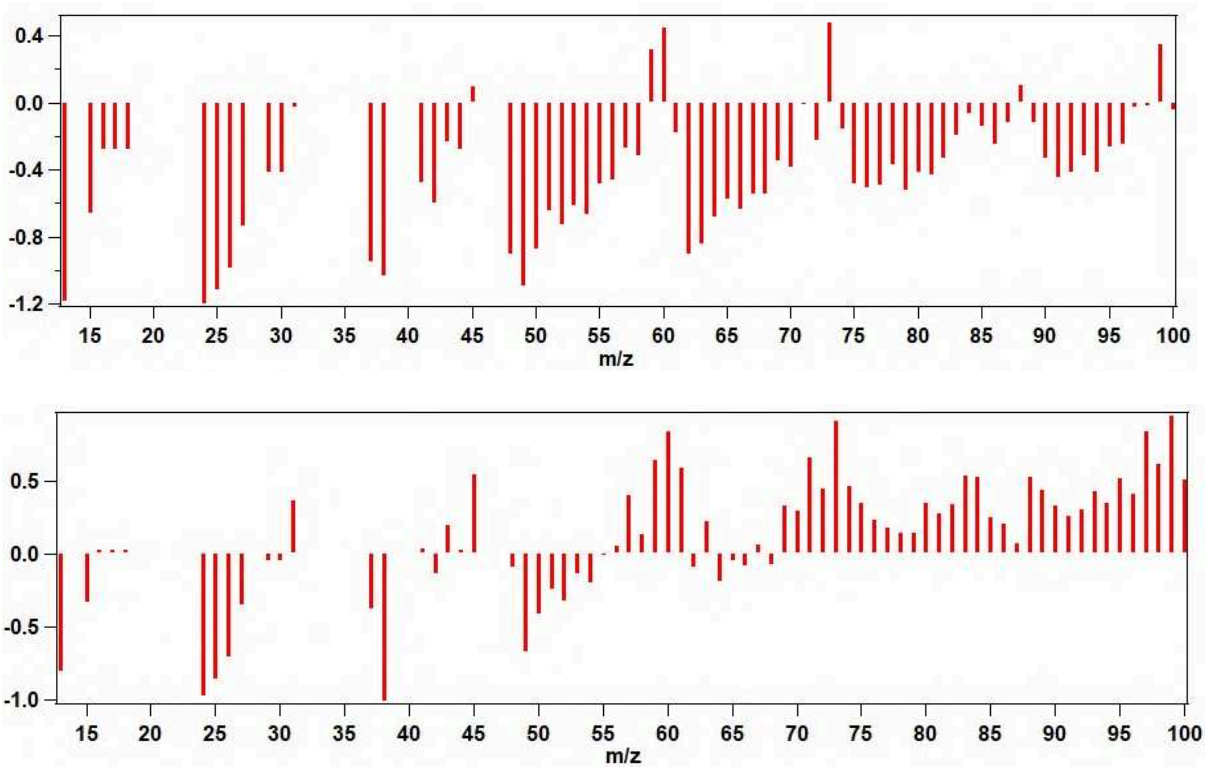

Figure S3: Differences between ACSM #1 and ACSM #2 for each m/z of the OA matrices. Upper panel: during the pre-campaign intercomparison exercise in Metz; Lower panel: during simultaneous measurements at both Strasbourg sites.

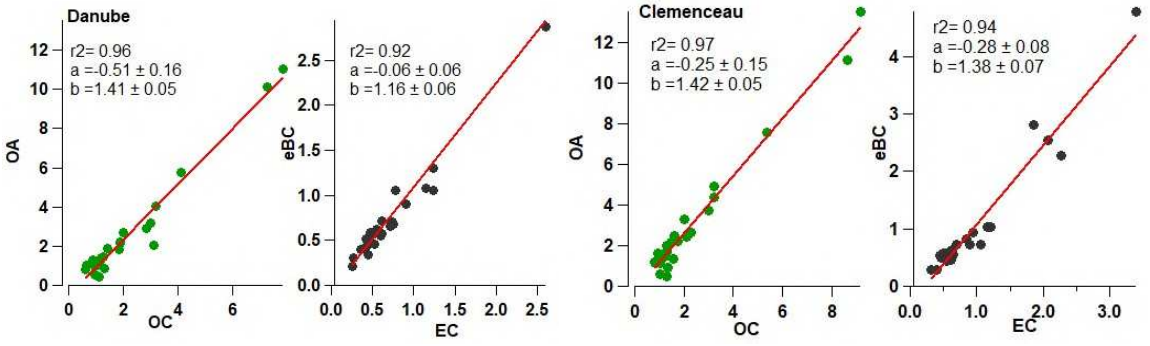

Figure S4: OA/OC and eBC/EC plots for both Strasbourg sites; Danube (left) and Clemenceau (right).

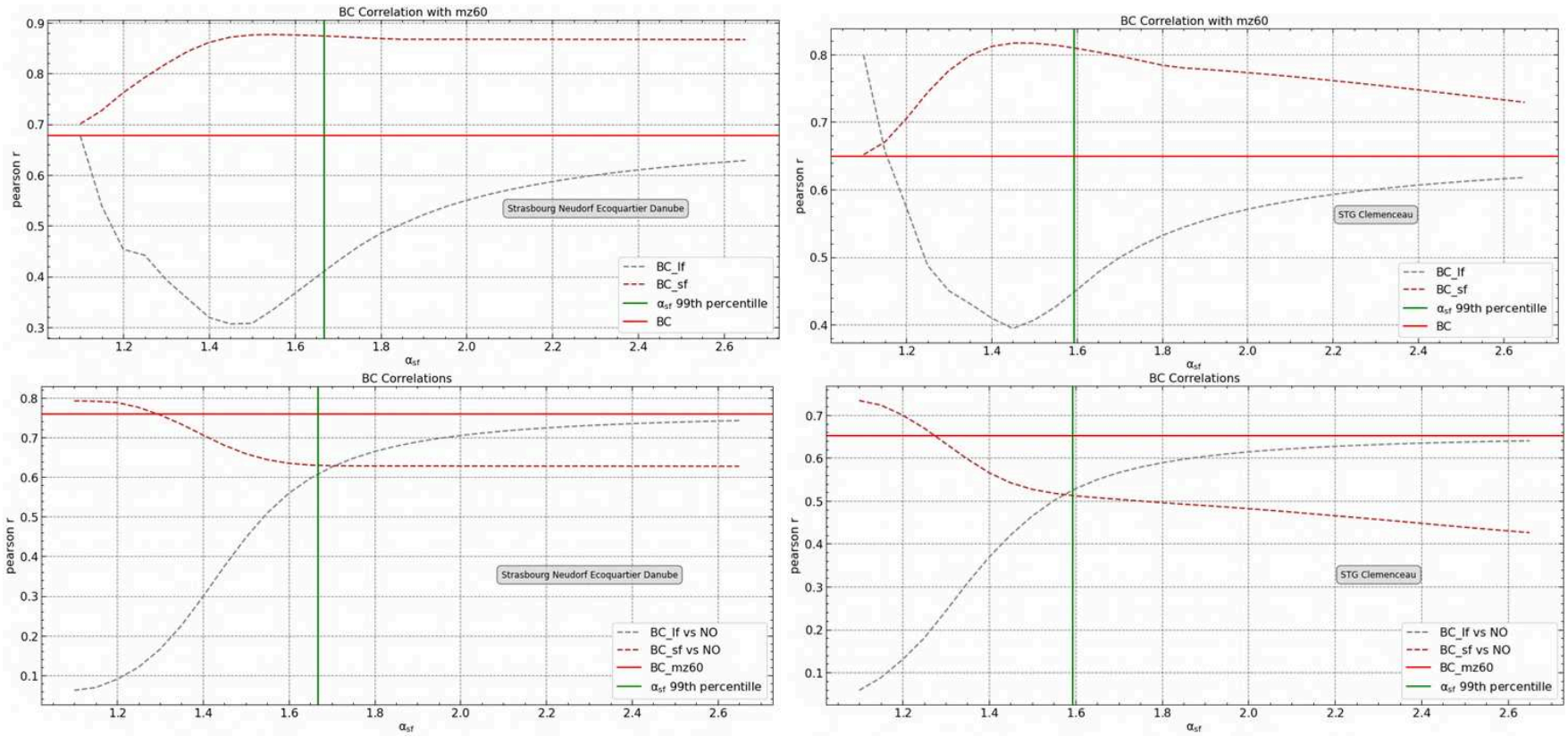

Figure S5: Determination of α_{ff} and α_{wb} values for the Danube (left) and Clemenceau (right) sites.

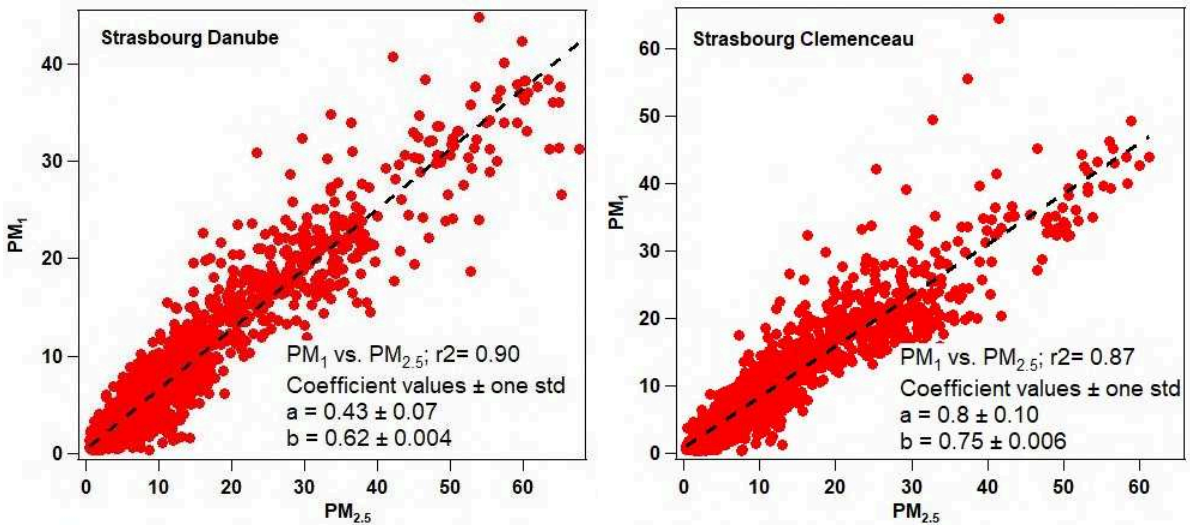

Figure S6: Comparison between PM_1 (ACSM + eBC) and $PM_{2.5}$ for Strasbourg Danube (left) and Strasbourg Clemenceau (right).

S1. Individual PMF analysis

The 5-factor solution was chosen for the Clemenceau site. The two primary factors HOA and COA-like were constrained using the reference profiles derived from Crippa et al. (2013). Multiple PMF tests were also carried out with a factor number ranging from 3 to 7. The 5-factor solution was selected. Increasing the number of factors is not relevant, as it leads to OOA factors split. A specific factor 58-OA was observed for solutions from 3 factors, highlighting the influence of this specific source. The 5 factors identified were HOA, COA-like, BBOA, 58-OA, and OOA. Their identification was based on the study of their mass spectra in comparison with reference profiles, their deil profiles, and correlations with external measurements.

The individual PMF applied for the Danube dataset was implemented in the same way as the Clemenceau site with multiple PMF runs tested to identify the better solution (a-values between 0 to 0.3 for the HOA and COA-like profiles, 3 to 7 number of factors). The presence of a COA-like was not relevant for this site, notably due to the absence of a peak at midday. As the Danube site is more residential, there may not be as many people returning for lunch, which could explain the only evening peak observed at this site. 5 factors were identified for this site as well: HOA, BBOA, COA-like, 58-OA, and OOA.

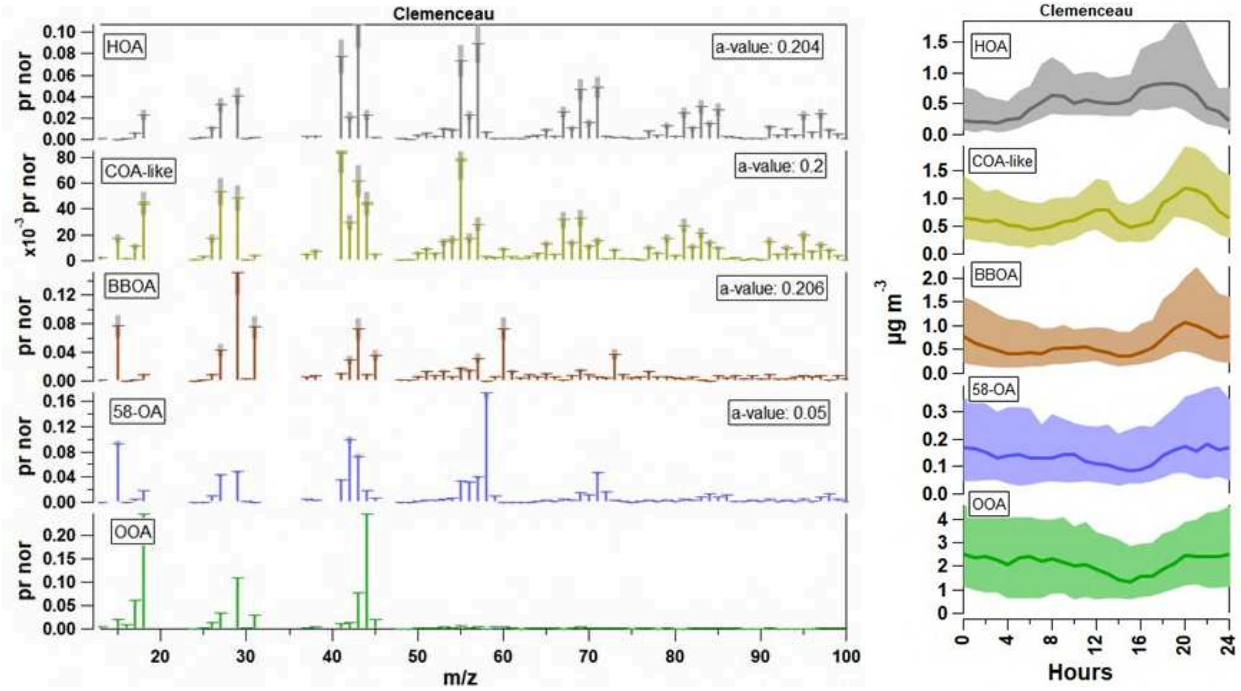

Figure S7: Mass spectra and diel cycles of OA factors for the Clemenceau site. The shaded areas represent the interquartile range and the bold line in the middle represents the median.

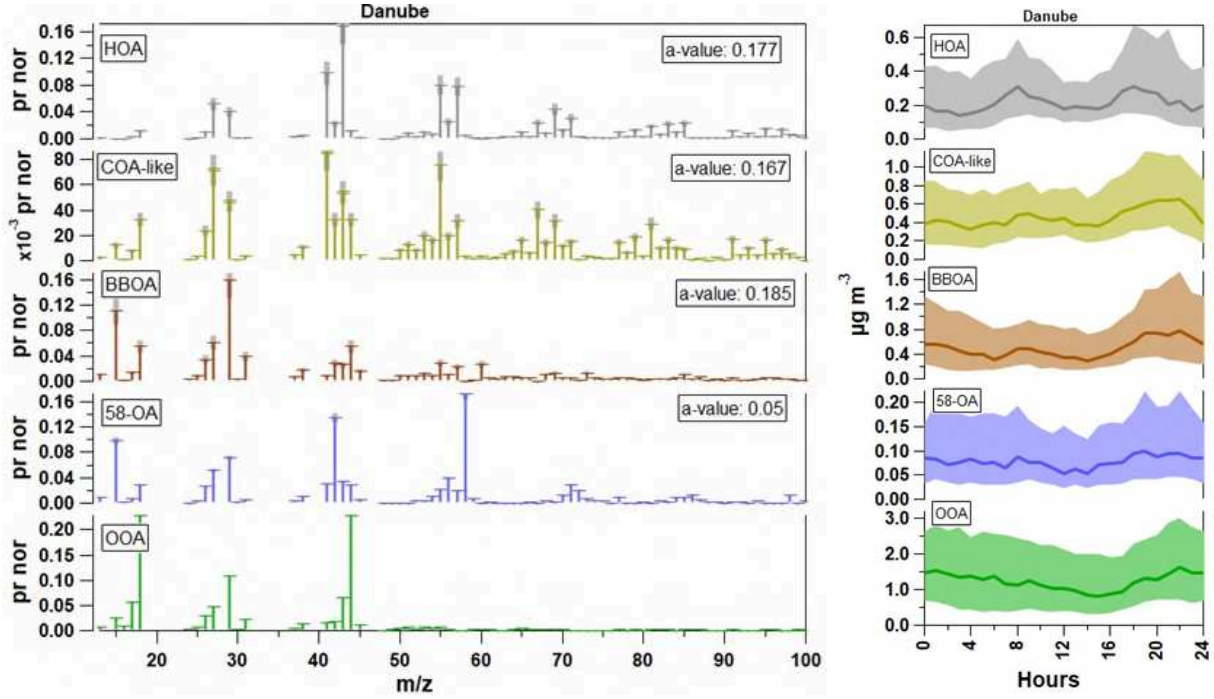

Figure S8: Mass spectra and diel cycles of OA factors for the Danube site. The shaded areas represent the interquartile range and the bold line in the middle represents the median.

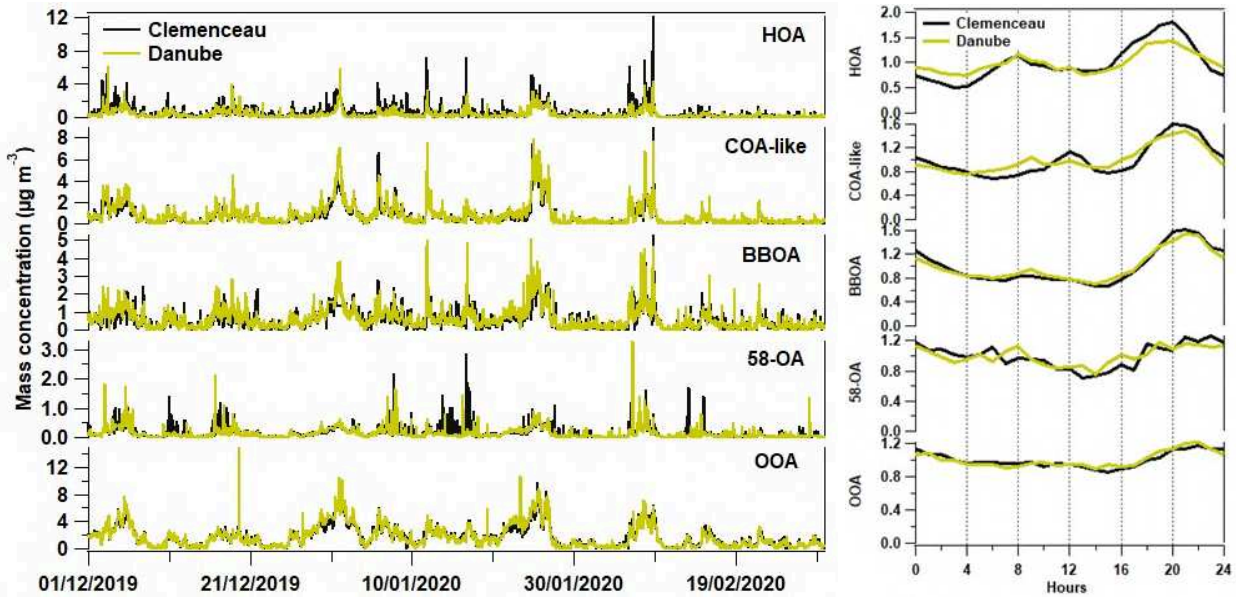

Figure S9: Time series of OA factors from individual PMF at both sites during the studied period.

S2. Combined PMF analysis

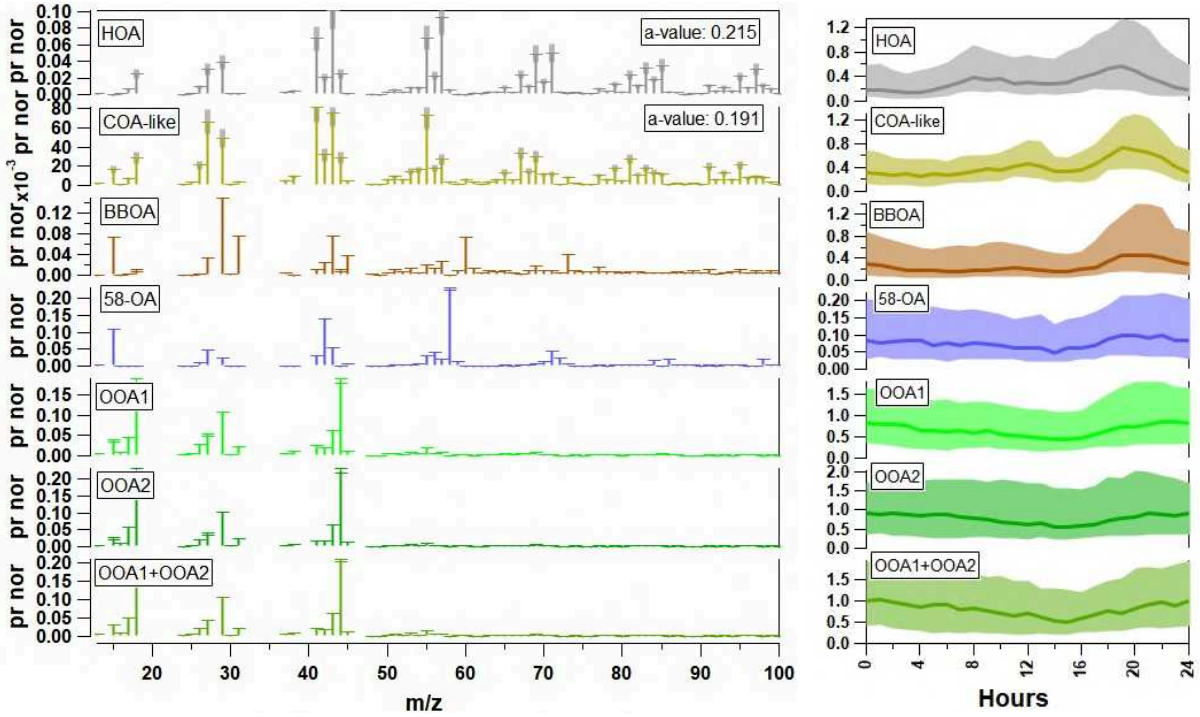

Figure S10: OA mass spectra for the combined PMF and diel profiles at both sites.

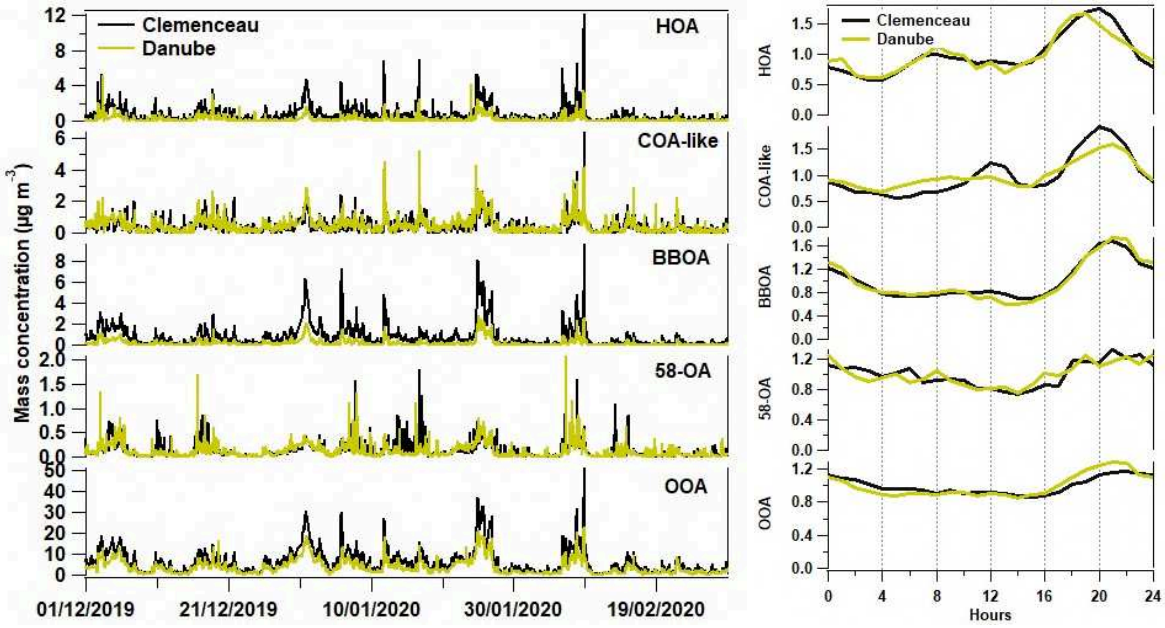

Figure S11: OA time series from combined PMF and the normalized diel profiles at both sites.

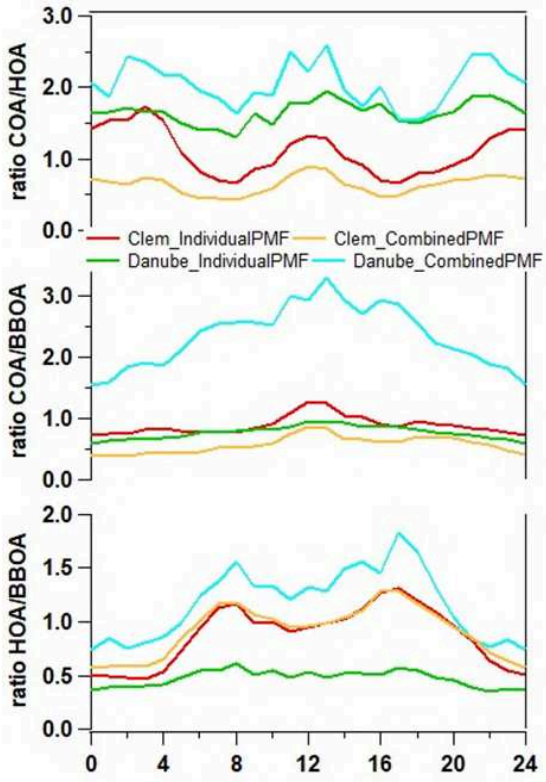

Figure S12: HOA/BBOA, COA-like/BBOA, and COA/HOA diel ratios for each PMF and site.

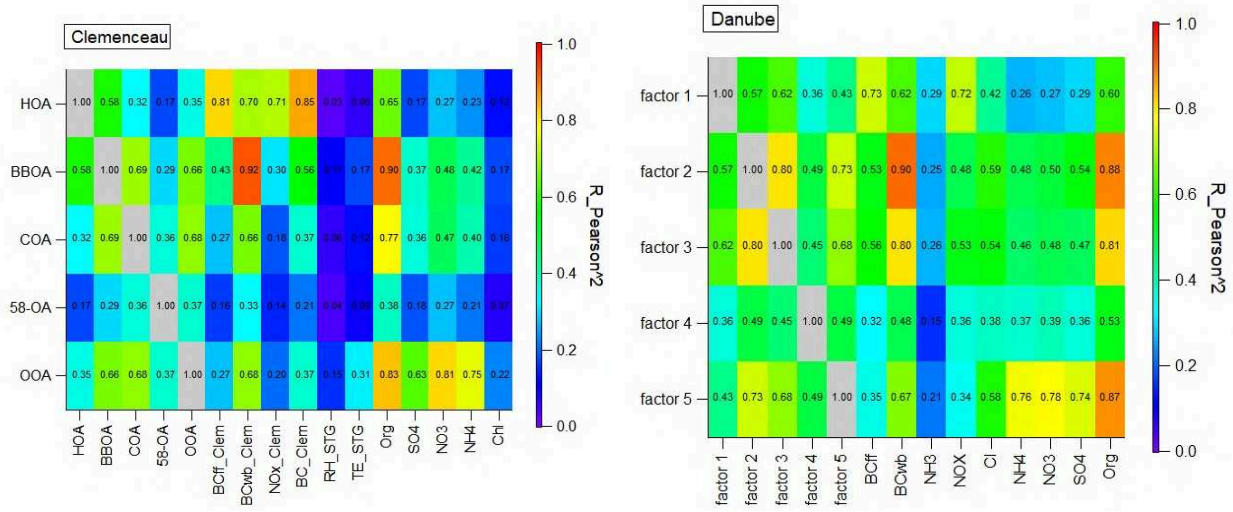

Figure S13: Correlations between OA factors and external variables for both Strasbourg sites

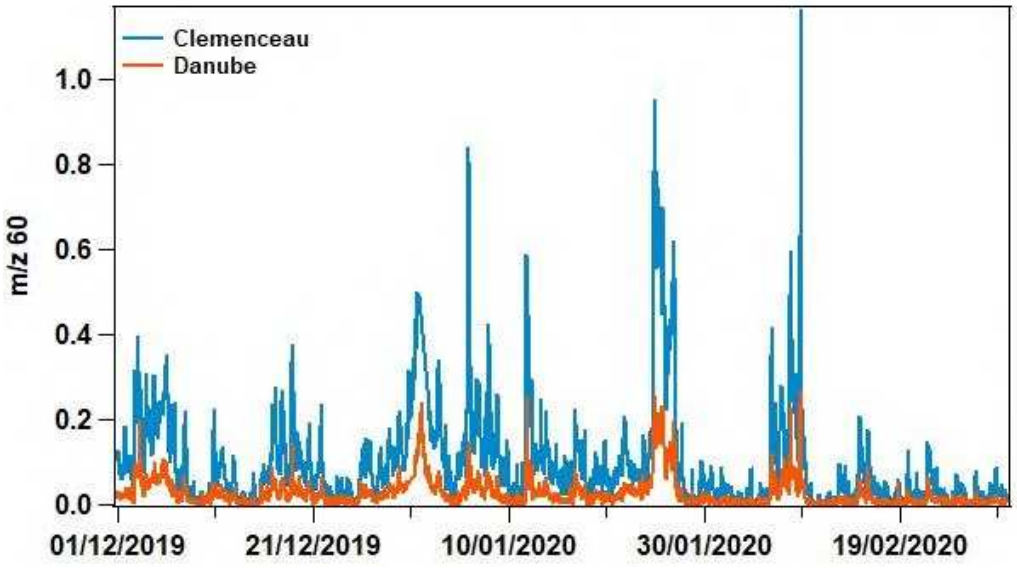

Figure S14: Time series of m/z 60 in Danube and Clemenceau sites.

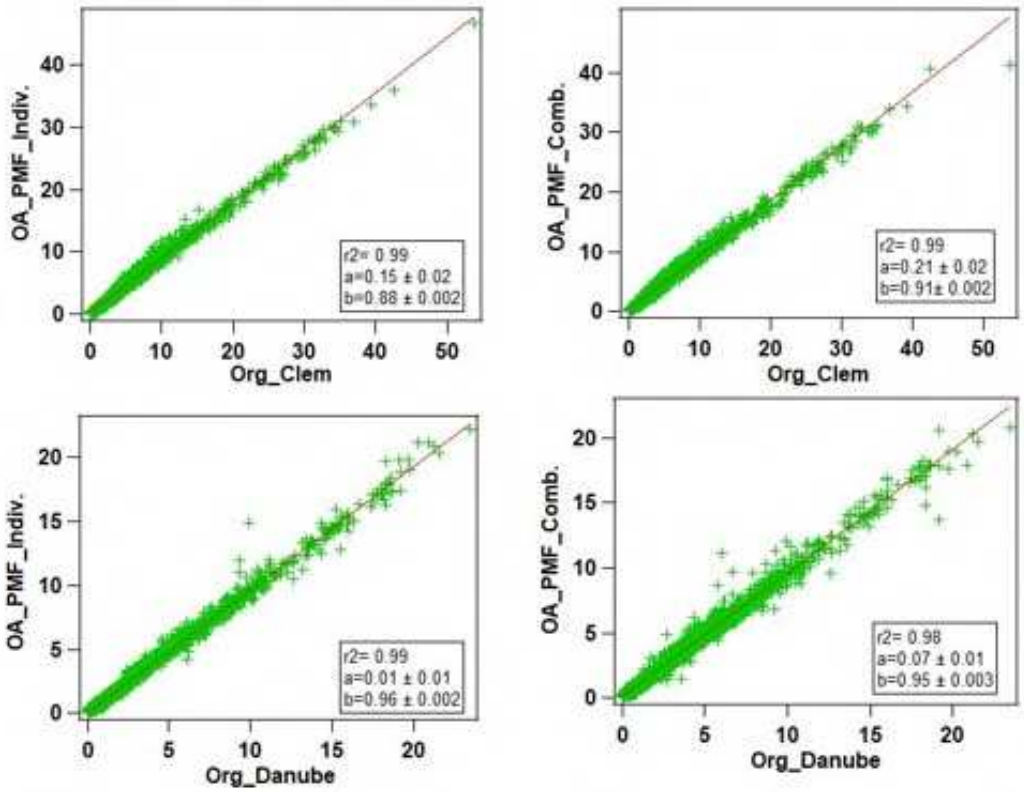

Figure S15: Scatterplots of OA (sum of different OA factors) resolved in both PMFs with the organics from ACSM at both sites.

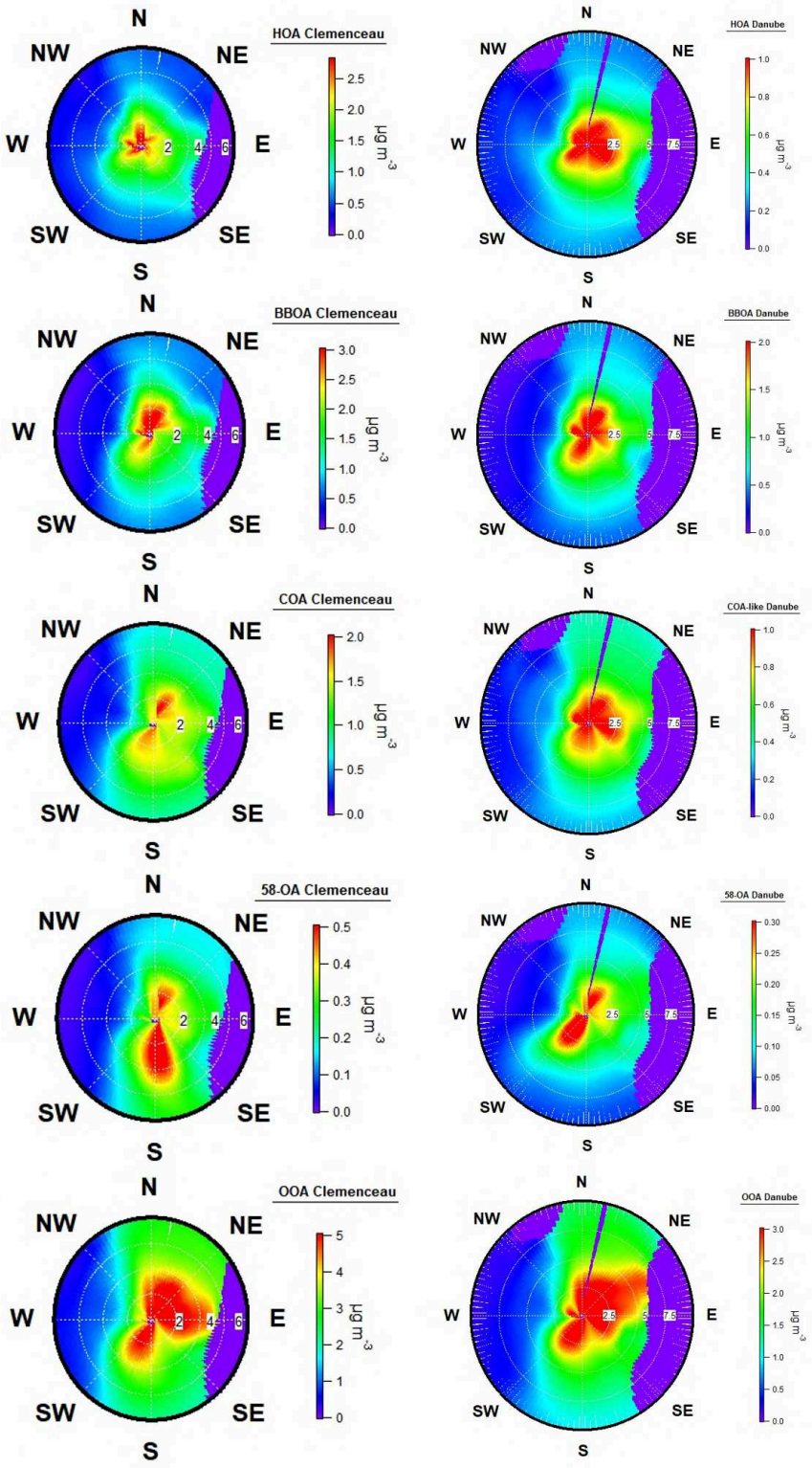

Figure S16: Pollution roses for OA factors, including HOA, BBOA, COA-like, 58-OA, and OOA at both sites: Clemenceau (left) and Danube (right).

Chapitre V. Étude pluriannuelle de la composition chimique des PM_1 et des sources d'aérosols organiques sur le site ATOLL dans le nord de la France

V.1. Résumé de l'article 3

Une limitation majeure de l'approche PMF classique est que les profils des sources AO sont statiques et donc leur variabilité temporelle potentielle n'est pas correctement modélisée. Les AO (primaires ou secondaires) présentent des tendances saisonnières distinctes qui doivent être prises en compte dans l'analyse PMF. Une nouvelle méthode mise en œuvre par Parworth et al. (2015) et affinée par Canonaco et al. (2021) a été utilisée pour tenir compte des changements temporels des facteurs sources. Cette méthode consiste à analyser l'ensemble du jeu de données en appliquant la PMF sur de courtes périodes (fenêtre PMF mobile), en s'appuyant sur des contraintes et des critères pertinents. De plus, cette méthode permet d'explorer l'ambiguïté rotationnelle et d'estimer les incertitudes des solutions PMF.

Cette méthode a été testée et validée au niveau européen dans le cadre de l'action COST COLOSSAL CA16109 (*Chemical On-Line cOmpoSition and Source Apportionment of fine aerosoL*; https://www.costcolossal.eu/objectives-and-content/) et présentée sous la forme de deux publications dont je suis co-auteure. La première publication (Chen et al., 2022a; voir annexe 4) vise à mieux comprendre les origines de l'AO en Europe, en utilisant l'ensemble des jeux de données de spectrométrie de masse AMS/ACSM recueillis sur 22 sites différents, en se concentrant sur une année de données, en particulier la période de 2016 à 2017 pour la plupart des sites. Cette étude a permis de créer un protocole harmonisé pour l'application de la PMF glissante. La deuxième publication (Via et al., 2022; voir annexe 5) est une étude comparative menée sur une sélection de ces 22 sites européens dont ATOLL, et qui a permis d'évaluer la pertinence de la PMF glissante pour les analyses à long terme en les comparant avec les résultats issus de l'application de la PMF classique (par saisons) pour ces mêmes jeux de données.

Cet article présente une première analyse multi-annuelle des mesures de composition chimique des particules initiées par le Centre Energie et Environnement de l'IMT Nord Europe depuis 2016 sur la plateforme ATOLL. Cette plateforme, localisée sur le toit du Département de

Physique sur le campus 'Cité Scientifique' de l'Université de Lille à Villeneuve d'Ascq, abrite depuis plusieurs décennies des mesures par télédétection des propriétés optiques et physiques des aérosols, menées par le Laboratoire d'Optique Atmosphérique (LOA).

L'objectif de cette analyse est de mieux caractériser les sources et les origines géographiques des particules fines dans le nord de la France, et d'étudier leur variabilité inter-annuelle. Après une brève description de la station et l'instrumentation, ainsi que la méthodologie suivie, l'article présente une analyse PMF saisonnière classique, réalisée sur la période d'octobre 2016 à août 2017, suivi d'une analyse PMF glissante en utilisant une fenêtre de 14 jours et un pas d'1 jour. Les résultats de ces deux types d'analyses ont été intégrés dans les deux publications européennes mentionnées ci-dessus, et ont permis d'identifier quatre facteurs à ATOLL, à savoir HOA lié au trafic routier, BBOA lié à la combustion de la biomasse, et deux facteurs OOA (LO-OOA et MO-OO).

Sur la base des résultats de l'analyse précédente conduite sur une année, la PMF glissante a été appliquée à l'ensemble des données présentées (d'octobre 2016 à décembre 2020). Les spectres de référence pour les facteurs primaires (HOA et BBOA), extraits de l'analyse saisonnière en hiver, ont été utilisés, mais avec des fenêtres de 28 jours et un pas de sept jours pour une meilleure efficacité de calcul. Le *bootstrap* a été effectué avec 50 itérations de PMF sur la fenêtre PMF, ce qui représente un total de 11 050 analyses PMF différentes pour cet ensemble de données. En utilisant des critères de sélection prédéfinis, basés sur les corrélations avec des variables externes, des critères de *monitoring* et de *sorting*, les meilleures solutions PMF ont été choisies, puis moyennées. La partie des résultats est divisée donc en trois axes : le premier porte sur la composition chimique des PM_1 observée sur la plateforme ATOLL entre fin 2016 et fin 2020, le deuxième traite des résultats PMF obtenus pour l'AO sur cette période, et le dernier concerne les origines géographiques en se basant sur une analyse des vents locaux et synoptiques (résultats du clustering basé sur l'étude des rétrotrajectoires).

L'analyse des mesures à long terme des particules à Lille a montré la prédominance de la matière organique avec une contribution de 46,5 %, suivie du NO_3 (28,9 %), du NH_4 (12,3 %), du SO_4 (8,6 %), du BC_{ff} (5,7 %) et du BC_{wb} (2,3 %). L'analyse PMF sur ce jeu de données pluriannuelles des aérosols organiques a permis d'identifier des sources primaires et secondaires d'AO. Parmi

elles, deux sont principalement associées aux processus de combustion, à savoir HOA (représentant 11,8 % de la masse totale AO) et BBOA, dont la proportion varie de 8,1 % à 18,5 %, atteignant son maximum pendant la saison hivernale en raison de l'augmentation du chauffage résidentiel. En parallèle, deux types d'AO secondaires oxygénées - LO-OOA (représentant 31,9 %) et MO-OOA (42,3 %) - ont été identifiés. Pendant l'hiver, 12 % de l'AO est associé au trafic et la moitié à la combustion résidentielle du bois (LO-OOA étant associé à BBOA en hiver). Pendant l'été, en plus des 10% d'AO liés au trafic, 34 % est lié aux sources biogéniques, le LO-OOA estival étant cette fois corrélé aux AOS biogéniques.

Cette analyse a révélé également une contribution importante des masses d'air continentales polluées provenant d'Europe centrale. En effet, le facteur MO-OOA est principalement lié aux masses d'air transportées sur de longues distances depuis les zones continentales. Les épisodes de pollution sont fortement influencés par des processus secondaires. En été, le facteur LO-OOA augmente avec l'augmentation des concentrations de PM_1, liée à une forte activité photochimique et à des épisodes de chaleur. En outre, le nitrate d'ammonium est également un composant de l'aérosol prédominant pendant les épisodes de pollution, associé à l'utilisation d'engrais et aux émissions dues à la circulation. En effet, pendant les saisons froides (hiver, printemps et automne) le nitrate d'ammonium, associé aux aérosols organiques oxydés (LO-OOA et MO-OOA), constitue un composant clé de la pollution particulaire.

L'analyse des vents et des rétrotrajectoires de masses d'air a montré que la pollution locale, en particulier celle provenant de la ville de Lille, avait un impact relativement faible sur le site d'échantillonnage par rapport à l'impact régional plus significatif.

Dans l'ensemble, cette étude a permis d'élucider les principales sources d'aérosols fins sur la plateforme ATOLL à Lille, en décrivant les interactions complexes entre le trafic régional, le chauffage au bois, les activités agricoles, les émissions biogéniques et le transport à longue distance dans cette région fortement urbanisée du nord-ouest de l'Europe.

V.2. Article 3

Investigation of four-year chemical composition and organic aerosol sources of submicron particles at the ATOLL site in Northern France

Hasna Chebaicheb[1,2,3], Joel F. de Brito[1*], Gang Chen[4,5], Emmanuel Tison[1], Caroline Marchand[2,3], André S. H. Prévôt[4], Olivier Favez[2,3], Véronique Riffault[1,3]

[1]IMT Nord Europe, Institut Mines-Télécom, Université de Lille, Centre for Energy and Environment, 59000 Lille, France
[2]Institut national de l'environnement industriel et des risques (INERIS), 60550 Verneuil-en-Halatte, France
[3]Laboratoire Central de surveillance de la Qualité de l'Air (LCSQA), F-60550 Verneuil-en-Halatte, France
[4]Laboratory of Atmospheric Chemistry, Paul Scherrer Institute, 5232 Villigen, Switzerland
[5]MRC Centre for Environment and Health, Environmental Research Group, Imperial College London, London, W120BZ, UK

Correspondence to: joel.brito@imt-nord-europe.fr

Published in Environmental Pollution on May 10th, 2023

Environmental Pollution 330 (2023) 121805

Contents lists available at ScienceDirect

Environmental Pollution

journal homepage: www.elsevier.com/locate/envpol

Investigation of four-year chemical composition and organic aerosol sources of submicron particles at the ATOLL site in northern France☆

Hasna Chebaicheb [a,b,c], Joel F. de Brito [a,*], Gang Chen [d,e], Emmanuel Tison [a], Caroline Marchand [b,c], André S.H. Prévôt [d], Olivier Favez [b,c], Véronique Riffault [a,c]

[a] IMT Nord Europe, Institut Mines-Télécom, Université de Lille, Centre for Energy and Environment, 59000, Lille, France
[b] Institut National de l'environnement Industriel et des Risques (INERIS), 60550, Verneuil-en-Halatte, France
[c] Laboratoire Central de Surveillance de la Qualité de l'Air (LCSQA), 60550, Verneuil-en-Halatte, France
[d] Laboratory of Atmospheric Chemistry, Paul Scherrer Institute, 5232, Villigen, Switzerland
[e] MRC Centre for Environment and Health, Environmental Research Group, Imperial College London, London, W120BZ, UK

ARTICLE INFO

Keywords:
Air quality
Urban pollution
Source apportionment
Rolling PMF
Particulate matter
ATOLL platform

ABSTRACT

This study presents the first long-term online measurements of submicron (PM_1) particles at the ATOLL (ATmospheric Observations in liLLe) platform, in northern France. The ongoing measurements using an Aerosol Chemical Speciation Monitor (ACSM) started at the end of 2016 and the analysis presented here spans through December 2020. At this site, the mean PM_1 concentration is 10.6 μg m^{-3}, dominated by organic aerosols (OA, 42.3%) and followed by nitrate (28.9%), ammonium (12.3%), sulfate (8.6%), and black carbon (BC, 8.0%). Large seasonal variations of PM_1 concentrations are observed, with high concentrations during cold seasons, associated with pollution episodes (e.g. over 100 μg m^{-3} in January 2017). To study OA origins over this multiannual dataset we performed source apportionment analysis using rolling positive matrix factorization (PMF), yielding two primary OA factors, a traffic-related hydrocarbon-like OA (HOA) and biomass-burning OA (BBOA), and two oxygenated OA (OOA) factors. HOA showed a homogeneous contribution to OA throughout the seasons (11.8%), while BBOA varied from 8.1% (summer) to 18.5% (winter), the latter associated with residential wood combustion. The OOA factors were distinguished between their less and more oxidized fractions (LO-OOA and MO-OOA, on average contributing 32% and 42%, respectively). During winter, LO-OOA is identified as aged biomass burning, so at least half of OA is associated with wood combustion during this season. Furthermore, ammonium nitrate is also a predominant aerosol component during cold-weather pollution episodes – associated with fertilizer usage and traffic emissions. This study provides a comprehensive analysis of submicron aerosol sources at the recently established ATOLL site in northern France from multiannual observations, depicting a complex interaction between anthropogenic and natural sources, leading to different mechanisms of air quality degradation in the region across different seasons.

1. Introduction

Air pollution remains a major environmental risk to humans, with fine particles $PM_{2.5}$ (Particulate matter with an aerodynamic diameter smaller than 2.5 μm) leading to cardiovascular and respiratory diseases and premature mortality (Kelly and Fussell, 2015). In Europe, more than 307 000 premature deaths have been attributed to fine particle exposure (Air quality in Europe, 2021). The north of France, in particular, is affected by relatively high PM concentrations, frequently exceeding the annual $PM_{2.5}$ concentration of 5 μg m^{-3} recommended by the WHO (WHO Air Quality Guidelines, 2021). The Hauts-de-France region is the 2nd most densely populated area in France with 6 million inhabitants. It is affected by intense traffic, residential, industrial, and agricultural emissions combined with transboundary pollution from nearby countries such as the United Kingdom, Belgium, the Netherlands, and Germany, making it an air pollution hotspot (Roig Rodelas et al., 2019; Thunis et al., 2021; Potier et al., 2019; Waked et al., 2014, 2018). While tighter emission controls are expected to decrease PM concentrations (e.

☆ This paper has been recommended for acceptance by Admir Créso Targino.
* Corresponding author.
E-mail address: joel.brito@imt-nord-europe.fr (J. F. de Brito).

https://doi.org/10.1016/j.envpol.2023.121805
Received 24 February 2023; Received in revised form 8 May 2023; Accepted 9 May 2023
Available online 10 May 2023

g., ban of new combustion engine vehicles by 2035 throughout the EU), quantifying the efficiency of mitigation strategies requires an in-depth understanding of current sources. This is particularly relevant when focusing on the finer aerosol fraction such as submicron particles (PM_1), which can be strongly affected by secondary formation (Pandis et al., 2016). Most notably, organic aerosols (OA), formed from a complex pool of compounds, are one of the dominant submicron aerosol species in Central Europe (Chen et al., 2022). For instance, in northern France, the OA and nitrates have been shown to dominate the non-refractory PM_1 (NR-PM_1) at background sites, whereas sulfate and nitrate were the most dominant species in summer at the industrial and coastal sites (Crenn et al., 2017, Zhang et al., 2021). Sulfate was also observed to be a major species during summertime in Marseille, in the south of France, attributed to the influence of local industrial activities and shipping (Chazeau et al., 2021).

The study of OA sources in recent years has largely been conducted using Positive Matrix Factorization (PMF, Paatero and Tapper, 1994) on Aerosol Mass Spectrometers (Allan et al., 2003), or its compact version, termed Aerosol Chemical Speciation Monitor (ACSM, Ng et al., 2011b). The PMF analysis of those observations has drastically improved our knowledge of key sources of OA in Europe over the past two decades (e.g. Crippa et al., 2014). Recently, Roig Rodelas et al. (2019) investigated the OA sources during a five-week wintertime field campaign in Douai, 30 km south of Lille, highlighting the significant contribution of oxygenated organic aerosols to the site, and the impact of air masses coming from Eastern Europe. Similarly, at an urban background site in Barcelona (Spain), both Oxygenated OA (OOA) fractions dominate the OA total mass over the two one-year study periods (Via et al., 2021), increased by air masses coming from inland Europe and the Mediterranean, especially the more oxidized OOA.

Whereas the PMF analysis applied on multiannual ACSM datasets hitherto yielded important results, notably allowing the identification of primary versus secondary OA (POA and SOA, respectively) sources across multiple seasons, the inherent limitation of fixed factors on traditional PMF method forces longer datasets to be split, typically into three months sub-sets (e.g. Canonaco et al., 2015; Zhang et al., 2019). This method has the drawback of requiring multiple independent PMF analyses, being labor-intensive, and prone to discrepancies between individual runs. Recently a rolling PMF method has been developed (Canonaco et al., 2021; Parworth et al., 2015; Chen et al., 2022), allowing the study of long-term datasets in a single iteration via a sliding time window, thus enabling inter and intra-seasonal variations of OA source profiles. The recently developed method has already been applied at several sites across Europe, although limited to one-year datasets (Atabakhsh et al., 2023; Canonaco et al., 2021; Chazeau et al., 2021; Chen et al., 2021; Tobler et al., 2021; Zografou et al., 2022).

In this context, we have studied PM_1 composition and OA sources since 2016 at a suburban site in Lille, known as the ATOLL (ATmospheric Observations in liLLe) platform. Recent studies at this site have shown a dominating effect of ammonium nitrate and organics on the aerosol optical properties (Velazquez-Garcia et al., 2023), as well as intense gas-to-particle conversion during spring and summer (Crumeyrolle et al., 2023). Thus, the objectives of this study are i) to apply for the first time the rolling PMF method on a multiannual dataset of organic aerosol at this site, and ii) to better understand PM_1 sources at the ATOLL platform. The results aim at better understanding aerosol sources via long-term analysis and quantify their contribution in the North-Western European region, therefore supporting the development of effective emission reduction strategies.

2. Methodology

2.1. Site description

The ATOLL platform (70 m a.s.l; 50.61° N; 3.14° E) is considered a suburban site, located on the rooftop of the University of Lille building in Villeneuve d'Ascq, within the Lille metropolitan area, one of the most densely populated areas in France. ATOLL is located roughly 4 km southeast of downtown Lille (Fig. S1). Furthermore, the region is located at the crossroads of transnational pollution transport including Belgium, Germany, the Netherlands, and the UK. This platform contributes to the French CARA program (Favez et al., 2021) and is a French National Facility of the European Aerosols, Clouds and Trace gases Research InfraStructure (ACTRIS), following the corresponding inlet setup and instrumentation deployment guidelines (https://www.actris-ecac.eu/measurement-guidelines.html). The period considered in this study lasts from October 2016 to December 2020 with some data gaps mostly due to instrument maintenance, calibrations, and temporary relocation for intensive field campaigns.

2.2. Instrumentation

The Quadrupole ACSM (Q-ACSM, Aerodyne Research Inc., USA) is based on aerosol mass spectrometery technology where ambient particles are sampled and the submicron fraction is focused by an aerodynamic lens onto a vaporizer heated at 600 °C after being pumped through a vacuum chamber. The vaporized compounds are ionized and fragmented by electron ionization at 70 eV, then detected with a quadrupole mass spectrometer (measurement range 0–200 amus). The analysis of the fragments allows reconstruction of their chemical composition, notably OA, sulfate (SO_4), nitrate (NO_3), ammonium (NH_4), and chloride (Cl) with a time resolution of 30 min and detection limits ranging from 0.01 to 0.28 μg m^{-3} for the different species (Ng et al., 2011a). The Cl contribution was negligible and is not addressed here.

The Q-ACSM sampling line (OD = 9.5 mm; ID = 6.5 mm; 2.3-m-long stainless tube; flow: 3 L min^{-1}) is equipped with a $PM_{2.5}$ cyclone (URG-2000-30EQ, URG Corp., USA) and a Nafion dryer to maintain relative humidity at the instrument entrance below 40%, which reduces artifacts from bouncing effects. ACSM chemical calibration is performed by injecting size-selected (typically 300 nm) ammonium nitrate and ammonium sulfate particles. This procedure allows for determining the response factor (RF) of NO_3 and the relative ionization efficiencies (RIE) of NH_4 and SO_4. The RF and RIE calibrations (summarized in Table S2) are stable and typically applied yearly Table S2. To obtain quantitative mass concentrations for ACSM species, a composition-dependent collection efficiency (CDCE) is applied to account for the incomplete detection of aerosol species (Middlebrook et al., 2012) (Fig. S3).

Ancillary measurements for this analysis include a 7-wavelength Aethalometer (AE33, Magee Scientific, USA). This instrument measures the optical attenuation and converts it into aerosol light absorption for each wavelength with a time resolution of 1 min (Drinovec et al., 2015). Ambient black carbon (BC) equivalent concentrations are derived at 880 nm, using the manufacturer's mass absorption efficiency (MAE) at this wavelength (7.77 m^2 g^{-1}), following ACTRIS guidelines. The AE33 sampling line (OD = 9.5 mm; ID = 6.5 mm; 2.6-m-long stainless tube and 1.85 m static dissipative tubing; flow: 5 L min^{-1}) is equipped with a PM_1 cyclone (BGI SCC1.197, Mesa Labs, USA). A Nafion dryer was installed in summer 2020 just before the dissipative tubing.

Meteorological variables (temperature, relative humidity, wind speed and direction) were collected from a weather station (Vantage Pro, DAVIS Inc, USA) collocated with the instruments. Temperature and relative humidity were measured every minute, while the wind direction and speed were obtained using an anemometer with a time stamp of 5 min. $PM_{2.5}$ measurements and nitrogen oxides ($NO + NO_2 = NO_x$) data were obtained from the air quality monitoring network ATMO HdF (at the Lille Fives station, 4.5 km from our site).

2.3. Wind analysis and back-trajectories for cluster calculations

Pollution roses and the diel plots by wind sectors are plotted considering the median concentrations using MATLAB. A wind speed

threshold above 0.3 m s^{-1} was imposed for these plots and analyzed over 22.5° wind sectors. We used the back-trajectories within the NOAA Hybrid Single Particle Lagrangian Integrated Trajectory (HYSPLIT; Draxler, 1999) model using 1° × 1° resolution Global Data Assimilation System (GDAS) files. The back-trajectories were ending at ATOLL from 2016 to 2019 for an arrival altitude of half the planetary boundary layer height at 1-h intervals, 72 h back in time. 4750 back-trajectories were clustered every 6 h using the HYSPLIT model. The method used for clustering analysis is based on the relative variation of the total spatial variance (TSV). The spatial variance is calculated as the sum of the squared distances between the endpoints of the trajectories and the mean of the trajectories in that cluster. The process continues until the last two clusters are combined, and the final number of clusters is determined by identifying the point where the total spatial variance increases rapidly.

2.4. Black Carbon source apportionment

The Aethalometer data are used to further separate BC into fossil fuel (BC_{ff}) and wood burning (BC_{wb}) as proposed by Sandradewi et al. (2008). The method is based on the assumption that wood combustion shows a pronounced absorption in the UV (i.e. high Absorption Angstrom Exponent, AAE) compared to fossil fuel (low AAE). At the ATOLL platform, BC_{ff} and BC_{wb} were separated using the AE33 manufacturer values of $AAE_{ff} = 1$ and $AEE_{wb} = 2$, using the absorption at 470 and 950 nm (Drinovec et al., 2015).

2.5. Source apportionment: the rolling PMF method

The PMF method assumes that concentrations measured at a receptor site can be explained as the linear product of a source matrix (F) and a contributing matrix (G), plus a residual matrix (E) that represents the non-modeled data, as in Eq. (1):

$$X = F.G + E, \tag{1}$$

The two matrices F and G are obtained by an interactive square minimization algorithm that iteratively minimizes the quantity Q which represents the total sum of the squares of the residuals of the model e_{ij} weighted by the measurement uncertainty σ_{ij} for all points ij.

$$Q = \sum_{i=1}^{n} \sum_{j=1}^{m} \left(\frac{e_{ij}}{\sigma_{ij}}\right)^2, \tag{2}$$

The application of PMF is subject to rotational ambiguity in which different combinations of G and F produce similar Q-values, some of which may contain mixed factors and/or unreasonable environmental descriptions of the data. If a priori source chemical information is known, the a-value approach allows overcoming this issue by constraining the expected factor profiles or time series using ME-2 according to Eq. (3) and Eq. (4):

$$f_{solution} = f_{reference}\ (1 \pm a), \tag{3}$$

$$g_{solution} = g_{reference}\ (1 \pm a), \tag{4}$$

This implies that an a-value of 0.1 allows each variable of a mass spectrum to vary by ±10% compared to the reference spectrum. Furthermore, to identify stable PMF solutions and estimate the statistical uncertainty of the analysis, the bootstrap technique is used. It allows a resampling of the original data, i.e. making sub-samples and checking that with these samples we can reach the same solutions and the same contributions of the factors as previously identified (Efron, 1979).

To perform a multi-annual analysis, standard PMF is first performed by seasons in a reference year to (i) determine the number of expected factors throughout the database and (ii) retrieve reference spectra. Afterward, a rolling PMF is applied combining spectra constraints on the primary factors and bootstrapping. The rolling method consists of breaking down the database into shorter periods (e.g. one-month windows, shifting by seven days), having the advantage of allowing some variability in the factor profiles throughout the observation period, across seasons and years.

The standard PMF analysis was performed on the reference year from October 2016 to August 2017, broken down by seasons (Autumn - September, October, November, SON; Winter - December, January, February, DJF; Spring - March, April, May, MAM; and Summer - June, July, August, JJA). This analysis allowed identifying four factors at ATOLL, namely HOA (Hydrocarbon-like OA) related to road traffic, BBOA (Biomass Burning OA) related to biomass combustion, and two OOA factors, including a Less-Oxidized OOA (LO-OOA) and a More-Oxidized one (MO-OOA). At the end of this standard analysis, the primary factor profiles, HOA and BBOA, were extracted from the winter bootstrap PMF solution to be used as a priori information for the rolling PMF analysis (further details are given in the SI, section S2). An initial one-year (2016–2017) rolling PMF analysis has been performed using a 14-day window and one-day step, which was integrated in a multi-site rolling PMF study (Chen et al., 2022), with a suggested criteria list and standardized protocol for this method.

Based on the results of the one-year analysis, rolling PMF was then conducted for the full dataset (October 2016 through December 2020) presented here, using the same reference spectra for the primary factors (HOA and BBOA), however with 28-day windows and seven-day shifting for increased computational efficiency. Section S3 of the SI shows comparable results of the rolling PMF time windows (14-day, shifting by one day vs. 28-day shifting by seven days). Bootstrap was performed with 50 PMF iterations of the rolling window, representing a total of 11 050 different PMF analyses for this four-year dataset. Using the selection criteria defined in Section S3, the best PMF solutions were chosen and then averaged. Rolling PMF was conducted using SoFi Pro software V8.0.6.0 (Source Finder Professional, Datalystica Ltd., Switzerland) with the ME-2 solver in the Igor Pro software environment (Igor Pro version 8.04, Wave Metrics, Inc., USA).

3. Results and discussion

3.1. Temporal variations of PM

Fig. 1 shows the monthly and overall averaged composition of PM_1 species at the ATOLL site for the observation period. The mean concentration of PM_1 for the period is 10.6 μg m^{-3}, with species seasonal concentrations depicted in Table S1. OA is the most abundant component with 41.8% of the total, followed by NO_3, NH_4, SO_4, BC_{ff}, and BC_{wb}, contributing 28.9%, 12.3%, 8.6%, 5.7%, and 2.3%, respectively. The contribution of OA to PM_1 falls within the range of other European urban sites (between 21 and 75%, Chen et al., 2022). The second most abundant species, NO_3, is also significant in PM_1 at other sites in Central Europe such as London, Paris, and at the Cabauw site in the Netherlands (Chen et al., 2022; Zhang et al., 2019; Schlag et al., 2016). Furthermore, Bressi et al. (2021) showed a higher contribution of NO_3 and a lower contribution of SO_4 for regional background sites in Central Europe compared to sites in Northern or Southern Europe.

Monthly mean PM_1 ranges from 3.5 to 20.6 μg m^{-3}, with higher values in winter, with hourly data showing peaks exceeding 80 μg m^{-3}, associated with either organics or inorganic species (Fig. S2). OA, the most abundant component of PM_1, has monthly mean values ranging from 1 to 8 μg m^{-3}, exhibiting higher concentrations in the cold months. NO_3, however, has a specific variability, displaying higher means in spring, associated with heightened ammonia (NH_3) from agricultural activities, and NOx from traffic coupled with favorable photochemical and low-temperature conditions for ammonium nitrate (AN; NH_4NO_3) formation (Bressi et al., 2021; Hendriks et al., 2016). Conversely, SO_4 and BC are fairly consistent, with monthly concentrations around 2 and 3 μg m^{-3}. To deconvolve the sources and processes influencing aerosol composition at the ATOLL site, multiannual rolling PMF was conducted

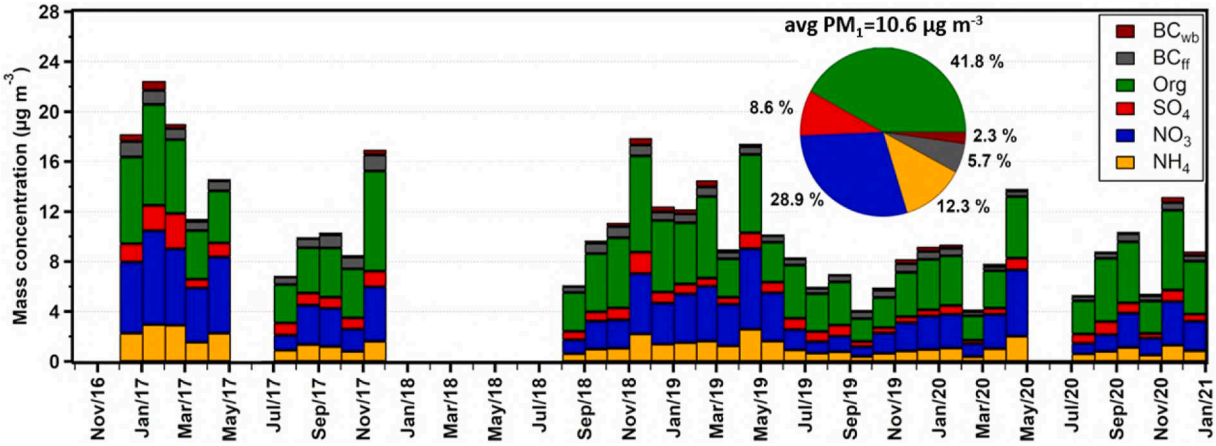

Fig. 1. Monthly means of PM_1 species at the ATOLL site.

on the OA spectra and is presented in the next section. The daily variation of inorganics and OA factors is presented in section 3.3.1.

3.2. Rolling PMF analysis: OA source apportionment

The mean OA factor profiles are presented in Fig. 2. The grey bars indicate the variability of each *m/z* of a factor compared to the reference factors described in section 2.5. The two primary factors HOA and BBOA are constrained with a mean a-value of 0.199 and 0.2, respectively, whereas oxygenated factors were left unconstrained, and were sorted during the analysis via the contribution of the m/z 44 fragment (CO_2^+). Typically, the HOA profile presents characteristic peaks at m/z 43, m/z 57 but also at m/z 41 and m/z 55, corresponding to alkyl and alkenyl fragments. The BBOA profile is characterized by a high contribution of the ions m/z 60 and m/z 73, tracers of biomass-burning combustion. MO-OOA is more oxidized than LO-OOA and presents a strong peak at m/z 44, whereas LO-OOA showed high variability in m/z 43 and 44 and also exhibits the influence of other ions i.e. m/z 29, 55, which is consistent with the mass spectra of other studies (Chen et al., 2021; Tobler et al., 2021; Zhang et al., 2019).

The monthly means of the PMF factors are shown in Fig. 3. The LO-OOA and MO-OOA factors are dominating with 31.9% and 42.3% of OA, respectively, followed by BBOA (14.0%) and HOA (11.8%). As expected, there is a clear seasonality for BBOA with higher concentrations during the cold months, associated with the use of wood for residential heating. Unlike BBOA, HOA is less variable throughout the whole period but with sporadic peaks (Fig. S7) that tend to be associated with BC_{ff}. The HOA factor and BC_{ff} present a correlation across different seasons of $r^2 = 0.48$ (Fig. S9). Indeed, the HOA factor varies from 9.8 % to 12.1% (Fig. S8), consistent with values obtained at other urban European sites (from 7.4% to 12.7%), whereas BBOA in wintertime reaches 18.5%, also comparable to other European sites for the season (8.5%–25.3%) as described in Chen et al. (2022). The MO-OOA factor shows generally a fairly good correlation with secondary inorganic aerosols (NO_3, SO_4, NH_4) across all seasons, and focusing on wintertime only (Figs. S9 and S10, respectively), being likely driven by meteorological conditions and long-range transport, without a clear source identification here.

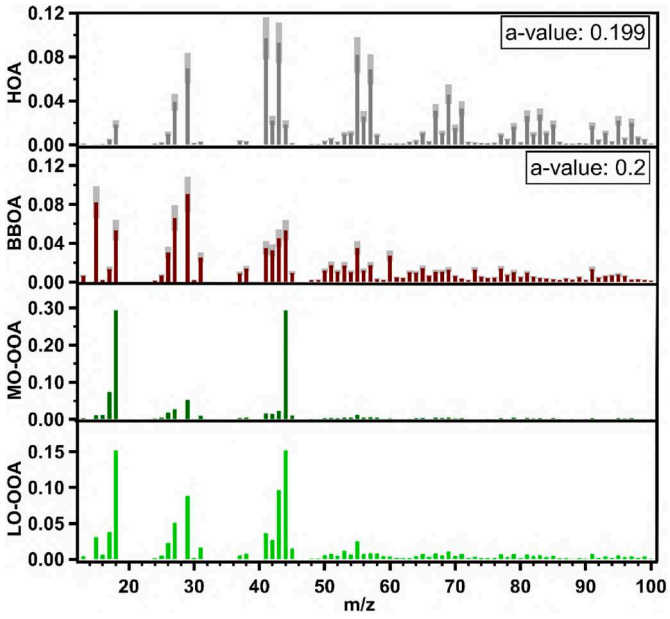

Fig. 2. Mass spectra of OA factors retrieved in the rolling PMF at the ATOLL site.

The LO-OOA factor could be related to different sources during the cold and warm seasons. During wintertime, LO-OOA is associated with aged BBOA, based on the correlation of LO-OOA with BC_{wb} ($r^2 = 0.60$), and BBOA ($r^2 = 0.63$), both shown in Fig. S10, as well as the presence in this factor of m/z 60 in wintertime compared to summertime (Fig. S11). Therefore, at the ATOLL site, the LO-OOA factor is associated with aged residential heating in wintertime, recently identified as a key source of oxidative potential in fine aerosol in Europe, and thus a potential source of deleterious health effects (Daellenbach et al., 2020). Furthermore, BBOA and LO-OOA in wintertime reach a mean contribution of wood combustion (fresh and aged) to OA of 50.4%. In summertime, LO-OOA also contributes to OA (34.0%; Fig. S8) and exhibits an increased m/z 43 and a decreased m/z 44 during warmer months (Fig. S11). Thus it tends to be associated with biogenic SOA following the analysis from Chen et al. (2022) and also depicting a clear trend of increasing LO-OOA with increasing afternoon temperatures in summertime (Fig. S12) (Zhang et al., 2019). Furthermore, summertime spectra of MO-OOA and LO-OOA have been further explored following the *f82* (i.e., m/z 82 ($C_5H_6O^+$)/OA) vs. *f44* plot as proposed by Hu et al. (2015), to verify the potential impact of isoprene epoxydiols (IEPOX) derived SOA. Whereas MO-OOA does not present any IEPOX-SOA signature, with very low *f82* concentrations (3‰), summertime LO-OOA depicts a trend of increasing *f82* with decreasing *f44* (Fig. S13), suggesting a potential role of IEPOX-SOA at this site. Nonetheless, the values of *f82* here for LO-OOA (<8‰) are below those of IEPOX-SOA dominated factors (10–40‰) proposed by Hu et al. (2015). New Particle Formation (NPF) events have additionally been frequently observed at ATOLL by Crumeyrolle et al. (2023) in spring and summer, also supporting strong gas-to-particle conversion in this period. Nevertheless, other processes (non-IEPOX isoprene SOA, monoterpene SOA, aromatics, etc.) could also be relevant for the LO-OOA factor during summertime, but cannot be determined

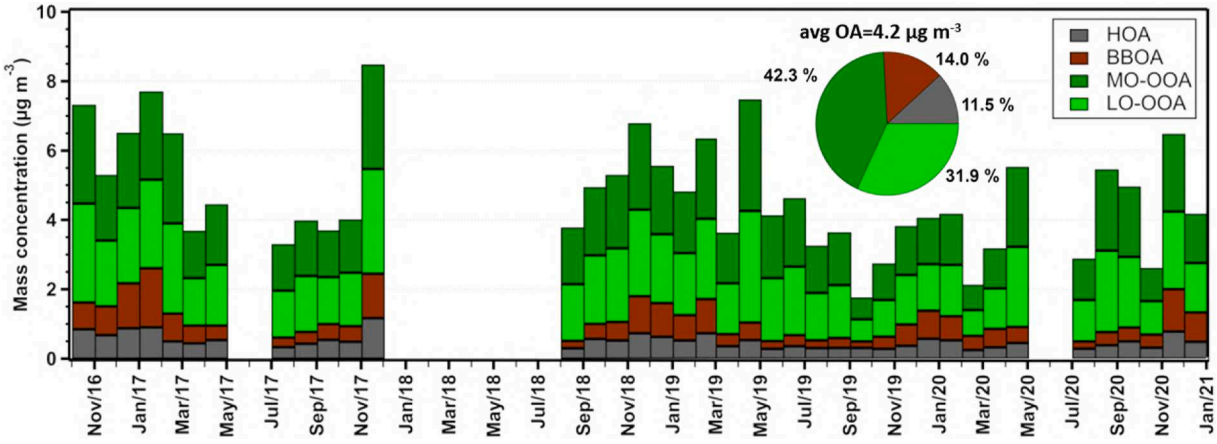

Fig. 3. Monthly averaged OA factor loadings and relative contributions to the total OA at ATOLL.

here.

Fig. 4 presents the mass fraction of aerosol species and OA factors as a function of total PM_1 for different seasons. The black circles show the PM_1 concentrations for each percentile (10–100%). In winter, the 10% highest PM_1 level nearly reaches 30 µg m^{-3}, in contrast with summer (15 µg m^{-3}), and spring and autumn with intermediate values. For winter, spring, and autumn, PM_1 values above the 30th percentile (roughly 5 µg m^{-3}) show an increasing dominance of NO_3 with PM_1 and fairly stable contributions of SO_4 and OA, albeit with a larger fraction being OOA factors. Therefore, as presented previously, NO_3 also plays a major role during pollution events for these colder periods, in agreement with observations at other Central European sites (Bressi et al., 2021; Petit et al., 2015). In summer PM_1 loadings are typically half of those observed in winter, and the composition during pollution episodes depict a different trend compared to other seasons. The SO_4 relative contribution decreases with increasing PM_1, thus not being significant during pollution events. Those, however, are driven by an increasing contribution of OOA fractions, and to a lesser extent, of NO_3. As discussed previously, summertime LO-OOA is particularly associated with biogenic SOA, a potential mechanism for pollution events during that season. It is interesting to note that BC_{ff} has a high contribution under the clean periods, potentially associated with northerly air masses impacted by shipping emissions from the Channel and the North Sea, which is further discussed in subsequent sections.

3.3. Geographic origins of aerosol species

3.3.1. Diel plots according to wind sectors

Diel profiles of aerosol concentrations according to the wind sectors for winter and summer, with contrasting meteorological conditions and aerosol sources, are presented in Figs. 5 and 6, whereas spring and autumn ones can be found in the SI, Figs. S15 and S16. Interestingly, most species present the highest concentrations when ATOLL is influenced by S, SE, E, and NE wind sectors for both seasons, but not when under the influence of the Lille city center (NW–N). It is important to note that wind sectors leading to maximum concentrations such as SE-

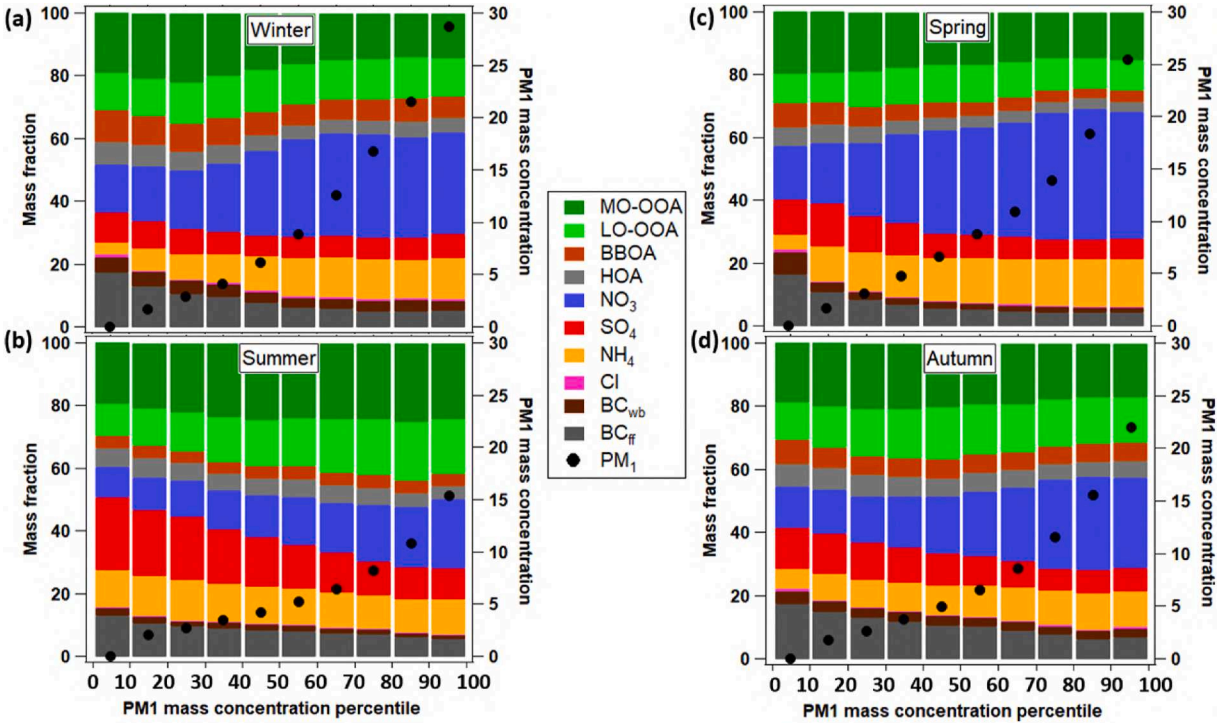

Fig. 4. Seasonal mass fraction of PM_1 species as a function of total PM_1 mass concentration, in a) winter, b) summer, c) spring, and d) autumn.

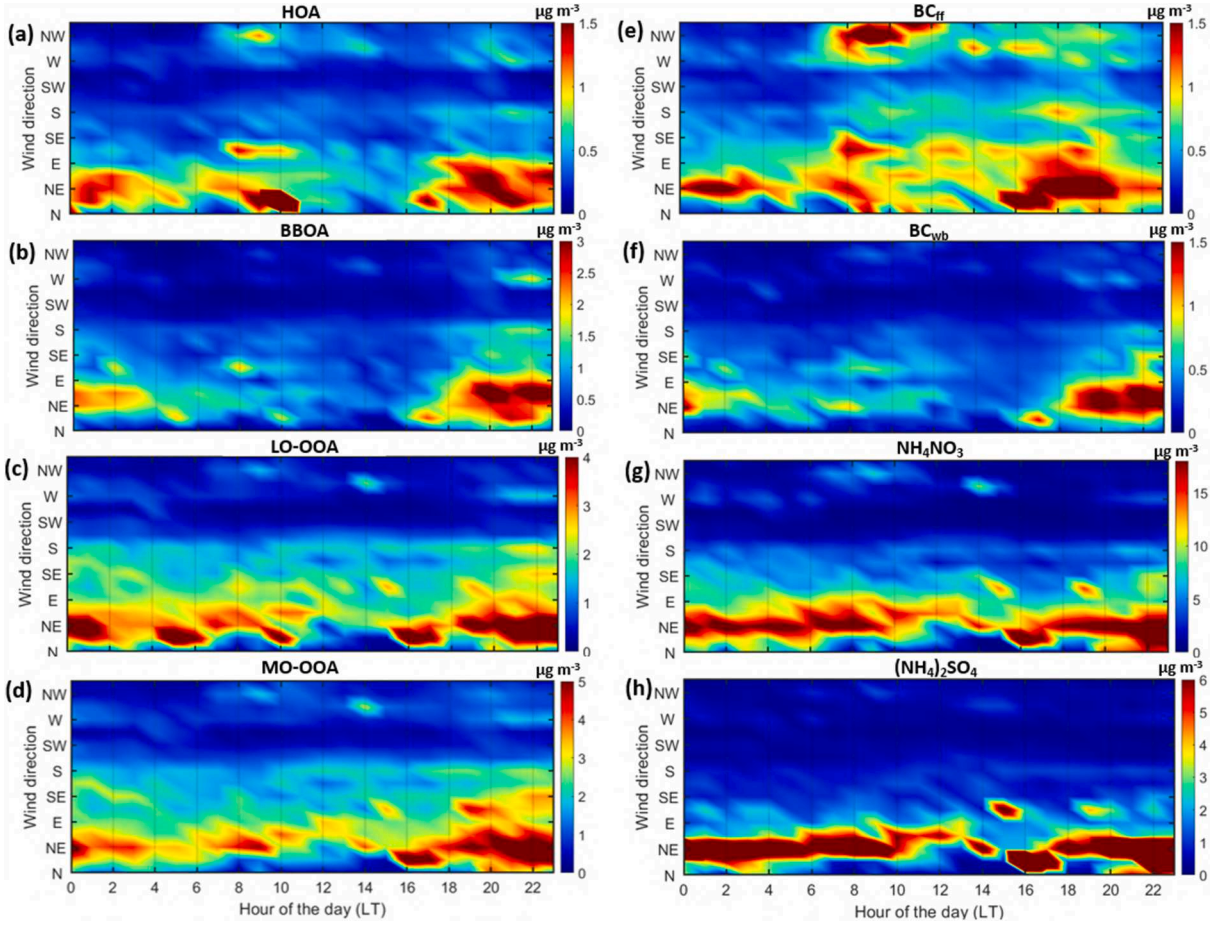

Fig. 5. Diel plots according to wind sectors during the wintertime for a) HOA, b) BBOA, c) LO-OOA, d) MO-OOA, e) BCff, f) BCwb, g) NH4NO3, and h) (NH4)2SO4. The Lille city center is located NW of the ATOLL site. The max value of the color scale represents the 90th percentile. (For interpretation of the references to color in this figure legend, the reader is referred to the Web version of this article.)

NE are prone to reduced wind speeds and pollution build-up conditions (Figs. S14 and S17). In winter, BC_{ff} is the only species that depict a comparable level across all directions, as the sampling site is surrounded by several major roads and highways, thus following fairly well-defined morning and evening rush hour peaks. The diel profile of HOA is generally similar to BC_{ff}, and BC_{wb} with BBOA, due to increased residential heating in the evening, mostly associated with the NE direction (Fig. 5). Considering all wind sectors, the rush hour peaks of HOA across seasons are identifiable, as well as the nighttime peak of BBOA during the colder months (Fig. S20), and the influence of stagnant conditions on the build-up of those primary components (Fig. S18). Both OOA factors follow comparable diel variability and show a similar cycle, with increased, and fairly constant loadings over the NE direction. For MO-OOA, the concentrations increase in the evening, suggesting an effect of the shallower boundary layer height which favors the accumulation of pollutants, in addition to its global regional feature. Furthermore, LO-OOA, follows roughly peak periods of BBOA and BC_{wb} in cold seasons, supporting the influence of biomass burning on this factor. The secondary inorganics, ammonium nitrate and ammonium sulfate, show small diel variability and strong enhancement in the NE sector, indicating a regional origin.

In summer, the diel profiles of HOA and BC_{ff} are less pronounced during the day than during wintertime, being related to the higher boundary layer variability under stronger temperature variations. Wood combustion-related aerosols, BBOA and BC_{wb}, present significantly lower concentrations than in winter, as expected, without a clear trend during the day. The MO-OOA factor depicts an increasing trend during the daytime, whereas LO-OOA has a fairly flat diel profile. Ammonium nitrate shows higher concentrations overnight till around 09:00 mostly from NW, N, and NE directions, followed by a strong decrease, likely caused by volatilization due to higher ambient air temperatures. Conversely, ammonium sulfate exhibits an enhancement in the afternoon. Such behaviors of inorganics have been previously described by Roig Rodelas et al. (2019), in a site 30 km south of ATOLL. During this study, they found correlated enhancement of SO_2 and SO_4, thus pointing towards the advection of sulfur-rich air masses towards the site, in contrast to the local formation of ammonium sulfate. The long-range transport of air masses associated with those higher concentrations is analyzed in more detail in the following section.

3.3.2. *Back-trajectory clustering results*

From the 4750 calculated back-trajectories, we derived six clusters shown in Fig. 7a (detailed in Fig. S21): C1 (southwest), C2 (local), C3 (south), C4 (north), C5 (east), C6 (northwest). Clusters C4 (6% of occurrence) and C6 (10%) from north and northwest are influenced mainly by marine air masses, but also potentially by the UK. Cluster C1 with 23% of occurrence, is affected also by oceanic air masses and contains a continental component (northern France). Cluster C2, the most frequent (37%), is more local and presents at the same time as the marine and continental air masses. Finally, clusters C3 (13%) and C5 (12%) represent continental air masses coming from the south (south of France and Europe) and eastern side of Europe (mainly affected by the industrialized areas in NW and central Germany as well as Belgium), respectively.

The chemical composition of the aerosol particles as well as the contribution of OA factors were averaged over the different air mass

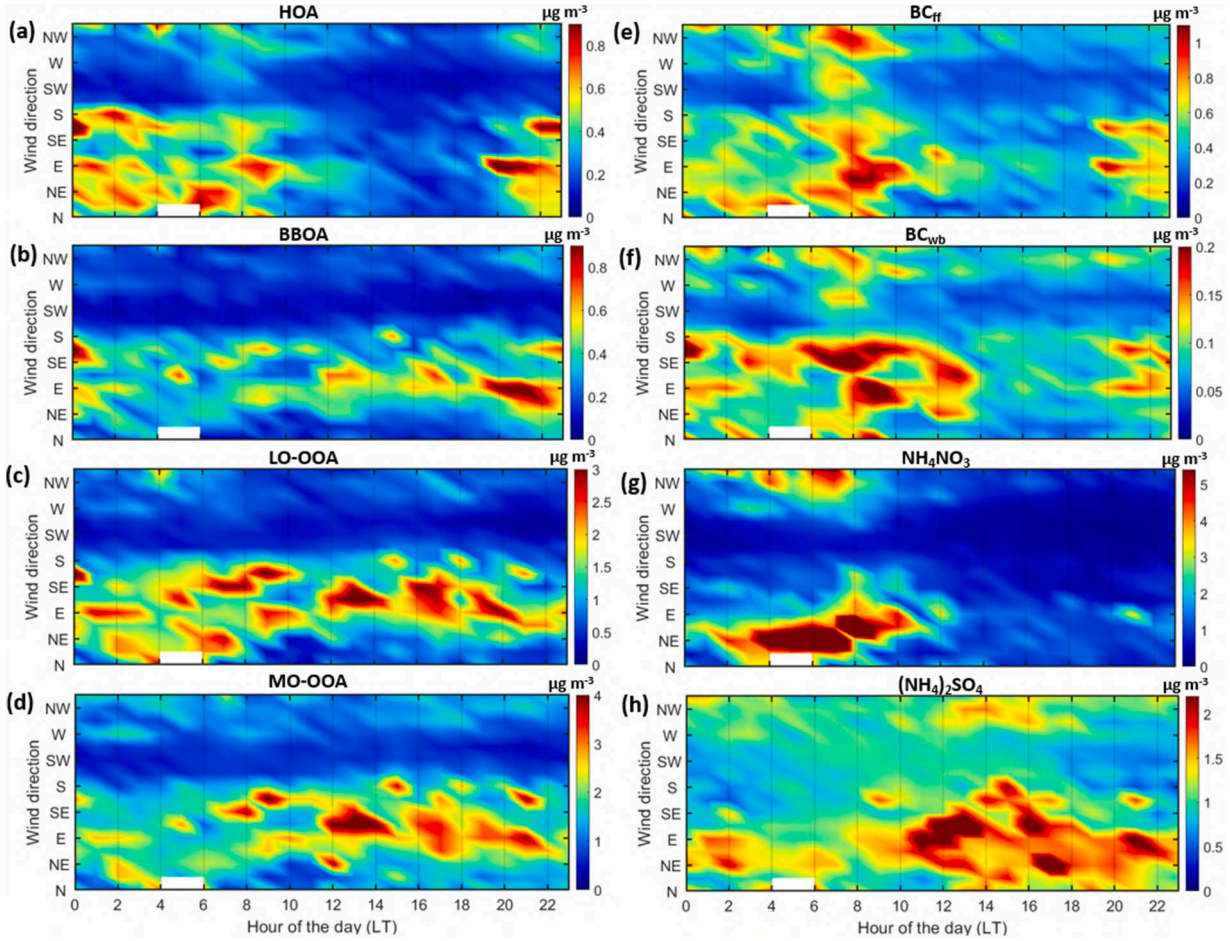

Fig. 6. Diel plots according to wind sectors during summertime for a) HOA, b) BBOA, c) LO-OOA, d) MO-OOA, e) BC_{ff}, f) BC_{wb}, g) NH_4NO_3, and h) $(NH_4)_2SO_4$. The Lille city center is located NW of the ATOLL site. The max value of the color scale represents the 90th percentile. (For interpretation of the references to color in this figure legend, the reader is referred to the Web version of this article.)

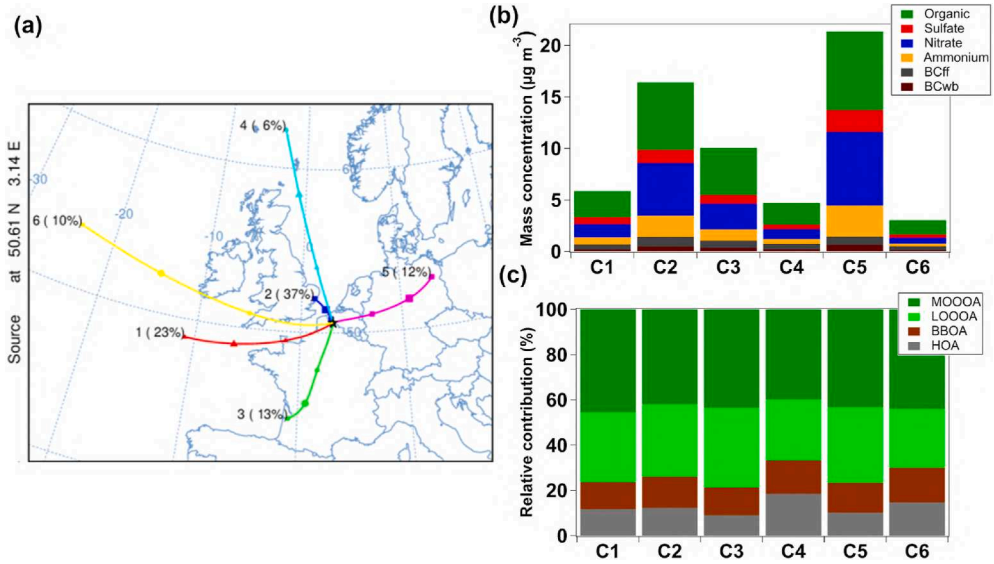

Fig. 7. Overview of the chemical composition and the OA factors for each cluster (C1 to C6), a) their trajectory map, b) the mean aerosol mass concentration associated with each cluster, and c) the relative contribution of the OA factors.

clusters and are presented in Fig. 7b and c. Overall, the highest particle mass concentrations were observed for clusters with the greatest continental influence (i.e., C3, south – 10.1 μg m^{-3}; C2, local – 16.5 μg m^{-3}; C5, east – 21.4 μg m^{-3}). The largest mass concentrations of nitrate, sulfate, and ammonium are also associated with these clusters, as well as a high contribution of LO-OOA and MO-OOA (more than 70%),

reflecting their regional origin or that of their gas-phase precursors. They are associated with the long-range transport of polluted continental air masses (C3 and C5) but are also related to local aged aerosol (C2). Those results are in line with receptor-based models and the chemistry-transport modeling applied by Potier et al. (2019), showing the important and frequent impact of "Near-East" areas (Belgium, Netherlands, Germany, etc.) on PM_{10} concentrations in the Northern France region. Meanwhile, the clusters C1, C4, and C6 with strong marine influence correspond to the lowest particle mass concentrations (C6, 3.0 μg $m^{-3;}$ C^4, 4.7 μg m^{-3}; C1, 5.9 μg m^{-3}) and they show a slight increase of POA PMF factor contributions (HOA and BBOA, 18.4% and 14.9% in C4, 14.6% and 15.5% in C6 respectively). These clusters are cleaner and mainly over water, thus HOA could be linked with shipping emissions over the Channel and North Sea, and northerly air masses with increased residential heating during wintertime. This analysis confirms the complex interaction between local and advected air masses on PM_1 concentrations and composition at the ATOLL platform.

4. Conclusion

Aerosol composition and sources in the newly established ATOLL site, near Lille in Northern France, are analyzed here from October 2016 to December 2020. During the studied period, PM_1 had a mean concentration of 10.6 μg m^{-3}, composed of OA (41.8%), NO_3 (28.9%), NH_4 (12.3%), SO_4 (8.6%), and BC (8.0%). For such a multi-annual dataset, source apportionment of organic aerosols has been performed using rolling PMF, allowing for a robust analysis through a clear set of criteria and constraints across seasons and years, in contrast to the season-by-season individual analysis method. A 28-day rolling PMF window shifted by one week over the four-year dataset yielded four factors, consisting of two primary OA, namely HOA (11.8% of total OA) mainly related to traffic, BBOA (ranging from 8.1% to 18.5% and peaking with the increase of residential heating in winter), and two oxygenated OA, LO-OOA (31.9%), and the MO-OOA (with a mean contribution of 42.3%). During wintertime, LO-OOA has been associated with aged biomass burning, identified recently as one of the key potential sources of negative health effects in Europe. Furthermore, the combined BBOA + LO-OOA attributes over 50% of OA to residential heating in winter at this site. Conversely, in summertime LO-OOA has been associated with biogenic SOA, also contributing significantly to OA (34.0%) during this season. The MO-OOA factor has been mostly linked with long-range transported air masses from continental areas. Pollution episodes are strongly linked with secondary processes. During summertime, LO-OOA increases with increasing PM_1 concentrations, linked with strong photochemical activity and high-temperature events, in agreement with enhanced new particle formation previously observed at this site and the expected SOA formation from increased emissions. In winter, spring, and autumn, ammonium nitrate, combined with oxidized organic aerosols (LO-OOA and MO-OOA) are key components during particulate pollution. Wind and trajectory analysis have shown a small impact of local pollution (Lille city) on the sampling site compared to the high regional impact. Overall, this study elucidates the main sources of fine aerosols at the ATOLL platform in Lille, describing the complex interactions between regional traffic, wood burning, agricultural activities, biogenic emissions, and long-range transport in this highly urbanized region of north-western Europe, towards developing effective mitigation policies. While exhaust traffic contribution to PM is expected to decrease in the coming years, wood burning (local and advected) will likely remain an important source of carbonaceous aerosols in Europe. Decreasing these primary sources could therefore lead to a decrease of both co-emitted precursor gases such as NOx and of secondary organic aerosols formed from anthropogenic precursors.

Author contributions

Hasna Chebaicheb: Data curation; Investigation; Methodology; Visualization; Writing – original draft. Joel F. de Brito: Supervision; Validation; Writing – original draft. Gang Chen: Methodology; Writing - review & editing. Emmanuel Tison: Data curation. Caroline Marchand: Supervision; Writing - review &editing. André S. H. Prévôt: Writing - review & editing. Olivier Favez: Supervision; Validation; Funding acquisition; Writing - review & editing.Véronique Riffault: Data curation; Validation; Funding acquisition; Supervision; Writing - review &editing.

Funding

H. Chebaicheb's PhD grant is supported by the LCSQA funded by the French Ministry of Environment. IMT Nord Europe acknowledges financial support from the Labex CaPPA project, which is funded by the French National Research Agency (ANR) through the PIA (Programme d'Investissement d'Avenir) under contract ANR-11-LABX-0005-01, and the CLIMIBIO and ECRIN projects, both financed by the Regional Council "Hauts-de-France" and the European Regional Development Fund (ERDF). IMT Nord Europe and INERIS participated in the COST COLOSSAL Action CA16109. The ATOLL site is one of the French ACTRIS National Facilities and contributes to the CARA program of the LCSQA funded by the French Ministry of Environment.

Declaration of competing interest

The authors declare that they have no known competing financial interests or personal relationships that could have appeared to influence the work reported in this paper.

Data availability

The data is freely available at the ACTRIS database (http://ebas-data.nilu.no/)

Acknowledgments

The authors are grateful to the staff at LOA, in particular Prof. P. Goloub, F. Auriol, and R. De Filippi, for supporting the technical and logistical implementation of the instruments, and to Dr. L.-H. Rivellini (now at the University of Toronto) for her early involvement. We thank T. Podvin (LOA) for providing the weather data at ATOLL, and the air quality monitoring network Atmo Hauts-de-France for providing $PM_{2.5}$ concentrations at the Lille Fives monitoring station.

Appendix A. Supplementary data

Supplementary data to this article can be found online at https://doi.org/10.1016/j.envpol.2023.121805.

References

Air quality in Europe 2021, 2021. European Environment Agency. URL. https://www.eea.europa.eu/publications/air-quality-in-europe-2021.

Allan, J.D., Jimenez, J.L., Williams, P.I., Alfarra, M.R., Bower, K.N., Jayne, J.T., Coe, H., Worsnop, D.R., 2003. Quantitative sampling using an Aerodyne aerosol mass spectrometer 1. Techniques of data interpretation and error analysis. J. Geophys. Res. Atmos. 108 https://doi.org/10.1029/2002JD002358.

Atabakhsh, S., Poulain, L., Chen, G., Canonaco, F., Prévôt, A.S.H., Pöhlker, M., Wiedensohler, A., Herrmann, H., 2023. A one-year ACSM source analysis of organic aerosol particle contributions from anthropogenic sources after long-range transport at the TROPOS research station Melpitz. Atmos. Chem. Phys. Discuss. 1–42. https://doi.org/10.5194/acp-2022-842.

Bressi, M., Cavalli, F., Putaud, J.P., Fröhlich, R., Petit, J.-E., Aas, W., Äijälä, M., Alastuey, A., Allan, J.D., Aurela, M., Berico, M., Bougiatioti, A., Bukowiecki, N., Canonaco, F., Crenn, V., Dusanter, S., Ehn, M., Elsasser, M., Flentje, H., Graf, P., Green, D.C., Heikkinen, L., Hermann, H., Holzinger, R., Hueglin, C., Keernik, H., Kiendler-Scharr, A., Kubelová, L., Lunder, C., Maasikmets, M., Makeš, O., Malaguti, A., Mihalopoulos, N., Nicolas, J.B., O'Dowd, C., Ovadnevaite, J., Petralia, E., Poulain, L., Priestman, M., Riffault, V., Ripoll, A., Schlag, P., Schwarz, J., Sciare, J., Slowik, J., Sosedova, Y., Stavroulas, I., Teinemaa, E., Via, M., Vodička, P.,

Williams, P.I., Wiedensohler, A., Young, D.E., Zhang, S., Favez, O., Minguillón, M.C., Prevot, A.S.H., 2021. A European aerosol phenomenology - 7: high-time resolution chemical characteristics of submicron particulate matter across Europe. Atmos. Environ. X 10, 100108. https://doi.org/10.1016/j.aeaoa.2021.100108.

Canonaco, F., Slowik, J.G., Baltensperger, U., Prévôt, A.S.H., 2015. Seasonal differences in oxygenated organic aerosol composition: implications for emissions sources and factor analysis. Atmos. Chem. Phys. 15, 6993–7002. https://doi.org/10.5194/acp-15-6993-2015.

Canonaco, F., Tobler, A., Chen, G., Sosedova, Y., Slowik, J.G., Bozzetti, C., Daellenbach, K.R., El Haddad, I., Crippa, M., Huang, R.-J., Furger, M., Baltensperger, U., Prévôt, A.S.H., 2021. A new method for long-term source apportionment with time-dependent factor profiles and uncertainty assessment using SoFi Pro: application to 1 year of organic aerosol data. Atmos. Meas. Tech. 14, 923–943. https://doi.org/10.5194/amt-14-923-2021.

Chazeau, B., Temime-Roussel, B., Gille, G., Mesbah, B., D'Anna, B., Wortham, H., Marchand, N., 2021. Measurement report: fourteen months of real-time characterisation of the submicronic aerosol and its atmospheric dynamics at the Marseille–Longchamp supersite. Atmos. Chem. Phys. 21, 7293–7319. https://doi.org/10.5194/acp-21-7293-2021.

Chen, G., Canonaco, F., Tobler, A., Aas, W., Alastuey, A., Allan, J., Atabakhsh, S., Aurela, M., Baltensperger, U., Bougiatioti, A., De Brito, J.F., Ceburnis, D., Chazeau, B., Chebaicheb, H., Daellenbach, K.R., Ehn, M., El Haddad, I., Eleftheriadis, K., Favez, O., Flentje, H., Font, A., Fossum, K., Freney, E., Gini, M., Green, D.C., Heikkinen, L., Herrmann, H., Kalogridis, A.-C., Keernik, H., Lhotka, R., Lin, C., Lunder, C., Maasikmets, M., Manousakas, M.I., Marchand, N., Marin, C., Marmureanu, L., Mihalopoulos, N., Močnik, G., Nęcki, J., O'Dowd, C., Ovadnevaite, J., Peter, T., Petit, J.-E., Pikridas, M., Matthew Platt, S., Pokorná, P., Poulain, L., Priestman, M., Riffault, V., Rinaldi, M., Różański, K., Schwarz, J., Sciare, J., Simon, L., Skiba, A., Slowik, J.G., Sosedova, Y., Stavroulas, I., Styszko, K., Teinemaa, E., Timonen, H., Tremper, A., Vasilescu, J., Via, M., Vodička, P., Wiedensohler, A., Zografou, O., Cruz Minguillón, M., Prévôt, A.S.H., 2022. European aerosol phenomenology − 8: harmonised source apportionment of organic aerosol using 22 Year-long ACSM/AMS datasets. Environ. Int. 166, 107325 https://doi.org/10.1016/j.envint.2022.107325.

Chen, G., Sosedova, Y., Canonaco, F., Fröhlich, R., Tobler, A., Vlachou, A., Daellenbach, K.R., Bozzetti, C., Hueglin, C., Graf, P., Baltensperger, U., Slowik, J.G., El Haddad, I., Prévôt, A.S.H., 2021. Time-dependent source apportionment of submicron organic aerosol for a rural site in an alpine valley using a rolling positive matrix factorisation (PMF) window. Atmos. Chem. Phys. 21, 15081–15101. https://doi.org/10.5194/acp-21-15081-2021.

Crenn, V., Fronval, I., Petitprez, D., Riffault, V., 2017. Fine particles sampled at an urban background site and an industrialized coastal site in Northern France - Part 1: seasonal variations and chemical characterization. Sci. Total Environ. 578, 203–218.

Crippa, M., Canonaco, F., Lanz, V.A., Äijälä, M., Allan, J.D., Carbone, S., Capes, G., Ceburnis, D., Dall'Osto, M., Day, D.A., DeCarlo, P.F., Ehn, M., Eriksson, A., Freney, E., Hildebrandt Ruiz, L., Hillamo, R., Jimenez, J.L., Junninen, H., Kiendler-Scharr, A., Kortelainen, A.-M., Kulmala, M., Laaksonen, A., Mensah, A.A., Mohr, C., Nemitz, E., O'Dowd, C., Ovadnevaite, J., Pandis, S.N., Petäjä, T., Poulain, L., Saarikoski, S., Sellegri, K., Swietlicki, E., Tiitta, P., Worsnop, D.R., Baltensperger, U., Prévôt, A.S.H., 2014. Organic aerosol components derived from 25 AMS data sets across Europe using a consistent ME-2 based source apportionment approach. Atmos. Chem. Phys. 14, 6159–6176. https://doi.org/10.5194/acp-14-6159-2014.

Crumeyrolle, S., Kontkanen, J.S.S., Rose, C., Velazquez Garcia, A., Bourrianne, E., Catalfamo, M., Riffault, V., Tison, E., Ferreira de Brito, J., Visez, N., Ferlay, N., Auriol, F., Chiapello, I., 2023. Measurement report: atmospheric new particle formation at a peri-urban site in Lille, northern France. Atmos. Chem. Phys. 23, 183–201. https://doi.org/10.5194/acp-23-183-2023.

Daellenbach, K.R., Uzu, G., Jiang, J., Cassagnes, L.-E., Leni, Z., Vlachou, A., Stefenelli, G., Canonaco, F., Weber, S., Segers, A., Kuenen, J.J.P., Schaap, M., Favez, O., Albinet, A., Aksoyoglu, S., Dommen, J., Baltensperger, U., Geiser, M., El Haddad, I., Jaffrezo, J.-L., Prévôt, A.S.H., 2020. Sources of particulate-matter air pollution and its oxidative potential in Europe. Nature 587, 414–419. https://doi.org/10.1038/s41586-020-2902-8.

Draxler, RR, 1999. HYSPLIT4 users's guide.

Drinovec, L., Močnik, G., Zotter, P., Prévôt, A.S.H., Ruckstuhl, C., Coz, E., Rupakheti, M., Sciare, J., Müller, T., Wiedensohler, A., Hansen, A.D.A., 2015. The "dual-spot" Aethalometer: an improved measurement of aerosol black carbon with real-time loading compensation. Atmos. Meas. Tech. 8, 1965–1979. https://doi.org/10.5194/amt-8-1965-2015.

Efron, B., 1979. Bootstrap methods: another look at the jackknife. Ann. Stat. 7, 1–26. https://doi.org/10.1214/aos/1176344552.

Favez, O., Weber, S., Petit, J.-E., Alleman, L., Albinet, A., Riffault, V., Chazeau, B., Amodeo, T., Salameh, D., Zhang, Y., Srivastava, D., Samaké, A., Aujay, R., Papin, A., Bonnaire, N., Boullanger, C., Chatain, M., Chevrier, F., Detournay, A., Leoz-Garziandia, E., 2021. Overview of the French Operational Network for in Situ Observation of PM Chemical Composition and Sources in Urban Unvironments (CARA Program). https://doi.org/10.20944/preprints202101.0182.v1.

Hendriks, C., Kranenburg, R., Kuenen, J.J.P., Van den Bril, B., Verguts, V., Schaap, M., 2016. Ammonia emission time profiles based on manure transport data improve ammonia modelling across north western Europe. Atmos. Environ. 131, 83–96. https://doi.org/10.1016/j.atmosenv.2016.01.043.

Hu, W.W., Campuzano-Jost, P., Palm, B.B., Day, D.A., Ortega, A.M., Hayes, P.L., Krechmer, J.E., Chen, Q., Kuwata, M., Liu, Y.J., de Sá, S.S., McKinney, K., Martin, S. T., Hu, M., Budisulistiorini, S.H., Riva, M., Surratt, J.D., Clair J M, St, Isaacman-Van Wertz, G., Yee, L.D., Goldstein, A.H., Carbone, S., Brito, J., Artaxo, P., de Gouw, J.A., Koss, A., Wisthaler, A., Mikoviny, T., Karl, T., Kaser, L., Jud, W., Hansel, A., Docherty, K.S., Alexander, M.L., Robinson, N.H., Coe, H., Allan, J.D., Canagaratna, M.R., Paulot, F., Jimenez, J.L., 2015. Characterization of a real-time tracer for isoprene epoxydiols-derived secondary organic aerosol (IEPOX-SOA) from aerosol mass spectrometer measurements. Atmos. Chem. Phys. 15, 11807–11833. https://doi.org/10.5194/acp-15-11807-2015.

Kelly, F.J., Fussell, J.C., 2015. Air pollution and public health: emerging hazards and improved understanding of risk. Environ. Geochem. Health 37, 631–649. https://doi.org/10.1007/s10653-015-9720-1.

Middlebrook, A.M., Bahreini, R., Jimenez, J.L., Canagaratna, M.R., 2012. Evaluation of composition-dependent collection efficiencies for the Aerodyne aerosol mass spectrometer using field data. Aerosol Sci. Technol. 46, 258–271. https://doi.org/10.1080/02786826.2011.620041.

Ng, N.L., Canagaratna, M.R., Jimenez, J.L., Zhang, Q., Ulbrich, I.M., Worsnop, D.R., 2011a. Real-time methods for estimating organic component mass concentrations from aerosol mass spectrometer data. Environ. Sci. Technol. 45, 910–916. https://doi.org/10.1021/es102951k.

Ng, N.L., Herndon, S.C., Trimborn, A., Canagaratna, M.R., Croteau, P.L., Onasch, T.B., Sueper, D., Worsnop, D.R., Zhang, Q., Sun, Y.L., Jayne, J.T., 2011b. An aerosol chemical speciation monitor (ACSM) for routine monitoring of the composition and mass concentrations of ambient aerosol. Aerosol Sci. Technol. 45, 780–794. https://doi.org/10.1080/02786826.2011.560211.

Paatero, P., Tapper, U., 1994. Positive matrix factorization: a non-negative factor model with optimal utilization of error estimates of data values. Environmetrics 5, 111–126. https://doi.org/10.1002/env.3170050203.

Pandis, S.N., Skyllakou, K., Florou, K., Kostenidou, E., Kaltsonoudis, C., Hasa, E., Presto, A.A., 2016. Urban particulate matter pollution: a tale of five cities. Faraday Discuss 189, 277–290. https://doi.org/10.1039/C5FD00212E.

Parworth, C., Fast, J., Mei, F., Shippert, T., Sivaraman, C., Tilp, A., Watson, T., Zhang, Q., 2015. Long-term measurements of submicrometer aerosol chemistry at the southern great plains (SGP) using an aerosol chemical speciation monitor (ACSM). Atmos. Environ. 106, 43–55. https://doi.org/10.1016/j.atmosenv.2015.01.060.

Petit, J.-E., Favez, O., Sciare, J., Crenn, V., Sarda-Estève, R., Bonnaire, N., Močnik, G., Dupont, J.-C., Haeffelin, M., Leoz-Garziandia, E., 2015. Two years of near real-time chemical composition of submicron aerosols in the region of Paris using an Aerosol Chemical Speciation Monitor (ACSM) and a multi-wavelength Aethalometer. Atmos. Chem. Phys. 15, 2985–3005. https://doi.org/10.5194/acp-15-2985-2015.

Potier, E., Waked, A., Bourin, A., Minvielle, F., Péré, J.C., Perdrix, E., Michoud, V., Riffault, V., Alleman, L.Y., Sauvage, S., 2019. Characterizing the regional contribution to PM10 pollution over northern France using two complementary approaches: chemistry transport and trajectory-based receptor models. Atmos. Res. 223, 1–14. https://doi.org/10.1016/j.atmosres.2019.03.002.

Roig Rodelas, R., Perdrix, E., Herbin, B., Riffault, V., 2019. Characterization and variability of inorganic aerosols and their gaseous precursors at a suburban site in northern France over one year (2015–2016). Atmos. Environ. 200, 142–157. https://doi.org/10.1016/j.atmosenv.2018.11.041.

Sandradewi, J., Prévôt, A.S.H., Szidat, S., Perron, N., Alfarra, M.R., Lanz, V.A., Weingartner, E., Baltensperger, U., 2008. Using aerosol light absorption measurements for the quantitative determination of wood burning and traffic emission contributions to particulate matter. Environ. Sci. Technol. 42, 3316–3323. https://doi.org/10.1021/es702253m.

Schlag, P., Kiendler-Scharr, A., Blom, M.J., Canonaco, F., Henzing, J.S., Moerman, M., Prévôt, A.S.H., Holzinger, R., 2016. Aerosol source apportionment from 1-year measurements at the CESAR tower in Cabauw, The Netherlands. Atmos. Chem. Phys. 16, 8831–8847. https://doi.org/10.5194/acp-16-8831-2016.

Thunis, P., Pisoni, E., Bessagnet, B., Wilson, J., Vignati, E., De Meij, A., Mascherpa, A., 2021. Urban PM2.5 Atlas [WWW Document]. JRC Publ. Repos. https://doi.org/10.2760/356670.

Tobler, A.K., Skiba, A., Canonaco, F., Močnik, G., Rai, P., Chen, G., Bartyzel, J., Zimnoch, M., Styszko, K., Nęcki, J., Furger, M., Różański, K., Baltensperger, U., Slowik, J.G., Prevot, A.S.H., 2021. Characterization of non-refractory (NR) PM_1 and source apportionment of organic aerosol in Kraków, Poland. Atmos. Chem. Phys. 21, 14893–14906. https://doi.org/10.5194/acp-21-14893-2021.

Velazquez-Garcia, A., Crumeyrolle, S., de Brito, J.F., Tison, E., Bourrianne, E., Chiapello, I., Riffault, V., 2023. Deriving composition-dependent aerosol absorption, scattering and extinction mass efficiencies from multi-annual high time resolution observations in Northern France. Atmos. Environ., 119613 https://doi.org/10.1016/j.atmosenv.2023.119613.

Via, M., Minguillón, M.C., Reche, C., Querol, X., Alastuey, A., 2021. Increase in secondary organic aerosol in an urban environment. Atmos. Chem. Phys. 21, 8323–8339. https://doi.org/10.5194/acp-21-8323-2021.

Waked, A., Bourin, A., Michoud, V., Perdrix, E., Alleman, L.Y., Sauvage, S., Delaunay, T., Vermeesch, S., Petit, J.-E., Riffault, V., 2018. Investigation of the geographical origins of PM10 based on long, medium and short-range air mass back-trajectories impacting Northern France during the period 2009–2013. Atmos. Environ. 193, 143–152. https://doi.org/10.1016/j.atmosenv.2018.08.015.

Waked, A., Favez, O., Alleman, L.Y., Piot, C., Petit, J.-E., Delaunay, T., Verlinden, E., Golly, B., Besombes, J.-L., Jaffrezo, J.-L., Leoz-Garziandia, E., 2014. Source apportionment of PM_{10} in a north-western Europe regional urban background site (Lens, France) using positive matrix factorization and including primary biogenic emissions. Atmos. Chem. Phys. 14, 3325–3346. https://doi.org/10.5194/acp-14-3325-2014.

WHO Air Quality Guidelines, 2021. URL https://www.c40knowledgehub.org/s/article/WHO-Air-Quality-Guidelines?language=en_US (accessed January.23.23).

Zhang, Y., Favez, O., Petit, J.-E., Canonaco, F., Truong, F., Bonnaire, N., Crenn, V., Amodeo, T., Prévôt, A.S.H., Sciare, J., Gros, V., Albinet, A., 2019. Six-year source apportionment of submicron organic aerosols from near-continuous highly time-

resolved measurements at SIRTA (Paris area, France). Atmos. Chem. Phys. 19, 14755–14776. https://doi.org/10.5194/acp-19-14755-2019.

Zhang, S., Tison, E., Dusanter, S., Beaugard, C., Gengembre, C., Augustin, P., Fourmentin, M., Delbarre, H., Riffault, V., 2021. Near real-time PM1 chemical composition measurements at a French urban background and coastal site under industrial influence over more than a year: Temporal variability and assessment of sulfur-containing emissions. Atmos. Environ. 244, 117960. https://doi.org/10.1016/j.atmosenv.2020.117960.

Zografou, O., Gini, M., Manousakas, M.I., Chen, G., Kalogridis, A.C., Diapouli, E., Pappa, A., Eleftheriadis, K., 2022. Combined organic and inorganic source apportionment on yearlong ToF-ACSM dataset at a suburban station in Athens, Atmospheric Meas. Technol. 15, 4675–4692. https://doi.org/10.5194/amt-15-4675-2022.

V.3. Supplementary Information de l'article 3

Supplementary Information

Investigation of four-year chemical composition and organic aerosol sources of submicron particles at the ATOLL site in Northern France

Hasna Chebaicheb[1,2,3], Joel F. de Brito[1*], Gang Chen[4,5], Emmanuel Tison[1], Caroline Marchand[2,3], André S. H. Prévôt[4], Olivier Favez[2,3], Véronique Riffault[1,3]

[1]IMT Nord Europe, Institut Mines-Télécom, Université de Lille, Centre for Energy and Environment, 59000 Lille, France
[2]Institut national de l'environnement industriel et des risques (INERIS), 60550 Verneuil-en-Halatte, France
[3]Laboratoire Central de surveillance de la Qualité de l'Air (LCSQA), F-60550 Verneuil-en-Halatte, France
[4]Laboratory of Atmospheric Chemistry, Paul Scherrer Institute, 5232 Villigen, Switzerland
[5]MRC Centre for Environment and Health, Environmental Research Group, Imperial College London, London, W120BZ, UK

Correspondence to: joel.brito@imt-nord-europe.fr

S1. Site location and Q-ACSM operation

Figure S1 below shows the location of the ATOLL site, on the University campus in Villeneuve-d'Ascq, roughly 4 km east of Lille.

Figure S1: Location of the ATOLL platform

Figure S2 shows the hourly time series of $PM_{2.5}$ from the air quality network at the Fives station, in downtown Lille, and the non-refractory species, as well as BC fractions at the ATOLL site. Their mean values during the observed period are presented in Table S1.

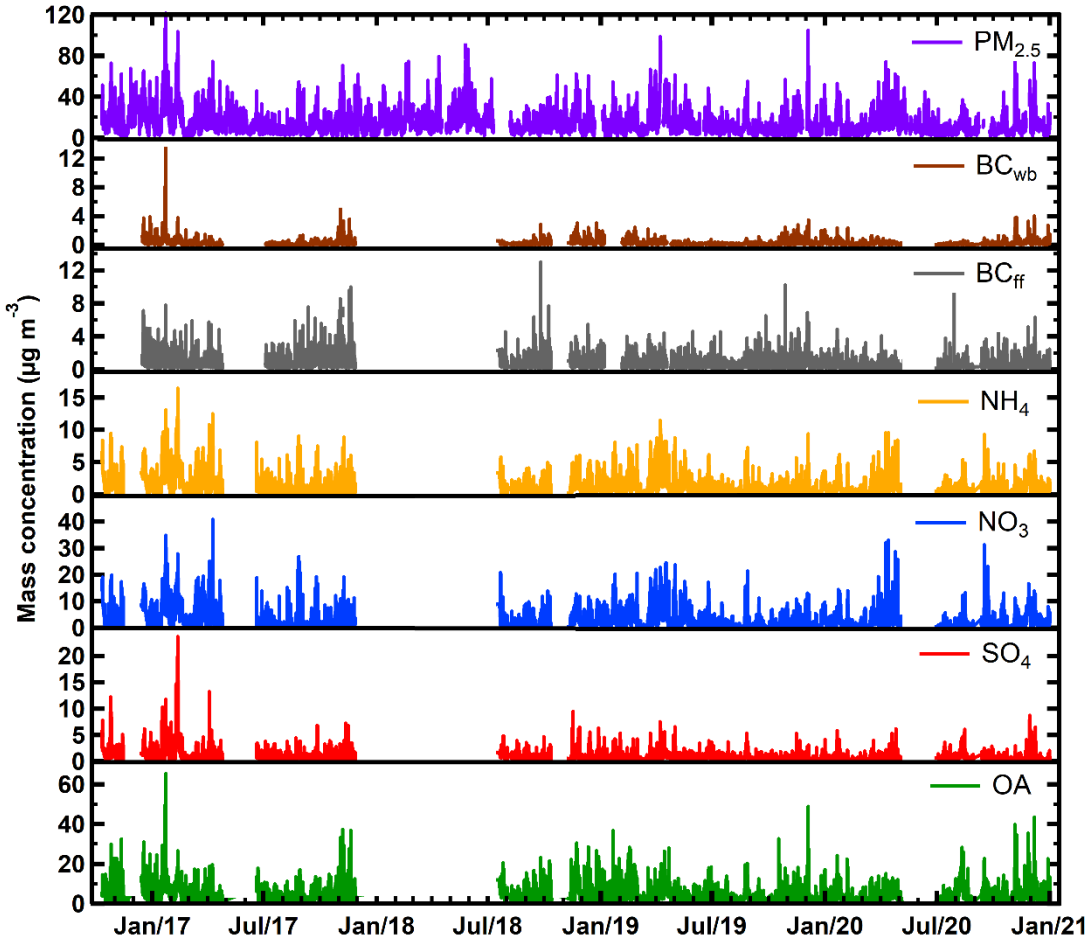

Figure S2: Mass concentrations of $PM_{2.5}$ and PM_1 components at the ATOLL platform

Table S1: Annual and seasonal mean values of ACSM species and BC (in µg m^{-3}), as well as BC fractions for 2016-2020

	Annual	Winter	Spring	Summer	Autumn
Org	4.42	5.20	3.97	3.72	4.53
SO_4	0.92	1.05	0.81	0.91	0.87
NO_3	3.06	3.91	4.38	1.48	2.70
NH_4	1.30	1.59	1.70	0.88	1.13
BC	0.93	1.18	0.76	0.62	1.06
BC_{ff}	0.67	0.74	0.56	0.51	0.78
BC_{wb}	0.26	0.44	0.20	0.10	0.28

During the observation period, calibration parameters reported in Table S2 were applied to the instrument.

Table S2: RF/RIE calibrations for ATOLL ACSM used from October 2016 to December 2020

Year	RF_{NO3} (10^{-11})	RIE_{NH4}	RIE_{SO4}
2016-2017	3.5	4	0.65
2018-2020	5.1	4.3	0.86

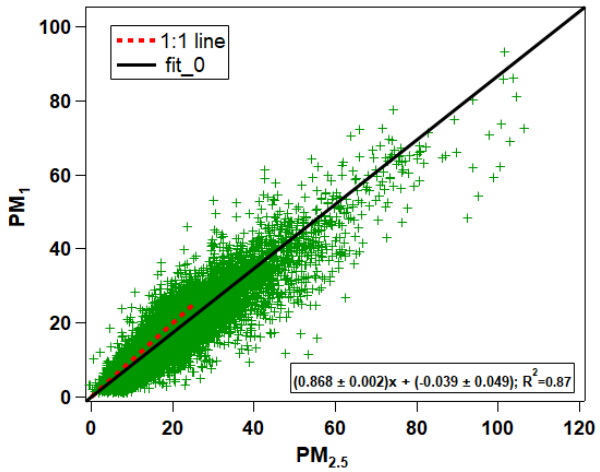

Figure S3: Correlation between PM_1 after applying CDCE at the ATOLL site and $PM_{2.5}$ at the Lille Fives station

S2. One-year (2016-2017) PMF analysis

In order to understand the main sources of organic aerosols (OA) at the ATOLL platform, PMF was performed for different seasons. First, the unconstrained PMF method was applied to define the potential number of factors (2-8 factor tests with ten PMF runs for each number of factors). Second, a constrained PMF was conducted using the reference profiles from Crippa et al. (2013) for hydrocarbon-like OA (HOA) and from Crippa et al. (2014) for biomass-burning OA (BBOA). Four PMF factors were identified, including two primary OA (HOA and BBOA) and two oxygenated OA (less oxidized LO-OOA and more oxidized MO-OOA). Table S3 represents the correlations of the four factors with reference spectra. The two oxygenated factors LO-OOA and

MO-OOA are separated according to their oxidation state, as shown in the f44 (m/z 44/OA) vs. f43 (m/z 43/OA) plot (Figure S4).

The primary factor profiles were extracted from the seasonal PMF and then bootstrapped to test the stability of the solutions. Chen et al. (2022) provide a step-by-step protocol to ensure the quality of the PMF solution for each season. Figure S5 presents the averaged bootstrapped solution for winter 2016-2017, where the extracted HOA and BBOA were used as reference profiles for rolling PMF analysis. This dataset contains 72 ions (m/z from 13 to 100). The *m/z* 12 mass was removed in the PMF analyses because of its negative signal.

Table S3: Uncentered correlation between OA PMF factors and reference profiles

External profiles (reference)	HOA	BBOA	MO-OOA	LO-OOA
HOA (Crippa et al., 2013)	0.98	0.61	0.20	0.53
HOA (Ng et al., 2011)	0.98	0.61	0.21	0.53
BBOA (Crippa et al., 2014)	0.54	0.93	0.36	0.66
BBOA (Ng et al., 2011)	0.86	0.93	0.44	0.77
OOA-I (Ng et al., 2011)	0.55	0.77	0.91	0.99
OOA-II (Ng et al., 2011)	0.83	0.87	0.53	0.85

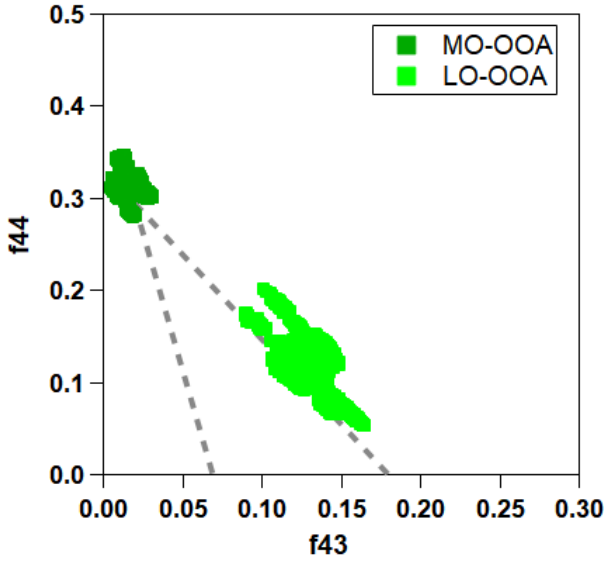

Figure S4: *f44* vs *f43* plot for LO-OOA and MO-OOA. The dashed lines are adopted from Ng et al. (2010)

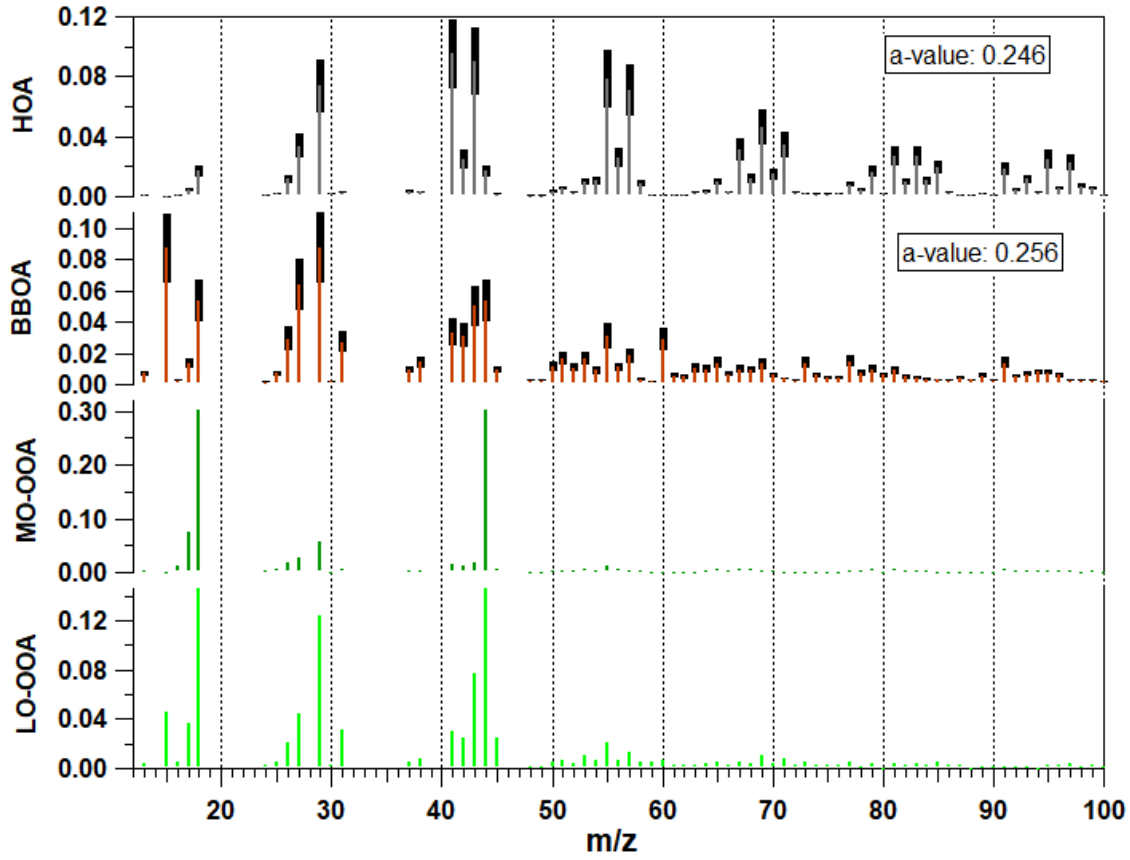

Figure S5: Factor profiles for winter 2016-2017 at the ATOLL site

Several tests were performed to select the optimum PMF window length, based on non-modelled points, considered PMF runs and Q/Q_{exp}, as defined in Canonaco et al. (2021).

Table S4: Rolling PMF window tests

PMF window length (with one-day shift)	**non-modelled points**	**Considered PMF runs**	**Q/Q_{exp}**
7 days	1 (0.01%)	7005 (42.98%)	0.55
14 days	1 (0.01%)	8848 (54.28%)	0.564
21 days	0 (0%)	9895 (60.71%)	0.567
28 days	0 (0%)	10534 (64.63%)	0.572

Table S4 shows the four tests performed. The results are very close in terms of the percentage of non-modelled points, the number of considered PMF runs, as well as the ratio Q/Q_{exp}. These similar results can be explained by the low temporal variabilities in the factor profiles of the data. Thus, the four options of the PMF window length could be used for this analysis. In the end, the 14-day PMF window shifted by one-day was chosen for the 2016-2017 dataset, as it is also recommended in other studies (Canonaco et al., 2021; Chen et al., 2021; Tobler et al., 2021).

S3. Choose the optimum PMF window for the rolling

To choose the optimum PMF window for a four-year rolling PMF, an inter-comparison of one-year to four-year was performed. The parameters and the criteria applied for the 2016-2017 rolling PMF are explained in table S5. As the 14-day window with a one-day shift is optimized, the 28-day window with a seven-day shift is tested to be used for the whole dataset as it reduces computation time.

Table S5: Comparison between two cases for rolling PMF 2016-2017 to choose the optimal length of the PMF window

2016-2017 Rolling PMF analysis	**Case 1: 14-day window and a one-day shift**	**Case 2: 28-day window and a seven-day shift**
Parameters	HOA & BBOA reference profiles from ATOLL winter; a-value = [0, 0.4];	
Criteria applied	Explained variation of *m/z* 60 of BBOA; Sorting of MO/LO-OOA based on f_{44}/f_{43}; Correlation HOA vs BC_{ff}	

The results of rolling PMF on these two cases have been compared in terms of factor loadings, mass spectra, contributions, correlations with externals, and residuals. Figure S6 presents the comparison of OA factor loadings and mass spectra between the 14-day and 28-day PMF windows. Both cases show similar and very close results. Therefore, considering the stable source profiles over time from this test, we used the 28-day rolling window and seven-day shift to save some computational time for the four-year rolling PMF analysis.

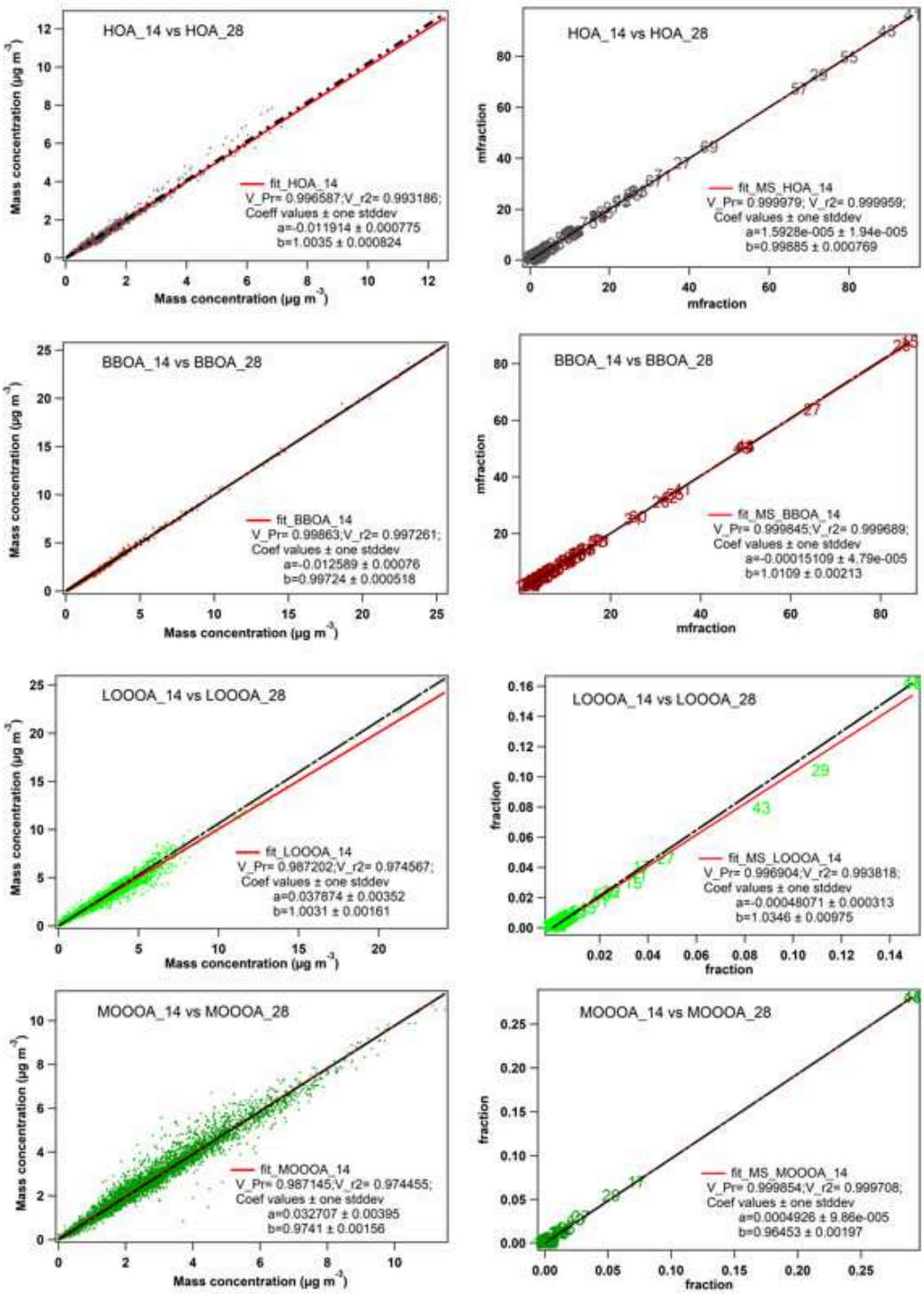

Figure S6: Comparison of OA factors between the two cases in terms of (left) factor loadings and (right) mass spectra

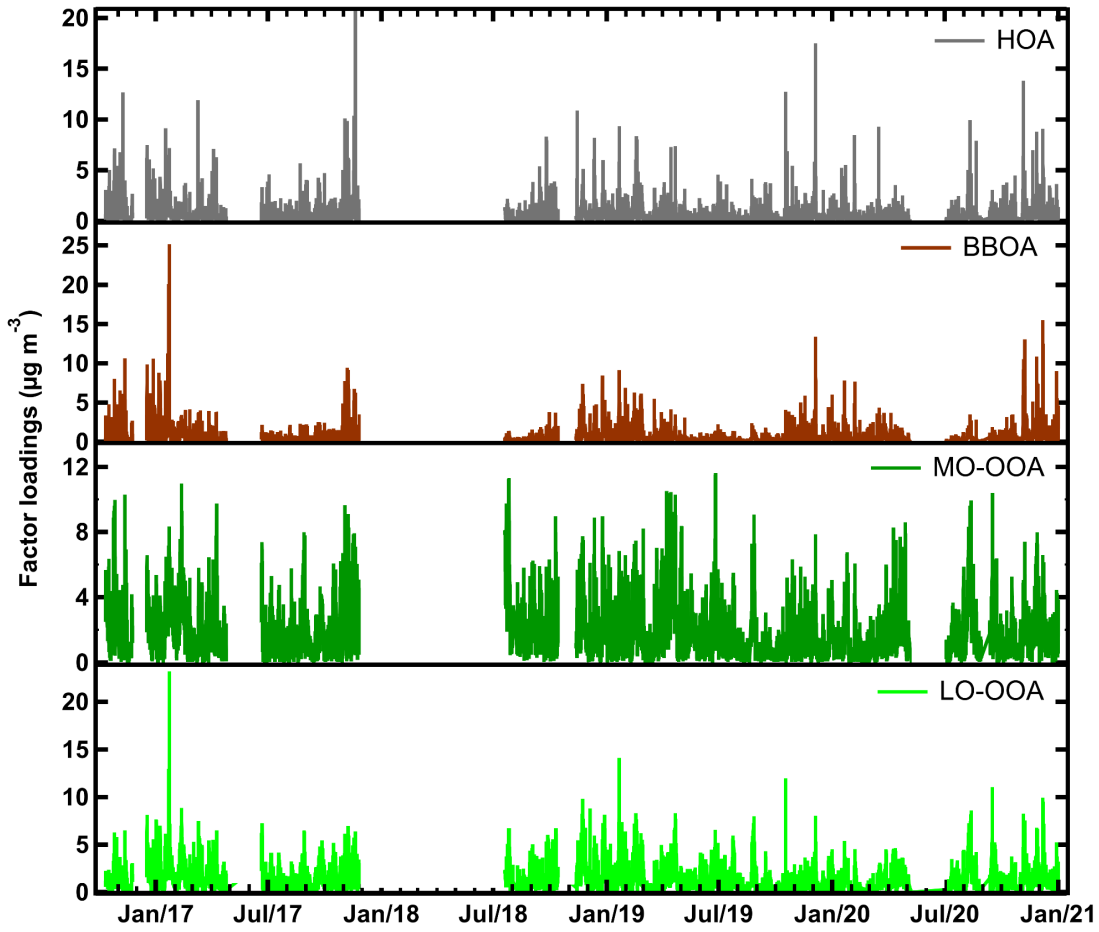

Figure S7: OA factor loadings from rolling PMF at the ATOLL site

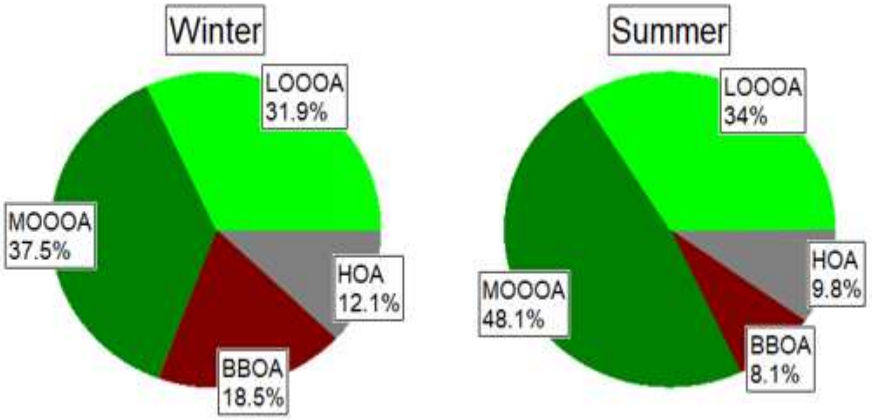

Figure S8: OA factor contributions in winter (left) and summer (right) during the whole period

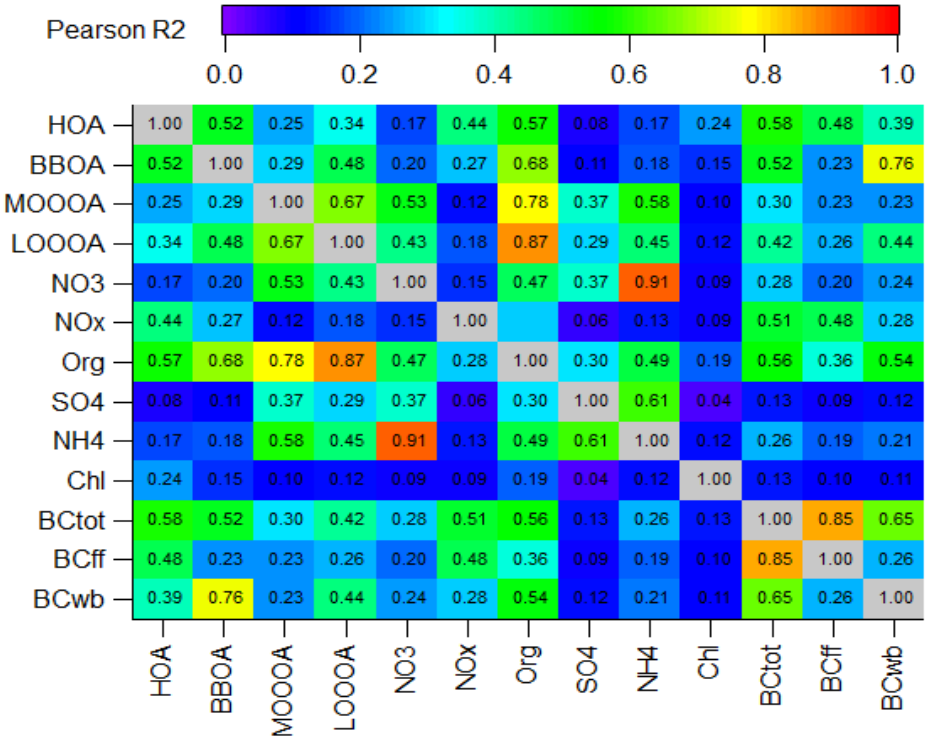

Figure S9: Correlations between the OA factors and the external variables for the entire period

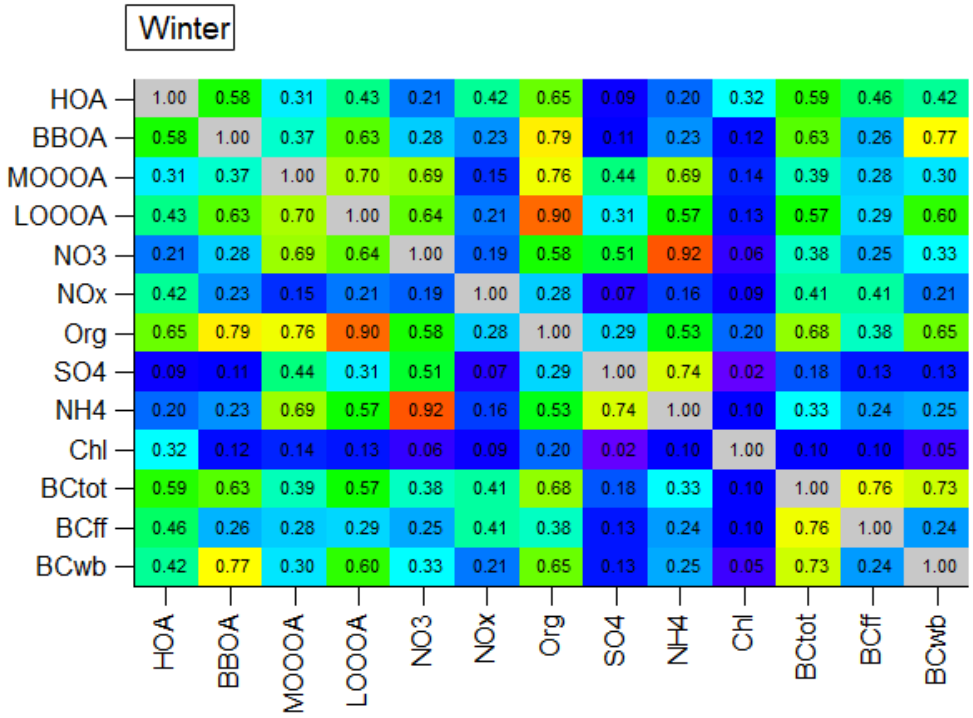

Figure S10: Correlations between the OA factors and the external variables for winter

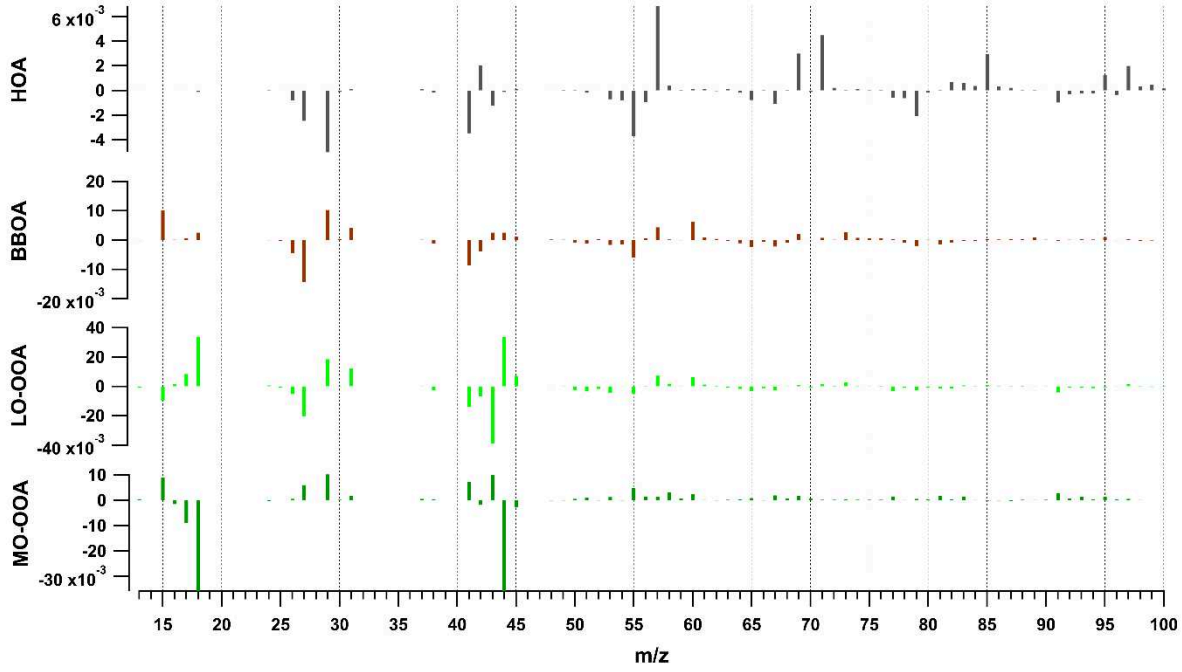

Figure S11: Difference of OA factors between wintertime and summertime

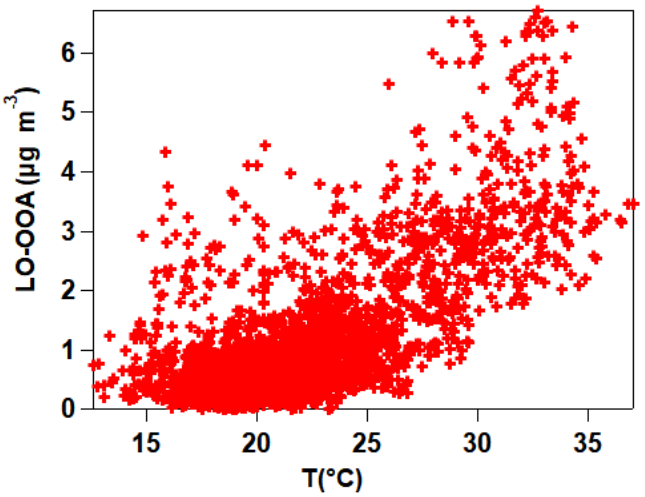

Figure S12: Summertime afternoon hours (12pm-5pm) LO-OOA loadings vs. temperature

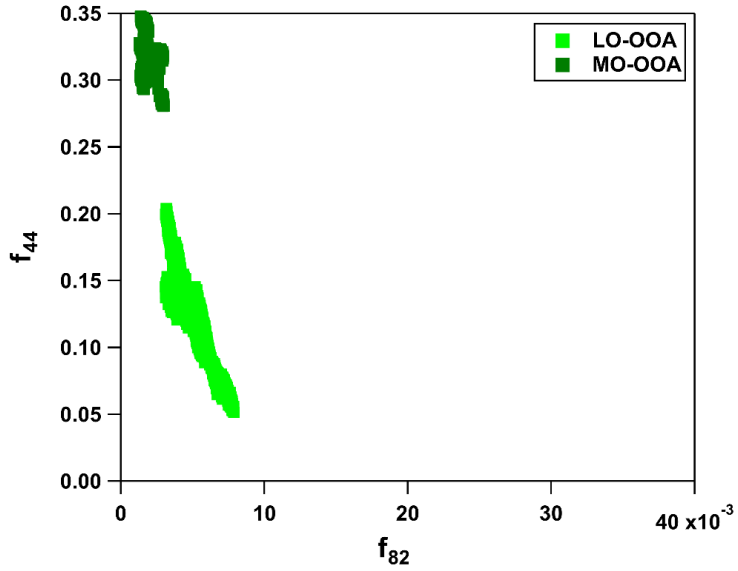

Figure S13: *f44* vs *f82* for MO-OOA and LO-OOA factors from rolling PMF in the summertime

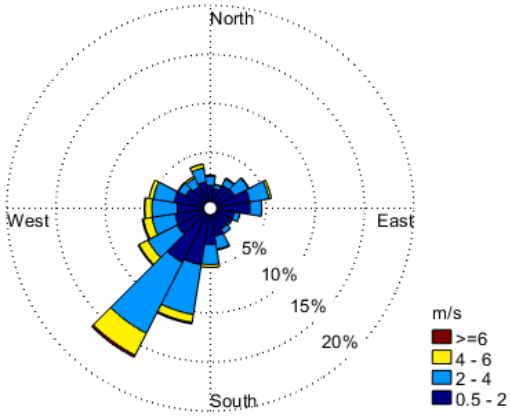

Figure S14: Wind rose from October 2016 to December 2020. The radial axis represents the wind occurrence (in %) and the color code, the wind speed in m s^{-1}

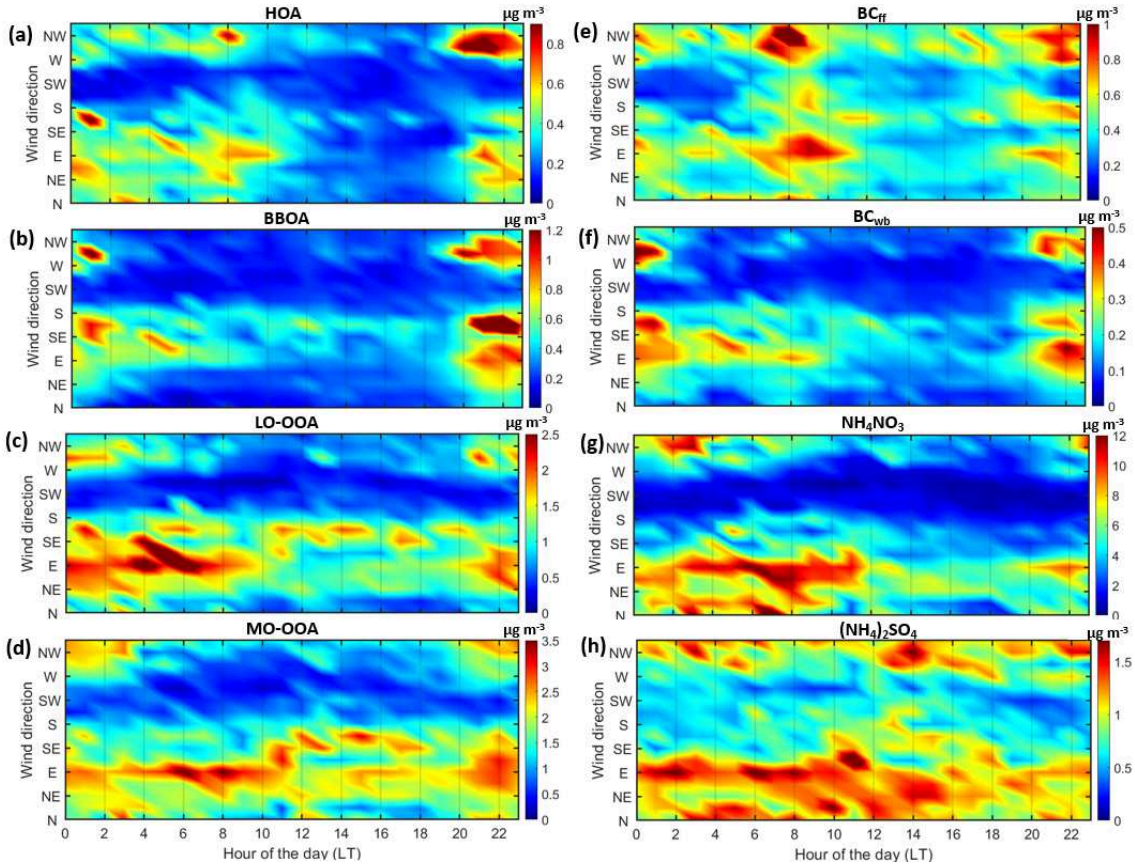

Figure S15: Diel plots according to wind sectors in spring for a) HOA, b) BBOA, c) LO-OOA, d) MO-OOA, e) BC_{ff}, f) BC_{wb}, g) NH_4NO_3, and h) $(NH_4)_2SO_4$. The Lille city center is located NW of the ATOLL site. The max value of the color scale represents the 90th percentile.

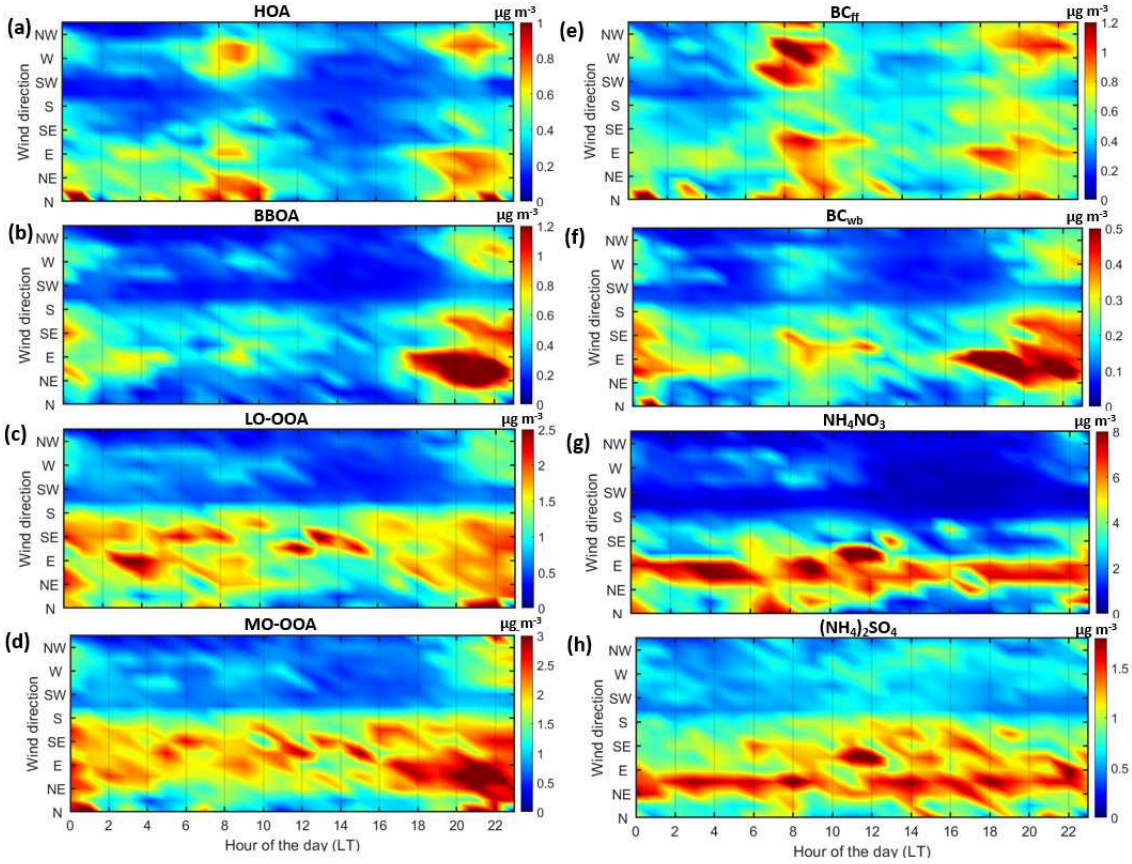

Figure S16: Diel plots according to wind sectors in autumn for a) HOA, b) BBOA, c) LO-OOA, d) MO-OOA, e) BC_{ff}, f) BC_{wb}, g) NH_4NO_3, and h) $(NH_4)_2SO_4$. The Lille city center is located NW of the ATOLL site. The max value of the color scale represents the 90th percentile.

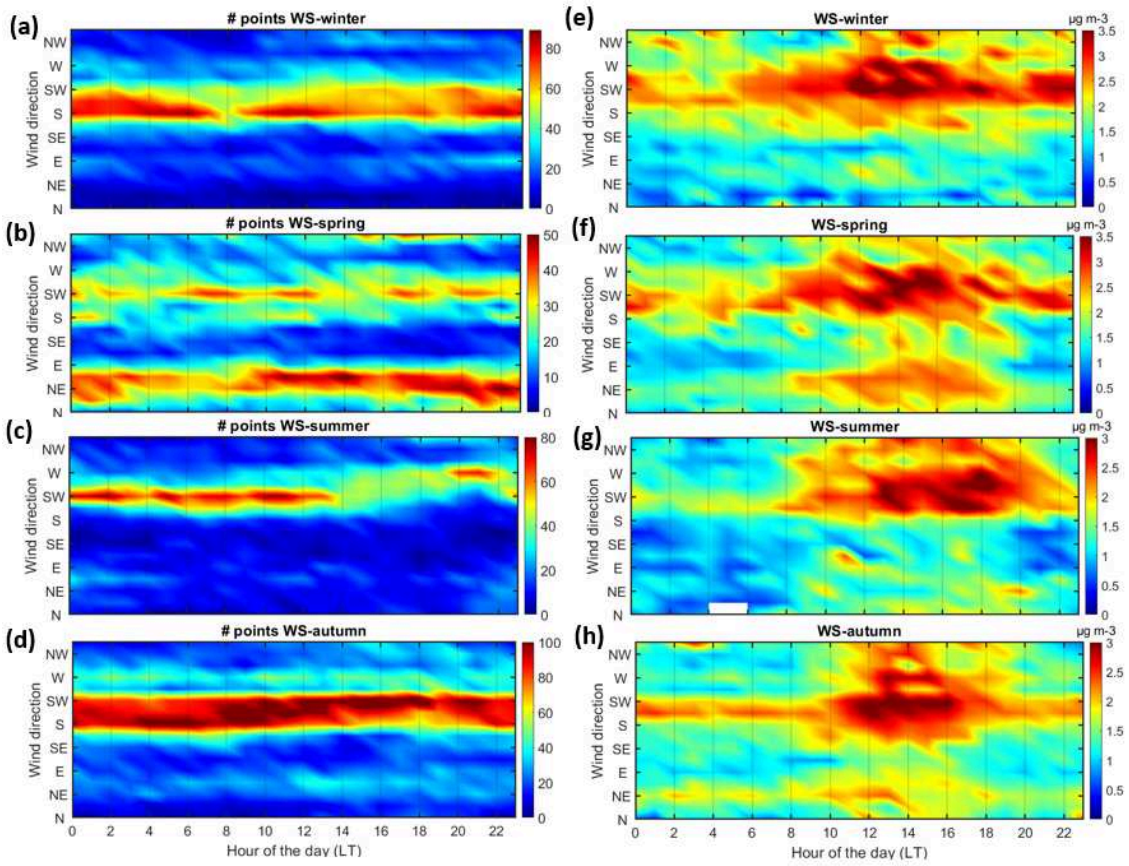

Figure S17: Diel plots of (left) number of points and (right) wind speed in m s^{-1} per wind sector in (a, e) winter, (b, f) spring, (c, g) summer and (d, h) autumn

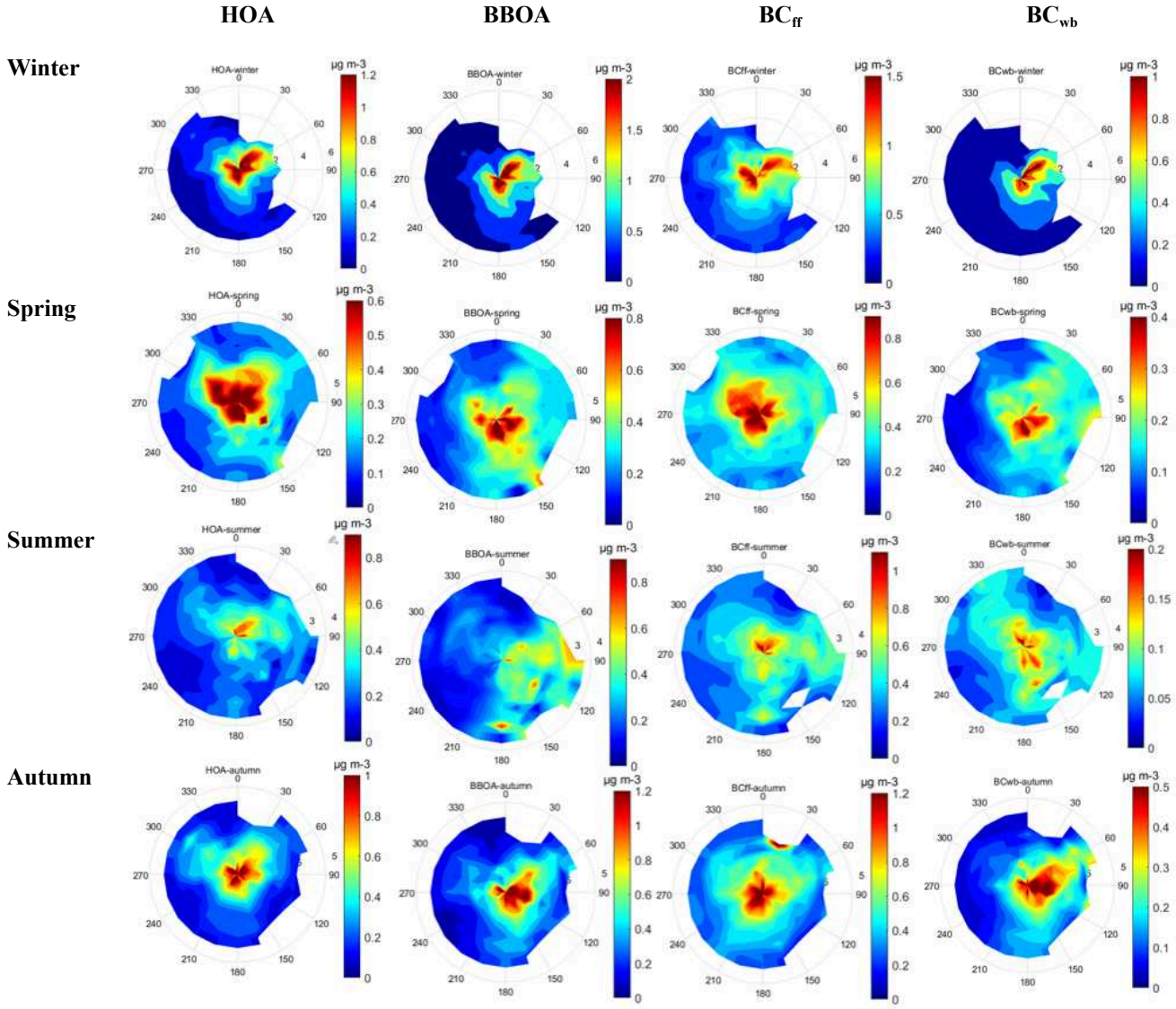

Figure S18: Pollution roses of POA PMF factors as well as BC fractions for each season

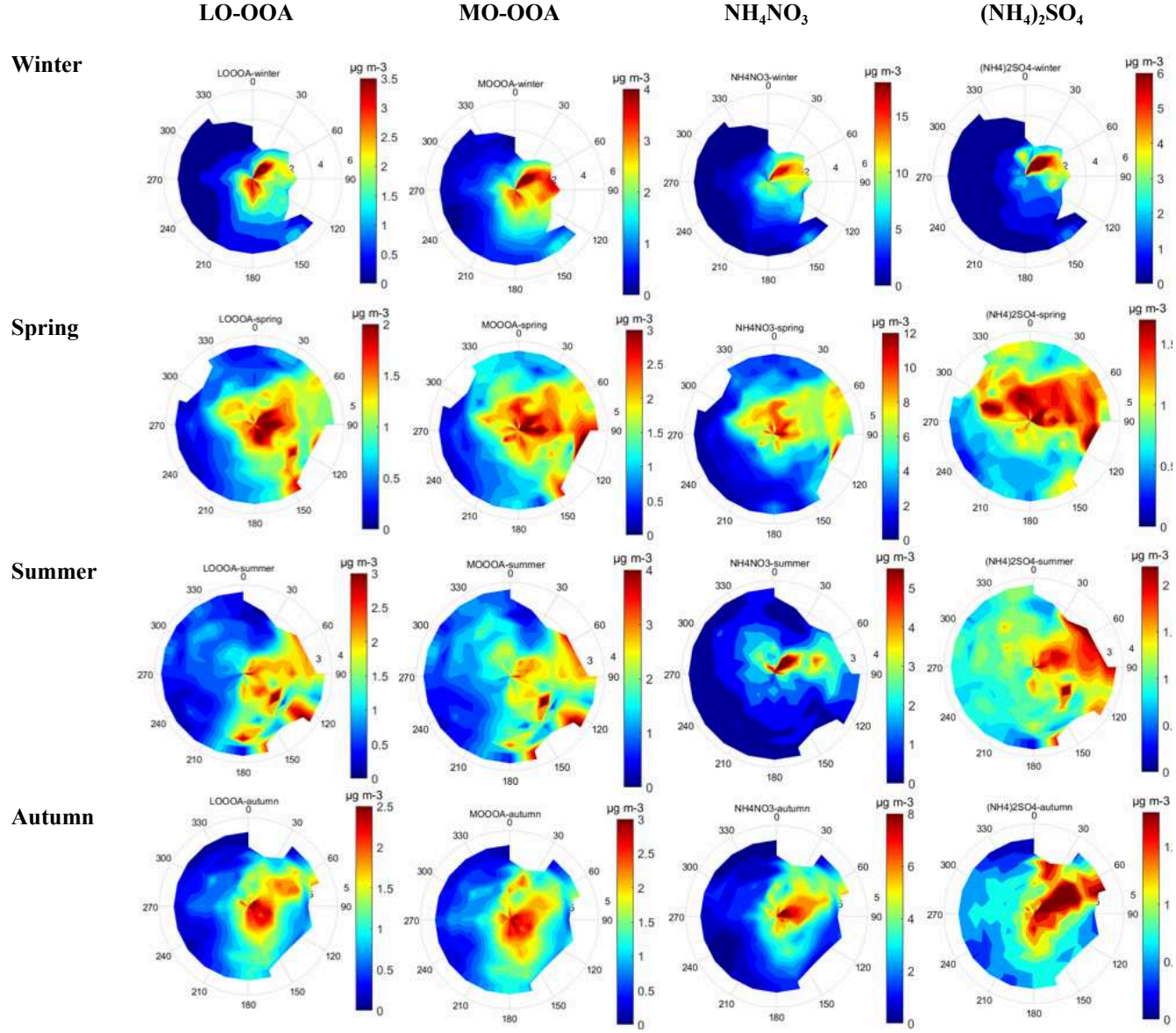

Figure S19: Pollution roses of SOA PMF factors as well as ACSM inorganic species for each season

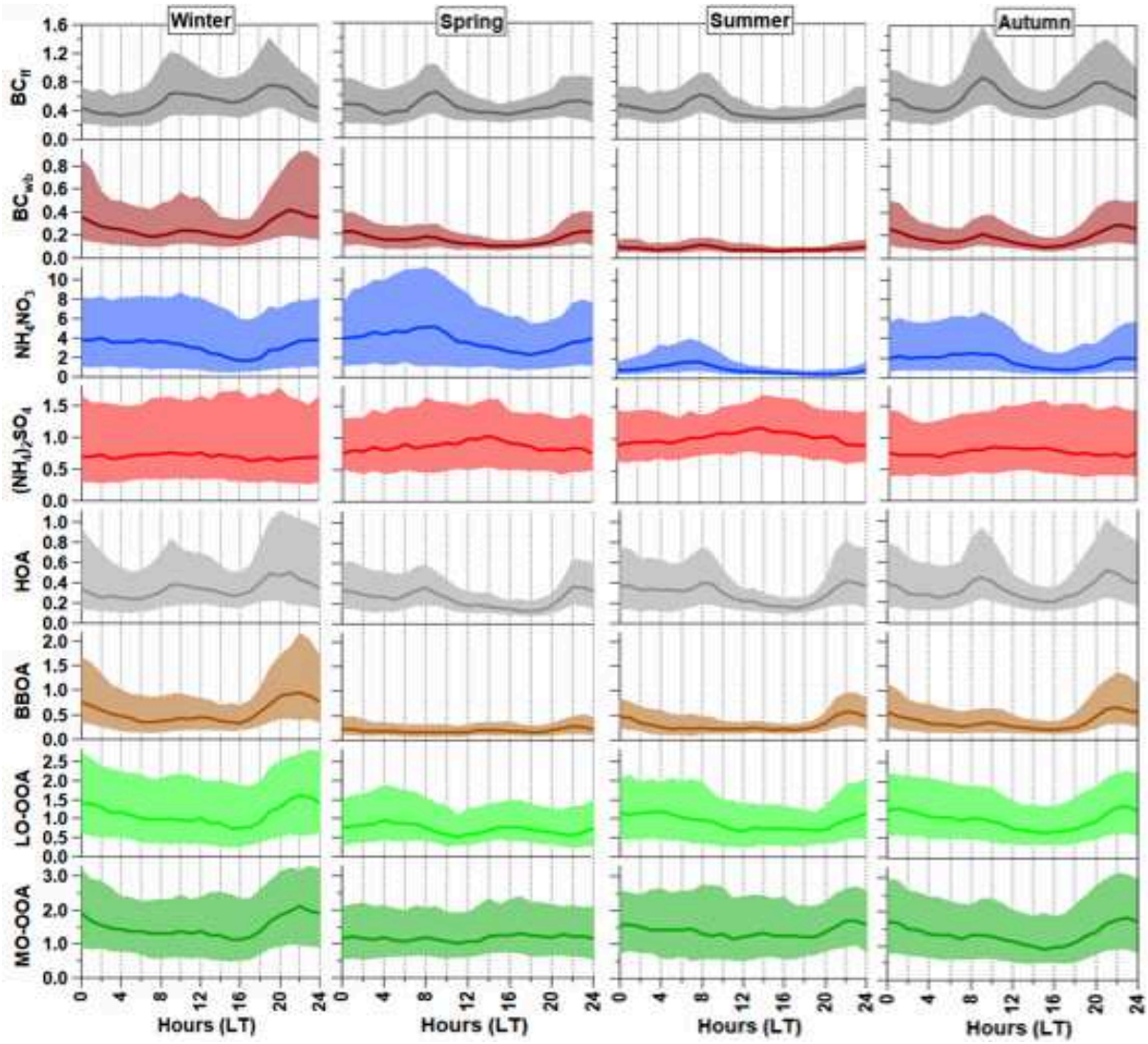

Figure S20: Diel cycles of the mass concentrations of BC fractions, NR-PM1 species and OA factors during each season. The shaded areas represent the interquartile range and the bold line in the middle represents the median

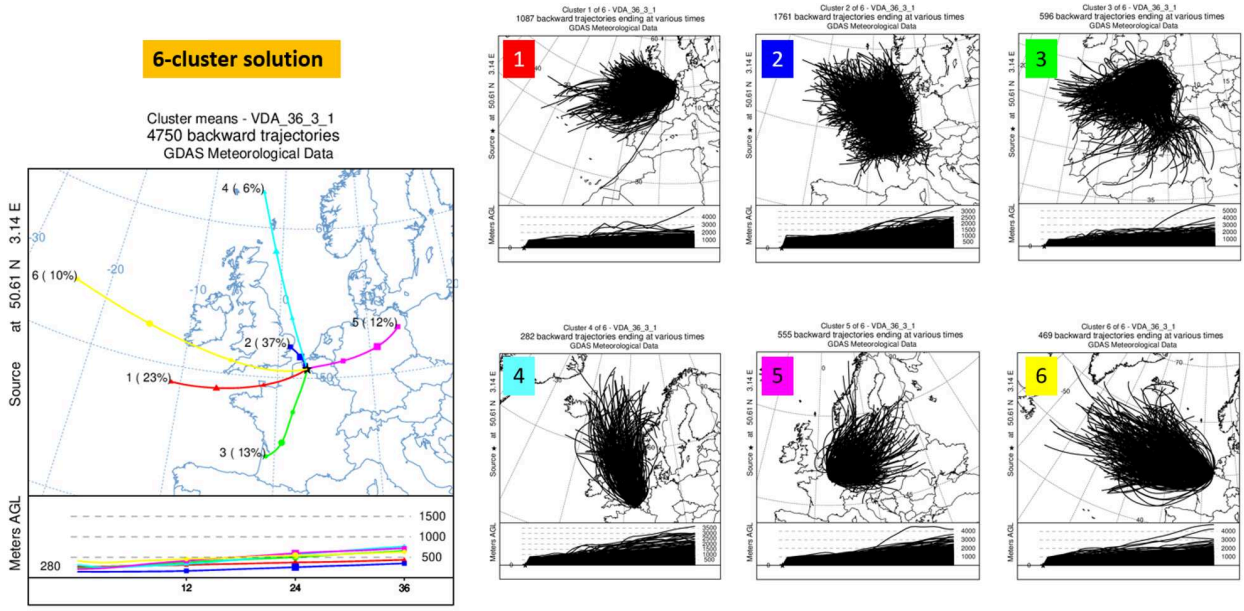

Figure S21: Cluster results retrieved from the back-trajectory analysis

References

Canonaco, F., Tobler, A., Chen, G., Sosedova, Y., Slowik, J. G., Bozzetti, C., Daellenbach, K. R., El Haddad, I., Crippa, M., Huang, R.-J., Furger, M., Baltensperger, U., and Prévôt, A. S. H.: A new method for long-term source apportionment with time-dependent factor profiles and uncertainty assessment using SoFi Pro: application to 1 year of organic aerosol data, Atmospheric Meas. Tech., 14, 923–943, https://doi.org/10.5194/amt-14-923-2021, 2021.

Chen, G., Sosedova, Y., Canonaco, F., Fröhlich, R., Tobler, A., Vlachou, A., Daellenbach, K. R., Bozzetti, C., Hueglin, C., Graf, P., Baltensperger, U., Slowik, J. G., El Haddad, I., and Prévôt, A. S. H.: Time-dependent source apportionment of submicron organic aerosol for a rural site in an alpine valley using a rolling positive matrix factorisation (PMF) window, Atmospheric Chem. Phys., 21, 15081–15101, https://doi.org/10.5194/acp-21-15081-2021, 2021.

Chen, G., Canonaco, F., Tobler, A., Aas, W., Alastuey, A., Allan, J., Atabakhsh, S., Aurela, M., Baltensperger, U., Bougiatioti, A., De Brito, J. F., Ceburnis, D., Chazeau, B., Chebaicheb, H., Daellenbach, K. R., Ehn, M., El Haddad, I., Eleftheriadis, K., Favez, O., Flentje, H., Font, A., Fossum, K., Freney, E., Gini, M., Green, D. C., Heikkinen, L., Herrmann, H., Kalogridis, A.-C., Keernik, H., Lhotka, R., Lin, C., Lunder, C., Maasikmets, M., Manousakas, M. I., Marchand, N., Marin, C., Marmureanu, L., Mihalopoulos, N., Močnik, G., Nęcki, J., O'Dowd, C., Ovadnevaite, J., Peter, T., Petit, J.-E., Pikridas, M., Matthew Platt, S., Pokorná, P., Poulain, L., Priestman, M., Riffault, V., Rinaldi, M., Różański, K., Schwarz, J., Sciare, J., Simon, L., Skiba, A., Slowik, J. G., Sosedova, Y., Stavroulas, I., Styszko, K., Teinemaa, E., Timonen, H., Tremper, A., Vasilescu, J., Via, M., Vodička, P., Wiedensohler, A., Zografou, O., Cruz Minguillón, M., and Prévôt, A. S. H.: European aerosol phenomenology − 8: Harmonised source apportionment of organic aerosol using 22 Year-long ACSM/AMS datasets, Environ. Int., 166, 107325, https://doi.org/10.1016/j.envint.2022.107325, 2022.

Crippa, M., DeCarlo, P. F., Slowik, J. G., Mohr, C., Heringa, M. F., Chirico, R., Poulain, L., Freutel, F., Sciare, J., Cozic, J., Di Marco, C. F., Elsasser, M., Nicolas, J. B., Marchand, N., Abidi, E., Wiedensohler, A., Drewnick, F., Schneider, J., Borrmann, S., Nemitz, E., Zimmermann, R., Jaffrezo, J.-L., Prévôt, A. S. H., and Baltensperger, U.: Wintertime aerosol chemical composition and source apportionment of the organic fraction in the metropolitan area of Paris, Atmospheric Chem. Phys., 13, 961–981, https://doi.org/10.5194/acp-13-961-2013, 2013.

Crippa, M., Canonaco, F., Lanz, V. A., Äijälä, M., Allan, J. D., Carbone, S., Capes, G., Ceburnis, D., Dall'Osto, M., Day, D. A., DeCarlo, P. F., Ehn, M., Eriksson, A., Freney, E., Hildebrandt Ruiz, L., Hillamo, R., Jimenez, J. L., Junninen, H., Kiendler-Scharr, A., Kortelainen, A.-M., Kulmala, M., Laaksonen, A., Mensah, A. A., Mohr, C., Nemitz, E., O'Dowd, C., Ovadnevaite, J., Pandis, S. N., Petäjä, T., Poulain, L., Saarikoski, S., Sellegri, K., Swietlicki, E., Tiitta, P., Worsnop, D. R., Baltensperger, U., and Prévôt, A. S. H.: Organic aerosol components derived from 25 AMS data sets across Europe using a consistent ME-2 based source apportionment approach, Atmospheric Chem. Phys., 14, 6159–6176, https://doi.org/10.5194/acp-14-6159-2014, 2014.

Ng, N. L., Canagaratna, M. R., Zhang, Q., Jimenez, J. L., Tian, J., Ulbrich, I. M., Kroll, J. H., Docherty, K. S., Chhabra, P. S., Bahreini, R., Murphy, S. M., Seinfeld, J. H., Hildebrandt, L., Donahue, N. M., DeCarlo, P. F., Lanz, V. A., Prévôt, A. S. H., Dinar, E., Rudich, Y., and Worsnop, D. R.: Organic aerosol components observed in Northern Hemispheric datasets from Aerosol Mass Spectrometry, Atmospheric Chem. Phys., 10, 4625–4641, https://doi.org/10.5194/acp-10-4625-2010, 2010.

Ng, N. L., Herndon, S. C., Trimborn, A., Canagaratna, M. R., Croteau, P. L., Onasch, T. B., Sueper, D., Worsnop, D. R., Zhang, Q., Sun, Y. L., and Jayne, J. T.: An Aerosol Chemical Speciation Monitor (ACSM) for Routine Monitoring of the Composition and Mass Concentrations of Ambient Aerosol, Aerosol Sci. Technol., 45, 780–794, https://doi.org/10.1080/02786826.2011.560211, 2011.

Tobler, A. K., Skiba, A., Canonaco, F., Močnik, G., Rai, P., Chen, G., Bartyzel, J., Zimnoch, M., Styszko, K., Nęcki, J., Furger, M., Różański, K., Baltensperger, U., Slowik, J. G., and Prevot, A. S. H.: Characterization of non-refractory (NR) PM_1 and source apportionment of organic aerosol in Kraków, Poland, Atmospheric Chem. Phys., 21, 14893–14906, https://doi.org/10.5194/acp-21-14893-2021, 2021.

Chapitre VI. Phénoménologie des sources d'aérosols organiques sur 12 sites de fond (péri-) urbains en France

VI.1. Résumé de l'article 4

Point d'orgue du présent travail de thèse, ce chapitre se concentre sur la détermination des sources de l'aérosol organique, espèce majeure des particules fines, sur les sites (péri-)urbains du programme CARA au cours de la même période que l'Article 1 (2015-2021). La méthodologie utilisée est la méthode PMF glissante (*rolling PMF)*, qui a été validée dans l'Article 3 sur la plateforme ATOLL, et qui permet de résoudre les principales sources d'AO sur les jeux de données multi-annuels (entre 1 et 7 ans, en fonction du site) à l'aide de l'approche *a-value* pour contraindre les facteurs primaires et l'approche *bootstrap* pour tester la stabilité de la solution PMF. Avant d'entamer ces PMF, une PMF classique sur un an de données a été réalisée sur 9 sites (à l'exception d'ATOLL, SIRTA et Marseille, où les analyses peuvent être trouvées dans Chebaicheb et al. 2023, Zhang et al. 2019 et Chazeau et al. 2021, respectivement). Ce travail a été réalisé en collaboration plus ou moins étroite avec les AASQA, en fonction des ressources dont elles disposaient ; les contributions de chacun ont été indiquées au Chapitre II, section II.7, Tableau II.3. Cette PMF a été appliquée sur quatre saisons (hiver, printemps, été et automne). L'objectif est d'identifier le nombre de facteurs pour chaque site, ceci permettant par la suite de fixer ce nombre dans la PMF glissante.

La PMF glissante a été effectuée sur une fenêtre de 28 jours avec un pas de 7 jours et 50 exécutions de PMF pour chaque fenêtre, avec l'inclusion de la méthode bootstrap. L'analyse a identifié les sources de facteurs communs d'AO, y compris les facteurs primaires (POA), l'AO de type hydrocarboné (HOA), de combustion de biomasse (BBOA) et celui lié aux activités de cuisson (COA). De plus, des facteurs secondaires d'AO oxygéné, plus (MO-OOA) ou moins oxydé (LO-OOA), ont été identifiés. Des facteurs d'AO spécifiques à certains sites ont également été résolus, tels qu'un facteur lié à des émissions portuaires et/ou industrielles à Marseille (ShInd-OA) et un facteur lié à des activités industrielles à Strasbourg et Creil (58-OA ou *amine-related-OA*). Un facteur MT-OA a également été résolu à Talence, qui pourrait être lié aux monoterpènes, et à l'environnement boisé constitué de forêts de pins.

Les résultats obtenus sont discutés dans cinq axes principaux. D'abord, les variations spatiales des facteurs identifiés ont été examinées en regardant leurs statistiques sur toute la période d'étude ainsi que leurs contributions. Les OOA dominent la masse totale d'AO sur tous les sites français avec une contribution moyenne de 74 %, proche de la moyenne obtenue sur 22 sites en Europe (71 %, Chen et al. 2022a). Ces facteurs oxygénés augmentent avec l'augmentation des niveaux d'AO en été, mettant l'accent sur l'importance de la formation secondaire. HOA et BBOA ont été résolus sur tous les sites et montrent des variabilités spatiales importantes. En moyenne annuelle, HOA varie entre 0.23 (Metz) et 0.93 µg m-³ à BPEST en raison de l'influence du trafic sur ce site routier. Les niveaux de HOA diffèrent aussi entre les régions, avec une moyenne de 0.6 µg m^{-3} au sud, 0.45 µg m^{-3} au nord, et une moyenne de 0.26 µg m^{-3} pour les sites dans la région Grand-Est. La contribution relative de HOA est de 12 % en France. Quant à BBOA, la moyenne relative est d'environ 14-15 % pour tous les sites, avec des contributions plus importantes au sud, en particulier en hiver (Favez et al., 2021) même si des contributions significatives sont également observées pour les autres stations. Un facteur de type COA a été identifié dans 8 sites avec des contributions comparables d'environ 13 % en moyenne, mais plus élevée à Paris Les Halles (18 %), ce qui reflète la spécificité de ce site au centre de Paris, proche de centres commerciaux et de nombreux restaurants, et au milieu d'une zone résidentielle particulièrement dense. Quatre autres facteurs spécifiques - identifiés sur un nombre limité de sites - ont des contributions minimales (ShInd-OA, 4 % et *amine related-OA*, 2 %). Les contributions des différents facteurs par rapport aux niveaux d'AO montrent une augmentation de BBOA lorsque l'AO augmente dans la majorité des sites, en particulier pendant l'hiver, suggérant un rôle particulier des émissions primaires de combustion de biomasse pendant les épisodes de pollution.

Dans un second temps, les variabilités saisonnières et journalières ont été examinées sur la période d'étude pour les facteurs communs à la plupart des sites, à savoir les facteurs primaires (HOA, BBOA et COA) et les facteurs secondaires (LO-OOA et MO-OOA), en s'intéressant à la médiane et l'écart interquartile (*InterQuartile Range*, IQR) des moyennes individuelles sur chaque site. Les facteurs primaires communs montrent une saisonnalité importante, très marquée pour le BBOA (augmentation des émissions de chauffage domestique) et moins pour HOA et COA. En général, les trois facteurs primaires augmentent pendant les mois hivernaux, ce qui peut s'expliquer par des conditions stagnantes (températures basses et vents faibles). Les deux facteurs

de type OOA restent plutôt stables sur toute la période, bien que LO-OOA présente des maxima saisonniers, en été et en hiver. Cette dualité suggère différentes sources et/ou mécanismes de formation à l'origine de ce type de spectres de masse en fonction du moment de l'année. Différents éléments suggèrent son association avec les AOS biogéniques (BSOA) en été, et avec la combustion de la biomasse en hiver. Ces hypothèses sont notamment étayées par l'analyse des variations journalières par saison, où le HOA présente deux pics aux heures de pointe du trafic et le COA montre un pic à midi et le soir, correspondant aux heures des repas. Ces deux facteurs présentent une saisonnalité faible par rapport à BBOA, qui montre un pic important le soir, surtout en hiver, en raison du chauffage domestique au bois. En revanche, les OOA ont une variabilité journalière stable, avec un LO-OOA hivernal corrélé avec BBOA, et un LO-OOA estival montrant une augmentation en journée, associé plutôt à la formation de BSOA. Quant à MO-OOA, il est plutôt stable, témoignant d'une origine plutôt régionale et vieillie pour ce facteur.

Les troisième et quatrième parties de cet article en préparation discutent des avantages de la méthode PMF utilisée. La troisième partie s'attache à l'étude du degré d'oxydation, et de ses variations saisonnières, en relation avec les origines possibles de l'AO. Cette analyse tire profit de la particularité de la PMF glissante qui permet d'étudier les variations saisonnières de la signature chimique des facteurs identifiés (Canonaco et al., 2015). Ceci est bien marqué pour les LO-OOA qui présentent une abondance relative de la masse m/z 44 vs. m/z 43 plus élevée en été qu'en hiver, suggérant l'influence principale du BSOA en saison chaude et d'émissions primaires de combustion de biomasse en période froide. En outre, la position des facteurs LO-OOA et MO-OOA sur le graphique qui présente les variations de f43 (Org_{43}/Org_{total}) en fonction de f44 (Org_{44}/Org_{total}), peut être fortement influencée par les spécificités des sites de mesure étudiés. En prenant l'exemple de Talence, un site caractérisé par une importante contribution des émissions de combustion de biomasse et une forte influence des SOA biogéniques, la position de LO-OOA reste ainsi du côté droit du graphique. Ce type d'analyse permet d'évaluer la diversité des origines des facteurs OOA, généralement décrit comme la fraction majoritaire de l'AO à l'échelle planétaire.

La quatrième partie s'attache à comparer les profils chimiques des différents facteurs PMF, en particulier les facteurs communs aux différents sites d'étude, en utilisant des tests de similarité, à

savoir *Pearson Distance* (PD) et *Similarity Identity Distance* (SID) (Belis et al., 2015). Les résultats obtenus montrent une grande cohérence entre les divers sites d'étude. Ceci est logiquement observé pour les facteurs HOA et COA, car ces facteurs ont été contraints dans la PMF, mais également pour les autres facteurs. En particulier le BBOA, le LO-OOA et le MO-OOA sont relativement stables sur tous les sites, mais avec une certaine dissemblance dans les fragments qui constituent les masses primaires du profil, traduisant tout de même des influences différentes en fonction de l'emplacement du site, de la nature et des conditions de combustion et du vieillissement chimique, mais également des éventuelles variations instrumentales, qui influencent les spectres de masse.

Enfin, le dernier axe illustre l'intérêt de l'ensemble de ces résultats PMF pour valider ou améliorer la performance des modèles de qualité de l'air. A titre d'exemple, une comparaison avec les simulations 3D CHIMERE - telle qu'introduite au chapitre 4 pour l'année 2018 - est approfondie ici pour neuf sites urbains français où les données sont disponibles, en se concentrant sur la fraction organique. Pour ce faire, nous avons comparé BBOA à la somme des espèces POA provenant de la combustion de biomasse sans leurs produits vieillis (BOA), HOA aux espèces POA provenant d'autres sources d'émission sans leurs produits vieillies, et OOA avec tous les composés SOA (y compris les produits de vieillissement des POA). En général, le modèle surestime le BBOA et sous-estime HOA et OOA. Le fait d'ajouter des POA vieillis pour les comparer avec HOA améliore la représentation du modèle, mais il subsiste un déficit notable. L'OOA est surtout sous-estimé en hiver, suggérant un manque de sources anthropiques dans le modèle. Mais en général, les corrélations entre les résultats PMF et le modèle sont plutôt bonnes. En hiver, LO-OOA corrèle bien avec les POA vieillis, les SOA anthropiques et les espèces BOA, et en été, avec les espèces SOA biogéniques du modèle, ce qui confirme nos conclusions concernant ce facteur. En revanche, MO-OOA ne montre aucune corrélation claire aux deux saisons.

VI.2. Article 4

Phenomenology of organic aerosol multi-annual source apportionment at 12 urban and suburban sites in France

Hasna Chebaicheb[1,2,3], Joel F. de Brito[1], Jean-Eudes Petit[4], Benjamin Chazeau[5,6], Mélodie Chatain[7], Gregory Abbou[8], Alexia Baudic[8], Raphaële Falhun[9], Florie Francony[10], Cyril Ratier[10], Didier Grenier[11], Nicolas Vigier[11], Shouwen Zhang[12], Emmanuel Tison[1], Laurent Meunier[2,3], Tanguy Amodeo[2,3], Nicolas Marchand[5], Florian Couvidat[2], Véronique Riffault[1,3], Olivier Favez[2,3]

[1]IMT Nord Europe, Institut Mines-Télécom, Université de Lille, Centre for Energy and Environment, 59000, Lille, France
[2]Institut National de l'environnement Industriel et des Risques (INERIS), 60550 Verneuil-en-Halatte, France
[3]Laboratoire Central de Surveillance de la Qualité de l'Air (LCSQA), 60550 Verneuil-en-Halatte, France
[4]Laboratoire des Sciences du Climat et de l'Environnement (LSCE), CNRS-CEA-UVSQ (UMR 8212), 91191 Gif-sur-Yvette, France
[5]Univ. Aix-Marseille, LCE (UMR7376), Marseille, France
[6]Atmo Sud, 13294 Marseille, France
[7]Atmo Grand Est, 67300 Schiltigheim, France
[8]Airparif, 75004 Paris, France
[9]Air Breizh, 35200 Rennes, France
[10]Atmo Nouvelle-Aquitaine, 33692 Mérignac, France
[11]Atmo Auvergne Rhône-Alpes, 69500 Bron, France
[12]Atmo Hauts de France, 59044 Lille, France

Correspondence to: hasna.chebaicheb@ineris.fr

In preparation

Abstract.

This study presents the first phenomenology of submicron organic aerosol (OA) source apportionment analysis in France, using highly time-resolved *Aerosol Chemical Spectrometer Mass* (ACSM) data from 12 (sub)urban sites spanning from one to seven years, with an average of four years. The rolling *Positive Matrix Factorization* (PMF) method was applied, following consistent constraints and criteria for all data sites. The analysis identifies common OA factor sources, including primary OA (POA) factors, hydrocarbon-like OA (HOA), biomass burning OA (BBOA), and cooking-like OA (COA), contributing to approximately 15 % of the total mass. Additionally, secondary oxygenated OA (OOA) factors, including Less Oxidized (LO-OOA) and More Oxidized OOA (MO-OOA), were identified, dominating the OA across all sites with a 74% contribution. Site-specific OA factors were also resolved, such as a mixed shipping and industrial OA factor in Marseille (ShInd-OA, 4%) and an amine-related OA factor in Strasbourg and Creil (58-OA, 2%).

POA factors exhibited significant seasonality, especially BBOA, which increased during winter due to residential heating, displaying the greatest spatial variability attributed to different wood types and combustion conditions. LO-OOA correlated with BBOA in winter, highlighting the contribution of biomass combustion, which needs more attention to reduce its emissions in order to improve air quality. In contrast, LO-OOA is associated with biogenic SOA in summer, at high temperatures. Therefore, OOA factors exhibited spatial and seasonal fluctuations linked to various biogenic and anthropogenic sources.

These findings hold great importance for many other scientific research, including epidemiological studies, and they also offer valuable insights for improving air quality models. In this regard, a comparison with model simulations of the CHIMERE model revealed an overestimation for BBOA and an underestimation of HOA and OOA, indicating the need to incorporate additional aerosol compounds, particularly anthropogenic ones, into the model.

Keywords. Organic aerosols, rolling PMF, source apportionment, urban pollution, air quality, France

1 Introduction

Atmospheric aerosol particles, arising from both natural sources and human activities, hold significant importance in influencing the Earth's climate and contributing to adverse effects on human health. Those aerosol particles, also known as Particulate Matter (PM), pose a significant threat to human health due to their small size, enabling them to penetrate deep into the lungs while carrying adsorbed toxic substances (Nyström, 2016). Exposure to ambient PM has been associated with a range of adverse health effects, including an elevated risk of cardiovascular and respiratory diseases leading to increased mortality, exacerbation of skin conditions, heightened blood pressure, elevated biomarkers of inflammation, coagulation, and lipid peroxidation, as well as a decrease in lung function (Boucher, 2015; Vicente and Alves, 2018). In Europe, PM values stipulated by the EU Directive 2008/50/EC are frequently exceeded in numerous regions, for both PM_{10} and $PM_{2.5}$, i.e. particle sizes below 10 and 2.5 µm, respectively (EEA, 2022). Furthermore, new air quality guidelines by the World Health Organization in 2021 (WHO, 2022) aim at lowering even further PM levels, often exceeded in France, as well as other European countries. Although average urban $PM_{2.5}$ concentrations at the regional level showed a decrease between the years 2000 and 2019, significant diversity in $PM_{2.5}$ concentration trends is observed among urban areas (Southerland et al., 2022). While public policies have been implemented to reduce fine particulate emissions from industrial processes, power generation, and transportation, residential wood combustion, which has been considered an interesting source of energy compared to fossil fuels with regard to the climate issue, has emerged as a primary source of organic aerosols and its impact on air quality has to better quantified (Cincinelli et al., 2019).

Given that the majority of the world's population resides in urban areas, understanding exposure to air pollution at this scale can play an important role in developing measures to reduce its effects (Southerland et al., 2022). In these regions, PM_1 components, notably organics, nitrate, and sulfate, represent the majority of the total particle mass (Bressi et al., 2021). In France, organic aerosols (OA) account for 43-60 % of PM_1 (Chebaicheb et al., in prep.). They constitute a complex mixture, originating from various sources (both biogenic and anthropogenic) and forming in the atmosphere through diverse mechanisms and reactions (known as secondary organic aerosols, SOA). Understanding their origins is essential for air pollution mitigation and improved understanding of their climatic and health effects (Crippa et al., 2013).

Several studies have conducted source apportionment (SA), and those focusing on OA have largely used positive matrix factorization (PMF; Paatero, and Tapper, 1994). These studies have employed real-time measurements obtained from aerosol mass spectrometry, including the Aerosol Mass Spectrometer (AMS) and the Aerosol Chemical Speciation Monitor (ACSM). Zhang et al. (2011) reviewed the different SA techniques applied to AMS data with a summary of the valuable insights into OA sources, then Crippa et al. (2014) conducted a comprehensive overview of OA sources throughout Europe using 25 datasets from AMS and provided guidelines for applying PMF method. Recently, Chen et al. (2022) have explored the main sources of OA at 22 European sites focusing on 1-year ACSM datasets through a standardized protocol and through the "rolling PMF" method. This approach enables the tracking of temporal variations in OA factors. This study evidenced several distinct sources of OA, including hydrocarbon-like OA (HOA, primarily associated with vehicular traffic emissions), biomass-burning OA (BBOA), cooking-like OA (COA), coal combustion OA (CCOA), and some site-specific OA originating from industrial and other activities. Additionally, the study identified oxidized oxygenated OA (OOA) resulting from secondary atmospheric transformations. Notably, OOA components contributed significantly to the overall fine OA mass, although our understanding of this fraction remains limited (Chen et al., 2022). Furthermore, the rolling PMF method has been recently applied to a multi-annual dataset at the ATmospheric Observations in liLLe (ATOLL), in Northern France, allowing to identify a significant role of residential heating during winter (>50% of OA), as well as a large contribution from secondary processes, including from biogenic sources (Chebaicheb et al., 2023). The main objective of this study is to expand the multi-annual analysis carried out at ATOLL into a phenomenology of OA sources at 12 (sub)urban sites in France with various source and climatological profiles, encompassing a period from 2015 to 2021. The OA phenomenology is further compared against state-of-the-art numerical modeling (Wang et al., 2022) for the 2018 reference year, allowing to gain insights into aerosol sources and processes, and provide directions for an improved numerical representation of the atmosphere across Europe.

2 Methodology

2.1 Sites and instrumentation

The present study encompasses 12 sites within the French operational CARA program network (Favez et al., 2021), 10 of which belong to the French Air Quality Networks (AASQAs), and are located within large urbanized areas. The list is complemented by two suburban observation platforms, namely ATOLL (located 4 km southeast from downtown Lille) and SIRTA (situated approximately 20 km southwest of the center of Paris). More details about each site can be found in Chebaicheb et al. (2023) for ATOLL, Zhang et al. (2019) for SIRTA, Chazeau et al. (2021) for Marseille, and Chebaicheb et al. (in prep.) for the other sites. Non-refractory PM_1 composition, along with equivalent black carbon (eBC), has been measured at all these sites using ACSM instruments (Aerodyne Reseach Inc., USA) and a multi-wavelength Aethalometer (model AE33, Magee Scientific, USA), respectively. Figure 1 reports the periods of concurrent ACSM and AE33 observations, corresponding to 7-year datasets for SIRTA and Lyon (2015-2021), followed by 4-5 years of data for three urban background sites in the southern part of France (Poitiers, Talence, and Marseille) and two urban sites in the north (ATOLL in Lille and Creil located 45 km north of Paris). Additionally, two years of data have been collected from two sites located in the east of France near the German border, Strasbourg and Metz. Finally, there are three sites within Paris - Gennevilliers, Paris Les Halles, and Boulevard Périphérique Est (BPEst) - with one year of data, the latter being characterized as a traffic station, with fewer measurements collected in 2022.

The datasets include 11 Quadrupole ACSM (Q-ACSM) instruments and one Time-of-Flight (ToF-ACSM) instrument (Marseille site). Briefly, the ACSM samples air through an inlet system composed of a critical orifice and an aerodynamic lens, to collect aerosol particles efficiently between about 100 and 1000 nm. Inside the instrument, the particles are vaporized at 600 °C, ionized through electron impact at 70 eV, and introduced into a mass spectrometer, where the ions are separated based on their mass-to-charge ratios (m/z). This separation enables the identification of different chemical species present in the aerosol particles, including organic compounds (OA), nitrate (NO_3), sulfate (SO_4), ammonium (NH_4), and chloride (Cl). A detailed description of the instrument can be found in Ng et al. (2011) for the Q-ACSM and Fröhlich et al. (2013) for the ToF-ACSM. To ensure the accuracy and reliability of ACSM measurements,

rigorous calibration exercises have been conducted periodically at the *Aerosol Chemical Monitor Calibration Centre* (ACMCC), as well as on-site calibrations.

On the other hand, the eBC concentrations were calculated at 880 nm, by normalizing the absorption coefficients (b_{abs}, considering a harmonization factor of 1.76 for the using the MF8060 filter tape) by a mass absorption cross-section (MAC) of 7.5 m^2 g^{-1}, following the current ACTRIS guidelines (https://actris-ecac.eu/particle-light-absorption.html). Furthermore, we have applied the Sandradewi model (Sandradewi et al. 2008) to differentiate between eBC sources associated with fossil fuel (eBC_{ff}) and wood burning (eBC_{wb}), using Ångström absorption exponents (AAE) of 1 (AAE_{ff}) and 2 (AAE_{wb}), respectively (Drinovec et al., 2015). Collection and treatment of NR-PM_1 and eBC follow the guidelines from ACTRIS (Aerosols, Clouds, and Trace gases Research Infrastructure, https://www.actris-ecac.eu/measurement-guidelines.html), and more details about their data processing can be found in Chebaicheb et al. (in prep.).

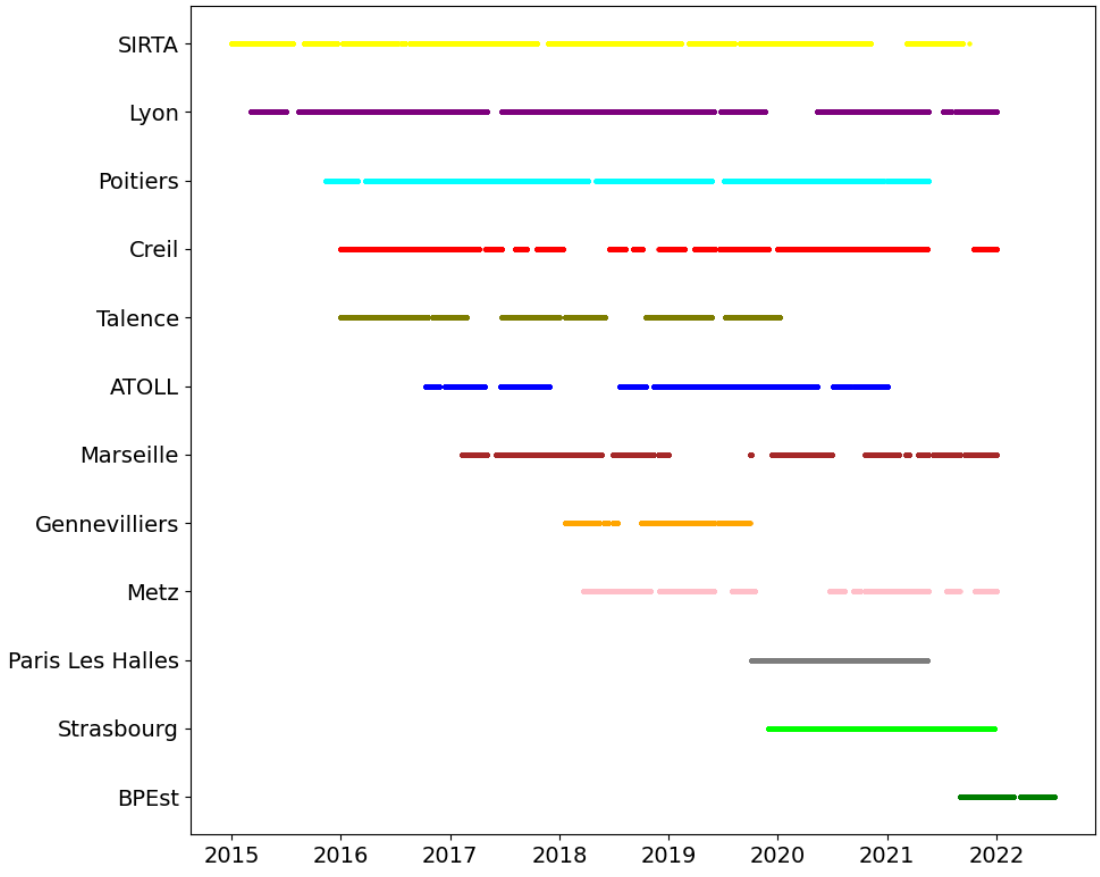

Figure 1: Temporal coverage of organic aerosol data.

2.2 Source apportionment of OA

Prior to conducting multi-year rolling PMF, it is necessary to perform "seasonal" PMF analyses over a one-year reference year, namely four PMF analyses per site to identify OA profiles at each given site under a range of different meteorological conditions. Once those profiles are identified, they are used to run rolling PMF through the entire multi-annual dataset. The rolling PMF was applied to the ATOLL site by Chebaicheb et al. (2023) for the period 2016-2020. Chazeau et al. (2022) also conducted a rolling PMF analysis on the Marseille Longchamps dataset but only for a single year (2017-2018). The rolling PMF at SIRTA was reported by Chen et al. (2022) for the year 2017 and a seasonal PMF has also been performed by Zhang et al. (2019) over a six-year period (2011-2018).

In this work, the PMF analyses were carried out using SoFi Pro V8 (Source Finder Professional, Datalystica Ltd., Switzerland) within the Igor Pro V8 software environment (Wavemetrics, Inc., USA). These PMF analyses were performed using the a-value approach and bootstrap analysis. The a-value approach, when a priori information is known, allows applying constraints on expected factor profiles or time series using the ME-2 solver (Paatero, 1999). The bootstrap analysis (Efron, 1979), involves data resampling to assess solution stability and estimate the uncertainties associated with the analysis.

2.2.1 Seasonal PMF analysis

First, an unconstrained PMF is performed for each season of a reference year across all sites, varying the number of factors from 3 to 8. The list of reference years per site is given in Table S1, with the reference year typically 2018 based on data coverage. This initial step aimed to pre-determine the potential number of factors for each site by evaluating the factor profiles, their time series, diel and weekly variations, scaled residuals, and their correlations with external data (such as eBC deconvolved data, secondary inorganic species, other atmospheric pollutants, etc.). For the majority of sites, four to six-factor solutions were obtained. These solutions revealed common primary factors across all sites, including HOA, BBOA and COA. However, site-specific factors also emerged, such as 'ShInd-OA' in Marseille, associated with a mixture of

industrial and shipping emissions, and an amine-related factor identified in Creil and Strasbourg, characterized by significant presence of m/z 58 (likely dominated by the ion $C_3H_8N^+$). A separate PMF study for Strasbourg is presented in another paper, including ACSM measurements at two sites and a comparison between individual and combined PMF analyses (Chebaicheb et al., in prep.).

HOA is characterized by a substantial contribution of hydrocarbon-like traffic masses (m/z 41, 43, 55, and 57) and a strong correlation with eBC_{ff}. The factor was typically constrained using the one from Crippa et al. (2013), using an a-value ranging from 0 to 0.3, except at sites strongly impacted by vehicular emissions (Creil and BPEst), which allowed for clear factor identification during unconstrained runs, particularly in autumn. This seasonal profile was chosen due to the intense vehicular activities (unlike summer, encompassing holidays) and reduced contributions from other sources such as residential heating in winter and agricultural activities during spring (e.g. Chebaicheb et al., 2023). The COA factor was identified at urban sites located close to city centers, where cooking emissions from nearby restaurants play a significant role and peaks are observed during meal times, around noon and in the evening. These urban sites encompass Gennevilliers, Creil, Paris Les Halles, Metz, Strasbourg, Lyon, Poitiers, and Marseille. For some sites where its occurrence was obvious, like Paris Les Halles, Creil, and Lyon, we directly extracted this factor from the unconstrained PMF analysis, while for other sites, we constrained it using the one from Crippa et al. (2013) with an a-value varying from 0 to 0.3. HOA and COA were constrained with these a-value ranges due to their observed similarities across various sites, as reported by Crippa et al. (2014) and Chen et al., (2022).

To extract the site-related BBOA factor, we conducted constrained PMF analyses that included HOA and/or COA factors. BBOA is characterized by a notable contribution of biomass burning tracers (m/z 29, 60, and 73), a distinct diel profile with a prominent nighttime peak, and a strong correlation with eBC_{wb}. This local factor was successfully identified at most sites, where it was extracted during periods of increased residential heating emissions, particularly during the winter season. For other sites, we constrained the BBOA profile using the one from Crippa et al. (2014), with an a-value ranging from 0 to 0.5. We chose this higher a-value range due to the observed higher spatial variability in BBOA profiles (Crippa et al., 2014).

Common secondary factors, identified as Oxygenated OA (OOA), were resolved at all sites. These OOA factors were further categorized into less oxidized (LO-OOA) and more oxidized

(MO-OOA) based on their oxidation degree and m/z 44/43 ratio. Consequently, these factors are not constrained, as they exhibit seasonal variations stemming from distinct precursor sources and atmospheric secondary processes. The exception is observed in Poitiers and Strasbourg, where only the MO-OOA factor was resolved. For these sites, including an additional factor would merely split existing components and would not contribute meaningfully to the PMF solution. In addition, at the Talence site, a monoterpene OA factor was identified. It is to be noted that this site is characterized by its proximity to many pine forests. The mass spectrum of this factor correlated well with the SOA one obtained in laboratory experiments for limonene ozonolysis (r^2=0.8). Its diel profile peaked between midnight and early morning hours (around 4 am) in summer, pointing at nighttime chemistry of monoterpenes, which are oxidized by NO_3 radicals at low temperatures (Figure S1). Additionally, the diel profile is comparable with the NightSOA1 factor identified by Stefenelli et al. (2019) in Zurich in summer. In contrast, in winter, the diel profile of this factor is correlated to the BBOA factor, indicating that this factor is probably related to domestic wood burning during this period of the year (i.e., pine cone burning).

Following the factor determination step for each site, we performed a bootstrap analysis where we constrained the primary factors using random a-values ranging from 0 to 0.4 with a step of 0.1 (Canonaco et al., 2021). This step was essential to assess the stability of the solutions. It involved running PMF 100 times and applying selected criteria (as outlined in Table S2) to choose reasonable solutions for averaging. Subsequently, the OA factor mass spectra from the constrained factors in the averaged bootstrap solution were used for the subsequent rolling PMF analysis.

2.2.2 Rolling PMF analysis

The rolling PMF analysis for these multi-year datasets (2015-2021) followed the same methodology as employed in Chebaicheb et al. (2023) for a four-year analysis at the ATOLL site and the protocol proposed by Chen et al. (2022). This approach allows for the application of PMF on small periods, referred to as PMF windows, which shift over the entire dataset with a given step, while maintaining consistent criteria and constraints. This method facilitates the capture of temporal variations in factor profiles (an example is illustrated in Figure S2).

In this study, a window length of 28 days, with a step of seven days, was employed for the rolling PMF analysis, with 50 repetitions for a fixed number of factors. Only at the Marseille site, the rolling PMF was applied with 5 to 6 factors, as the BBOA factor is very limited during the summer season (Chazeau et al., 2022).

The primary factors, including HOA, COA, and BBOA were constrained using the averaged solutions derived from the bootstrap seasonal analysis, with a random a-value ranging from 0 to 0.4 (Canonaco et al. 2021). Oxygenated OA factors were left unconstrained to explore the secondary processes of OA, while the specific site-related factors were constrained with an a-value of 0.05 so as not to mix with other - more predominant - factors.

Furthermore, the bootstrap analysis was incorporated into this analysis to account for model uncertainties. A criterion-based selection process was applied using SoFi Pro to evaluate the PMF solutions and choose the most suitable PMF runs. These criteria were based on correlations with external factors, utilizing the t-test to filter out unreasonable results, as well as monitoring and factor sorting criteria. A detailed list of these criteria can be found in Table S2.

2.3 Statistical data analysis

The different temporal variabilities (annual, monthly, weekly, and diel) for the rolling PMF results are determined from the entire dataset (2015-2022) for all sites using the median and the InterQuartile Range (IQR; 25th and 75th percentiles) calculated from the individual mean values for each site, if more than 75 % of the values are present for each month/day, etc.

The tests of similarity between factor profiles are calculated using the Pearson Distance (PD) and Similarity Identity Distance (SID) similarity metrics (Belis et al. 2015), following these equations:

$$PD = 1 - r^2 \quad \text{(Eq. 1)}$$

$$SID = \frac{\sqrt{2}}{m} \sum_{j=1}^{m} \frac{|x_j - y_j|}{x_j + y_j} \quad \text{(Eq. 2)}$$

where r^2 is the Pearson coefficient, x and y represent the relative mass to the total OA of two different factors and j=1 to m common m/z in x and y. Briefly, these two metrics allow comparing

two profiles by analyzing their shared chemical relative mass composition. The PD metric is particularly responsive to changes in the primary mass fractions of the OA, whereas the SID metric exhibits equal sensitivity to all components. As per the guidelines outlined by Pernigotti and Belis, (2018), profiles are considered similar when PD is less than 0.4 and SID is less than 1, meeting the acceptable criteria for profile similarity.

2.4 The CHIMERE model

Finally, in order to compare the PMF results to modeled SOA contributions, 3D simulations were conducted with the CHIMERE CTM model (Menut et al. 2021). CHIMERE was coupled with the SSH-aerosol model v1.3 (Sartelet et al., 2020), which allows the computation of gas-particle partitioning with the SOAP thermodynamic module (Couvidat et al., 2015). Thermodynamic equilibrium was assumed for gas-particle partitioning.

The simulations were performed with reduced mechanisms obtained with the GENOA algorithm (*GENerator of reduced Organic Aerosol* mechanisms v2.0). This algorithm was used to reduce the SOA mechanisms for monoterpenes and sesquiterpenes from the Master Chemical Mechanism (Saunders et al., 2003) coupled with PRAM (in order to account for SOA formation from monoterpenes by autoxidation) (Roldin et al., 2019). Full details on the reduced mechanisms by GENOA are available in Wang et al., (2022, 2023).

Primary organic aerosols (POA) are assumed to be semi-volatile: the compounds are thus partitioned between the gas and aerosol phases and can undergo aging. POA were distributed by volatility following the dilution curve of May et al. (2013) for wood burning and Robinson et al. (2007) for other emission sources.

The simulations were performed over France for the year 2018 at a resolution of around 7 km. The simulation was nested by a simulation over Europe at a resolution of 0.25° × 0.4°. Boundary conditions of the European simulation are taken from CAMS CIFS global model simulations, and meteorology data from the operational analysis of the Integrated Forecasting System (IFS) model of the European Centre for Medium-Range Weather Forecasts (ECMWF) (Flentje et al., 2021). The emissions inventory used for this simulation was CAMS-REG 2018 REF2.1 (Kuenen et al.,

2022), including the corresponding PM speciation data. Notably, the simulation did not include emissions of intermediate volatile organic compounds (IVOC).

3 Results

This section presents the results of rolling PMF analysis applied to multiple multi-year datasets across France, highlighting their distinct spatial (3.1) and temporal variabilities (3.2), as well as detailed OA profile analysis (3.3 and 3.4). Finally, section 3.5 provides a comparative analysis with state-of-the-art 3D modeling results, allowing insights into both factor sources/properties as well as the improvement directions for the model.

3.1 Spatial variations

Figure 2 illustrates the PMF results of OA for 12 multi-year (sub)urban datasets for the different stations across France, while Figure 3 represents some key statistics across the whole period. The chemical composition of PM_1 (NR-PM_1 + eBC) for these datasets was previously discussed in Chebaicheb et al. (in prep.), highlighting spatial and temporal variations from 2015 to 2021. The average PM_1 concentration was 9.4 ± 8.3 µg m^{-3}, which is lower than the average mass concentrations at urban stations in Europe (12.2 ± 9.3 µg m^{-3}) reported by Chen et al. (2022). PM_1 are dominated by OA across France (52 % on average), which aligns with the contribution (reported on the one-year analyses conducted in Europe (around 50 % of PM_1 in urban sites, Chen et al., 2022). The mean OA mass concentration ranged from 3.3 µg m^{-3} in Strasbourg up to 6.0 µg m^{-3} at the BPEst site, primarily due to traffic-related influence at that location.

The pie charts show the predominance of secondary factors (corresponding to OOA, whether split or not into LO-OOA+MO-OOA, and MT-OA in Talence), ranging from 55-59 % in Marseille, Poitiers and Paris Les Halles up to 74-75 % at SIRTA, ATOLL, Metz and BPEst, with an average contribution of 74 % in France, consistent with the average across Europe (71.1 %; Chen et al., 2022). LO-OOA was resolved at 10 sites, with mass concentrations varying from 0.86 µg m^{-3} in Metz to 1.76 µg m^{-3} at BPEst, and MO-OOA at all sites ranging from 1.06 µg m^{-3} at Paris Les Halles to 2.75 µg m^{-3} at BPEst. Regarding relative contributions in total OA across France, LO-OOA varied between 19-20 % (in Talence and Marseille) and 32 % (at ATOLL),

while MO-OOA ranged between 29 % (in Talence) and 61 % (in Strasbourg). Furthermore, the secondary MT-OA factor, resolved only at the Talence site, accounted for 17 %.

The contributions of primary combustion factors (HOA and BBOA) exhibit substantial variability across sites. BPEst showed the highest HOA contribution, accounting for 16 % with a mass concentration of 0.93 μg m^{-3}, while the lowest contributions were observed in Metz (7 %, 0.23 μg m^{-3}) and Lyon (7 %, 0.35 μg m^{-3}) sites. On average, HOA constitutes 11.6 % of the total OA mass at all urban sites in France. Overall, the mass concentrations of HOA vary across sites, with relatively high levels in the south of France, averaging 0.6 μg m^{-3}, followed by comparable levels in the north and central regions (ATOLL, Paris, Lyon), averaging 0.45 μg m^{-3}. Lower levels are observed at eastern sites (Strasbourg, Metz), with an average of 0.26 μg m^{-3}.

The BBOA factor ranges from 9 % at Metz and BPEst sites (with a mass concentration of 0.31 μg m^{-3} and 0.55 μg m^{-3}, respectively) to 22 % (1.21 μg m^{-3}) at the Talence site. This variability highlights significant contributions from biomass burning, especially at the southern sites (Talence, Poitiers, Marseille), where biomass burning activity is prominent, particularly during winter (Favez et al. 2021). Additionally, notable relative contributions of BBOA are observed in Creil (18 %), Strasbourg (17 %), and SIRTA (15 %). On average, BBOA constitutes 14.2 % of the total OA across all sites.

The COA factor was identified at eight urban sites, with concentrations ranging from 0.35 μg m^{-3} in Metz and Strasbourg to around 0.7 μg m^{-3} in Marseille and Paris Les Halles. In terms of relative contribution, COA contributions are relatively consistent, with an average of 13 %, except for a higher contribution at Paris Les Halles (18 %), likely due to its proximity to surrounding commercial and residential areas. These averages are quite similar to the ones reported at urban European sites by Chen et al. (2022).

Other specific-site factors resolved at some sites contribute minimally, such as the ShInd-OA factor in Marseille (4 %), related to the mixing of shipping and industrial emissions, and the 58-OA factor associated with industries in Strasbourg and Creil (2 %).

The barplots depicting the relative contributions of different OA factors as a function of OA mass concentration at each site (in Figure 2) also highlight the predominance of the OOA fraction in green. The BBOA factor increases with rising OA levels and dominates during pollution episodes at the majority of sites, particularly during wintertime (Figure S3). This suggests the role of primary emissions from biomass combustion during the polluted periods (Zhang et al., 2019;

Chen et al., 2022). Conversely, the HOA and COA factors remain relatively stable across OA levels. In Creil, Gennevilliers, Paris Les Halles, Poitiers, and Talence, HOA increases at high OA mass concentrations, which indicates that traffic emissions continue to have a significant impact during periods of elevated OA mass concentrations, and their influence remains significant even when the overall OA mass concentration is minimal. The ShInd-OA factor in Marseille and the MT-SOA factor in Talence show higher contributions during clean periods with lower OA loadings and a decrease at higher levels of OA mass concentration during wintertime. During summertime, primary factors decrease as OA levels rise, and the OOA fraction increases, dominating during high OA mass concentration episodes. This suggests the impact of secondary formation of OA during the summer months.

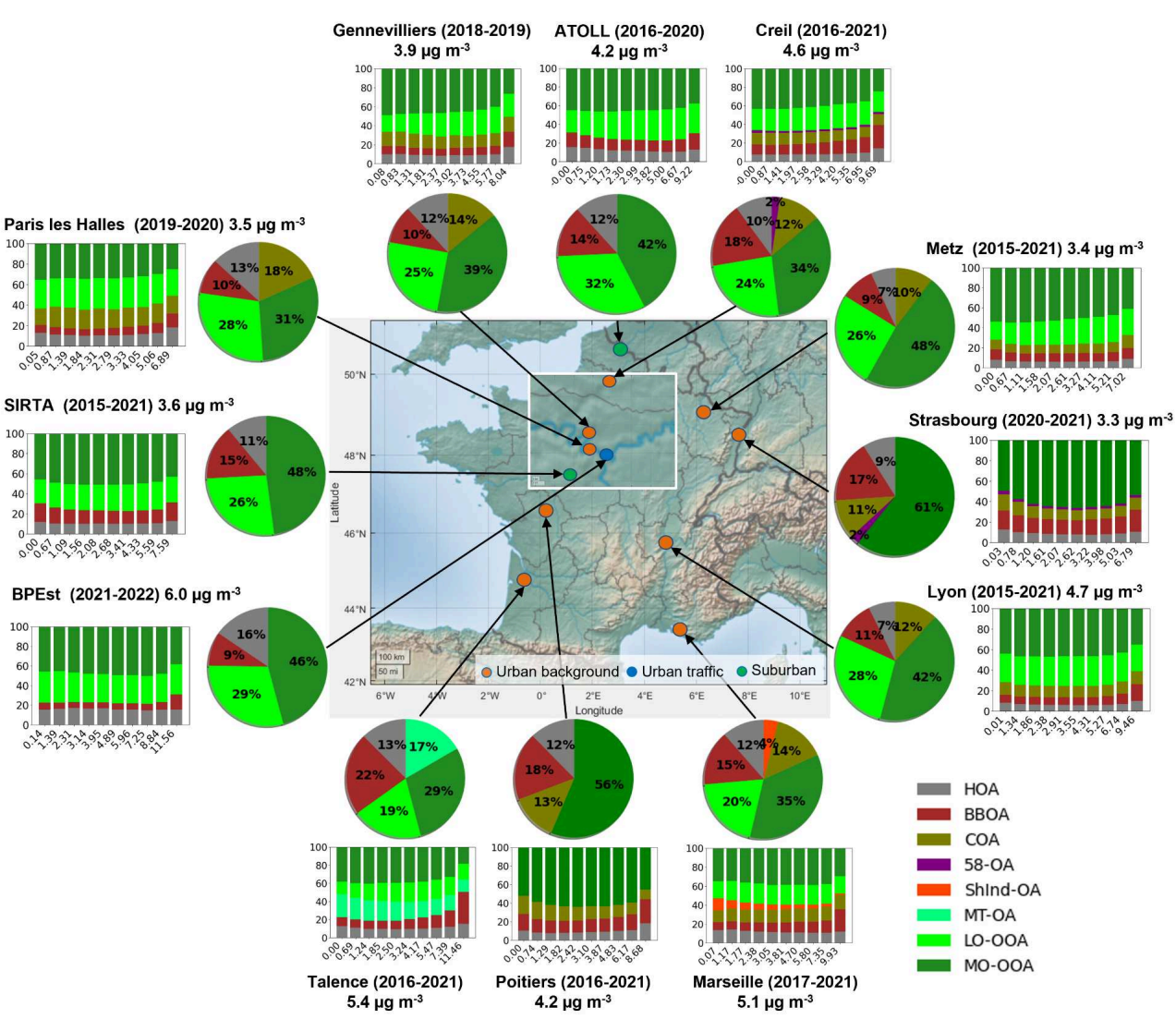

Figure 2: Location, time span, and average OA mass concentration of the 12 sites used in this study. Pie charts indicate the contributions of different OA factors, and bar graphs their relative contribution according to OA decile levels.

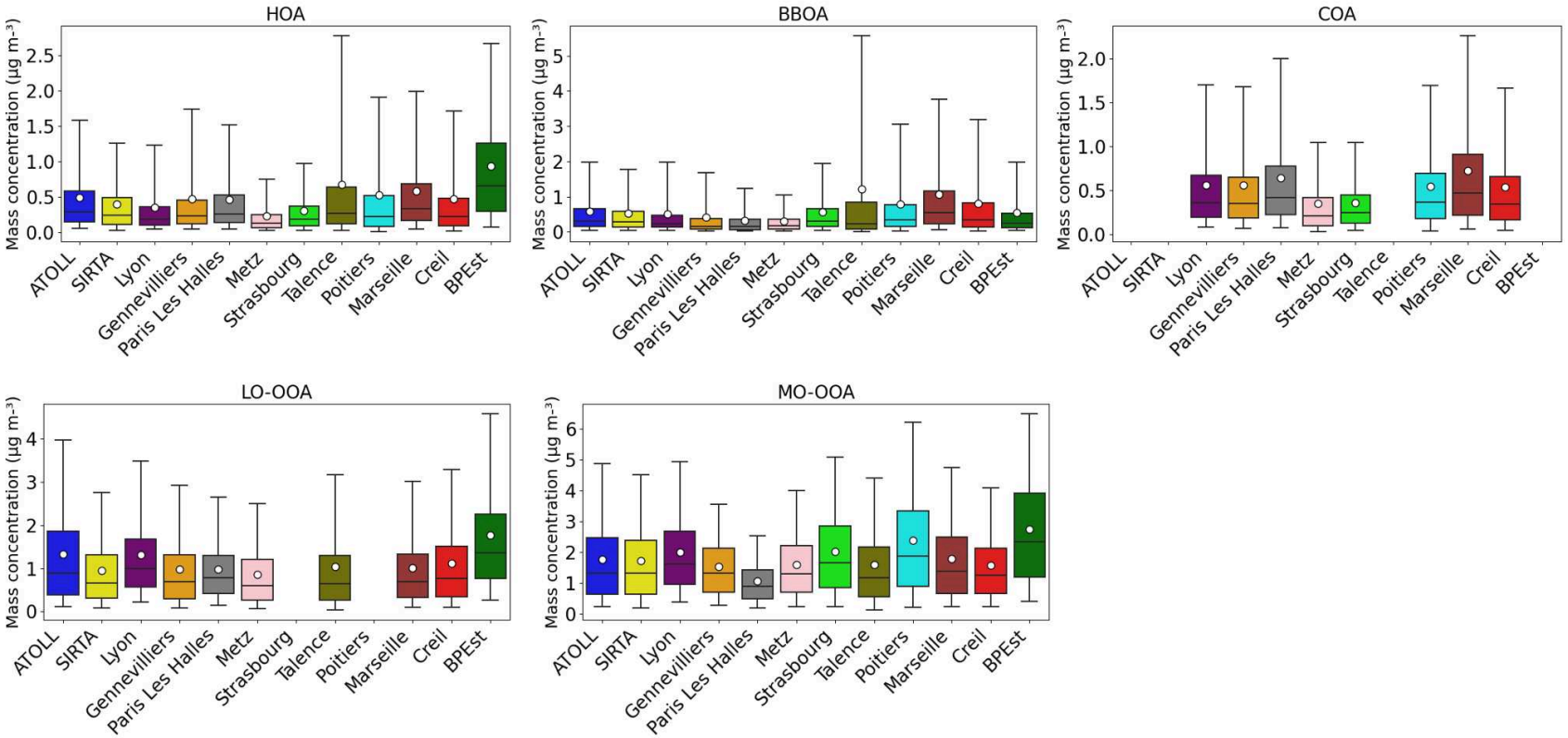

Figure 3: Box plots (median and 5th, 25th, 75th, and 95th percentiles, means as circles) of common OA factors between the 12 sites.

3.2 Temporal variabilities and external ratios

In this section, we explore the diel and seasonal variabilities of common OA factors (HOA, BBOA, COA, LO-OOA, and MO-OOA) across the different French urban sites during the measurement period. Figure 4 presents the yearly variability of the most common OA factors. The three primary factors show higher loadings during the colder months, with a ratio of monthly max/min of 6.5, 3.0, and 1.9 for BBOA, HOA, and COA, respectively. The highest loadings of primary factors during winter can be explained by stagnant conditions, including low temperatures and winds, along with a shallower boundary layer, as well as increased emissions from domestic heating in winter for BBOA and possibly enhanced condensation processes of semi-volatile organics. Conversely, the OOA factors depict less pronounced yearly variability, MO-OOA depicting no clear trends, whereas LO-OOA depicts an enhancement during summer (JJA) and winter (DJF). Previous studies have associated summertime LO-OOA with biogenic SOA (Chebaicheb et al., 2023; Chen et al., 2022; Zhang et al., 2019), and wintertime LO-OOA with aged BBOA (Chebaicheb et al., 2023). The enhancement observed here suggests that this is relevant across France, and it will be discussed in further detail in the following sections.

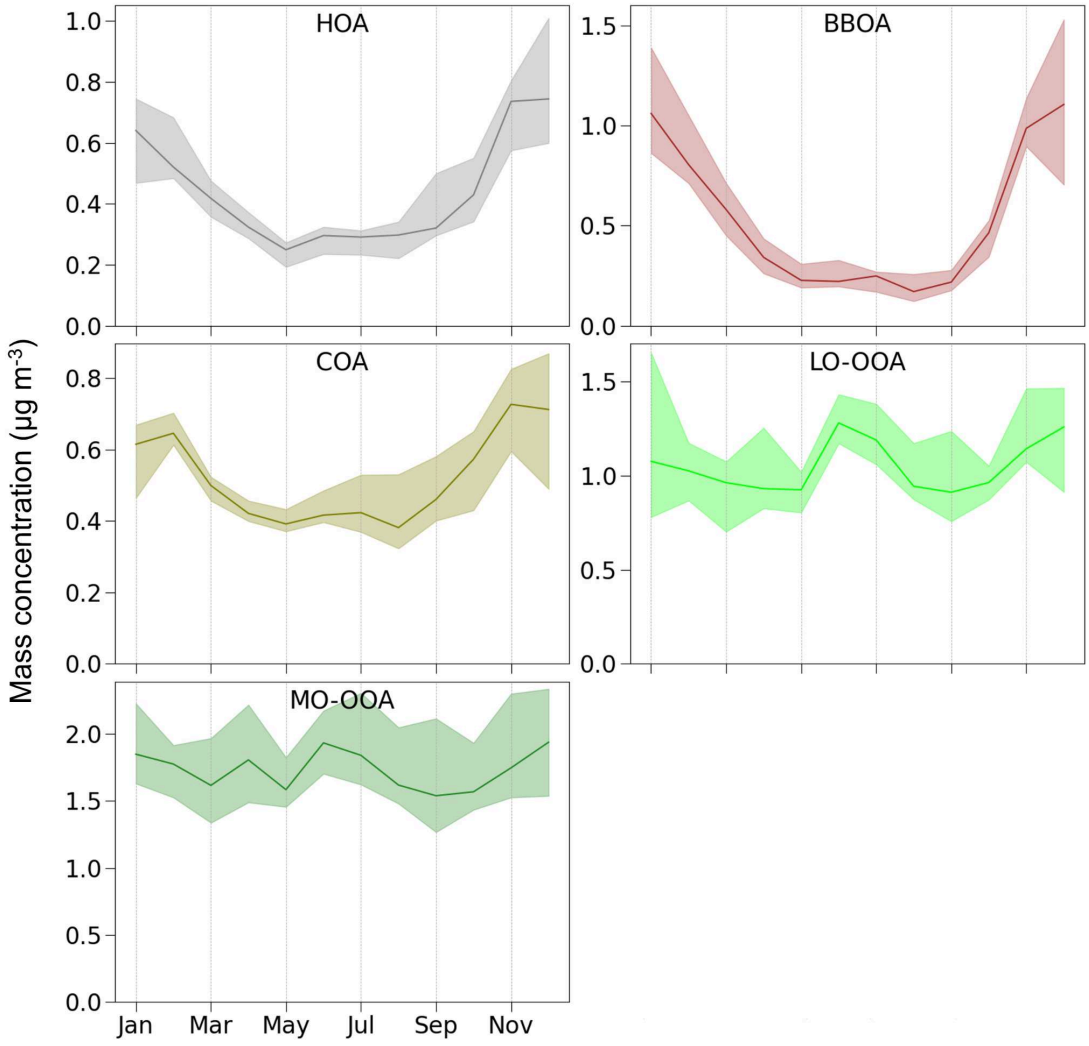

Figure 4: Monthly median and IQR (25th and 75th percentiles) for each common OA factor across all sites.

The diel variability of the OA factors across different seasons is presented in Figure 5. In general, all OA factor loadings increase during the evening, likely associated with a shallower boundary layer. As expected, the HOA factor exhibits two distinct peaks associated with morning and evening rush traffic hours, comparable to eBC_{ff} (Chebaicheb et al., in preparation). These are particularly pronounced during the winter and autumn months when traffic activity is more intense, and they diminish somewhat in spring and summer. However, there is considerable variability in these patterns among the 12 sites, particularly during cold periods when concentrations are enhanced. A noticeable seasonality is observed for the BBOA factor, characterized by a prominent nighttime peak corresponding to residential heating emissions,

consistent with eBC_{wb} (Chebaicheb et al., in preparation). Substantial variability among different sites is observed, especially in wintertime, while BBOA remains relatively low and stable during the summer months, indicating a probable heterogeneity of sources impacting different sites. On the other hand, the COA factor displays two peaks corresponding to meal hours at noon and in the evening, but no strong seasonality, and there is less variability observed between the eight urban sites where it was observed (Figure S5).

The OOA factors maintain a relatively stable diel profile, with some spatial differences observed between sites, especially for LO-OOA. The diel cycles of LO-OOA are well correlated with BBOA during wintertime, displaying a significant nighttime peak. Furthermore, they exhibited a temporal correlation (r^2) varying between 0.6 and 0.87 (Table S5), suggesting the influence of aged BBOA in the LO-OOA factor, as demonstrated in previous studies (e.g., Chebaicheb et al. 2023, Kodros et al. 2020). Combining BBOA and LO-OOA during wintertime would yield a contribution of residential heating (both fresh and aged) to OA ranging from 37 % up to 50 % (Table S3). Conversely, during summertime, LO-OOA remains stable, showing a slight increase in the early morning and during the day, which may be related to the influence of biogenic SOA in summer, contributing an average of 32 % to the total OA. The MO-OOA factor remains rather consistent across different seasons, pointing mostly towards a regional background of OA, overlaid by increases during daytime in summer (associated with photochemistry induced processes), and in the evening in winter (probably related to residential heating and boundary layer dynamics).

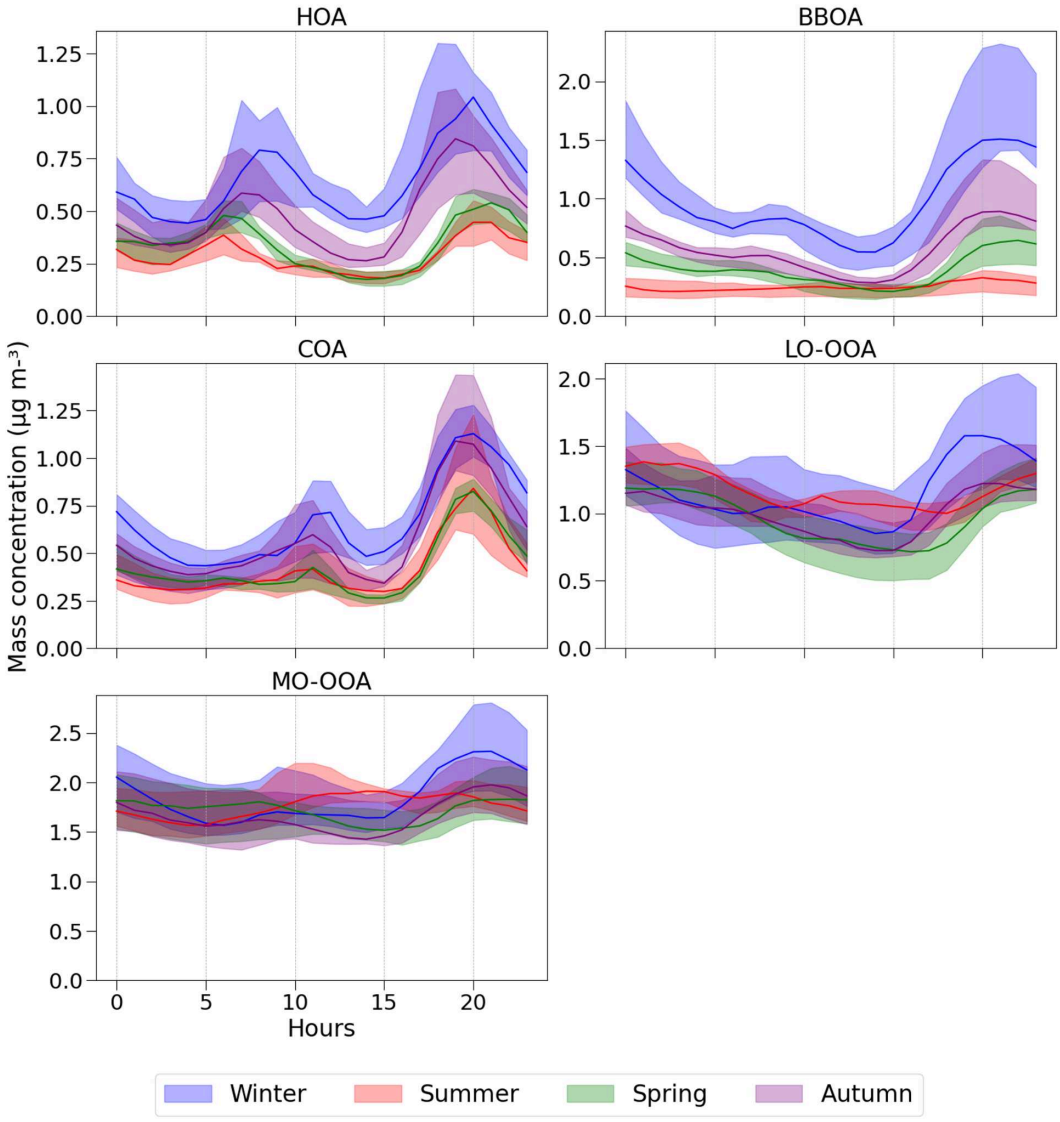

Figure 5: Seasonal daily median and IQR across all sites for each common OA factor.

Figure 6 illustrates the correlations (r^2) and average ratios between HOA and eBC_{ff}, as well as BBOA and eBC_{wb}. BBOA and eBC_{wb} exhibited strong correlations (r^2 values ranging from 0.6 to 0.85), and ratios spanning from 2.5 in Metz up to 6.5 in Marseille, whereas for the remaining sites it hovers around 4, indicating the influence of wood combustion (Ball et al., 2008). The correlation between HOA and eBC_{ff} is more variable between different sites, ranging from r^2 around 0.3 in Poitiers up to 0.7 in Genevilliers, the others typically around 0.5. The ratios varied between 0.4 (traffic station BPEst) and 1.2 (ATOLL, Talence, Poitiers), with the other sites falling within the range of 0.6 to 0.8. The ratios HOA/eBC_{ff} and BBOA/eBC_{wb} can be to a certain extent

compared with literature values of Organic and Elemental Carbons (OC and EC, respectively), approximating eBC components as EC, and primary OA factors as 1.3 × OC (Aiken et al., 2008). By applying those ratios, we see that generally French sites agree with the literature, with ratios of OA factor to eBC component >2.4 being associated with wood combustion, between 0.6 and 2.4 to gasoline vehicles, and lower than 0.6 to diesel powered vehicles (Brito et al., 2013). All the sites fall within the expected range for wood combustion, and traffic related analysis show that some of the sites depict ratios compatible to diesel (BPEst, Gennneviliers, Lyon, Metz, Strasbourg), while others fall into gasoline powered ranges. There is a caveat about the approximations performed, assuming the entirety of HOA and eBC_{ff} to originate from local traffic. As an example, a recent analysis of eBC sources at ATOLL has identified that vehicular traffic corresponds to only about 40 % of eBC_{ff} at that site, the rest being associated to shipping and industrial emissions (Velazquez-Garcia et al., in prep.). This identification of different sources for eBC_{ff} suggests the possibility of a range of HOA origins, thus explaining the variability of ratios observed among different sites.

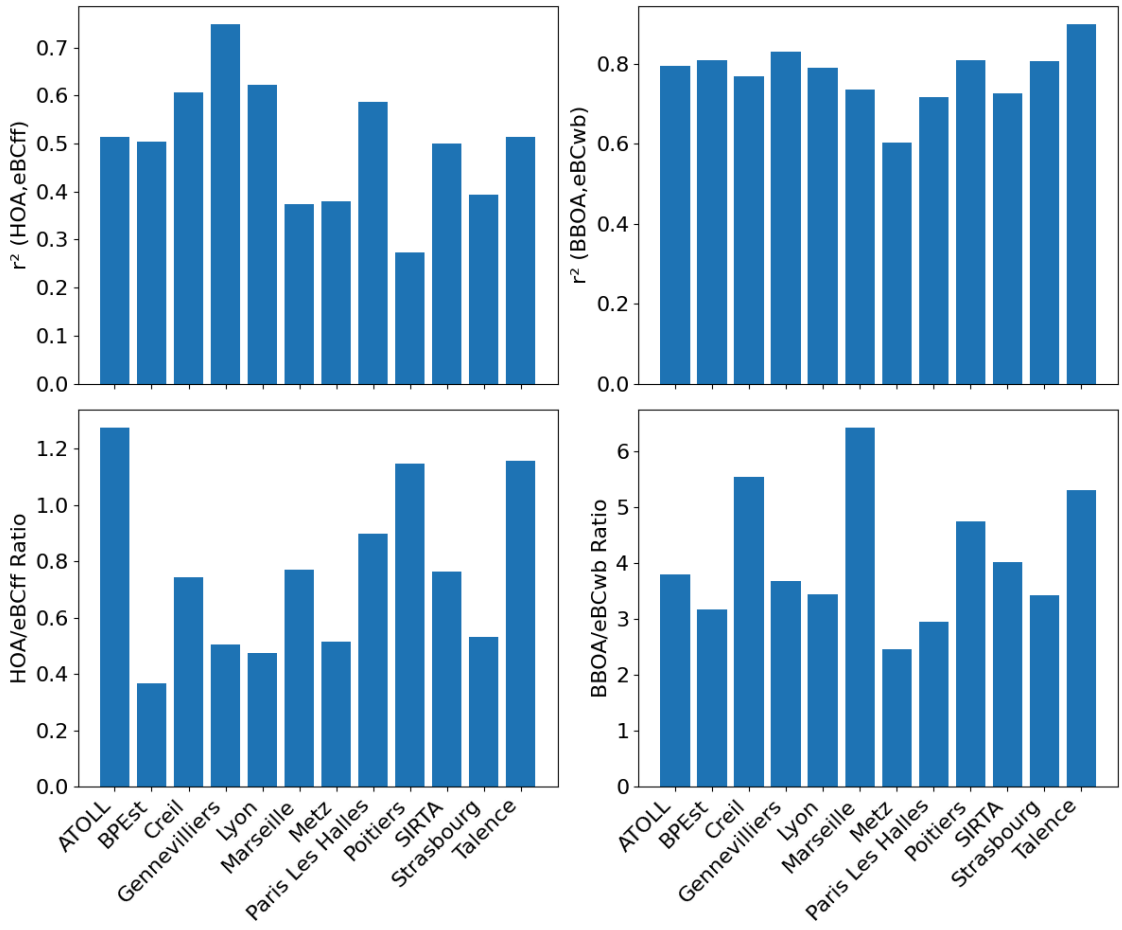

Figure 6: Correlations (r^2, top) and ratios of HOA to eBC_{ff} (left) and BBOA to eBC_{wb} (right) at 12 sites in France.

3.3 f_{44} vs. f_{43} variations

Figure 7 displays the f_{44} vs. f_{43} plots for secondary OA factors (LO-OOA, MO-OOA, MT-OA, OOA) during winter and summer periods for different sites. In general, during the summer months, LO-OOA tends to shift toward the right side of the plot (increased f_{43}), typically associated with a biogenic influence during this season (Canonaco et al. 2015). Conversely, in winter, the LO-OOA factor tends to cluster closer to the center of the f_{44} vs. f_{43} plot, associated with the influence from biomass burning emissions (Ng et al. 2010). However, it is important to note that there are exceptions to this pattern, where specific site characteristics can affect the position of LO-OOA. For instance, in Talence, the LO-OOA factor is consistently positioned on

the right side of the graph for both seasons, while the MT-OA factor remains centered within the triangle but shifts slightly to the right during the summer season. Typically, Talence is characterized by a significant contribution from biomass burning emissions, especially in winter, and associated with a substantial formation of biogenic SOA during the summer season, given its proximity to various forests, such as the Landes forest.

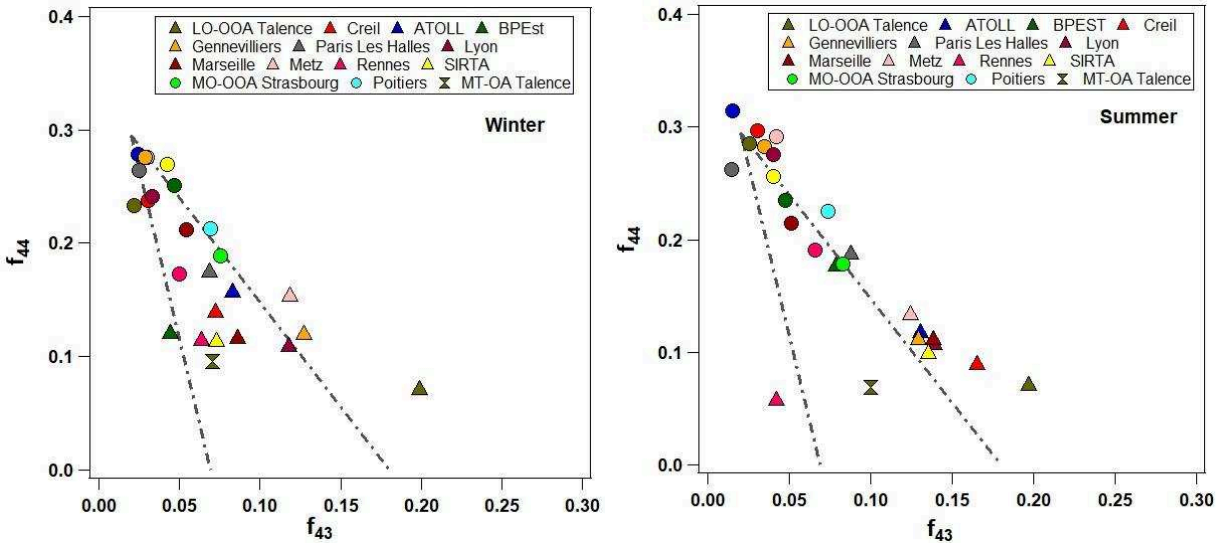

Figure 7: f_{44} vs. f_{43} fractions for secondary OA factors in winter (left) and summer (right).

3.4 Comparison of chemical profiles for different OA factors

In this section, we examined the similarities among all the chemical profiles identified in this study. We conducted a comparative analysis of the PMF factor profiles, using the PD and SID similarity metrics defined in section 2.3. Figure 8 illustrates the mean and standard deviation of distances between pairs of factor profiles categorized in the SID-PD space. Initially, we see that numerous factor/source profiles exhibit low PD and SID values (mean ± standard deviation) of PD < 0.4 and SID < 0.4, which is within the acceptance criteria (section 2.3). This observation suggests that these profiles remain consistent across the various sites, including the HOA and COA factors which were constrained in the PMF.

On the other hand, the remaining factors, specifically BBOA, LO-OOA and MO-OOA, also display relative stability across all sites but demonstrate more dissimilarity when assessed using

the PD metric (although they exhibit minimal variance in SID). This variance in PD suggests a substantial discrepancy in the chemical components that constitute the primary masses of the profile. This result is not surprising, since these factors depend on site location, combustion conditions, and chemical aging, all of which influence their mass spectrum.

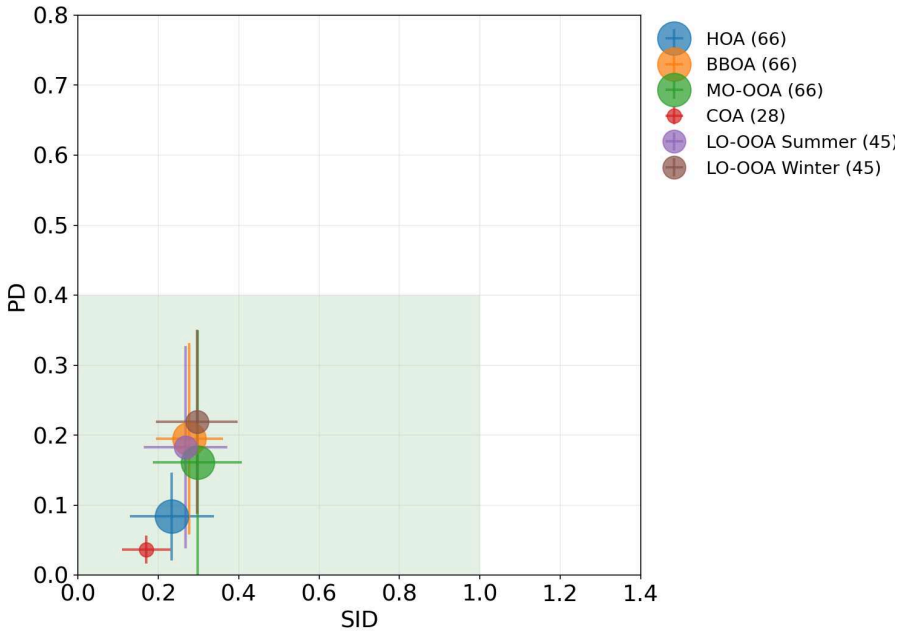

Figure 8: Similarity plot generated for every pair of factor profiles obtained from the different sites with mean and standard deviation. The size of each circle corresponds to the number of available profile pairs (ranging from 28 to 66, as indicated in parentheses in the legend). The shaded area represents the region considered acceptable for profile similarity, according to Pernigotti and Belis, 2018.

3.5 Comparison with model simulations

The PMF results were compared with the CHIMERE simulation results for nine urban sites for the year 2018. Specifically, we compared BBOA to the sum of POA species from biomass burning without their aging products. Similarly, HOA was compared to POA species from other emission sources without their aging products, whereas OOA was compared to all SOA

compounds (including the aging products of POA). This methodology is similar to other PMF comparison studies in the literature (Giani et al., 2019).

As discussed in Chebaicheb et al., (in prep.), the total OA fraction is underestimated in the model by a factor of around 2-3. Figure 9 shows the comparison between observed primary OA (HOA, BBOA, COA, ShInd-OA, 58-OA) and secondary OA (LO-OOA, MO-OOA, MT-OA), and the model-simulated primary and secondary species. The OOA annual concentrations are strongly underestimated by the model at all sites (around a mean of 72 %). However, POA are well captured by the model at most sites, except for Marseille (73 % of underestimation), Poitiers (55 %) and Creil (30 %). Looking into POA, especially HOA and BBOA (Figure 10), the model tends to strongly underestimate the HOA factor (86 %) and overestimate BBOA (46 %), except in Marseille where the observations are higher. Their times series are presented in the SI, Figure S8. As the model underestimates HOA, it is possible that other organic aerosol compounds need to be considered within the HOA category. Adding aged POA to the model HOA (Figure S9) shows some improvement in the model representation, although there is still a noticeable deficiency in capturing HOA.

Figure 11 illustrates the diel profiles comparing observations and the model results of HOA, BBOA, and total OOA during winter and summer. The model generally captures the diel evolution of HOA well in both seasons, but there is an underestimation compared to observations. As previously mentioned, the addition of aged HOA improves the model representation, a pattern also evident in the diel profiles (Figure S10). However, the model keeps overestimating BBOA. In winter, the model adequately captures the same behavior but with a smoother increase of the nighttime peak. Conversely, in summer, the observed BBOA concentrations remain relatively stable throughout the day, while the model parametrization produces the same pattern throughout the year. It is important to note that summertime BBOA is likely composed of a myriad of sources (barbecues, green waste burning - even if prohibited in most regions, forest fires). The model underestimates OOA, especially during winter months, displaying distinct behaviors in observations and model representations for both winter and summer. This may imply that a portion of BBOA in the CHIMERE model might be misclassified as OOA in the winter PMF results.

Figure 12 shows some statistical parameters, including mean bias, RMSE and correlation coefficient r, between the OA factors and result simulations for each site, using daily averages. In

general, good correlations are obtained between the PMF results and model simulations, with values between 0.6 and 0.8. The mean bias and RMSE confirm the model robustness.

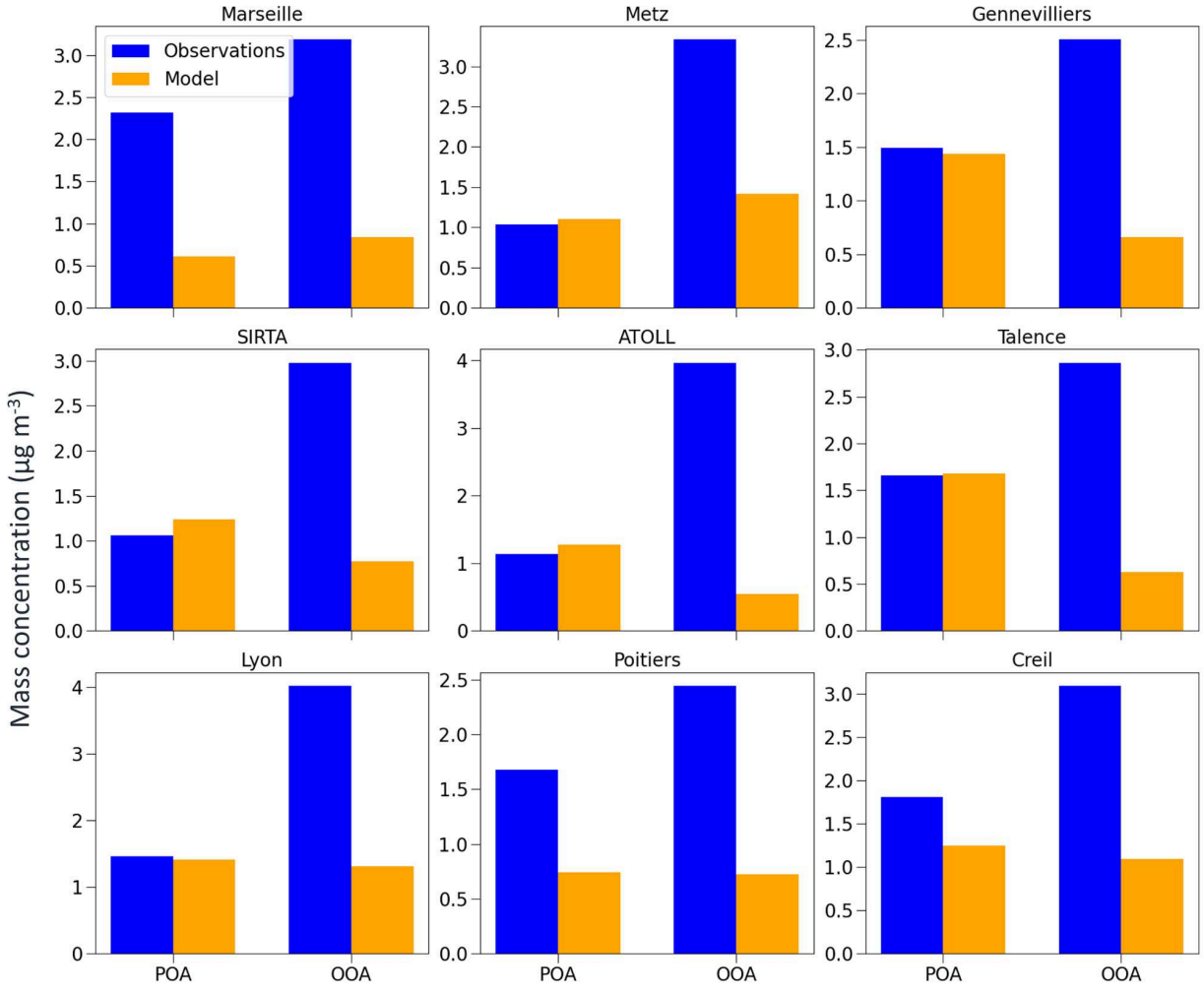

Figure 9: Mean mass concentration (in µg m^{-3}) of primary (POA) and secondary OA (OOA) for observations (in blue) and simulations (in orange) at nine French sites.

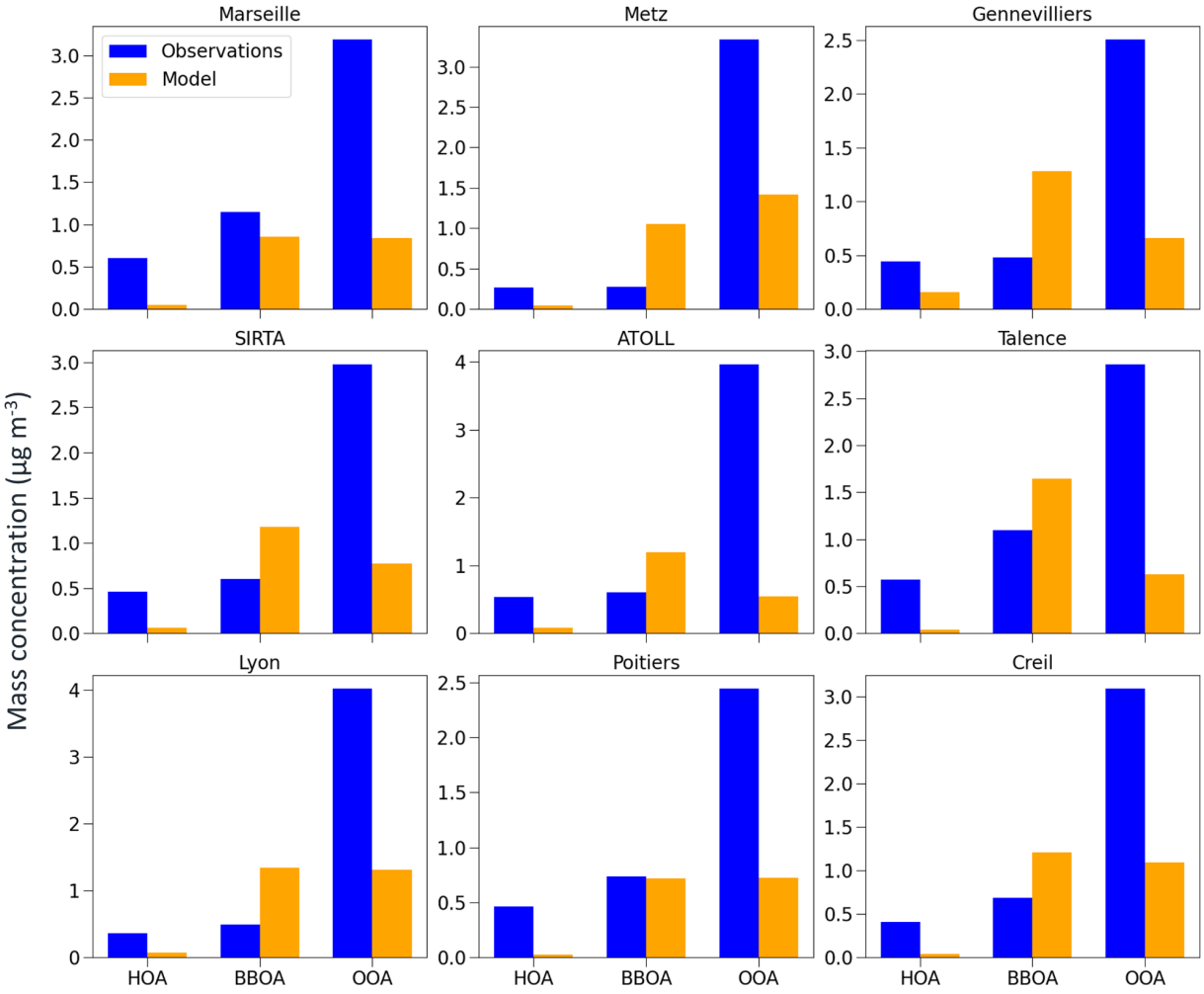

Figure 10: Mean mass concentration (in µg m^{-3}) of HOA, BBOA and OOA for observations (in blue) and simulations (in orange) at nine French sites.

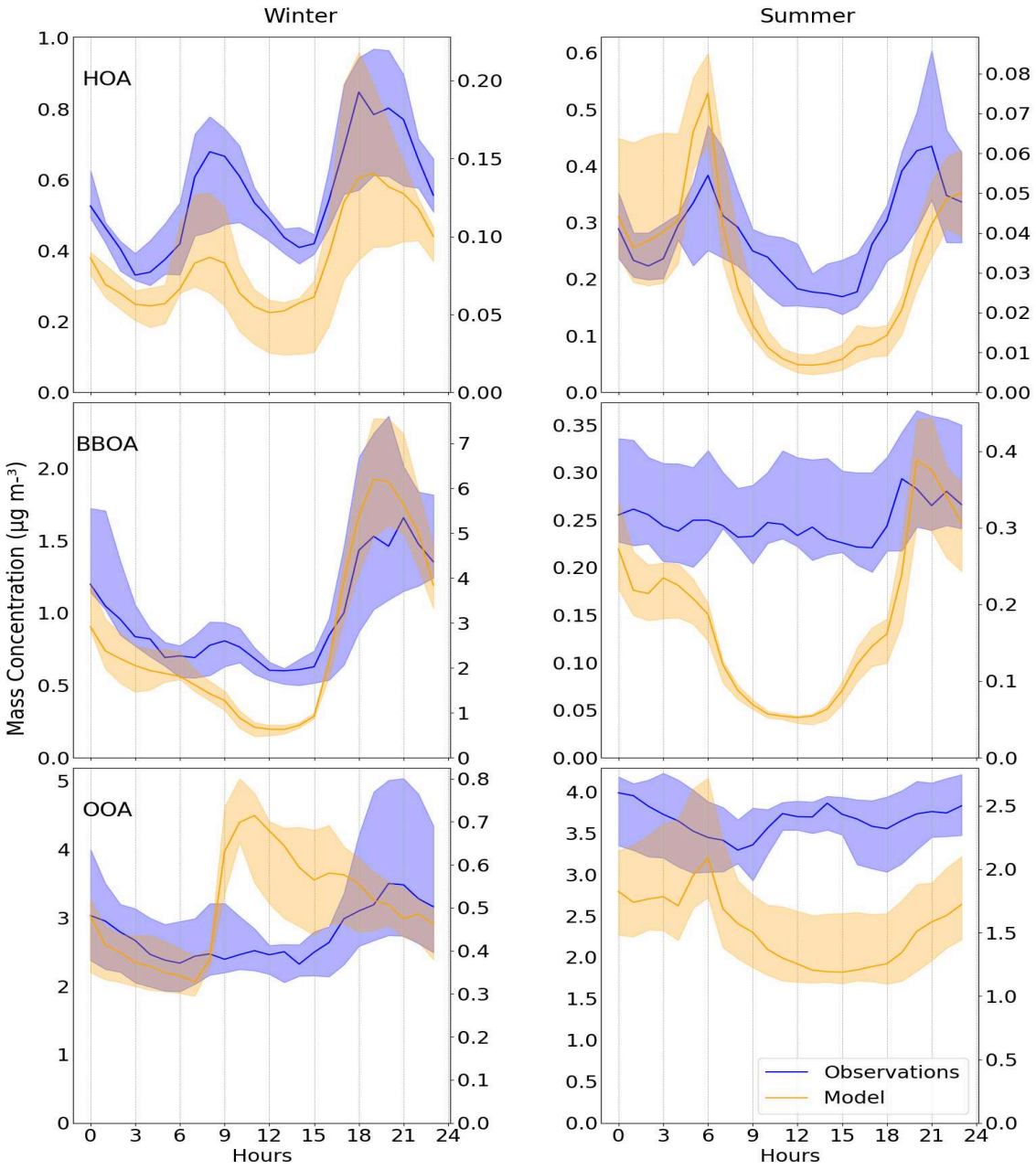

Figure 11: Observed (in blue, left axis) and modeled (in orange, right axis) diel OA profiles (from top to bottom: HOA, BBOA and OOA; median and IQR) during winter and summer of 2018 across 9 French sites.

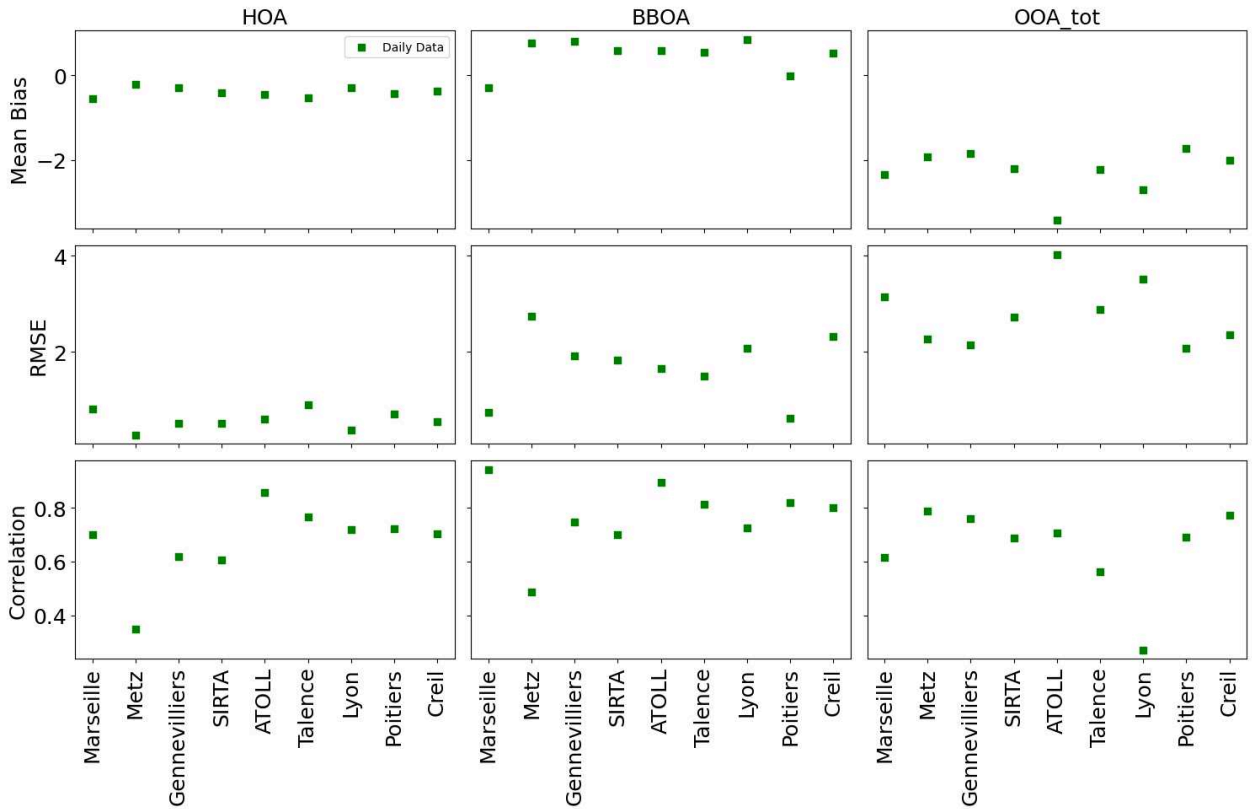

Figure 12: Statistic parameters (from top to bottom: mean bias, RMSE, and correlation coefficient r) for different species at each site, using daily averages.

Figure S12 shows correlations between OA factors and different species within the model, examining both winter and summer seasons. During the winter months, primary BOA species (corresponding to wood combustion) exhibit a strong correlation with BBOA (r = 0.5-0.8), while also displaying a moderate correlation (r around 0.5) with COA. At all sites, HOA shows a high correlation with anthropogenic POA species (r = 0.4-0.7), but also with wood combustion POA (r = 0.3-0.6). Interestingly, HOA shows a high correlation with non-speciated primary PM (PPM) (r = 0.4-0.7), raising questions about speciation accuracy. The LO-OOA factor correlates well (r around 0.6) with anthropogenic SOA and aged POA, as well as with primary BOA species, while the MO-OOA factor exhibits no clear correlation. In the summer season, POA surprisingly lacks a clear correlation with any CHIMERE species, prompting questions about potentially missing sources in the model. LO-OOA, on the other hand, exhibits high correlations with some biogenic SOA species (r = 0.4-0.8), while MO-OOA does not display any clear correlations with any species for that season.

4 Conclusions

Rolling PMF analysis was applied to 12 multi-annual datasets from observational sites across France. This study provides, for the first time, an overview of the main OA urban sources at the national level using highly time-resolved multisite datasets from ACSM for the period ranging from 2015 to 2021. Common primary OA factors were resolved, including HOA, BBOA, COA, and secondary ones such as LO-OOA and MO-OOA. Site-specific factors were also resolved, such as the mixed shipping/industrial OA (ShInd-OA) factor in Marseille, the amine-related OA (58-OA) in Strasbourg and Creil, and a monoterpene OA (MT-OA) factor in Talence. Oxidized OA (aged/secondary) dominated organic matter across all sites, accounting for 74 % of the total organic aerosol. The POA factors, including HOA, BBOA and COA, contributed to about 13% each of the total OA mass, respectively, with substantial differences across sites. During elevated PM_1 levels, BBOA had a predominant role, associated with residential heating. In contrast, during summer, OOA factors tended to dominate higher PM_1 levels, highlighting the impact of secondary formation in this season.

Factors associated with primary traffic and residential heating (HOA and BBOA) have shown strong seasonality, with maximum concentrations during wintertime, related to stagnant meteorological conditions and to wood combustion. In addition, BBOA shows the highest spatial variability among the POA factors, with IQR/median ratios among sites falling within the ranges of 0.24 to 0.79. This is associated with the heterogeneity of meteorological conditions across France, compounded with wood specificities as a heating fuel, such as wood types, combustion conditions, and potential chemical aging. A strong correlation (r^2 between 0.60 and 0.87) between LO-OOA and BBOA in winter increases biomass combustion contribution (between 37 and 50 %) during cold periods and highlights the importance of biomass combustion during pollution episodes. LO-OOA also exhibits an enhancement in summer, which can be associated with biogenic SOA. In contrast, MO-OOA did not show any clear seasonality, which can be related to a larger variety of sources and processes.

The ratio f_{44} vs. f_{43} in the OOA factors (LO-OOA and MO-OOA) showed spatial and seasonal variabilities. These fluctuations were associated with biogenic sources during summer, while during winter, they are predominantly associated with anthropogenic sources (these sources could entail the oxidation of emissions from vehicular traffic or the combustion of biomass, depending

on the specific time periods). These variabilities are also highlighted in the SID-PD space, which shows variance in the PD metric for the BBOA, LO-OOA and MO-OOA factors, confirming the divergence of their chemical components, which vary according to the site location, nature and conditions of burning and chemical aging.

Finally, the comparison with CHIMERE simulations shows a good agreement for the primary OA, however, the model consistently underestimates HOA, possibly requiring the inclusion of additional organic aerosol compounds, while overestimating BBOA. OOA is highly underestimated, especially in winter, suggesting a lack of anthropogenic aerosol sources in the model.

References

Air quality in Europe 2022 — European Environment Agency: https://www.eea.europa.eu/publications/air-quality-in-europe-2022, last access: 31 July 2023.

Belis, C. A., Pernigotti, D., Karagulian, F., Pirovano, G., Larsen, B. R., Gerboles, M., and Hopke, P. K.: A new methodology to assess the performance and uncertainty of source apportionment models in intercomparison exercises, Atmos. Environ., 119, 35–44, https://doi.org/10.1016/j.atmosenv.2015.08.002, 2015.

Bressi, M., Cavalli, F., Putaud, J. P., Fröhlich, R., Petit, J.-E., Aas, W., Äijälä, M., Alastuey, A., Allan, J. D., Aurela, M., Berico, M., Bougiatioti, A., Bukowiecki, N., Canonaco, F., Crenn, V., Dusanter, S., Ehn, M., Elsasser, M., Flentje, H., Graf, P., Green, D. C., Heikkinen, L., Hermann, H., Holzinger, R., Hueglin, C., Keernik, H., Kiendler-Scharr, A., Kubelová, L., Lunder, C., Maasikmets, M., Makeš, O., Malaguti, A., Mihalopoulos, N., Nicolas, J. B., O'Dowd, C., Ovadnevaite, J., Petralia, E., Poulain, L., Priestman, M., Riffault, V., Ripoll, A., Schlag, P., Schwarz, J., Sciare, J., Slowik, J., Sosedova, Y., Stavroulas, I., Teinemaa, E., Via, M., Vodička, P., Williams, P. I., Wiedensohler, A., Young, D. E., Zhang, S., Favez, O., Minguillón, M. C., and Prevot, A. S. H.: A European aerosol phenomenology - 7: High-time resolution chemical characteristics of submicron particulate matter across Europe, Atmospheric Environ. X, 10, 100108, https://doi.org/10.1016/j.aeaoa.2021.100108, 2021.

Canonaco, F., Slowik, J. G., Baltensperger, U., and Prévôt, A. S. H.: Seasonal differences in oxygenated organic aerosol composition: implications for emissions sources and factor analysis, Atmospheric Chem. Phys., 15, 6993–7002, https://doi.org/10.5194/acp-15-6993-2015, 2015.

Canonaco, F., Tobler, A., Chen, G., Sosedova, Y., Slowik, J. G., Bozzetti, C., Daellenbach, K. R., El Haddad, I., Crippa, M., Huang, R.-J., Furger, M., Baltensperger, U., and Prévôt, A. S. H.: A new method for long-term source apportionment with time-dependent factor profiles and uncertainty assessment using SoFi Pro: application to 1 year of organic aerosol data, Atmospheric Meas. Tech., 14, 923–943, https://doi.org/10.5194/amt-14-923-2021, 2021.

Chazeau, B., Temime-Roussel, B., Gille, G., Mesbah, B., D'Anna, B., Wortham, H., and Marchand, N.: Measurement report: Fourteen months of real-time characterisation of the submicronic aerosol and its

atmospheric dynamics at the Marseille–Longchamp supersite, Atmospheric Chem. Phys., 21, 7293–7319, https://doi.org/10.5194/acp-21-7293-2021, 2021.

Chazeau, B., El Haddad, I., Canonaco, F., Temime-Roussel, B., D'Anna, B., Gille, G., Mesbah, B., Prévôt, A. S. H., Wortham, H., and Marchand, N.: Organic aerosol source apportionment by using rolling positive matrix factorization: Application to a Mediterranean coastal city, Atmospheric Environ. X, 14, 100176, https://doi.org/10.1016/j.aeaoa.2022.100176, 2022.

Chebaicheb, H., F. de Brito, J., Chen, G., Tison, E., Marchand, C., Prévôt, A. S. H., Favez, O., and Riffault, V.: Investigation of four-year chemical composition and organic aerosol sources of submicron particles at the ATOLL site in northern France, Environ. Pollut., 330, 121805, https://doi.org/10.1016/j.envpol.2023.121805, 2023.

Chebaicheb, H et al., Multi-year high time resolution datasets of fine PM at 13 sites of the French Operational Network (CARA program): Data processing and chemical composition, in preparation.

Chebaicheb, H et al., Lessons learned from the comparison and combination of fine carbonaceous aerosol source apportionment at two locations in the city of Strasbourg, France, in preparation.

Chen, G., Canonaco, F., Tobler, A., Aas, W., Alastuey, A., Allan, J., Atabakhsh, S., Aurela, M., Baltensperger, U., Bougiatioti, A., De Brito, J. F., Ceburnis, D., Chazeau, B., Chebaicheb, H., Daellenbach, K. R., Ehn, M., El Haddad, I., Eleftheriadis, K., Favez, O., Flentje, H., Font, A., Fossum, K., Freney, E., Gini, M., Green, D. C., Heikkinen, L., Herrmann, H., Kalogridis, A.-C., Keernik, H., Lhotka, R., Lin, C., Lunder, C., Maasikmets, M., Manousakas, M. I., Marchand, N., Marin, C., Marmureanu, L., Mihalopoulos, N., Močnik, G., Nęcki, J., O'Dowd, C., Ovadnevaite, J., Peter, T., Petit, J.-E., Pikridas, M., Matthew Platt, S., Pokorná, P., Poulain, L., Priestman, M., Riffault, V., Rinaldi, M., Różański, K., Schwarz, J., Sciare, J., Simon, L., Skiba, A., Slowik, J. G., Sosedova, Y., Stavroulas, I., Styszko, K., Teinemaa, E., Timonen, H., Tremper, A., Vasilescu, J., Via, M., Vodička, P., Wiedensohler, A., Zografou, O., Cruz Minguillón, M., and Prévôt, A. S. H.: European aerosol phenomenology − 8: Harmonised source apportionment of organic aerosol using 22 Year-long ACSM/AMS datasets, Environ. Int., 166, 107325, https://doi.org/10.1016/j.envint.2022.107325, 2022.

Chrit, M., Sartelet, K., Sciare, J., Pey, J., Marchand, N., Couvidat, F., Sellegri, K., and Beekmann, M.: Modelling organic aerosol concentrations and properties during ChArMEx summer campaigns of 2012 and 2013 in the western Mediterranean region, Atmospheric Chem. Phys., 17, 12509–12531, https://doi.org/10.5194/acp-17-12509-2017, 2017.

Cincinelli, A., Guerranti, C., Martellini, T., and Scodellini, R.: Residential wood combustion and its impact on urban air quality in Europe, Curr. Opin. Environ. Sci. Health, 8, 10–14, https://doi.org/10.1016/j.coesh.2018.12.007, 2019.

Couvidat, F. and Sartelet, K.: The Secondary Organic Aerosol Processor (SOAP v1.0) model: a unified model with different ranges of complexity based on the molecular surrogate approach, Geosci. Model Dev., 8, 1111–1138, https://doi.org/10.5194/gmd-8-1111-2015, 2015.

Crilley, L. R., Bloss, W. J., Yin, J., Beddows, D. C. S., Harrison, R. M., Allan, J. D., Young, D. E., Flynn, M., Williams, P., Zotter, P., Prevot, A. S. H., Heal, M. R., Barlow, J. F., Halios, C. H., Lee, J. D., Szidat, S., and Mohr, C.: Sources and contributions of wood smoke during winter in London: assessing local and regional influences, Atmospheric Chem. Phys., 15, 3149–3171, https://doi.org/10.5194/acp-15-3149-2015, 2015.

Crippa, M., DeCarlo, P. F., Slowik, J. G., Mohr, C., Heringa, M. F., Chirico, R., Poulain, L., Freutel, F., Sciare, J., Cozic, J., Di Marco, C. F., Elsasser, M., Nicolas, J. B., Marchand, N., Abidi, E., Wiedensohler, A., Drewnick, F., Schneider, J., Borrmann, S., Nemitz, E., Zimmermann, R., Jaffrezo, J.-L., Prévôt, A. S. H., and Baltensperger, U.: Wintertime aerosol chemical composition and source apportionment of the organic fraction in the metropolitan area of Paris, Atmospheric Chem. Phys., 13, 961–981, https://doi.org/10.5194/acp-13-961-2013, 2013.

Crippa, M., Canonaco, F., Lanz, V. A., Äijälä, M., Allan, J. D., Carbone, S., Capes, G., Ceburnis, D., Dall'Osto, M., Day, D. A., DeCarlo, P. F., Ehn, M., Eriksson, A., Freney, E., Hildebrandt Ruiz, L., Hillamo, R., Jimenez, J. L., Junninen, H., Kiendler-Scharr, A., Kortelainen, A.-M., Kulmala, M., Laaksonen, A., Mensah, A. A., Mohr, C., Nemitz, E., O'Dowd, C., Ovadnevaite, J., Pandis, S. N., Petäjä, T., Poulain, L., Saarikoski, S., Sellegri, K., Swietlicki, E., Tiitta, P., Worsnop, D. R., Baltensperger, U., and Prévôt, A. S. H.: Organic aerosol components derived from 25 AMS data sets across Europe using a consistent ME-2 based source apportionment approach, Atmospheric Chem. Phys., 14, 6159–6176, https://doi.org/10.5194/acp-14-6159-2014, 2014.

Drinovec, L., Močnik, G., Zotter, P., Prévôt, A. S. H., Ruckstuhl, C., Coz, E., Rupakheti, M., Sciare, J., Müller, T., Wiedensohler, A., and Hansen, A. D. A.: The "dual-spot" Aethalometer: an improved measurement of aerosol black carbon with real-time loading compensation, Atmospheric Meas. Tech., 8, 1965–1979, https://doi.org/10.5194/amt-8-1965-2015, 2015.

Europe's air quality status 2023 — European Environment Agency:
https://www.eea.europa.eu/publications/europes-air-quality-status-2023, last access: 22 August 2023.

Favez, O., Weber, S., Petit, J.-E., Alleman, L., Albinet, A., Riffault, V., Chazeau, B., Amodeo, T., Salameh, D., Zhang, Y., Srivastava, D., Samaké, A., Aujay, R., Papin, A., Bonnaire, N., Boullanger, C., Chatain, M., Chevrier, F., Detournay, A., and Leoz-Garziandia, E.: Overview of the French Operational Network for In Situ Observation of PM Chemical Composition and Sources in Urban Unvironments (CARA Program), https://doi.org/10.3390/atmos12020207, 2021.

Flentje, H., Mattis, I., Kipling, Z., Rémy, S., and Thomas, W.: Evaluation of ECMWF IFS-AER (CAMS) operational forecasts during cycle 41r1–46r1 with calibrated ceilometer profiles over Germany, Geosci. Model Dev., 14, 1721–1751, https://doi.org/10.5194/gmd-14-1721-2021, 2021.

Fröhlich, R., Cubison, M. J., Slowik, J. G., Bukowiecki, N., Prévôt, A. S. H., Baltensperger, U., Schneider, J., Kimmel, J. R., Gonin, M., Rohner, U., Worsnop, D. R., and Jayne, J. T.: The ToF-ACSM: a portable aerosol chemical speciation monitor with TOFMS detection, Atmospheric Meas. Tech., 6, 3225–3241, https://doi.org/10.5194/amt-6-3225-2013, 2013.

Kodros, J. K., Papanastasiou, D. K., Paglione, M., Masiol, M., Squizzato, S., Florou, K., Skyllakou, K., Kaltsonoudis, C., Nenes, A., and Pandis, S. N.: Rapid dark aging of biomass burning as an overlooked source of oxidized organic aerosol, Proc. Natl. Acad. Sci., 117, 33028–33033, https://doi.org/10.1073/pnas.2010365117, 2020.

Kuenen, J., Dellaert, S., Visschedijk, A., Jalkanen, J.-P., Super, I., and Denier van der Gon, H.: CAMS-REG-v4: a state-of-the-art high-resolution European emission inventory for air quality modelling, Earth Syst. Sci. Data, 14, 491–515, https://doi.org/10.5194/essd-14-491-2022, 2022.

Menut, L., Bessagnet, B., Briant, R., Cholakian, A., Couvidat, F., Mailler, S., Pennel, R., Siour, G., Tuccella, P., Turquety, S., and Valari, M.: The CHIMERE v2020r1 online chemistry-transport model, Geosci. Model Dev., 14, 6781–6811, https://doi.org/10.5194/gmd-14-6781-2021, 2021.

Ng, N. L., Canagaratna, M. R., Zhang, Q., Jimenez, J. L., Tian, J., Ulbrich, I. M., Kroll, J. H., Docherty, K. S., Chhabra, P. S., Bahreini, R., Murphy, S. M., Seinfeld, J. H., Hildebrandt, L., Donahue, N. M., DeCarlo, P. F., Lanz, V. A., Prévôt, A. S. H., Dinar, E., Rudich, Y., and Worsnop, D. R.: Organic aerosol components observed in Northern Hemispheric datasets from Aerosol Mass Spectrometry, Atmospheric Chem. Phys., 10, 4625–4641, https://doi.org/10.5194/acp-10-4625-2010, 2010.

Ng, N. L., Herndon, S. C., Trimborn, A., Canagaratna, M. R., Croteau, P. L., Onasch, T. B., Sueper, D., Worsnop, D. R., Zhang, Q., Sun, Y. L., and Jayne, J. T.: An Aerosol Chemical Speciation Monitor (ACSM) for Routine Monitoring of the Composition and Mass Concentrations of Ambient Aerosol, Aerosol Sci. Technol., 45, 780–794, https://doi.org/10.1080/02786826.2011.560211, 2011.

Pernigotti, D. and Belis, C. A.: DeltaSA tool for source apportionment benchmarking, description and sensitivity analysis, Atmos. Environ., 180, 138–148, https://doi.org/10.1016/j.atmosenv.2018.02.046, 2018.

Roldin, P., Ehn, M., Kurtén, T., Olenius, T., Rissanen, M. P., Sarnela, N., Elm, J., Rantala, P., Hao, L., Hyttinen, N., Heikkinen, L., Worsnop, D. R., Pichelstorfer, L., Xavier, C., Clusius, P., Öström, E., Petäjä, T., Kulmala, M., Vehkamäki, H., Virtanen, A., Riipinen, I., and Boy, M.: The role of highly oxygenated organic molecules in the Boreal aerosol-cloud-climate system, Nat. Commun., 10, 4370, https://doi.org/10.1038/s41467-019-12338-8, 2019.

Sandradewi, J., Prévôt, A. S. H., Szidat, S., Perron, N., Alfarra, M. R., Lanz, V. A., Weingartner, E., and Baltensperger, U.: Using Aerosol Light Absorption Measurements for the Quantitative Determination of Wood Burning and Traffic Emission Contributions to Particulate Matter, Environ. Sci. Technol., 42, 3316–3323, https://doi.org/10.1021/es702253m, 2008.

Sartelet, K., Couvidat, F., Wang, Z., Flageul, C., and Kim, Y.: SSH-Aerosol v1.1: A Modular Box Model to Simulate the Evolution of Primary and Secondary Aerosols, Atmosphere, 11, 525, https://doi.org/10.3390/atmos11050525, 2020.

Saunders, S. M., Jenkin, M. E., Derwent, R. G., and Pilling, M. J.: Protocol for the development of the Master Chemical Mechanism, MCM v3 (Part A): tropospheric degradation of non-aromatic volatile organic compounds, Atmospheric Chem. Phys., 3, 161–180, https://doi.org/10.5194/acp-3-161-2003, 2003.

Southerland, V. A., Brauer, M., Mohegh, A., Hammer, M. S., Donkelaar, A. van, Martin, R. V., Apte, J. S., and Anenberg, S. C.: Global urban temporal trends in fine particulate matter (PM2·5) and attributable health burdens: estimates from global datasets, Lancet Planet. Health, 6, e139–e146, https://doi.org/10.1016/S2542-5196(21)00350-8, 2022.

Velazquez-Garcia, A., F. de Brito, J., Crumeyrolle, S., Chiapello, I., and Riffault, V.: Assessment of light-absorbing carbonaceous aerosol origins and properties at the ATOLL site in Northern France, in preparation.

Wang, Z., Couvidat, F., and Sartelet, K.: GENerator of reduced Organic Aerosol mechanism (GENOA v1.0): an automatic generation tool of semi-explicit mechanisms, Geosci. Model Dev., 15, 8957–8982, https://doi.org/10.5194/gmd-15-8957-2022, 2022.

Wang, Z., Couvidat, F., and Sartelet, K.: Implementation of a parallel reduction algorithm in the GENerator of reduced Organic Aerosol mechanisms (GENOA v2.0): Application to multiple

monoterpene aerosol precursors, J. Aerosol Sci., 174, 106248, https://doi.org/10.1016/j.jaerosci.2023.106248, 2023.

Wang, Z.: Influence of anthropogenic emissions on organic aerosol formation depending on the physico chemical characteristics of the environment, phd thesis, École des Ponts ParisTech, 2023.

Zhang, Q., Jimenez, J. L., Canagaratna, M. R., Ulbrich, I. M., Ng, N. L., Worsnop, D. R., and Sun, Y.: Understanding atmospheric organic aerosols via factor analysis of aerosol mass spectrometry: a review, Anal. Bioanal. Chem., 401, 3045–3067, https://doi.org/10.1007/s00216-011-5355-y, 2011.

VI.3. Supplementary Information de l'article 4

Phenomenology of organic aerosol multi-annual source apportionment at 12 urban and suburban sites in France

Hasna Chebaicheb[1,2,3], Joel F. de Brito[1], Jean-Eudes Petit[4], Benjamin Chazeau[5,6], Mélodie Chatain[7], Gregory Abbou[8], Alexia Baudic[8], Raphaële Falhun[9], Florie Francony[10], Cyril Ratier[10], Didier Grenier[11], Nicolas Vigier[11], Shouwen Zhang[12], Emmanuel Tison[1], Laurent Meunier[2,3], Tanguy Amodeo[2,3], Nicolas Marchand[5], Florian Couvidat[2], Véronique Riffault[1,3], Olivier Favez[2,3]

[1]IMT Nord Europe, Institut Mines-Télécom, Université de Lille, Centre for Energy and Environment, 59000, Lille, France
[2]Institut National de l'environnement Industriel et des Risques (INERIS), 60550 Verneuil-en-Halatte, France
[3]Laboratoire Central de Surveillance de la Qualité de l'Air (LCSQA), 60550 Verneuil-en-Halatte, France
[4]Laboratoire des Sciences du Climat et de l'Environnement (LSCE), CNRS-CEA-UVSQ (UMR 8212), 91191 Gif-sur-Yvette, France
[5]Univ. Aix-Marseille, LCE (UMR7376), Marseille, France
[6]Atmo Sud, 13294 Marseille, France
[7]Atmo Grand Est, 67300 Schiltigheim, France
[8]Airparif, 75004 Paris, France
[9]Air Breizh, 35200 Rennes, France
[10]Atmo Nouvelle-Aquitaine, 33692 Mérignac, France
[11]Atmo Auvergne Rhône-Alpes, 69500 Bron, France
[12]Atmo Hauts de France, 59044 Lille, France

Correspondence to: hasna.chebaicheb@ineris.fr

In preparation

Table S1: Seasonal PMF periods selected for each site.

Sites	**Seasonal PMF period**
ATOLL	2016/2017
Marseille	2017/2018
SIRTA	2016/2017
Gennevilliers	2018/2019
Paris Les Halles	2019/2020
BPEst	2021/2022
Creil	2016/2017
Lyon	2018/2019
Metz	2018/2019
Strasbourg	2019/2020
Talence	2017/2018
Poitiers	2017/2018

Table S2: Criteria-based selection

Facteur	Criterion	Selection
HOA	- Correlation with eBC_{ff} (or eBC) - Correlation with NO_x	p-value ≤ 0.05 p-value ≤ 0.05
BBOA	- Explained variation of *m/z* 60 - Correlation with eBC_{wb}	p-value ≤ 0.05 All
COA	- Ratio of COA lunch peak	> 1
LO-OOA and MO-OOA	- m/z 43 and 44 - Sorting based on f_{44}/f_{43}	> 0

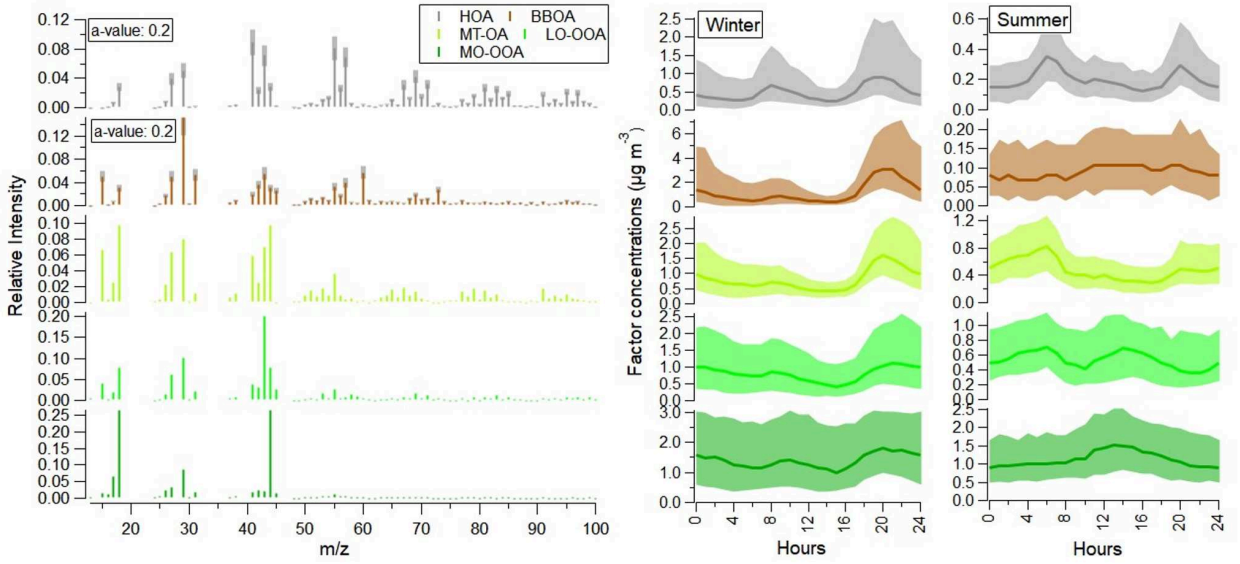

Figure S1: Rolling PMF solution for Talence.

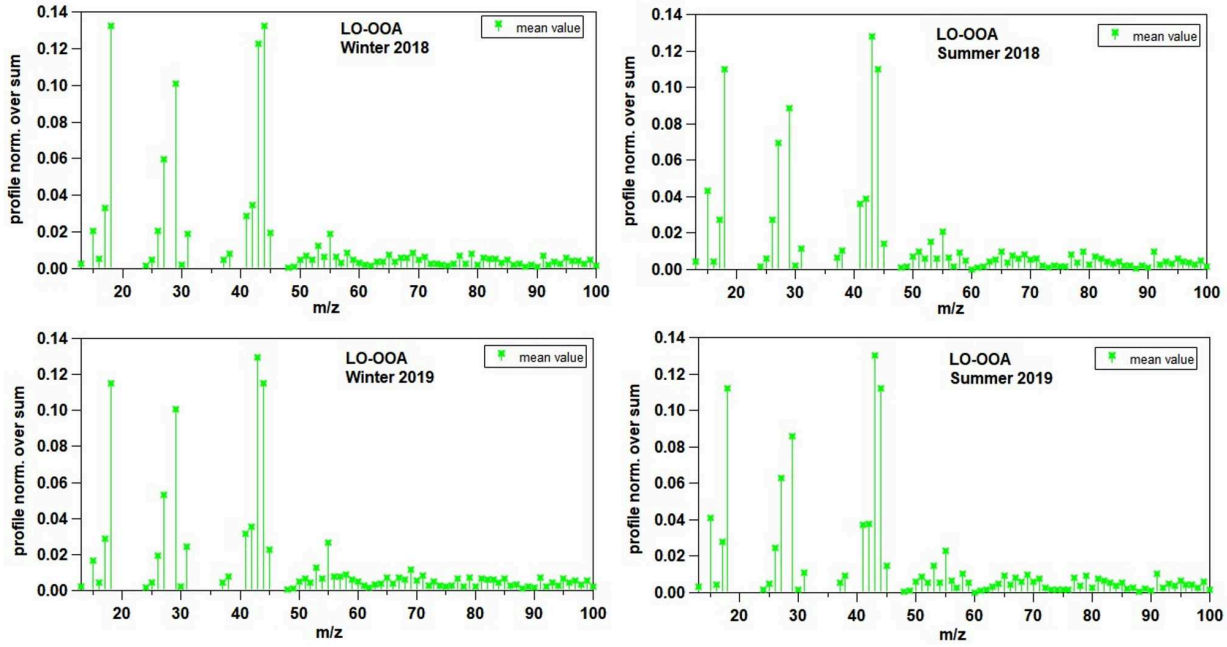

Figure S2: Temporal variations in factor profiles (example of the Gennevilliers site).

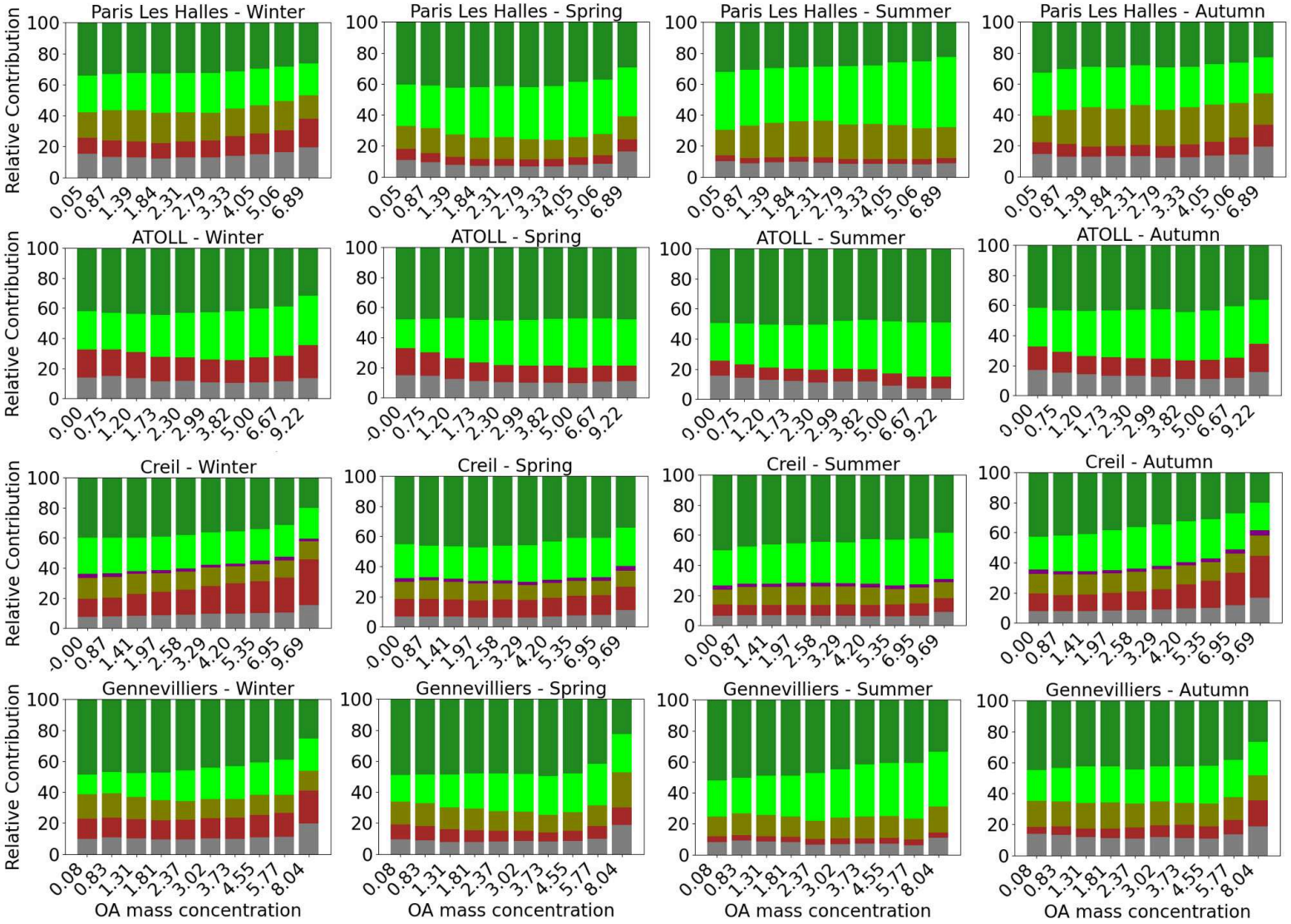

Figure S3: Relative contribution of PMF factors as a function of OA centiles by season (continued).

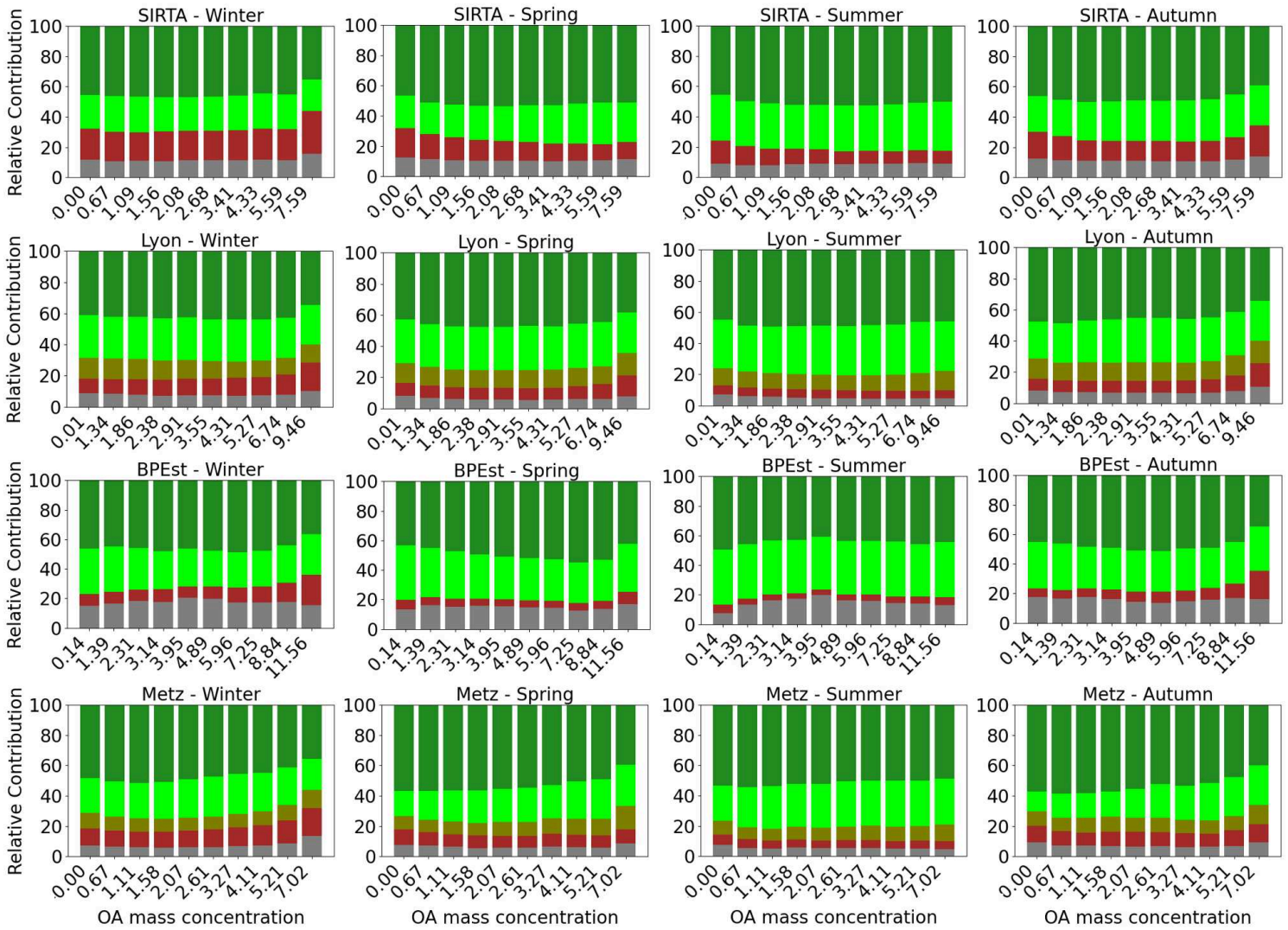
SIRTA - Winter
SIRTA - Spring
SIRTA - Summer
SIRTA - Autumn
Lyon - Winter
Lyon - Spring
Lyon - Summer
Lyon - Autumn
BPEst - Winter
BPEst - Spring
BPEst - Summer
BPEst - Autumn
Metz - Winter
Metz - Spring
Metz - Summer
Metz - Autumn
Relative Contribution
OA mass concentration

Figure S3: Relative contribution of PMF factors as a function of OA centiles by season (continued).

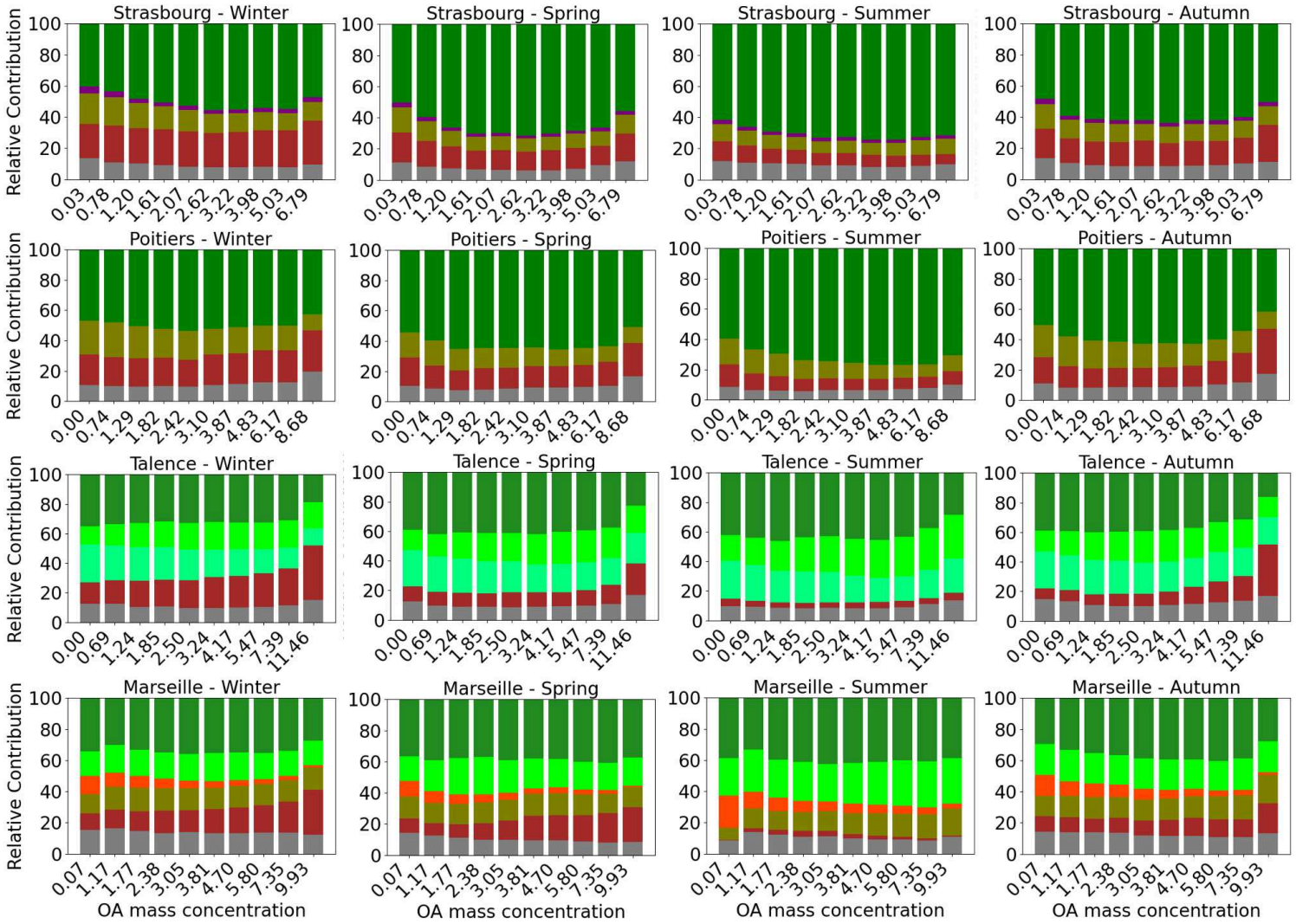

Figure S3: Relative contribution of PMF factors as a function of OA centiles by season.

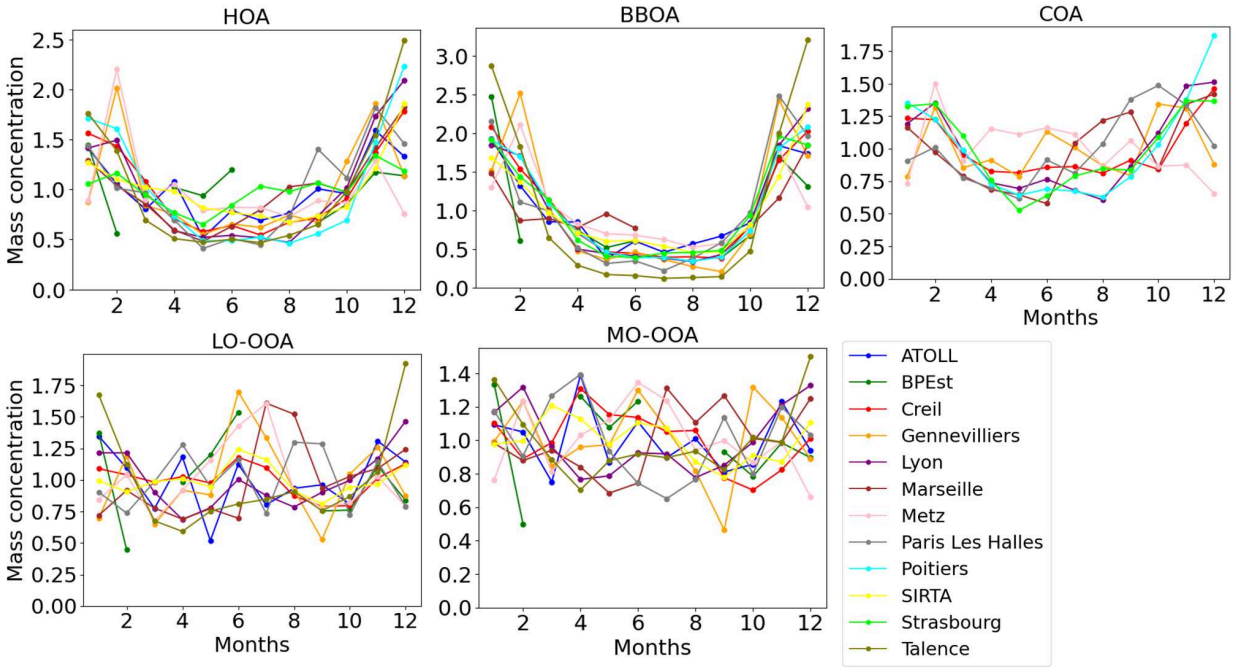

Figure S4: Monthly cycles for each PMF factor at different sites, normalized by the annual mean for each site.

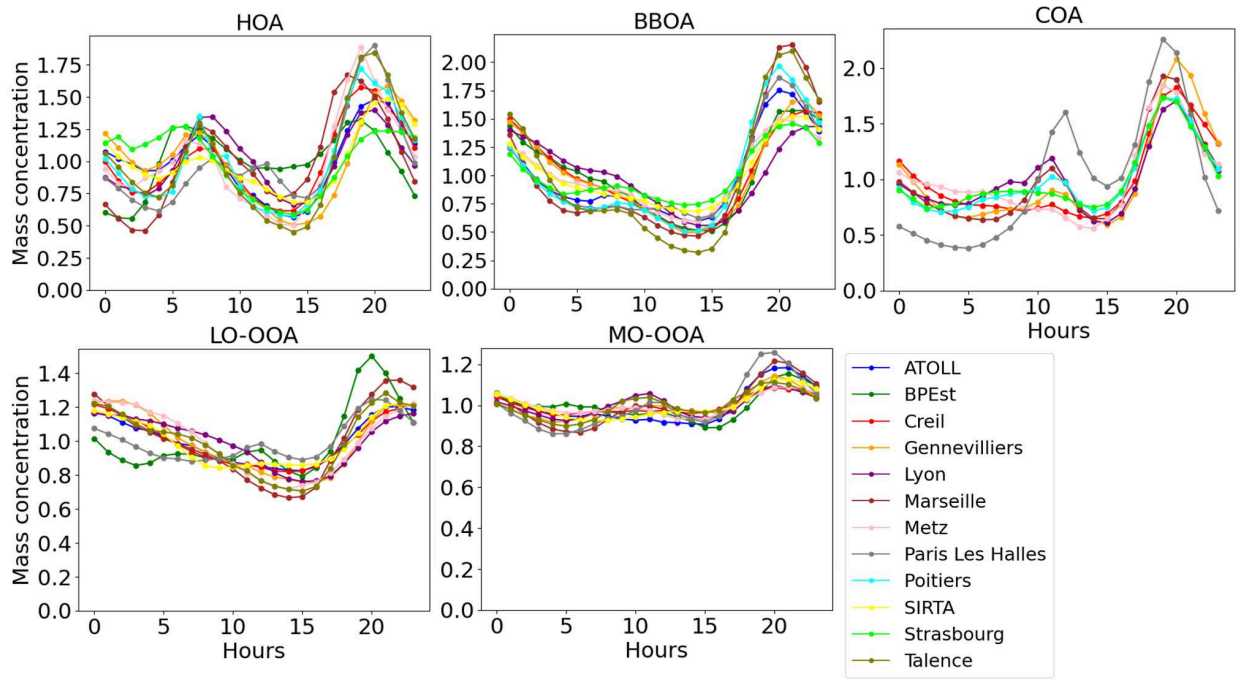

Figure S5: Diel profiles for each PMF factor at different sites.

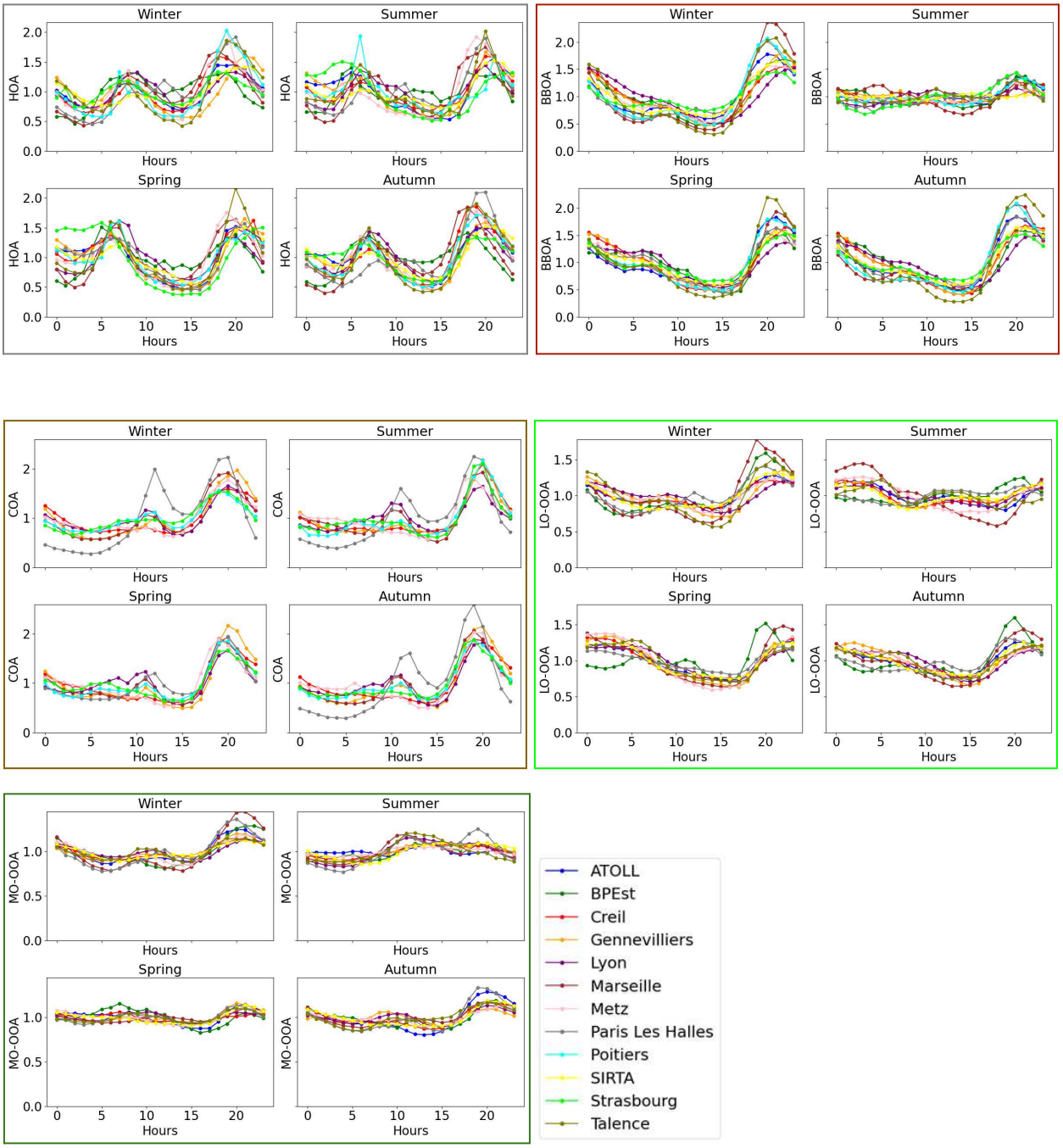

Figure S6: Seasonal diel concentration profiles, normalized by site-specific daily averages.

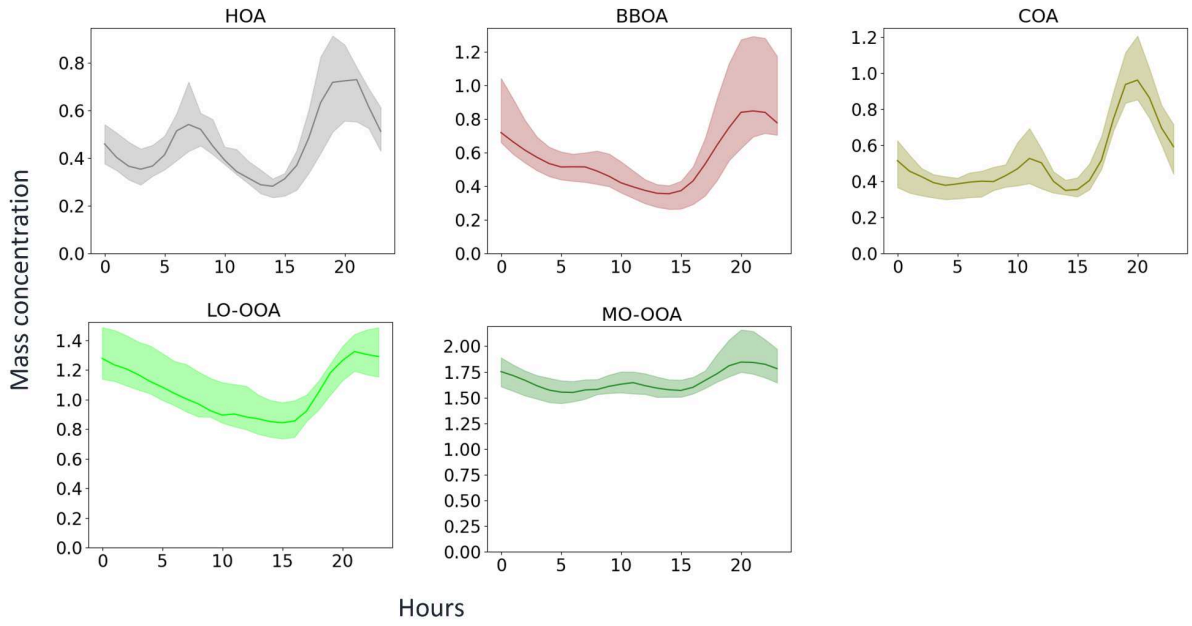

Figure S7: Diel median and IQR for each species across all sites.

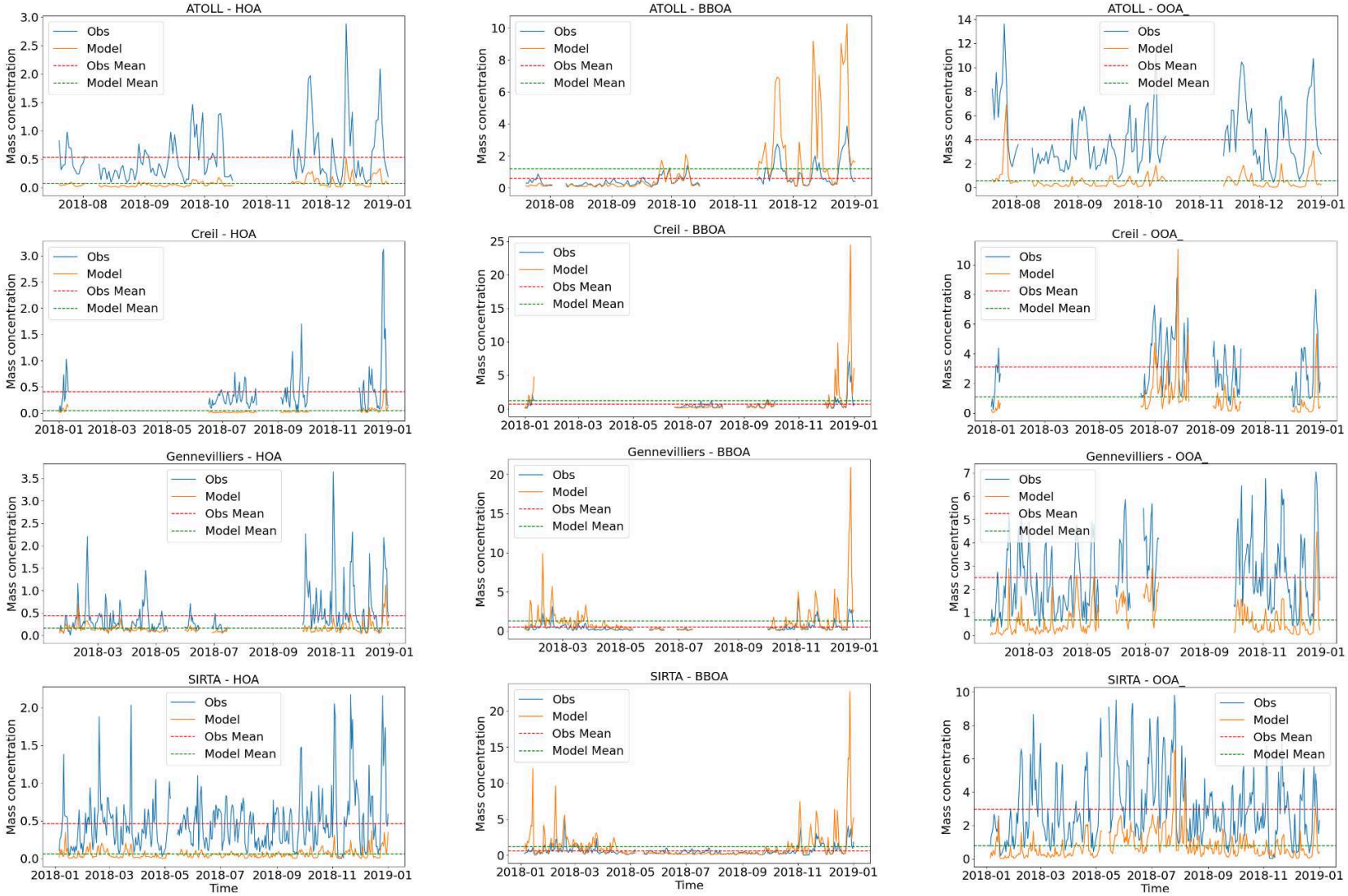
ATOLL - HOA
ATOLL - BBOA
ATOLL - OOA_
Creil - HOA
Creil - BBOA
Creil - OOA_
Gennevilliers - HOA
Gennevilliers - BBOA
Gennevilliers - OOA_
SIRTA - HOA
SIRTA - BBOA
SIRTA - OOA_
Obs
Model
Obs Mean
Model Mean
Mass concentration
Time

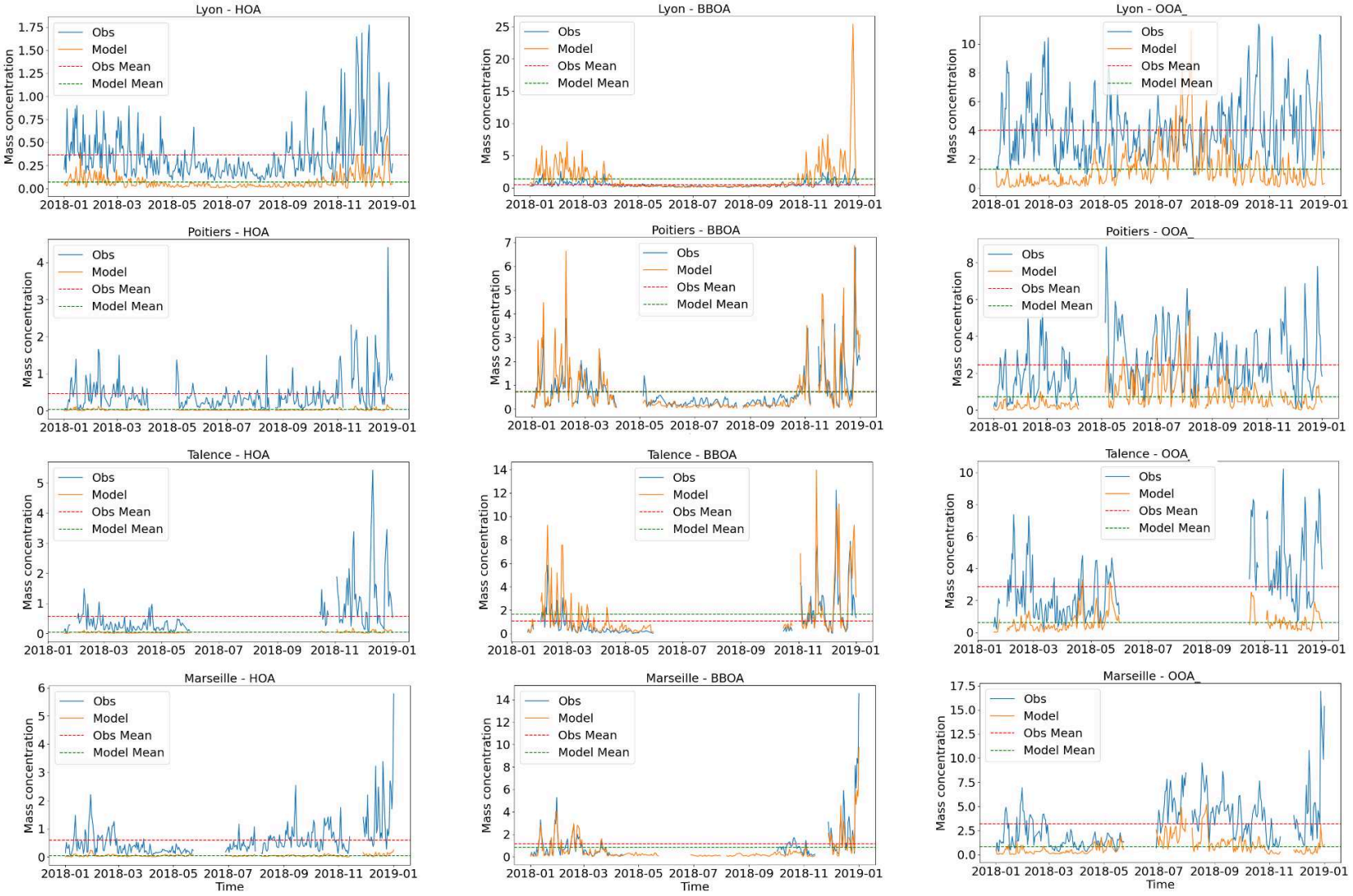

Figure 8: Comparison between PMF results and simulations for all sites (daily resolution).

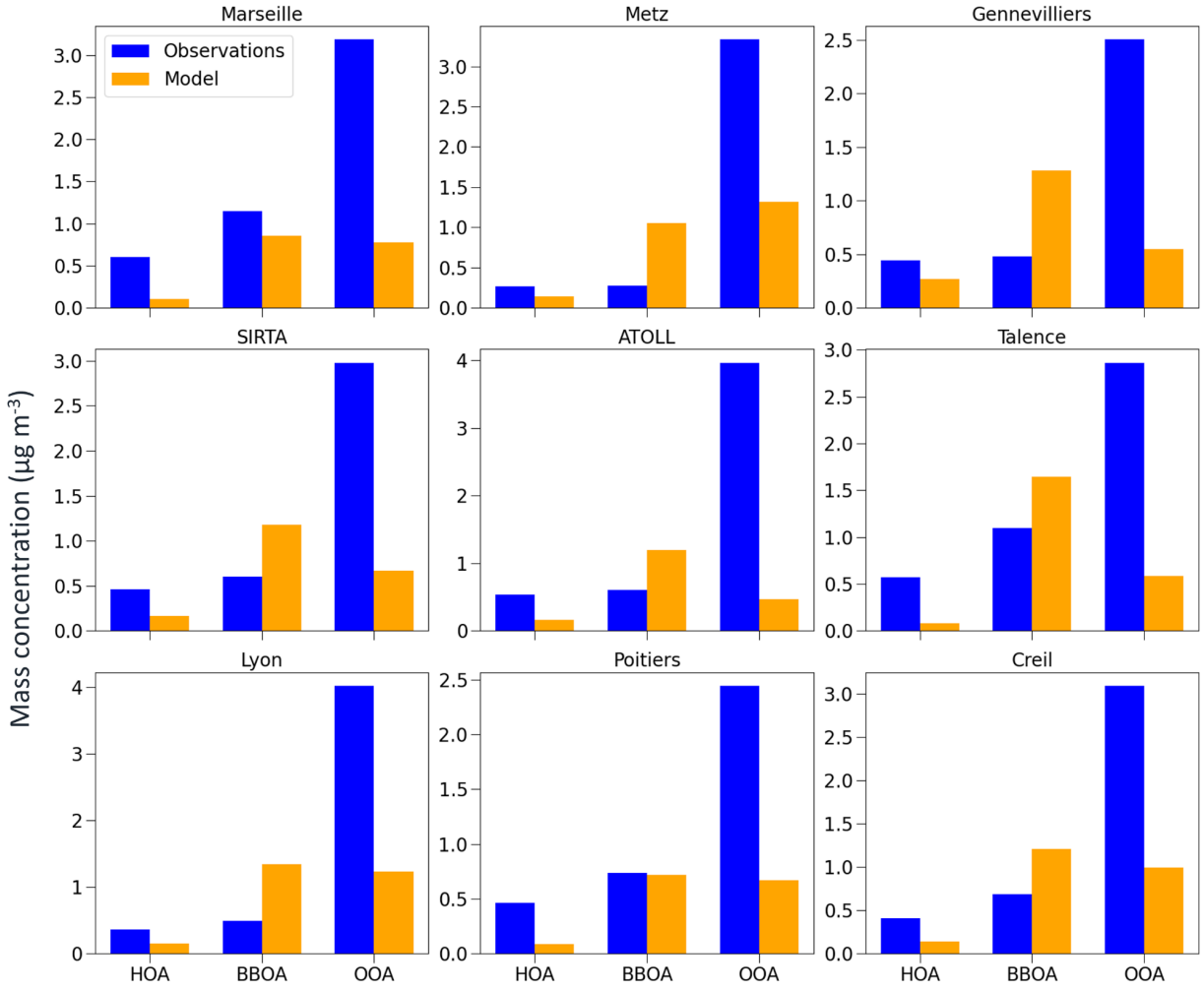

Figure S9: Mean mass concentration (in µg m^{-3}) for observations (in blue) and simulations (in orange) at nine French sites of HOA (POA and aged POA in the model), BBOA and OOA.

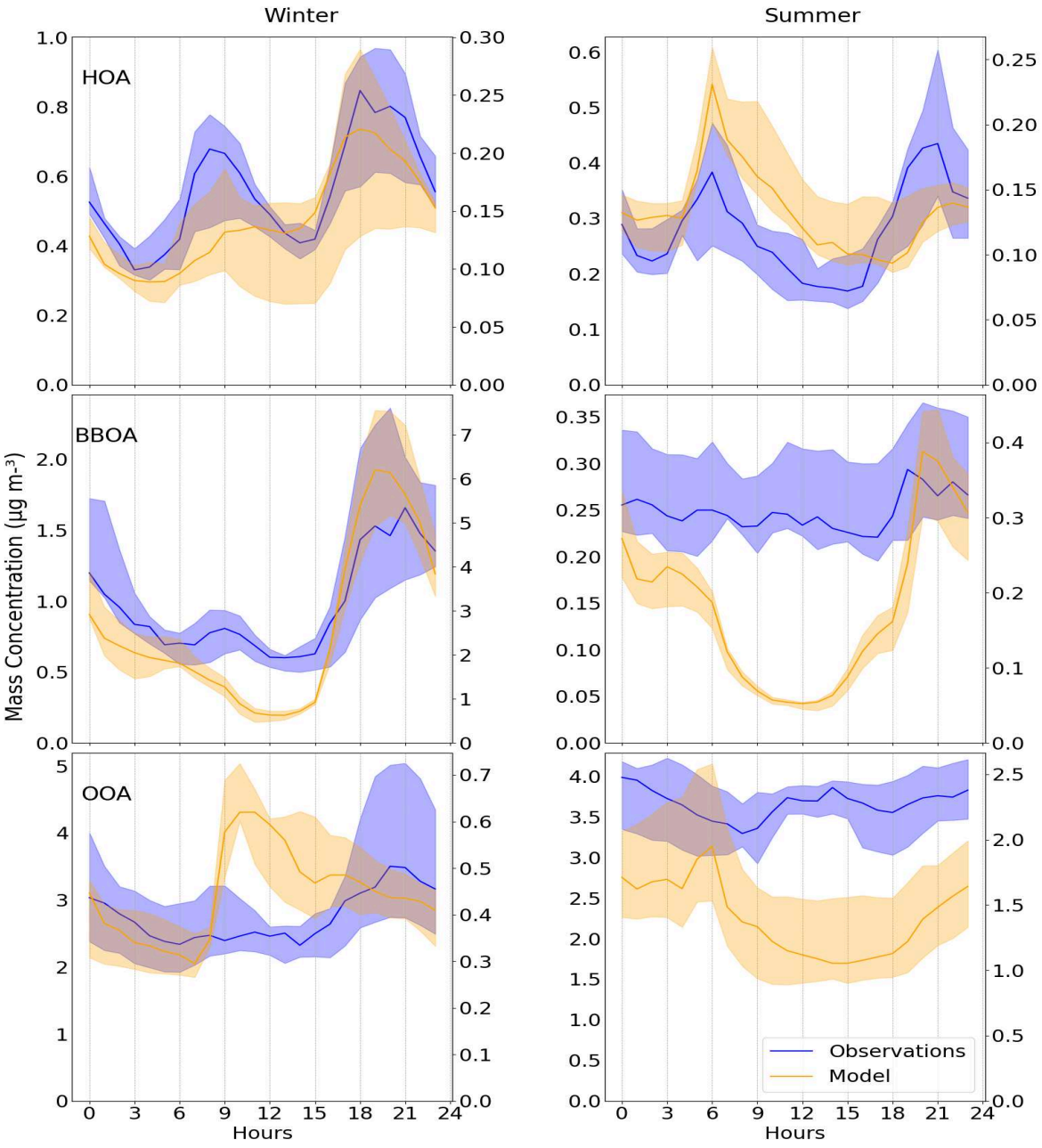

Figure S10: Observed and modeled diel OA profiles during winter and summer of 2018 across 9 French sites (HOA in the model presented as POA and aged POA).

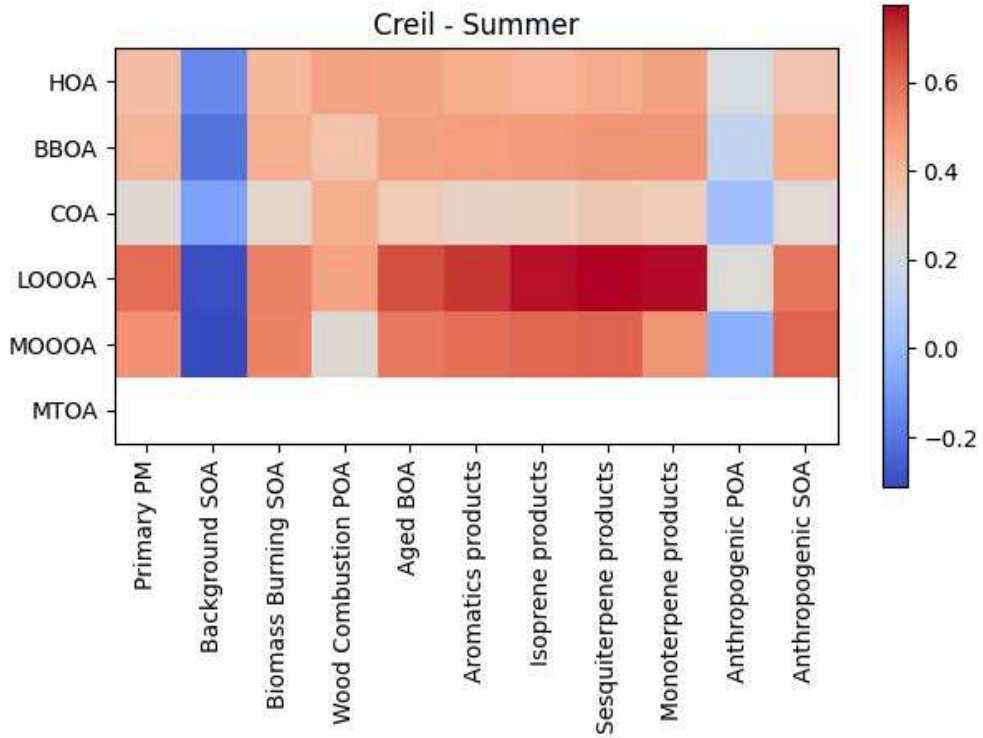
Creil - Summer
HOA
BBOA
COA
LOOOA
MOOOA
MTOA
Primary PM
Background SOA
Biomass Burning SOA
Wood Combustion POA
Aged BOA
Aromatics products
Isoprene products
Sesquiterpene products
Monoterpene products
Anthropogenic POA
Anthropogenic SOA
0.6
0.4
0.2
0.0
−0.2

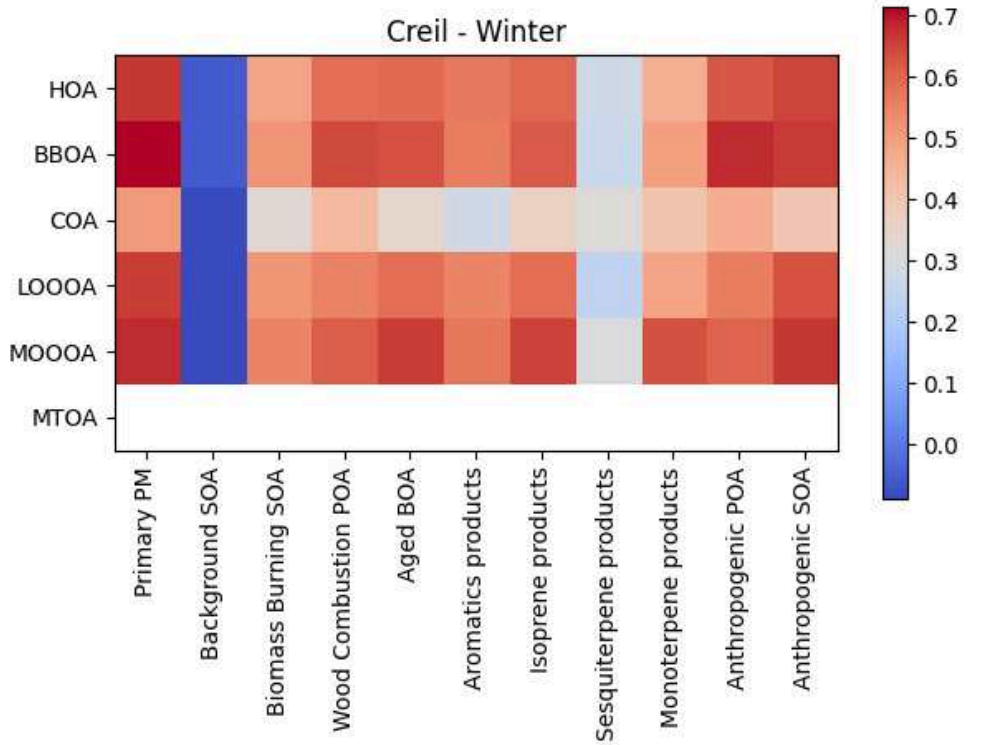
Creil - Winter
HOA
BBOA
COA
LOOOA
MOOOA
MTOA
Primary PM
Background SOA
Biomass Burning SOA
Wood Combustion POA
Aged BOA
Aromatics products
Isoprene products
Sesquiterpene products
Monoterpene products
Anthropogenic POA
Anthropogenic SOA
0.7
0.6
0.5
0.4
0.3
0.2
0.1
0.0

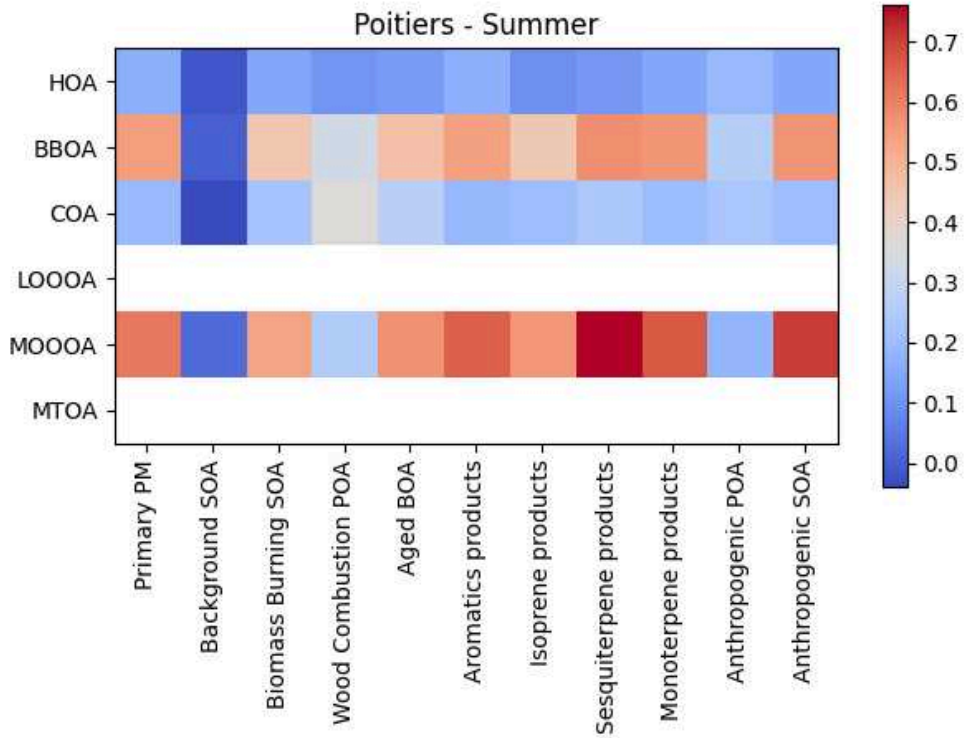
Poitiers - Summer
HOA
BBOA
COA
LOOOA
MOOOA
MTOA
Primary PM
Background SOA
Biomass Burning SOA
Wood Combustion POA
Aged BOA
Aromatics products
Isoprene products
Sesquiterpene products
Monoterpene products
Anthropogenic POA
Anthropogenic SOA
0.7
0.6
0.5
0.4
0.3
0.2
0.1
0.0

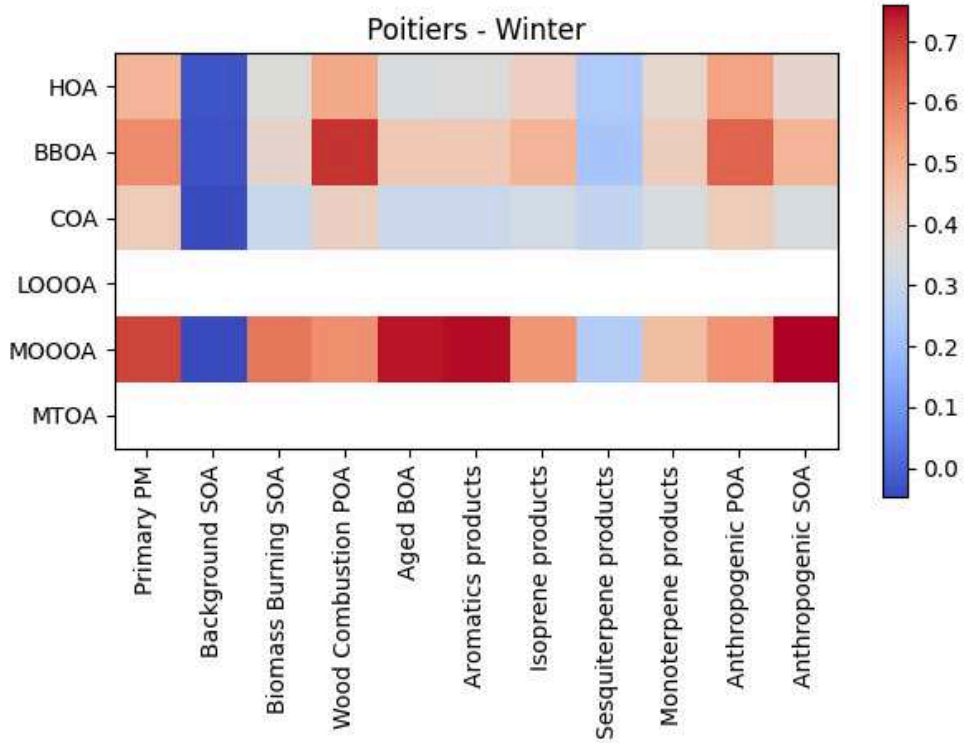
Poitiers - Winter
HOA
BBOA
COA
LOOOA
MOOOA
MTOA
Primary PM
Background SOA
Biomass Burning SOA
Wood Combustion POA
Aged BOA
Aromatics products
Isoprene products
Sesquiterpene products
Monoterpene products
Anthropogenic POA
Anthropogenic SOA
0.7
0.6
0.5
0.4
0.3
0.2
0.1
0.0

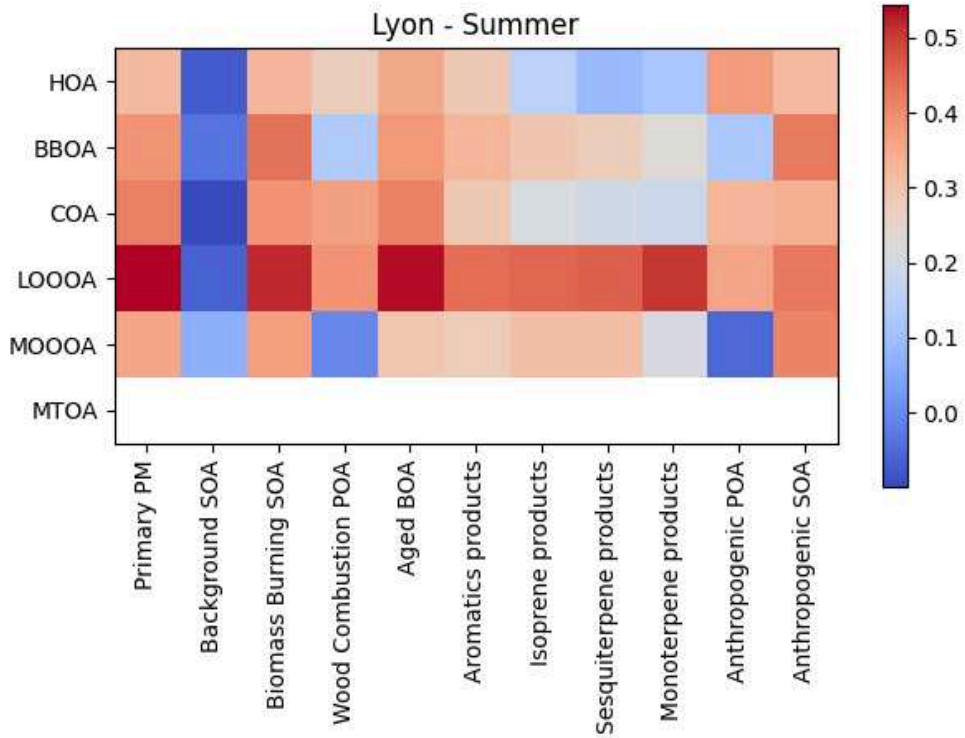
Lyon - Summer
HOA
BBOA
COA
LOOOA
MOOOA
MTOA
Primary PM
Background SOA
Biomass Burning SOA
Wood Combustion POA
Aged BOA
Aromatics products
Isoprene products
Sesquiterpene products
Monoterpene products
Anthropogenic POA
Anthropogenic SOA
0.5
0.4
0.3
0.2
0.1
0.0

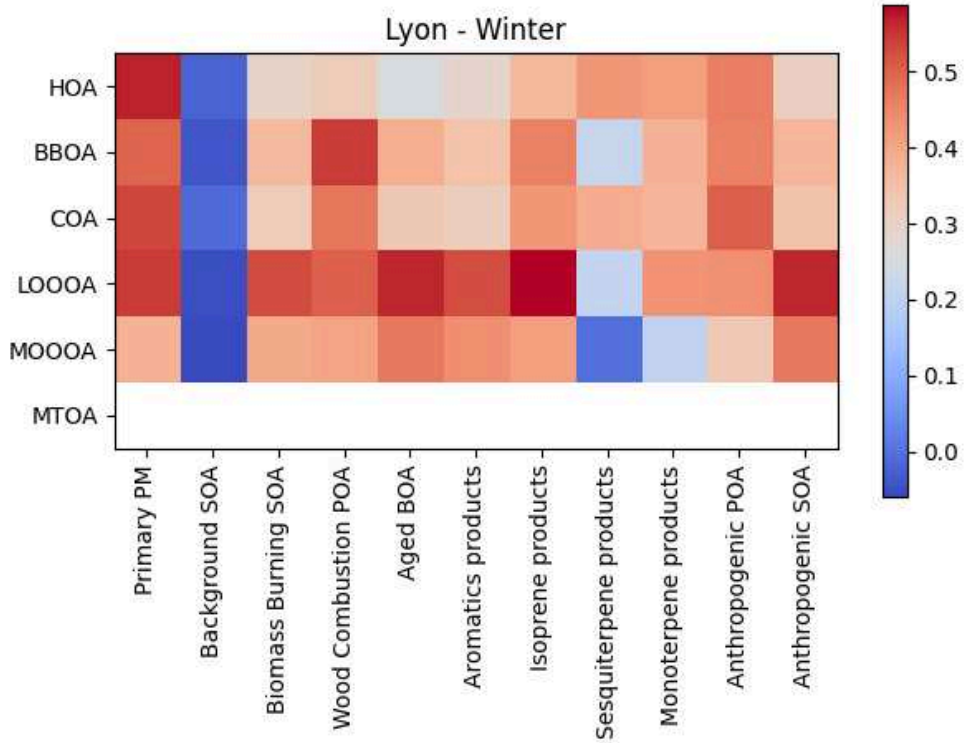
Lyon - Winter
HOA
BBOA
COA
LOOOA
MOOOA
MTOA
Primary PM
Background SOA
Biomass Burning SOA
Wood Combustion POA
Aged BOA
Aromatics products
Isoprene products
Sesquiterpene products
Monoterpene products
Anthropogenic POA
Anthropogenic SOA
0.5
0.4
0.3
0.2
0.1
0.0

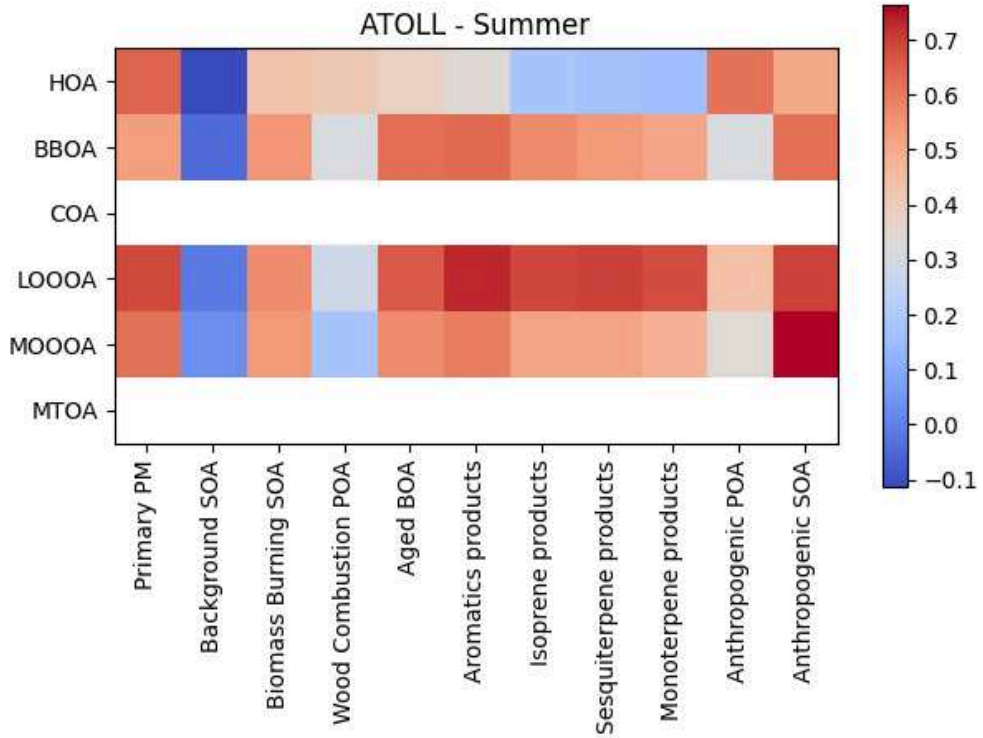
ATOLL - Summer
HOA
BBOA
COA
LOOOA
MOOOA
MTOA
Primary PM
Background SOA
Biomass Burning SOA
Wood Combustion POA
Aged BOA
Aromatics products
Isoprene products
Sesquiterpene products
Monoterpene products
Anthropogenic POA
Anthropogenic SOA
0.7
0.6
0.5
0.4
0.3
0.2
0.1
0.0
−0.1

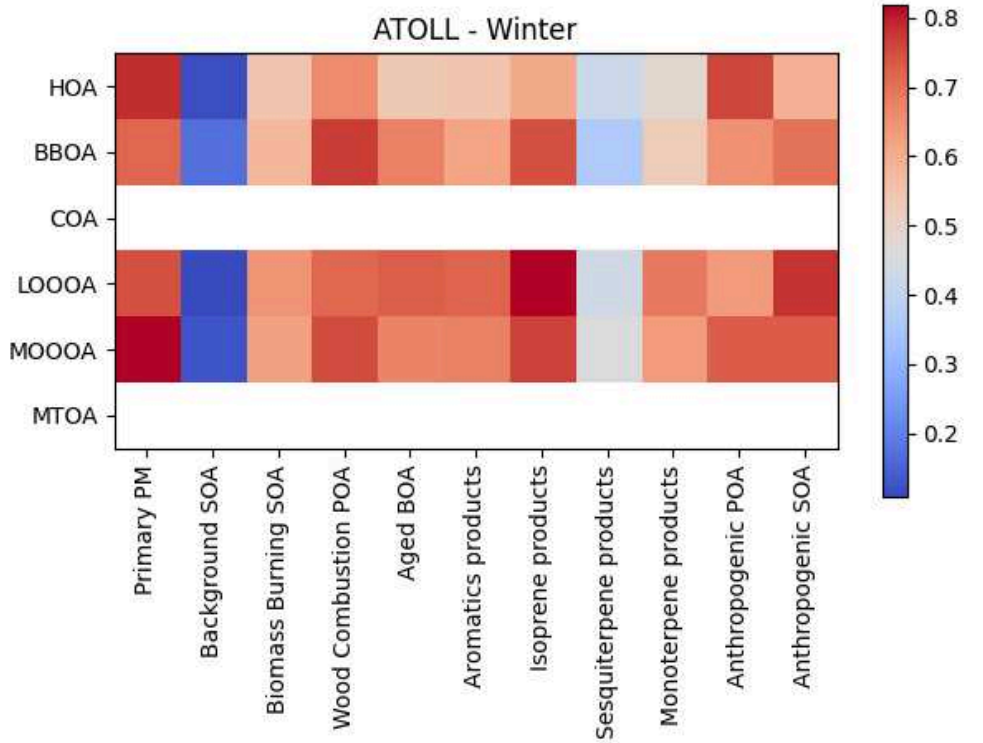
ATOLL - Winter
HOA
BBOA
COA
LOOOA
MOOOA
MTOA
Primary PM
Background SOA
Biomass Burning SOA
Wood Combustion POA
Aged BOA
Aromatics products
Isoprene products
Sesquiterpene products
Monoterpene products
Anthropogenic POA
Anthropogenic SOA
0.8
0.7
0.6
0.5
0.4
0.3
0.2

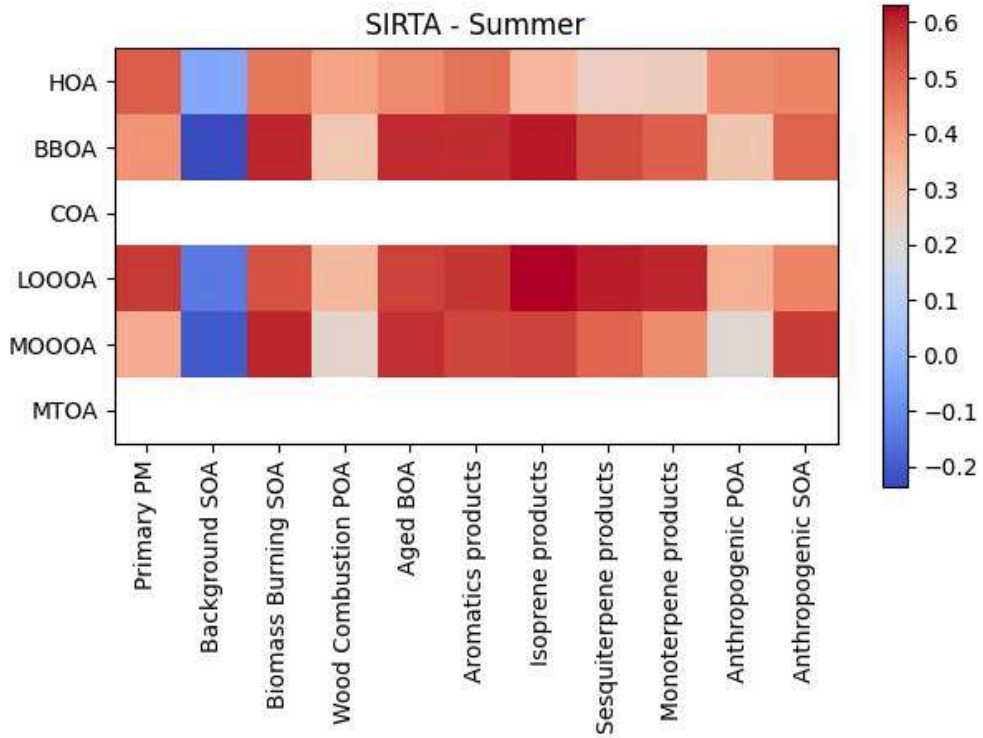
SIRTA - Summer
HOA
BBOA
COA
LOOOA
MOOOA
MTOA
Primary PM
Background SOA
Biomass Burning SOA
Wood Combustion POA
Aged BOA
Aromatics products
Isoprene products
Sesquiterpene products
Monoterpene products
Anthropogenic POA
Anthropogenic SOA
0.6
0.5
0.4
0.3
0.2
0.1
0.0
−0.1
−0.2

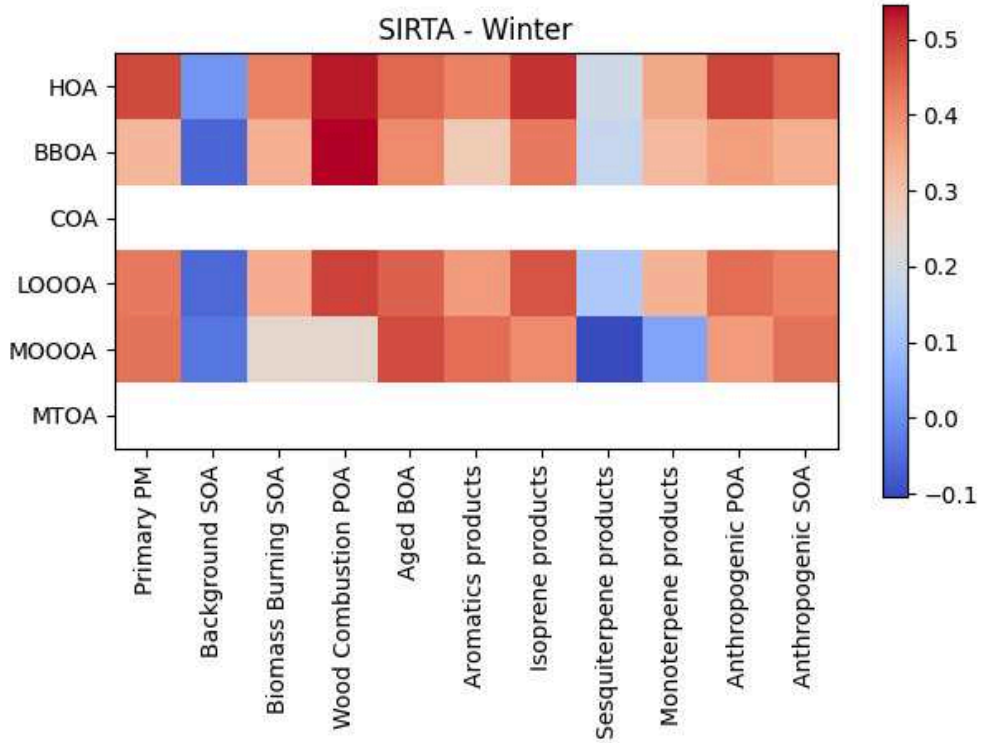
SIRTA - Winter
HOA
BBOA
COA
LOOOA
MOOOA
MTOA
Primary PM
Background SOA
Biomass Burning SOA
Wood Combustion POA
Aged BOA
Aromatics products
Isoprene products
Sesquiterpene products
Monoterpene products
Anthropogenic POA
Anthropogenic SOA
0.5
0.4
0.3
0.2
0.1
0.0
−0.1

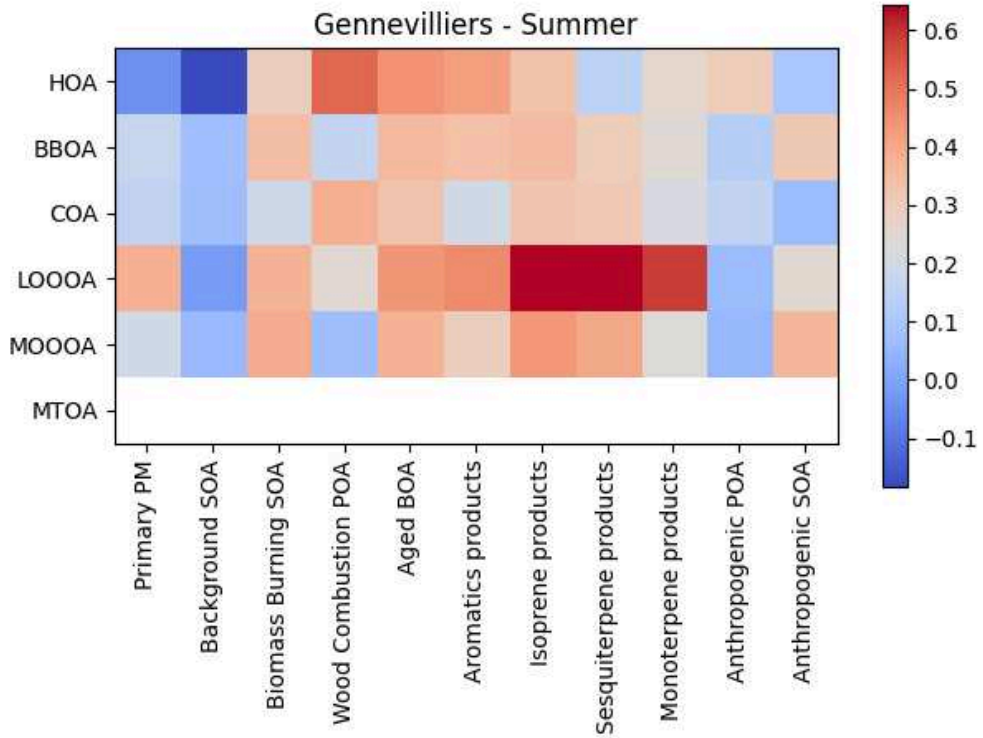
Gennevilliers - Summer
HOA
BBOA
COA
LOOOA
MOOOA
MTOA
Primary PM
Background SOA
Biomass Burning SOA
Wood Combustion POA
Aged BOA
Aromatics products
Isoprene products
Sesquiterpene products
Monoterpene products
Anthropogenic POA
Anthropogenic SOA
0.6
0.5
0.4
0.3
0.2
0.1
0.0
−0.1

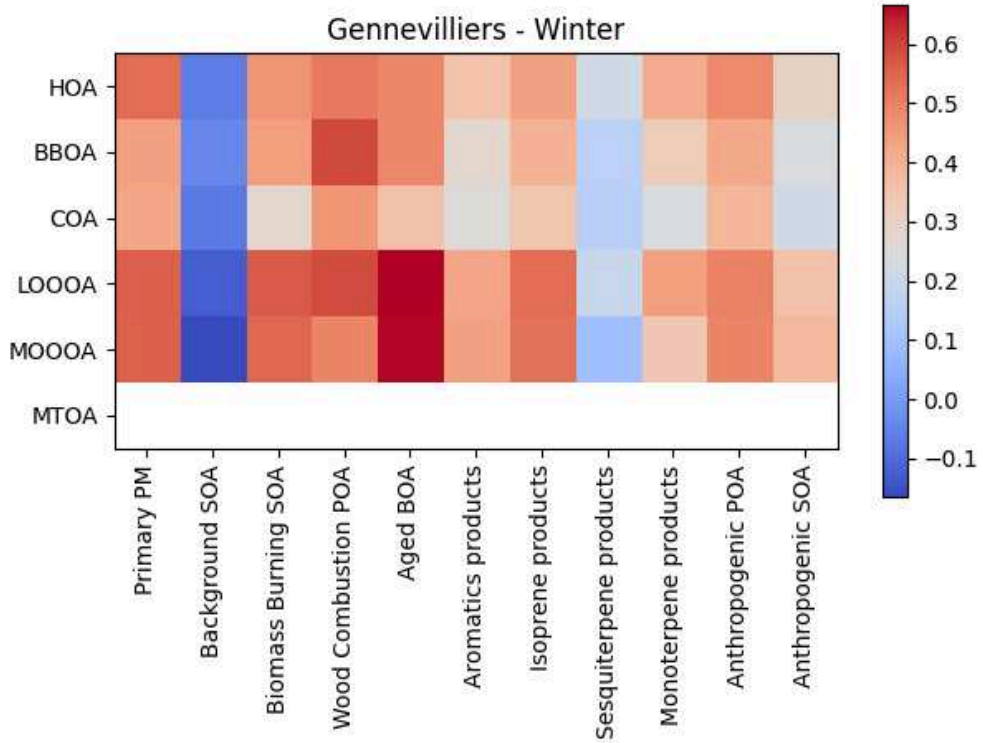
Gennevilliers - Winter
HOA
BBOA
COA
LOOOA
MOOOA
MTOA
Primary PM
Background SOA
Biomass Burning SOA
Wood Combustion POA
Aged BOA
Aromatics products
Isoprene products
Sesquiterpene products
Monoterpene products
Anthropogenic POA
Anthropogenic SOA
0.6
0.5
0.4
0.3
0.2
0.1
0.0
−0.1

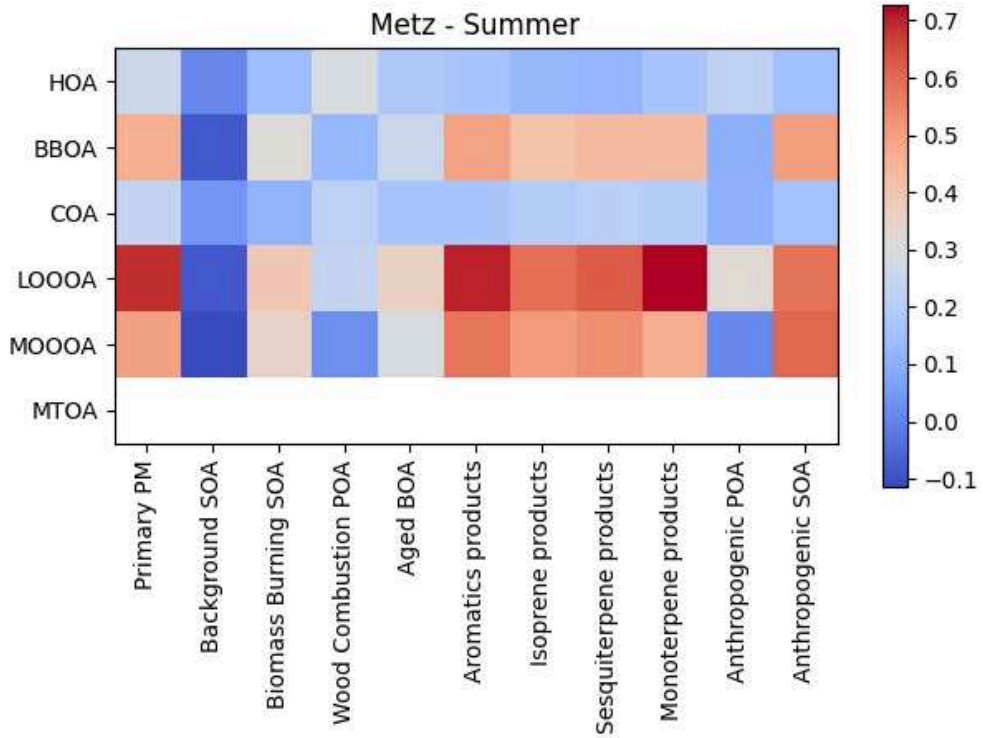
Metz - Summer
HOA
BBOA
COA
LOOOA
MOOOA
MTOA
Primary PM
Background SOA
Biomass Burning SOA
Wood Combustion POA
Aged BOA
Aromatics products
Isoprene products
Sesquiterpene products
Monoterpene products
Anthropogenic POA
Anthropogenic SOA
0.7
0.6
0.5
0.4
0.3
0.2
0.1
0.0
−0.1

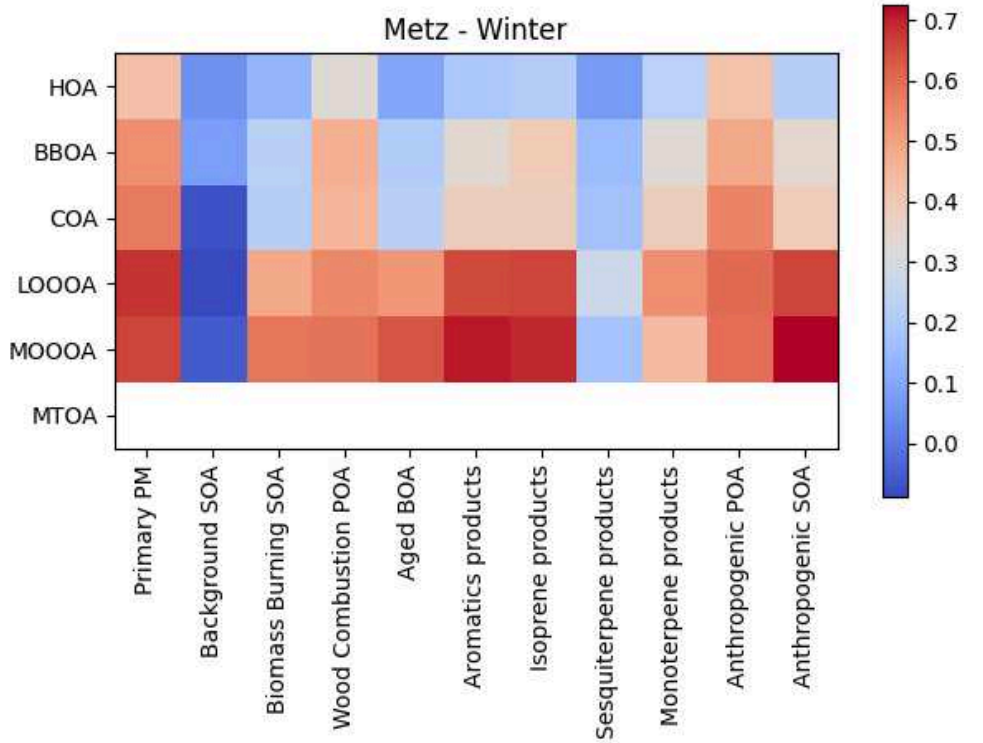
Metz - Winter
HOA
BBOA
COA
LOOOA
MOOOA
MTOA
Primary PM
Background SOA
Biomass Burning SOA
Wood Combustion POA
Aged BOA
Aromatics products
Isoprene products
Sesquiterpene products
Monoterpene products
Anthropogenic POA
Anthropogenic SOA
0.7
0.6
0.5
0.4
0.3
0.2
0.1
0.0

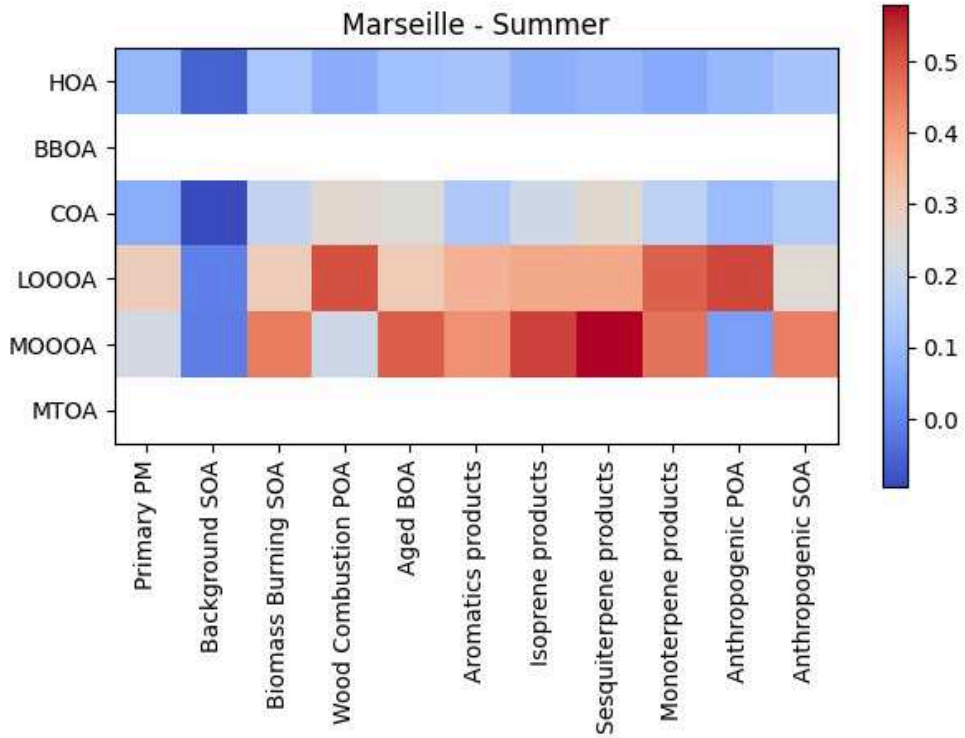
Marseille - Summer
HOA
BBOA
COA
LOOOA
MOOOA
MTOA
Primary PM
Background SOA
Biomass Burning SOA
Wood Combustion POA
Aged BOA
Aromatics products
Isoprene products
Sesquiterpene products
Monoterpene products
Anthropogenic POA
Anthropogenic SOA
0.5
0.4
0.3
0.2
0.1
0.0

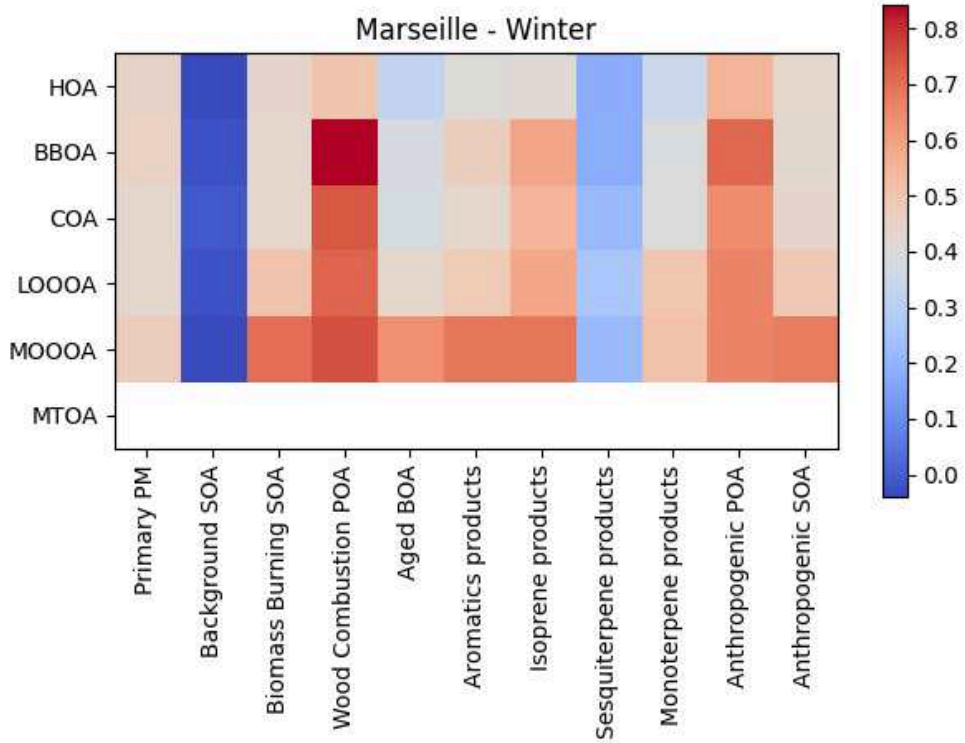
Marseille - Winter
HOA
BBOA
COA
LOOOA
MOOOA
MTOA
Primary PM
Background SOA
Biomass Burning SOA
Wood Combustion POA
Aged BOA
Aromatics products
Isoprene products
Sesquiterpene products
Monoterpene products
Anthropogenic POA
Anthropogenic SOA
0.8
0.7
0.6
0.5
0.4
0.3
0.2
0.1
0.0

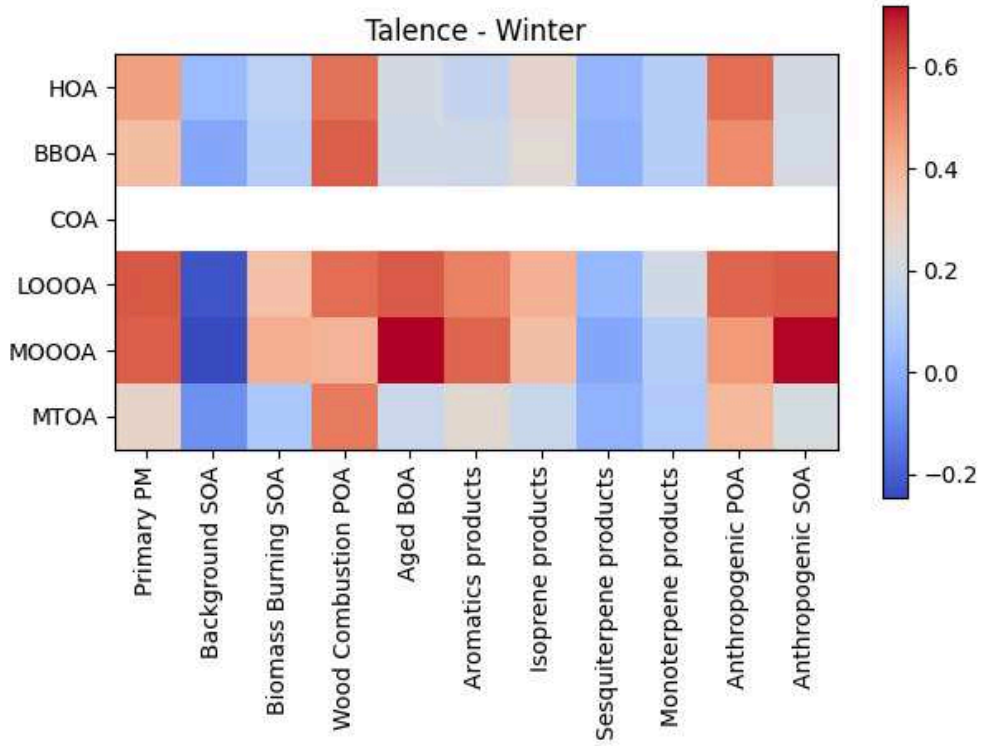

Figure S12: Correlations (r) of OA factors with CHIMERE species at French sites for winter and summer.

Table S3: Contributions (in %) of OA components for each season and site.

Site	**ATOLL**				**BPEst**				**Creil**				**Gennevilliers**				**Paris Les Halles**				**SIRTA**			
Season	SON	MAM	JJA	DJF	SON	MAM	JJA	DJF	SON	MAM	JJA	DJF	SON	MAM	JJA	DJF	SON	MAM	JJA	DJF	SON	MAM	JJA	DJF
HOA	13.1	10.6	9.7	12.2	15.7	14.5	14.8	16.8	11.4	7.9	6.9	12.5	14.4	10.3	7.9	15	15.6	9.4	8.8	15.8	11.6	10.6	8.8	13.3
BBOA	14.5	11	8	18.7	10.1	5.7	4.6	14.4	19	13.1	7.9	25.2	11	8	3.7	17	10.7	5.6	3.3	14.1	15.2	12	9	23.9
COA									13	10.3	11	12	15.5	14.6	14.2	13	22.3	13.7	22	17.6				
LO-OOA	31.6	30.6	33.3	31.9	28.6	29.3	36.5	26.4	24.1	25.1	29	21	22.8	24.3	33.1	21	25.3	33.3	39	22.9	27	25.5	30.9	22.1
MO-OOA	40.7	47.7	48.9	37.2	45.7	50.5	44.1	42.4	29.9	41.3	43	27.4	36.3	42.7	41	35	26.1	38	27	29.6	46.2	51.9	51.3	40.7
58-OA									2.7	2.3	2.2	2												
MT-OA																								
ShInd-OA																								

Site	**Marseille**				**Talence**				**Poitiers**				**Metz**				**Strasbourg**				**Lyon**			
Season	SON	MAM	JJA	DJF	SON	MAM	JJA	DJF	SON	MAM	JJA	DJF	SON	MAM	JJA	DJF	SON	MAM	JJA	DJF	SON	MAM	JJA	DJF
HOA	12	9.4	9.8	13.1	13.5	10.4	9.4	13.4	11.7	10.6	7.3	15.9	7.4	6.6	5.1	8.8	9.9	8.2	9.2	8.7	8.1	6.2	4.8	8.9
BBOA	13	15.9	2	22.5	19.5	11.7	4	31.9	18.8	15.9	8.1	24.1	10.3	8.5	5.2	14	18.5	13.9	7.7	25	10.5	8.9	5.2	15.3
COA	15.3	13.1	14.5	14.1					14.4	11.7	10	13.5	10.3	11.3	9.7	9.9	11.4	9.9	8.7	12.3	12.9	11.9	10.3	11.3
LO-OOA	19.6	19.4	27.6	16.4	18.1	19.9	25.5	17.9					23.5	24.4	29.9	24					27.2	27.8	31.7	26
MO-OOA	35.8	38.5	40.4	30.9	29.4	37.9	41.9	23.3	55.2	61.8	74	46.5	48.5	49.2	50.1	43	57.5	65.9	72	51.3	41.3	45.2	48	38.6
58-OA																	2.7	2.1	2.1	2.8				
MT-OA					19.5	19.9	19.2	13.4																
ShInd-OA	4.2	3.6	5.5	2.9																				

Table S4: Determination coefficient (r^2) between OA factors and external data.

R^2	HOA vs. eBC	BBOA vs. eBC_{wb}	LO-OOA vs. NO_3	MO-OOA vs. SO_4
ATOLL	0.62	0.80	0.42	0.37
BPEst	0.56	0.81	0.11	0.33
Creil	0.66	0.77	0.25	0.31
Gennevilliers	0.78	0.83	0.19	0.40
Lyon	0.69	0.79	0.40	0.40
Marseille	0.50	0.74	0.16	0.23
Metz	0.41	0.60	0.15	0.36
Paris Les Halles	0.69	0.72	0.22	0.34
Poitiers	0.42	0.81		0.28
SIRTA	0.65	0.73	0.22	0.37
Strasbourg	0.43	0.81		0.39
Talence	0.73	0.90	0.30	0.24

Table S5: Determination coefficient (r^2) between LO-OOA factor and BBOA, eBC_{wb} in winter.

R^2	LO-OOA vs. BBOA	LO-OOA vs. eBC_{wb}
ATOLL	0.64	0.61
BPEst	0.88	0.80
Creil	0.52	0.47
Gennevilliers	0.78	0.75
Lyon	0.71	0.68
Marseille	0.45	0.43
Metz	0.60	0.61
Paris Les Halles	0.67	0.68
SIRTA	0.63	0.62
Talence	0.78	0.55

Conclusions et perspectives

L'objectif principal de la thèse était d'étudier la phénoménologie à la fois de la composition chimique des particules fines et des sources d'aérosols organiques en France à partir de données pluriannuelles à haute résolution temporelle. Pour atteindre cet objectif, plusieurs étapes ont été suivies.

Dans un premier temps, un ensemble de jeux de données obtenues par mesures ACSM et AE33 a été collecté et consolidé pour la période 2015-2021. Ces données correspondent à 13 sites (péri-)urbains du programme CARA du dispositif national de surveillance de la qualité de l'air. 11 sites font partie des réseaux régionaux opérés par les AASQA suivantes : ATMO Hauts-de-France, ATMO Grand Est, AirParif, Air Breizh, ATMO Auvergne Rhône-Alpes, ATMO Nouvelle-Aquitaine, et ATMO Sud (ce dernier en partenariat avec le Laboratoire de Chimie de l'Environnement, Université Aix-Marseille). Les deux autres sites - ATOLL et SIRTA - correspondent à des plateformes d'observation intégrées à l'infrastructure de recherche européenne ACTRIS. Les opérations de nettoyage et de contrôle qualité des données ACSM ont été réalisées à l'aide du logiciel "acsm local" en utilisant des procédures éprouvées dans le cadre de ce programme de recherche ainsi que de précédents travaux du LCSQA. De la même manière, les données AE33 ont été validées et traitées selon les consignes des guides méthodologiques du dispositif national LCSQA et du centre d'expertise ECAC pour la mesure in situ des aérosols au sein d'ACTRIS. En particulier, un facteur d'harmonisation a été utilisé dans le calcul du coefficient d'absorption, puis les concentrations d'eBC ont été recalculées en normalisant les valeurs de coefficients d'absorption par une valeur de *Mass Absorption Cross-section* considérée comme représentative des conditions de fond en Europe. Les deux fractions d'eBC - i.e., eBC_{ff} et eBC_{wb}, considérées ici comme provenant essentiellement des échappements automobiles et de la combustion de biomasse, respectivement - ont ensuite pu être déterminées par application du modèle Aethalomètre de déconvolution.

Dans un deuxième temps, l'analyse de la composition chimique des particules fines a été effectuée en étudiant les différences géographiques et les variations journalières et saisonnières. En moyenne annuelle, les concentrations de PM_1 varient entre 6.8 (à Rennes) et 16.0 µg m^{-3} (à BPEst) avec une moyenne globale d'environ 10 (± 8) µg m^{-3} en France. Les résultats obtenus

indiquent clairement la domination de l'AO (40 à 60 %) en milieu urbain en France avec des concentrations massiques d'AO généralement plus élevées dans les stations du centre et du sud (Marseille, Poitiers, Talence et Lyon), ce qui s'explique en partie par des processus de formation secondaire plus intenses. À l'inverse, les contributions de NO_3 sont plus prononcées dans les sites au nord (ATOLL, Creil, Gennevilliers, …), en raison de conditions plus favorables à la formation de particules de nitrate d'ammonium. En général, les concentrations de NO_3 en France diminuent du nord au sud et d'est en ouest. Il constitue le deuxième contributeur le plus important, représentant de 15 à 30 % de la masse totale des PM_1. Le SO_4 est le troisième contributeur, avec des contributions allant de 8 à 14 %. Il montre une variation mensuelle relativement stable, avec des niveaux plus élevés observés en été, dues à l'augmentation des processus photochimiques qui favorisent sa formation. Les variations de la composition chimique en fonction des niveaux de PM_1 montrent la dominance de l'AO à des concentrations élevées de PM_1, soulignant l'influence de la combustion de la biomasse lors des épisodes de pollution en hiver et l'impact de la formation secondaire de composés organiques (AOS) en été, ceci en particulier pour les sites du sud de la France. L'AO diminue cependant à partir du 30e centile des niveaux de PM_1 avec une augmentation du NO_3 dans les sites du nord de la France en particulier au printemps, jouant un rôle important lors des épisodes de pollution.

Dans un troisième temps, les efforts ont porté sur la comparaison et l'évaluation qualitative de la cohérence des mesures ainsi que les résultats des analyses de répartition des sources d'aérosols carbonés effectuées sur deux sites urbains voisins à Strasbourg (Danube et Clemenceau) pendant l'hiver 2019/2020. Cette étude de cas permet d'évaluer la sensibilité des outils de déconvolution de sources mis en œuvre dans le cadre de cette thèse. Les résultats ont montré des concentrations légèrement plus élevées sur le site Clemenceau (imputée à la proximité du trafic automobile sur ce site) par rapport au site Danube. La comparaison des sources d'AO a été effectuée en appliquant deux approches PMF pour les deux sites: l'une classique et l'autre combinée. Les deux méthodes ont résolu cinq facteurs : HOA, BBOA, COA-like, OOA et un facteur spécifique (*amine-related OA*) caractérisé par une forte contribution de m/z 58, qui semble associé à une source industrielle spécifique. La PMF a également révélé des contributions plus élevées de HOA sur le site Clemenceau et des contributions de BBOA équivalentes entre les deux stations, en accord avec la comparaison des mesures de lévoglucosane. Ce dernier résultat paraît

contradictoire avec des concentrations plus élevées estimées à Clemenceau pour eBC_{wb} (en raison du choix des coefficients α_{ff} et α_{wb} pour la déconvolution) et m/z 60 (visiblement en lien avec certaines spécificités techniques de l'instrument). La PMF combinée a permis d'améliorer le profil journalier de COA, en particulier pour le site Clemenceau, mais elle conduit probablement à une sous-estimation des facteurs HOA et BBOA (et donc une surestimation de la fraction OOA) à la station Danube. Par conséquent, cette étude met en lumière des discordances dans les mesures d'aérosols carbonés entre ces deux sites, ainsi que dans les solutions de répartition des sources, malgré l'utilisation d'instruments identiques. Cela souligne la difficulté et les précautions nécessaires dans l'interprétation des résultats PMF obtenus pour ce genre d'études.

Un autre cas d'étude est ensuite mis en avant dans ce manuscrit, avec l'analyse approfondie des résultats obtenus pour le site de l'agglomération lilloise. En effet, afin de résoudre les sources d'AO sur de longues séries de données (comprises entre 1 et 7 ans, selon le site), une nouvelle méthode récemment développée dans SoFi Pro a été utilisée pour tenir compte des changements temporels dans les facteurs sources. Cette méthode, de type "PMF glissante", a d'abord été appliquée dans le cadre de ma thèse au site ATOLL dans le nord de la France. Au préalable, une série d'analyses PMF classiques par saison, a été réalisée sur la période allant d'octobre 2016 à août 2017. Elle a permis d'identifier quatre facteurs, à savoir HOA, BBOA, LO-OOA et MO-OOA. Sur la base de ces résultats, la PMF glissante a ensuite été appliquée à l'ensemble des données (d'octobre 2016 à décembre 2020), en utilisant une fenêtre de 28 jours et un pas de sept jours. La solution finale a été obtenue en utilisant des critères de sélection prédéfinis pour sélectionner les meilleures solutions PMF. L'analyse permet d'associer en hiver, 12 % de l'AO au trafic routier et la moitié à la combustion résidentielle du bois (LO-OOA étant identifié comme un BBOA vieilli) ; et en été, 10 % de l'AO au trafic et 34 % aux sources biogéniques (LO-OOA étant cette fois associé aux AOS biogéniques). Cette analyse a révélé également une contribution importante des masses d'air continentales polluées provenant d'Europe centrale et mis en lumière la complexité des interactions entre les sources anthropiques et naturelles, conduisant à différents mécanismes de dégradation de la qualité de l'air dans la région.

Finalement, cette approche de PMF glissante testée sur la série pluri-annuelle d'ATOLL a été appliquée aux autres ensembles de données. L'analyse a montré l'existence de facteurs d'AO communs entre les différentes stations, comprenant les facteurs primaires tels que HOA, BBOA

et COA, et les facteurs oxygénés secondaires, notamment LO-OOA et MO-OOA. Des facteurs d'AO spécifiques à chaque site ont été également identifiés, comme un facteur associé aux émissions portuaires et/ou industrielles à Marseille (ShInd-OA) et un facteur lié aux activités industrielles à Strasbourg et Creil (58-OA). À Talence, un facteur relativement proche des spectres de masse de type LO-OOA, a également été mis en évidence. En été, ce facteur pourrait être directement lié aux AOS issus de l'oxydation des monoterpènes. L'ensemble de ces résultats illustre également la prédominance des OOA sur tous les sites français avec une contribution moyenne de 74 %. Ces facteurs oxygénés augmentent avec l'augmentation des niveaux d'AO en été, mettant l'accent sur l'importance de la formation secondaire. Le HOA et le BBOA ont été résolus sur tous les sites, montrant une variabilité spatiale importante. La contribution relative de HOA est de 12 % en France. Quant à BBOA, sa moyenne annuelle est d'environ 15 % sur tous les sites, avec des contributions importantes dans les sites du sud, mettant en évidence l'influence de la combustion de biomasse, en particulier en hiver. Le facteur de type COA a été identifié sur 8 sites avec des contributions comparables d'environ 10-15 % de l'AO submicronique. Les quatre autres facteurs spécifiques ont des contributions minimales (ShInd-OA, 4 % et *amine related-OA*, 2 %). Les contributions des différents facteurs en fonction des niveaux d'AO montrent une augmentation de BBOA lorsque l'AO augmente dans la majorité des sites, en particulier pendant l'hiver, suggérant le rôle des émissions primaires de la combustion de biomasse pendant les épisodes de pollution. Les variabilités saisonnières et journalières ont été également examinées pour les facteurs communs dans la plupart des sites sur la période d'étude. Les POA présentent une saisonnalité marquée, avec une variation particulièrement prononcée pour BBOA, attribuable à l'augmentation des émissions de chauffage domestique, tandis que HOA et COA montrent une variation moins marquée. En général, ces trois facteurs augmentent pendant les mois hivernaux, ce qui peut s'expliquer par des conditions atmosphériques stagnantes, caractérisées par des températures basses et des vents faibles. LO-OOA présente généralement une augmentation en été et une autre en hiver. Cette tendance suggère une association avec les AOS biogéniques en été, et avec la combustion de la biomasse en hiver. Quant à MO-OOA, il montre une relative stabilité, indiquant une origine plutôt régionale pour ce facteur.

Ainsi, l'origine des 2 facteurs oxygénés (LO-OOA et MO-OOA, classiquement attribués aux AOS) reste relativement mal caractérisée. Leur séparation en fonction de leur degré d'oxydation

n’apporte malheureusement aucun élément d’information sur leurs précurseurs gazeux (e.g., anthropiques vs. biogéniques), bien que l’on suppose que les OOA sont principalement formés par l'oxydation de composés organiques volatils biogéniques en été, et de composés liés aux émissions anthropiques (notamment combustion de biomasse et trafic routier) en hiver. Par conséquent, d'autres travaux sont nécessaires pour mieux comprendre ces facteurs oxygénés. Dans le cadre d’un programme opérationnel tel que CARA, ces futurs travaux peuvent notamment inclure des exercices de comparaisons avec des modèles déterministes (e.g., CHIMERE ou PSAT). Dans cette optique, nous avons initié la comparaison avec des simulations 3D issues d’une version récente du modèle CHIMERE (couplé au modèle SSH-aérosol v1.3, et utilisant le model GENOA v2.0 (Wang et al., 2022, 2023) pour réduire les mécanismes AOS des monoterpènes et des sesquiterpènes) pour l'année 2018, englobant les données de neuf sites en France. Les différents facteurs PMF ont été comparés avec les différentes espèces du modèle CHIMERE. En général, le modèle surestime BBOA et sous-estime HOA et OOA. L'ajout des POA vieillis pour les comparer avec HOA améliore la représentation du modèle, mais il persiste un déficit notable. L'OOA est principalement surestimé en hiver, suggérant un manque de sources anthropiques dans le modèle. LO-OOA montre de bonnes corrélations avec les espèces primaires vieillis et les SOA anthropiques en hiver, et en été, avec les espèces SOA biogéniques du modèle, ce qui confirme nos conclusions concernant ce facteur. En revanche, MO-OOA ne montre aucune corrélation claire aux deux saisons. Il reste donc des défis à relever pour améliorer le modèle et espérer en retirer des informations fiables sur les différentes origines de ces deux fractions OOA. Ce type d’étude, combinant l’analyse des mesures in situ et les sorties de modèles, nécessite par ailleurs l’élaboration d’une méthodologie harmonisée de classification des sous-familles d’OA issues des différentes approches pouvant être directement comparées entre elles.

De futurs travaux de recherche pourront également faire appel à l'utilisation de traceurs moléculaires analysés en parallèle des mesures ACSM, le programme CARA incluant également la collecte d’échantillons sur filtres pour des analyses différées ultérieures en laboratoire. La combinaison dans une même analyse PMF des données correspondant aux spectres de masse de l’AO, aux concentrations des autres espèces chimiques majeures, et aux mesures de traceurs organiques (obtenus par exemple à partir des mesures sur filtres) sur une période plus longue permet en effet une meilleure distinction et compréhension des sources d’AO des processus

chimiques associés (Srivastava et al., 2019, Via et al., 2023). Ce type d'approche permet d'améliorer notre connaissance des différentes fractions de l'AO secondaire, mais aussi d'étudier plus spécifiquement les sources de certains facteurs spécifiques comme le COA-like (qu'on suppose lié principalement à la cuisson). Ceci est également applicable pour d'autres facteurs spécifiques identifiés comme le 58-OA à Strasbourg et Creil, et ShInd-OA à Marseille, à condition de trouver d'autres traceurs spécifiques de ces activités.

En parallèle, il conviendra de développer les outils d'analyse combinée des données ACSM et AE33 avec d'autres mesures automatiques en cours de déploiement sur certains sites du programme CARA, tels que les analyseurs automatiques de métaux, les granulomètres de type MPSS (*Mobility Particle Size Spectrometer*) ainsi que les instruments de mesures de NH_3 ou de COVs en continu. Ces mesures complémentaires des propriétés physico-chimiques des aérosols et/ou de leurs éventuels précurseurs gazeux pourraient effectivement permettre d'affiner notre compréhension des origines des différents facteurs d'OA issus de l'application de la PMF aux mesures ACSM, mais également d'élargir le nombre de sous-familles de Black Carbon obtenues par l'étude des données d'Aethalomètre multi-longueurs d'onde.

Quoi qu'il en soit, l'ensemble des résultats présentés ici constitue une compilation innovante et unique à ce jour des mesures d'observation réalisées sous influences anthropiques, apportant une vision globale des principales sources d'AO en milieu urbain en France. Cette thèse a également permis de répondre à la mission de soutien scientifique et technique du LCSQA à la fois auprès du ministère, en permettant d'orienter les politiques publiques de réduction des émissions et d'amélioration de la qualité de l'air, et auprès des Associations Agréées de Surveillance de la Qualité de l'Air (AASQA), en assurant la montée en compétences de leur personnel sur le traitement avancé des mesures de composition chimique en ligne, notamment via des sessions de formation et la rédaction d'un guide opérationnel de mise en oeuvre de la modélisation statistique sources-récepteur.

Cette thèse de doctorat constitue ainsi la base de futures études de tendances qui pourront être mises en œuvre à moyen terme pour la surveillance au long cours de la nature et des origines des particules fines sur les sites du programme CARA. Il est également à noter que les différents résultats de répartition des sources d'AO obtenus pour l'ensemble de ces sites pourront être

utilisés dans le cadre du déploiement d'outils de déconvolution de sources des particules carbonées en temps réel. En effet, la détermination initiale des principaux facteurs influençant le site de mesure est actuellement un prérequis indispensable et crucial des approches automatisées développées récemment (Chen et al., 2022b). Cependant, de futures réflexions seront à mener concernant les facteurs de référence utilisés dans la PMF. Actuellement, les facteurs issus de Crippa et al. (2013, 2014) sont très largement utilisés pour différentes études conduites à travers l'Europe. Pour exemple, les facteurs étudiés dans l'étude de dimension continentale de Chen et al. (2022a) ont été fortement contraints sur la base de ces profils. Cette approche, également privilégiée dans le cadre de la présente thèse, permet une harmonisation des pratiques pour une meilleure comparabilité des résultats obtenus d'une étude à l'autre. Néanmoins, il conviendra de se montrer vigilant à d'éventuelles modifications significatives des profils spécifiques de sources primaires au cours du temps. En outre, il serait bénéfique de développer davantage la procédure de sélection des critères de choix des solutions PMF à retenir dans SoFi Pro, notamment via la détermination de critères statistiques concernant les ensembles de données sélectionnés.

Soulignons enfin que l'ensemble des différents jeux de données français issus de ce travail de thèse revêt une grande importance pour différentes communautés scientifiques partenaires partageant l'objectif d'améliorer la qualité de l'air et de réduire les émissions de polluants. Outre leur utilisation dans des exercices de comparaison mesures-modèles (tel qu'évoqué ci-dessus), il est particulièrement intéressant d'envisager la réalisation d'études épidémiologiques visant à quantifier les effets des aérosols sur la santé, également en lien avec les travaux actuels sur le potentiel oxydant des particules (Daellenbach et al., 2020; Weber et al., 2021). Selon la taille des agglomérations étudiées et la nature des données sanitaires pouvant être mises en regard des mesures atmosphériques, des séries temporelles de l'ordre de 3 ans peuvent en effet s'avérer suffisantes à la réalisation de ce genre d'analyse. A ce titre, ces données pourront être directement utilisées dans le cadre du projet européen RI-URBANS (2021-2025), qui vise à relever les défis et les besoins sociétaux liés à la qualité de l'air dans les villes européennes. L'objectif est de réduire considérablement la pollution de l'air en Europe et de mettre en place une stratégie d'évaluation des impacts de la pollution de l'air sur la santé des citoyens.

Références bibliographiques

AASQA: Rapport Caractérisation des particules à Rennes Bilan 2020, 2022.

Aiken, A. C., DeCarlo, P. F., Kroll, J. H., Worsnop, D. R., Huffman, J. A., Docherty, K. S., Ulbrich, I. M., Mohr, C., Kimmel, J. R., Sueper, D., Sun, Y., Zhang, Q., Trimborn, A., Northway, M., Ziemann, P. J., Canagaratna, M. R., Onasch, T. B., Alfarra, M. R., Prevot, A. S. H., Dommen, J., Duplissy, J., Metzger, A., Baltensperger, U., and Jimenez, J. L.: O/C and OM/OC Ratios of Primary, Secondary, and Ambient Organic Aerosols with High-Resolution Time-of-Flight Aerosol Mass Spectrometry, Environ. Sci. Technol., 42, 4478–4485, https://doi.org/10.1021/es703009q, 2008.

Air quality in Europe 2021 — European Environment Agency: https://www.eea.europa.eu/publications/air-quality-in-europe-2021, last access: 10 January 2022.

Air quality in Europe 2022 — European Environment Agency: https://www.eea.europa.eu/publications/air-quality-in-europe-2022, last access: 31 July 2023.

Alastuey, A., Querol, X., García, M., Trechera, P., Savadkoohi, M., Karanasiou, A., Minguillón, M. C., Fiebig, M., Dallënbach, K. R., Salameh, T., Sauvage, S., and Petäjä, T.: Deliverable D1 (D1.1): Guidelines, datasets of non-regulated pollutants incl. metadata, methods, 2022.

Allan, J. D., Jimenez, J. L., Williams, P. I., Alfarra, M. R., Bower, K. N., Jayne, J. T., Coe, H., and Worsnop, D. R.: Quantitative sampling using an Aerodyne aerosol mass spectrometer 1. Techniques of data interpretation and error analysis, J. Geophys. Res. Atmospheres, 108, https://doi.org/10.1029/2002JD002358, 2003.

Allan, J. D., Delia, A. E., Coe, H., Bower, K. N., Alfarra, M. R., Jimenez, J. L., Middlebrook, A. M., Drewnick, F., Onasch, T. B., Canagaratna, M. R., Jayne, J. T., and Worsnop, D. R.: A generalised method for the extraction of chemically resolved mass spectra from Aerodyne aerosol mass spectrometer data, J. Aerosol Sci., 35, 909–922, https://doi.org/10.1016/j.jaerosci.2004.02.007, 2004.

Almeida, S. M., Manousakas, M., Diapouli, E., Kertesz, Z., Samek, L., Hristova, E., Šega, K., Alvarez, R. P., Belis, C. A., and Eleftheriadis, K.: Ambient particulate matter source apportionment using receptor modelling in European and Central Asia urban areas, Environ. Pollut., 266, 115199, https://doi.org/10.1016/j.envpol.2020.115199, 2020.

Amato, F., Favez, O., Pandolfi, M., Alastuey, A., Querol, X., Moukhtar, S., Bruge, B., Verlhac, S., Orza, J. A. G., Bonnaire, N., Le Priol, T., Petit, J.-F., and Sciare, J.: Traffic induced particle resuspension in Paris: Emission factors and source contributions, Atmos. Environ., 129, 114–124, https://doi.org/10.1016/j.atmosenv.2016.01.022, 2016.

APUR:https://cities.newstank.fr/article/view/148500/paris-180000-250000-vehicules-jour-peripherique-selon-apur.html, last access: 22 August 2023.

Aymoz, G., Jaffrezo, J. L., Chapuis, D., Cozic, J., and Maenhaut, W.: Seasonal variation of PM_{10} main constituents in two valleys of the French Alps. I: EC/OC fractions, Atmospheric Chem. Phys., 7, 661–675, https://doi.org/10.5194/acp-7-661-2007, 2007.

Beekmann, M., Prévôt, A. S. H., Drewnick, F., Sciare, J., Pandis, S. N., Denier van der Gon, H. a. C., Crippa, M., Freutel, F., Poulain, L., Ghersi, V., Rodriguez, E., Beirle, S., Zotter, P., von der Weiden-Reinmüller, S.-L., Bressi, M., Fountoukis, C., Petetin, H., Szidat, S., Schneider, J., Rosso, A., El Haddad, I., Megaritis, A., Zhang, Q. J., Michoud, V., Slowik, J. G., Moukhtar, S., Kolmonen, P., Stohl, A., Eckhardt, S., Borbon, A., Gros, V., Marchand, N., Jaffrezo, J. L., Schwarzenboeck, A., Colomb, A., Wiedensohler, A., Borrmann, S., Lawrence, M., Baklanov, A., and Baltensperger, U.: In situ, satellite measurement and model evidence on the dominant regional contribution to fine particulate matter levels in the Paris megacity, Atmospheric Chem. Phys., 15, 9577–9591, https://doi.org/10.5194/acp-15-9577-2015, 2015.

Belis, C. A., Favez, O., Harrison, R. M., Larsen, B. R., Amato, F., El Haddad, I., Hopke, P. K., Nava, S., Paatero, P., Prévôt, A., Quass, U., Vecchi, R., Viana, M., European Commission, Joint Research Centre, and Institute for Environment and Sustainability: European guide on air pollution source apportionment with receptor models., Publications Office, Luxembourg, 2014.

Belis, C. A., Pernigotti, D., Karagulian, F., Pirovano, G., Larsen, B. R., Gerboles, M., and Hopke, P. K.: A new methodology to assess the performance and uncertainty of source apportionment models in intercomparison exercises, Atmos. Environ., 119, 35–44, https://doi.org/10.1016/j.atmosenv.2015.08.002, 2015.

Bonvalot, L., Tuna, T., Fagault, Y., Jaffrezo, J.-L., Jacob, V., Chevrier, F., and Bard, E.: Estimating contributions from biomass burning, fossil fuel combustion, and biogenic carbon to carbonaceous aerosols in the Valley of Chamonix: a dual approach based on radiocarbon and levoglucosan, Atmospheric Chem. Phys., 16, 13753–13772, https://doi.org/10.5194/acp-16-13753-2016, 2016.

Borlaza, L. J. S., Weber, S., Uzu, G., Jacob, V., Cañete, T., Micallef, S., Trébuchon, C., Slama, R., Favez, O., and Jaffrezo, J.-L.: Disparities in particulate matter (PM_{10}) origins and oxidative potential at a city scale (Grenoble, France) – Part 1: Source apportionment at three neighbouring sites, Atmospheric Chem. Phys., 21, 5415–5437, https://doi.org/10.5194/acp-21-5415-2021, 2021a.

Borlaza, L. J. S., Weber, S., Jaffrezo, J.-L., Houdier, S., Slama, R., Rieux, C., Albinet, A., Micallef, S., Trébluchon, C., and Uzu, G.: Disparities in particulate matter (PM_{10}) origins and oxidative potential at a city scale (Grenoble, France) – Part 2: Sources of PM_{10} oxidative potential using multiple linear regression analysis and the predictive applicability of multilayer perceptron neural network analysis, Atmospheric Chem. Phys., 21, 9719–9739, https://doi.org/10.5194/acp-21-9719-2021, 2021b.

Boucher, O.: Atmospheric Aerosols: Properties and Climate Impacts, Springer, 322 pp., 2015.

Bressi, M., Sciare, J., Ghersi, V., Mihalopoulos, N., Petit, J.-E., Nicolas, J. B., Moukhtar, S., Rosso, A., Féron, A., Bonnaire, N., Poulakis, E., and Theodosi, C.: Sources and geographical

origins of fine aerosols in Paris (France), Atmospheric Chem. Phys., 14, 8813–8839, https://doi.org/10.5194/acp-14-8813-2014, 2014.

Bressi, M., Cavalli, F., Putaud, J. P., Fröhlich, R., Petit, J.-E., Aas, W., Äijälä, M., Alastuey, A., Allan, J. D., Aurela, M., Berico, M., Bougiatioti, A., Bukowiecki, N., Canonaco, F., Crenn, V., Dusanter, S., Ehn, M., Elsasser, M., Flentje, H., Graf, P., Green, D. C., Heikkinen, L., Hermann, H., Holzinger, R., Hueglin, C., Keernik, H., Kiendler-Scharr, A., Kubelová, L., Lunder, C., Maasikmets, M., Makeš, O., Malaguti, A., Mihalopoulos, N., Nicolas, J. B., O'Dowd, C., Ovadnevaite, J., Petralia, E., Poulain, L., Priestman, M., Riffault, V., Ripoll, A., Schlag, P., Schwarz, J., Sciare, J., Slowik, J., Sosedova, Y., Stavroulas, I., Teinemaa, E., Via, M., Vodička, P., Williams, P. I., Wiedensohler, A., Young, D. E., Zhang, S., Favez, O., Minguillón, M. C., and Prevot, A. S. H.: A European aerosol phenomenology - 7: High-time resolution chemical characteristics of submicron particulate matter across Europe, Atmospheric Environ. X, 10, 100108, https://doi.org/10.1016/j.aeaoa.2021.100108, 2021.

Brito, J., Carbone, S., A. Monteiro dos Santos, D., Dominutti, P., de Oliveira Alves, N., V. Rizzo, L., and Artaxo, P.: Disentangling vehicular emission impact on urban air pollution using ethanol as a tracer, Sci. Rep., 8, 10679, https://doi.org/10.1038/s41598-018-29138-7, 2018.

Calas, A., Uzu, G., Besombes, J.-L., Martins, J. M. F., Redaelli, M., Weber, S., Charron, A., Albinet, A., Chevrier, F., Brulfert, G., Mesbah, B., Favez, O., and Jaffrezo, J.-L.: Seasonal Variations and Chemical Predictors of Oxidative Potential (OP) of Particulate Matter (PM), for Seven Urban French Sites, Atmosphere, 10, 698, https://doi.org/10.3390/atmos10110698, 2019.

Canonaco, F., Crippa, M., Slowik, J. G., Baltensperger, U., and Prévôt, A. S. H.: SoFi, an IGOR-based interface for the efficient use of the generalized multilinear engine (ME-2) for the source apportionment: ME-2 application to aerosol mass spectrometer data, Atmospheric Meas. Tech., 6, 3649–3661, https://doi.org/10.5194/amt-6-3649-2013, 2013.

Canonaco, F., Slowik, J. G., Baltensperger, U., and Prévôt, A. S. H.: Seasonal differences in oxygenated organic aerosol composition: implications for emissions sources and factor analysis, Atmospheric Chem. Phys., 15, 6993–7002, https://doi.org/10.5194/acp-15-6993-2015, 2015.

Canonaco, F., Tobler, A., Chen, G., Sosedova, Y., Slowik, J. G., Bozzetti, C., Daellenbach, K. R., El Haddad, I., Crippa, M., Huang, R.-J., Furger, M., Baltensperger, U., and Prévôt, A. S. H.: A new method for long-term source apportionment with time-dependent factor profiles and uncertainty assessment using SoFi Pro: application to 1 year of organic aerosol data, Atmospheric Meas. Tech., 14, 923–943, https://doi.org/10.5194/amt-14-923-2021, 2021.

Canagaratna, M. r., Jayne, J. t., Jimenez, J. l., Allan, J. d., Alfarra, M. r., Zhang, Q., Onasch, T. b., Drewnick, F., Coe, H., Middlebrook, A., Delia, A., Williams, L. r., Trimborn, A. m., Northway, M. j., DeCarlo, P. f., Kolb, C. e., Davidovits, P., and Worsnop, D. r.: Chemical and microphysical characterization of ambient aerosols with the aerodyne aerosol mass spectrometer, Mass Spectrom. Rev., 26, 185–222, https://doi.org/10.1002/mas.20115, 2007.

Cesari, D., Merico, E., Grasso, F. M., Decesari, S., Belosi, F., Manarini, F., De Nuntiis, P., Rinaldi, M., Volpi, F., Gambaro, A., Morabito, E., and Contini, D.: Source Apportionment of

PM2.5 and of its Oxidative Potential in an Industrial Suburban Site in South Italy, Atmosphere, 10, 758, https://doi.org/10.3390/atmos10120758, 2019.

Charron, A., Polo-Rehn, L., Besombes, J.-L., Golly, B., Buisson, C., Chanut, H., Marchand, N., Guillaud, G., and Jaffrezo, J.-L.: Identification and quantification of particulate tracers of exhaust and non-exhaust vehicle emissions, Atmospheric Chem. Phys., 19, 5187–5207, https://doi.org/10.5194/acp-19-5187-2019, 2019.

Chazeau, B., Temime-Roussel, B., Gille, G., Mesbah, B., D'Anna, B., Wortham, H., and Marchand, N.: Measurement report: Long-term real-time characterisation of the submicronic aerosol and its atmospheric dynamic in a Mediterranean coastal city: Tracking the polluted events at the Marseille-Longchamp supersite, Atmospheric Chem. Phys. Discuss., 1–44, https://doi.org/10.5194/acp-2020-1015, 2020.

Chazeau, B., Temime-Roussel, B., Gille, G., Mesbah, B., D'Anna, B., Wortham, H., and Marchand, N.: Measurement report: Fourteen months of real-time characterisation of the submicronic aerosol and its atmospheric dynamics at the Marseille–Longchamp supersite, Atmospheric Chem. Phys., 21, 7293–7319, https://doi.org/10.5194/acp-21-7293-2021, 2021.

Chebaicheb, H., F. de Brito, J., Chen, G., Tison, E., Marchand, C., Prévôt, A. S. H., Favez, O., and Riffault, V.: Investigation of four-year chemical composition and organic aerosol sources of submicron particles at the ATOLL site in northern France, Environ. Pollut., 330, 121805, https://doi.org/10.1016/j.envpol.2023.121805, 2023.

Chen, G., Canonaco, F., Tobler, A., Aas, W., Alastuey, A., Allan, J., Atabakhsh, S., Aurela, M., Baltensperger, U., Bougiatioti, A., De Brito, J. F., Ceburnis, D., Chazeau, B., Chebaicheb, H., Daellenbach, K. R., Ehn, M., El Haddad, I., Eleftheriadis, K., Favez, O., Flentje, H., Font, A., Fossum, K., Freney, E., Gini, M., Green, D. C., Heikkinen, L., Herrmann, H., Kalogridis, A.-C., Keernik, H., Lhotka, R., Lin, C., Lunder, C., Maasikmets, M., Manousakas, M. I., Marchand, N., Marin, C., Marmureanu, L., Mihalopoulos, N., Močnik, G., Nęcki, J., O'Dowd, C., Ovadnevaite, J., Peter, T., Petit, J.-E., Pikridas, M., Matthew Platt, S., Pokorná, P., Poulain, L., Priestman, M., Riffault, V., Rinaldi, M., Różański, K., Schwarz, J., Sciare, J., Simon, L., Skiba, A., Slowik, J. G., Sosedova, Y., Stavroulas, I., Styszko, K., Teinemaa, E., Timonen, H., Tremper, A., Vasilescu, J., Via, M., Vodička, P., Wiedensohler, A., Zografou, O., Cruz Minguillón, M., and Prévôt, A. S. H.: European aerosol phenomenology − 8: Harmonised source apportionment of organic aerosol using 22 Year-long ACSM/AMS datasets, Environ. Int., 166, 107325, https://doi.org/10.1016/j.envint.2022.107325, 2022a.

Chen, G., Canonaco, F., Slowik, J. G., Daellenbach, K. R., Tobler, A., Petit, J.-E., Favez, O., Stavroulas, I., Mihalopoulos, N., Gerasopoulos, E., El Haddad, I., Baltensperger, U., and Prévôt, A. S. H.: Real-Time Source Apportionment of Organic Aerosols in Three European Cities, Environ. Sci. Technol., 56, 15290–15297, https://doi.org/10.1021/acs.est.2c02509, 2022b.

Chrit, M., Sartelet, K., Sciare, J., Pey, J., Marchand, N., Couvidat, F., Sellegri, K., and Beekmann, M.: Modelling organic aerosol concentrations and properties during ChArMEx summer campaigns of 2012 and 2013 in the western Mediterranean region, Atmospheric Chem. Phys., 17, 12509–12531, https://doi.org/10.5194/acp-17-12509-2017, 2017.

Climate_Change:https://www.dropbox.com/sh/lwofyzcqk7ux3xf/AACLkK-eFYMpvD9uPyJt9Dcva?dl=0, last access: 22 March 2021.

Couvidat, F. and Sartelet, K.: The Secondary Organic Aerosol Processor (SOAP v1.0) model: a unified model with different ranges of complexity based on the molecular surrogate approach, Geosci. Model Dev., 8, 1111–1138, https://doi.org/10.5194/gmd-8-1111-2015, 2015.

Crippa, M., DeCarlo, P. F., Slowik, J. G., Mohr, C., Heringa, M. F., Chirico, R., Poulain, L., Freutel, F., Sciare, J., Cozic, J., Di Marco, C. F., Elsasser, M., Nicolas, J. B., Marchand, N., Abidi, E., Wiedensohler, A., Drewnick, F., Schneider, J., Borrmann, S., Nemitz, E., Zimmermann, R., Jaffrezo, J.-L., Prévôt, A. S. H., and Baltensperger, U.: Wintertime aerosol chemical composition and source apportionment of the organic fraction in the metropolitan area of Paris, Atmospheric Chem. Phys., 13, 961–981, https://doi.org/10.5194/acp-13-961-2013, 2013.

Crippa, M., Canonaco, F., Lanz, V. A., Äijälä, M., Allan, J. D., Carbone, S., Capes, G., Ceburnis, D., Dall'Osto, M., Day, D. A., DeCarlo, P. F., Ehn, M., Eriksson, A., Freney, E., Hildebrandt Ruiz, L., Hillamo, R., Jimenez, J. L., Junninen, H., Kiendler-Scharr, A., Kortelainen, A.-M., Kulmala, M., Laaksonen, A., Mensah, A. A., Mohr, C., Nemitz, E., O'Dowd, C., Ovadnevaite, J., Pandis, S. N., Petäjä, T., Poulain, L., Saarikoski, S., Sellegri, K., Swietlicki, E., Tiitta, P., Worsnop, D. R., Baltensperger, U., and Prévôt, A. S. H.: Organic aerosol components derived from 25 AMS data sets across Europe using a consistent ME-2 based source apportionment approach, Atmospheric Chem. Phys., 14, 6159–6176, https://doi.org/10.5194/acp-14-6159-2014, 2014.

Daellenbach, K. R., Stefenelli, G., Bozzetti, C., Vlachou, A., Fermo, P., Gonzalez, R., Piazzalunga, A., Colombi, C., Canonaco, F., Hueglin, C., Kasper-Giebl, A., Jaffrezo, J.-L., Bianchi, F., Slowik, J. G., Baltensperger, U., El-Haddad, I., and Prévôt, A. S. H.: Long-term chemical analysis and organic aerosol source apportionment at nine sites in central Europe: source identification and uncertainty assessment, Atmospheric Chem. Phys., 17, 13265–13282, https://doi.org/10.5194/acp-17-13265-2017, 2017.

Daellenbach, K. R., Uzu, G., Jiang, J., Cassagnes, L.-E., Leni, Z., Vlachou, A., Stefenelli, G., Canonaco, F., Weber, S., Segers, A., Kuenen, J. J. P., Schaap, M., Favez, O., Albinet, A., Aksoyoglu, S., Dommen, J., Baltensperger, U., Geiser, M., El Haddad, I., Jaffrezo, J.-L., and Prévôt, A. S. H.: Sources of particulate-matter air pollution and its oxidative potential in Europe, Nature, 587, 414–419, https://doi.org/10.1038/s41586-020-2902-8, 2020.

Drinovec, L., Močnik, G., Zotter, P., Prévôt, A. S. H., Ruckstuhl, C., Coz, E., Rupakheti, M., Sciare, J., Müller, T., Wiedensohler, A., and Hansen, A. D. A.: The "dual-spot" Aethalometer: an improved measurement of aerosol black carbon with real-time loading compensation, Atmospheric Meas. Tech., 8, 1965–1979, https://doi.org/10.5194/amt-8-1965-2015, 2015.

Efron, B.: Bootstrap Methods: Another Look at the Jackknife, Ann. Stat., 7, 1–26, https://doi.org/10.1214/aos/1176344552, 1979.

Europe's air quality status 2023 — European Environment Agency: https://www.eea.europa.eu/publications/europes-air-quality-status-2023, last access: 22 August 2023.

Exposure & health impacts of air pollution: https://www.who.int/teams/environment-climate-change-and-health/air-quality-and-health/health-impacts/exposure-air-pollution, last access: 22 August 2023.

Favez, O., Cachier, H., Sciare, J., Sarda-Estève, R., and Martinon, L.: Evidence for a significant contribution of wood burning aerosols to PM2.5 during the winter season in Paris, France, Atmos. Environ., 43, 3640–3644, https://doi.org/10.1016/j.atmosenv.2009.04.035, 2009.

Favez, O., El Haddad, I., Piot, C., Boréave, A., Abidi, E., Marchand, N., Jaffrezo, J.-L., Besombes, J.-L., Personnaz, M.-B., Sciare, J., Wortham, H., George, C., and D'Anna, B.: Inter-comparison of source apportionment models for the estimation of wood burning aerosols during wintertime in an Alpine city (Grenoble, France), Atmospheric Chem. Phys., 10, 5295–5314, https://doi.org/10.5194/acp-10-5295-2010, 2010.

Favez, O., Weber, S., Petit, J.-E., Alleman, L., Albinet, A., Riffault, V., Chazeau, B., Amodeo, T., Salameh, D., Zhang, Y., Srivastava, D., Samaké, A., Aujay, R., Papin, A., Bonnaire, N., Boullanger, C., Chatain, M., Chevrier, F., Detournay, A., and Leoz-Garziandia, E.: Overview of the French Operational Network for In Situ Observation of PM Chemical Composition and Sources in Urban Environments (CARA Program), https://doi.org/10.3390/atmos12020207, 2021.

Flentje, H., Mattis, I., Kipling, Z., Rémy, S., and Thomas, W.: Evaluation of ECMWF IFS-AER (CAMS) operational forecasts during cycle 41r1–46r1 with calibrated ceilometer profiles over Germany, Geosci. Model Dev., 14, 1721–1751, https://doi.org/10.5194/gmd-14-1721-2021, 2021.

Freney, E., Zhang, Y., Croteau, P., Amodeo, T., Williams, L., Truong, F., Petit, J.-E., Sciare, J., Sarda-Esteve, R., Bonnaire, N., Arumae, T., Aurela, M., Bougiatioti, A., Mihalopoulos, N., Coz, E., Artinano, B., Crenn, V., Elste, T., Heikkinen, L., Poulain, L., Wiedensohler, A., Herrmann, H., Priestman, M., Alastuey, A., Stavroulas, I., Tobler, A., Vasilescu, J., Zanca, N., Canagaratna, M., Carbone, C., Flentje, H., Green, D., Maasikmets, M., Marmureanu, L., Minguillon, M. C., Prevot, A. S. H., Gros, V., Jayne, J., and Favez, O.: The second ACTRIS inter-comparison (2016) for Aerosol Chemical Speciation Monitors (ACSM): Calibration protocols and instrument performance evaluations, Aerosol Sci. Technol., 53, 830–842, https://doi.org/10.1080/02786826.2019.1608901, 2019.

Fröhlich, R., Cubison, M. J., Slowik, J. G., Bukowiecki, N., Prévôt, A. S. H., Baltensperger, U., Schneider, J., Kimmel, J. R., Gonin, M., Rohner, U., Worsnop, D. R., and Jayne, J. T.: The ToF-ACSM: a portable aerosol chemical speciation monitor with TOFMS detection, Atmospheric Meas. Tech., 6, 3225–3241, https://doi.org/10.5194/amt-6-3225-2013, 2013.

Giani, P., Balzarini, A., Pirovano, G., Gilardoni, S., Paglione, M., Colombi, C., Gianelle, V. L., Belis, C. A., Poluzzi, V., and Lonati, G.: Influence of semi- and intermediate-volatile organic compounds (S/IVOC) parameterizations, volatility distributions and aging schemes on organic

aerosol modelling in winter conditions, Atmos. Environ., 213, 11–24, https://doi.org/10.1016/j.atmosenv.2019.05.061, 2019.

Gilardoni, S., Massoli, P., Paglione, M., Giulianelli, L., Carbone, C., Rinaldi, M., Decesari, S., Sandrini, S., Costabile, F., Gobbi, G. P., Pietrogrande, M. C., Visentin, M., Scotto, F., Fuzzi, S., and Facchini, M. C.: Direct observation of aqueous secondary organic aerosol from biomass-burning emissions, Proc. Natl. Acad. Sci., 113, 10013–10018, https://doi.org/10.1073/pnas.1602212113, 2016.

Hopke, P. K., Dai, Q., Li, L., and Feng, Y.: Global review of recent source apportionments for airborne particulate matter, Sci. Total Environ., 740, 140091, https://doi.org/10.1016/j.scitotenv.2020.140091, 2020.

Insee: https://www.insee.fr/fr/statistiques/4481460, last access: 13 October 2021.

IPCC: AR6 Synthesis Report: Climate Change 2023 — IPCC, 2023.

Jiang, J., Aksoyoglu, S., El-Haddad, I., Ciarelli, G., Denier van der Gon, H. A. C., Canonaco, F., Gilardoni, S., Paglione, M., Minguillón, M. C., Favez, O., Zhang, Y., Marchand, N., Hao, L., Virtanen, A., Florou, K., O'Dowd, C., Ovadnevaite, J., Baltensperger, U., and Prévôt, A. S. H.: Sources of organic aerosols in Europe: a modeling study using CAMx with modified volatility basis set scheme, Atmospheric Chem. Phys., 19, 15247–15270, https://doi.org/10.5194/acp-19-15247-2019, 2019.

Jimenez, J. L., Canagaratna, M. R., Donahue, N. M., Prevot, A. S. H., Zhang, Q., Kroll, J. H., DeCarlo, P. F., Allan, J. D., Coe, H., Ng, N. L., Aiken, A. C., Docherty, K. S., Ulbrich, I. M., Grieshop, A. P., Robinson, A. L., Duplissy, J., Smith, J. D., Wilson, K. R., Lanz, V. A., Hueglin, C., Sun, Y. L., Tian, J., Laaksonen, A., Raatikainen, T., Rautiainen, J., Vaattovaara, P., Ehn, M., Kulmala, M., Tomlinson, J. M., Collins, D. R., Cubison, M. J., E, Dunlea, J., Huffman, J. A., Onasch, T. B., Alfarra, M. R., Williams, P. I., Bower, K., Kondo, Y., Schneider, J., Drewnick, F., Borrmann, S., Weimer, S., Demerjian, K., Salcedo, D., Cottrell, L., Griffin, R., Takami, A., Miyoshi, T., Hatakeyama, S., Shimono, A., Sun, J. Y., Zhang, Y. M., Dzepina, K., Kimmel, J. R., Sueper, D., Jayne, J. T., Herndon, S. C., Trimborn, A. M., Williams, L. R., Wood, E. C., Middlebrook, A. M., Kolb, C. E., Baltensperger, U., and Worsnop, D. R.: Evolution of Organic Aerosols in the Atmosphere, Science, 326, 1525–1529, https://doi.org/10.1126/science.1180353, 2009.

Kelly, F. J. and Fussell, J. C.: Air pollution and public health: emerging hazards and improved understanding of risk, Environ. Geochem. Health, 37, 631–649, https://doi.org/10.1007/s10653-015-9720-1, 2015.

Kuenen, J., Dellaert, S., Visschedijk, A., Jalkanen, J.-P., Super, I., and Denier van der Gon, H.: CAMS-REG-v4: a state-of-the-art high-resolution European emission inventory for air quality modelling, Earth Syst. Sci. Data, 14, 491–515, https://doi.org/10.5194/essd-14-491-2022, 2022.

LCSQA: Guide méthodologique : mesure de la composition chimique des particules submicroniques non réfractaires par Aerosol Chemical Speciation Monitor (ACSM) :

https://www.lcsqa.org/fr/rapport/2016/ienris/guide-methodologique-mesure-composition-chimique-particules-submicroniques-non-0, 2018.

LCSQA: Guide méthodologique pour la mesure du « Black Carbon » par Aethalomètre multi longueur d'onde AE33 dans l'air ambiant (Version 2020), 2020.

LCSQA: CAHIER DES CHARGES POUR L'ETALONNAGE DES Q-ACSM, 2022.

Lim, C.-H., Ryu, J., Choi, Y., Jeon, S. W., and Lee, W.-K.: Understanding global PM2.5 concentrations and their drivers in recent decades (1998–2016), Environ. Int., 144, 106011, https://doi.org/10.1016/j.envint.2020.106011, 2020.

Lin, C., Ceburnis, D., Xu, W., Heffernan, E., Hellebust, S., Gallagher, J., Huang, R.-J., O'Dowd, C., and Ovadnevaite, J.: The impact of traffic on air quality in Ireland: insights from the simultaneous kerbside and suburban monitoring of submicron aerosols, Atmospheric Chem. Phys., 20, 10513–10529, https://doi.org/10.5194/acp-20-10513-2020, 2020.

Medina Sylvia, Adélaïde Lucie, Wagner Vérène, de Crouy Chanel Perrine, Real Elsa, Colette Augustin, Couvidat Florian, Bessagnet Bertrand, Durou Amélie, Host Sabine, Hulin Marion, Corso Magali, Pascal Mathilde: Impact de pollution de l'air ambiant sur la mortalité en France métropolitaine. Réduction en lien avec le confinement du printemps 2020 et nouvelles données sur le poids total pour la période 2016-2019, 2021.

Menut, L., Bessagnet, B., Briant, R., Cholakian, A., Couvidat, F., Mailler, S., Pennel, R., Siour, G., Tuccella, P., Turquety, S., and Valari, M.: The CHIMERE v2020r1 online chemistry-transport model, Geosci. Model Dev., 14, 6781–6811, https://doi.org/10.5194/gmd-14-6781-2021, 2021.

Middlebrook, A. M., Bahreini, R., Jimenez, J. L., and Cana-Garatna, M. R.: Evaluation of Composition-Dependent Collection Efficiencies for the Aerodyne Aerosol Mass Spectrometer using Field Data, Aerosol Sci Technol, 46, 258–271, 2011.

Ng, N. L., Herndon, S. C., Trimborn, A., Canagaratna, M. R., Croteau, P. L., Onasch, T. B., Sueper, D., Worsnop, D. R., Zhang, Q., Sun, Y. L., and Jayne, J. T.: An Aerosol Chemical Speciation Monitor (ACSM) for Routine Monitoring of the Composition and Mass Concentrations of Ambient Aerosol, Aerosol Sci. Technol., 45, 780–794, https://doi.org/10.1080/02786826.2011.560211, 2011.

Oberdörster, G., Maynard, A., Donaldson, K., Castranova, V., Fitzpatrick, J., Ausman, K., Carter, J., Karn, B., Kreyling, W., Lai, D., Olin, S., Monteiro-Riviere, N., Warheit, D., Yang, H., and A report from the ILSI Research Foundation/Risk Science Institute Nanomaterial Toxicity Screening Working Group: Principles for characterizing the potential human health effects from exposure to nanomaterials: elements of a screening strategy, Part. Fibre Toxicol., 2, 8, https://doi.org/10.1186/1743-8977-2-8, 2005.

Paatero, P. and Tapper, U.: Positive matrix factorization: A non-negative factor model with optimal utilization of error estimates of data values, Environmetrics, 5, 111–126, https://doi.org/10.1002/env.3170050203, 1994.

Paatero, P.: User's guide for positive matrix factorization programs PMF2 and PMF3. In: University of Helsinki, Helsinki, Finland, 2010.

Paglione, M., Gilardoni, S., Rinaldi, M., Decesari, S., Zanca, N., Sandrini, S., Giulianelli, L., Bacco, D., Ferrari, S., Poluzzi, V., Scotto, F., Trentini, A., Poulain, L., Herrmann, H., Wiedensohler, A., Canonaco, F., Prévôt, A. S. H., Massoli, P., Carbone, C., Facchini, M. C., and Fuzzi, S.: The impact of biomass burning and aqueous-phase processing on air quality: a multi-year source apportionment study in the Po Valley, Italy, Atmospheric Chem. Phys., 20, 1233–1254, https://doi.org/10.5194/acp-20-1233-2020, 2020.

Pandis, S. N., Skyllakou, K., Florou, K., Kostenidou, E., Kaltsonoudis, C., Hasa, E., and Presto, A. A.: Urban particulate matter pollution: a tale of five cities, Faraday Discuss., 189, 277–290, https://doi.org/10.1039/C5FD00212E, 2016.

Parworth, C., Fast, J., Mei, F., Shippert, T., Sivaraman, C., Tilp, A., Watson, T., and Zhang, Q.: Long-term measurements of submicrometer aerosol chemistry at the Southern Great Plains (SGP) using an Aerosol Chemical Speciation Monitor (ACSM), Atmos. Environ., 106, 43–55, https://doi.org/10.1016/j.atmosenv.2015.01.060, 2015.

Petit, J.-E., Favez, O., Sciare, J., Canonaco, F., Croteau, P., Močnik, G., Jayne, J., Worsnop, D., and Leoz-Garziandia, E.: Submicron aerosol source apportionment of wintertime pollution in Paris, France by double positive matrix factorization (PMF^2) using an aerosol chemical speciation monitor (ACSM) and a multi-wavelength Aethalometer, Atmospheric Chem. Phys., 14, 13773–13787, https://doi.org/10.5194/acp-14-13773-2014, 2014.

Petit, J.-E., Pallares, C., Favez, O., Alleman, L., Bonnaire, N., and Rivière, E.: Sources and Geographical Origins of PM 10 in Metz (France) Using Oxalate as a Marker of Secondary Organic Aerosols by Positive Matrix Factorization Analysis, Atmosphere, 10, 370, https://doi.org/10.3390/atmos10070370, 2019.

Petzold, A., Ogren, J. A., Fiebig, M., Laj, P., Li, S.-M., Baltensperger, U., Holzer-Popp, T., Kinne, S., Pappalardo, G., Sugimoto, N., Wehrli, C., Wiedensohler, A., and Zhang, X.-Y.: Recommendations for reporting "black carbon" measurements, Atmospheric Chem. Phys., 13, 8365–8379, https://doi.org/10.5194/acp-13-8365-2013, 2013.

Putaud, J.-P., Van Dingenen, R., Alastuey, A., Bauer, H., Birmili, W., Cyrys, J., Flentje, H., Fuzzi, S., Gehrig, R., Hansson, H. C., Harrison, R. M., Herrmann, H., Hitzenberger, R., Hüglin, C., Jones, A. M., Kasper-Giebl, A., Kiss, G., Kousa, A., Kuhlbusch, T. A. J., Löschau, G., Maenhaut, W., Molnar, A., Moreno, T., Pekkanen, J., Perrino, C., Pitz, M., Puxbaum, H., Querol, X., Rodriguez, S., Salma, I., Schwarz, J., Smolik, J., Schneider, J., Spindler, G., ten Brink, H., Tursic, J., Viana, M., Wiedensohler, A., and Raes, F.: A European aerosol phenomenology – 3: Physical and chemical characteristics of particulate matter from 60 rural, urban, and kerbside sites across Europe, Atmos. Environ., 44, 1308–1320, https://doi.org/10.1016/j.atmosenv.2009.12.011, 2010.

Rapport CITEPA: https://www.citepa.org/fr/secten/, last access: 25 August 2023.

Rivellini, L.-H., Chiapello, I., Tison, E., Fourmentin, M., Féron, A., Diallo, A., N'Diaye, T., Goloub, P., Canonaco, F., Prévôt, A. S. H., and Riffault, V.: Chemical characterization and source apportionment of submicron aerosols measured in Senegal during the 2015 SHADOW campaign, Atmospheric Chem. Phys., 17, 10291–10314, https://doi.org/10.5194/acp-17-10291-2017, 2017.

Roig Rodelas, R., Chakraborty, A., Perdrix, E., Tison, E., and Riffault, V.: Real-time assessment of wintertime organic aerosol characteristics and sources at a suburban site in northern France, Atmos. Environ., 203, 48–61, https://doi.org/10.1016/j.atmosenv.2019.01.035, 2019.

Roldin, P., Ehn, M., Kurtén, T., Olenius, T., Rissanen, M. P., Sarnela, N., Elm, J., Rantala, P., Hao, L., Hyttinen, N., Heikkinen, L., Worsnop, D. R., Pichelstorfer, L., Xavier, C., Clusius, P., Öström, E., Petäjä, T., Kulmala, M., Vehkamäki, H., Virtanen, A., Riipinen, I., and Boy, M.: The role of highly oxygenated organic molecules in the Boreal aerosol-cloud-climate system, Nat. Commun., 10, 4370, https://doi.org/10.1038/s41467-019-12338-8, 2019.

Samaké, A., Jaffrezo, J.-L., Favez, O., Weber, S., Jacob, V., Canete, T., Albinet, A., Charron, A., Riffault, V., Perdrix, E., Waked, A., Golly, B., Salameh, D., Chevrier, F., Oliveira, D. M., Besombes, J.-L., Martins, J. M. F., Bonnaire, N., Conil, S., Guillaud, G., Mesbah, B., Rocq, B., Robic, P.-Y., Hulin, A., Le Meur, S., Descheemaecker, M., Chretien, E., Marchand, N., and Uzu, G.: Arabitol, mannitol, and glucose as tracers of primary biogenic organic aerosol: the influence of environmental factors on ambient air concentrations and spatial distribution over France, Atmospheric Chem. Phys., 19, 11013–11030, https://doi.org/10.5194/acp-19-11013-2019, 2019.

Samaké, A., Martins, J. M. F., Bonin, A., Uzu, G., Taberlet, P., Conil, S., Favez, O., Thomasson, A., Chazeau, B., Marchand, N., and Jaffrezo, J.-L.: Variability of the Atmospheric PM10 Microbiome in Three Climatic Regions of France, Front. Microbiol., 11, 2021.

Sandradewi, J., Prévôt, A. S. H., Szidat, S., Perron, N., Alfarra, M. R., Lanz, V. A., Weingartner, E., and Baltensperger, U.: Using Aerosol Light Absorption Measurements for the Quantitative Determination of Wood Burning and Traffic Emission Contributions to Particulate Matter, Environ. Sci. Technol., 42, 3316–3323, https://doi.org/10.1021/es702253m, 2008.

Sartelet, K., Couvidat, F., Wang, Z., Flageul, C., and Kim, Y.: SSH-Aerosol v1.1: A Modular Box Model to Simulate the Evolution of Primary and Secondary Aerosols, Atmosphere, 11, 525, https://doi.org/10.3390/atmos11050525, 2020.

Saunders, S. M., Jenkin, M. E., Derwent, R. G., and Pilling, M. J.: Protocol for the development of the Master Chemical Mechanism, MCM v3 (Part A): tropospheric degradation of non-aromatic volatile organic compounds, Atmospheric Chem. Phys., 3, 161–180, https://doi.org/10.5194/acp-3-161-2003, 2003.

Savadkoohi, M., Pandolfi, M., Reche, C., Niemi, J. V., Mooibroek, D., Titos, G., Green, D. C., Tremper, A. H., Hueglin, C., Liakakou, E., Mihalopoulos, N., Stavroulas, I., Artiñano, B., Coz, E., Alados-Arboledas, L., Beddows, D., Riffault, V., De Brito, J. F., Bastian, S., Baudic, A., Colombi, C., Costabile, F., Chazeau, B., Marchand, N., Gómez-Amo, J. L., Estellés, V., Matos, V., van der Gaag, E., Gille, G., Luoma, K., Manninen, H. E., Norman, M., Silvergren, S., Petit, J.-E., Putaud, J.-P., Rattigan, O. V., Timonen, H., Tuch, T., Merkel, M., Weinhold, K., Vratolis, S.,

Vasilescu, J., Favez, O., Harrison, R. M., Laj, P., Wiedensohler, A., Hopke, P. K., Petäjä, T., Alastuey, A., and Querol, X.: The variability of mass concentrations and source apportionment analysis of equivalent black carbon across urban Europe, Environ. Int., 178, 108081, https://doi.org/10.1016/j.envint.2023.108081, 2023.

Seibert, R., Nikolova, I., Volná, V., Krejčí, B., and Hladký, D.: Air Pollution Sources' Contribution to PM2.5 Concentration in the Northeastern Part of the Czech Republic, Atmosphere, 11, 522, https://doi.org/10.3390/atmos11050522, 2020.

Southerland, V. A., Brauer, M., Mohegh, A., Hammer, M. S., Donkelaar, A. van, Martin, R. V., Apte, J. S., and Anenberg, S. C.: Global urban temporal trends in fine particulate matter (PM2·5) and attributable health burdens: estimates from global datasets, Lancet Planet. Health, 6, e139–e146, https://doi.org/10.1016/S2542-5196(21)00350-8, 2022.

Srivastava, D., Favez, O., Bonnaire, N., Lucarelli, F., Haeffelin, M., Perraudin, E., Gros, V., Villenave, E., and Albinet, A.: Speciation of organic fractions does matter for aerosol source apportionment. Part 2: Intensive short-term campaign in the Paris area (France), Sci. Total Environ., 634, 267–278, https://doi.org/10.1016/j.scitotenv.2018.03.296, 2018.

Srivastava, D., Favez, O., Petit, J.-E., Zhang, Y., Sofowote, U. M., Hopke, P. K., Bonnaire, N., Perraudin, E., Gros, V., Villenave, E., and Albinet, A.: Speciation of organic fractions does matter for aerosol source apportionment. Part 3: Combining off-line and on-line measurements, Sci. Total Environ., 690, 944–955, https://doi.org/10.1016/j.scitotenv.2019.06.378, 2019.

Sun, Y., Xu, W., Zhang, Q., Jiang, Q., Canonaco, F., Prévôt, A. S. H., Fu, P., Li, J., Jayne, J., Worsnop, D. R., and Wang, Z.: Source apportionment of organic aerosol from 2-year highly time-resolved measurements by an aerosol chemical speciation monitor in Beijing, China, Atmospheric Chem. Phys., 18, 8469–8489, https://doi.org/10.5194/acp-18-8469-2018, 2018.

Taylor, M. and Duncan, P.: Revealed: almost everyone in Europe is breathing toxic air, The Guardian, 20th September, 2023.

Tobler, A., Bhattu, D., Canonaco, F., Lalchandani, V., Shukla, A., Thamban, N. M., Mishra, S., Srivastava, A. K., Bisht, D. S., Tiwari, S., Singh, S., Močnik, G., Baltensperger, U., Tripathi, S. N., Slowik, J. G., and Prévôt, A. S. H.: Chemical characterization of PM2.5 and source apportionment of organic aerosol in New Delhi, India, Sci. Total Environ., 745, 140924, https://doi.org/10.1016/j.scitotenv.2020.140924, 2020.

Tobler, A. K., Skiba, A., Canonaco, F., Močnik, G., Rai, P., Chen, G., Bartyzel, J., Zimnoch, M., Styszko, K., Nęcki, J., Furger, M., Różański, K., Baltensperger, U., Slowik, J. G., and Prevot, A. S. H.: Characterization of non-refractory (NR) PM_1 and source apportionment of organic aerosol in Kraków, Poland, Atmospheric Chem. Phys., 21, 14893–14906, https://doi.org/10.5194/acp-21-14893-2021, 2021.

Toubasi, A. and Al-Sayegh, T. N.: Short-term Exposure to Air Pollution and Ischemic Stroke: A Systematic Review and Meta-analysis, Neurology, https://doi.org/10.1212/WNL.0000000000207856, 2023.

Via, M., Chen, G., Canonaco, F., Daellenbach, K. R., Chazeau, B., Chebaicheb, H., Jiang, J., Keernik, H., Lin, C., Marchand, N., Marin, C., O'Dowd, C., Ovadnevaite, J., Petit, J.-E., Pikridas, M., Riffault, V., Sciare, J., Slowik, J. G., Simon, L., Vasilescu, J., Zhang, Y., Favez, O., Prévôt, A. S. H., Alastuey, A., and Cruz Minguillón, M.: *Rolling* vs. *seasonal* PMF: real-world multi-site and synthetic dataset comparison, Atmospheric Meas. Tech., 15, 5479–5495, https://doi.org/10.5194/amt-15-5479-2022, 2022.

Via, M., Yus-Díez, J., Canonaco, F., Petit, J.-E., Hopke, P., Reche, C., Pandolfi, M., Ivančič, M., Rigler, M., Prevôt, A. S. H., Querol, X., Alastuey, A., and Minguillón, M. C.: Towards a better understanding of fine PM sources: Online and offline datasets combination in a single PMF, Environ. Int., 177, 108006, https://doi.org/10.1016/j.envint.2023.108006, 2023.

Waked, A., Favez, O., Alleman, L. Y., Piot, C., Petit, J.-E., Delaunay, T., Verlinden, E., Golly, B., Besombes, J.-L., Jaffrezo, J.-L., and Leoz-Garziandia, E.: Source apportionment of PM_{10} in a north-western Europe regional urban background site (Lens, France) using positive matrix factorization and including primary biogenic emissions, Atmospheric Chem. Phys., 14, 3325–3346, https://doi.org/10.5194/acp-14-3325-2014, 2014.

Wang, B., Eum, K.-D., Kazemiparkouhi, F., Li, C., Manjourides, J., Pavlu, V., and Suh, H.: The impact of long-term PM2.5 exposure on specific causes of death: exposure-response curves and effect modification among 53 million U.S. Medicare beneficiaries, Environ. Health Glob. Access Sci. Source, 19, 20, https://doi.org/10.1186/s12940-020-00575-0, 2020.

Wang, Z., Couvidat, F., and Sartelet, K.: GENerator of reduced Organic Aerosol mechanism (GENOA v1.0): an automatic generation tool of semi-explicit mechanisms, Geosci. Model Dev., 15, 8957–8982, https://doi.org/10.5194/gmd-15-8957-2022, 2022.

Wang, Z., Couvidat, F., and Sartelet, K.: Implementation of a parallel reduction algorithm in the GENerator of reduced Organic Aerosol mechanisms (GENOA v2.0): Application to multiple monoterpene aerosol precursors, J. Aerosol Sci., 174, 106248, https://doi.org/10.1016/j.jaerosci.2023.106248, 2023.

Watson, John G. "Overview of receptor model principles." *Journal of the Air Pollution Control Association* 34.6 (1984): 619-623.

Watson, T. B.: Aerosol Chemical Speciation Monitor (ACSM) Instrument Handbook, https://doi.org/10.2172/1375336, 2017.

Watson, T., Aiken, A,. Zhang, Q., Croteau, P., Onasch, T., Williams, L., and Flynn, C.: Second ARM Aerosol Chemical Speciation Monitor Users' Meeting Report: https://www.arm.gov/publications/programdocs/doe-sc-arm-tr-249.pdf, 2020.

Weber, S., Salameh, D., Albinet, A., Alleman, L. Y., Waked, A., Besombes, J.-L., Jacob, V., Guillaud, G., Meshbah, B., Rocq, B., Hulin, A., Dominik-Sègue, M., Chrétien, E., Jaffrezo, J.-L., and Favez, O.: Comparison of PM10 Sources Profiles at 15 French Sites Using a Harmonized Constrained Positive Matrix Factorization Approach, Atmosphere, 10, 310, https://doi.org/10.3390/atmos10060310, 2019.

Weber, S., Uzu, G., Favez, O., Borlaza, L. J. S., Calas, A., Salameh, D., Chevrier, F., Allard, J., Besombes, J.-L., Albinet, A., Pontet, S., Mesbah, B., Gille, G., Zhang, S., Pallares, C., Leoz-Garziandia, E., and Jaffrezo, J.-L.: Source apportionment of atmospheric PM_{10} oxidative potential: synthesis of 15 year-round urban datasets in France, Atmospheric Chem. Phys., 21, 11353–11378, https://doi.org/10.5194/acp-21-11353-2021, 2021.

Zanatta, M., Gysel, M., Bukowiecki, N., Müller, T., Weingartner, E., Areskoug, H., Fiebig, M., Yttri, K. E., Mihalopoulos, N., Kouvarakis, G., Beddows, D., Harrison, R. M., Cavalli, F., Putaud, J. P., Spindler, G., Wiedensohler, A., Alastuey, A., Pandolfi, M., Sellegri, K., Swietlicki, E., Jaffrezo, J. L., Baltensperger, U., and Laj, P.: A European aerosol phenomenology-5: Climatology of black carbon optical properties at 9 regional background sites across Europe, Atmos. Environ., 145, 346–364, https://doi.org/10.1016/j.atmosenv.2016.09.035, 2016.

Zhang, Q., Jimenez, J. L., Canagaratna, M. R., Ulbrich, I. M., Ng, N. L., Worsnop, D. R., and Sun, Y.: Understanding atmospheric organic aerosols via factor analysis of aerosol mass spectrometry: a review, Anal. Bioanal. Chem., 401, 3045–3067, https://doi.org/10.1007/s00216-011-5355-y, 2011.

Zhang, R., Wang, G., Guo, S., Zamora, M. L., Ying, Q., Lin, Y., Wang, W., Hu, M., and Wang, Y.: Formation of Urban Fine Particulate Matter, Chem. Rev., 115, 3803–3855, https://doi.org/10.1021/acs.chemrev.5b00067, 2015.

Zhang, Y., Favez, O., Petit, J.-E., Canonaco, F., Truong, F., Bonnaire, N., Crenn, V., Amodeo, T., Prévôt, A. S. H., Sciare, J., Gros, V., and Albinet, A.: Six-year source apportionment of submicron organic aerosols from near-continuous highly time-resolved measurements at SIRTA (Paris area, France), Atmospheric Chem. Phys., 19, 14755–14776, https://doi.org/10.5194/acp-19-14755-2019, 2019.

Annexes

Annexe 1. Valorisation scientifique

Publications dans des revues à comité de lecture

1) G. CHEN, F. CANONACO, A. TOBLER, W. AAS, A. ALASTUEY, J. ALLAN, S. ATABAKHSH, M. AURELA, U. BALTENSPERGER, A. BOUGIATIOTI, J. F. DE BRITO, D. CEBURNIS, B. CHAZEAU, **H. CHEBAICHEB**, K. R. DAELLENBACH, M. EHN, I. EL HADDAD, K. ELEFTHERIADIS, O. FAVEZ, H. FLENTJE, A. FONT, K. FOSSUM, E. FRENEY, M. GINI, D. C. GREEN, L. HEIKKINEN, H. HERRMANN, A.-C. KALOGRIDIS, H. KEERNIK, R. LHOTKA, C. LIN, C. LUNDER, M. MAASIKMETS, M. I. MANOUSAKAS, N. MARCHAND, C. MARIN, L. MARMUREANU, N. MIHALOPOULOS, G. MOCNIK, J. NECKI, C. O'DOWD, J. OVADNEVAITE, T. PETER, J.-E. PETIT, M. PIKRIDAS, S. M. PLATT, P. POKORNÁ, L. POULAIN, M. PRIESTMAN, V. RIFFAULT, M. RINALDI, K. ROZANSKI, J. SCHWARZ, J. SCIARE, L. SIMON, A. SKIBA, J. SLOWIK, Y. SOSEDOVA, I. STAVROULAS, K. STYSZKO, E. TEINEMAA, H. TIMONEN, A. TREMPER, J. VASILESCU, M. VIA, P. VODICKA, A. WIEDENSOHLER, O. ZOGRAFOU, M. C. MINGUILLON, A. S. H. PREVOT, *European Aerosol Phenomenology - 8: Harmonised Source Apportionment of Organic Aerosol using 22 Year-long ACSM/AMS Datasets*, Environment International 166, 107325 (2022), DOI 10.1016/j.envint.2022.107325.

2) M. VIA, G. CHEN, F. CANONACO, K. R. DAELLENBACH, B. CHAZEAU, **H. CHEBAICHEB**, J. JIANG, H. KEERNIK, C. LIN, N. MARCHAND, C. MARIN, C. O'DOWD, J. OVADNEVAITE, J.-E. PETIT, M. PIKRIDAS, V. RIFFAULT, J. SCIARE, J. G. SLOWIK, L. SIMON, J. VASILESCU, Y. ZHANG, O. FAVEZ, A. S. H. PREVOT, A. ALASTUEY, M. C. MINGUILLON, *Rolling vs. Seasonal PMF: Real-world multi-site and synthetic dataset comparison*, Atmospheric Measurement Techniques 15, 5479–5495 (2022), DOI 10.5194/amt-15-5479-2022.

3) **H. CHEBAICHEB**, G. CHEN, J. FERREIRA DE BRITO, O. FAVEZ, E. TISON, C. MARCHAND, A. PREVOT, V. RIFFAULT, *Investigation of 4-year chemical composition and organic aerosol sources of submicron particles at the ATOLL site in Northern France*, Environmental Pollution 330, 121805 (2023), DOI 10.1016/j.envpol.2023.121805.

4) **H. CHEBAICHEB** et al., *Multi-year high time resolution datasets of fine PM at 13 sites of the French Operational Network (CARA program): Data processing and chemical composition*, in preparation.

5) **H. CHEBAICHEB** et al., *Lessons learned from the comparison and combination of fine carbonaceous aerosol source apportionment at two locations in the city of Strasbourg, France*, in preparation.

6) **H. CHEBAICHEB** et al., *Phenomenology of organic aerosol multi-annual source apportionment at 12 urban and peri-urban sites in France*, in preparation.

Colloques et conférences internationales

H. CHEBAICHEB, J. BRITO, O. FAVEZ, C. MARCHAND, V. RIFFAULT, *Source apportionment analysis on one-year ACSM data of organic aerosols from Lille, Northern France, using Rolling PMF*, **Communication orale**, SoFi Users Meeting 2021, Online, 13-16 avril 2021.

M. VIA, G. CHEN, F. CANONACO, **H. CHEBAICHEB**, V. RIFFAULT, A. S. H. PREVOT, A. ALASTUEY, M. C. MINGUILLON, *Comparison Rolling vs. Seasonal PMF*, **Communication orale**, SoFi Users Meeting 2021, Online, 13-16 avril 2021.

H. CHEBAICHEB, J. FERREIRA DE BRITO, O. FAVEZ, C. MARCHAND, V. RIFFAULT, *Source apportionment analysis on one-year ACSM data of organic aerosols from Lille, Northern France, using Rolling PMF*, **Poster**, European Aerosol Conference, Online, 30 août – 3 septembre 2021.

J. F. DE BRITO, **H. CHEBAICHEB**, E. STRATIGOU, A. BOURIN, S. DUSANTER, V. RIFFAULT, *Studying regional SOA formation using source apportionment, organic tracers and box modelling during the COBIACC field campaign*, **Communication orale**, European Aerosol Conference, Online, 30 août – 3 septembre 2021.

H. CHEBAICHEB, O. FAVEZ, J. BRITO, V. RIFFAULT, *Exploring the error matrix calculation for Q-ACSM used in the PMF analysis*, **Communication orale**, SoFi Users Meeting 2022, Online, 19-22 avril 2022.

M. VIA, G. CHEN, F. CANONACO, K. DAELLENBACH, B. CHAZEAU, **H. CHEBAICHEB**, J. JIANG, H. KEERNIK, C. LIN, N. MARCHAND, C. MARIN, C. O'DOWD, J. OVADNEVAITE, J.-E.

PETIT, M. PIKRIDAS, V. RIFFAULT, J. SCIARE, J. G. SLOWIK, L. SIMON, J. VASILESCU, Y. ZHANG, O. FAVEZ, A. S. H. PREVOT, A. ALASTUEY, M. C. MINGUILLON, *Rolling vs. Seasonal PMF: Real-world multi-site and synthetic dataset comparison*, **Communication orale**, SoFi Users Meeting 2022, Online, 19-22 avril 2022.

A. VELAZQUEZ-GARCIA, **H. CHEBAICHEB**, J. F. DE BRITO, E. TISON, S. CRUMEYROLLE, O. FAVEZ, I. CHIAPELLO, V. RIFFAULT, *Multi-annual source apportionment and absorbing properties of organic aerosols in northern France*, **Communication orale**, 13th International Conference on Air Quality, Thessaloniki (Greece) & Online, 27 juin – 1er juillet 2022.

M. VIA, G. CHEN, F. CANONACO, K. R. DAELLENBACH, B. CHAZEAU, **H. CHEBAICHEB**, J. JIANG, H. KEERNIK, C. LIN, N. MARCHAND, C. MARIN, C. O'DOWD, J. OVADNEVAITE, J-E. PETIT, M. PIKRIDAS, V. RIFFAULT, J. SCIARE, J. G. SLOWIK, L. SIMON, J. VASILESCU, Y. ZHANG, O. FAVEZ, A. S. PRÉVÔT, A. ALASTUEY, M. C. MINGUILLÓN, *Rolling vs. Seasonal PMF: Multi-site and synthetic dataset comparisons*, **Communication orale**, 11th International Aerosol Conference, Athens (Greece) & Online, 4-9 septembre 2022.

H. CHEBAICHEB, J. F. DE BRITO, O. FAVEZ, C. MARCHAND, V. RIFFAULT, *5-year analysis of submicron aerosol chemical composition and organic aerosol source apportionment at a suburban site in North-Western Europe*, **Communication orale**, 11th International Aerosol Conference, Athens (Greece) & Online, 4-9 septembre 2022.

H. CHEBAICHEB, O. FAVEZ, J. BRITO, V. RIFFAULT, *Identification/Investigation of some Q-ACSM issues to ensure QA/QC of data for proper export for PMF analysis*, **Communication orale**, AMS/ACSM Users's meeting, Athens (Greece), 10-11 septembre 2022.

H. CHEBAICHEB, O. FAVEZ, J. F. DE BRITO, B. CHAZEAU, J.-E. PETIT, N. MARCHAND, C. MARCHAND, V. RIFFAULT, *Multi-year datasets of PM_1 chemical composition and organic aerosol sources in different French urban and suburban areas*, **Poster**, American Association for Aerosol Research 41st Annual Conference, Portland, Oregon, 2-6 octobre 2023.

Colloques et conférences nationales

H. CHEBAICHEB, J. F. DE BRITO, O. FAVEZ, C. MARCHAND, V. RIFFAULT, *5-year analysis of submicron aerosol chemical composition and organic aerosol source apportionment at a suburban site in North-Western Europe*, **Communication orale**, Workshop ACTRIS-FR, Autrans, France, 10-13 octobre 2022.

H. CHEBAICHEB, J. BRITO, O. FAVEZ, C. MARCHAND, V. RIFFAULT, *Multi-year datasets of PM1 chemical composition and organic aerosol sources in different French urban and suburban areas*, **Communication orale**, Journée scientifique du Labex CaPPA, Villeneuve d'Ascq, France, 10 mars 2023.

S. CRUMEYROLLE, J. F. DE BRITO, A. VELAZQUEZ GARCIA, **H. CHEBAICHEB**, E. BOURRIANNE, R. DE FILIPPI, M. CATALFAMO, E. TISON, O. FAVEZ, C. MARCHAND, F. AURIOL, I. CHIAPELLO, V. RIFFAULT, *Some recent ATOLL results from in situ measurements*, **Communication orale**, Workshop ACTRIS-FR, Aussois, France, 9-13 mai 2023.

H. CHEBAICHEB, O. FAVEZ, J. F. DE BRITO, B. CHAZEAU, J.-E. PETIT, N. MARCHAND, C. MARCHAND, V. RIFFAULT, *Étude de la composition chimique des PM_1 et des sources de l'aérosol organique sur différents sites français à partir de jeux de données pluriannuels à haute résolution temporelle*, **Communication orale**, Atelier Atmosphère, Climat et environnements urbains, Paris, France, 8-9 juin 2023.

Annexe 2. Procédure d'évaluation des incertitudes

Pour faire suite au calcul des incertitudes des mesures mentionné dans le chapitre 2, section II.5, le bruit électronique est calculé alors en prenant en compte l'écart-type de ce signal (V_Sdev) selon cette équation :

$$e_{Noise} = 6.24e18 \times DwellTW[p] \times V\_Sdev \,/\, gainW[p] \quad \text{(Eq. 12)}$$

où le paramètre DwellTW fait référence au temps pendant lequel les données sont moyennées pour calculer le spectre de masse (*dwell time*), et représente le produit de la fenêtre d'intégration m/z (ka_amu_window), du temps d'attente du DAQ (Prisma scan rate) et du nombre de points par amu (no. Sets), comme indiqué dans l'équation suivante :

$$dwellTW = 2{\times}ka\_amu\_window \times no.\ Sets[p] \times 0.001{\times}Prisma\ scan\ rate[p] \quad \text{(Eq. 13)}$$

Et le $gainW = (gain \,/\, smCorr\_w[p]){\times}(\ Extractor\ set\ value\ [p]/Pressure[p])$ (Eq. 14)

avec la référence gain pour les mesures est : gain = 20000.

Ensuite, le tableau de fragmentation est appliqué aux deux matrices 'organiques' et leurs 'incertitudes', ainsi que la correction Airbeam (Time series correction).

Il faut signaler que dans la matrice d'incertitudes, les erreurs très faibles sont remplacées par une erreur minimum calculée comme suit :

$$minErrorW = 1.2\sqrt{2}{\times}GainW[p]/(6.24{\times}1018{\times}DwellTW[p]) \quad \text{(Eq. 15)}$$

Pour quelques cas de traitement de données ACSM, ces erreurs minimums pour quelques m/z sont très faibles (d'un ordre de grandeur ou plus) par rapport aux autres incertitudes, ce qui nécessite une correction de ces erreurs. Dans certaines versions de l'ACSM Local, cela peut être résolu en changeant la variable "ka_baseline" à 1 dans la procédure de l'ACSM Local, ou en appliquant la fonction "ACSM_ReprocessAll()", mais ce n'est pas toujours le cas. Cela peut corriger certaines erreurs, mais pas toutes. Pour ce travail, nous avons modifié la procédure de l'ACSM Local pour calculer l'erreur en considérant la valeur absolue de ces signaux. Cela permet de résoudre le problème des faibles incertitudes.

$$e_{I_{open}} = abs\,(1.2\sqrt{I_{open}}) \quad \text{(Eq. 16)}$$

$$e_{I_{closed}} = abs\,(1.2\sqrt{I_{closed}}) \quad \text{(Eq. 17)}$$

À ce stade du processus d'exportation, un certain nombre de paramètres doivent être examinés et vérifiés, car ils peuvent malheureusement présenter des bogues en fonction de la version de l'ACSM Local utilisée. Il s'agit notamment du paramètres 'DwellTime' et 'no of Sets'. La paramètre 'DwellTime' peut être égal à zéro pour certaines périodes et qui doit être corrigé pour atteindre la valeur par défaut de 200. Le paramètre "no of Sets" peut aussi parfois être réglé sur une valeur autre que 28, ce qui entraîne des incertitudes élevées. Les périodes dont la valeur du paramètre "no of Sets" est différente de 28 doivent être supprimées.

Les incertitudes des masses "importantes" (e.g. m/z 43, 44, 55, 57, 60, etc.) sont également vérifiées en regardant l'ordre de grandeur des écarts-types et d'erreurs moyennes calculées pour ces m/z. Par conséquent, le ratio entre l'écart-type et l'erreur moyenne sur une période de faibles concentrations pour ces m/z devrait être inférieur à 10.

Annexe 3. Guide de l'utilisateur pour le traitement des données ACSM et l'application PMF à l'aide de SoFi Pro

IMT Nord Europe
École Mines-Télécom
IMT-Université de Lille

INERIS
maîtriser le risque
pour un développement durable

User guide for ACSM data processing and PMF application using SoFi Pro

Hasna Chebaicheb, Véronique Riffault

(Reviewed by Mélodie Chatain)

Objective: This document is intended for everyone who wants to investigate source apportionment using the PMF method on SoFi Pro software. This version is specifically designed for the analysis of ACSM data. It details all the steps for the preparation of data in Igor within the ACSM data acquisition software (ACSM Local, Aerodyne Research Inc.) and then the steps to perform PMF using SoFi (Source Finder Datalystica Ltd., Villigen, Switzerland).

LCSQA
Laboratoire Central de
Surveillance de la Qualité de l'Air

Datalystica

Table of contents

Chapter 1: Preparation of PMF input using ACSM Local software

There are many steps to follow in order to clean the ACSM data and then export the "Organic" and "Error" matrices:

I. Initialize ACSM Local

First, the user should open a new Igor experiment, and then add the procedures by drag and drop:

- Global_Util.ipf

- acsm_local_xxxx.ipf (xxxx: version number)

Secondly, the user should compile the procedures and then close the windows by clicking on "Hide".

This method can be used to integrate the ACSM tab punctually, but it is also possible to save the procedures so that the user always has them on IGOR. To do so, simply place them in this folder :

C:\Program Files (x86)\WaveMetrics\Igor Pro Folder\Igor Procedures

In the top bar, an "ACSM" menu appeared. The user should click on "Panel Tools", then "Build, Rebuild, or Bring to Front ACSM Panel".

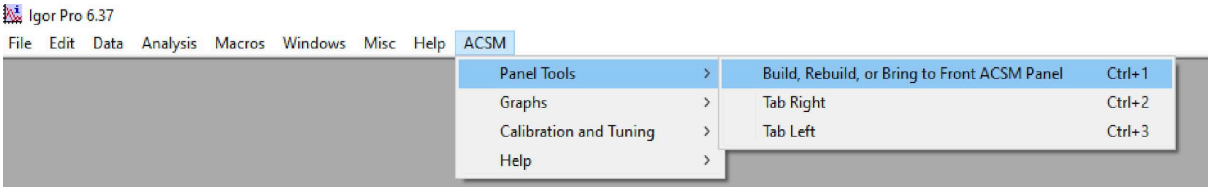

Figure 1: Initialize ACSM Local

The user should also import the fragmentation table by dragging and dropping the ms_mats wave that is in the fragmentation file (C:\ACSM_Local\FragmentDataDirectory\ms_mats) into root:ms_mats in "Data Browser".

II. Import data

After initializing ACSM Local, the user can import the data by clicking on "source" in the "Dataload" tab, then choose the path where there are the ScanData ACSM files which should be in the format 'aaaammjj' as mentioned in the figure below.

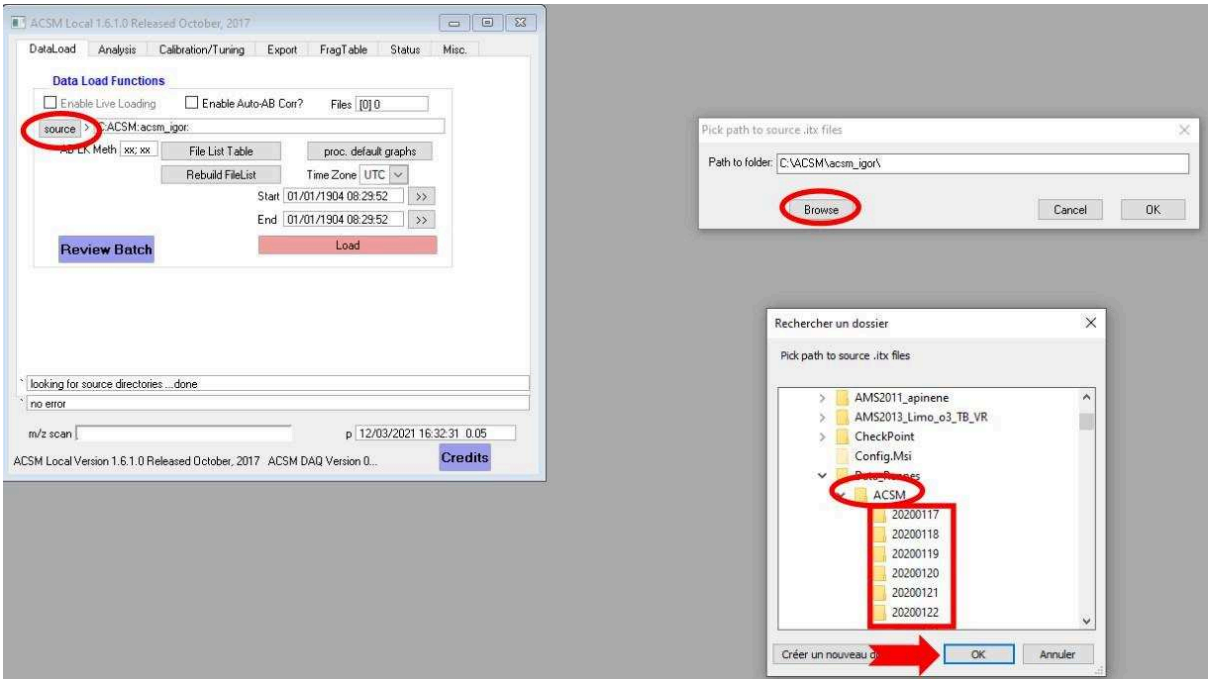

Figure 2: Import data

When the data loading is finished, the number of directories and files are displayed in the upper right corner, and the start and end dates of the dataset are displayed in 'Start' and 'End'.

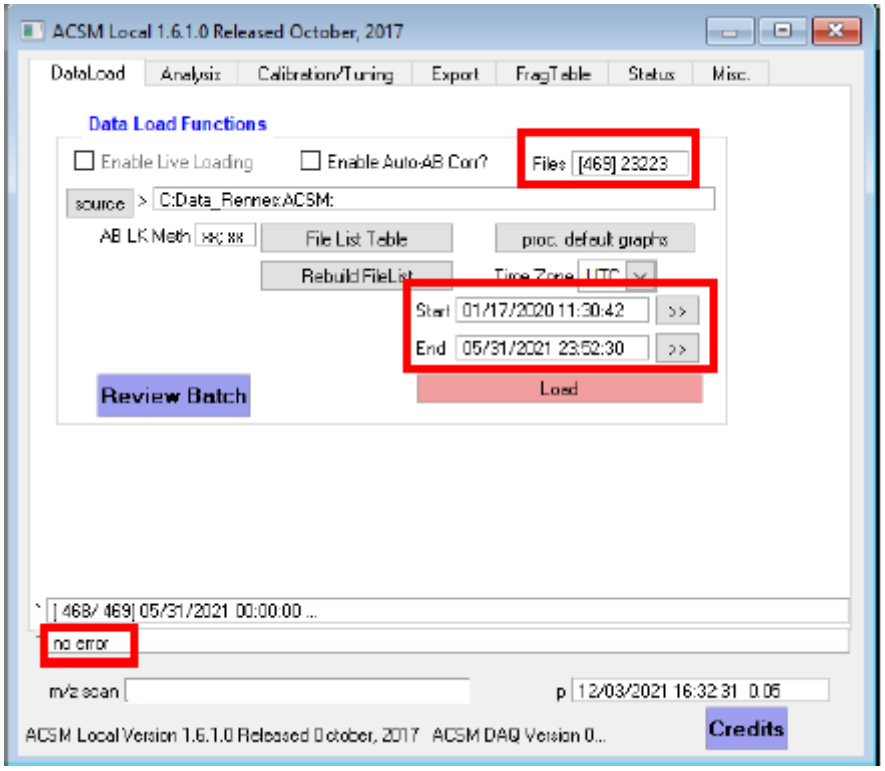

Figure 3: Import data

Then, the user should click on “Load” in order to load ACSM data:

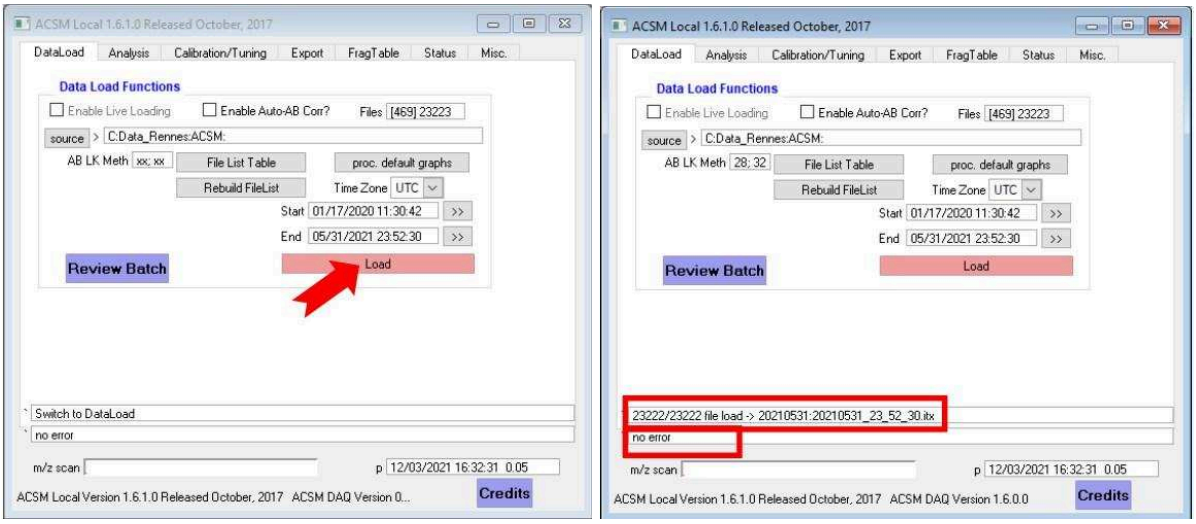

Figure 4: Load data

III. Verification of calibration parameters

The calibration parameters are defined in the “Review Batch” button. So, the user can click on this button in order to check which RF and RIE values are considered (default values when opening a new file).

For RIE, in the button 'Review Batch': the user can modify the values of the RIE column.

For RF(NO3) presented by the variable ‘Masscalib_nitrate’, it can be modified here and also in the 'Analysis' tab, button 'Time Series correction'.

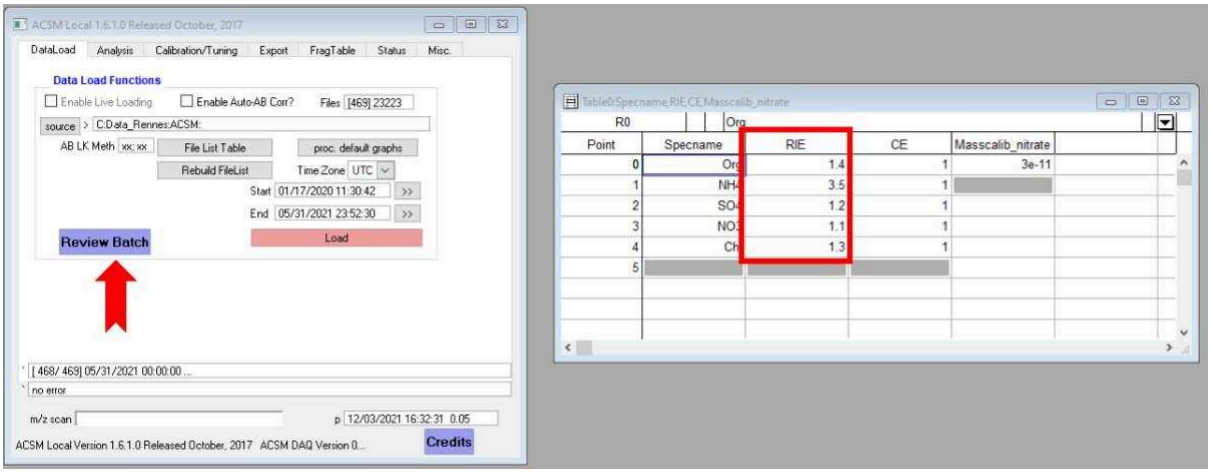

Figure 5: Review Batch

IV. QA/QC of data

- Basic diagnostics

In the "Analysis" tab, the user can check the diagnostics and tuning plots. So, in the "Basic Diagnostics" tab in the upper right corner, the user should check "diagnostics" and "tuning", and then click on “Plot!”

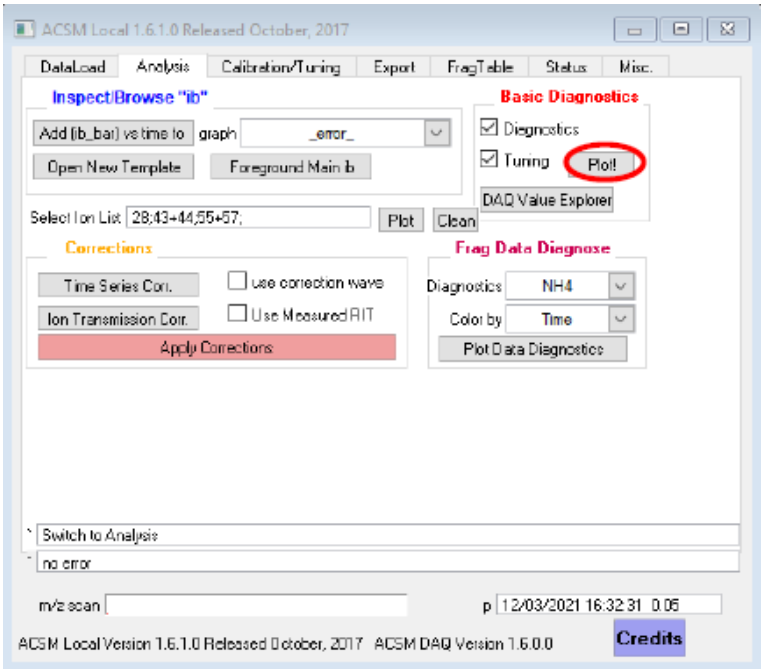

Figure 6: Basic diagnostics

In the “tuning plot”: the user needs to check all the parameters to verify that there has been no accidental modification of the unchecked parameters (theoretically identical after the initial tuning of the instrument on site).

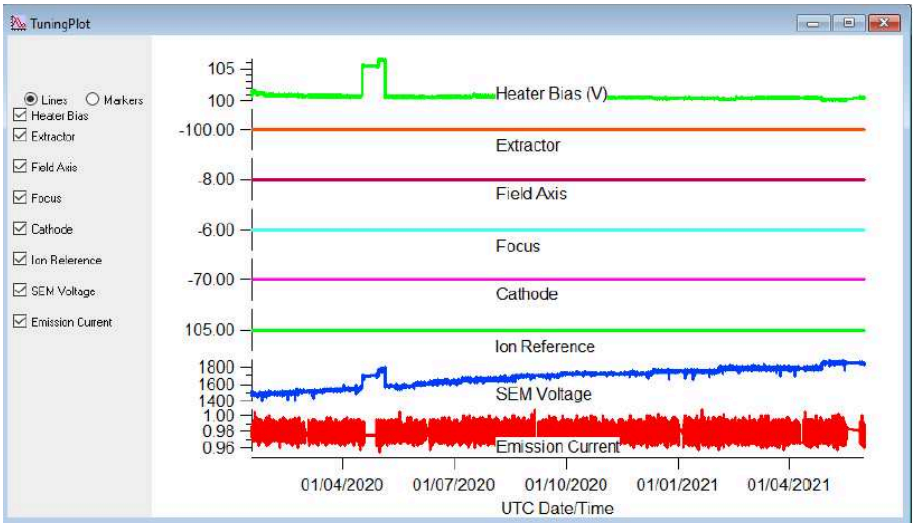

Figure 7: Tuning plot

On the 3 default parameters (Heater Bias, SEM voltage, and Emission current), the user can identify possible problematic periods (to be kept in memory to see if more noise or PMF problems later ...).

Here is an example of a stop of the instrument with tuning at the restart on the detector probably not stabilized enough.

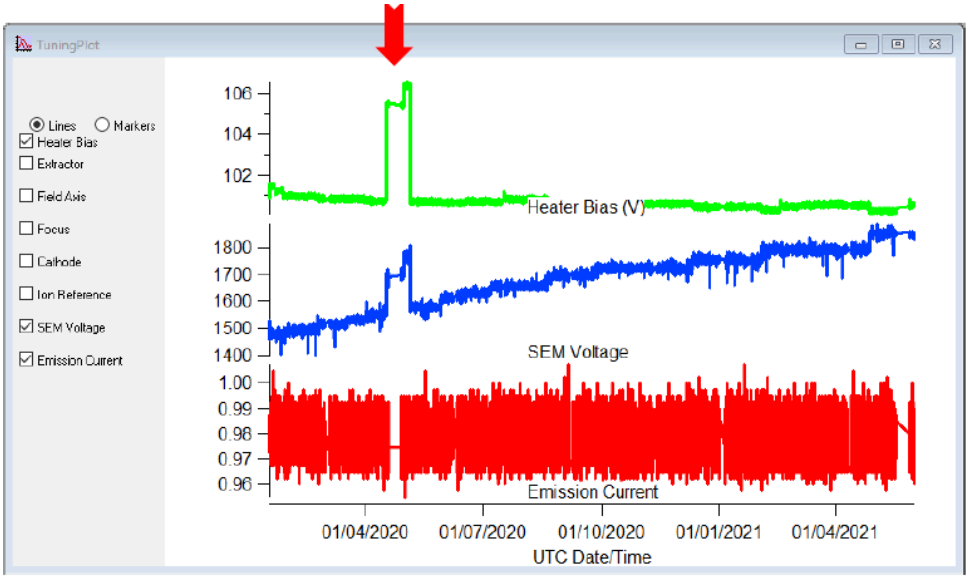

Figure 8: Tuning plot

In the "diagnostics plot": the user can check other parameters (Airbeam, Inlet pressure, ...).

The user can choose "markers" to have a good look at the plots and check if there are any outliers or brutal variations or settings indicating a problem (tensions, clogging of the critical orifice ...).

In this figure, there are some outliers of inlet pressure and airbeam, as well as restart periods where the temperature of the vaporizer is not stabilized.

The user should note the points to be invalidated.

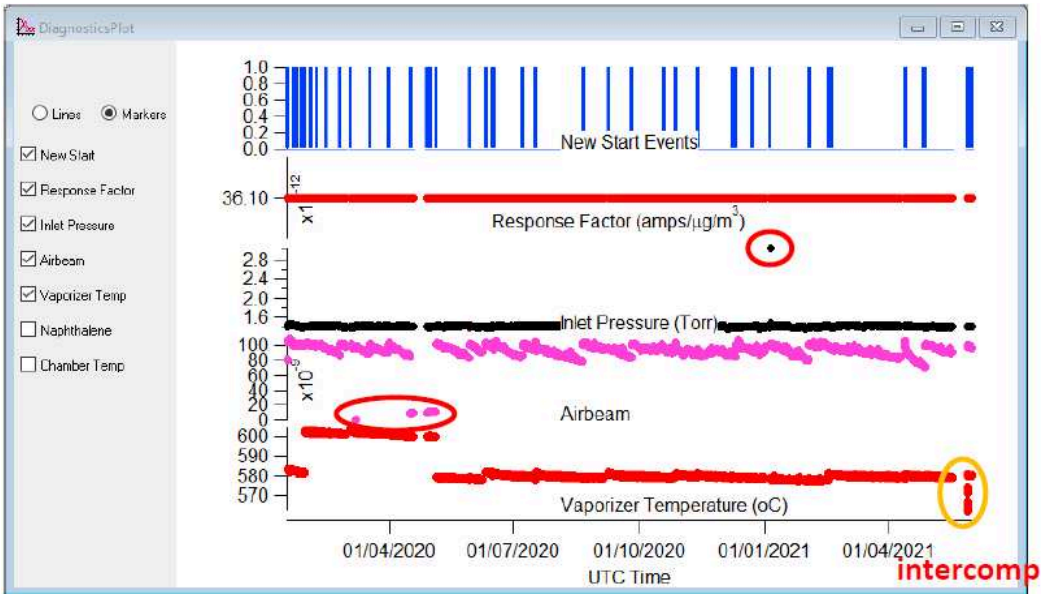

Figure 9: Diagnostics plot

- Checking specific ions:

The user can have a look at some main ions in order to have more information about the data. So, in the "Select Ion List" tab, the user can copy this list of masses:

18;28;32;35;36;40;43;44;55;60

that present the ions corresponding to water (*m/z* 18), air (*m/z* 28, 32, and 40), chlorides (*m/z* 35 and 36), and some organics (*m/z* 43, 44, and 55) including the levoglucosan fragment (*m/z* 60). Therefore, it allows to:

- Check the influence of some sources (sea salts, biomass combustion, AOS, traffic ...)

- Invalidate points for which the air and/or water signals seem aberrant.

Then the user can click on “Plot” to clean the dataset:

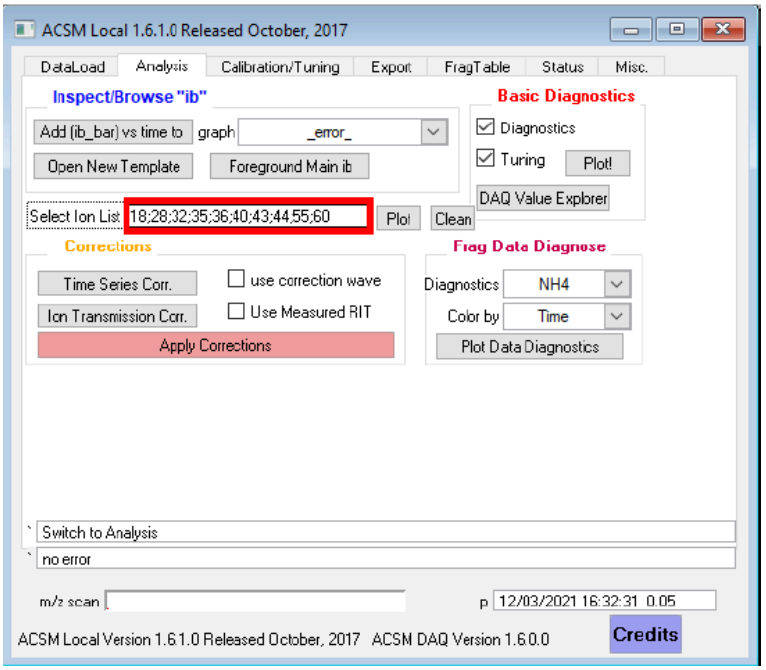

Figure 10: Select Ion List

This step can be done by using 3 ways or tools:

- First, by using the "Blacklist" button that can be added to any graph from the "Macros" menu, then the user can clean up the graph manually using the cursor(s).

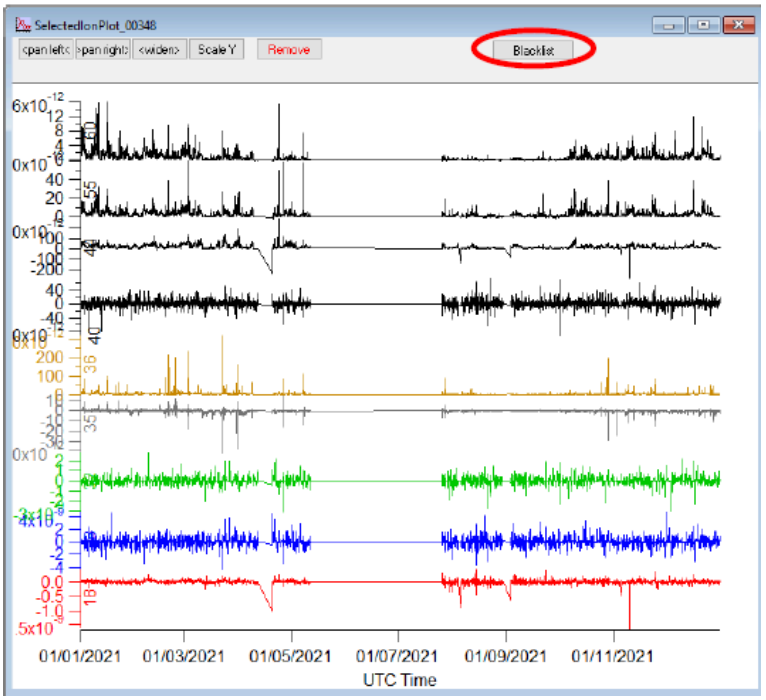

Figure 11: Graphs of selected ions

- Second, the user can use 3 scatter plots: *m/z* 18 vs *m/z* 28; *m/z* 32 vs *m/z* 28; *m/z* 40 vs *m/z* 28 which allows determining the noise levels for each *m/z*.

The 1st graph is supposed to be anisotropic but symmetrical to the vertical. The next 2 graphs are supposed to be isotropic, as shown in the example below.

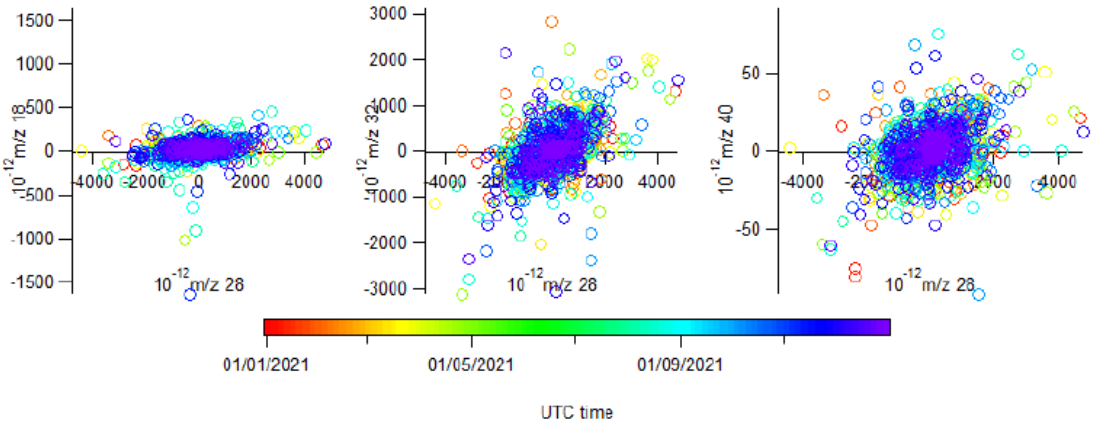

Figure 12: Scatter plots of selected ions

This is an example of manual cleaning with the cursors and the "Blacklist" button:

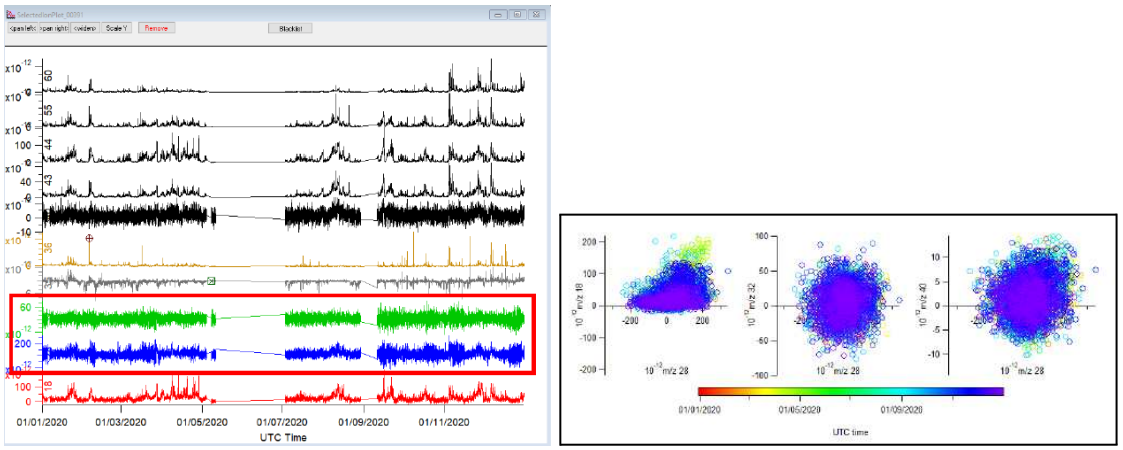

Figure 13: Example of manual cleaning of selected ions

- Third, by using a function 'ACSM_CleanSpikes' different from those proposed by Aerodyne Research in the 'ACSM_SpikeRemover.ipf' file. It is applied to *m/z* 18, 28, 32, and 40 and allows to remove spikes based on positive or negative deviations from zero in the "SelectedIonPlot" plot. It reproduces the manual cleaning performed previously, unlike Aerodyne's functions which are based on a difference between 2 points in the filtered and ambient air signals.

The procedures of the 3 tools are attached in the annex.

- TIS and RIT Corrections

In the part "Corrections", the user can click on "Time Series Corr." to check the variability of the detector sensitivity. This window displays on the right the technical parameters of the

ACSM ("reference" N_2, O_2, Ar, P, T, Naph., and RF) i.e. as measured during calibration. It also reports some important time series of Pressure, the Airbeam (N_2), and the value of the RF.

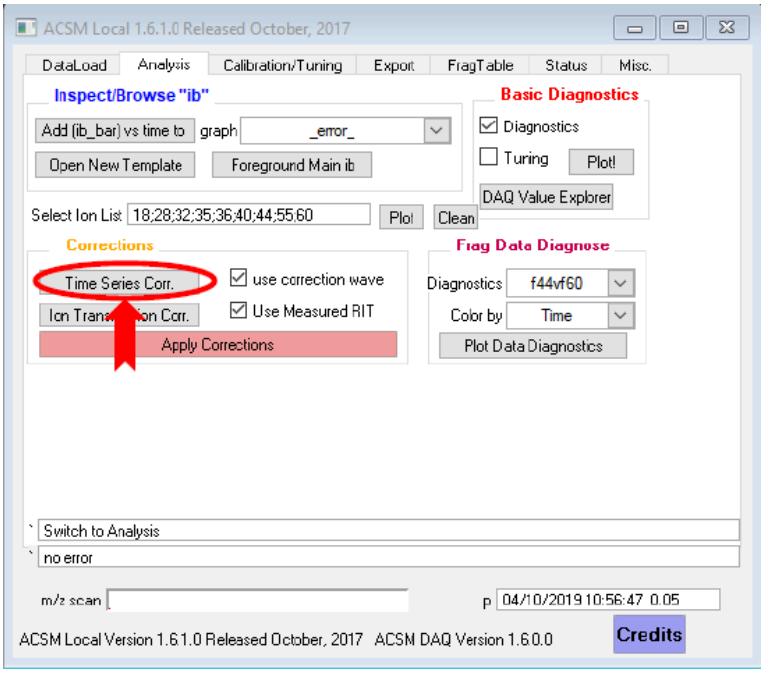

Figure 14: Time series correction

In this plot, the user can check the Airbeam signal which should be around $1e^{-7}$. Then, the user clicks on "Continue to Corrections Panel" and "Re-smooth" the correction.

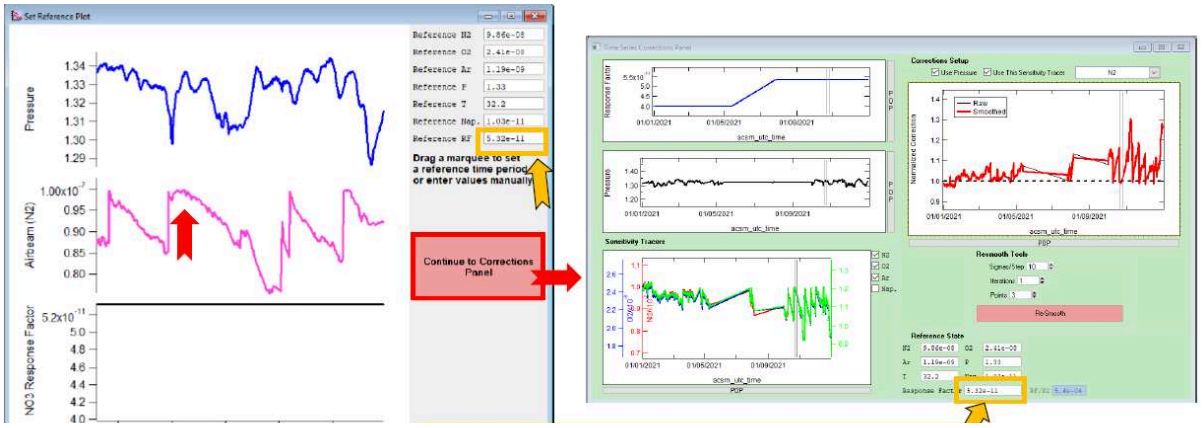

Figure 15: Time series correction panel

Second, the user can click on "Ion Transmission Corr." to check the relative ion transmission that is based on the naphthalene peaks. It corresponds to the transmission efficiency of the ACSM which decreases for the highest masses.

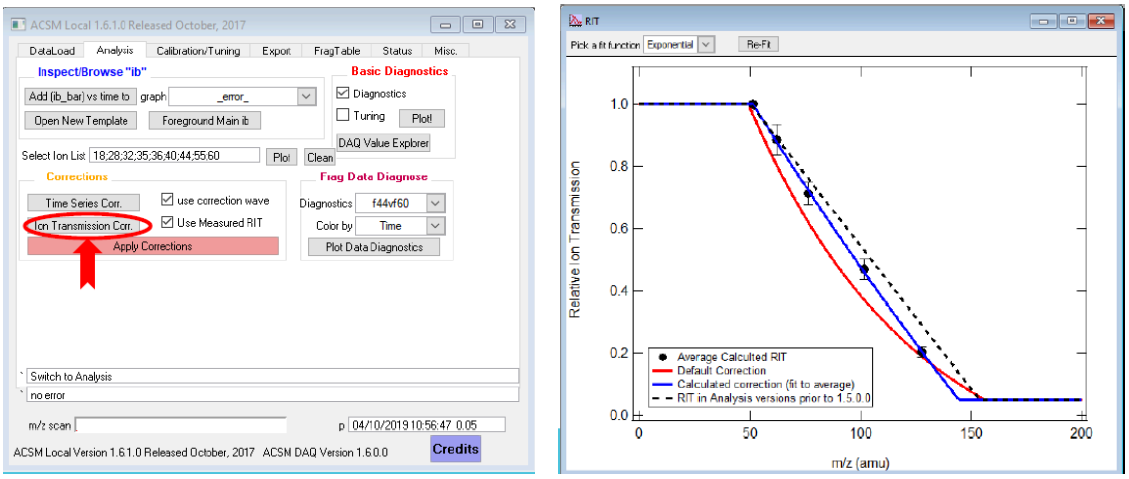

Figure 16: Relative Ion Transmission (RIT) correction

To pay attention:

When the error bars of the average calculated RIT are very large, it is important to check the time series of RIT ions (*m/z* 62, 76, 102, and 128; normalized to 1 for the 1st mass 51). (the procedure in the annex).

Here is an example of the time series of RIT masses with no RIT problem in the data:

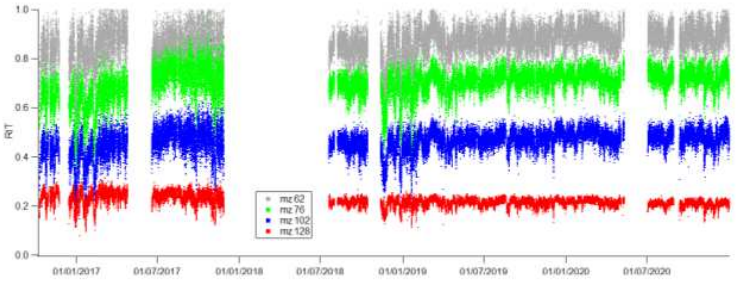

Figure 17: Example of RIT masses with no problem RIT

On the other hand, this is an example of a dataset with the RIT problem:

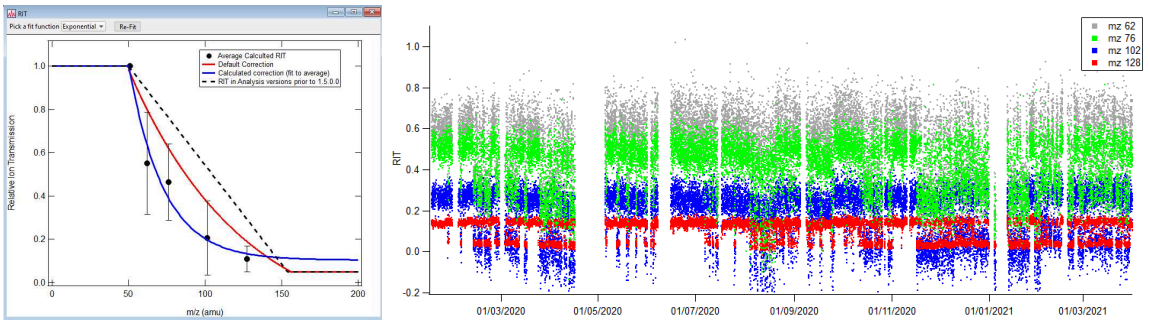

Figure 18: Example of RIT masses with a problem RIT

To filter the bad data, we applied a criterion on the RIT of m/z 128 in order to take into account only the values of m/z 128 between 0.11 and 0.19, as shown in the figure below:

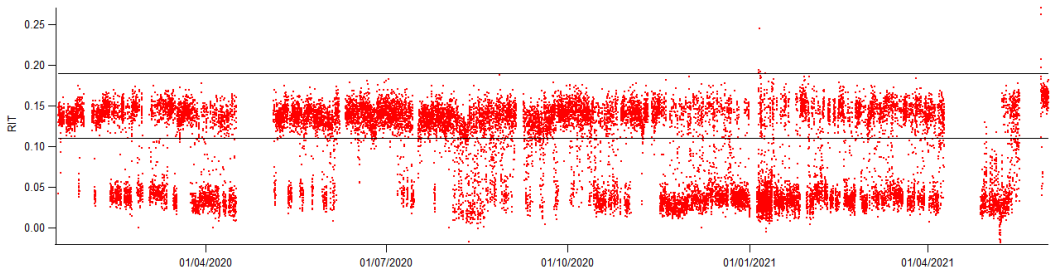

Figure 19: The RIT of m/z 128

So, these figures present the RIT after cleaning the dataset; 58% of the dataset remains, with more points in the first 2/3 of the period. Still, a few problematic points at other *m/z* (e.g. 102), but should not bias the RIT average too much.

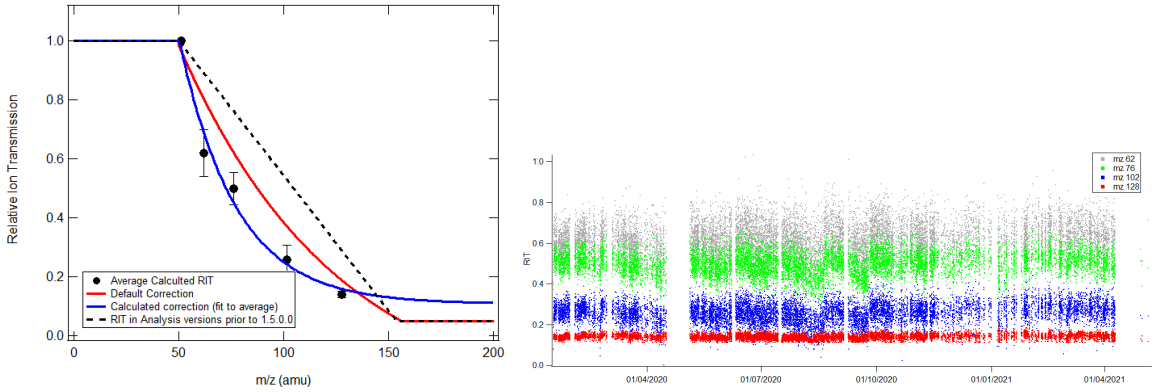

Figure 20: The RIT after cleaning the dataset

To be Careful:

Sometimes, the averaged RIT looks good but the time series does not, as shown in the graphs below. Therefore, the user needs to check the time series of individual naphthalene masses, not only the average RIT.

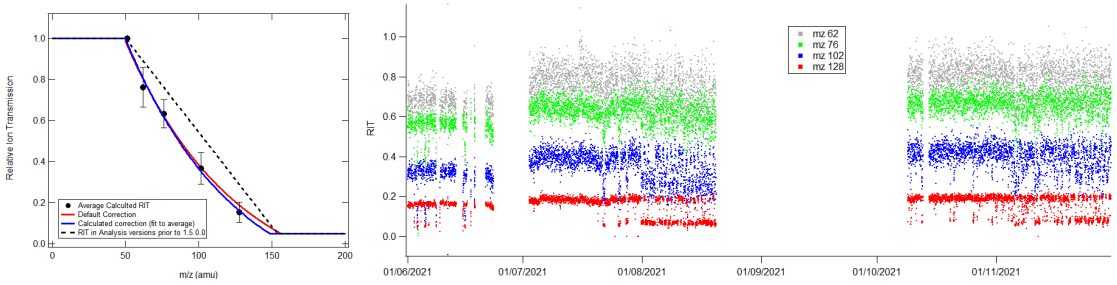

Figure 21: Example of the averaged RIT and the time series of individual RIT masses

So, the user should check or tick the two corrections “Use correction wave” for the Airbeam variation and “Use measured RIT” for the RIT variation, and then click on “Apply corrections”. Depending on the size of the dataset, this step may take some time.

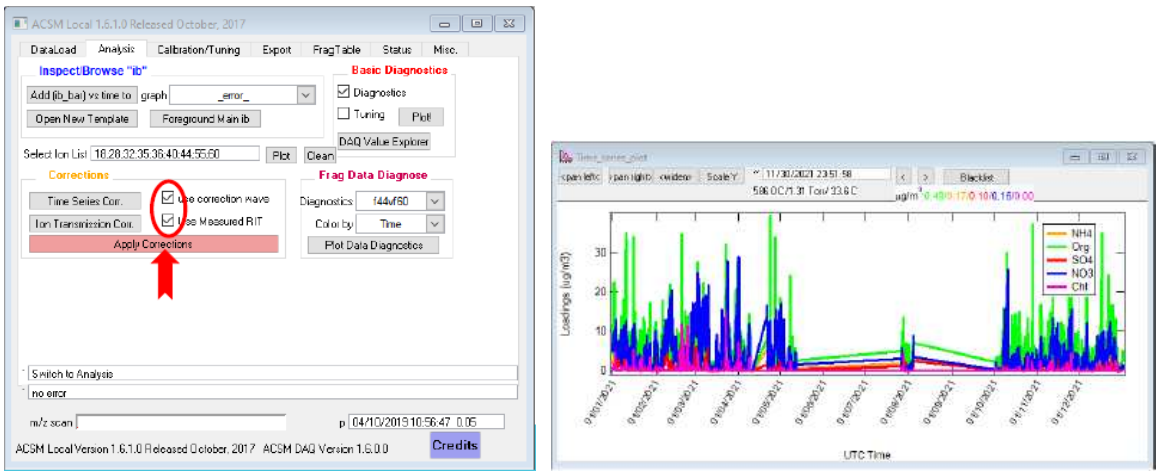

Figure 22: Apply corrections

V. CE correction

The collection efficiency (CE) correction is based on the Middlebrook algorithm (CE = 1 by default in the batch; the minimum value of CE of 0.5 and LD_{NH4} = 0.1 µg m^{-3}). LD variable depending on the instruments (blanks). (see the procedure in the annex that allows calculating the CE_dry by using the function CalCE_dry with a minimum value of 0.5 (determined during the 2013 CIL).

Pay attention:
The procedure is only applied to the waves of the different ACSM species (Org, SO_4, NO_3, NH_4 and Chl).

The user can then check the time series of CE_dry, the scatter plots of different ACSM species before and after applying the CE correction.

VI. Verification of NH_4 neutralization

In the tab "Frag Data Diagnose", the user can check diagnostics of NH_4, NO_3, SO_4, org_{44} vs org_{43}, f_{44} vs f_{60} and then click on "plot data diagnostics".

This is an important step in the validation of ACSM data that allows the validation of the RIE values of NH_4 and SO_4. The user should verify that the ammonium concentration measured by the instrument is close to the "predicted" ammonium concentrations. The slope of the measured NH_4 versus the predicted NH_4 should be around 1+10%.

This ratio can be temporarily lowered during certain pollution episodes with the presence of acid aerosols or SO_4 or NO_3 linked to organic matter (organo-nitrate, organo-sulfate). In these cases, the predicted ammonium would be overestimated and the ratio would be reduced.

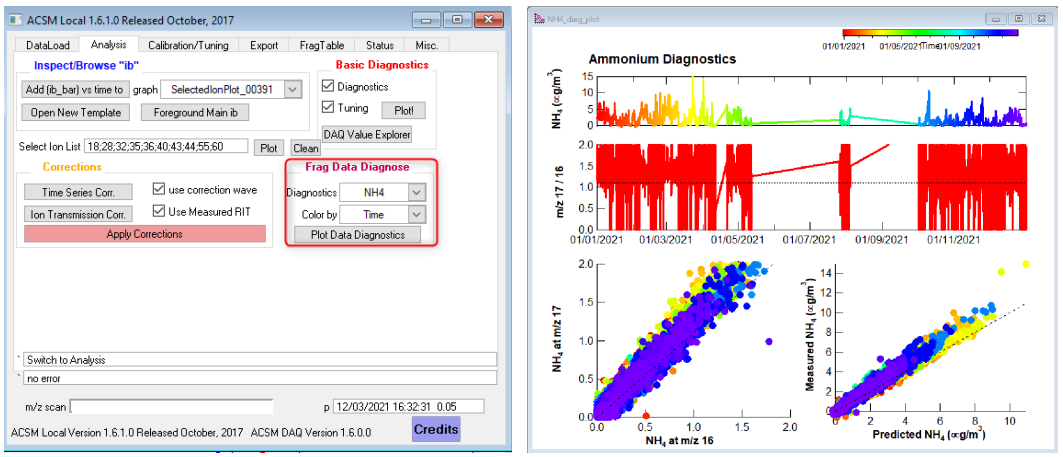

Figure 23: Verification of NH_4 neutralization

VII. Verification and correction of the wave ACSM_LocalTime

The wave 'ACSM_LocalTime' is modified ONLY when the Prisma is stopped/restarted after the time change (so sometimes weeks/months later). Therefore, it should be corrected **before the PMF export** because it conditions the calculated **daily profiles** of species and organic fragments.

=> Springtime change: last Sunday of March; at 2 am, it is 3 am.

=> Fall time change: last Sunday in October; at 3 am it is 2 am.

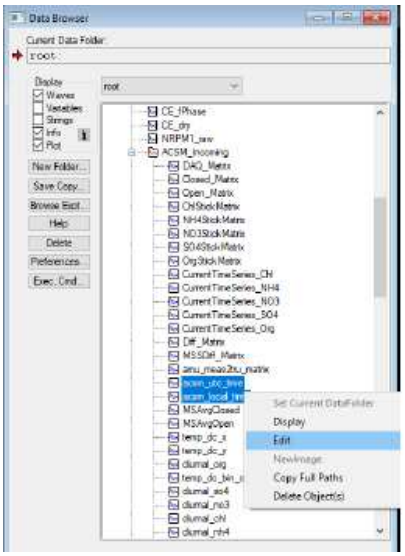

Figure 24: Verification of ACSM_LocalTime

VIII. PMF exporting

After the process of validating the ACSM species, the user can export the matrices of organic concentrations and their uncertainties in order to perform PMF. This can be done in the tab "Export", as shown in the figure below.

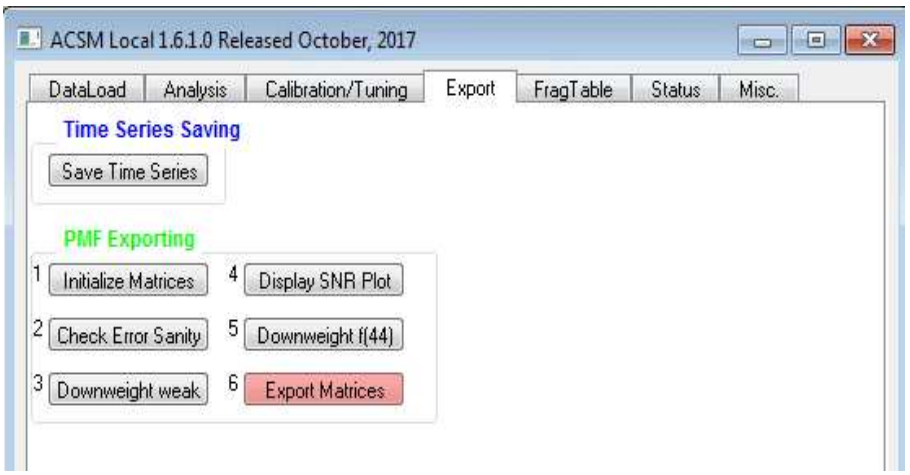

Figure 25: Export matrices

In ACSM Local software, there are five steps before extracting both matrices, however for SoFi, only the first two should be performed ("Initialize Matrices" and "Check Error Sanity"), before exporting the data, as SoFI will execute the last three (THIRD, Fourth, and FIFTH, related to downweight) as data preparation. This is particularly important for the downweight CO_2 masses, which should be only performed in SoFi.

So, first, the user should click on "Initialize Matrices" in order to create the matrix of organic fragments (concentrations and uncertainties).

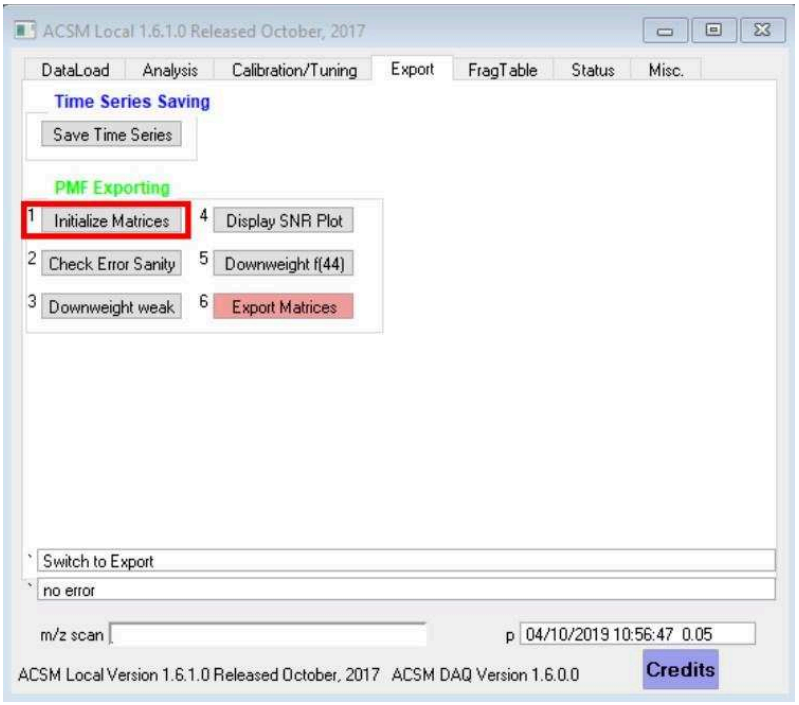

Figure 26: Initialize matrices

The CE correction procedure was NOT applied to the individual organic fragments that are generated in the export matrix for PMF. This step must be performed in SoFi before performing the PMF analysis.

The user should follow the steps shown in the figure below to create the matrices:

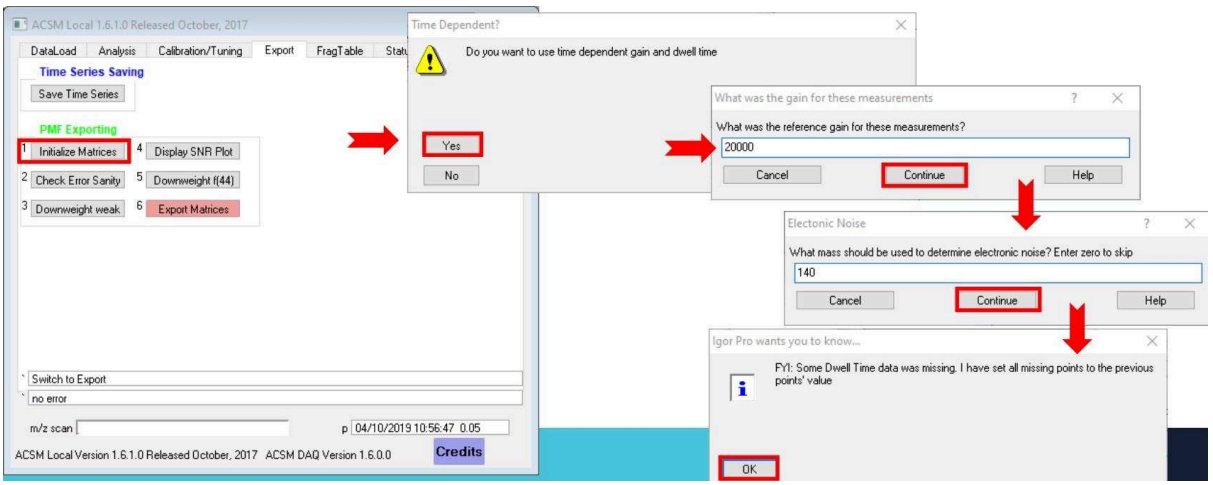

Figure 27: Initialize matrices

The matrices are created in a new directory 'PMFMats' directory in the Data Browser.

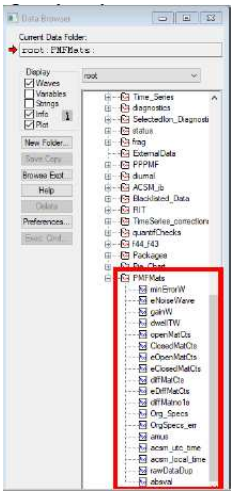

Figure 28: 'PMFMats' directory

Secondly, the user should click on “Check error sanity” in order to verify the error level of all masses *m/z*.

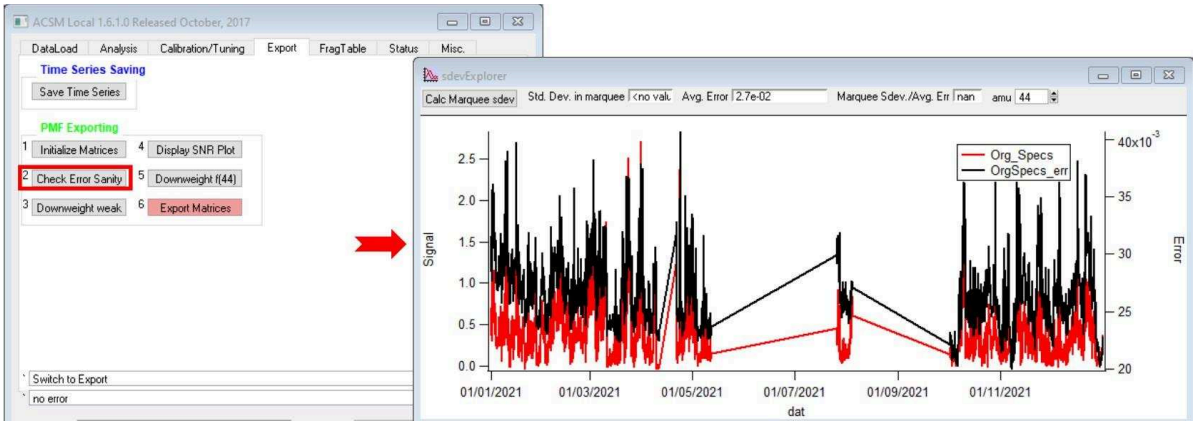

Figure 29: Check error sanity

For "important" masses in the classical PMF factors (*m/z* 43, 44, 55, 57, 60 ...), the user should make sure that the standard deviations and the mean error calculated for this *m/z* are of the same order of magnitude.

So, first, the user should select a period of low concentration (red) for this *m/z* and then right-click on this selection and choose “Calculate Mark Std. Deviation” in order to check the ratio between the 2 values (the std Dev. and the avg. error) which should be lower than 10.

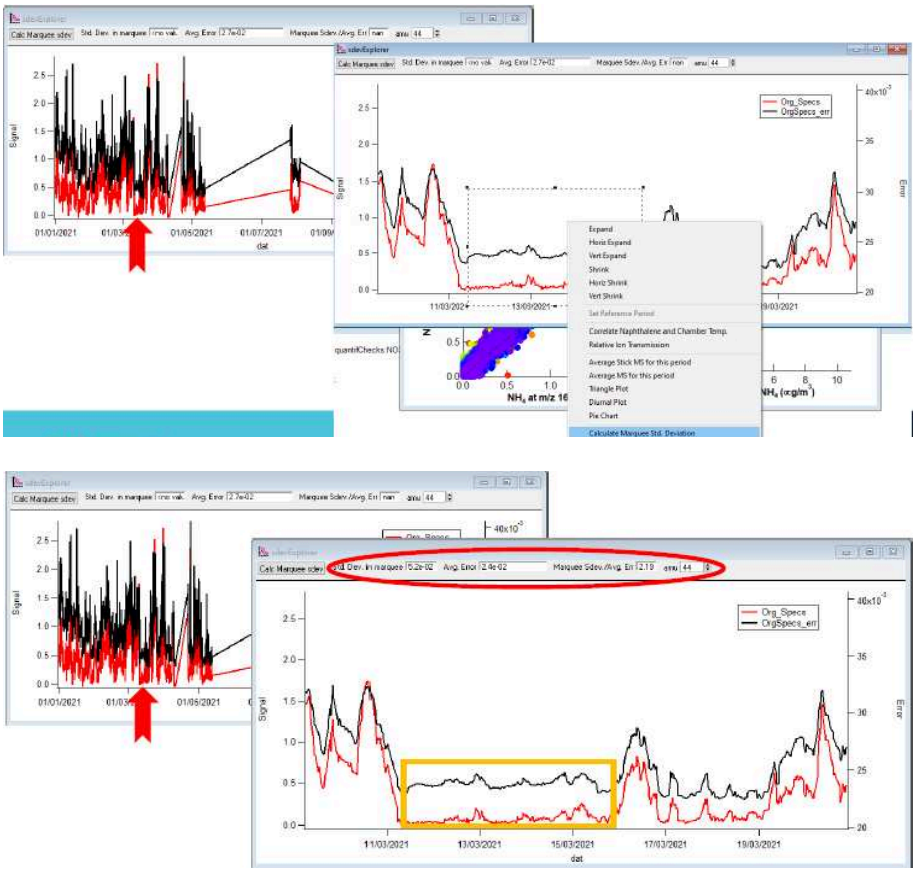

Figure 30: Check error sanity

To pay attention:
As mentioned before, the user should check the error sanity for all m/z before exporting the matrices. This step is very important because it is possible to have some issues during the calculation of the error matrix. So, the user must check the uncertainties of all the m/z.

There are some issues linked with the calculation of input (error) matrices:

- **An issue related to the minError**

Very low uncertainties are observed for some m/z’s as shown in this figure:

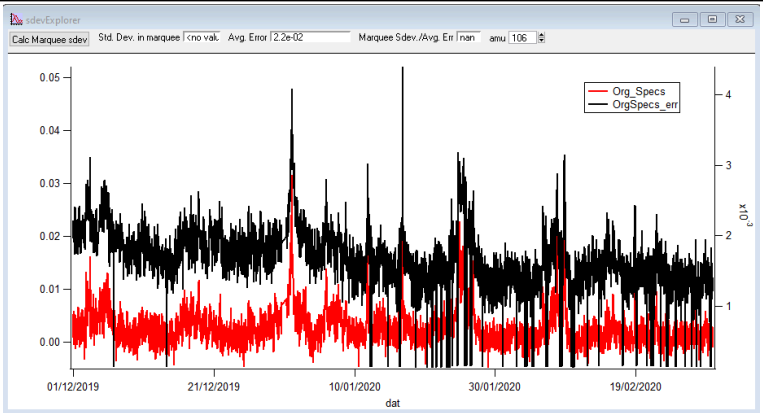

Figure 31: Example of very low uncertainties

The errors corresponding to the closed signal for some points were not calculated because they were negative values (below MS baseline), therefore we have NaNs. NaNs are replaced with zeros in the process of generating the error matrix and then replaced with the minError values. The minError wave seems much too low (factor of 10) compared to other datapoint uncertainties.

eClosed=$1.2\sqrt{closed}$ and eOpen=$1.2\sqrt{Open}$

eDiffMat=$\sqrt{eOpen^2 + eClosed^2}$

In some ACSM Local versions, this can be solved by changing the variable "ka_baseline" to 1 in the ACSM Local procedure, or by applying the function "ACSM_ReprocessAll()", but it is not always the case. This can correct some errors but not all.

On the other hand, in ACSM local, the **minError** is determined as follows:

minErrorW = $1.2\sqrt{2}$GainW[p]/(6.24e18*DwellTW[p])
GainW = (gain / smCorr_w[p])*(daq_matrix[p][85]/daq_matrix[p][1])
DwellTW = 2*ka_amu_window * daq_matrix[p][54] * 0.001*daq_matrix[p][75]

Therefore, the other possibility is to calculate these errors and/or minError differently.
In the figure below, we modify the ACSM local procedure to calculate the error by considering the absolute value of these signals. This solves this issue of low uncertainties.

acsm_local_1616.ipf

```
//Calculate difference and its error in cts
//MatrixOp/O eOpenMatCts = a*powr(OpenMatCts,0.5)
//MatrixOp/O eClosedMatCts = a*powr(ClosedMatCts,0.5)
//////////Test for negative values in open and closed signals
MatrixOp/O eOpenMatCts = a*powr(abs(OpenMatCts),0.5)
MatrixOp/O eClosedMatCts = a*powr(abs(ClosedMatCts),0.5)
```

Figure 32: Acsm local procedure

- **An issue related to DwellTime equal to zero**

The DwellTime is sometimes given as null for some periods:

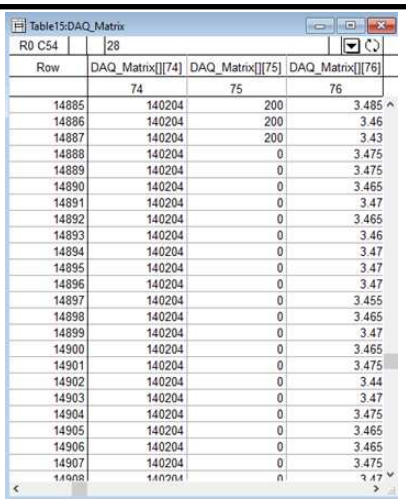

Figure 33: DAQ matrix waves

This problem is a bug of the ACSM local, and it can be solved manually by correcting the zero values by 200.

- **An issue related to nb. of sets**

The user should verify the “nb. of sets” wave because sometimes, this wave is not always equal to 28. So it gives high uncertainties, therefore, the user should remove the periods where the nb. of sets is different than 28, as shown in this figure.

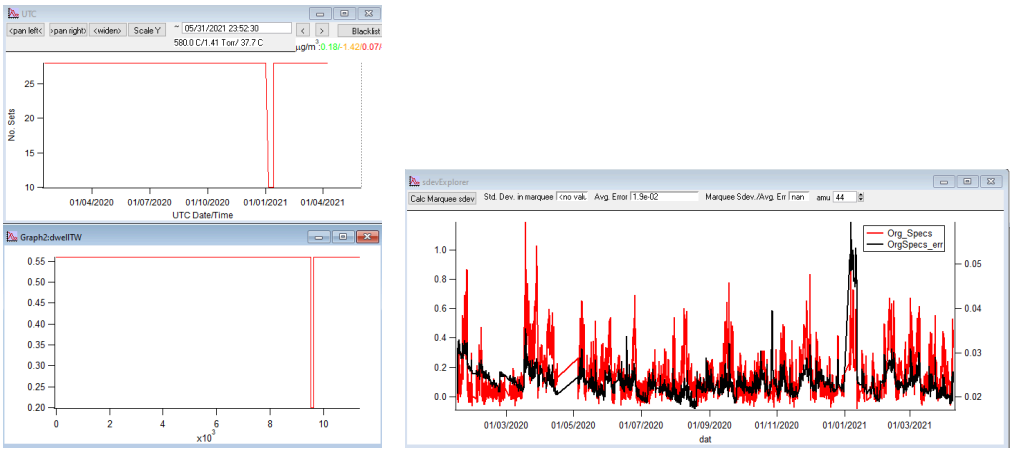

Figure 34: Example of number of sets issue

The last step is to “Export matrices” in order to create the input file for the PMF analysis, as shown in the figure below.

As mentioned before, to avoid inadvertently applying twice the weighting of "weak" or "bad" m/z, here and in SoFi, all the weighting steps (downweight) are performed in SoFi.

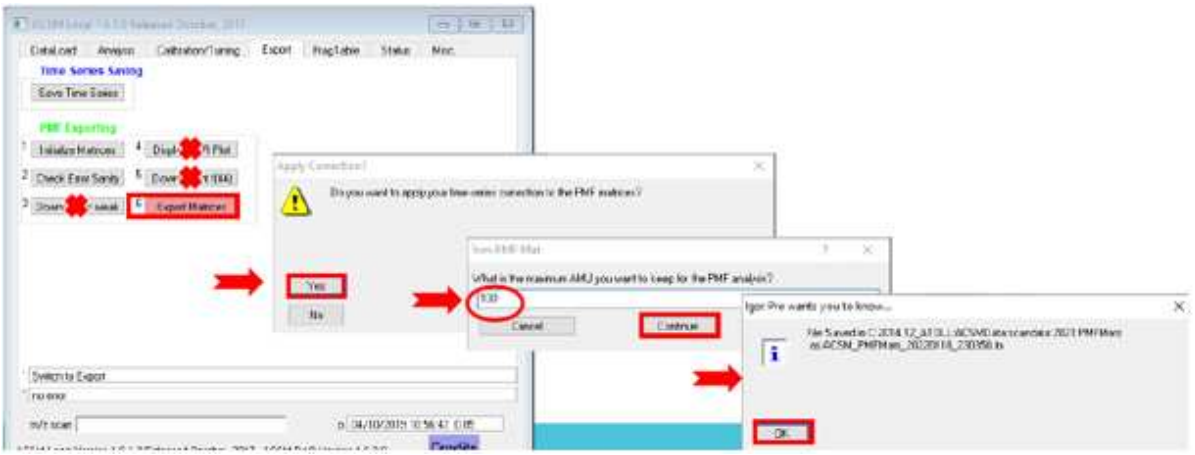

Figure 35: Export matrices

The file created contains the following waves:

- Org_Specs => mass concentrations (in µg m^{-3}) of organic fragments (uncorrected for CE).

- OrgSpecs_err => errors (in µg m^{-3}) associated with the concentrations (idem)

- amus => list of m/z

- acsm_local_time => local date and time

- acsm_utc_time => TU date and time

It can be directly imported (by drag and drop) in the experiment containing the SoFi Pro. The CE_dry should be imported as well with the ACSM species.

To resume, these are the main points to be checked in order to have a clean matrix to be used in the PMF analysis:

- Application of the calibration parameters
- Data cleaning (air/water peak removal)
- Application of the TIS and RIT corrections
- Application of the CE correction
- Error checks for all m/z
- No downweighting of data on ACSM Local software
- Verification and correction of the ACSM_Local_Time wave
- Export of matrices up to m/z 100

Chapter 2: Installing and initializing SoFi

To install SoFi, the user should follow these steps:

Step 1: Have Igor installed on the machine with a valid license (It's best to have the latest version of Igor and therefore for SoFi).

Step 2: Install the HDF5 interface

- Create a shortcut to the following file:

C:\Program Files\WaveMetrics\Igor Pro Folder\More Extensions\File Loaders\HDF5.xop

- Place the shortcut into:

C:\Documents\WaveMetrics\Igor Pro User Files\Igor Extensions\HDF5.xop

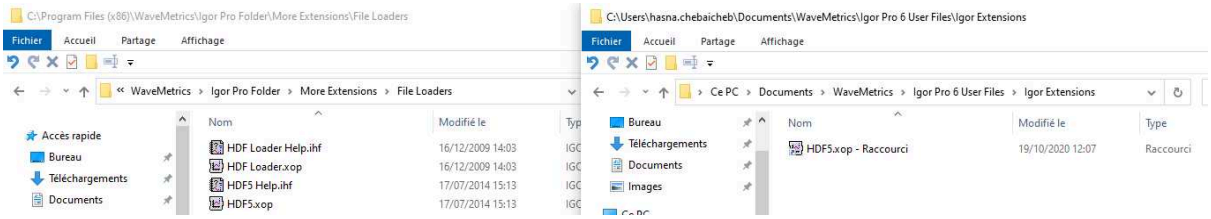

Figure 36: HDF5 interface installation

Step3: Installing the ME2 solver

- Download the ME2: https://www.datalystica.com/userdata/filemanager/data/ME2_engine.zip
- Place the ME2_engine folder in the local drive C (must be save in this folder to avoid any issues)
- Buy a license key for ME2: https://datalystica.onfastspring.com/
- Place the license in the ME2_engine folder
- Execute ME2 (ME2.exe)

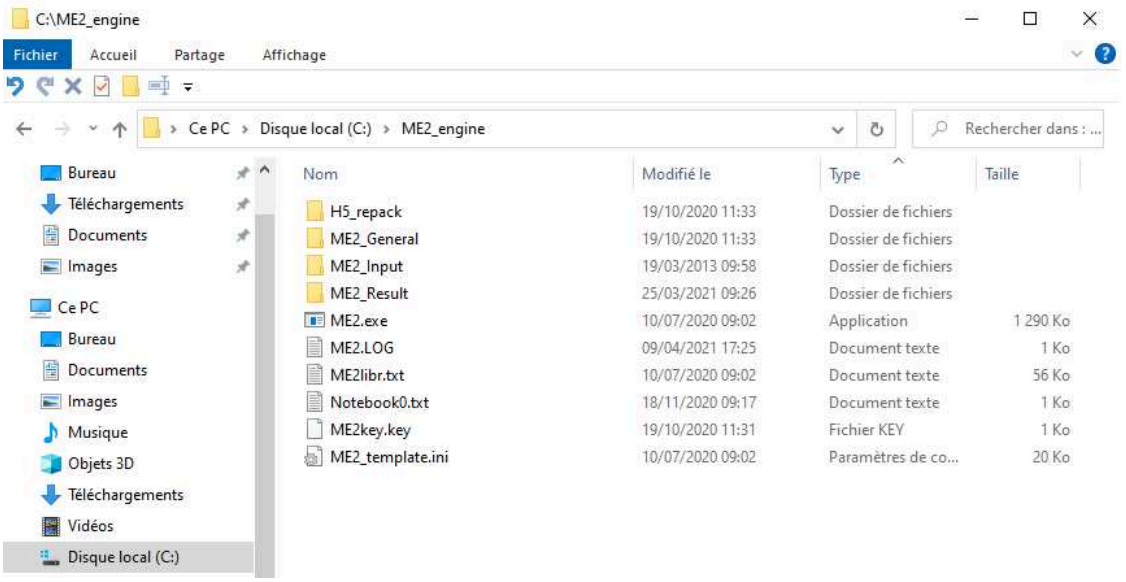

Figure 37: ME2 solver installation

Step 4: Install SoFi Pro

- Download the latest version of SoFi on the Datalystica website (SoFi.ipf)
- Place this version (SoFi.ipf) with the SoFi Pro key (SoFi_key.ipf) in this path: C:/ME2_engine/ME2_General/SoFi

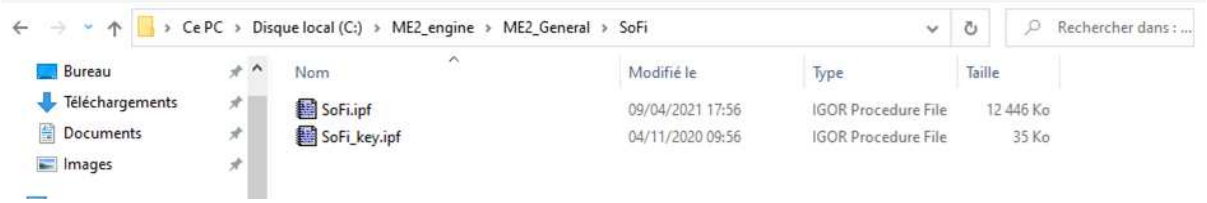

Figure 38: SoFi Pro installation

Step 5: Initialize SoFi

- Open a new IGOR experiment
- Double-click on the SoFi procedure file (SoFi.ipf)
- Click on "Compile" to compile the SoFi procedure

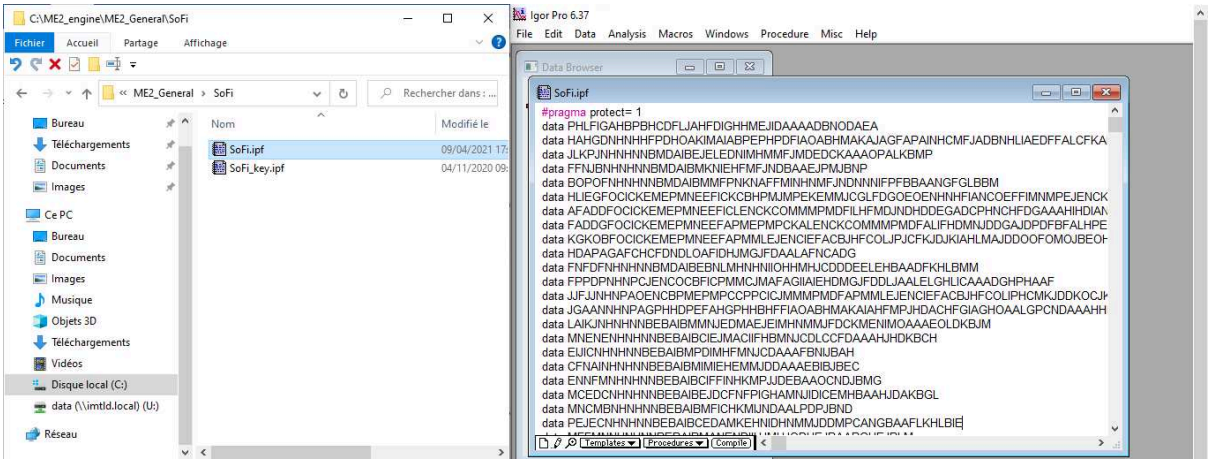

Figure 39: SoFi initialization

- Click on the new tab that appears in the IGOR main menu "SoFi" and "Initialize SoFi"

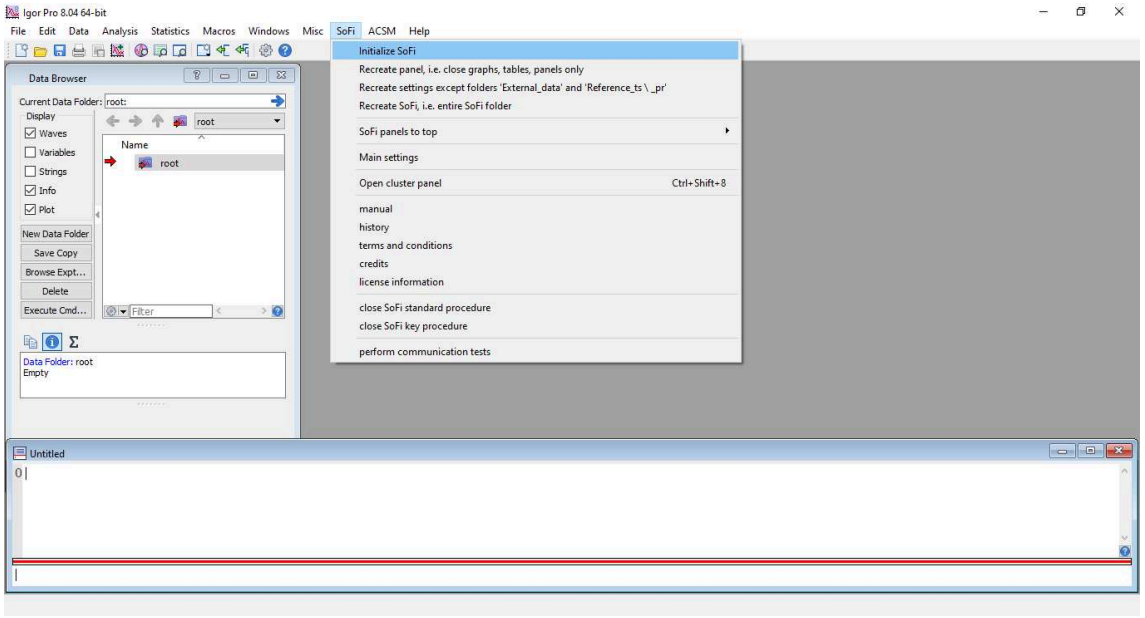

Figure 40: SoFi initialization

- Accept the terms and conditions
- Activate the SoFi Pro license (SoFi_key.ipf)

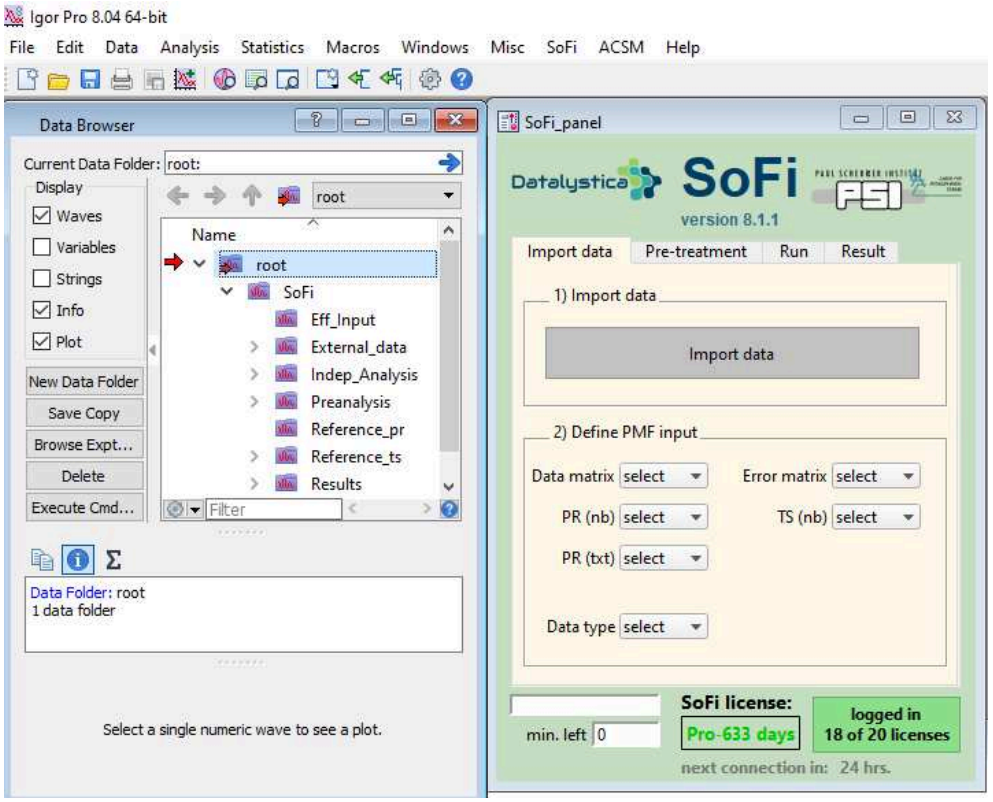

Figure 41: SoFi initialization

Step 6: Update each time the recent version of SoFi Pro

- Replace in the path C:/ME2_engine/ME2_General/SoFi the last version with the recent version of SoFi without changing the name (SoFi.ipf)

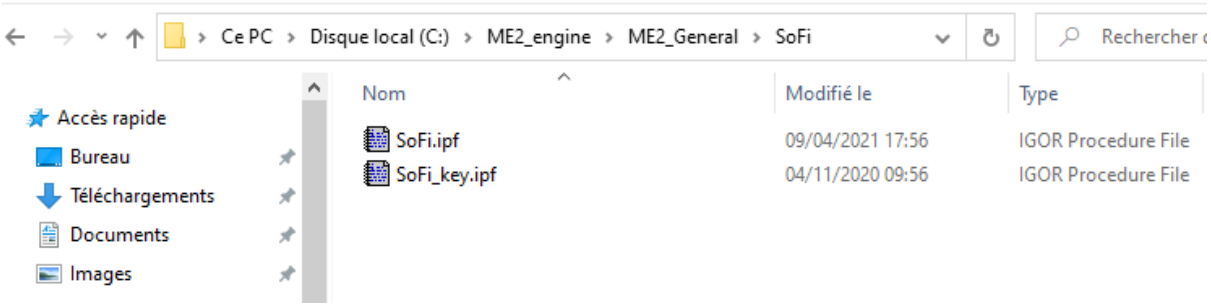

Figure 42: SoFi path

- Reopen the Igor experiment and check in the SoFi menu the downloaded version

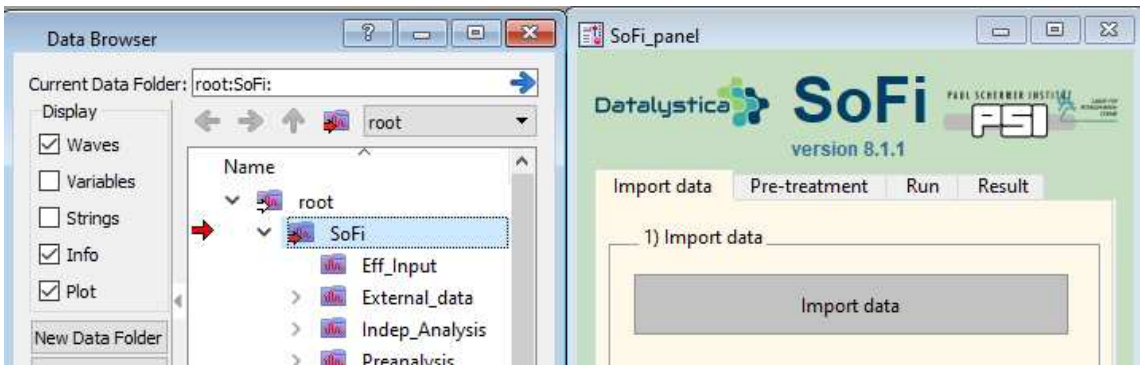

Figure 43: SoFi initialization

- **The folder structure in Data Browser**

Once SoFi is launched, the main folder SoFi appears (Figure 1, left panel), and each step completed in the SoFi panel goes to a folder in the Data browser (Figure 1, right panel). For example, everything imported in the "Import panel" in the SoFi panel is going to the "External data" folder in the Data browser.

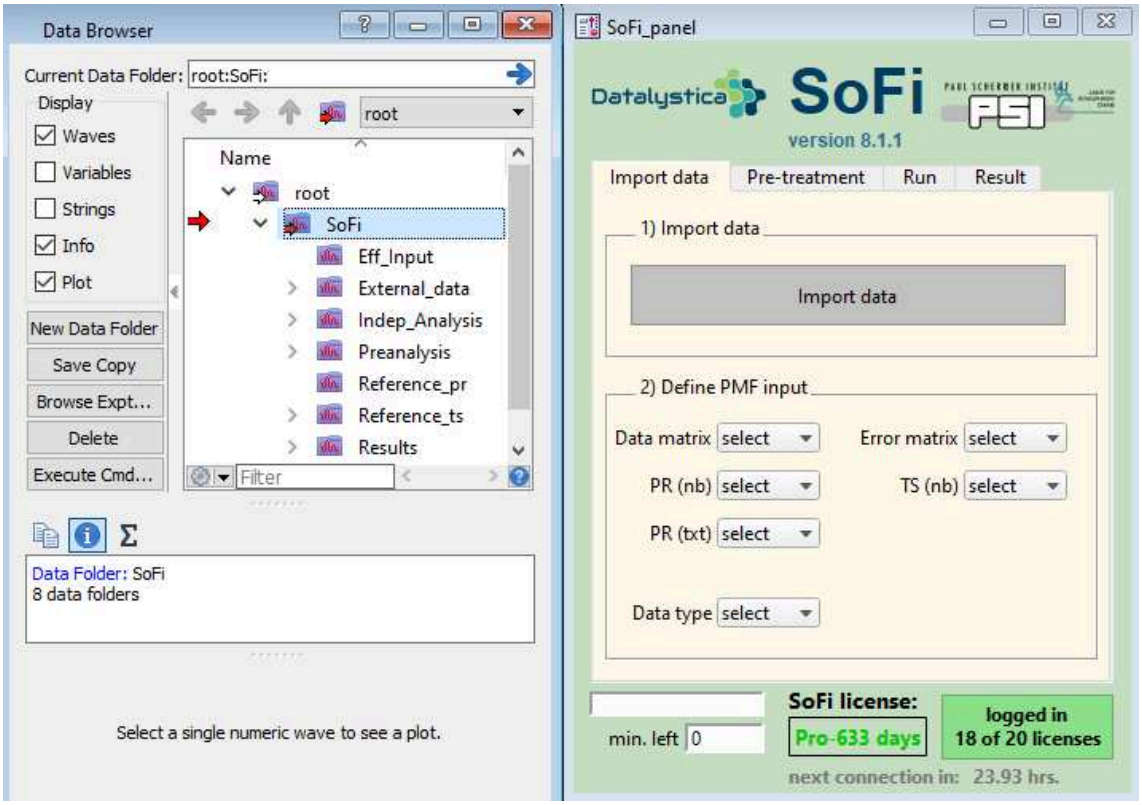

Figure 44: SoFi panel and Data Browser

Chapter 3: Steps to perform PMF on ACSM data using SoFi Pro

In this chapter, we detailed the steps to be followed in order to conduct a PMF analysis using ACSM data in SoFi Pro software.

I. Import data and Pretreatment

The first step is to import data to be analyzed in SoFi. The data can be imported in a different type of file (.xls, .csv, .dat, etc.) but this document will focus on IGOR text file (.itx) data, which is the most straightforward method. This step goes through 2 stages:

1) Import data

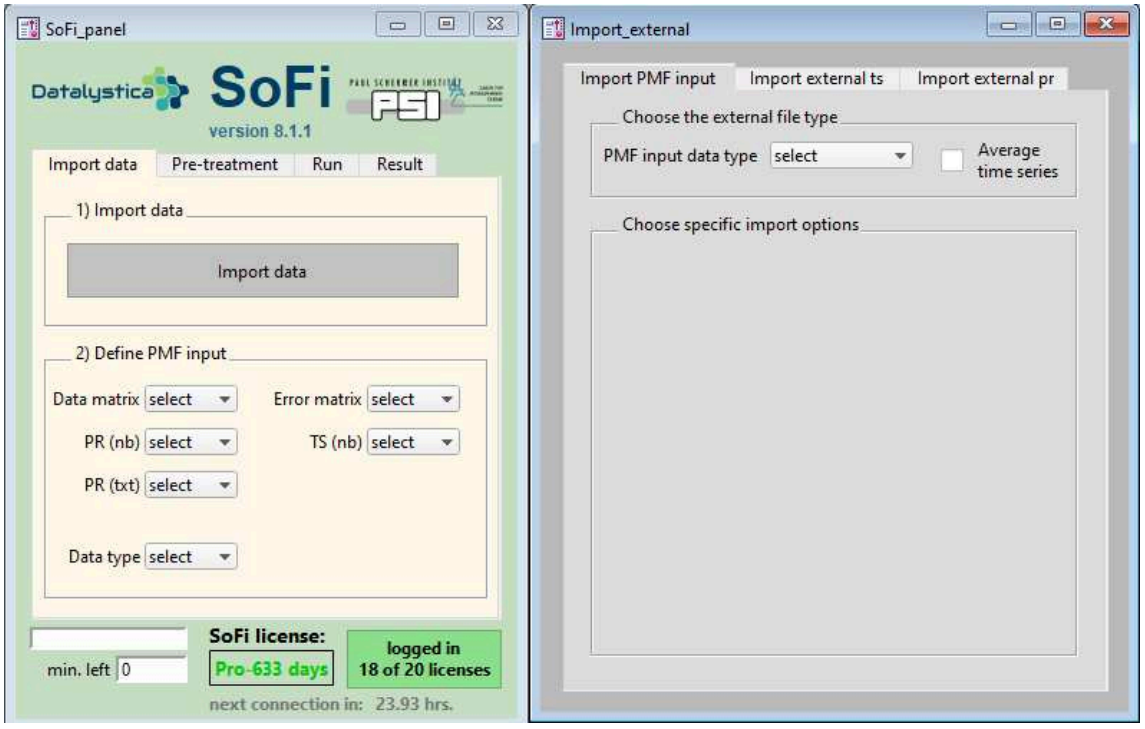

Figure 45: Import data

- PMF input

First, the user should import the PMF input, namely the corrected Organic and Error matrices, which will be defined at a later step. So, the user defines the type of file which is in this case ".itx". Then, the user chooses the path of the file and then imports the file containing the PMF input. The user can also define the PMF input unit which is by default µg m^{-3}.

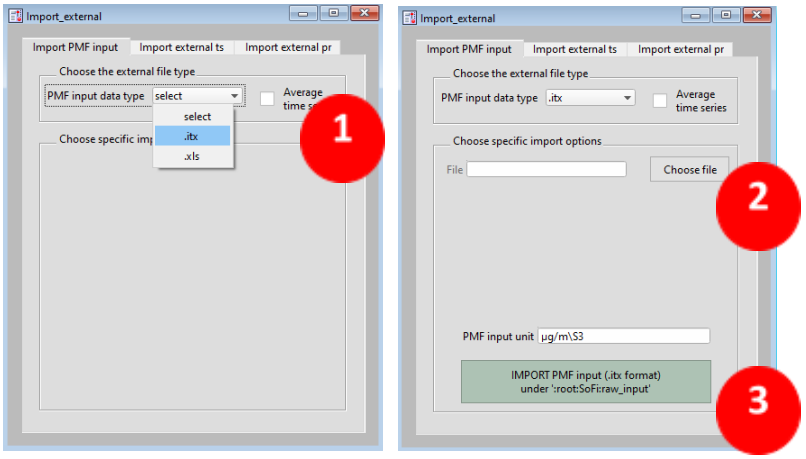

Figure 46: Import PMF input

CE correction

An important point is the correction of collection efficiency (CE). Unfortunately, the ACSM data analysis software does not apply CE correction prior to exporting to SoFi, so it needs to be done manually (in Igor or other software). In Igor, before running the PMF analysis in SoFi, the user should import the CDCE wave (time-dependent CE), then divide the Org and Error matrix by the CE (or CDCE) manually before running PMF. To do so, type this command:

•Make /O/N = (nb_lin,nb_col) Org_Specs_corrected=Org_Specs/CE for CE Or

Org_Specs _corrected[][]=Org_Specs [p][q]/CDCE[p] for CDCE

•Make /O/N = (nb_lin,nb_col) OrgSpecs_Err_corrected=OrgSpecs_Err/CE for CE Or OrgSpecs_Err_corrected[][]=OrgSpecs_Err [p][q]/CDCE[p] for CDCE

- External time series

It is possible to also import external time series; this step can be performed at the beginning or later. This typically encompasses any external data available in the site, i.e. inorganic species (SO_4, NO_3, NH_4, and Chl), $PM_{2.5}$ concentrations, Black Carbon data, NOx data, or meteorological data, in order to support PMF analysis. The file can be in any file format, and SoFi allows any format to be used. Thus, the user chooses the file format (.itx, .xls, .csv, .dat, .txt, or even AE33 data), then defines the file path, and then clicks on "Import files".

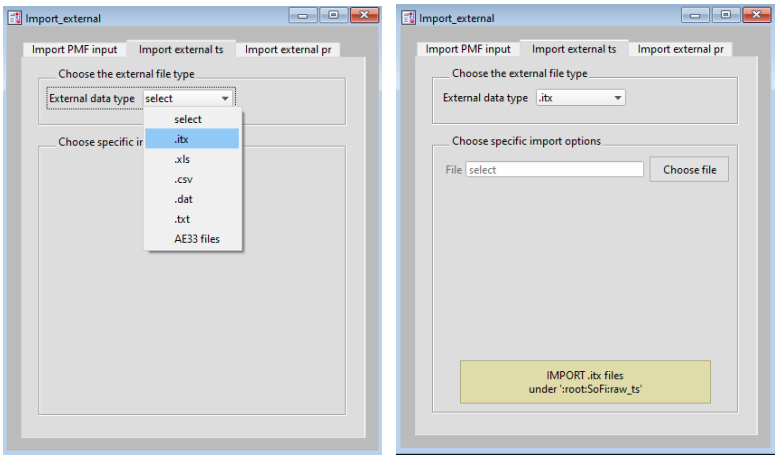

Figure 47: Import external time series

- External profiles

It can also be interesting to import external profiles, whether for comparison or for constraint. A database of external profiles is available at http://cires1.colorado.edu/jimenez-group/AMSsd/. Again, the user must select the type of file, then choose its path and click on "Import Files".

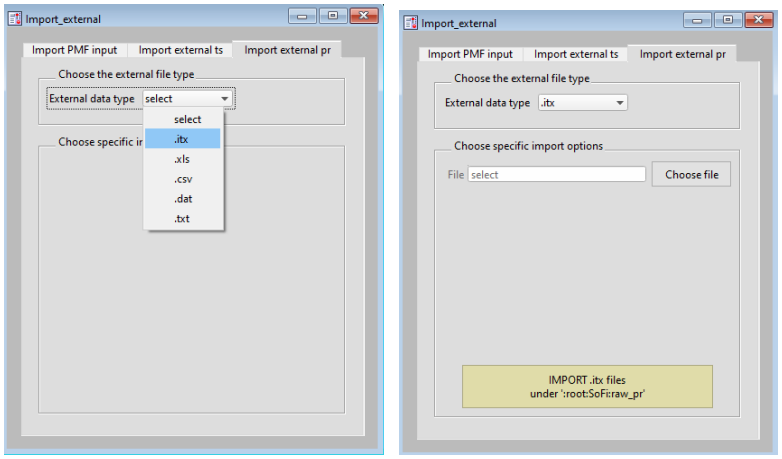

Figure 48: Import external profiles

The data imported are stored under path root: External_data in “Data_Browser”.

2) Define PMF input

After importing the data, now the user should define the input data:

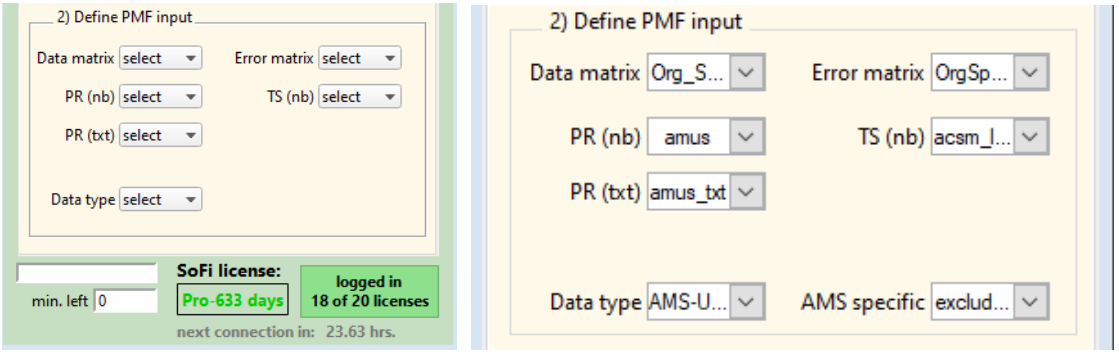

Figure 49: Define PMF input

- **Data matrix** is the Organic matrix (e.g., Org_Specs);
- **Error matrix** is the Error matrix (e.g., OrgSpecs_err), if the PMF input is imported from an excel file, SoFi can calculate the error matrix based on two different projects (Polissar et al. 1998) or (Norris et al. 2014);
- **PR (nb):** PR is the profiles (e.g., amus), they present the variables (i.e., the mass fragments for ACSM), here it is imported in numeric format. Then SoFi asks if the user has it in text wave, otherwise, SoFi will create it automatically;
- **PR (txt):** is the text information of the variables. This information is important for defining the labels of the graphs, especially in the case of HR-AMS data;
- **TS (nb):** TS is the time series of the data in local time (e.g., acsm_local_time);
- **Data type:** several options of data type (AMS-UMR/Q-ACSM, Tof-ACSM, HR-AMS, filter data, or other), this is basically where is defined in the case of Aerodyne instruments the fragmentation table, in this case, the user should select Q-ACSM;
- Then the **AMS specific** box appears and then the user has two options: “consider all variables” or “exclude CO2-related variables”. In fact, in Aerodyne instruments, some of the variables are related to CO2 (*m/z* 44) and are not directly measured, they are calculated in the fragmentation table from CO_2. So, if the user considers all variables, the *m/z* 44 is over-estimated. So, it is more interesting to select the option “exclude CO2-related variables”. Typically, they are excluded from PMF calculation but they will be re-inserted in the step of results.

3) Pre-treatment

Once the import of the data is finished, the user should move to the "Pre-treatment" tab to process the data and understand it. This section contains 4 important steps:

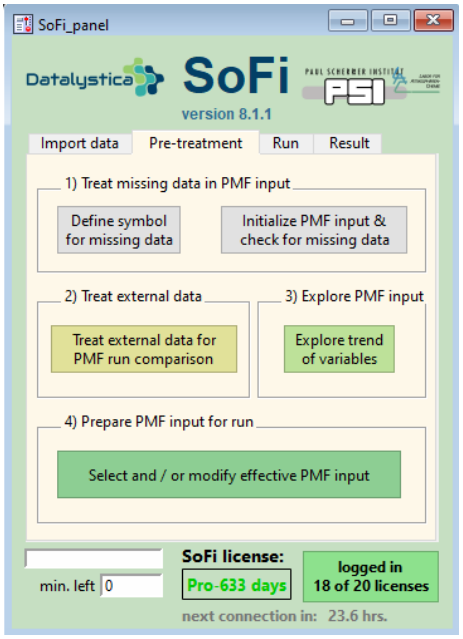

Figure 50: Pre-treatment section

a) Treat missing data in PMF input

First of all, the user needs to check for missing data and then initialize the PMF input. This step is therefore divided into two parts:

- **Define the symbol for missing data**

The user defines a symbol for missing data, this is what is inserted into the data matrix if there is no measurement for that point, and SoFi simply checks the entire rows and columns that don't have any information, in order to fill them with this symbol. In the case of Q-ACSM, the user uses **NaN** (or 0 for AMS data for example), then clicks on "Continue".

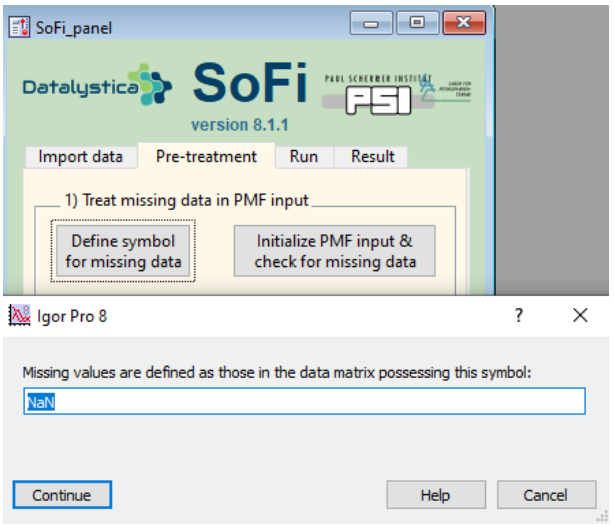

Figure 51: Treat missing data in PMF input

- **Initialize PMF input & check for missing data**

Once the missing data is defined, the user should pass to the second part and click on "initialize PMF input & check for missing data", so then the entire columns and rows are removed. When the initialization is finished, the PMF input will be under the "Eff_Input" folder in the Data Browser.

b) Treat external data

In the 2nd step, the user can initialize the external data in order to match them to the PMF input data. The external data must be at the same dimension as the PMF input. So, the user should click on "Treat external data for PMF run comparison". There are two options for the "External data" button:

- **Profiles**

The x-axis is the text information of the external profile (e.g., number_text) and SoFi will compare the text information of the PMF input (PR (text)) with that of the external profile and then the user selects the profiles, and click then on "Extract information" button. The external profiles will be placed under the "reference_pr" folder in the data browser panel.

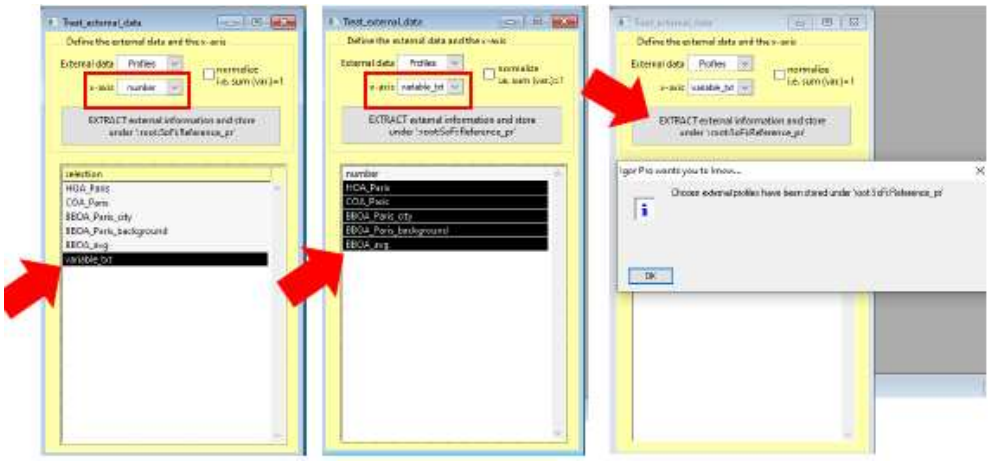

Figure 52: Treat external data

- **Time series**

For time series: the user selects the x-axis which is the time series of the external data, then selects the variables to be extracted, and then the option of extraction "type". The user can choose the type: "EXTRACT" if the external data has the same time points as the PMF input (e.g., ACSM species). "INTERPOLATE" option, if the time resolution of the external data is similar but not equal, to interpolate the rest of the points. And the "AVERAGE" option (save start, middle, or end time) if the time resolution of the external data is higher. The difference between 3 types of "Average" option is the data backup time: the Tof-ACSM, for example, creates the file with a timestamp at the beginning, then measures for the next 30 min and save it at the start time, however, the Q-ACSM measures and then save at the end. So, the user chooses the type of data and then can click on "REGRID the data information" in order to be

saved under the "reference_ts" folder. This part will generate graphs for this data with different resolutions to get an idea of the distribution of those external data.

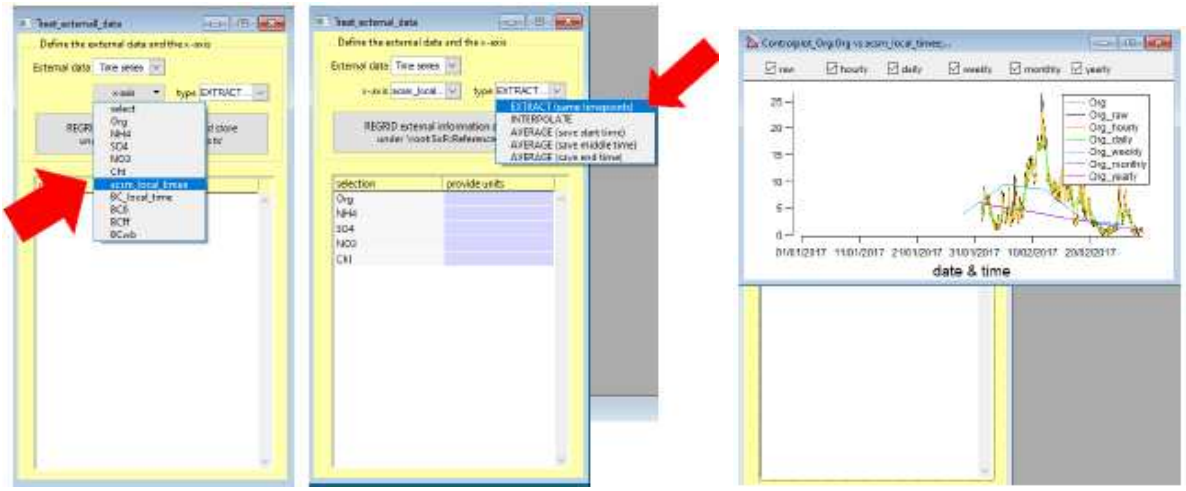

Figure 53: Extraction of external time series information

c) Explore PMF input

After initializing the input data and before running PMF, it is important to explore the data to better understand it and have a preliminary idea about its main sources. So, the user should click on "Explore trend of variables". This part allows having some interesting information about the data. This could be done by checking for example the diurnal variation of the main masses (i.e., *m/z* 43, 44, 55, 57, 60, 73), comparing with the external data (e.g., making correlations), or looking at the *f44/43* space in fractions if there are any particular trends or outliers. It is also possible to add both mz data and external data to compare a specific mz with a source tracer (mz 60 vs BC_{wb} as example). There are different options for fitting and graph representation in this panel as mentioned in the figure below.

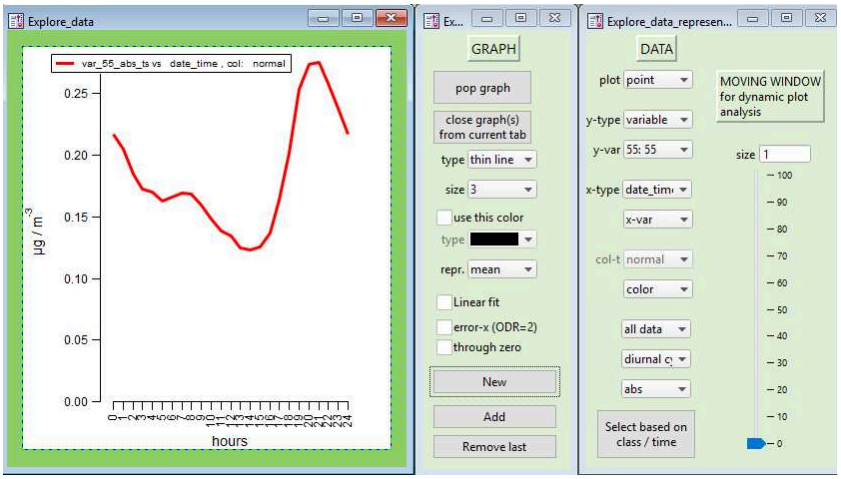

Figure 54: Explore PMF input data; an example of the daily profile of *m/z* 55

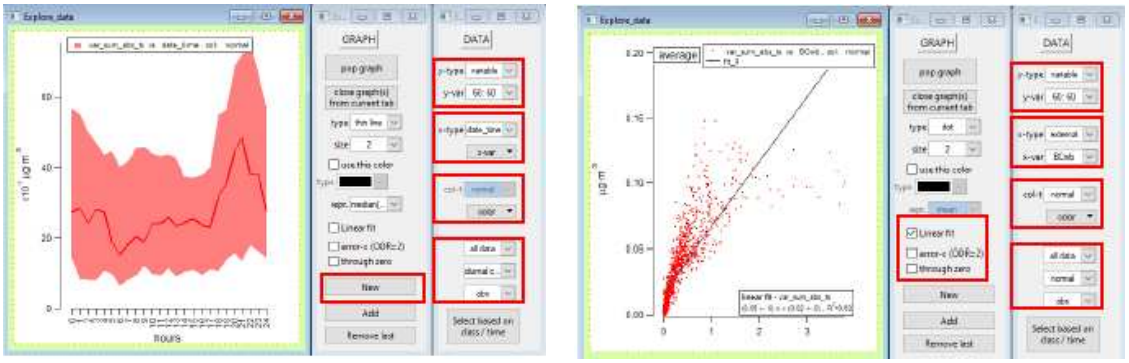

Figure 55: Examples to xplore PMF input data

d) Prepare PMF input for the run

In this step, the user can select and/or modify the effective PMF input. In this panel, the user has options to blacklist certain items and select what the PMF should be, in terms of profiles and time series.

- **Profiles**

In the input of the profile, the user can check the mass spectra of profiles (i.e. negative masses, number of variables). Thus, in the right panel, the user can select the variables he wants to keep for the PMF, so the unwanted variables are deselected, then the user clicks on "APPLY SELECTION" to blacklist them. For example, the m/z 12 is removed in many cases because of its negative signal.

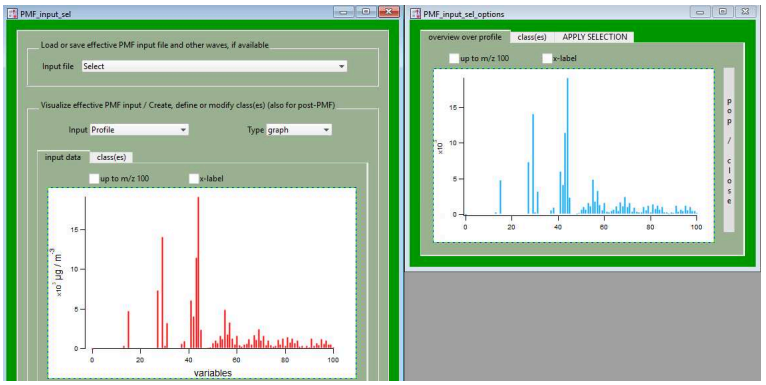

Figure 56: Input data selection

There is also an option to create and add classes by clicking on the “class(es)” panel. The user can create or add classes as additional metrics. It is useful, especially in the case of having 2 types of data, so it is possible to separate them by using classes.

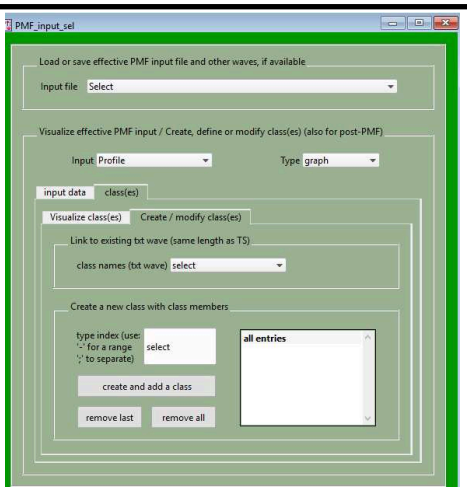

Figure 57: PMF input panel to control user-specified PMF

- **Time series**

The same for "time series" input. The user can select the period to be analyzed using the "PMF_input_sel_options" panel. This can be done by checking the months (or days, hours, years) in the "time-selection" tab or by making the selection in the "overview over time" tab. Then, the user can blacklist the unselected part by clicking on the "APPLY SELECTION" tab. For example, the user can make a selection based on different seasons in order to perform the seasonal PMF.

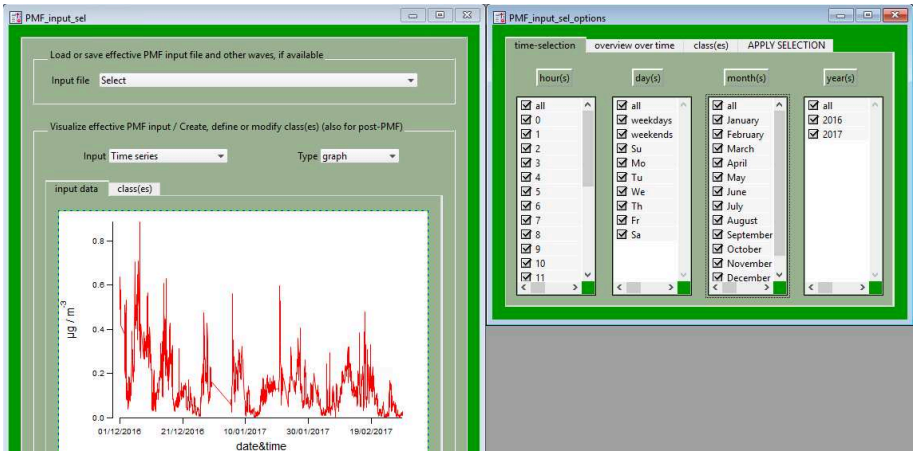

Figure 58: PMF input panel to prepare for running

The user also can create and add classes (e.g. create separate classes of offline data by automatically selecting their files, or do it in index time by creating a class from index p to q).

II. Run the PMF "Unconstrained PMF"

After defining the input data (variables and time series), the user can move to the 3rd tab to run PMF and define its several settings.

First, the user can start with unconstrained PMF in order to identify the number of possible sources of organic aerosols (OA) for the studied site.

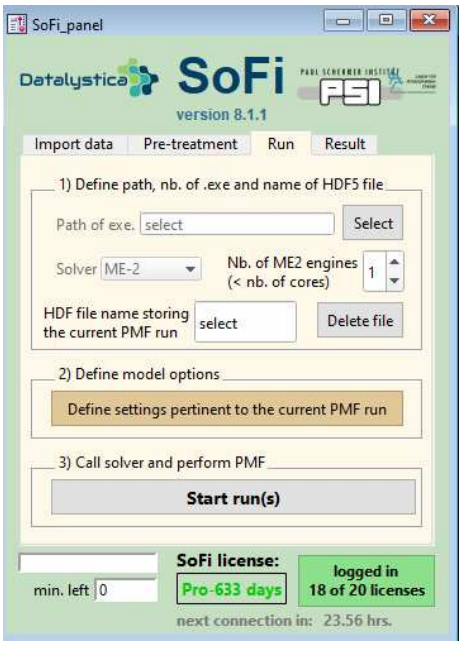

Figure 59: PMF run tab

1) Define the path and name of the HDF5 file

First of all, the user should define the path of the ME2_engine file by clicking on the "Folder of executable" button and selecting the file, and then define the name of the HDF file by writing the name on the box and clicking on "Enter". Once the HDF file is created, all results will be stored in this HDF file.

Next, the user selects the number of cores that should be used to run PMF. This number must be less than the number of cores in the computer. In SoFi Pro, it is possible to use all the cores, but it is better to not select all the cores because it can block other computer operations (e.g., if there are 4 cores in the computer then the user should put 3 for the number of executables for running PMF).

Next, you need to define the name of your results file in the "HDF file name storing the current PMF run" section. Be careful: give it a specific, unique name, because if you use the same name as an existing file, you won't get an error message, but the new results will overwrite it. Also pay attention to the length of the name, as you may get an error message (max 15 characters).

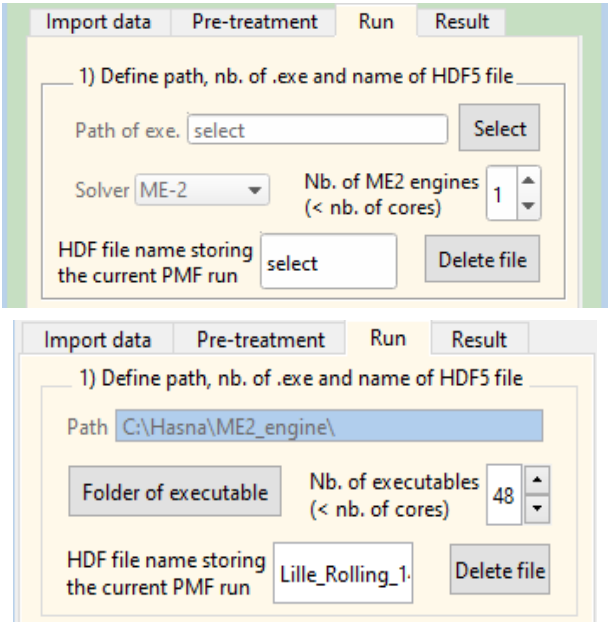

Figure 60: Define Path and HDF file

2) Define model options

After defining the HDF file for the PMF results, the user should define many settings for the PMF model. This part is considered one of the important parts of the PMF analysis. It contains 4 panels: the first one contains general parameters and the others depend on the analysis that the user wants to perform (unconstrained PMF, constrained PMF, Bootstrap analysis, or Rolling PMF). Rolling PMF for example requires going through all these steps by defining the number of factors in the first panel, applying constraints in the second panel, using the bootstrap in the third panel, and defining the parameters of rolling PMF in the last panel.

So, for the unconstrained PMF, the user should define the general settings for the PMF analysis:

- **GENERAL settings**

In this part, the user should define general information to run PMF.

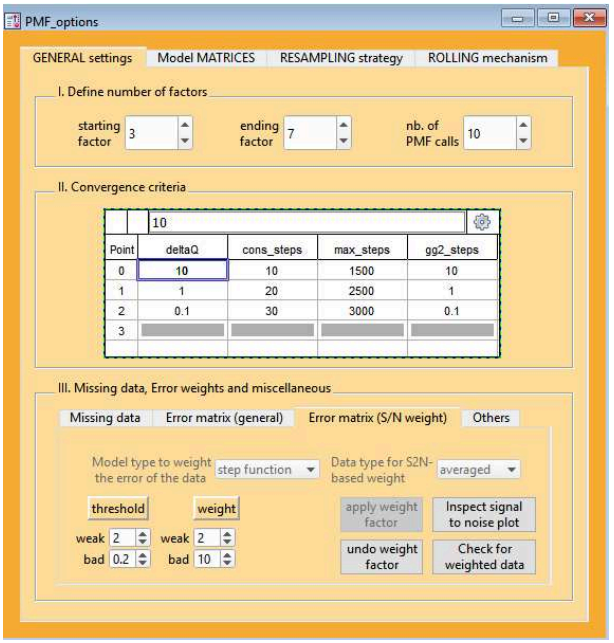

Figure 61: PMF settings, tab General settings

✔ Define the number of factors

First, the user should define the number of factors by specifying the number of factors to start with and the number of factors to end with, as well as the number of PMF calls that present the number of iterations. For example, starting factor with **3 factors**, and the ending factor with **8 factors** with **10 nb. of PMF calls for a first unconstrained PMF**.

In general, the choice of the number of factors depends on the number of possible sources for the site.

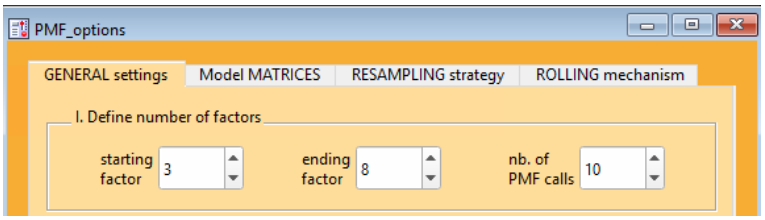

Figure 62: Define the number of factors

✔ Convergence criteria

This part of the convergence criteria is important to control the quality of the fit during the PMF. It is necessary to achieve convergence. Typically, **the user doesn't have to change it.**

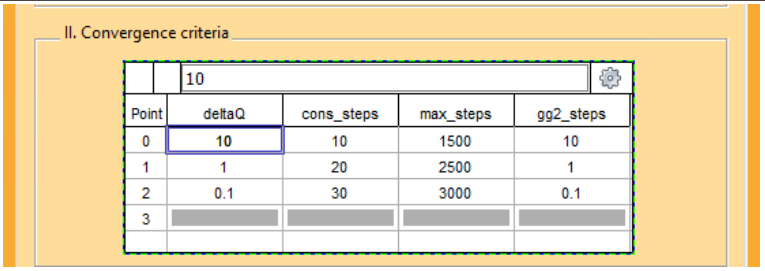

Figure 63: Convergence criteria

✔ Miscellaneous setting

This part defines many settings about missing data, error matrix, and others.

- Missing data

This part contains other missing data parameters, especially for empty single cells. **The user doesn't change anything in this part.** The "Define values for matrix cells containing no data" button allows to define the missing values, in this case, they are NaNs, all these NaNs will be replaced with a certain value, in this case, the value is -100, and the corresponding errors will be replaced with the highest error.

In the second stage, a threshold value (e.g. -99) means that everything smaller than -99 should not be considered, that's why the missing cells or the cells that have no data are replaced with a value lower than -99.

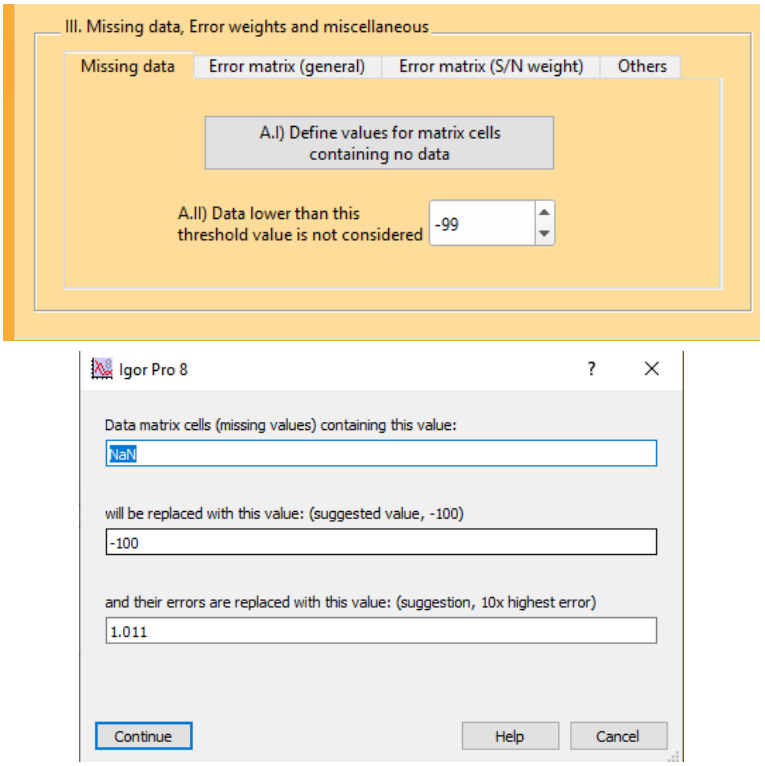

Figure 64: Missing data tab

- Error matrix (general)

This part corresponds to the C-values approach. In many cases, **this option is disabled**. The user can enable it in case of having data from different instruments, then it is necessary to make sure that the error from both instruments is rescaled to achieve an effective PMF. In other words, this option is enabled in the case of applying a combined PMF with two different types of data.

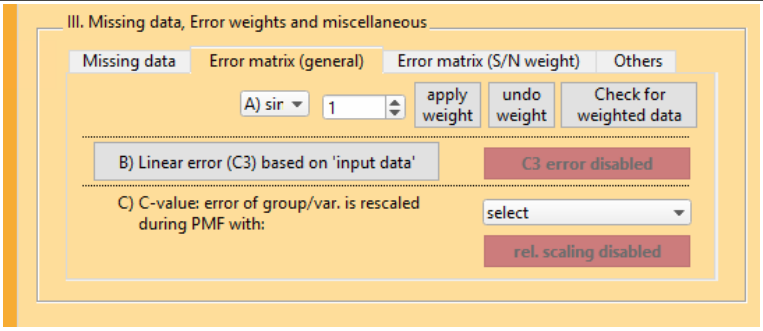

Figure 65: Error matrix (general) tab

- Error matrix (weight)

In this part, the user can downweight some variables/masses *m/z*. So, first, the user should select the "model type to weight the error of the data" and "Data type for S2N-based weight". There are 2 different options of model type: "step function" and "1/S2N function". It is recommended to choose the **"step function"**, in order to define the threshold and the weight for weak and bad values, and then choose the **"average"** option for the data type for the S2N box (Figure 16).

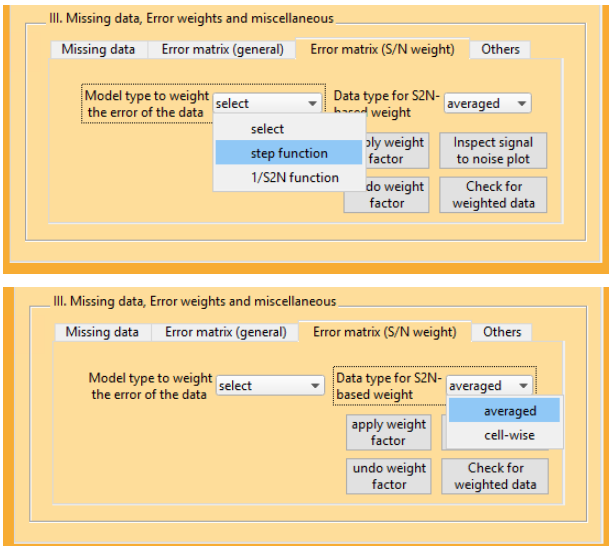

Figure 66: Error matrix (weight) tab

The weak and bad variables are defined through the recommendations of (Paatero et Hopke 2003) and (Ulbrich et al. 2009); i.e. weak variables with a signal-to-noise ratio 0.2 <(S/N) <2 increased by a factor of 2, and bad variables with (S/N) <0.2 increased by a factor of 10.

So, the user can change the S2N ratio, for the variables whose S2N is lower, the weighting is reduced by a factor of 2, if the S2N is lower than 0.2, the variable is considered as bad and its weighting is reduced by a factor of 10 (Figure 17).

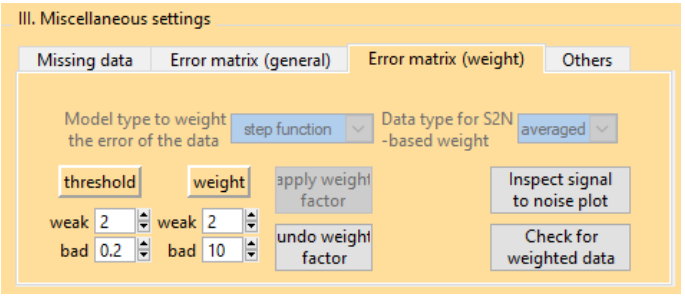

Figure 67: main settings for error matrix, CO2-related buttons

The user can then check the graph of S2N where the average of the S2N ratio for each variable is presented, with weak variables in green and bad variables in black (Figure 18).

Then, the user clicks on the "**apply weight factor**" box and checks the graph of weighted data (e.g. Figures 17 and 18).

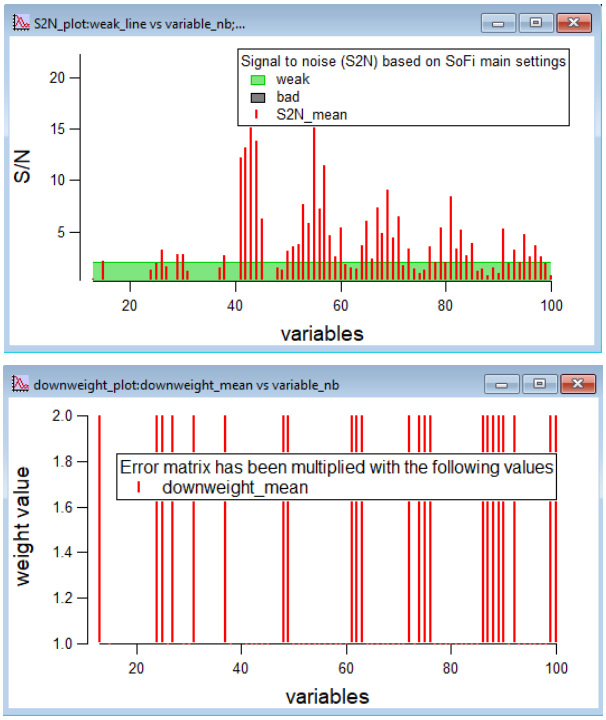

Figure 68: S2N and weighted errors for the averaged data

- Others

This part contains 4 other settings to make. **Some options are generally not changed**.

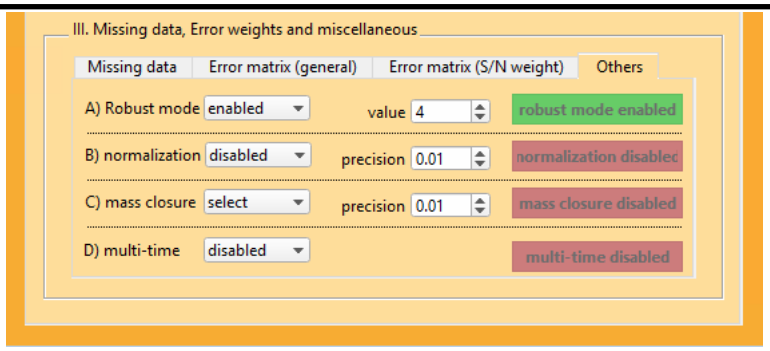

Figure 69: Others settings tab

- Robust mode

Robust mode is always enabled. The PMF method runs in robust mode to prevent the PMF from drifting due to outliers; this means that large outliers are simply re-sequenced from value 4.

The next three parameters are disabled in many cases.

- Normalization

This option allows normalization during the PMF. In the default case of SoFi, this normalization is disabled; this means that there is no normalization equation during PMF because typically SoFi is used to constrain profiles using a-value. In the case of using a pulling equation to constraining factors, this normalization should be enabled over factors, and the value 0.01 is considered the weight of the pulling equation.

- Mass closure

This option allows adjusting the sum of all factor contributions to a certain mass (PM_1, $PM_{2.5}$, …). This mass closure is also related to the pulling equation and normalization.

- Multi-time

This option is enabled when combining data from different instruments with different time resolutions (see an example at the end for the use of this option).

3) Call ME2 and perform PMF

After defining all the major settings, the user can run the PMF by clicking on **"Start run(s)"**. At the end of the PMF running, if the user obtains the message below in the console (the figure below), it means that the model is finished and the PMF runs are completed. Then the user can open the result folder and import the PMF results from the HDF file.

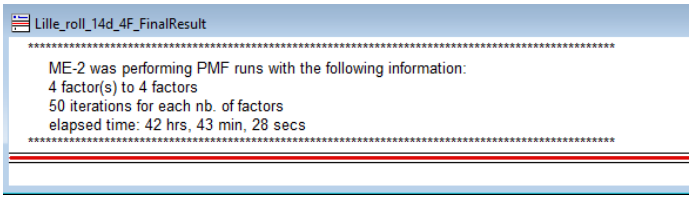

Figure 70: PMF execution

4) PMF results

The objective of this step is to select and analyze the main results obtained.

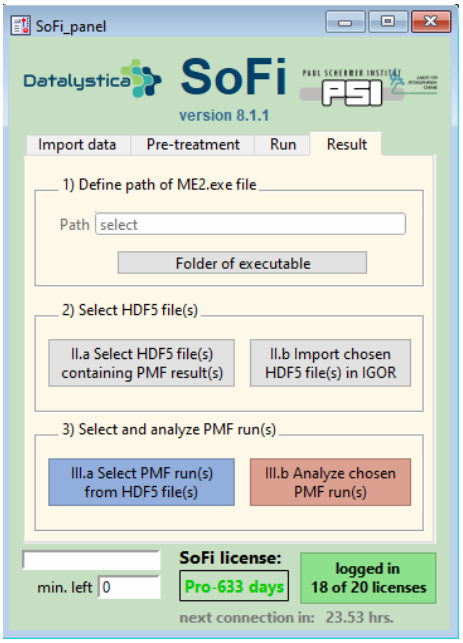

Figure 71: Result panel

a) Define the path of the ME2.exe file

First, the user should define the path of the ME2 folder (where ME2.exe resides). This is the same path defined in the previous step of the section of run PMF.

b) Select HDF5 file

Next, the selection of the HDF file contains the results. When the user clicks on the button "select HDF5 file", he will find a list of all the HDF files that exist in the folder. Then he can just select the one he needs (or use ctrl or shift to select multiple ones) and then close the box by clicking on its button again. Then, click on the "Import chosen HDF5 file into IGOR" button to import the HDF file, this takes some time depending on the amount of data.

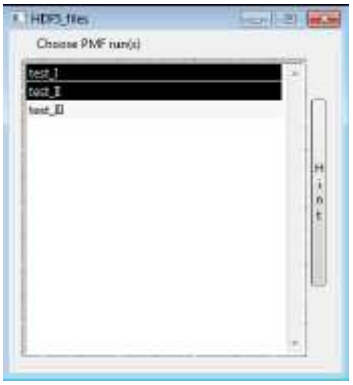

Figure 72: list of HDF5 files to be chosen for the PMF analysis

c) Select and analyze PMF run

Then, the user selects the results to be analyzed. This part consists of two important steps:

o Select PMF run(s) from HDF5 file(s)

There are 2 options: the choice based on “manual” or on “automated selection” which leads to the criteria based-selection. Automated selection is important especially to select the best runs and differentiate between unconstrained factors and have the same position for each factor, and also for computing the average solution.

- Manual selection of PMF runs

For a simple PMF run, the “**manual selection**” is the most option used for unconstrained PMF with “**no average**” for the PMF runs. Then, the user should select the HDF file and see in the graph below the sticks that show the PMF runs (Figure 22). Then he can select with a marquee the runs to analyze in detail. In this step, it would be better to select all PMF runs to check all possibilities of PMF results.

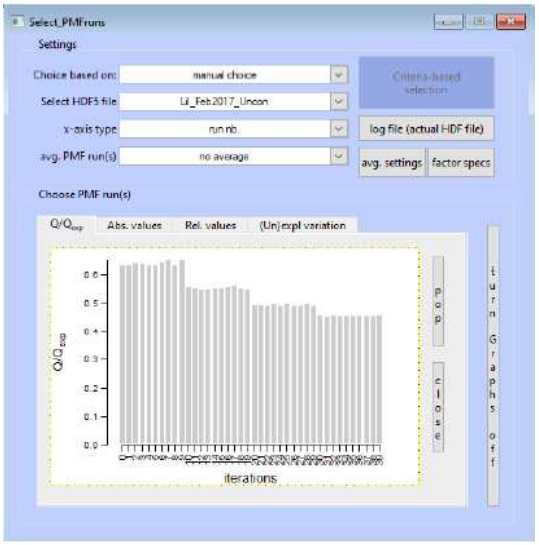

Figure 73: selecting some solutions from the HDF file

The Q/Q_{exp} decreases with the number of factors. The slopes of this graph (The deviations between the different numbers of factors) allow for identifying the possible number of PMF factors for this site.

For the x-axis, there are many options (nb. of factors, nb. of runs, …). In the box of graphs, there are 4 types: the overview of Q/Q_{exp} values, graphs about factors in absolute and relative terms, and the unexplained variation (this one normally should be less than 25%).

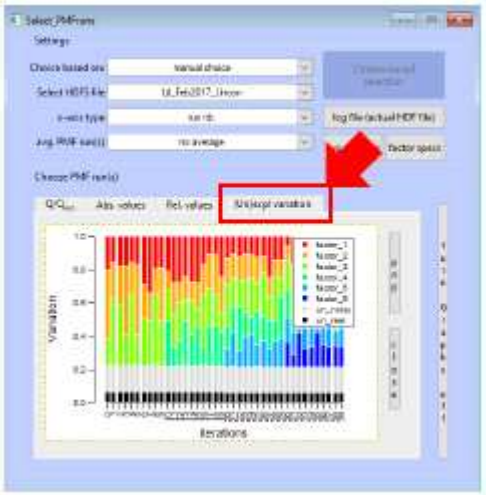

Figure 74: Graph of unexplained variation

There are other boxes:
***Log file (actual HDF file)** where it is indicated what has been chosen; it is a file that resumes the settings of the experiment.
***Avg. settings** to choose the type of resolution and which data should be imported.
***Factor specs** to define the names of the factors (e.g. HOA, BBOA, OOA1, OOA2…), or add factors like the sum of OOA1 and OOA2.

- Analyze chosen PMF run(s)

Once the selection of PMF runs is done, the user should click on "**Analyze the chosen PMF runs"** in the red box, and wait for the analysis to finish. Then, the user can check the results.

- General information

In the first panel, there is some general information about the experiment. On the left, is a list of the PMF runs that present all the sticks highlighted before, whether from one HDF file or more. On the right, is some average information. And below is the "log file" for the selected runs. And then the "swap factor position" to change the positions of the factors but this is applied only for the experiment Igor not for the HDF file.

Figure 75: General information tab

After selecting the runs, the user can proceed to check the different plots to get an overview of the total PMF runs. Here, for these unconstrained PMF results, the user should check each run to identify the main organic aerosol factors for the site.

- Overview plots

In this panel, the user can check the time series and mass spectra plots of the PMF results.

First, the user can start by checking the profiles, looking at the *m/z* of each factor, and checking their contribution, to know how much each variable contributes to each factor. The graph below shows the case of the 4 factors. 2 first factors are primary OA (HOA - Hydrocarbon-like Organic Aerosol, BBOA - Biomass Burning Organic Aerosol), and 2 last ones are secondary oxygenated OA with the important contribution of *m/z* 43 and 44. The HOA factor is characterized by peaks corresponding to aliphatic hydrocarbons (*m/z* 27, 41, 43, 55, 57, 69, 71, etc.), mainly related to road traffic, and the BBOA factor is characterized by anhydrous sugar fragments such as levoglucosan (*m/z* 29, 60, 73). BBOA is strongly influenced by wood type, burning conditions, etc., and thus is more variable from site to site.

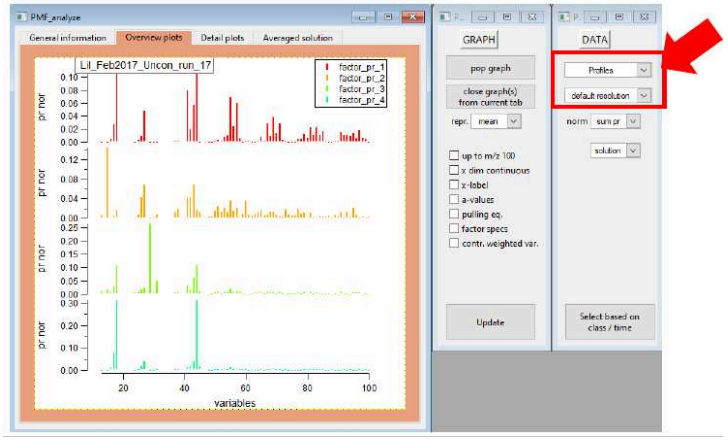

Figure 76: Overview plots tab

Then the user can select the time series in the default resolution, and look at the solution in the normal time resolution to plot the time series of the factors. The user should check as well the diurnal cycle of the factors, as the residuals (abs, scaled, Q_res ...). It is possible also to do a selection for some months, weekends to have an overview, or for certain periods to see special things.

The primary OA factors have a pronounced diurnal pattern. HOA is characterized by two peaks in the morning and evening linked to traffic hours, and BBOA is characterized by a strong peak at night corresponding to residential heating in cold periods. However, the oxygenated oxidized OA (OOA) factors have a flat daily cycle.

Regarding the residuals, the daily cycle structure of the scaled residuals could indicate missing or poorly separated sources. In addition, some peaks in the time series of this residual still require attention, suggesting high uncertainties for these points or instrumentation issues.

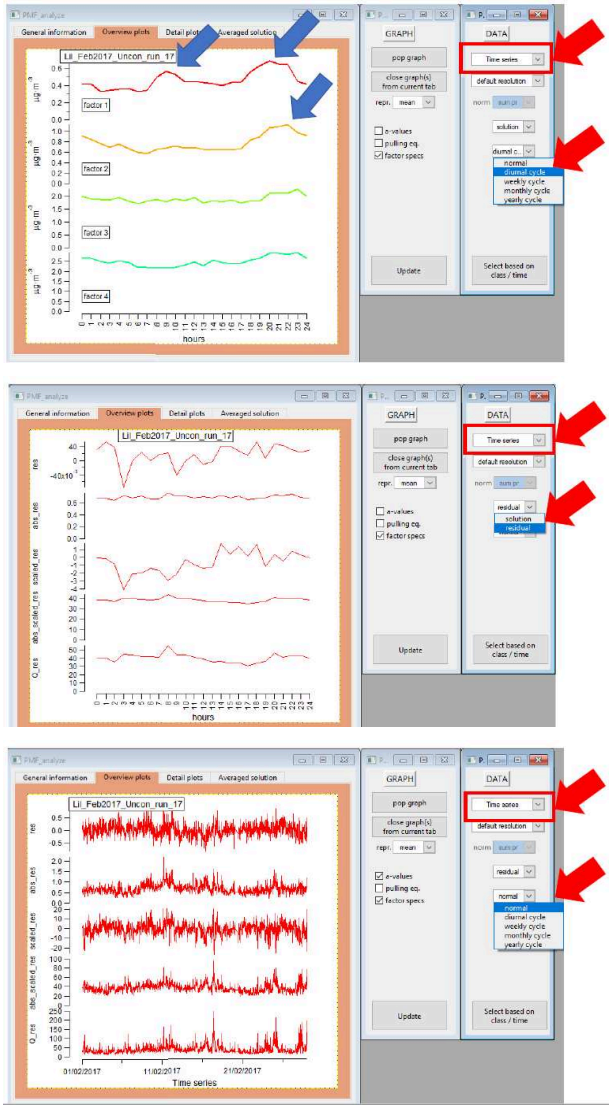

Figure 77: Different plots to make in the overview panel

- Detail plots

In the detail plots panel, there are different sets and graphs: “Fraction”, “Standard”, “Scatter”, “Residuals” and “Correlation”. These plots provide more information about the PMF factors, e.g., their contribution, their correlation with external variables, etc.

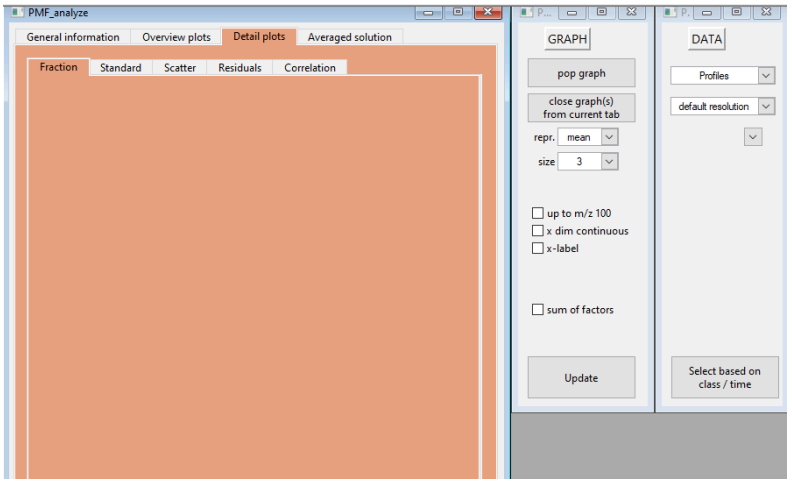

Figure 78: Detail plots tab

***In the fraction panel,** it is possible to plot a pie chart of contribution, of explained variation, and also the pie chart of concentration. These graphs show the contribution of each OA factor and each variable. SoFi allows as well to include the contribution of ACSM species. It is also possible to plot a bar graph of contribution. The graph of the explained variation presents the unexplained noisy part (the grey part) related to the noisy data, and the unexplained real part corresponds to what the model was not able to reproduce during this test.

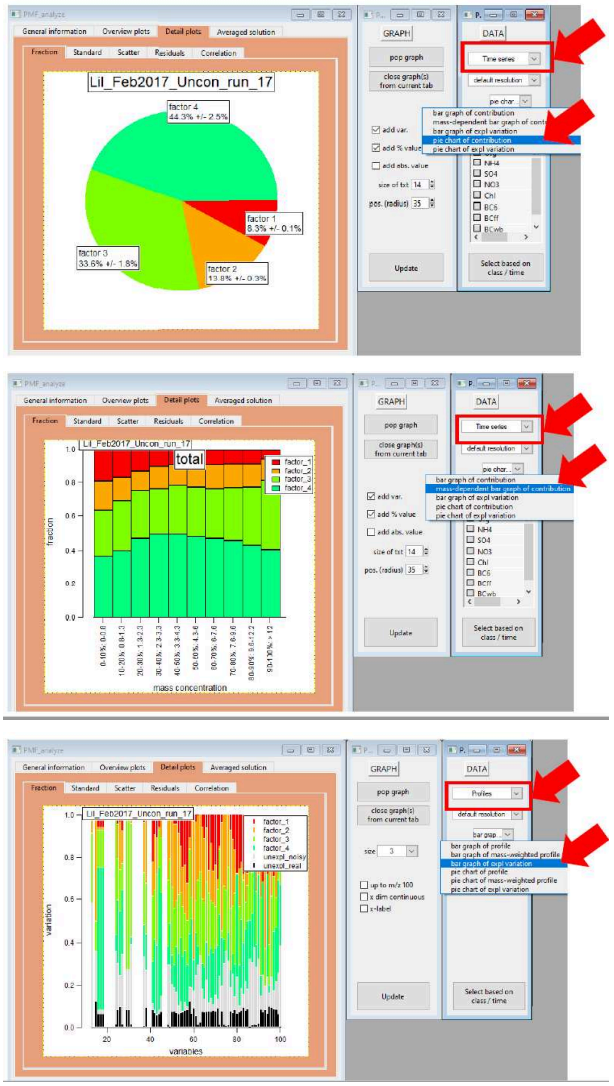

Figure 79: Different plots to make in Detail plots panel; Fraction tab

***In the standard panel,** the user can plot different graphs for profiles and times series. In this panel, there are more options than in the panel before, i.e. plot solution, residuals, the time series of the factors, and the external data. It is also possible to look at the variation of each variable of the solution.

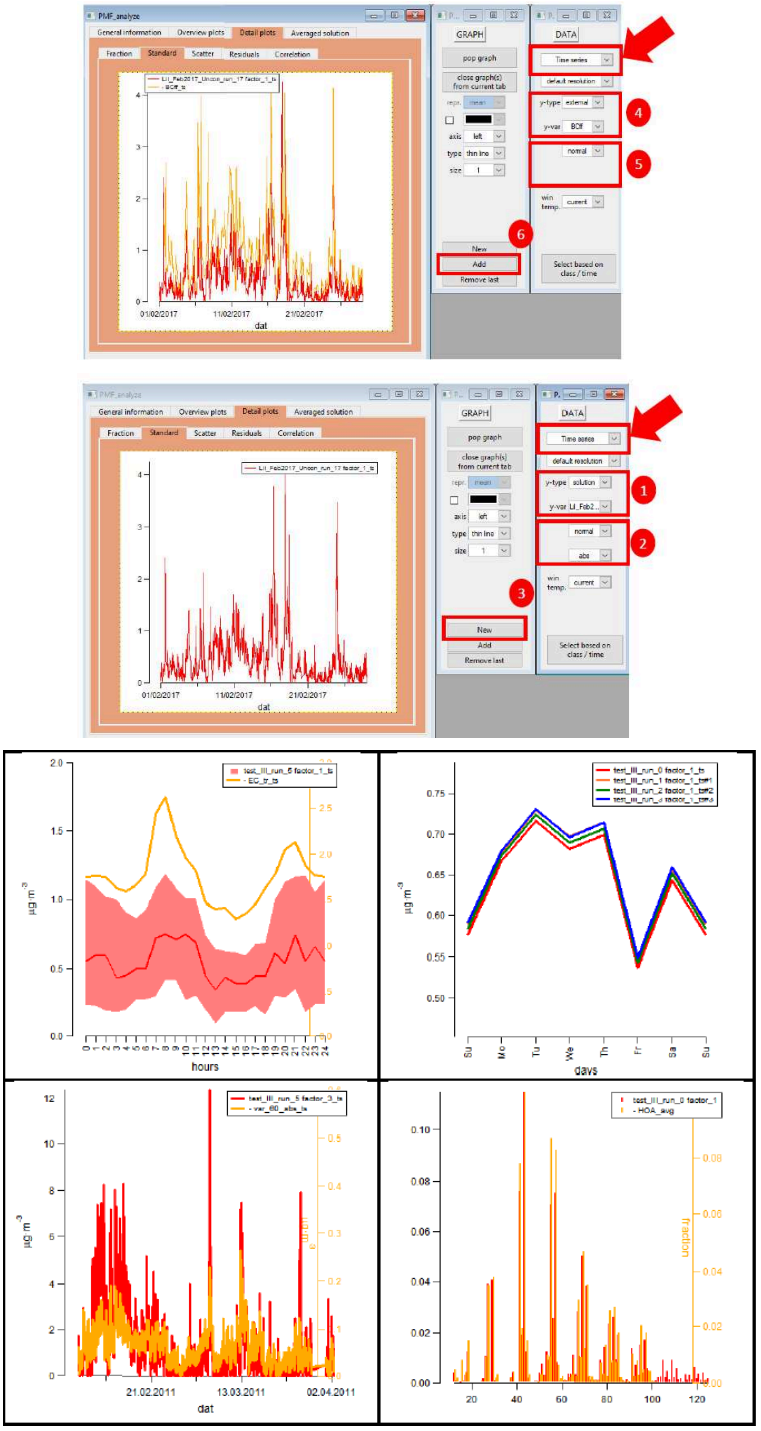

Figure 80: Different plots to make in Detail plots panel; Standard tab

***Then scatter plot panel**, for additional options. The "scatter" tab allows to represent information in the form of a scatter plot and to color-code it according to other information over time or on over variables. e.g. plot the scatter plot of factors with the external data.

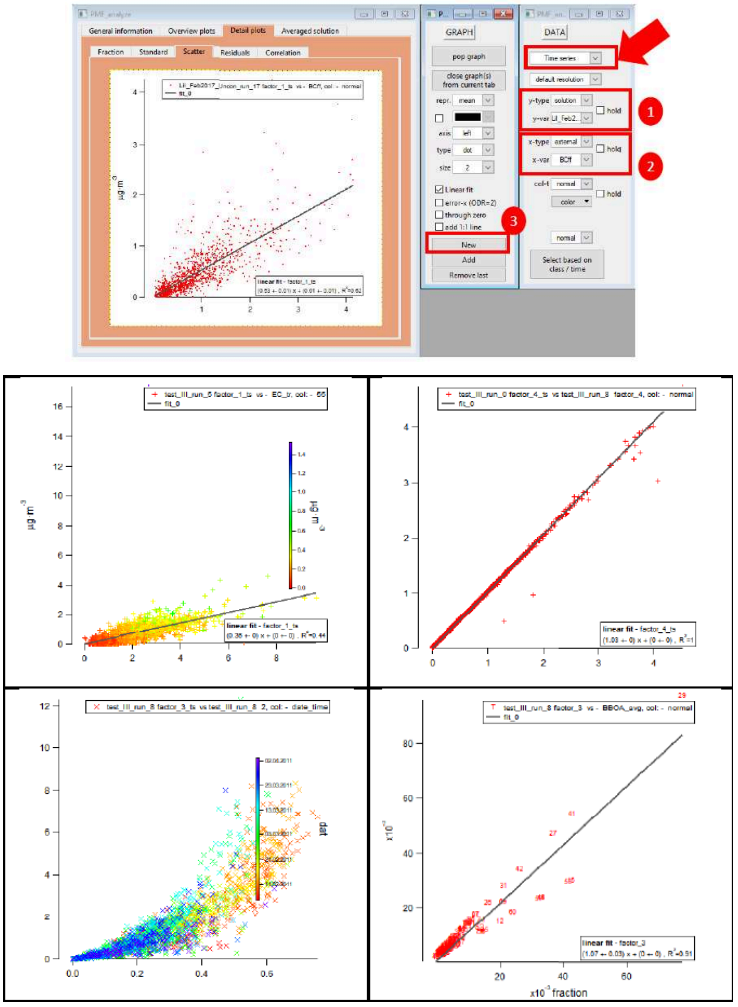

Figure 81: Some possible graphs from the "scatter" tab

This tab is also important to look into the *f44/43* space. To do so, the user should choose "model subtraction" for the x-type and the y-type in fraction terms, and select the secondary factors for example to subtract the primary factors, colored by date, and then see the difference between the two OOA in *f44/43* plot.

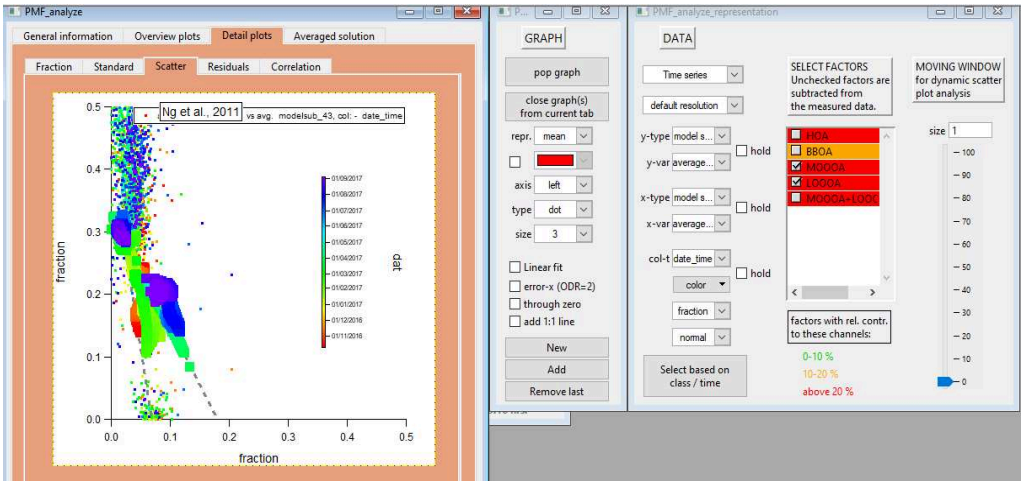

Figure 82: Outcome of the model subtraction option for f44 vs f43

*Then some more information about **residuals** in **the residuals panel**, where the user can look over the entire matrix or histograms, and choose the residual type (for example the entire matrix of scaled residuals). The user can also check the residuals for each variable at each timepoint, and present it as a histogram to see the distribution of the residuals and to detect any problem in the data.

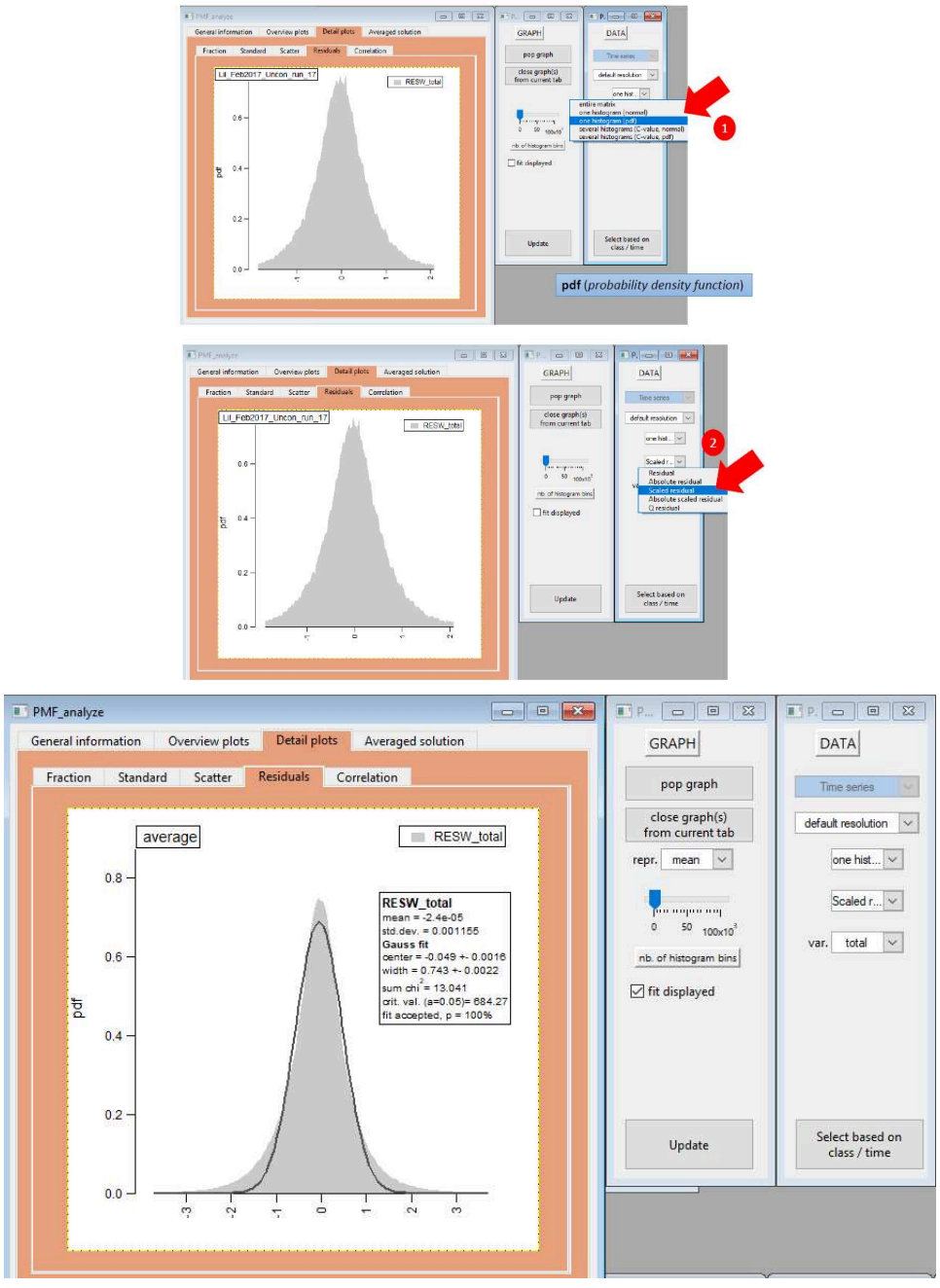

Figure 83: Scaled residuals histogram

*Then in **the correlation panel**, the user can check the correlation (matrix or table) between factor time series (or factor profiles) with external data. It is possible to plot the R or P values in table or image format, and the type of correlation. The user obtains this correlation by checking in the x-list and y_list and then displaying it, as shown in the figures below.

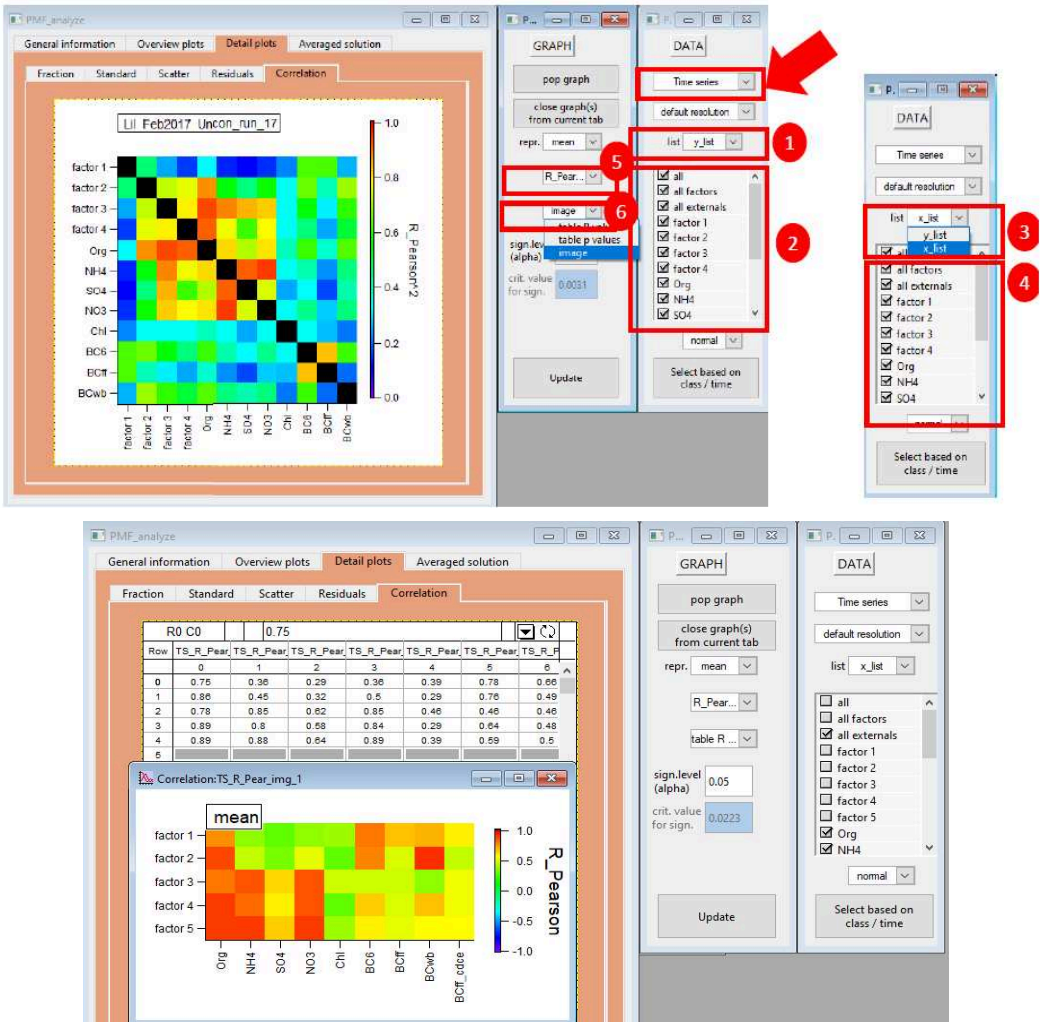

Figure 84: Correlation tab; correlation image plot and correlation table

To summarize the "unconstrained PMF":

For the unconstrained PMF, the user should run from 3 to 8 factors to test all the possibilities, check the daily profiles of factors, the correlation with the external data available, etc. in order to determine the number of possible factors/sources. If the factors identified are not proper, then the user can proceed to the "constrained PMF" presented in the next section.

III. Run the "constrained PMF"

To start another PMF, the user should create a new HDF file as shown in the previous section, and save the experiment. To define constraints, the user should click on the "Model Matrices" panel.

- **Model MATRICES**

In this part, the user can perform the constrained PMF where it is possible to constrain factors or time series. This paragraph is concise in the case of constrained factors.

3 options of constraints can be applied: **fpeak, a-value, and pulling equations**. "**seed"** option is for defining the reference profiles or time series. It means the starting value, from which it should start running PMF, and based on those starting values, the factors are constrained. "**factor specs**" option is for defining names for factors (figure 33).

In a PMF analysis, the most used options are the "seed" and the "a-value". But in this guide, all options will be detailed.

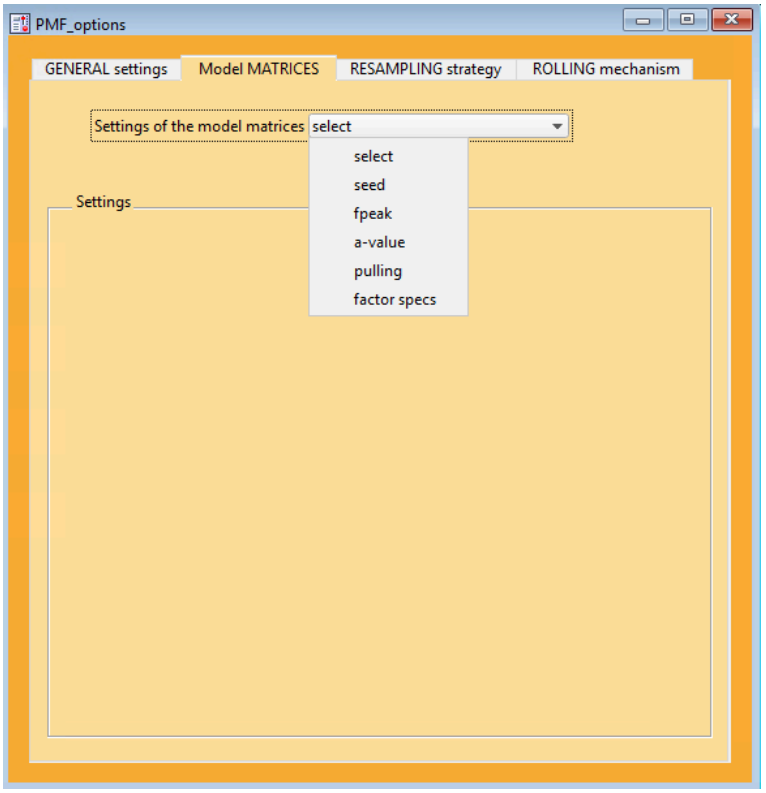

Figure 85: Model matrices panel

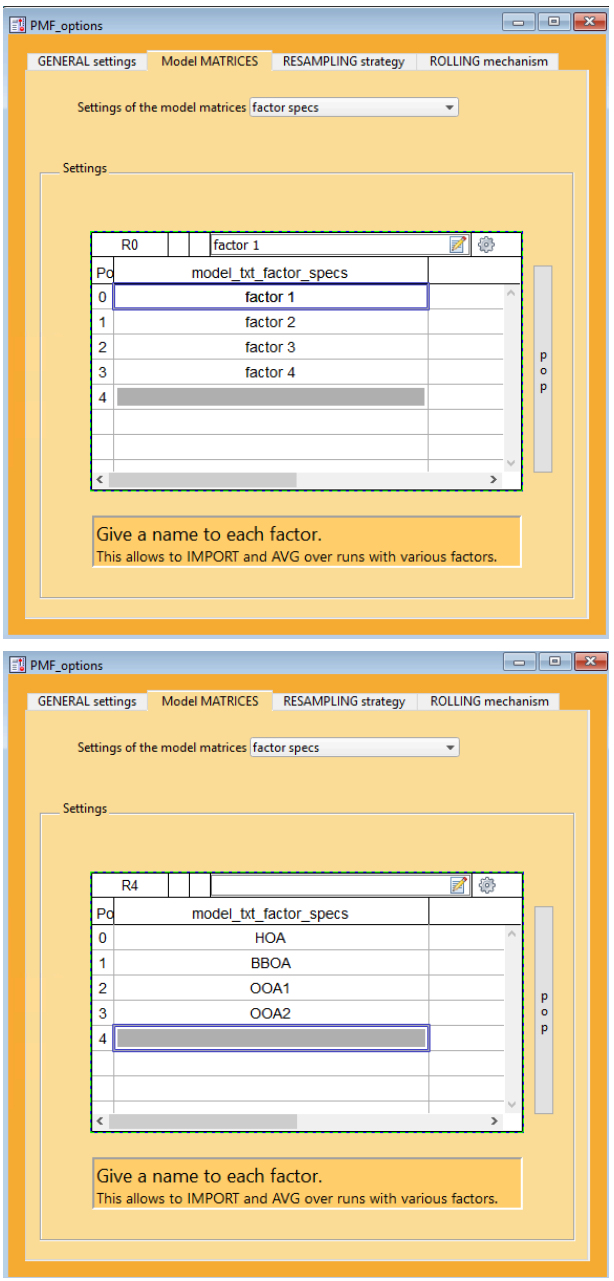

Figure 86: factor specs tab, default names (left), and user-defined names (right)

- Seed

Seed as mentioned before means the number of PMF starts, i.e. the initial values. It is used to initialize the reference factors (or time series).

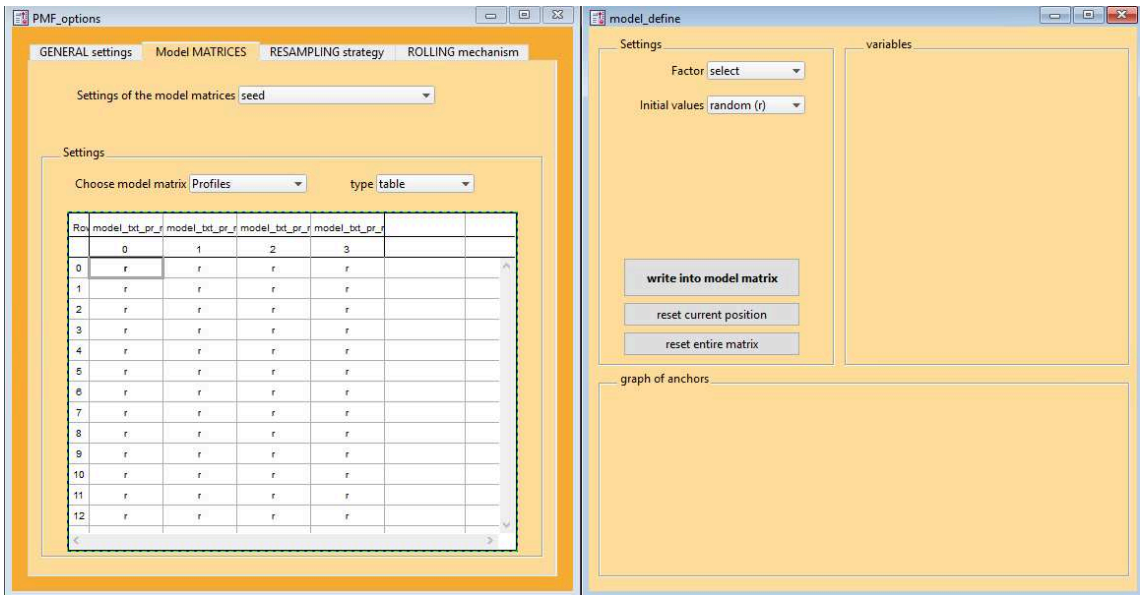

Figure 87: seed tab

So first, the user selects the "**factor**" and the "**initial values**": "random", "pseudo-random" or "from vector". If the user wants to keep specific features in the same way, "**pseudo-random**" means initialize only once and then keep the same random initial value, the "**random**" orientation always has completely random entries, any time PMF is running, SoFi initializes random completely; random for profiles and for time series. "**from vector**" option is used if the user wants to constrain the factor from a vector, so SoFi automatically goes into the "reference_pr" folder to import the factor chosen by the user. Then, for the "variables" option, it is possible to constrain "single ions" of the vector or "all variables", and see below the graph of the reference profile, where the variables selected are presented in red. Then, the option to "normalize" or "non-normalize" the factor; if the full profile is constrained so the factor should be normalized to the sum of 1. Then, the user clicks on "write into the model matrix" to import the profile. In the table on the left, the user can check the *m/z* and their corresponding values, and the yellow field "all model var. of factor defined" becomes green which means that the factor is written. The same settings are for other factors.

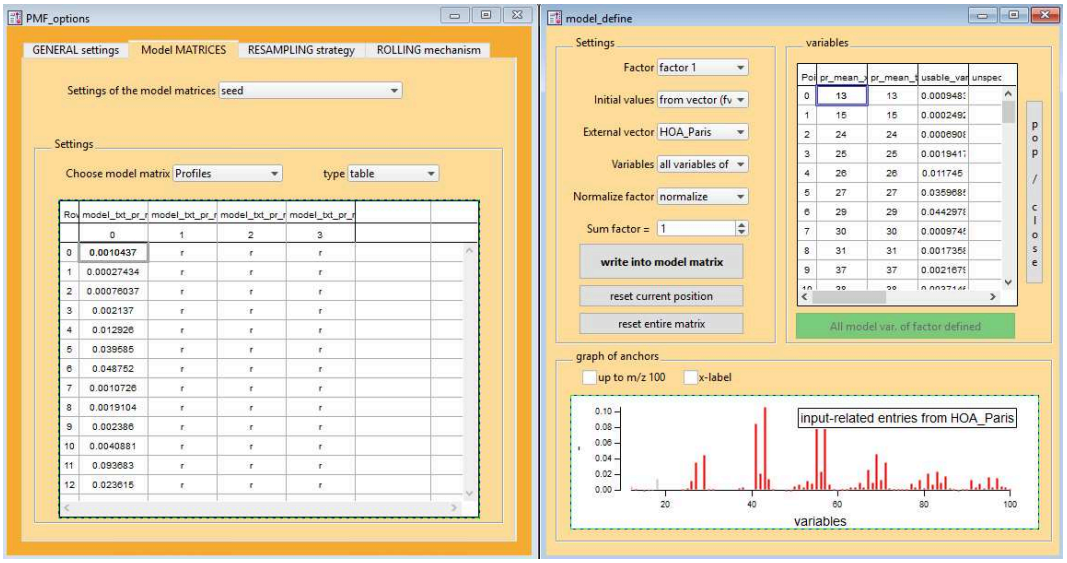

Figure 88: Initial model values from vector

- a-value approach

The "a-value" approach means measuring how much the final profile is allowed to differ from the constraint profile. This means that we define a range of variation for the reference factor we initialized in the seed part. This step is a continuity of the seed approach. There are several types of constraints for the a-value approach: "exact a-value", "random a-value" and "test of sensitivity" with different dimensions. This approach allows as well to constrain profiles and time series. This part focuses on profiles.

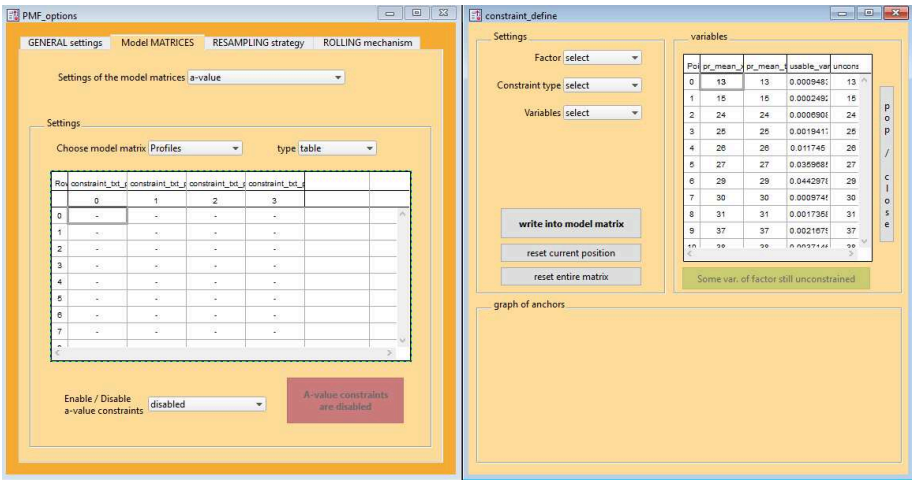

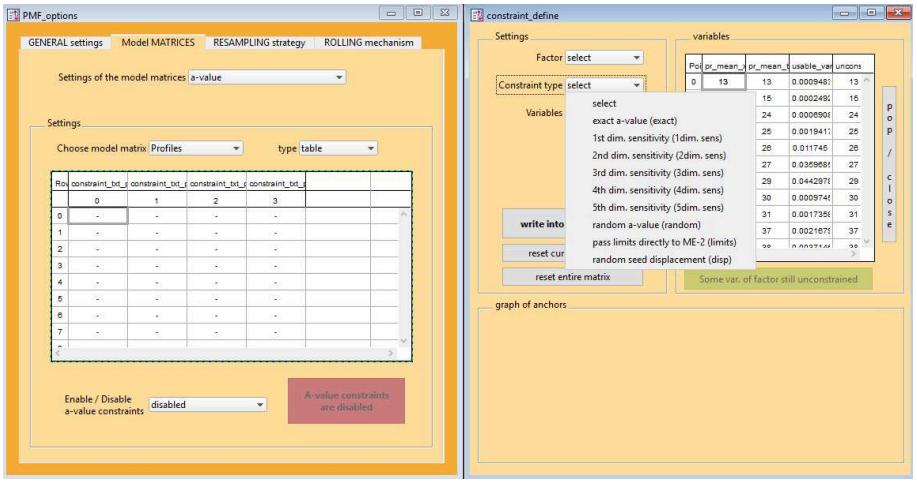

Figure 89: a-value tab

So first, the user needs to define the seed values as explained before, and then define the parameters for the a-value approach. In the left tab, the user chooses the "model matrix": "Profiles" or "Time series". In most cases, constraint profiles are more used. Then, in the right tab, the user chooses the "factor" and the "Constraint type". There are different constrain types: **Exact a-value** with a specific a-value, i.e. a-value=0.1 means that the factor profile can differ by ±10 %, **sensitivity analysis** with different sensitivity tests of a-value, for example running PMF once with the constraint of factor 1 using 1st dimension of sensitivity and starting with a certain a-value for example from 0 to 1 with a step of 0.1, so, in this case, PMF runs 11 times with one run having an a-value of 0, a second one with an a-value of 0.1, a third one with 0.2 and so on. With sensitivity analysis, there are different dimensions of sensitivity which means that if the user constrains multiple profiles, the a-values of all profiles can be changed at the same time or individually. For example, to constrain only one factor, the user can use 1st dim. of sensitivity. To constrain 2 factors, the user can constrain the first factor with 1st dim. of sensitivity and the second factor with 2nd dim. of sensitivity. So, while the a-value for the first factor stays at 0, the a-value of the second factor is increased from 0 to 1, and then the a-value of the first factor is increased to 0.1, and the a-value of the second factor is increased to the same range. So, with sensitivity analysis, all the different possibilities for the a-values can be tested. The third option of the a-value approach is to use a **random a-value** where the user specifies an upper and lower end a-value, so basically to have a random value in between, with specifying an a-delta which presents the increment. There is another option namely "pass limits directly to ME2" in order to have different limits for the profile. But it is not very used.

Thus, for the first tests, the user can constrain factors using exact a-value, but then can choose a random a-value to investigate a range of values: Ideally for HOA: a =0.05-0.1 but consider a larger range (0-0.3); For BBOA: a =0.3-0.5 but consider a larger range (0-0.5)

After choosing the constraint type, the user should select the variables that have to use this a-value. There is an option to define a-values for each ion. And another option is to apply a-value for all variables: "all model variables" or "all variables of external vector". If the external vector has all variables so the 2 options are correct and the user can choose "all

model variables". There are some cases where they are different like the case of using HR data.

Afterward, the user can click on "write into the model matrix" to insert the settings made in the left table. The same operation can be done for the other factors. The primary factors are the recommended factors to be constrained. In the end, the user should enable the a-value approach.

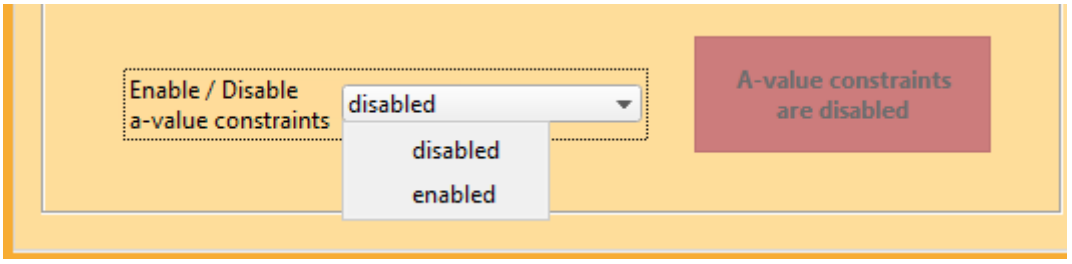

Figure 90: a-value tab

- **Example of applying the sensitivity analysis:**

Sensitivity analysis can help to not automatically change these a-values, for example, if the profile is taken from a study and the user wants to fit it to the data, he can test it with an a-value using sensitivity analysis. There are 5 dimensions of sensitivity, which means 5 independent sensitivity analyses (5 dimensions of a-values matrix). It is also possible to put the same dimension for all factors if the user wants to have one sensitivity analysis. It depends on what the user wants to use.

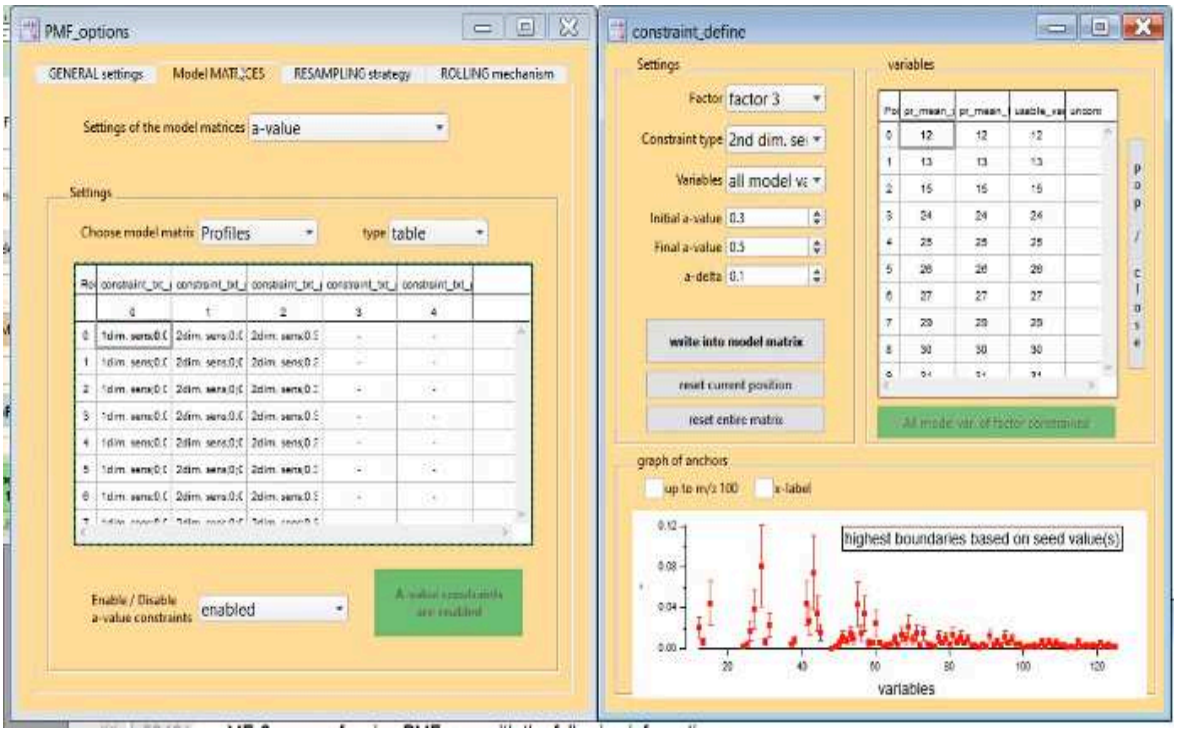

Figure 91: a-value parameters

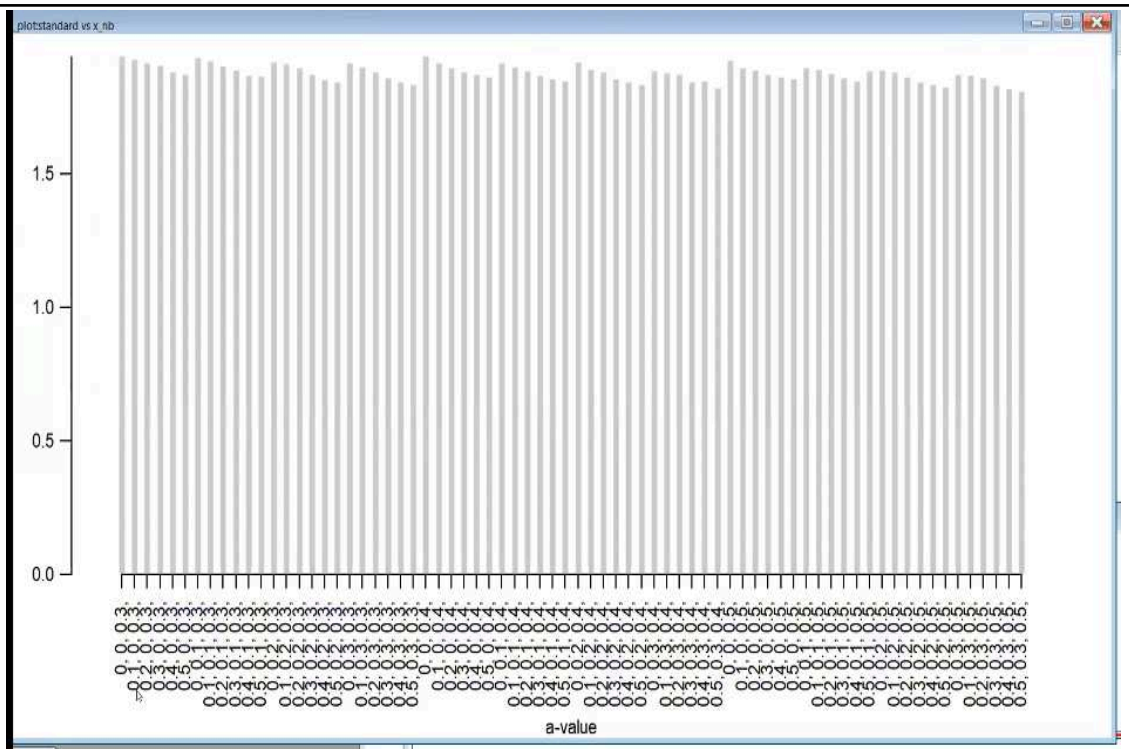

Figure 92: Sensitivity analysis

In this example in figure 38, a sensitivity analysis is applied on BBOA (a-value from 0.3 to 0.5 with a step of 0.1), COA (a-value from 0 to 0.3 with a step of 0.1), and HOA (a-value from 0 to 0.5 with a step of 0.1).

- fpeak

Two features of fpeak: “global fpeak” and “individual fpeak”. The fpeak approach allows for locations. The **global fpeak** allows for rotating all factors, i.e. full rotations between all the combinations. The **individual fpeak** allows to look at how other solutions come up, it is important, especially for specific rotations. If the user enables global fpeak, 3 options are possible: “exact fpeak”, “sensitivity analysis” and “random fpeak”. Global fpeak allows forcing rotations of unconstrained parts. **The exact fpeak** has only one fpeak value. **Sensitivity analysis** has a range of fpeaks; “initial” and “final fpeak” and a “user-defined fpeak resolution”. **Random fpeak** generates fpeak between -1 and 1 with a step of 0.1. If the individual fpeak is enabled, the user has the rotational matrix, i.e. if the user constraints 5 factors, it can be a matrix of 5 fpeaks, and then the user passes the positions that are supposed to be rotated.

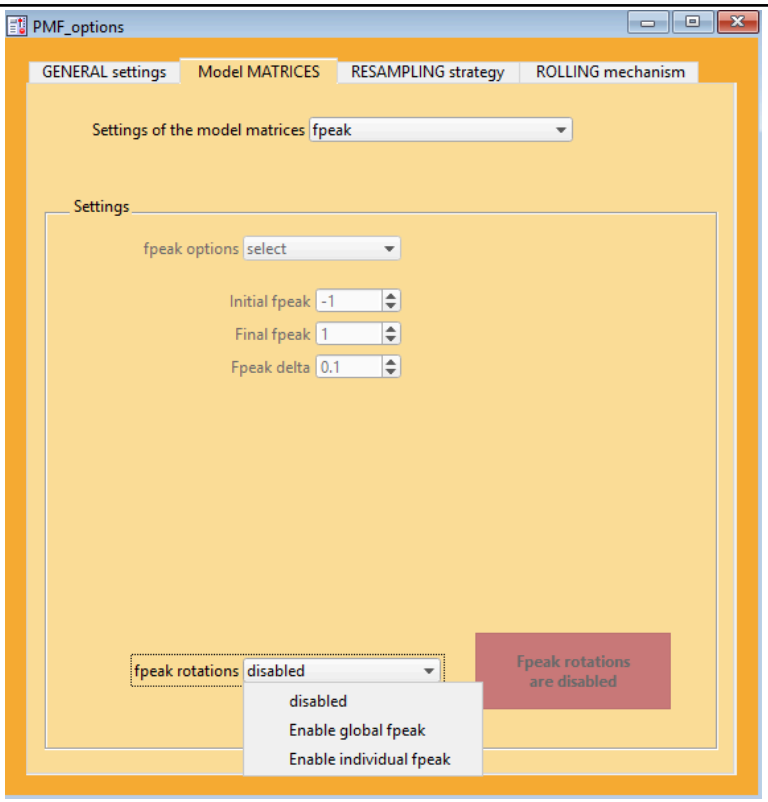

Figure 93: fpeak tab

- Pulling equation

Pulling equations are additional equations that can be added to the PMF model.

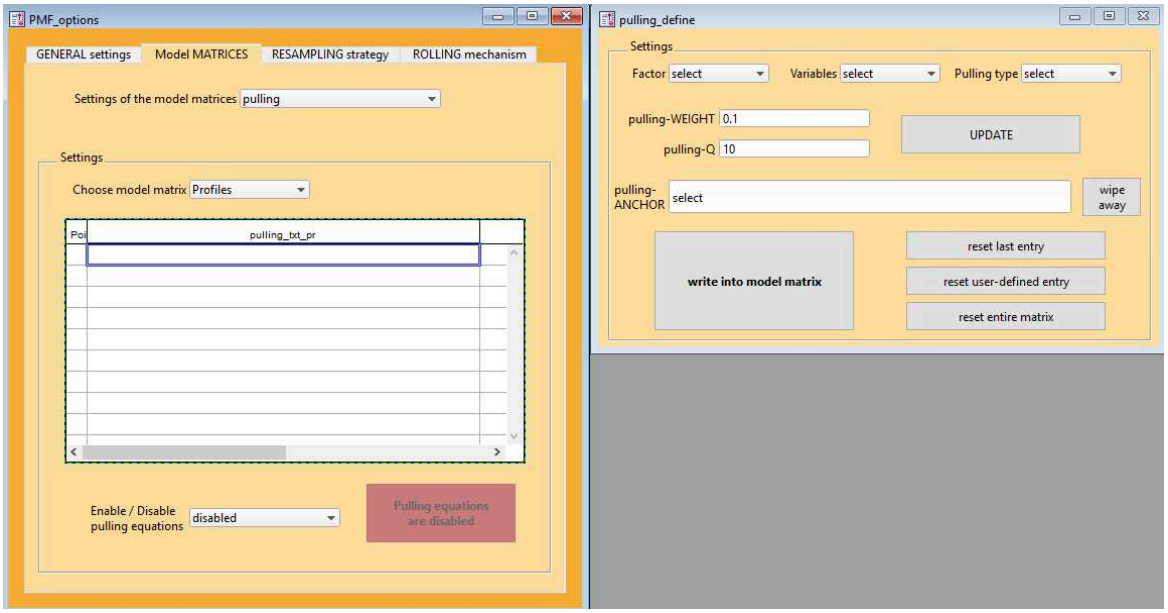

Figure 94: Pulling equations tab

Bellow an example to constrain BBOA using the pulling equation:
For example, the user can define an equation for the variable m/z 60 of the biomass burning factor (BBOA). So first the user needs to define the ANCHOR (the value to pull) and the WEIGHT (the pulling weight 0.1, which means the uncertainty passed to the model, is used

to rest the pulling equation), so the user can change the value in the equation, then click on "write into model matrix" and then it appears in the table on the left. The user needs to enable the pulling equation to apply the defined equations.

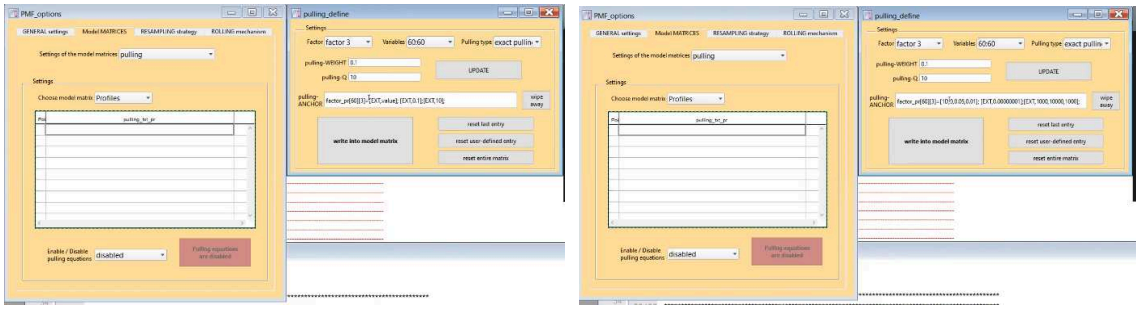

Figure 95: Example of constraining BBOA using pulling equation

The user can also test the sensitivity analysis using the pulling equation:

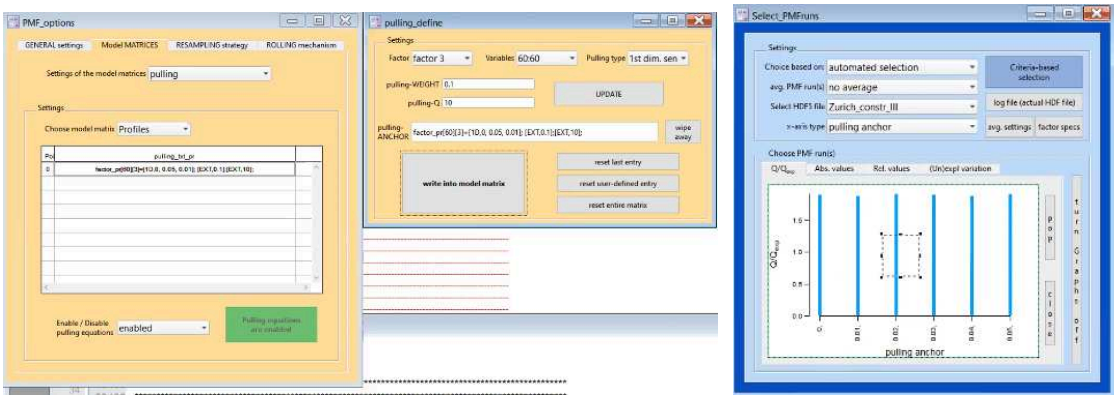

Figure 96: Example of constraining BBOA using pulling equation with sensitivity analysis

IV. Use the "Bootstrap"

- **RESAMPLING strategy**

This strategy consists of enabling Bootstrap resampling. The bootstrap is used to test the stability of the results. It generates a new input matrix of the original input data in order to verify the robustness of the result. It is important to enable Bootstrap, especially for the final PMF results to estimate the statistical uncertainties.

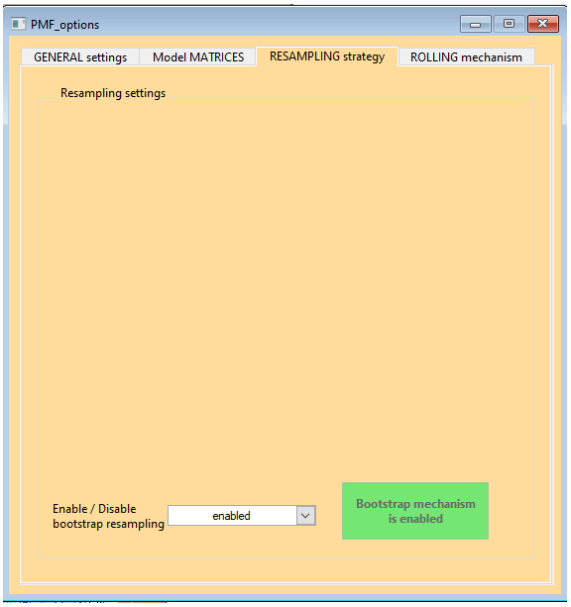

Figure 97: Resampling strategy panel

V. Run the "rolling PMF"

- **ROLLING mechanism**

The rolling mechanism consists of defining a small window that is moved in 1d increments across the entire dataset and thus captures seasonal variations of the factor profiles. This is useful especially for long-term datasets because running PMF over the entire dataset can take time to import and check results, so it would be better to use rolling PMF that consists of applying small windows over the data. For each PMF window, the uncertainties are propagated for the PMF results with for example a time window of 14 days and a 1-day shift, which is about 14 repeats.

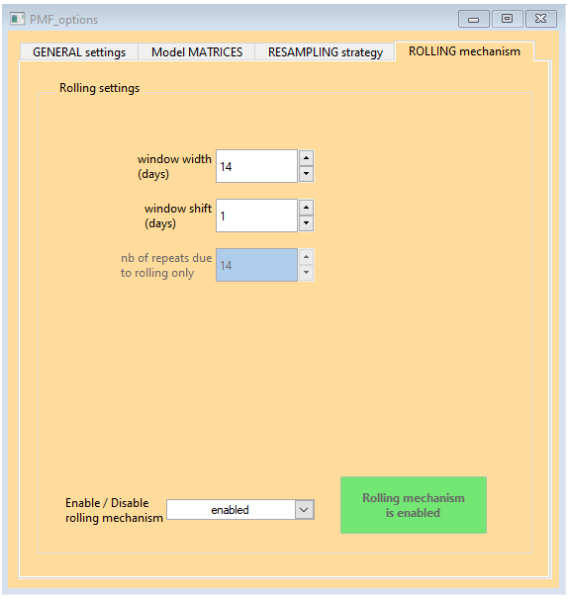

Figure 98: Rolling mechanism tab

In this part, the user must define the window length and window shift. The default values for these parameters are 14 days for each window and 1-day shift, as mentioned in Canonaco et al. 2021. Otherwise, the user should test different time windows in order to finally choose the one that presents the results well. To do so, the user can check the variation of Q/Q_{exp} and non-modeled points (or missing points that correspond to the time points that not satisfied the user-defined criteria for all runs) with different time windows and at the end, the user chooses the window with less Q/Q_{exp} and less non-modeled points (Figure 45). The time window with the upper value of s_{win} (window size), a_{max} (maximum a-value), and x_{PMF} (PMF repeats) are the desired ones.

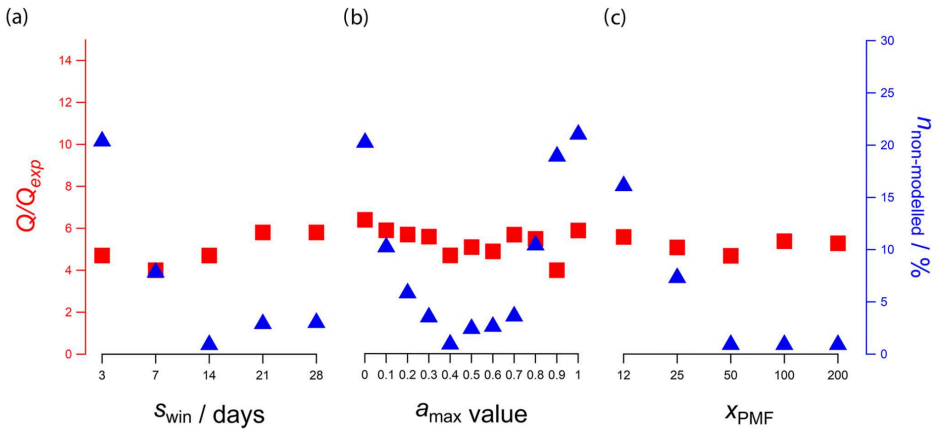

Figure 99: Q/Q_{exp} and the percent of non-modeled time points over the entire dataset as a function of window size (swin), maximum a-value (a_{max}), and number of PMF repeats per window (x_{PMF}) (Canonaco et al. 2021)

VI. Criteria-based selection

The criteria-based selection is used especially for rolling PMF results or bootstrap results for which there are many runs in order to choose the best ones.

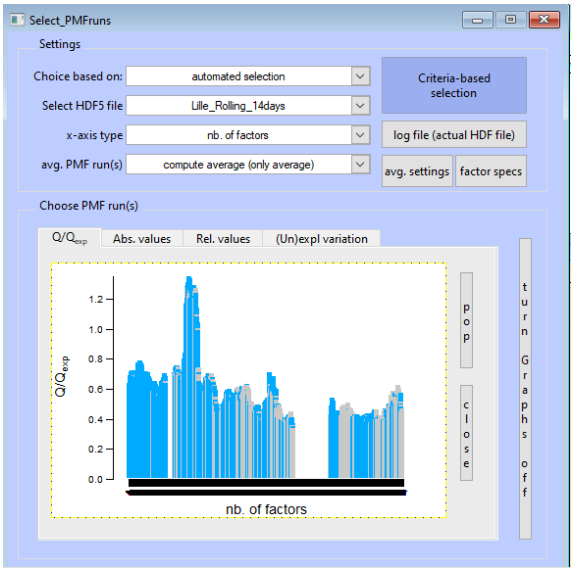

Figure 100: Select PMF runs based on the criteria panel

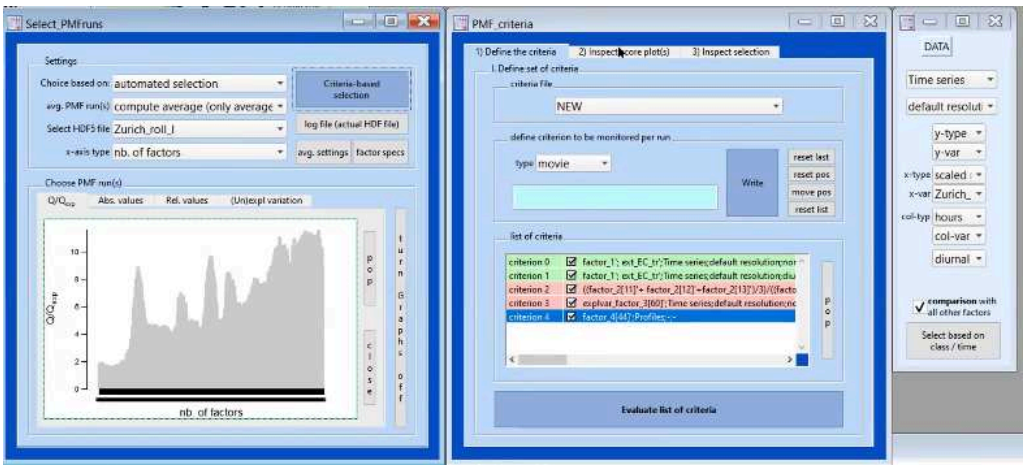

Figure 101: PMF criteria panel

There are three panels for PMF Criteria:

1) The first one is “Define the criteria” where the user specifies the criteria, for example, the correlation between factors and the external data using the DATA panel and it is possible to change the cycle (diurnal, weekly, monthly, …) and the type (abs or fraction), and then the user can click on “Write” button to add the criterion to the list. Many examples are given in the SoFi manual (« Manual - Datalystica Knowledge Base »), where there are different selection or monitoring criteria. Then, the user evaluates the criteria that their boxes are checked, by clicking on the box “Evaluate list of criteria” button.
2) The Second one is “Inspect score plots” where there are different options to select the main runs. In the DATA panel, in the CRITERIA part, the user chooses the criterion. Here, for example in figure 48 the first criteria present the correlation between factor 1 and BCtr, i.e. the complete representation of correlation over time, with each point presenting a PMF run. Clicking on “Pop batch table” allows checking the table that resumes the main settings of criteria.

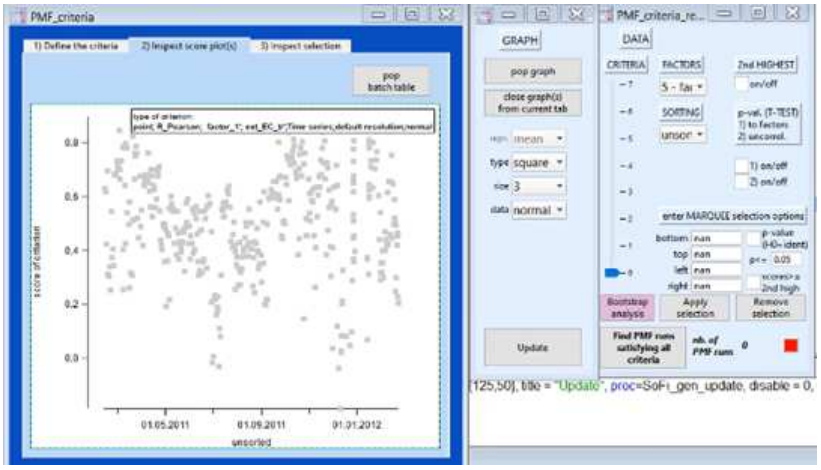

Figure 102: first criteria "correlation between Factor 1 and BCtr"

On the right side (figure 39), there are options to select the best runs with some statistics like T-TEST. If the box “comparison with all other factors” in the first panel is unchecked, it

means that SoFi only calculates the scores for these criteria, but if it is enabled, SoFi compares with other factors and makes all combinations. So, the "2nd Highest" button in the second panel means that SoFi also calculates with other factors. Then, after clicking on "apply selection", the blue dots present the correlation between factor 1 and BCtr and the black dots present the correlation between factor 2 or factor 3 with BCtr. For the T-TEST, there are 2 options: "to factors" (to select the points with a significant correlation compared to other factors) and "uncorrel. option" (for a significant correlation between factor 1 and BCtr). There are also options for the "p-value" and for the axis. There is also an option to sort the factors and change the solutions of the factors.

In SoFi 8 and 9, there are other criteria types such as image or movie, not just point.

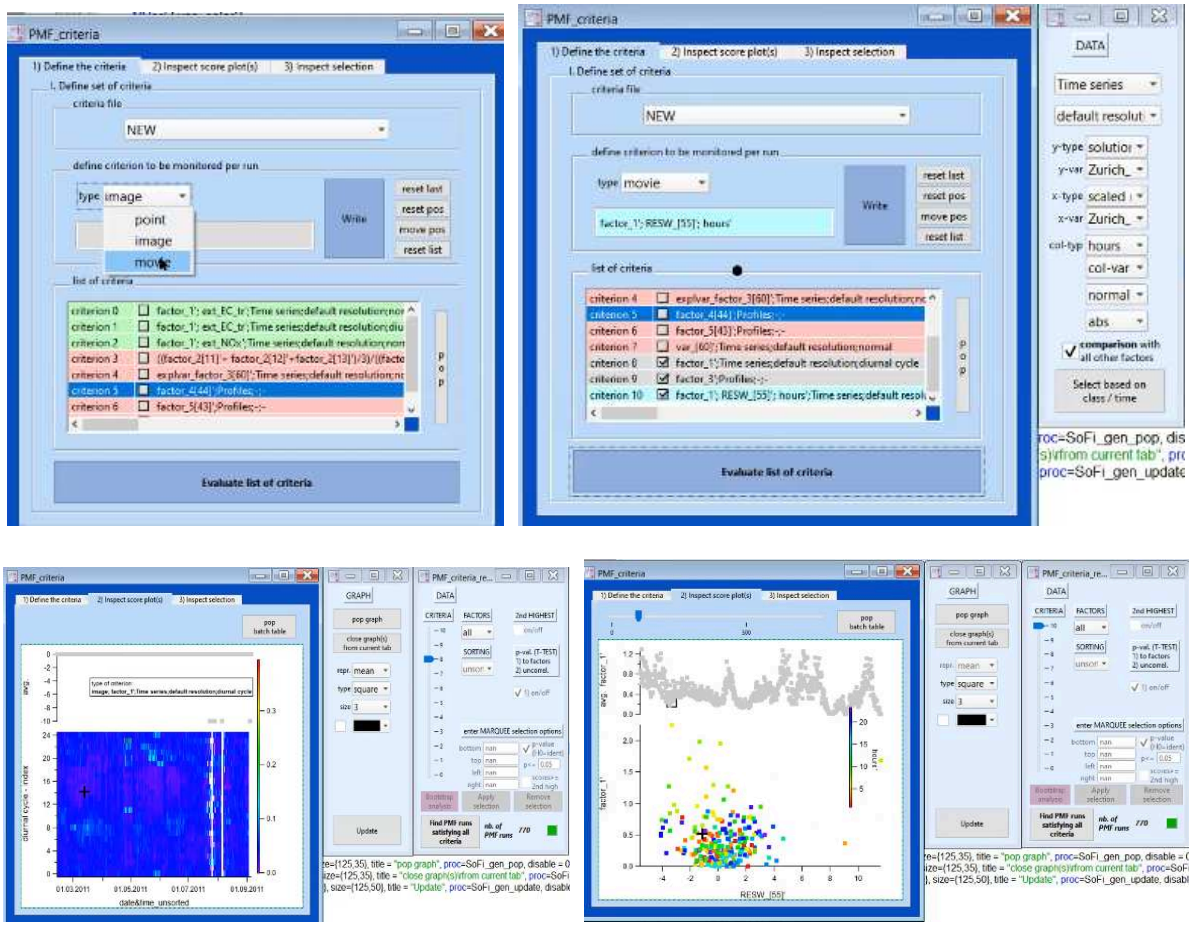

Figure 103: Defining criteria; type image or movie in SoFi 8

3) After that, the user clicks on "Find PMF runs satisfying all criteria" and the number of chosen PMF runs appears, then he passes to the third panel to "Inspect selection". The blue points are the selected points and the green points present all the PMF runs.

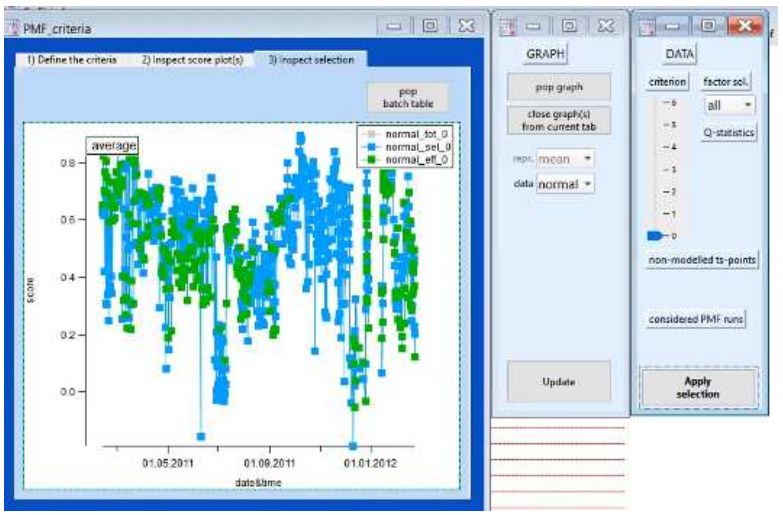

Figure 104: Inspect the selection panel

Then the user must click on “apply selection” to save the modifications, then close this window. In the main panel, the selection is done. Then, the user chooses the averages option.

VII. Averaged solution

This one corresponds to the case of the option “averaged” in the last panel. It is just available for the averaged solution.

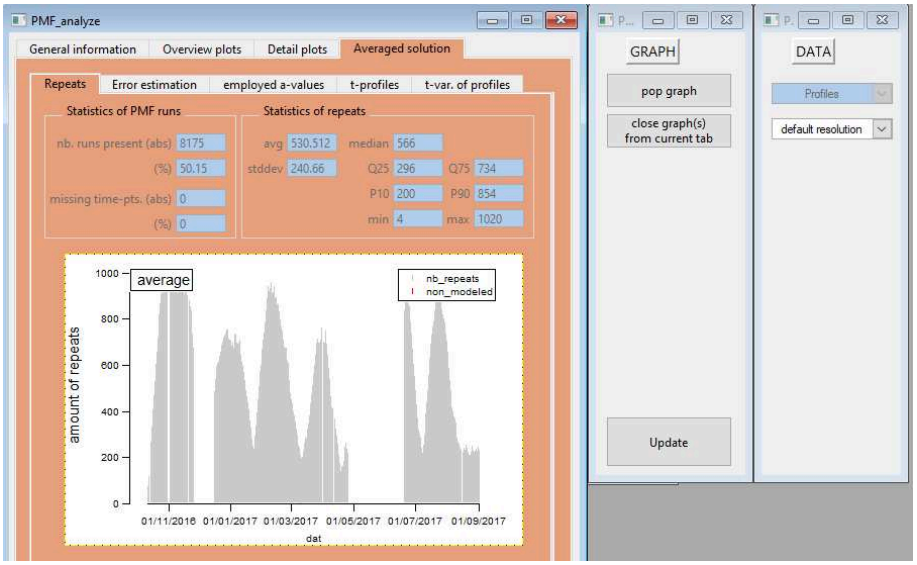

Figure 105: Averaged solution panel

In this tap, there are many panels about the averaged solution (i.e. settings and statistics of the PMF): “repeats” (statistics about repeats), “error estimation” (the uncertainties and rotational uncertainties, to explore these in scatter plots or histogram by plotting the stddev/mean, PMF errors), “employed a-values” (the a-values statistics), “t-profiles” (the time-dependent profile, variables over time), “t-var of profiles” (time-dependent variables, variables of each factor how it looks over time).

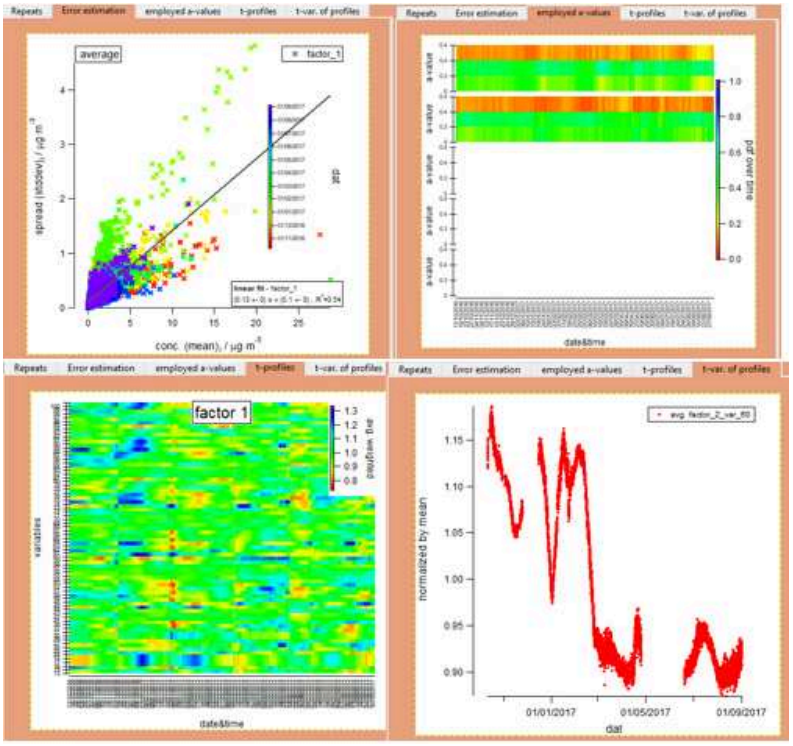

Figure 106: some graphs from the "Averaged" tab

❖ It is possible to define colors for PMF factors in the main setting of SoFi and they will be applied to all plots generated in the experiment Igor.

Chapter 4: Specific examples

I. Example of classic PMF

To perform a classic PMF, the user should follow the same steps as mentioned in the guide. First, the user should import the data in the "Import data" panel and then treat it in the "Pretreatment" panel. The next step is to specify the main settings to run PMF.

1) Start with unconstrained PMF (from 2 to 8 factors) where the user can check the mass spectra of the factor profiles, their diel cycles and correlation with available tracers (e.g. NO_x, BC,..) in order to identify the possible number of factors. If the factors are OK, see point 4.

2) If not, the user needs to perform constrained PMF, especially for the primary factors, by performing many tests of the a-values and testing many reference profiles. Starting with HOA (e.g., Crippa et al. (2013)), then HOA and BBOA (e.g., Ng et al., (2011)).

3) Test specific primary OA profiles when in doubt about their presence or hesitating between N and N+1 factors: cooking OA (COA), coal combustion OA (CCOA), ... So the user constrains the mass spectra of the factor (for example COA with Crippa et al., (2013) to see if the daily profile is reasonable).

4) Once the best base case (i.e., the reasonable PMF solution) has been chosen, the user should then test the stability of this solution by enabling the Bootstrap approach with e.g., 50 repeats.

If the user disposes of long-term data, e.g. one year, it is preferable to perform a seasonal PMF analysis. The user should therefore follow these steps for each season (winter, spring, summer, autumn) and try to have a consistent number of oxygenated OA factors for the different seasons if environmentally reasonable. The profiles extracted from the bootstrap can be used to constrain profiles for rolling or real-time PMF analyses.

II. Example of Rolling PMF

The rolling PMF is a continuation of the classic PMF, where the dataset is analyzed at once, constraining the profiles with reference profiles or specific site profiles obtained from the seasonal PMF results. The user should enable the rolling approach by defining the window width and window shift. After running the model, the user obtains the HdF file and defines criteria to choose the best PMF solutions.

- Steps to define the PMF run settings:

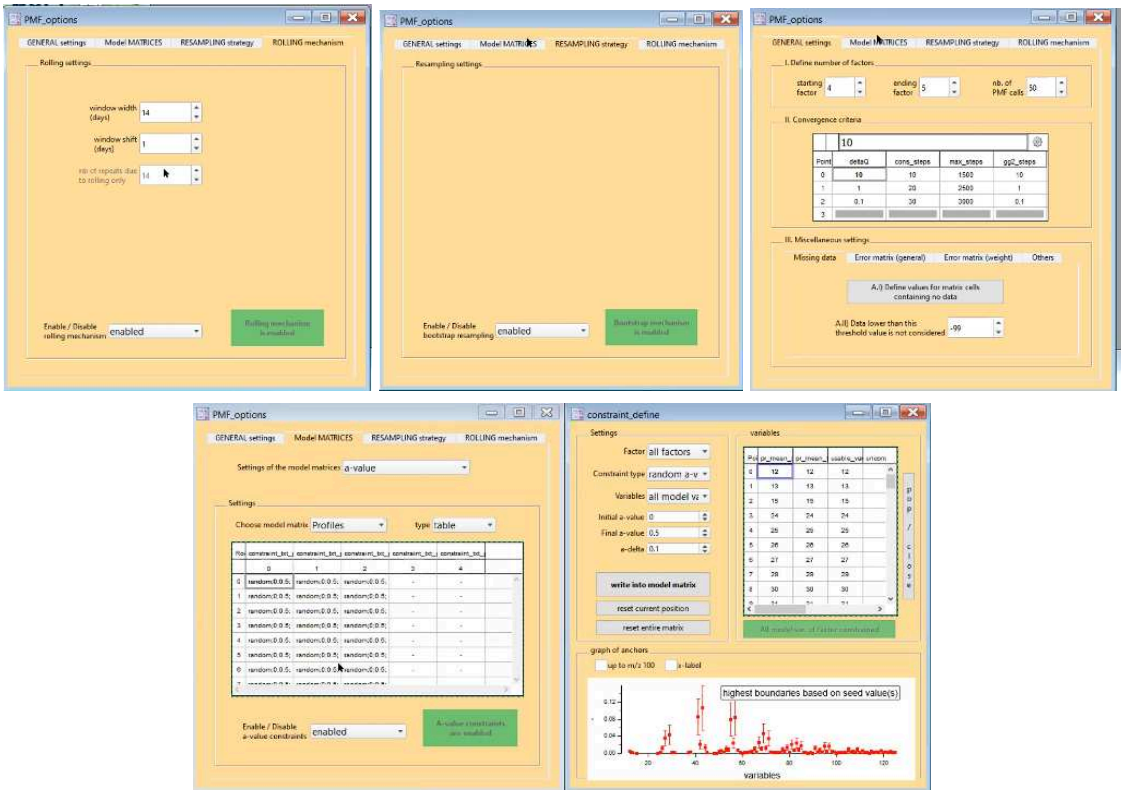

Figure 107: Steps to define the PMF run settings

- Steps to define criteria:

The user can define criteria for each factor. There are different types of criteria. Some criteria for selection and others for monitoring. If the user has two unconstrained factors, for example, he can sort them. For example, sort the criteria with the highest *m/z* 44 so the user should click on this criterion, the black color means that it is a sorting criterion.

Below, an example of a criterion for the variability of *m/z* 60 in factor 3, each point of the graph presents the explained variation of *m/z* 60 in factor 3.

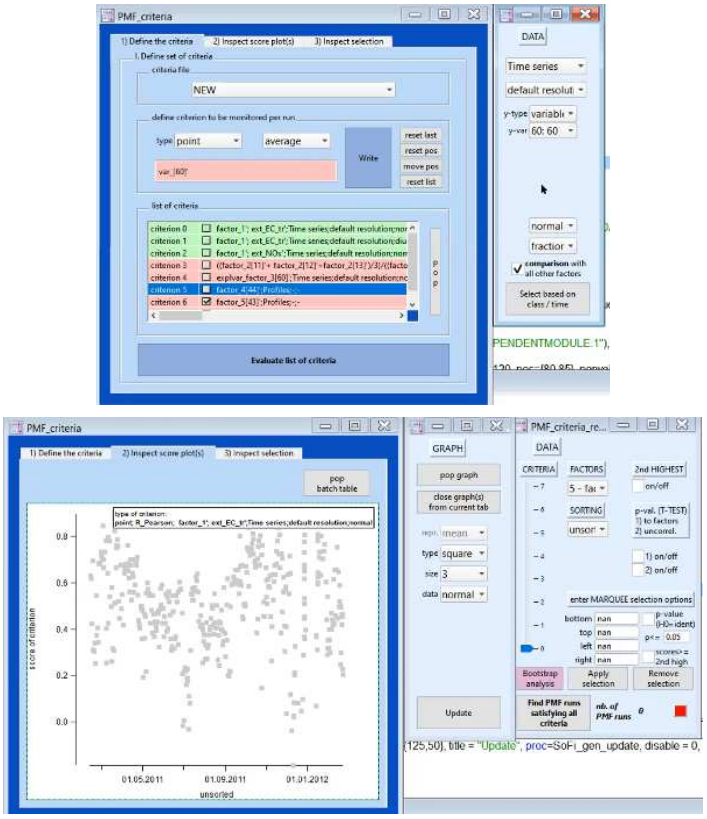

Figure 108: Steps to define criteria

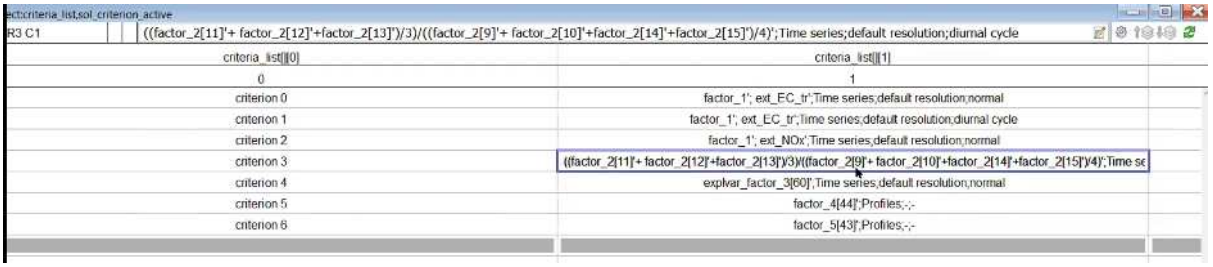

Figure 109: List of some based-selection criteria

III. Example to illustrate the multi-time feature

The multi-time feature is useful to combine data with different time resolutions.

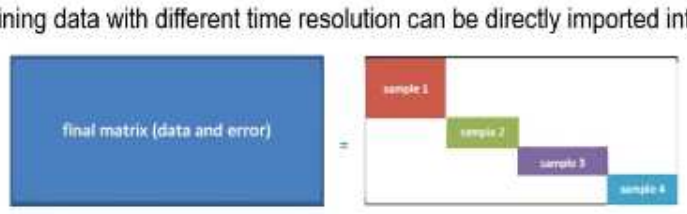

First, the user imports the two datasets in the "Import data" panel in the matrix specs (the ACSM data and the other dataset), and the error matrix. And then define the two-time dimensions.

In the second panel “Pretreatment”, the user should define classes in terms of time series. Either he can import the two classes or define them using an index, the same for the profile to define 2 classes.

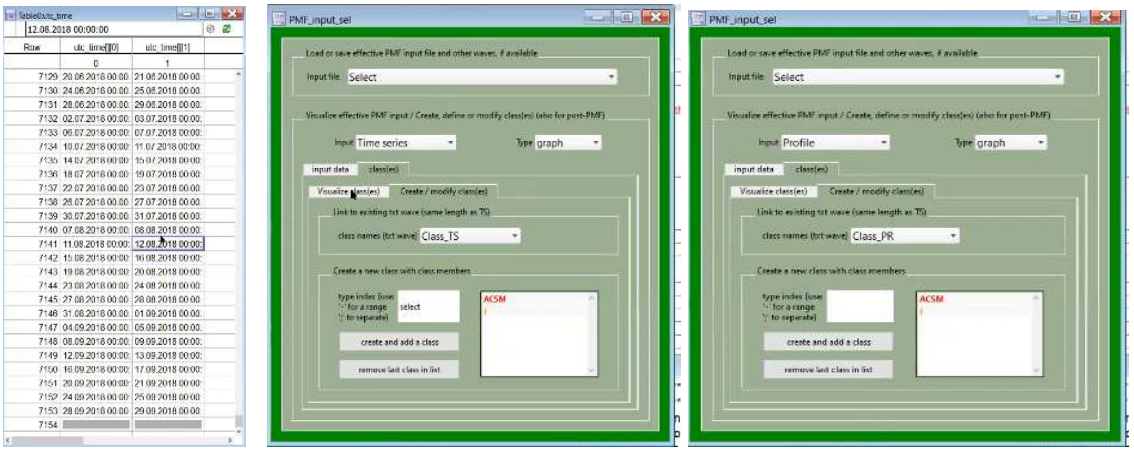

Figure 110: Pre-treatment panel; Prepare PMF input

Then the user can enable the multi-time option.

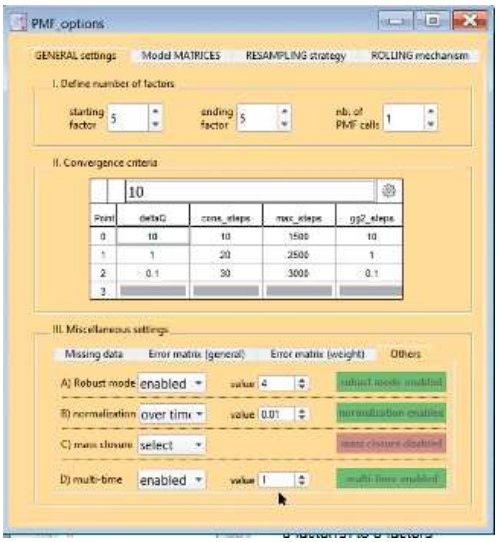

Figure 111: Run PMF panel; define model options

Then run the PMF and check the result.

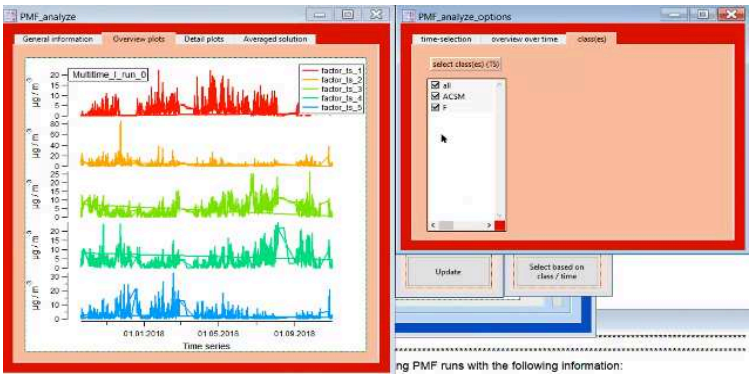

Figure 112: Overview plots panel

The user can check the residuals for the 2 datasets/classes:

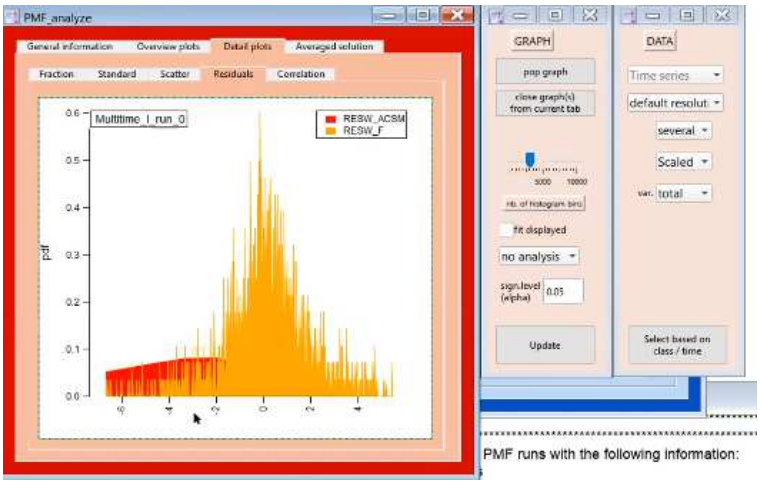

Figure 113: Detail plots panel; residuals tab

To correct this in order to have the same underlying distribution for (scaled) residuals, the user can use the C-value approach (see SoFi manual, pages 117-118).

References

Canonaco, Francesco, Anna Tobler, Gang Chen, Yulia Sosedova, Jay Gates Slowik, Carlo Bozzetti, Kaspar Rudolf Daellenbach, et al. 2021. « A New Method for Long-Term Source Apportionment with Time-Dependent Factor Profiles and Uncertainty Assessment Using SoFi Pro: Application to 1 Year of Organic Aerosol Data ». *Atmospheric Measurement Techniques* 14 (2): 923‑43. https://doi.org/10.5194/amt-14-923-2021.

Development, Office of Research &. s. d. « EPA Positive Matrix Factorization (PMF) 5.0 Fundamentals and User Guide ». Consulté le 5 juillet 2021. https://cfpub.epa.gov/si/si_public_record_report.cfm?Lab=NERL&direntryid=308292

« Manual - Datalystica Knowledge Base ». s. d. Consulté le 5 juillet 2021. https://datalystica.helpscoutdocs.com/article/19-manual.

Paatero, Pentti, et Philip K. Hopke. 2003. « Discarding or Downweighting High-Noise Variables in Factor Analytic Models ». *Analytica Chimica Acta*, Papers presented at the 8th International Conference on Chemometrics and Analytical Chemistry, 490 (1): 277‑89. https://doi.org/10.1016/S0003-2670(02)01643-4.

Polissar, Alexandr V., Philip K. Hopke, Pentti Paatero, William C. Malm, et James F. Sisler. 1998. « Atmospheric Aerosol over Alaska: 2. Elemental Composition and Sources ». *Journal of Geophysical Research: Atmospheres* 103 (D15): 19045‑57. https://doi.org/10.1029/98JD01212.

Ulbrich, I M, M R Canagaratna, Q Zhang, D R Worsnop, et J L Jimenez. 2009. « Interpretation of Organic Components from Positive Matrix Factorization of Aerosol Mass Spectrometric Data ». *Atmos. Chem. Phys.*, 28.

Annex

Macro of Blacklist Button

```
#pragma rtGlobals=3      // Use modern global access method and strict wave access.
Macro BL_Button()
   PauseUpdate; Silent 1            // building window...
   ShowInfo
   //ShowTools
         controlinfo kwcontrolbar

   Variable width = 55, height = 22
   Variable line = v_height, col_1 = 0 * width+5 , col_2 = width + 5, col_3 = 2 * width + 5 , col_4 = 3
* width + 5,col_5 = 4 * width + 15

   ControlBar line + height * 1 // this 1 means there is only one line of buttons right now
         Button BL_but, pos={463,2}, size={80,20},title="Blacklist",proc=BLWindowProc
EndMacro
```

Macro of Clean Spikes Graphs

```
Window CleanUpSpikes() : Graph
   PauseUpdate; Silent 1            // building window...
   String fldrSav0= GetDataFolder(1)
   SetDataFolder root:SelectedIon_Diagnostic:
   Display /W=(766.5,336.5,1410.75,591.5)/L=L_18/B=B_28_18 mz18 vs mz28
   AppendToGraph/L=L_32/B=B_28_32 mz32 vs mz28
   AppendToGraph/L=L_40/B=B_28_40 mz40 vs mz28
   SetDataFolder fldrSav0
   ModifyGraph margin(bottom)=85
   ModifyGraph mode=3
   ModifyGraph marker=8
   ModifyGraph
zColor(mz18)={:ACSM_Incoming:acsm_utc_time,*,*,Rainbow},zColor(mz32)={:ACSM_Incoming:
acsm_utc_time,*,*,Rainbow}
   ModifyGraph zColor(mz40)={:ACSM_Incoming:acsm_utc_time,*,*,Rainbow}
   ModifyGraph standoff=0
   ModifyGraph notation=1
   ModifyGraph lblPos(L_18)=45,lblPos(B_28_18)=80,lblPos(L_32)=47,lblPos(B_28_32)=80
   ModifyGraph lblPos(L_40)=40,lblPos(B_28_40)=80
   ModifyGraph zapTZ=1
   ModifyGraph prescaleExp=12
   ModifyGraph freePos(L_18)=0
   ModifyGraph freePos(B_28_18)={0,L_18}
   ModifyGraph freePos(L_32)={0.35,kwFraction}
   ModifyGraph freePos(B_28_32)={0,L_32}
   ModifyGraph freePos(L_40)={0.7,kwFraction}
   ModifyGraph freePos(B_28_40)={0,L_40}
   ModifyGraph axisEnab(B_28_18)={0,0.25}
```

```
    ModifyGraph axisEnab(B_28_32)={0.35,0.6}
    ModifyGraph axisEnab(B_28_40)={0.7,1}
    Label L_18 "\\um/z 18"
    Label B_28_18 "\\um/z 28"
    Label L_32 "\\um/z 32"
    Label B_28_32 "\\um/z 28"
    Label L_40 "\\um/z 40"
    Label B_28_40 "\\um/z 28"
    SetAxis/A=2/E=2 L_18
    SetAxis/A/E=2 B_28_18
    SetAxis/A=2/E=2 L_32
    SetAxis/A/E=2 B_28_32
    SetAxis/A=2/E=2 L_40
    SetAxis/A/E=2 B_28_40
    ColorScale/C/N=text0/F=0/B=1/A=MC/X=0.13/Y=-76.78 trace=mz18, vert=0, height=10
    ColorScale/C/N=text0 widthPct=70, lblMargin=0
    AppendText "UTC time"
EndMacro
```

Procedure of Clean Spikes

```
//Function adapted from the Aerodyne ACSM_SpikeRemover.ipf functions by V. Riffault (IMT Nord Europe)
// to mimic the manual cleaning of data using the Selected Ion Plot in ACSM Local and stay consistent with previous manual procedure
////////////////////////////////////////////////////////////////////////////////////////////////////////////////////////
// Better be cautious and save the experiment before blacklisting too many points! //
////////////////////////////////////////////////////////////////////////////////////////////////////////////////////////
Function ACSM_CleanSpikes(mz,deltapos,deltaneg)
variable deltapos,deltaneg, mz
// mz's should typically be air beam ions (28, 32,40) or water signal at mz18 (which can show more variation so exert carefully!)
// deltapos and deltaneg are positive values in the function.
// The positive and negative values for delta
// The 2 deltas are mostly to account for differences in the variation of mz18, while mz28, mz32 and mz40 should exhibit a symmetrical level of noise. They must be set cautiously, according to the level of noise for each mz.
wave mz18 = root:SelectedIon_Diagnostic:mz18
wave mz28 = root:SelectedIon_Diagnostic:mz28
wave mz32 = root:SelectedIon_Diagnostic:mz32
wave mz40 = root:SelectedIon_Diagnostic:mz40
wave time_w = root:Acsm_incoming:acsm_utc_time
variable i
switch(mz)
   case 18:
         for (i=0; i<numpnts(time_w); i += 1)
               if ((mz18[i] > deltapos) || (mz18[i] < -deltaneg))
                     BlackList(i,i)
                     i=i-1
```

```
                endif
        endfor
        break
    case 28:
        for (i=0; i<numpnts(time_w); i += 1)
                if ((mz28[i] > deltapos) || (mz28[i] < -deltaneg))
                        BlackList(i,i)
                        i=i-1
                endif
        endfor
        break
    case 32:
        for (i=0; i<numpnts(time_w); i += 1)
                if ((mz32[i] > deltapos) || (mz32[i] < -deltaneg))
                        BlackList(i,i)
                        i=i-1
                endif
        endfor
        break
    case 40:
        for (i=0; i<numpnts(time_w); i += 1)
                if ((mz40[i] > deltapos) || (mz40[i] < -deltaneg))
                        BlackList(i,i)
                        i=i-1
                endif
        endfor
        break
    default:
        print "Wrong mz. You must choose 18, 28, 32 or 40"
    break
endswitch
SIMZP_Make()
end
```

Procedure of RIT Time series

```
Window RIT_TS() : Graph
    PauseUpdate; Silent 1          // building window...
    String fldrSav0= GetDataFolder(1)
    SetDataFolder root:RIT:
    Display /W=(450,56,1413,439.25) RIT_Mat[*][1] vs ::ACSM_Incoming:acsm_utc_time
    AppendToGraph RIT_Mat[*][3] vs ::ACSM_Incoming:acsm_utc_time
    AppendToGraph RIT_Mat[*][4] vs ::ACSM_Incoming:acsm_utc_time
    AppendToGraph RIT_Mat[*][2] vs ::ACSM_Incoming:acsm_utc_time
    SetDataFolder fldrSav0
    ModifyGraph mode=2
    ModifyGraph lSize=1.5
    ModifyGraph
rgb(RIT_Mat)=(43520,43520,43520),rgb(RIT_Mat#1)=(0,0,65280),rgb(RIT_Mat#3)=(0,65280,0)
```

```
   ModifyGraph lblMargin(left)=15
   ModifyGraph dateInfo(bottom)={0,0,0}
   Label left "RIT"
   Label bottom " "
   ShowInfo
   Legend/C/N=text0/J/H={0,5,10}/X=1.68/Y=-1.22 "\\s(RIT_Mat) mz 62\r\\s(RIT_Mat#3) mz
76\r\\s(RIT_Mat#1) mz 102\r\\s(RIT_Mat#2) mz 128"
   ControlBar 22
   Button BL_but,pos={463,2},size={80,20},proc=BLWindowProc,title="Blacklist"
EndMacro
```

Procedure of CDCE application

```
#pragma rtGlobals=3      // Use modern global access method and strict wave access.
// NH4_DL = ammonium detection limit
// CE_lowNH4 = CE for points where ammonium is below its detection limit
// 1) All species must be calculated using CE=1 in the batch.
// 2) Run this procedure to create a wave for time dependant CE.
// 3) ?????
// The sampling line relative humidity (if measured) should be named "RH_SL"
// e.g., CalcCE_fPhase(0.1, 0.5)
Function CalcCE_fPhase(NH4_DL,CE_lowNH4)
Variable NH4_DL,CE_lowNH4
SetDataFolder root:
wave RH_SL
// Create waves of each species to smooth for the calculations.
duplicate/o root:time_series:SO4 SO4_raw
duplicate/o root:time_series:NH4 NH4_raw
duplicate/o root:time_series:NO3 NO3_raw
duplicate/o root:time_series:Chl Chl_raw
duplicate/o root:time_series:Org Org_raw
Variable i
Duplicate/o root:time_series:SO4 PredNH4_CE1, NH4_MeasToPredict, ANMF
Duplicate/o root:time_series:SO4 CE_dry,CE_fPhase
CE_dry=0.5
CE_fPhase=0.5
// Equation 3
PredNH4_CE1=18*(SO4_raw/96*2+NO3_raw/62+Chl_raw/35.45)
NH4_MeasToPredict=NH4_raw/PredNH4_CE1
// Equation 5
ANMF=(80/62)*NO3_raw/(NO3_raw+SO4_raw+NH4_raw+Org_raw+Chl_raw)
// Calculate the dry collection efficiency, CE_dry
For (i=0;i<(numpnts(SO4_raw));i+=1)
// Nan negative NH4_MeasToPredict points
   If (NH4_MeasToPredict[i]<0)
         NH4_MeasToPredict[i]=0
   EndIf
// Nan ANMF points if negative or more than 1
   If (ANMF[i]<0)
```

```
        ANMF[i]=0
   ElseIf (ANMF[i]>1)
        ANMF[i]=1
   EndIf
   If (NH4_raw[i]<NH4_DL)
// In general, do not calculate CE for these points.
        CE_dry[i]=0.5
// In the CE paper, applied CE for low ammonium mass
// CE_dry[i]=CE_lowNH4
   ElseIf (NH4_MeasToPredict[i]>=0.75)
// Apply Equation 4
        CE_dry[i]= 0.0833+0.9167*ANMF[i]
   ElseIf (NH4_MeasToPredict[i]<0.75)
// Apply Equation 6
        CE_dry[i]= 1-0.73*NH4_MeasToPredict[i]
   EndIf
EndFor
// Make CE_dry between 0.5 and 1
CE_dry=min(1,(max(0.5,CE_dry)))
If (WaveExists(RH_SL)==1)
// Apply Equation 7
   CE_fPhase=(5*CE_dry-4)+(1-CE_dry)/20*RH_SL
   For (i=0;i<numpnts(CE_fPhase)+1;i+=1)
        If (RH_SL[i]<80 || numtype(RH_SL[i])==2 )
            CE_fPhase[i]=CE_dry[i]
        EndIf
   EndFor
Else
   CE_fPhase=CE_dry
EndIf
Edit root:ACSM_Incoming:acsm_utc_time, CE_dry, CE_fPhase
KillWaves PredNH4_CE1
// Create CE-corrected waves for each species and their sum
SetDataFolder root:Time_Series:
wave NRPM1_CEcorr
Make/O/N=(numpnts(Org_raw)) Org=Org_raw/CE_fPhase
Make/O/N=(numpnts(Org_raw)) SO4=SO4_raw/CE_fPhase
Make/O/N=(numpnts(Org_raw)) NH4=NH4_raw/CE_fPhase
Make/O/N=(numpnts(Org_raw)) NO3=NO3_raw/CE_fPhase
Make/O/N=(numpnts(Org_raw)) Chl=Chl_raw/CE_fPhase
Make/O/N=(numpnts(Org)) NRPM1_CEcorr=Org+SO4+NH4+NO3+Chl
End
```

Procedure of CE correction for PMF matrices

```
#pragma rtGlobals=3      // Use modern global access method and strict wave access.
// Written by Hasna Chebaicheb then verified and commented by Veronique Riffault (IMT Nord
Europe)
```

// This function corrects the organic fragments matrix, as well as the associated error matrix, both generated for PMF analysis, for the composition-dependent collection efficiency (CDCE) which is not currently calculated within the ACSM_Local when creating these matrices.
// The CE_dry (or CE_fPhase) wave (named "CalCE_dry" in this function) needs to be imported into the PMF Igor experiment root folder prior to using this function.

Function CorrCE_ForPMF() // Written by Hasna Chebaicheb & verified by Veronique Riffault (IMT Nord Europe)

```
wave Org_mat = root:SoFi:External_data:Raw_input:Org_Specs
wave Err_mat = root:SoFi:External_data:Raw_input:OrgSpecs_err
wave CE = root:CalCE_dry
variable i,j
variable numOfRows = dimsize(Org_mat, 0)
variable numOfCols = dimsize(Org_mat, 1)

SetDataFolder root:SoFi:External_data:Raw_input:
make/O/N=(numOfRows,numofCols) Org_MxCE // This is the matrix that will need to be further selected for Org species concentrations.
make/O/N=(numOfRows,numofCols) Err_MxCE // This is the matrix that will need to be further selected for Org species errors.for (i=0; i<numOfRows; i += 1)

for (i=0; i<numOfRows; i += 1)
	for (j=0; j<numOfCols; j += 1)
		Org_MxCE[i][j]=Org_mat[i][j]/CE[i]
		Err_MxCE[i][j]=Err_mat[i][j]/CE[i]
	endfor
endfor
end
```

Annexe 4. European aerosol phenomenology − 8: Harmonised source apportionment of organic aerosol using 22 Year-long ACSM/AMS datasets; Chen et al. (2022)

Environment International 166 (2022) 107325

Contents lists available at ScienceDirect

Environment International

journal homepage: www.elsevier.com/locate/envint

Full length article

European aerosol phenomenology – 8: Harmonised source apportionment of organic aerosol using 22 Year-long ACSM/AMS datasets

Gang Chen [a], Francesco Canonaco [a,b], Anna Tobler [a,b], Wenche Aas [c], Andres Alastuey [d], James Allan [e,f], Samira Atabakhsh [g], Minna Aurela [h], Urs Baltensperger [a], Aikaterini Bougiatioti [i], Joel F. De Brito [j], Darius Ceburnis [k], Benjamin Chazeau [a,l,m], Hasna Chebaicheb [j,n], Kaspar R. Daellenbach [a], Mikael Ehn [o], Imad El Haddad [a], Konstantinos Eleftheriadis [p], Olivier Favez [n], Harald Flentje [q], Anna Font [r,1], Kirsten Fossum [k], Evelyn Freney [s], Maria Gini [p], David C Green [r,t], Liine Heikkinen [o,2], Hartmut Herrmann [g], Athina-Cerise Kalogridis [p], Hannes Keernik [u,v], Radek Lhotka [w,x], Chunshui Lin [k], Chris Lunder [c], Marek Maasikmets [u], Manousos I. Manousakas [a], Nicolas Marchand [l], Cristina Marin [y,z], Luminita Marmureanu [y], Nikolaos Mihalopoulos [i], Griša Močnik [aa,ab], Jaroslaw Nęcki [ac], Colin O'Dowd [k], Jurgita Ovadnevaite [k], Thomas Peter [ad], Jean-Eudes Petit [ae], Michael Pikridas [af], Stephen Matthew Platt [c], Petra Pokorná [w], Laurent Poulain [g], Max Priestman [r], Véronique Riffault [j], Matteo Rinaldi [ag], Kazimierz Różański [ac], Jaroslav Schwarz [w], Jean Sciare [af], Leïla Simon [n,ae], Alicja Skiba [ac], Jay G. Slowik [a], Yulia Sosedova [b], Iasonas Stavroulas [i,af], Katarzyna Styszko [ah], Erik Teinemaa [u], Hilkka Timonen [h], Anja Tremper [r,t], Jeni Vasilescu [y], Marta Via [d,ai], Petr Vodička [w], Alfred Wiedensohler [g], Olga Zografou [p], María Cruz Minguillón [d,*], André S.H. Prévôt [a,*]

[a] Laboratory of Atmospheric Chemistry, Paul Scherrer Institute, 5232 Villigen, Switzerland
[b] Datalystica Ltd., Park innovAARE, 5234 Villigen, Switzerland
[c] NILU - Norwegian Institute for Air Research, 2007 Kjeller, Norway
[d] Institute of Environmental Assessment and Water Research (IDAEA), Spanish Council for Scientific Research (CSIC), Barcelona, 08034, Spain
[e] Department of Earth and Environmental Sciences, University of Manchester, Manchester, UK
[f] National Centre for Atmospheric Science, University of Manchester, Manchester, UK
[g] Department of Chemistry of the Atmosphere Leibniz Institute for Tropospheric Research, Permoser Straße 15, 04318 Leipzig, Germany
[h] Atmospheric Composition Research, Finnish Meteorological Institute, P.O. Box 503, 00101 Helsinki, Finland
[i] Institute for Environmental Research and Sustainable Development, National Observatory of Athens, Palaia Penteli, 15236 Athens, Greece
[j] IMT Nord Europe, Institut Mines-Télécom, Univ. Lille, Centre for Energy and Environment, 59000 Lille, France
[k] School of Physics, Ryan Institute's Centre for Climate and Air Pollution Studies, National University of Ireland Galway, University Road, Galway H91 CF50, Ireland
[l] Aix Marseille Univ., CNRS, LCE, Marseille, France
[m] AtmoSud, Regional Network for Air Quality Monitoring of Provence-Alpes-Côte-d'Azur, Marseille, France
[n] Institut National de l'Environnement Industriel et des Risques, Parc Technologique ALATA, 60550, Verneuil en Halatte, France
[o] Institute for Atmospheric and Earth System Research (INAR)/Physics, University of Helsinki, Helsinki, Finland
[p] Environmental Radioactivity Laboratory, Institute of Nuclear & Radiological Sciences & Technology, Energy & Safety, N.C.S.R. "Demokritos", 15310 Athens, Greece
[q] Deutscher Wetterdienst, Meteorologisches Observatorium Hohenpeißenberg, 82383 Hohenpeißenberg, Germany
[r] MRC Centre for Environment and Health, Environmental Research Group, Imperial College London, 86 Wood Lane, London W12 0BZ, UK
[s] Laboratoire de Météorologie Physique, UMR6016, Université Clermont Auvergne-CNRS, Aubière, France
[t] HPRU in Environmental Exposures and Health, Imperial College London, UK
[u] Air Quality and Climate Department, Estonian Environmental Research Centre (EERC), Marja 4D, Tallinn, Estonia
[v] Department of Software Science, Tallinn University of Technology, 19086 Tallinn, Estonia
[w] Institute of Chemical Process Fundamentals of the CAS, Rozvojová 135/1, 16502 Prague, Czech Republic
[x] Institute for Environmental Studies, Faculty of Science, Charles University, Benátská 2, 12801 Prague, Czech Republic
[y] National Institute of Research and Development for Optoelectronics INOE 2000, 77125 Magurele, Romania
[z] Department of Physics, Politehnica University of Bucharest, Bucharest,Romania

* Corresponding authors.
E-mail addresses: mariacruz.minguillon@idaea.csic.es (M. Cruz Minguillón), andre.prevot@psi.ch (A.S.H. Prévôt).

https://doi.org/10.1016/j.envint.2022.107325
Received 24 December 2021; Received in revised form 5 May 2022; Accepted 26 May 2022
Available online 30 May 2022

[aa] Condensed Matter Physics Department, J. Stefan Institute, Ljubljana, Slovenia
[ab] Center for Atmospheric Research, University of Nova Gorica, Ajdovščina, Slovenia
[ac] AGH University of Science and Technology, Faculty of Physics and Applied Computer Science, Department of Applied Nuclear Physics, Kraków, Poland
[ad] Institute for Atmospheric and Climate Sciences, ETH Zürich, Zürich, 8092, Switzerland
[ae] Laboratoire des Sciences du Climat et de l'Environnement, UMR 8212, CEA/Orme des Merisiers, 91191 Gif-sur-Yvette, France
[af] Climate & Atmosphere Research Centre (CARE-C), The Cyprus Institute, Nicosia, 2121, Cyprus
[ag] Institute of Atmospheric Sciences and Climate (ISAC), National Research Council (CNR), 40129 Bologna, Italy
[ah] AGH University of Science and Technology, Faculty of Energy and Fuels, Department of Coal Chemistry and Environmental Sciences, Kraków, Poland
[ai] Department of Applied Physics, University of Barcelona, Barcelona 08028, Spain

ARTICLE INFO

Handling Editor: Adrian Covaci

Keywords:
European Overview
Source apportionment
Harmonised Protocol
Organic Aerosol
Long-term Datasets
Rolling PMF

ABSTRACT

Organic aerosol (OA) is a key component of total submicron particulate matter (PM_1), and comprehensive knowledge of OA sources across Europe is crucial to mitigate PM_1 levels. Europe has a well-established air quality research infrastructure from which yearlong datasets using 21 aerosol chemical speciation monitors (ACSMs) and 1 aerosol mass spectrometer (AMS) were gathered during 2013–2019. It includes 9 non-urban and 13 urban sites. This study developed a state-of-the-art source apportionment protocol to analyse long-term OA mass spectrum data by applying the most advanced source apportionment strategies (i.e., rolling PMF, ME-2, and bootstrap). This harmonised protocol was followed strictly for all 22 datasets, making the source apportionment results more comparable. In addition, it enables quantification of the most common OA components such as hydrocarbon-like OA (HOA), biomass burning OA (BBOA), cooking-like OA (COA), more oxidised-oxygenated OA (MO-OOA), and less oxidised-oxygenated OA (LO-OOA). Other components such as coal combustion OA (CCOA), solid fuel OA (SFOA: mainly mixture of coal and peat combustion), cigarette smoke OA (CSOA), sea salt (mostly inorganic but part of the OA mass spectrum), coffee OA, and ship industry OA could also be separated at a few specific sites. Oxygenated OA (OOA) components make up most of the submicron OA mass (average = 71.1%, range from 43.7 to 100%). Solid fuel combustion-related OA components (i.e., BBOA, CCOA, and SFOA) are still considerable with in total 16.0% yearly contribution to the OA, yet mainly during winter months (21.4%). Overall, this comprehensive protocol works effectively across all sites governed by different sources and generates robust and consistent source apportionment results. Our work presents a comprehensive overview of OA sources in Europe with a unique combination of high time resolution (30–240 min) and long-term data coverage (9–36 months), providing essential information to improve/validate air quality, health impact, and climate models.

1. Introduction

Atmospheric aerosols are liquid or solid particles suspended in the atmosphere (Hinds, 1999), which cause serious adverse health effects, reduce visibility, and interact with ecosystems and climate (IPCC, 2021). Despite all efforts, Europe is still suffering from poor air quality. Specifically, the European Environment Agency (EEA) (2021) reported that 2% of the reporting countries exceeded the annual $PM_{2.5}$ (atmospheric particulate matter (PM) with an aerodynamic diameter of 2.5 μm or less) limit value of EU legislation (25 $\mu g/m^3$) in 2019. Following the even stricter 2021 WHO $PM_{2.5}$ guidelines (5 $\mu g/m^3$), all reporting countries, except Estonia, were over the limit that year (European Environment Agency (EEA), 2021; World Health Organization, 2021). Therefore, it is more important than ever to mitigate the air pollution levels. Moreover, premature deaths attributed to long-term exposure to $PM_{2.5}$ in 27 EU member states reached 307,000 in 2019 (European Environment Agency (EEA), 2021). As one of the most significant aerosol components, organic aerosol (OA) gained extensive interest since it represents 20 to 90% of the mass of the total submicron aerosol (Crippa et al., 2014; Jimenez et al., 2009; Zhang et al., 2011, 2007). Importantly, a simple reduction of $PM_{2.5}$ or even OA might not be an effective strategy to mitigate the health impacts of aerosol because OA components from different sources have different toxicities (Daellenbach et al., 2020). In addition, various sources/compositions of OA can also have significant differences in climate forcing (Yang et al., 2018). Therefore, a comprehensive knowledge of the OA sources could provide more information for regional, global climate, or air quality models for emission inventories, parameterization, or validation.

Typically, OA sources are identified using the receptor model positive matrix factorisation (PMF) on data from an Aerodyne aerosol mass spectrometer (AMS; (Jayne et al., 2000)). Many studies have reported a broad spatial overview of OA sources, providing the chemical composition of the bulk non-refractory PM_1 and, more recently, also $PM_{2.5}$ (Elser et al., 2016; Xu et al., 2017). Zhang et al. (2007) first reviewed the use of factor analysis to investigate OA sources in urban and rural/remote sites in the Northern Hemisphere. Jimenez et al. (2009) provided an overview of PM_1 chemical composition and OA sources worldwide (including eight European sites), while Ng et al. (2010) provided a big picture of OA sources over the Northern Hemisphere in various environments (including 43 AMS datasets). PM_1 chemical composition and OA sources in Central Europe, including Switzerland, Germany, Austria, France, and Liechtenstein, have been described more specifically in Lanz et al. (2010). Finally, an overview of the OA sources across Europe using 25 AMS datasets, combined with guidelines for source apportionment (SA) applications to AMS data, resulted from the work of (Crippa et al., 2014). However, the AMS requires labour-intensive maintenance, making it extremely difficult to run continuously over a long period. Most of the AMS datasets in previous studies only covered time periods up to a few months, and the seasonal variations of OA sources in Europe remain mostly unknown without consistent long-term SA studies. Therefore, a network of on-line chemical composition measurements has been built up within the well-established European Aerosol, Clouds and Trace gases Research InfraStructure (ACTRIS, http://actris.eu), consisting of 1 AMS and 21 Aerodyne Aerosol Chemical Speciation Monitors (ACSM, (Fröhlich et al., 2013; Ng et al., 2011b)), the latter being a simpler and more robust version of the AMS. With these data, it is possible to address a critical knowledge gap in the literature, i.e., the seasonal, diurnal, and spatial variabilities of OA sources across Europe.

An important limitation of the conventional PMF applications for long-term datasets is that OA sources are assumed to be static over the entire sampling period, although the source profiles of OA have substantial seasonal variations (Canonaco et al., 2015; Crippa et al., 2014;

[1] Now at: IMT Nord Europe, Institut Mines-Télécom, Univ. Lille, Centre for Energy and Environment, 59000 Lille, France.
[2] Now at: Department of Environmental Science & Bolin Centre for Climate Research, Stockholm University, Stockholm, Sweden.

Zhang et al., 2019). This study applies a novel SA technique, rolling PMF (Canonaco et al., 2021; Parworth et al., 2015), to account for the temporal variabilities of the factor profiles. Instead of running PMF for the whole dataset, this work applies a smaller time window (e.g., varying from 7 to 28 days), moving with daily steps over the entire dataset (typically around one year). This allows the model to gradually adapt the factor profiles across different observational periods. In addition, the rolling technique has been equipped with random input resampling and random variation of the constraints allowing for a quantitative estimate of the statistical and rotational uncertainties of the PMF solutions (Canonaco et al., 2021; Chen et al., 2021). Meanwhile, rolling PMF can facilitate the analysis while handling the long-term ACSM/AMS datasets by saving computational time compared to conventional seasonal bootstrap PMF.

The comparison of SA results from different sites is challenging, as they are not always equivalent due to the subjective decisions made by the analysts during the different PMF analysis steps, especially regarding the optimal number of factors, their identification, and validation. For that reason, a standardised protocol (Section 2.3) has been developed to ensure comparability between results obtained from different sites/instruments. According to this protocol, rolling PMF is performed following the latest and most advanced statistical features present within the Source Finder Professional (SoFi Pro) package (Datalystica Ltd., Villigen, Switzerland, (Canonaco et al., 2021, 2013)) integrated into the Igor Pro software (WaveMetrics Inc., Lake Oswego, OR, USA). Although subjective judgements cannot be avoided entirely, the developed protocol aims to minimise the number of decisions to be made by the user.

This highly time-resolved information of OA sources in Europe could substantially improve the development, validation, and prediction of regional/global air quality/climate models by providing extra independent information. These results could also be helpful to health-related studies when trying to accurately predict the toxicity of atmospheric aerosol since OA has significantly different health impacts depending on its origin (Daellenbach et al., 2020). Multiple years of data are finally needed to assess the impact of particulate matter sources on morbidity and mortality due to chronic exposure (Liu et al., 2019; Yang et al., 2019). Eventually, this work will provide valuable information for policymakers to take the most effective mitigation measures for aerosol-related environmental problems. Overall, this study presents a comprehensive overview of OA sources across Europe by following a thoroughly-designed and harmonised protocol (Section 2.3). Specifically, the seasonal/spatial variability of OA sources regarding time series and source profiles are unfolded in the following sections.

2. Measurements and instrumentation

This study is the main outcome of the Chemical On-Line cOmpoSition and Source Apportionment of fine aerosoL (COLOSSAL) project (https://www.costcolossal.eu/), based on measurements performed within ACTRIS. In total, 22 year-long datasets were used here from 14 different countries via ACSM/AMS since 2013 (Fig. 1). This study includes data from 18 Q-ACSM (quadrupole ACSM, (Ng et al., 2011b)), 3 ToF-ACSM (Time-of-Flight ACSM (Fröhlich et al., 2013)), and 1 C-ToF-AMS (compact time-of-flight AMS (Drewnick et al., 2005)).

Overall, the ACSM and AMS considered here apply similar techniques. Briefly, the air is passing through a critical orifice into an aerodynamic lens, where atmospheric aerosol is focused and accelerated (the smaller the aerodynamic size, the higher the velocity) into a vacuum chamber (10^{-5} Torr) and impacts on the surface of a standard vaporiser heated at 600 °C. The resulting vapours are then ionised by electron ionisation (70 eV), and these ions are further extracted into the mass analyzer. Compared to the AMS, the ACSM is more robust, affordable, and easier to operate, making it suitable for long-term monitoring purposes. However, it cannot measure the size-resolved chemical composition and its time and mass resolutions are poorer compared to the AMS. Most of the ACSMs deployed here participated in an inter-comparison activity conducted by the Aerosol Chemical Monitor Calibration Centre (ACMCC) at SIRTA (https://sirta.ipsl.fr/) and reported consistent results as long as proper calibrations were conducted (Crenn et al., 2015; Freney et al., 2019). One of the objectives of the COLOSSAL project is to deliver a harmonised standard operating procedure (SOP) for ACSMs (COLOSSAL, 2021), and most of the 22 datasets were collected by following this SOP. However, the recommended relative ionisation efficiency (RIE) calibration procedures have varied over the long-time span of these datasets (2013–2019). For instance, some of the datasets conducted RIE calibration only on specific *m/z* values (jump scan) as recommended earlier, instead of scanning the entire mass range (*m/z* 10 to 150) of the mass spectrometer (Freney et al., 2019). Considering the nitrate interference on the CO_2^+ signal at *m/z* 44 (so-called Pieber effect) is time-dependent (Freney et al., 2019; Fröhlich et al., 2015; Pieber et al., 2016) and *m/z* 44 is not measured in jump scan RIE calibrations, it is thus impossible to do a post-correction consistently. Therefore, none of the datasets was corrected for the Pieber

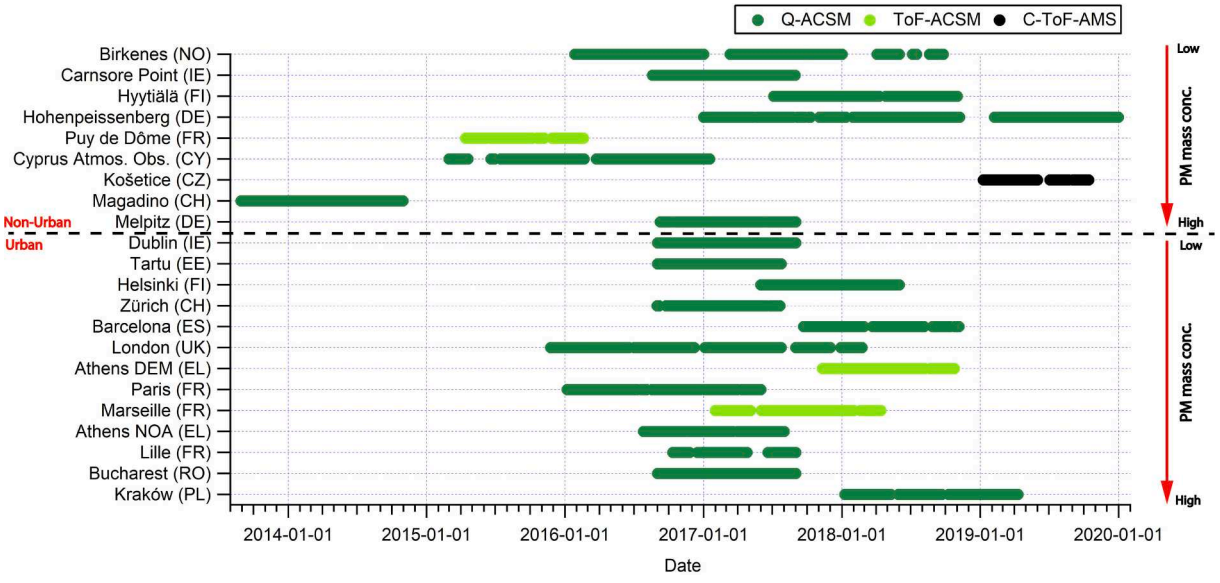

Fig. 1. ACSM/AMS measurement periods considered in this study.

effect. However, it is assumed that such artefact would not represent more than 25% (as maximum, e.g., during severe ammonium nitrate pollution episodes) of total OA readings by AMS/ACSM used for the present study.

Complementary to ACSM/AMS measurements, equivalent black carbon (eBC) was also monitored at all sites using filter-based absorption photometers. It was typically measured using Multi Angle Absorption Photometer (MAAP) (Thermo) or Aethalometer Model AE33 (Magee Scientific) devices and predominantly with default settings as proposed by the manufacturer (i.e., with no extra data correction procedures). In the case of multi-wavelength instruments (e.g., AE33 or former AE31 devices), eBC concentrations were reported from measurements at 880 nm, and solid/liquid fuel-burning eBC subfractions (noted eBC_{wb} and eBC_{ff}, for wood burning, and fossil fuel, respectively, hereafter) were distinguished from each other based on the application of the so-called Aethalometer model (Sandradewi et al., 2008; Zotter et al., 2017).

The 22 sampling sites are classified based on their geographic locations as urban (13 sites, including four flagged as suburban: Athens DEM, Lille, Paris, and Bucharest) or non-urban (9 sites, Table S1). The chemical composition of some of these 22 datasets have already been reported (Barreira et al., 2021; Bressi et al., 2021). This study focuses on the overview of OA source apportionment results and includes new sites in our analysis. More details about source apportionment results at some of these sites can be found in the following published papers: (Barreira et al., 2021; Canonaco et al., 2021; Chazeau et al., 2022, 2021; Chen et al., 2021; Farah et al., 2021; Heikkinen et al., 2021; Lin et al., 2019; Minguillón et al., 2015; Petit et al., 2021; Poulain et al., 2020; Stavroulas et al., 2019; Tobler et al., 2021; Via et al., 2021; Yttri et al., 2021; Zhang et al., 2019).

2.1. Positive matrix factorisation (PMF) and multilinear engine (ME-2)

PMF has been customarily performed to conduct source apportionment of ambient aerosol data (e.g., ACSM/AMS data) in many previous studies (Lanz et al., 2007; Ulbrich et al., 2009; Zhang et al., 2011). PMF model was first introduced by Paatero and Tapper, (1994) as follows:

$$x_{ij} = \sum_{k=1}^{p} g_{ik} \times f_{kj} + e_{ij} \quad (1)$$

where x_{ij} is the elements of the matrices for the measurements, g_{ik} is the factor time series, f_{kj} is the factor profiles, and e_{ij} is the PMF residuals. The subscripts i, j, and k represent time, m/z, and a discrete factor, respectively. The superscript, p represents the number of factors. PMF finds the model solution by using the least-squares algorithm by iteratively minimising the following quantity:

$$Q = \sum_{i=1}^{n} \sum_{j=1}^{m} \left(\frac{e_{ij}}{\sigma_{ij}}\right)^2 \quad (2)$$

where σ_{ij} is the measurement uncertainty.

However, the PMF model does not provide a mathematically unique solution, an issue which is usually referred to as rotational ambiguity (Paatero et al., 2002). Specifically, the model can deliver the identical value of Q for a combination of the matrices **G** (time series) and **F** (factor profiles) and for a combination of their rotations $\boldsymbol{G}_{-}$ and F_{-} (with $G_{-} = \boldsymbol{G} \bullet T$ and $F_{-} = T^{-1} \bullet F$). In this case, Q is the same, despite the solution being possibly entirely different. Even though the non-negativity constraints limit the number of allowed rotations, there are still many possible rotations and thus solutions. In order to reduce the rotational ambiguity of the PMF model, Paatero and Hopke (2009) proposed a multilinear engine (ME-2) algorithm, which allows the addition of *a priori* information into the model (e.g., source profiles or time series of external data (i.e., data external to the PMF input matrices)) to avoid unrealistic rotations and to generate more unique solutions. Using a priori information allows the user to guide the model towards an environmentally reasonable solution. Canonaco et al. (2013) implemented an ME-2 solver (Paatero, 1999) into the Igor-based software package, Source Finder (SoFi). SoFi enables the users to have enhanced rotational control over the factor solutions by imposing constraints via, e.g., the *a*-value approach, on one or more elements of **F** and/or **G** (Paatero and Hopke, 2009). For instance, the a value (ranging from 0 to 1) is the tolerated relative deviation of a factor profile (f_k) or time series (g_k) from the chosen a priori input profile (F_k) or time series (G_k) during the iterative least-square minimization, as demonstrated in Equations (3a) and (3b) (Canonaco et al., 2013):

$$f_k = F_k \pm a \bullet F_k \quad (3a)$$

$$g_k = G_k \pm a \bullet G_k \quad (3b)$$

2.2. Rolling PMF analysis with bootstrap and random a-value approach

Conventional PMF is conducted over the whole dataset, with the assumption that the OA source profiles are static, which can lead to high errors when it comes to long-term datasets considering that OA chemical fingerprints are expected to vary over time (Paatero et al., 2014). For instance, (Canonaco et al., 2015) showed a substantial seasonal variability of oxygenated organic aerosol (OOA) factor profiles. Parworth et al. (2015) first proposed to run PMF analysis on a smaller time window (e.g., 14 days) to roll over the whole dataset with a certain step. This technique was further refined by Canonaco et al. (2021). The rolling PMF window mechanism allows the PMF model to adapt the temporal variations of the source profiles (e.g., biogenic versus biomass burning influences on OOA), which usually provides well-separated OA factors. In addition, with the help of the bootstrap strategy (Efron, 1979) and the random *a*-value approach, users can estimate the statistical and rotational uncertainties of the PMF results (Canonaco et al., 2021).

2.3. A standardised protocol of SA for a long-term dataset using SoFi pro

This work presents a standardised protocol to identify main OA components. These guidelines work well for all 22 datasets despite the various pollution sources and OA levels at the different stations. All 22 datasets were analysed by following the protocol described in this study to minimise user subjectivity. Fig. S1 provides the general working flow of this protocol, while the more detailed step-by-step guideline is summarised in Table 1. Detailed explanations of each step are unfolded in the following subsections.

2.3.1. Seasonal PMF pre-tests

To effectively implement rolling PMF analysis, knowing potential sources for each season for any given site is crucial. Seasonal PMF *pre-tests* allow us to retrieve reasonable seasonal PMF results (so-called base case). The first step of the *pre-tests* is to conduct unconstrained PMF with varying factors from 2 to 8 for each season. Based on the time series, diel patterns, factor profiles, and correlation with external data, the number of factors for each season could potentially be pre-determined. Examining a solution up to a relatively high number of factors (8 in this case) is crucial as some primary factors (e.g., HOA, BBOA, COA, and CCOA) might only appear in the PMF solution when the number of factors increases. Given the similar chemical fingerprints of some of the primary sources, it is possible that for a low number of factors, they remain mixed (e.g., HOA and COA). In this section, the approach used to identify each source type effectively is covered in the following paragraphs.

For a site potentially impacted by traffic, it is suggested to constrain the HOA mass spectrum using the one from Crippa et al. (2013) with a tight a value (0.05–0.1) and a narrower range of factors (3–7). Typically, the HOA factor has a pronounced diel pattern with distinct morning and evening rush hour peaks, and the HOA factor profile is typically similar among different sites (Crippa et al., 2014). However, when the diel pattern does not show the typical variability expected from traffic emissions, one should consider using the HOA mass spectrum from

Table 1
Step-by-step protocol for running rolling PMF.

	Detailed steps
1. **Seasonal PMF *pre-tests***	1.1. Unconstrained runs (2–8 factors) 1.2. Test for the presence of OA factors (in order of hydrocarbon-like OA (HOA), biomass burning OA (BBOA), cooking-like OA (COA), coal combustion OA (CCOA), special local factors (if applicable), and OOA factors) 1.3. Residual analysis (no structural patterns in diel profiles/time series/mass spectra) 1.4. *a*-value sensitivity analysis for constrained factors (i.e., primary OA factors (POAs))
2. **Seasonal bootstrap analysis**	2.1. Constrain the POAs and site-specific factor(s) in mass spectra retrieved from base case (the satisfactory solutions from seasonal *pre-tests*) 2.2. Combine the bootstrap resampling strategy with random *a*-values with an upper *a*-value of 0.4–0.5 for POAs and site-specific factor(s) and a repeat of 100–1000 times 2.3. Use the same technique as mentioned in step 4 (see later) to filter out PMF runs that are not environmentally reasonable 2.4. Quality check for the bootstrapped solution
3. **Rolling PMF**	3.1. Constrain primary factor MS using published profiles or averaged site-specific profiles from seasonal bootstrapped solutions 3.2. Constrain site-specific factor MS (if those exist) using random *a*-value approach within a range of 0–0.4 and a step of 0.1. An upper limit of 0.5 for BBOA *a*-value could be considered 3.3. Enable bootstrap and set the length of the PMF window (7, 14 or 28 days) 3.4. Set the range of the number of factors based on the number of factors obtained during the seasonal analysis
4. **Criteria-based selection for PMF runs** (Table S2)	4.1. Define a sorting criterion for more oxidised-oxygenated OA (MO-OOA) (f_{44} for the MO-OOA) in case there are two unconstrained OOA factors 4.2. Selection criteria of PMF solutions based on correlations with external tracers 4.3. Selection criteria of PMF solutions based on time series (e.g., hours of COA, explained variation of key ions by specific factor) 4.4. Define the "best" PMF runs using the relevant/appropriate statistical tests (e.g., *t*-test approach) 4.5. Optimize time windows (compare non-modelled points and Q/Q_{exp} among different time windows)

unconstrained PMF runs or loosen the *a-value* for HOA from Crippa et al. (2013). When a BBOA-like factor exists in both unconstrained and HOA-constrained runs, the "local" BBOA spectrum retrieved from these runs are recommended to be used as a constraint/reference profile in the next step of the PMF analysis. This is because of the relatively large spatial variabilities of BBOA factor profiles (Crippa et al., 2014). The expected BBOA factor usually has a pronounced contribution of *m/z* 29, 60, and 73 signals and a distinct diel pattern with high concentration during nighttime. If the BBOA factor was not present in previous steps, it should be checked if f_{60} (i.e., the fraction of *m/z* 60 to the total organic mass) is above the background level of 0.3% (Cubison et al., 2011), and also has a clear temporal pattern beyond the noise. However, f_{60} should not be the only criterion to determine the existence of BBOA (the background level of f_{60} is instrument-dependent). Constrained PMF runs with a reference BBOA spectrum (Crippa et al., 2013; Ng et al., 2011a) and a relatively high *a*-value (0.3–0.5) need to be performed to seek more proof of its existence by (i) comparing the solution without a BBOA factor; (ii) by checking the correlation factor between HOA vs eBC_{ff}, BBOA vs eBC_{wb}; and (HOA + BBOA) vs eBC_{total}; (iii) by checking if the solution has smaller scaled residuals of *m/z* 60, etc. One should keep in mind that the model performance metrics should determine the choice of reference BBOA profile.

If different slopes in f_{55} vs f_{57} plots at different hours of the day point towards the presence of COA (Mohr et al., 2012), it should be constrained tightly using the corresponding spectrum from Crippa et al. (2013) with an *a* value of 0.05–0.1. Then, it should be checked if the diel pattern (mass concentration or mass fraction) is reasonable, i.e., it peaks during the time of expected cooking-related activities (noon/afternoon and evening peaks). The COA factor is typically only present in urban environments close to residential and commercial areas.

For an environment with potential coal combustion sources, looking for a "local" CCOA factor mass spectrum from unconstrained or HOA-constrained PMF runs is recommended. However, it is typically challenging to identify the CCOA factor with ACSM data when its contribution is not significant because of the relatively low *m/z* resolution and since the mass range (up to 100/120 for Q-ACSM) does not include polyaromatic hydrocarbons (PAHs). In addition, the similar spectral pattern of hydrocarbon ions (e.g., $C_nH_{2n-1}^+$ and $C_nH_{2n+1}^+$) between HOA, BBOA and CCOA makes it challenging for PMF to resolve these two factors (Sun et al., 2016). Therefore, the existence of CCOA should be justified at least by the most significant contribution of *m/z* 115 (mainly $C_9H_7^+$) and the absence of the morning rush hour peak.

Sometimes, PMF can also help picking up a site-specific factor with special fingerprints in previous steps (besides some common primary organic aerosols (POAs) and OOAs). In that case, the key ions should be checked to investigate potential sources, then the fragmentation table to understand how these key ions are calculated. Most importantly, OOA components should not be constrained as they are expected to vary season by season due to different precursor sources and oxidation capacity of the atmosphere. Typically, more and less oxidised-oxygenated OA (MO-OOA and LO-OOA, respectively) are found within the unconstrained factor(s). Here, the MO-OOA and low volatility oxygenated OA (LV-OOA) are interchangeable. The same applies to LO-OOA and semi volatile-oxygenated OA (SV-OOA). But we refer to these two OOA factors as MO-OOA and LO-OOA in the rest of the text. However, a static number of OOA factors for different seasons is highly recommended if it is environmentally reasonable since it remains challenging to objectively justify the exact transition period for the different number of factors at different periods.

Scaled residuals should be monitored throughout the PMF analysis. Structure in the scaled residuals' daily cycle might indicate missing or incompletely separated sources. In addition, spikes and structural patterns in the time series of the scaled residuals always require extra attention, as they suggest some high uncertainties of the current model for these points/periods or instrument issues. Also, if the constrained profiles cause systematic patterns in the residuals, they should be reconsidered or tested with a larger *a* value. Last but not least, the *a*-value sensitivity analysis for constrained factors should be conducted to optimise (i.e., towards enhanced correlation with externals, reasonable factor profiles, and small scaled residual, etc.) the constrained factor to the dataset of interest. Then, once the reasonable PMF solution has been determined (so-called base case result), the mass spectra for all constrained factors are used as input factors for bootstrap analysis in the next step.

2.3.2. Seasonal bootstrap analysis

A bootstrap resampling strategy (Efron, 1979) is recommended to test the stability of the base case solutions. Therefore, all the mass spectra of constrained factors (i.e., POAs and site-specific factors) should be constrained using the random *a*-value technique (Canonaco et al., 2021; Chen et al., 2021) with an upper *a* value of 0.4–0.5 and repeats of 100–1000. Next, the same technique mentioned in Section 2.3.4 should be used to filter out "incorrect" (not environmentally reasonable) solutions. As a next step, the quality of the averaged solution of selected PMF runs should be checked in terms of the uncertainties of factor profiles, time series, and percentage of selected runs. If the bootstrap solution shows significant uncertainties, the base case needs to be re-evaluated. The mass spectra for all constrained factors resulting from the bootstrap phase should be saved and used for the rolling PMF analysis in the

next step.

2.3.3. Rolling PMF

The mass spectra from bootstrapped solutions are recommended as the reference profiles to constrain POA and site-specific factors during rolling PMF. BBOA is known as the most spatiotemporally variable factor compared to all other POA factors (Crippa et al., 2014). Also, considering that the highest mass concentrations of BBOA occur in winter, the BBOA mass spectrum from the bootstrapped winter solution is recommended as the constraint, as it is more representative of the dataset. Alternatively, the published profiles (HOA and COA from Crippa et al. (2013) and BBOA from Ng et al. (2011a) or Crippa et al. (2013)) could be used (Canonaco et al., 2021). Canonaco et al. (2021) suggested using a random *a*-value technique (randomly select *a* values for each constraint within a certain range) and bootstrap resampling strategy to estimate the rotational uncertainties of rolling PMF. Based on the seasonal bootstrap analysis, the upper *a* value for the site-specific factors can be determined by the seasonal variation and uncertainties. Canonaco et al. (2021) showed that an upper value of 0.4 for POAs is sufficient to cover the temporal variabilities. However, an upper *a* value of 0.5 for BBOA is suggested when high temporal variabilities of the BBOA mass spectrum are expected. When the number of factors is not identical for all the seasons, the rolling PMF should be conducted with both n and $n + 1$ factors over the entire dataset.

2.3.4. Criteria-based selection for PMF runs

With the large number of PMF runs expected for rolling analysis (e.g., >15,000 runs for a one-year dataset with 30-min time-resolution), inspecting each single PMF run is not feasible. Therefore, a criteria-based selection should be used to (i) evaluate the quality of the PMF runs quantitatively and relatively objectively and (ii) sort out the unconstrained factors in the same order for further averaging. The criteria-based selection has been explicitly explained in Canonaco et al. (2021). In short, SoFi Pro enables the user to define criteria based on the time series and/or factor profiles to select environmentally reasonable solutions. In addition, this criteria-based selection function can also serve to reposition unconstrained factors as unconstrained factors can appear in random order in a different iteration of the PMF. The inexact sorting criteria can result in a mixing of the unconstrained factors. Therefore, it is crucial to use the most representative sorting criterion, i.e., f_{44} for the MO-OOA (criterion #7 in Table S2), as suggested by Chen et al. (2021). At the same time, it is also recommended to monitor f_{44} in MO-OOA and f_{43} in LO-OOA to reject zero-values of these two criteria. The criterion of f_{44}/f_{43} for MO-OOA is not recommended because it could accept PMF solutions with smaller f_{44} in MO-OOA than LO-OOA when f_{43} is extremely small. Statistical tests such as the *t*-test (Chen et al., 2021) for time series based criteria (#4, #5 and #7 in Table S2) and correlation-based criteria (#1, #2 and #3 in Table S2) should be performed to minimise subjective decisions. With a p value ≤ 0.05, it is possible to select PMF runs with statistically significantly higher scores compared to the same criterion for other factors (for time series based criteria) or statistically higher correlation with each other (for correlation-based criteria). This technique allows the user to select environmentally reasonable PMF solutions with minimal subjective judgements. Last but not least, the optimum length of the time window should be determined by minimising non-modelled data points and Q/Q_{exp} while applying the same criteria and thresholds to these PMF runs with different time windows (7, 14 or 28 days) (Canonaco et al., 2021; Chen et al., 2021). Based on our study, a 14-day window size is the most commonly selected one, which is consistent with previous studies (Canonaco et al., 2021; Chen et al., 2021).

2.3.5. Special cases and limitations of the current protocol

For all the 22 ACSM/AMS datasets, this standardised protocol works well in general. However, different numbers of factors at different periods remain challenging for rolling PMF. There are three special cases that this protocol could not cover. Specifically, the BBOA factor is not present in the warm period for the Barcelona, Cyprus, and Marseille datasets. However, this protocol could not cover such situations with a proper criterion to objectively include/exclude certain OA factors (e.g., BBOA) in certain time periods. The distribution of the correlation between BBOA and eBC_{wb} was utilised for the Marseille data, which appears to have a bimodal Fisher distribution. Thus, the 10th percentile results from the separated distributions were used as thresholds to define the existence of BBOA (Chazeau et al., 2022). For the Barcelona and Cyprus datasets, the criterion to decide the existence of BBOA is the explained variation of f_{60} by BBOA. A *t*-test was conducted with the null hypothesis that the variation of f_{60} explained by BBOA is not significantly larger than that of other factors. The presence of BBOA is only considered when the p value was ≤ 0.05. In addition, as discussed before, a different number of factors often suffers from more uncertainties at the edge of the transition period by averaging different numbers of factor solutions simultaneously. One strategy to avoid averaging over different numbers of factor solutions is to unselect any data point in a range of *edge* $\pm$ *window length/2*. However, it could potentially lead to relatively more non-modelled points during the transition period. Therefore, keeping a static number of factors in the rolling analysis as much as possible is recommended if that is environmentally feasible. Thus, it remains challenging to objectively define the transition point to an improved source apportionment for rolling PMF analysis with a different number of OA factors.

3. Results and discussions

Figure 2 provides an overview of the mean OA mass fractions and their main components at 22 stations across Europe. Overall, the total PM_1 (sum of OA, eBC, nitrate (NO_3), sulfate (SO_4), ammonium (NH_4), and chloride (Chl)) mass concentration has an average of 9.7 ± 7.9 μg/m^3, with generally higher concentrations at urban stations (brown circles, avg = 12.2 ± 9.3 μg/m^3) compared to non-urban ones (green circles, avg = 6.2 ± 3.3 μg/m^3). Kraków is the most polluted site (40.4 μg/m^3), and Birkenes is the cleanest (1.3 μg/m^3). The OA contribution to the total submicron aerosol ranges from 21 to 75%, which is consistent with previous results based on shorter campaigns (Jimenez et al., 2009). For other main chemical species, eBC, NO_3, SO_4, NH_4, and Chl exhibit an average contribution to the total PM_1 of 10.0%, 15.0%, 16.2%, 9.9% and 1.2%, respectively. eBC and NO_3 show higher contributions at the urban sites (12.1% and 16.2%) than at the non-urban ones (6.8% and 13.3%).

3.1. Overview of the primary and secondary OA

Primary and secondary OA factors are identified for each station in Fig. 2. In this study, all the OA factors except MO-OOA and LO-OOA are considered as POA factors. Overall, the well-known POA factors have been resolved, including HOA and BBOA. All datasets identify HOA except Hyytiälä (non-urban). BBOA is resolved in 19 datasets (12 urban and 7 non-urban sites) with the exceptions being Hyytiälä, Puy de Dôme, and Helsinki. In general, both HOA and BBOA present considerable fractions of the total submicron aerosol with average contributions of 5.0% and 5.6%, respectively. Also, they both show higher contributions at the urban sites (HOA: 5.7% and BBOA: 6.3%) than at the non-urban ones (HOA: 4.0% and BBOA 4.5%). COA is identified in three southern European cities (i.e., Athens, Marseille, and Barcelona), a megacity (London), and a central European city (Zürich). It has an average contribution to the total PM_1 of 6.3%. CCOA is resolved in Kraków (Tobler et al., 2021) and Melpitz (non-urban) with contributions of 5.8% and 6.9%, respectively. SFOA, which likely originates from peat and coal combustion, appears at the two Irish sites (Dublin (urban) and Carnsore Point (non-urban), with contributions of 12.2% and 6.0%, respectively. In addition, local factors (i.e., specific to a single monitoring site) are highlighted in this study: an m/z 58-related OA (58-OA) in Magadino (1.2%); a coffee roaster OA factor in Helsinki (3.0%); a sea salt factor at

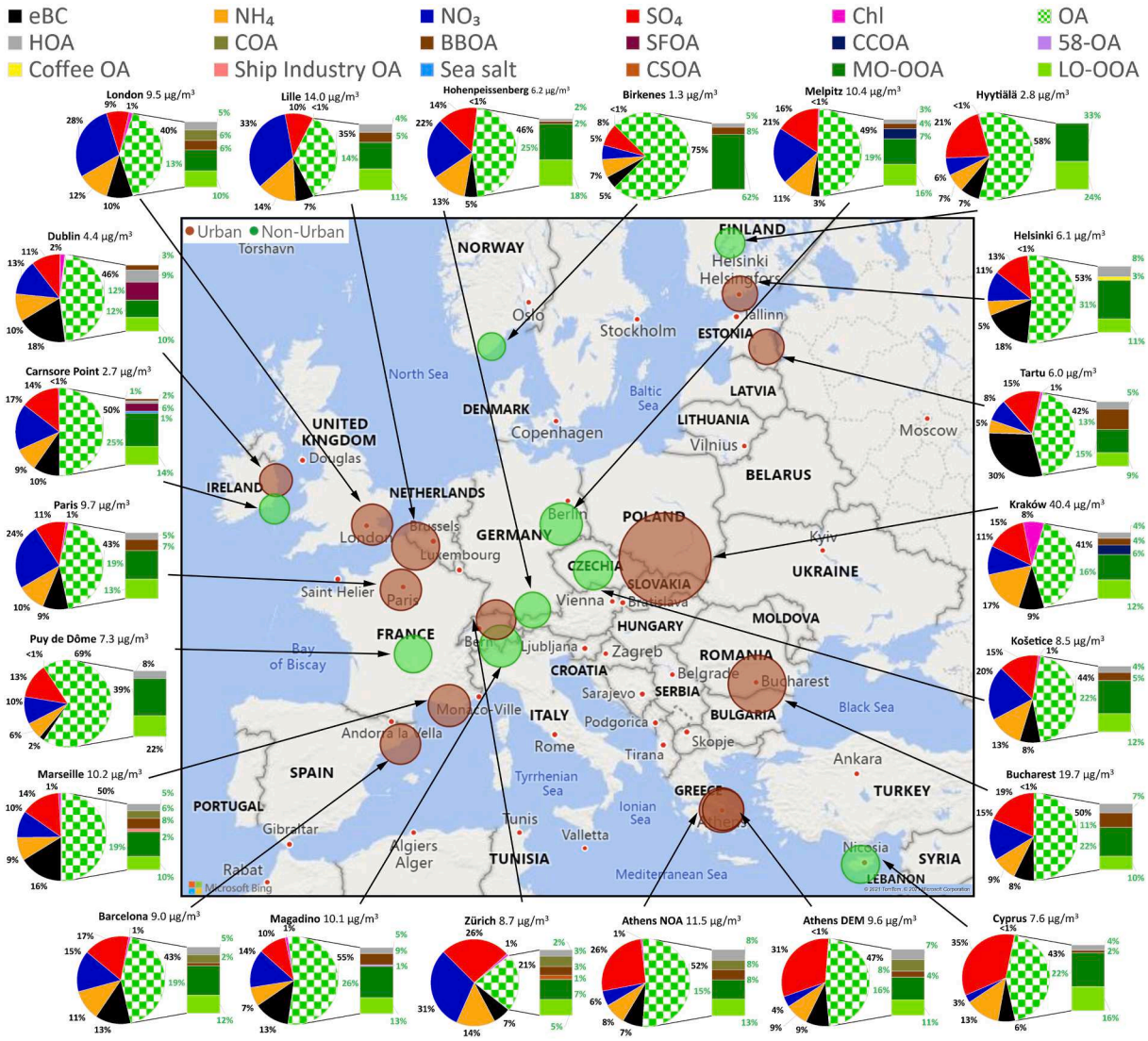

Fig. 2. Submicron particulate matter (PM_1) mass concentration (in $\mu g/m^3$) and mass fractions of non-refractory inorganic species, equivalent black carbon (measured by online filter-based methods), and organic aerosol measured with the 22 ACSM/AMS at multiple locations in Europe covering all seasons. The size of the markers corresponds to the PM_1 mass concentration. The brown colour of the marker indicates an urban site, while the green marker indicates a non-urban site. The checkered green/white shading of the pie charts denotes the organic aerosol (OA) fraction in PM_1, and the bar charts represent the contributions of each OA factor to the total OA mass.

Carnsore Point (1.5%); cigarette smoking OA (CSOA) in Zürich (Qi et al., 2019; Stefenelli et al., 2019); and a mixed ship-industry factor in Marseille (2.2%, Chazeau et al., 2022). Finally, two secondary OOA factors (MO-OOA and LO-OOA) are present at all sites except for Birkenes (MO-OOA only). The MO-OOA and LO-OOA contribute to the total PM_1 with an average of 22.0% and 13.1%, respectively. Both MO-OOA and LO-OOA show drastic differences among urban (16.7% and 10.6%) and non-urban sites (29.6% and 17.2%), which is expected since more primary sources are present in the urban environment. When summing up MO-OOA and LO-OOA (Total OOA), Fig. 2 suggests that secondary OA is the main contributor to total submicron PM (average = 34.5%, range from 11.7 to 62.4%) and dominates OA (average = 71.1%, range from 47.3 to 100%) across Europe.

In addition, the resolved OA factors have been validated using data external to the PMF input matrices as well as the mass conc. of m/z 60 in the organic matrix (Table S4). These external data include NH_4, NO_3, SO_4, which were obtained from ACSM/AMS, and eBC was measured by AE33/AE31/MAAP. Regarding the PMF errors (Equation (6) in Canonaco et al. (2021)), they are estimated by logarithmic probability density functions (pdf) of the standard deviations of each time point i divided by the mean concentration of each time point i for corresponding OA factors. The PMF errors of major OA components are presented in Table S6. In general, POAs often have smaller PMF errors than OOA factors since they are always constrained.

3.2. OA composition changes as a function of OA loading

To understand how the OA composition changes under different loadings, each dataset is divided into ten bins containing the same number of points based on the OA mass concentrations. As shown in Fig. 3, apart from Zürich and Helsinki, all urban as well as two non-urban sites (Magadino and Melpitz) report larger POA contributions under high OA loadings. It is most likely because primary emissions substantially contribute to OA mass concentrations in relatively polluted areas under stagnant conditions (Tobler et al., 2021; Zhang et al., 2019). Specifically, HOA shows a relatively constant contribution even when the OA mass concentration increases at non-urban sites, while it increases as the OA mass concentration increases at urban sites. This

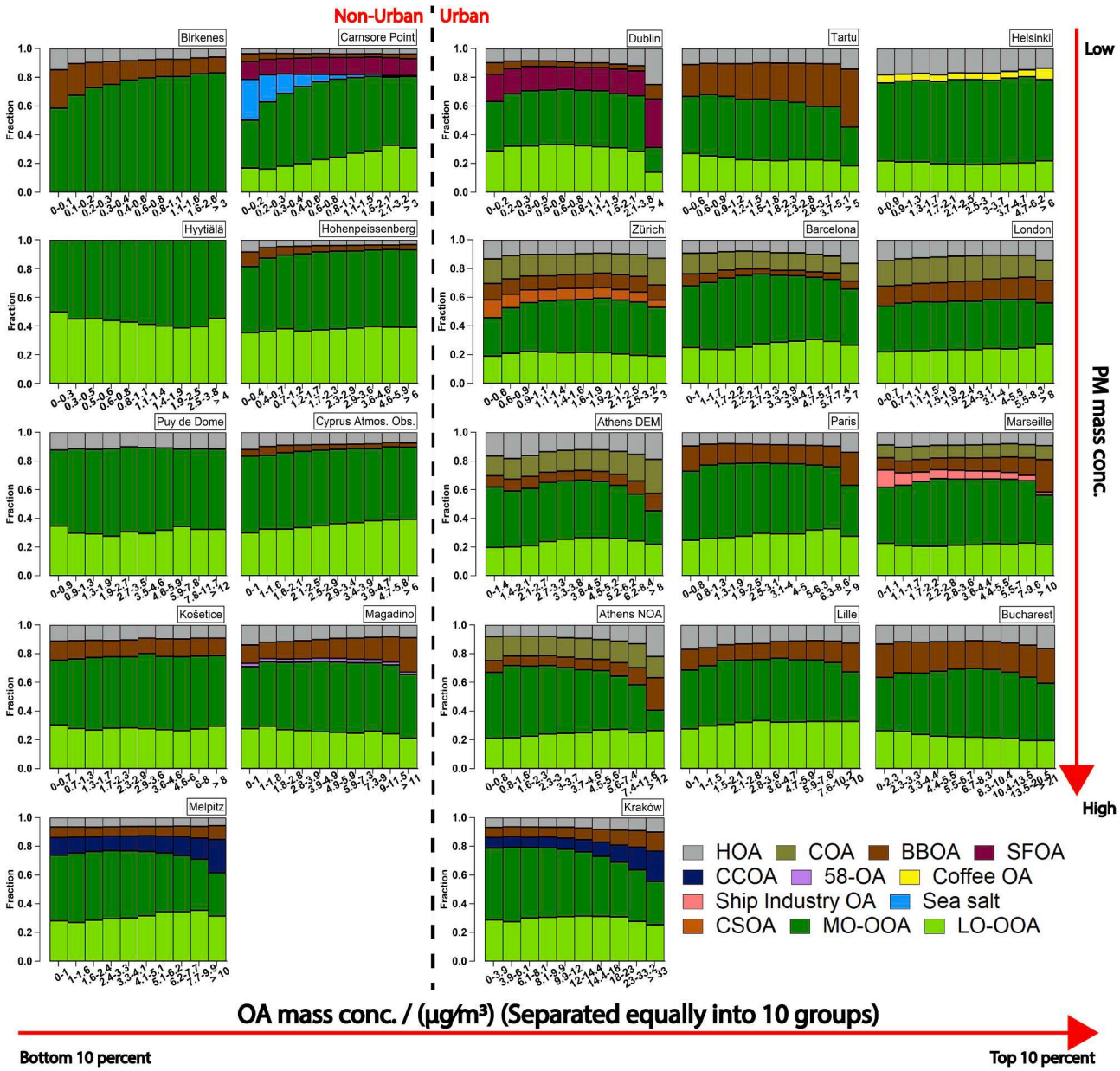

Fig. 3. Mass fraction of each organic aerosol (OA) component for 22 stations with 10 equally distributed bins based on OA mass concentration. Non-urban and urban sites have been separated by the dashed vertical line divided into left and right panels. The sites are sorted based on the submicron total particulate matter (PM_1) mass concentration. In general, oxygenated OA (OOA, dark and light green bars) is dominant at all sites over the whole mass range. However, with an increase of the total OA mass concentration, an increase in the primary OA fraction is often observed.

suggests that traffic emissions still play a considerable role during high OA mass concentration periods, and it remains important even when the total OA mass concentration is low. In particular, all factors related to the combustion of solid fuel (i.e., BBOA, SFOA, and CCOA) show the most pronounced enhancement when the OA mass loading increases, especially during winter seasons (Fig. S3 in the Supplement), which suggests solid fuel combustion is the main driver for the polluted episodes. The sea salt factor at Carnsore Point, in turn, has the highest contribution in the bottom 10 percent of OA mass loadings since high wind speeds favour high sea salt emissions and low OA mass concentrations at the same time.

3.3. Diel cycles for resolved OA components

The highly time-resolved long-term ACSM/AMS data allow investigating the diel cycles of the OA components. Figure 4 shows the averages (solid lines) and standard deviations (shaded areas) of diel profiles of the major OA components (HOA, BBOA, COA-like, MO-OOA, LO-OOA and Total OOA), normalised by the annual average of the corresponding OA component mass concentration for each site at both non-urban and urban sites. Birkenes and Hyytiälä datasets are not included because they only have 4-hour and 3-hour time resolutions, respectively. Overall, all OA components exhibit increases during the evening since accumulation occurs in a shallow boundary layer during that time of the day. However, the decreasing trends from midnight to sunrise are caused by decreased emissions and relatively higher wind speed, and the dilution of OA components after sunrise is caused by the rising boundary layer which introduces clean airmasses (Stull, 1988).

HOA shows a distinct pattern at urban sites with characteristic morning and evening rush-hour peaks. By contrast, at non-urban locations, HOA does not follow the same pattern, indicating that this factor is likely associated with transported traffic emissions or with non-traffic

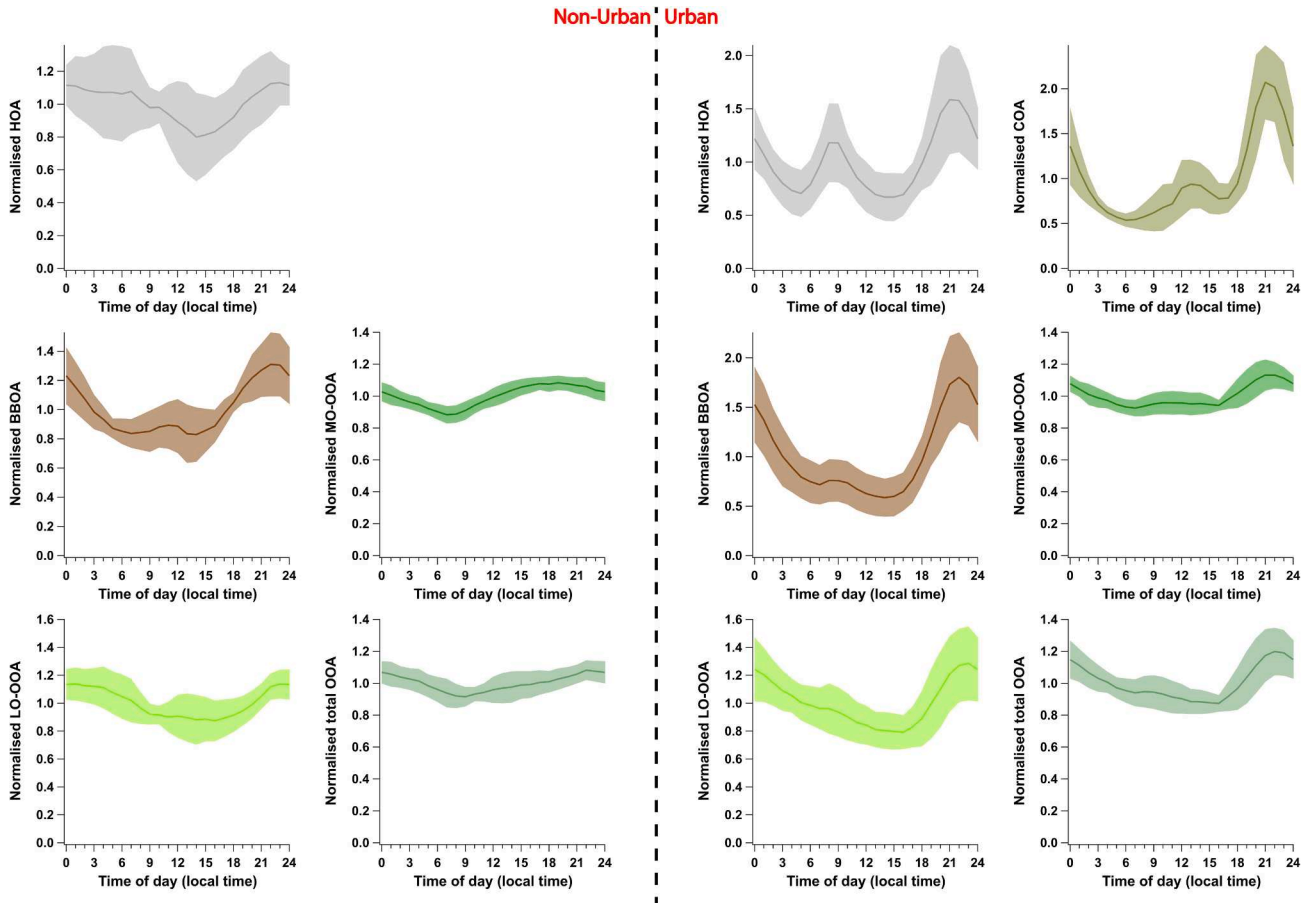

Fig. 4. Normalised diel profiles for HOA, COA, BBOA, MO-OOA, LO-OOA, and Total OOA (MO-OOA + LO-OOA). The solid lines and shaded areas represent the averages and standard deviations, respectively, of the diel profiles for the non-urban and urban datasets (normalised by the annual average of the corresponding OA component mass concentration for each site). The POA factors generally show more pronounced variability than the OOA factors. In addition, the urban sites have stronger patterns with less spatial variability than the non-urban sites.

primary hydrocarbon emissions at these sites. COA, as mentioned resolved at six urban sites, shows distinct noon and evening peaks with minor standard deviations, which suggests small spatial variabilities of cooking emissions. BBOA has a similar diel cycle at urban and non-urban sites with reduced values during the day and a marked evening peak, which indicates that most likely, (residential) heating emissions are the main contributor to BBOA. However, at the urban sites, the evening peak of BBOA is more pronounced than at the non-urban sites, which suggests that the urban BBOA is more local and synchronised to domestic heating than at the non-urban sites. The delayed morning peaks and broader span of non-urban BBOA diel profiles further indicate relatively distant BBOA sources at non-urban sites.

The MO-OOA diel trend at both urban and non-urban sites shows the most stable pattern. A slight decrease is observed during the night starting after 23:00 and continuing until 06:00–07:00, probably due to the decrease in the formation rates of MO-OOA in the absence of photochemical activity. By contrast, the MO-OOA concentrations increase slightly from morning to afternoon at the non-urban sites, potentially due to photochemistry. Moreover, the long-range transported origin could also play a role in this stable diel trend of MO-OOA. The enhancement of MO-OOA after 18:00 at urban sites is due to the accumulation of pollutants in a shallow boundary layer. This includes both OOA precursors and POA, both of which may be oxidized by OH or NO_3 radicals. The diel cycles of LO-OOA at the urban and non-urban sites reveal nighttime maxima with a slight decrease at noon, suggesting local production or enhanced vapour partitioning onto pre-existing aerosol in the shallow nocturnal boundary layer. Urban LO-OOA shows much stronger evening peaks than at non-urban sites, potentially caused by nighttime chemistry yielding urban OOA from POA oxidation (where POA includes both HOA, BBOA, and other primary sources). Kodros et al. (2020) and Tiitta et al. (2016) demonstrated how dark ageing of BBOA could potentially yield substantial amounts of OOA. Such ageing is likely to explain some of our observations at the urban sites (Zhang et al., 2020). Both urban and non-urban sites show small spatial variability for the Total OOA, but the diel cycle for urban sites has a more substantial evening peak again due to the strong LO-OOA increase. In general, the POA factors show more temporal variability than the OOA factors at both urban and non-urban sites.

In addition, Fig. S5 shows the averages of normalized weekly cycles for the non-urban and urban sites separately (with Birkenes and Hyytiälä datasets included among the non-urban sites). Each weekly cycle has been normalised by the annual average of the corresponding OA component mass concentration for each site. Compared with the diel cycles, the weekly ones are generally much weaker. In addition, POA shows a stronger variability compared to the OOA factors, similar to the averaged diel cycles (Fig. 4). HOA shows lower values during the weekend than on weekdays at both urban (-2.6%) and non-urban (-3.5%) sites. Except for HOA, the non-urban weekly cycles are much less pronounced than the ones at the urban sites. Specifically, BBOA increases during the weekend, with 19.9% and 12.3% higher values than on the weekdays for urban and non-urban sites, respectively. This is because more wood-burning activities (e.g., open fire grills and residential heating) are expected during weekends (Fuller et al., 2014). COA shows a similar trend as it increases during the weekends (+18.8% at urban sites), suggesting that cooking activities are more pronounced. All OOA factors (MO-OOA, LO-OOA, and Total OOA) do not present strong

weekly cycles (<6.3% difference between the weekdays and the weekend), with relatively larger spatial variability for OOA at the urban sites, indicated by larger standard deviations.

3.4. Spatial and seasonal variability of OA contributions

The time series of daily-averaged OA fractions for each site is shown in Fig. S2, which presents an overall picture of the entire source apportionment result. It indicates significant spatial and temporal variabilities of OA contributions across Europe. To study the seasonal variation of OA and its sources, data was divided into four seasons: winter (DJF: December, January, and February), spring (MAM: March, April, and May), summer (JJA: June, July, and August), and autumn (SON: September, October, and November). Figure 5 indicates a relatively small spatial variability of the relative OA contributions at both urban and non-urban datasets, and there is no clear pattern between the OA fraction and PM_1 loading. Urban sites have higher POA contributions in OA than non-urban sites. However, each dataset shows an apparent seasonal variability with higher POA contributions and mass concentrations in cold seasons than in warm ones (Fig. 5 and Fig. S6). The contributions of POA also appear to be higher when the total PM_1 mass concentration increases at all non-urban sites, as shown in Fig. 5.

Specifically, urban sites show higher HOA contributions (overall average contribution of 12.7 ± 2.9%) than non-urban sites (7.4 ± 2.7%), which is expected due to more traffic emissions in urban areas. Moreover, for both urban and non-urban sites, the HOA contribution shows a distinct seasonality with the lowest contribution in summer (8.8 ± 3.4%) and the highest in winter (12.0 ± 4.8%), and similar contributions in spring (10.9 ± 4.3%) and autumn (11.5 ± 4.6%). This might be due to the lower boundary layer with stagnant conditions in the cold season favouring the accumulation of primary and local pollutants and/or reduced photochemistry. In addition, the heating-related sources (i.e., BBOA, CCOA, and SFOA) are obviously more pronounced during the cold seasons than the warm ones. Specifically, BBOA has an average contribution of 8.3 ± 4.7% in summer but 16.9 ± 8.4% in winter. CCOA was only found in Kraków and Melpitz, and its contributions varied from season to season, with substantially enhanced contribution during winter (Kraków: 18.2% and Melpitz: 23.1%) compared to summer (Kraków: 4.5% and Melpitz: 8.7%). The drastic seasonal variations in Kraków are due to the widespread use of coal-burning for residential heating purposes in winter (note that these measurements took place before the government imposed a ban on the use of solid fuels for residential heating in the city of Krakow (Casotto et al., 2022; Tobler et al., 2021)). In Melpitz, coal combustion is less dependent on local sources, but likely more affected by emissions from Poland or other eastern European countries that are rapidly transported by advection in winter, leading to the observed seasonality. For the Dublin dataset, the SFOA (heavily affected by both peat and coal combustion sources (Lin et al., 2019, 2018)) shows an enhanced contribution in winter (32.9%) and a decreased contribution in summer (13.2%). The SFOA in Carnsore Point station shows less seasonality because of the absence of local sources but still has a higher contribution in winter (13.3%) than in summer (9.2%). The COA contribution shows almost no seasonality, ranging from 14.3 ± 2.7% in summer to 15.4 ± 3.3% in autumn at the six urban sites where this factor is resolved, suggesting that the cooking emission contribution is constant and non-negligible in

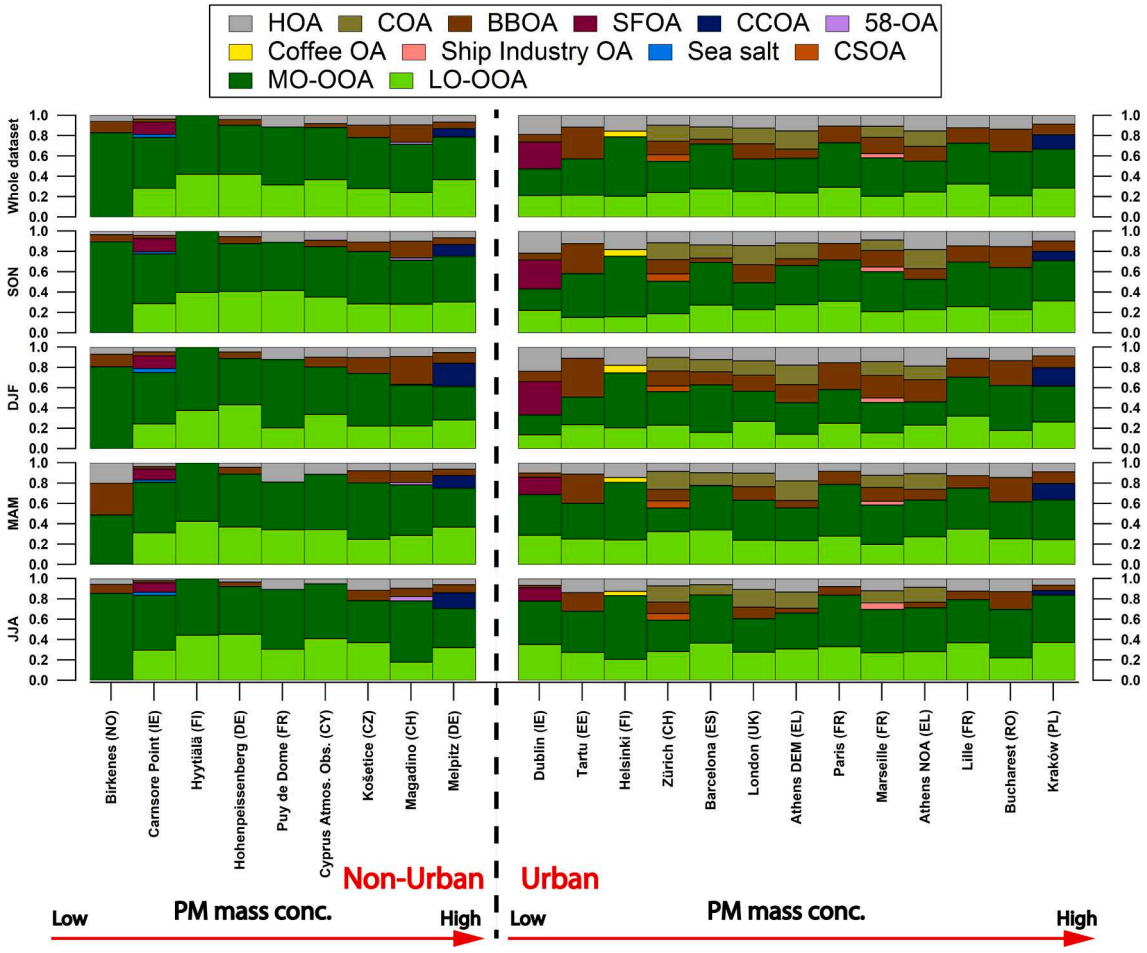

Fig. 5. Relative contributions of all OA components at each station grouped by season (see text). The stations are categorised into non-urban (left) and urban sites (right), where each subset is ordered by PM_1 mass concentration.

European cities in all seasons. The specific contributions of all OA components for all datasets and all seasons are summarised in Table S6, in which all POA except HOA, BBOA and COA are summed up as "other OA".

3.5. Spatial and seasonal variabilities of f_{44} vs f_{43} in the OOA factors

Canonaco et al. (2015) analysed the seasonal variability of major ion intensities (i.e., *m/z* 44 and *m/z* 43) in the OOA factors in Zürich. They suggested that biomass burning emissions, the most important precursor of SOA in that city during winter, cause the LO-OOA factor to be at the left half of the triangular region shown by (Ng et al., 2010) within the f_{44} vs f_{43} space, consistent with biomass burning emissions as shown by Heringa et al. (2011). In contrast, biogenic SOA from terpene oxidation may "push" the LO-OOA factors to the right side of the triangle in summer (Pfaffenberger et al., 2013).

This study explores the seasonality of f_{44} vs f_{43} for MO-OOA, LO-OOA and the Total OOA factors for both seasons at all sites, as shown in Fig. 6. It shows that the rolling PMF provides a good separation between MO-OOA and LO-OOA in both winter and summer (Fig. 6***a***), which is consistent with what Canonaco et al. (2021) and Chen et al. (2021) reported for two Swiss datasets. However, the positions of MO-OOA for the different stations in the f_{44} vs f_{43} space show large spatial variability (Fig. 6***a***), mainly attributed to the complex and various ageing processes in different locations under different meteorological conditions. In general, all LO-OOAs during the summer (JJA) shift to the right side of the triangle by a different extent when compared to the winter (DJF) seasons (Fig. 6***a***), which is most likely due to the enhanced biogenic emissions with higher temperatures during summer seasons (Canonaco et al., 2015). The right-side shift from summer to winter is more apparent when summing up the LO-OOA and MO-OOA into the Total OOA factors (Fig. 6***b***).

At the same time, some site-specific ions could significantly influence the LO-OOA position. For instance, due to the pronounced biomass burning influence in Bucharest during summer, the LO-OOA factor has considerable contributions of *m/z* 55, 57, 60 and 73, which is accompanied by a low f_{43} in LO-OOA during summer. The LO-OOA factors of the Tartu and Hyytiälä datasets stay on the right side of the triangle even during the winter season. Tartu appears to have a significant BBOA contribution throughout the year (18.2% in summer). Considering biomass burning OA oxidises rapidly, the biomass burning influence is more pronounced in the MO-OOA factor than in the LO-OOA factor during the whole year. That is why the LO-OOA factor in winter remains on the right side of the triangle. Hyytiälä is located in the boreal forest with high biogenic SOA formation in summer (Heikkinen et al., 2021; Yli-Juuti et al., 2021), which explains the high f_{43} in summer. In addition, no POA factors were deconvolved from this dataset following the presented protocol. By utilizing machine learning techniques, Heikkinen et al. (2021) resolved a slightly aged POA factor that could neither be further separated into HOA nor BBOA. This factor appeared only in winter and coincided with a LO-OOA drop to near-zero loadings when utilizing k-mean clustering approach (Heikkinen et al., 2021).

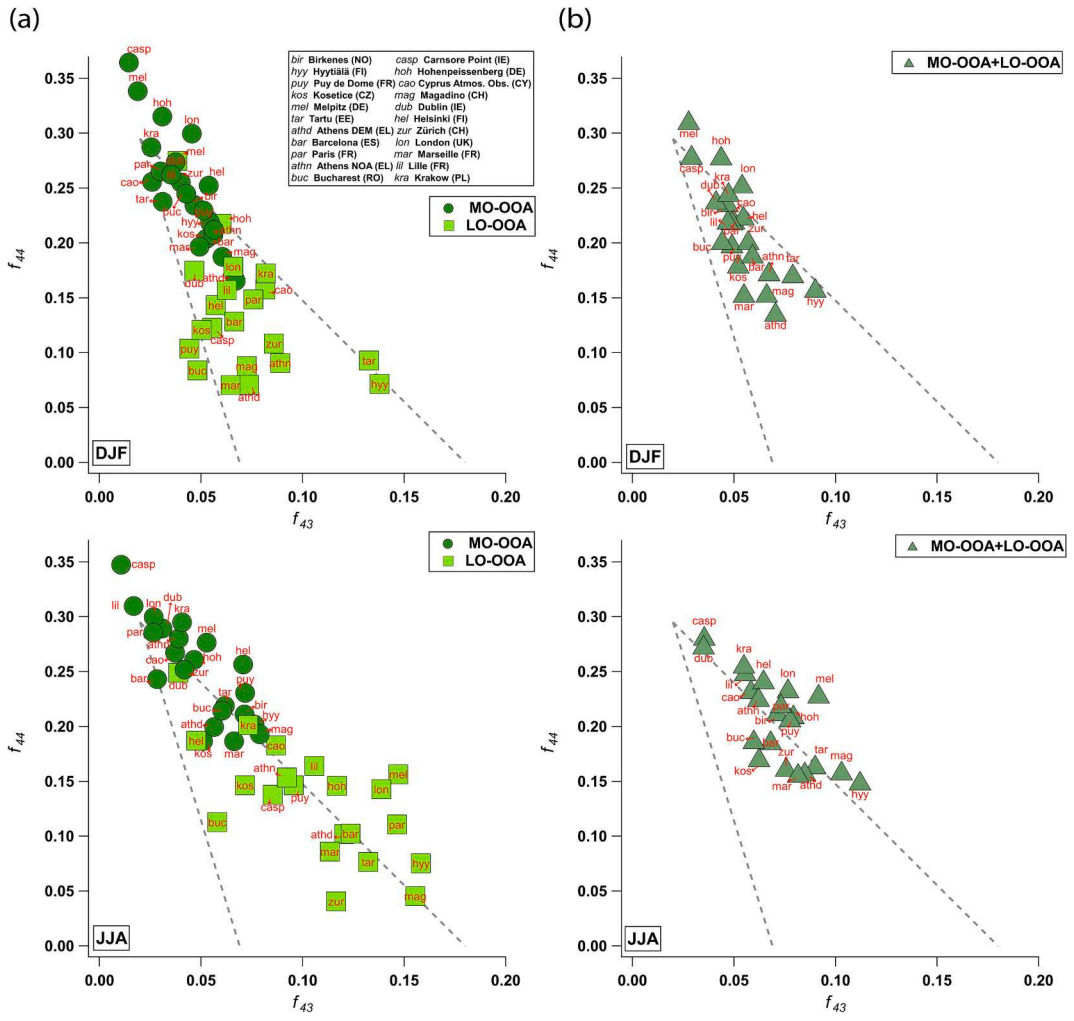

Fig. 6. (a) f_{44} vs f_{43} intensity in (top) winter and (bottom) summer for (a) resolved MO-OOA (dark green) and LO-OOA (light green); (b) the Total OOA (MO-OOA + LO-OOA).

Therefore, it is very likely that the Hyytiälä LO-OOA shown in this study is influenced by aged POA in winter, which keeps the LO-OOA f_{43} high. Also, the potential terpene emission from the Korkeakoski sawmills (ca. 7 km NE of the monitoring station) could also keep the LO-OOA on the right side (Äijälä et al., 2017). The combined effects of high summertime biogenic SOA contribution to LO-OOA and wintertime POA mixing to LO-OOA could explain why LO-OOA in Hyytiälä always stays on the right side of the triangle. When considering the rest of the sites, both the LO-OOA and Total OOA factors generally shift to the right side of the triangle during summer compared to winter.

3.6. Spatial and temporal variabilities of key ions in resolved OA factors

This study also investigates key ions' spatial and monthly variabilities in common OA factors (i.e., *m/z* 55 and *m/z* 57 for HOA and COA; *m/z* 60 and *m/z* 73 for BBOA; *m/z* 44 and *m/z* 43 for MO-OOA, LO-OOA, and the Total OOA). All monthly intensities of these key ions in these OA factors were averaged across the 22 datasets to see possible monthly trends (Fig. 7). Overall, the key ions for HOA, COA, MO-OOA and Total OOA factors barely show a monthly trend. In contrast, f_{60} and f_{73} in BBOA are substantially higher in the cold months compared to the warmer months. The main reason is likely that levoglucosan and thus *m/z* 60 is less stable in the aerosol with higher temperature as well as the change in the biomass burning source during different seasons (e.g., residential heating and outdoor open fire) (Bertrand et al., 2018; Bougiatioti et al., 2014; Xie et al., 2014). The most dominating ions (*m/z* 44 and *m/z* 43) in the LO-OOA factor show a relatively strong monthly trend compared with MO-OOA and Total OOA. Specifically, f_{44} is smaller, and f_{43} is higher in LO-OOA during the warm months, which is a further indication that the enhancement of biogenically-formed SOA could increase the intensity of f_{43} in LO-OOA when the temperature is increased (which eventually "pushes'' the LO-OOA factors to the right side of the triangle as presented in Fig. 6, (Canonaco et al., 2015)). Monthly trends of these key ions of these OA factors for each station are

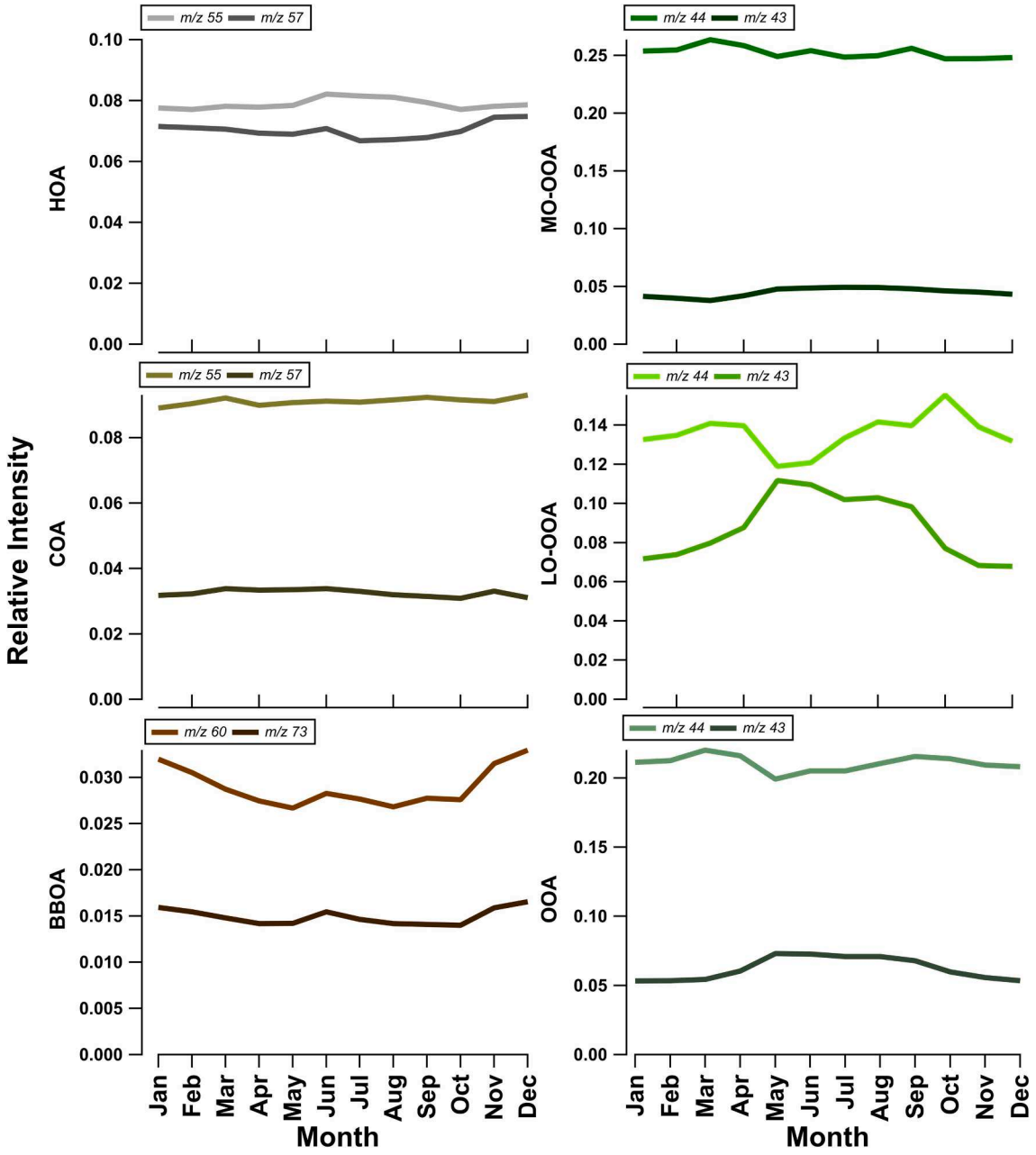

Fig. 7. Monthly average relative intensities of key ions in the corresponding factor profiles over all the datasets.

shown in Fig. S6.

In order to compare the spatial variations of key ions in the different OA factors, the interquartile range (IQR) of the monthly site-averaged intensities was normalised by their median (Table 2). In general, f_{55} for HOA and COA shows a relatively small IQR/median ratio with averages of 0.15 ± 0.03 and 0.16 ± 0.07, respectively. The f_{57} for HOA and COA shows similar consistency across 22 sites with averages of 0.20 ± 0.03 and 0.09 ± 0.05, respectively. Overall, the HOA and COA factors are generally consistent across different locations. It agrees well with the previous findings reported by Crippa et al. (2014). However, the most essential fingerprint ions of BBOA, f_{60} and f_{73}, appear to have the largest spatial variability among the POA factors with IQR/median ratios in a range of 0.28–0.39 and 0.20–0.36, respectively. This is expected since the type of wood and burning conditions, as well as chemical ageing, can affect the BBOA mass spectrum considerably (Bertrand et al., 2018; Bougiatioti et al., 2014; Grieshop et al., 2009; Heringa et al., 2011; Weimer et al., 2008; Xie et al., 2014). Thus, as discussed previously, retrieving site-specific BBOA factor profiles using unconstrained PMF analysis instead of published BBOA factor profiles is strongly recommended.

The most dominating ion in MO-OOA, f_{44}, has a somewhat smaller IQR/median ratio, ranging from 0.16 to 0.34, and the f_{43} in MO-OOA has an IQR/median ratio in a range of 0.45–0.83. This is because different datasets could have significantly variable ageing processes, precursors, and meteorological conditions, which appear to affect the degrees of oxygenation (the relative intensities of m/z 44 and m/z 43). In addition, MO-OOA remains dominated mainly by f_{44} (average f_{44} = 0.25), but with a much smaller f_{43} intensity (average f_{43} = 0.04). Therefore, the slight changes in the intensity of f_{43} could have a larger effect on the IQR/median ratio for this ion.

Due to enhanced biogenic emissions, the f_{43} in LO-OOA shows consistently larger intensities in the warmer months (May-September), as shown in Fig. 7. Consequently, the f_{44} in LO-OOA decreases during the warm seasons and is related to the seasonal differences in f_{44} vs f_{43} of Fig. 7. In addition to the dynamic monthly trends observed in LO-OOA, there are also strong spatial variabilities for these two key ions (i.e., m/z 44 and m/z 43). The IQR/median ratios of f_{44} and f_{43} in LO-OOA are in the range 0.38–0.94 and 0.39–0.60, respectively. This is expected considering LO-OOA has never been constrained, and various ageing processes, precursors, and meteorological conditions could contribute to the large spatial variabilities. When we sum up the LO-OOA and MO-OOA to the Total OOA factor, m/z 44 is still the dominating ion with an average of 0.21, but it is smaller than that of MO-OOA alone due to the much smaller f_{44} in LO-OOA with an average of 0.14. Overall, f_{43} in the Total OOA factor still shows an increasing trend during warm seasons like the LO-OOA factor, which indicates that the effect of enhanced biogenic emissions on the intensity of f_{43} in the Total OOA might be rather considerable. Moreover, f_{43} in the Total OOA shows relatively smaller spatial variabilities (compared to MO-OOA and LO-OOA) with an IQR/median ratio of 0.26–0.41. The f_{44} in the Total OOA has slightly larger spatial variabilities than MO-OOA with an IQR/median ratio of 0.21–0.40, but it is still more stable than LO-OOA. It is expected considering the large spatial variabilities in LO-OOA. However, the sum of the OOA factors shows little monthly trends except for the increasing f_{43} (thus, decreasing f_{44}) in warmer months (May-September).

4. Conclusion

A state-of-the-art standardised protocol for source apportionment of long-term ACSM/AMS organic aerosol mass spectrum datasets was developed. Our protocol was validated systematically and strictly applied to 22 sites with year-long measurements. It demonstrates the consistency of this protocol with comprehensive source apportionment results, even though each dataset was analysed by each research group individually. Our source apportionment strategy has been significantly improved compared to conventional seasonal PMF by utilising rolling windows, bootstrap, and ME-2 techniques, which were first introduced by Canonaco et al. (2021). As addressed by Chen et al. (2021) and Tobler et al. (2021), this strategy allows us to retrieve robust source apportionment results by considering temporal variations of source profiles. Importantly, the success of the rolling mechanism is an essential step to make real-time source apportionment possible (Chen et al., 2022). However, the current protocol/strategy remains challenging to objectively define the transition point to an improved source apportionment for rolling PMF analysis when a different number of OA factors is necessary for different periods. More tools should be tested to address this challenge in the near future.

Overall, this work provides a comprehensive overview of the OA sources in Europe with highly time-resolved source apportionment results. The OA fraction in PM_1 is high (23–75%) across Europe and seasons. With the help of this advanced source apportionment strategy, many common POA factors have been resolved, including HOA, COA, BBOA, CCOA, and SFOA, together with secondary OOA factors, i.e., MO-OOA and LO-OOA in these 22 datasets. Moreover, some local OA components have been identified at specific stations, like a coffee roastery OA factor in Helsinki, a ship industry OA factor in Marseille, a sea salt factor in Carnsore Point, and a cigarette smoke OA factor in Zürich. The OOA factors together constitute the main contributor (47.3–100%) to OA and generally show more stable diel and weekly cycles than POA factors. The contributions of POA increase with increasing total OA mass concentration in most of the polluted regions. It suggests that the control of primary emissions could help mitigate OA mass concentration or at least decrease the likelihood of highly polluted episodes. Also, most POA factors show enhanced contribution/mass concentrations during cold seasons compared to warm seasons due to residential heating. Lower boundary layer heights (lower temperature) combined with stagnant

Table 2
Normalised spatial variations for key ions using the interquartile range (IQR) divided by the medians of average monthly intensities across the 22 datasets.

Factors	HOA		COA		BBOA		MO-OOA		LO-OOA		Total OOA	
m/z	*55*	*57*	*55*	*57*	*60*	*73*	*44*	*43*	*44*	*43*	*44*	*43*
Jan	0.13	0.21	0.11	0.04	0.36	0.29	0.30	0.46	0.52	0.46	0.34	0.34
Feb	0.16	0.19	0.12	0.04	0.33	0.35	0.25	0.57	0.60	0.54	0.31	0.29
Mar	0.15	0.19	0.10	0.11	0.37	0.25	0.28	0.45	0.57	0.39	0.26	0.39
Apr	0.12	0.22	0.06	0.10	0.36	0.25	0.27	0.69	0.60	0.60	0.32	0.39
May	0.17	0.24	0.09	0.11	0.36	0.23	0.34	0.83	0.86	0.53	0.37	0.36
Jun	0.19	0.17	0.11	0.17	0.34	0.20	0.27	0.81	0.63	0.53	0.40	0.33
Jul	0.19	0.21	0.18	0.17	0.32	0.21	0.27	0.65	0.38	0.40	0.29	0.29
Aug	0.21	0.27	0.27	0.14	0.28	0.22	0.26	0.69	0.50	0.43	0.29	0.30
Sep	0.19	0.21	0.24	0.04	0.32	0.23	0.25	0.70	0.94	0.41	0.36	0.33
Oct	0.11	0.18	0.25	0.06	0.39	0.21	0.27	0.49	0.46	0.59	0.30	0.26
Nov	0.11	0.13	0.19	0.08	0.34	0.36	0.19	0.60	0.50	0.55	0.21	0.41
Dec	0.12	0.22	0.14	0.02	0.33	0.36	0.16	0.77	0.74	0.42	0.29	0.39
Mean	0.15 ± 0.03	0.20 ± 0.03	0.16 ± 0.07	0.09 ± 0.05	0.34 ± 0.03	0.26 ± 0.06	0.26 ± 0.05	0.64 ± 0.13	0.61 ± 0.16	0.49 ± 0.08	0.40 ± 0.05	0.34 ± 0.05

conditions can readily cause the accumulation of pollutants. In particular, HOA (traffic emissions) is a non-negligible OA source with a rather consistent contribution across different stations (10.7 ± 3.8%). Six urban sites display a significant COA factor (i.e., two Athens datasets, Zürich, London, Barcelona, and Marseille) with an overall average contribution to OA of 14.5 ± 2.5%. Moreover, most of the datasets show a resolved BBOA component (except Hyytiälä, Puy de Dôme, and Helsinki) with important contributions to OA (annual average:12.4 ± 6.9%), which increases substantially in winter, with a contribution of 16.9 ± 8.4%. Melpitz and Kraków present a CCOA factor (annual average: 14.7 ± 0.8%, winter average: 20.6 ± 3.5%), while SFOA is found to be heavily affected by peat and coal combustion sources at Carnsore Point and Dublin (annual average: 19.3 ± 10.4%, winter average: 22.7 ± 14.4%). All of these results confirm that the reduction of solid fuel-burning for residential heating is one of the key leverages to mitigate fine PM levels in Europe, especially in winter.

This study reveals the spatial and seasonal concentration variability of the MO-OOA, LO-OOA, and Total OOA factors. MO-OOA and Total OOA show little variability, while LO-OOA varies considerably across spatial and seasonal domains. This is expected since the ageing processes, abundances/types of precursors and meteorological conditions can differ both temporally and spatially. In particular, the seasonality of the LO-OOA factor in most of the datasets agrees well with the findings reported by Canonaco et al. 2015), with increasing f_{43} (thus, decreasing f_{44}) intensity in warm seasons likely due to the enhanced biogenic emissions.

Moreover, with the help of the rolling PMF technique, time-dependent OA factor profiles have been retrieved. Therefore, this study also investigates the monthly trends (averaged over 22 datasets) and corresponding variabilities (IQR/median ratio) across sites for key ions in the commonly resolved OA factors. While these key ions barely show monthly trends in HOA, COA, MO-OOA, and Total OOA, BBOA key ion (f_{60} and f_{73}) intensities increase during the cold seasons due to the abundance of biomass burning sources and the lower reactivity of levoglucosan. The increased f_{43} of LO-OOA during warm seasons is most likely due to enhanced biogenic SOA formation. In terms of spatial variabilities, key ions for HOA and COA factors show a small IQR/median ratio with a range of 0.06–0.27 due to both factor contributions being consistent (if present), as reported in previous studies. However, the key ions for the BBOA factor show a relatively larger spatial variability with the IQR/median ratio ranging from 0.20 to 0.39, which suggests potentially different combustion conditions, type of woods, etc., contribute to this variability in the real-world scenarios. In addition, the f_{43} intensities in MO-OOA and LO-OOA show large spatial variability, with the IQR/median ratio ranging from 0.45 to 0.83 and 0.39 to 0.60, respectively. The f_{44} in LO-OOA has a large IQR/median ratio range of 0.38–0.94, but the f_{44} in MO-OOA is rather less variable across sites with a relatively small IQR/median ratio range of 0.16–0.34. This is expected, since OOA factors are never constrained combined and complex ageing processes are affected by different locations and meteorological conditions. OOA is the dominant contributor to OA, but ACSM data alone is insufficient for its apportionment to specific sources and formation mechanisms. Back-trajectory analysis could support the understanding of the source regions and transportation pathways for long-range transported OOA. Model – measurement assessments may be used to further constrain the secondary organic aerosol formation sources and pathways. In addition, higher m/z resolving ability and time resolution instrumentation (e.g., FIGAERO (Lopez-Hilfiker et al., 2014), EESI-TOF (Lopez-Hilfiker et al., 2019), and EESI-Orbitrap (Lee et al., 2020)) could provide more information at the molecular level of OA, which can help us to separate OOA factors better when conducting PMF (Qi et al., 2019; Stefenelli et al., 2019). Such instruments are not yet developed for long-term use, but they could be used in campaigns or for filter analyses that are taken concurrently with the on-line data. Moreover, offline-AMS (Daellenbach et al., 2016) analyses could be useful to better explain seasonal variabilities of the dominant contributors of OOA. With the help of this state-of-the-art source apportionment protocol, this study has retrieved highly time-resolved, long-term (>9 months), and robust OA source information consistently, with minimum subjective judgements. This highly time-resolved comprehensive OA source information can be useful inputs/constraints to improve/validate climate, health, and air quality models.

Finally, this work suggests that policymakers should address the major combustion sources (i.e., biomass burning, coal combustion, and peat) that affect air quality in Europe. Besides, more attention should be paid to the traffic source, even though it is quite constant across places because it is significant in organic aerosols and is also a proxy for non-exhaust emissions. Due to regional transport, decreasing the emissions of primary factors would also decrease the secondary factors observed at the non-urban sites.

CRediT authorship contribution statement

Gang Chen: Conceptualization, Data curation, Formal analysis, Investigation, Methodology, Project administration, Software, Validation, Visualization, Writing – original draft, Writing – review & editing. **Francesco Canonaco:** Methodology, Software, Writing – review & editing. **Anna Tobler:** Data curation, Formal analysis, Investigation, Software, Visualization, Writing – review & editing. **Wenche Aas:** Data curation, Funding acquisition, Supervision. **Andres Alastuey:** Data curation, Funding acquisition, Supervision. **James Allan:** Investigation. **Samira Atabakhsh:** Data curation, Formal analysis, Investigation. **Minna Aurela:** Data curation, Formal analysis, Investigation, Writing – review & editing. **Urs Baltensperger:** Supervision, Validation, Writing – review & editing. **Aikaterini Bougiatioti:** Data curation, Formal analysis, Investigation. **Joel F. De Brito:** Formal analysis, Investigation. **Darius Ceburnis:** Funding acquisition, Supervision. **Benjamin Chazeau:** Data curation, Formal analysis, Investigation, Software. **Hasna Chebaicheb:** Data curation, Formal analysis, Investigation. **Kaspar R. Daellenbach:** Investigation. **Mikael Ehn:** Funding acquisition, Supervision. **Imad El Haddad:** . **Konstantinos Eleftheriadis:** Formal analysis, Funding acquisition, Investigation, Supervision. **Olivier Favez:** Funding acquisition, Supervision. **Harald Flentje:** Data curation. **Anna Font:** Data curation, Formal analysis, Investigation, Writing – review & editing. **Kirsten Fossum:** Data curation, Formal analysis. **Evelyn Freney:** Data curation, Formal analysis, Investigation, Writing – review & editing. **Maria Gini:** Data curation, Formal analysis, Investigation. **David C Green:** Data curation, Funding acquisition, Investigation, Supervision. **Liine Heikkinen:** Data curation, Formal analysis, Investigation, Writing – review & editing. **Hartmut Herrmann:** Funding acquisition, Investigation, Supervision. **Athina-Cerise Kalogridis:** Resources. **Hannes Keernik:** Data curation, Formal analysis, Investigation. **Radek Lhotka:** Data curation, Formal analysis, Investigation. **Chunshui Lin:** Data curation, Formal analysis. **Chris Lunder:** Data curation, Investigation. **Marek Maasikmets:** Funding acquisition. **Manousos I. Manousakas:** Data curation. **Nicolas Marchand:** Formal analysis, Funding acquisition, Investigation, Writing – review & editing. **Cristina Marin:** Data curation. **Luminita Marmureanu:** Data curation. **Nikolaos Mihalopoulos:** Formal analysis, Funding acquisition, Investigation, Supervision. **Griša Močnik:** Investigation, Resources. **Jaroslaw Nęcki:** Resources. **Colin O'Dowd:** Funding acquisition, Supervision. **Jurgita Ovadnevaite:** Data curation, Funding acquisition, Investigation, Supervision. **Thomas Peter:** Supervision. **Jean-Eudes Petit:** Data curation, Formal analysis, Investigation, Supervision. **Michael Pikridas:** Data curation, Formal analysis. **Stephen Matthew Platt:** Formal analysis, Writing – review & editing, Investigation. **Petra Pokorná:** Data curation, Funding acquisition, Investigation, Supervision. **Laurent Poulain:** Data curation, Formal analysis, Funding acquisition, Investigation, Supervision. **Max Priestman:** Data curation, Investigation. **Véronique Riffault:** Data curation, Formal analysis, Funding acquisition, Investigation, Supervision, Writing – review & editing. **Matteo Rinaldi:** Funding acquisition, Supervision. **Kazimierz Różański:**

Supervision. **Jaroslav Schwarz:** Formal analysis, Funding acquisition. **Jean Sciare:** Funding acquisition, Writing – review & editing. **Leïla Simon:** Data curation, Formal analysis, Investigation, Supervision. **Alicja Skiba:** Investigation. **Jay G. Slowik:** Funding acquisition, Investigation, Methodology, Software, Writing – review & editing. **Yulia Sosedova:** Formal analysis, Data curation. **Iasonas Stavroulas:** Data curation, Funding acquisition, Investigation, Supervision. **Katarzyna Styszko:** Investigation, Resources. **Erik Teinemaa:** Funding acquisition. **Hilkka Timonen:** Funding acquisition. **Anja Tremper:** Writing – review & editing. **Jeni Vasilescu:** Formal analysis, Funding acquisition, Investigation, Writing – review & editing. **Marta Via:** Data curation, Formal analysis, Investigation. **Petr Vodička:** Data curation, Investigation. **Alfred Wiedensohler:** Funding acquisition, Investigation, Supervision. **Olga Zografou:** Data curation, Formal analysis, Investigation. **María Cruz Minguillón:** Conceptualization, Funding acquisition, Investigation, Project administration, Resources. **André S. H. Prévôt:** Conceptualization, Funding acquisition, Investigation, Supervision, Methodology, Project administration, Resources, Validation, Writing – review & editing.

Declaration of Competing Interest

The authors declare that they have no known competing financial interests or personal relationships that could have appeared to influence the work reported in this paper.

Acknowledgement

This work would not have been possible without the following contributions: All co-authors were supported by the cost action of Chemical On-Line cOmpoSition and Source Apportionment of fine aerosol (COLOSSAL, CA16109). The Paul Scherrer Institute (PSI) team acknowledges the support of the Swiss Data Science Centre (SDSC) and the Swiss Federal Office of Environment (FOEN) within the Project Aurora. GC and AT were supported by a COST related project of the Swiss National Science Foundation, Source apportionment using long-term Aerosol Mass Spectrometry and Aethalometer Measurements (SAMSAM, IZCOZ0_177063), as well as the EU Horizon 2020 Framework Programme via the Research Infrastructures Services Reinforcing Air Quality Monitoring Capacities in European Urban & Industrial AreaS (RI-URBANS) project (GA-101036245), the ERA-PLANET projects SMURBS and iCUPE (grant agreement no. 689443). LP and SA were supported by ACTRIS (grant nos. ACTRIS (262254) and ACTRIS-2 (654109)). HC, VR, and JFB acknowledge financial support from the Labex CaPPA project, which is funded by the French National Research Agency (ANR) through the PIA (Programme d'Investissement d'Avenir) under contract ANR-11-LABX-0005-01, and the CLIMIBIO project, both financed by the Regional Council "Hauts-de-France" and the European Regional Development Fund (ERDF). In addition, The ATOLL (Lille), Longchamp (Marseille), and SIRTA (Paris region) platforms are part of the so-called LCSQA-CARA program, co-funded by the French Ministry of Environment. JV, CM, LM were supported by a grant of the Romanian Ministry of Research, Innovation and Digitalization, CNCS - UEFISCDI, project number PN-III-P1-1.1-TE-2019-0340, within PNCDI III and by Romanian National Core Program contract 18N/2019. European Union's Horizon 2020 research and innovation programme (project FORCeS under grant agreement No 821205). Consolidator grant INTERGRATE No 865799 and starting grant COALA No 638703). RL, PP, JS and PV were supported by ICPF CAS acknowledges financial support from the MEYS's of the Czech Republic within the INTER-EXCELLENCE INTERCOST program under grant agreements No. LTC18068 and by under grant Actris CZ LM2018122, and by the GACR under grant P209/19/06110Y. IDAEA-CSIC acknowledges financial support from Generalitat de Catalunya (AGAUR 2017 SGR41), the Spanish Ministry of Science and Innovation through CAIAC project (PID2019-108990RB-I00) and FEDER funds, through EQC2018-004598-P. IDAEA-CSIC is a Centre of Excellence Severo Ochoa (Spanish Ministry of Science and Innovation, Project CEX2018-000794-S). The Cyprus Atmospheric Observatory team acknowledges funding from the European Union's Horizon 2020 Research and Innovation Programme (under grant agreement no. 856612) and the Cyprus Government. Operational program Competitiveness, Entrepreneurship and Innovation (RESEARCH-CREATE-INNOVATE) project code: T1EDK-03437. KRD acknowledges support by the SNSF Ambizione grant PZPGP2_201992. The LCE team acknowledges financial support from the PACA region (PRISM project; grant n°2017_08809). TROPOS has been supported by the German Federal Environment Ministry (BMU) grants F&E 370343200 (German title: "Erfassung der Zahl feiner und ultrafeiner Partikel in der Außenluft"),2008–2010, and F&E 71143232 (German title: "Trendanalysen gesundheitsgefährdender Fein- und Ultrafeinstaubfraktionen unter Nutzung der im German Ultrafine Aerosol Network (GUAN) ermittelten Immissionsdaten durch Fortführung und Interpretation der Messreihen"), 2012–2014. KS and ASk were supported by the subsidy from the Ministry of Science and Higher Education, grant numbers: 16.16.220.842 B02, 16.16.210.476 and by the EU Project POWR.03.02.00-00-I004/16. EF, JEP and OF gratefully acknowledge CNRS-INSU for supporting measurements performed at SIRTA and CO-PDD, within the long-term monitoring aerosol program SNO-CLAP, both of which are components of the ACTRIS French Research Instructure, and whose data is hosted at the AERIS data center (https://www.aeris-data.fr/). LS gratefully acknowledges DIM Qi^2 research network for financial support of her doctoral work. National University of Ireland Galway work was supported by the EPA Research Programme 2021-2030, AEROSOURCE Project (2016-CCRP-MS-31). The EPA Research Programme is a Government of Ireland initiative funded by the Department of Environment, Climate and Communications. GM acknowledges the support of the Slovenian Research Agency (grant no. P1- 0385). NOA team (IS, AB, NM (Nikolaos Mihalopoulos)) acknowledges support by the "PANhellenic infrastructure for Atmospheric Composition and climatE change" (MIS 5021516) which is implemented under the Action "Reinforcement of the Research and Innovation Infrastructure", funded by the Operational Programme "Competitiveness, Entrepreneurship and Innovation" (NSRF 2014-2020) and co-financed by Greece and the European Union (European Regional Development Fund). JS and MP acknowledge the support of the European Union's Horizon 2020 Research and Innovation Programme (under grant agreement no. 856612) and of the Cyprus Government.

Moreover, we also want to thank Krista Luoma for Hyytiälä aethalometer data. Helsinki Region Environmental Services Authority HSY and Metropolia University of Applied Sciences for providing auxiliary Helsinki site data. The authors gratefully acknowledge the Romanian National Air Quality Monitoring Network (NAQMN, www.calitateaer.ro) for NOx data providing.

Data availability

The time series of resolved source apportionment results and corresponding external data as well as detailed description of rolling PMF settings are publicly available (DOI: 10.5281/zenodo.6522811).

Appendix A. Supplementary material

Supplementary data to this article can be found online at https://doi.org/10.1016/j.envint.2022.107325.

References

Äijälä, M., Heikkinen, L., Fröhlich, R., Canonaco, F., Prévôt, A.S.H., Junninen, H., Petäjä, T., Kulmala, M., Worsnop, D., Ehn, M., 2017. Resolving anthropogenic aerosol pollution types – deconvolution and exploratory classification of pollution events. Atmos. Chem. Phys. 17, 3165–3197. https://doi.org/10.5194/acp-17-3165-2017.

Barreira, L.M.F., Ylisirniö, A., Pullinen, I., Buchholz, A., Li, Z., Lipp, H., Junninen, H., Hõrrak, U., Noe, S.M., Krasnova, A., Krasnov, D., Kask, K., Talts, E., Niinemets, Ü., Ruiz-Jimenez, J., Schobesberger, S., 2021. The importance of sesquiterpene oxidation products for secondary organic aerosol formation in a springtime hemiboreal forest. Atmos. Chem. Phys. 21, 11781–11800. https://doi.org/10.5194/acp-21-11781-2021.

Bertrand, A., Stefenelli, G., Jen, C.N., Pieber, S.M., Bruns, E.A., Ni, H., Temime-Roussel, B., Slowik, J.G., Goldstein, A.H., El Haddad, I., Baltensperger, U., Prévôt, A. S.H., Wortham, H., Marchand, N., 2018. Evolution of the chemical fingerprint of biomass burning organic aerosol during aging. Atmos. Chem. Phys. 18, 7607–7624. https://doi.org/10.5194/acp-18-7607-2018.

Bougiatioti, A., Stavroulas, I., Kostenidou, E., Zarmpas, P., Theodosi, C., Kouvarakis, G., Canonaco, F., Prévôt, A.S.H., Nenes, A., Pandis, S.N., Mihalopoulos, N., 2014. Processing of biomass-burning aerosol in the eastern Mediterranean during summertime. Atmos. Chem. Phys. 14, 4793–4807. https://doi.org/10.5194/acp-14-4793-2014.

Bressi, M., Cavalli, F., Putaud, J.P., Fröhlich, R., Petit, J.-E., Aas, W., Äijälä, M., Alastuey, A., Allan, J.D., Aurela, M., Berico, M., Bougiatioti, A., Bukowiecki, N., Canonaco, F., Crenn, V., Dusanter, S., Ehn, M., Elsasser, M., Flentje, H., Graf, P., Green, D.C., Heikkinen, L., Hermann, H., Holzinger, R., Hueglin, C., Keernik, H., Kiendler-Scharr, A., Kubelová, L., Lunder, C., Maasikmets, M., Makeš, O., Malaguti, A., Mihalopoulos, N., Nicolas, J.B., O'Dowd, C., Ovadnevaite, J., Petralia, E., Poulain, L., Priestman, M., Riffault, V., Ripoll, A., Schlag, P., Schwarz, J., Sciare, J., Slowik, J., Sosedova, Y., Stavroulas, I., Teinemaa, E., Via, M., Vodička, P., Williams, P.I., Wiedensohler, A., Young, D.E., Zhang, S., Favez, O., Minguillón, M.C., Prevot, A.S.H., 2021. A European aerosol phenomenology - 7: High-time resolution chemical characteristics of submicron particulate matter across Europe. Atmos. Environ. X 10, 100108. https://doi.org/10.1016/j.aeaoa.2021.100108.

Canonaco, F., Crippa, M., Slowik, J.G., Baltensperger, U., Prévôt, A.S.H., 2013. SoFi, an IGOR-based interface for the efficient use of the generalized multilinear engine (ME-2) for the source apportionment: ME-2 application to aerosol mass spectrometer data. Atmos. Meas. Tech. 6, 3649–3661. https://doi.org/10.5194/amt-6-3649-2013.

Canonaco, F., Slowik, J.G., Baltensperger, U., Prévôt, A.S.H., 2015. Seasonal differences in oxygenated organic aerosol composition: implications for emissions sources and factor analysis. Atmos. Chem. Phys. 15, 6993–7002. https://doi.org/10.5194/acp-15-6993-2015.

Canonaco, F., Tobler, A., Chen, G., Sosedova, Y., Slowik, J.G., Bozzetti, C., Daellenbach, K.R., El Haddad, I., Crippa, M., Huang, R.-J., Furger, M., Baltensperger, U., Prévôt, A.S.H., 2021. A new method for long-term source apportionment with time-dependent factor profiles and uncertainty assessment using SoFi Pro: application to 1 year of organic aerosol data. Atmos. Meas. Tech. 14, 923–943. https://doi.org/10.5194/amt-14-923-2021.

Casotto, R., Skiba, A., Rauber, M., Strähl, J., Tobler, A., Bhattu, D., Lamkaddam, H., Manousakas, M.I., Salazar, G., Ryś, A., Haddad, I.E., Kasper-Giebl, A., Baltensperger, U., Necki, J., Szidat, S., Styszko, K., Slowik, J.G., Daellenbach, K.R., 2022. Organic aerosol sources in Krakow, Poland, before implementation of a solid fuel residential heating ban. Sci. Total Environ. (submitted for publication).

Chazeau, B., El Haddad, I., Canonaco, F., Temime-Roussel, B., D'Anna, B., Gille, G., Mesbah, B., Prévôt, A.S.H., Wortham, H., Marchand, N., 2022. Organic aerosol source apportionment by using rolling positive matrix factorization: application to a Mediterranean coastal city. Atmospheric Environ.: X 14, 100176. https://doi.org/10.1016/j.aeaoa.2022.100176.

Chazeau, B., Temime-Roussel, B., Gille, G., Mesbah, B., D'Anna, B., Wortham, H., Marchand, N., 2021. Measurement report: fourteen months of real-time characterisation of the submicronic aerosol and its atmospheric dynamics at the Marseille-Longchamp supersite. Atmos. Chem. Phys. 21, 7293–7319. https://doi.org/10.5194/acp-21-7293-2021.

Chen, G., Canonaco, F., Slowik, J.G., Dallenbach, K.R., Tobler, A.K., Petit, J., Favez, O., Stavroulas, I., Mihalopoulos, N., Gerasopoulos, E., Baltensperger, U., Prévôt, A.S.H., 2022. Real-time source apportionment of organic aerosols in three european cities. Environmental Science & Technology. Submitted for publication.

Chen, G., Sosedova, Y., Canonaco, F., Fröhlich, R., Tobler, A., Vlachou, A., Daellenbach, K.R., Bozzetti, C., Hueglin, C., Graf, P., Baltensperger, U., Slowik, J.G., El Haddad, I., Prévôt, A.S.H., 2021. Time-dependent source apportionment of submicron organic aerosol for a rural site in an alpine valley using a rolling positive matrix factorisation (PMF) window. Atmospheric Chem. Phys. https://doi.org/10.5194/acp-21-15081-2021.

COLOSSAL, 2021. Guidelines for comparison of ACSM measurements with co-located external data [WWW Document]. URL http://www.actris-ecac.eu/pmc-non-refractory-organics-and-inorganics.html%0A (accessed 12.20.21).

Crenn, V., Sciare, J., Croteau, P.L., Verlhac, S., Fröhlich, R., Belis, C.A., Aas, W., Äijälä, M., Alastuey, A., Artiñano, B., Baisnée, D., Bonnaire, N., Bressi, M., Canagaratna, M., Canonaco, F., Carbone, C., Cavalli, F., Coz, E., Cubison, M.J., Esser-Gietl, J.K., Green, D.C., Gros, V., Heikkinen, L., Herrmann, H., Lunder, C., Minguillón, M.C., Močnik, G., O'Dowd, C.D., Ovadnevaite, J., Petit, J.-E., Petralia, E., Poulain, L., Priestman, M., Riffault, V., Ripoll, A., Sarda-Estève, R., Slowik, J.G., Setyan, A., Wiedensohler, A., Baltensperger, U., Prévôt, A.S.H., Jayne, J.T., Favez, O., 2015. ACTRIS ACSM intercomparison – Part 1: Reproducibility of concentration and fragment results from 13 individual Quadrupole Aerosol Chemical Speciation Monitors (Q-ACSM) and consistency with co-located instruments. Atmos. Meas. Tech. 8, 5063–5087. https://doi.org/10.5194/amt-8-5063-2015.

Crippa, M., Canonaco, F., Lanz, V.A., Äijälä, M., Allan, J.D., Carbone, S., Capes, G., Ceburnis, D., Dall'Osto, M., Day, D.A., DeCarlo, P.F., Ehn, M., Eriksson, A., Freney, E., Hildebrandt Ruiz, L., Hillamo, R., Jimenez, J.L., Junninen, H., Kiendler-Scharr, A., Kortelainen, A.-M., Kulmala, M., Laaksonen, A., Mensah, A.A., Mohr, C., Nemitz, E., O'Dowd, C., Ovadnevaite, J., Pandis, S.N., Petäjä, T., Poulain, L., Saarikoski, S., Sellegri, K., Swietlicki, E., Tiitta, P., Worsnop, D.R., Baltensperger, U., Prévôt, A.S.H., 2014. Organic aerosol components derived from 25 AMS data sets across Europe using a consistent ME-2 based source apportionment approach. Atmos. Chem. Phys. 14 (12), 6159–6176. https://doi.org/10.5194/acp-14-6159-2014.

Crippa, M., DeCarlo, P.F., Slowik, J.G., Mohr, C., Heringa, M.F., Chirico, R., Poulain, L., Freutel, F., Sciare, J., Cozic, J., Di Marco, C.F., Elsasser, M., Nicolas, J.B., Marchand, N., Abidi, E., Wiedensohler, A., Drewnick, F., Schneider, J., Borrmann, S., Nemitz, E., Zimmermann, R., Jaffrezo, J.-L., Prévôt, A.S.H., Baltensperger, U., 2013. Wintertime aerosol chemical composition and source apportionment of the organic fraction in the metropolitan area of Paris. Atmos. Chem. Phys. 13, 961–981. https://doi.org/10.5194/acp-13-961-2013.

Cubison, M.J., Ortega, A.M., Hayes, P.L., Farmer, D.K., Day, D., Lechner, M.J., Brune, W. H., Apel, E., Diskin, G.S., Fisher, J.A., Fuelberg, H.E., Hecobian, A., Knapp, D.J., Mikoviny, T., Riemer, D., Sachse, G.W., Sessions, W., Weber, R.J., Weinheimer, A.J., Wisthaler, A., Jimenez, J.L., 2011. Effects of aging on organic aerosol from open biomass burning smoke in aircraft and laboratory studies. Atmos. Chem. Phys. 11 (23), 12049–12064. https://doi.org/10.5194/acp-11-12049-2011.

Daellenbach, K.R., Bozzetti, C., Křepelová, A., Canonaco, F., Wolf, R., Zotter, P., Fermo, P., Crippa, M., Slowik, J.G., Sosedova, Y., Zhang, Y., Huang, R.-J.-J., Poulain, L., Szidat, S., Baltensperger, U., El Haddad, I., Prévôt, A.S.H., 2016. Characterization and source apportionment of organic aerosol using offline aerosol mass spectrometry. Atmos. Meas. Tech. 9, 23–39. https://doi.org/10.5194/amt-9-23-2016.

Daellenbach, K.R., Uzu, G., Jiang, J., Cassagnes, L.-E., Leni, Z., Vlachou, A., Stefenelli, G., Canonaco, F., Weber, S., Segers, A., Kuenen, J.J.P., Schaap, M., Favez, O., Albinet, A., Aksoyoglu, S., Dommen, J., Baltensperger, U., Geiser, M., El Haddad, I., Jaffrezo, J.-L., Prévôt, A.S.H., 2020. Sources of particulate-matter air pollution and its oxidative potential in Europe. Nature 587, 414–419. https://doi.org/10.1038/s41586-020-2902-8.

Drewnick, F., Hings, S.S., DeCarlo, P., Jayne, J.T., Gonin, M., Fuhrer, K., Weimer, S., Jimenez, J.L., Demerjian, K.L., Borrmann, S., Worsnop, D.R., 2005. A new time-of-flight aerosol mass spectrometer (TOF-AMS)—instrument description and first field deployment. Aerosol Sci. Technol. 39, 637–658. https://doi.org/10.1080/02786820500182040.

Efron, B., 1979. Bootstrap methods: another look at the jackknife. Ann. Stat. 7, 1–26.

Elser, M., Bozzetti, C., El-Haddad, I., Maasikmets, M., Teinemaa, E., Richter, R., Wolf, R., Slowik, J.G., Baltensperger, U., Prévôt, A.S.H., 2016. Urban increments of gaseous and aerosol pollutants and their sources using mobile aerosol mass spectrometry measurements. Atmos. Chem. Phys. Discuss. 2016, 7117–7134. https://doi.org/10.5194/acp-2016-31.

European Environment Agency (EEA), 2021. Air quality in Europe 2021. Copenhagen, Denmark. 10.2800/549289.

Farah, A., Freney, E., Canonaco, F., Prévôt, A.S.H., Pichon, J., Abboud, M., Farah, W., Sellegri, K., 2021. Altitude aerosol measurements in central france: seasonality, sources and free-troposphere/boundary layer segregation. Earth Sp. Sci. 8 https://doi.org/10.1029/2019EA001018.

Freney, E., Zhang, Y., Croteau, P., Amodeo, T., Williams, L., Truong, F., Petit, J.E., Sciare, J., Sarda-Esteve, R., Bonnaire, N., Arumae, T., Aurela, M., Bougiatioti, A., Mihalopoulos, N., Coz, E., Artinano, B., Crenn, V., Elste, T., Heikkinen, L., Poulain, L., Wiedensohler, A., Herrmann, H., Priestman, M., Alastuey, A., Stavroulas, I., Tobler, A., Vasilescu, J., Zanca, N., Canagaratna, M., Carbone, C., Flentje, H., Green, D., Maasikmets, M., Marmureanu, L., Minguillon, M.C., Prevot, A. S.H., Gros, V., Jayne, J., Favez, O., 2019. The second ACTRIS inter-comparison (2016) for Aerosol Chemical Speciation Monitors (ACSM): Calibration protocols and instrument performance evaluations. Aerosol Sci. Technol. 53, 830–842. https://doi.org/10.1080/02786826.2019.1608901.

Fröhlich, R., Crenn, V., Setyan, A., Belis, C.A., Canonaco, F., Favez, O., Riffault, V., Slowik, J.G., Aas, W., Aijälä, M., Alastuey, A., Artiñano, B., Bonnaire, N., Bozzetti, C., Bressi, M., Carbone, C., Coz, E., Croteau, P.L., Cubison, M.J., Esser-Gietl, J.K., Green, D.C., Gros, V., Heikkinen, L., Herrmann, H., Jayne, J.T., Lunder, C.R., Minguillón, M.C., Močnik, G., O'Dowd, C.D., Ovadnevaite, J., Petralia, E., Poulain, L., Priestman, M., Ripoll, A., Sarda-Estève, R., Wiedensohler, A., Baltensperger, U., Sciare, J., Prévôt, A.S.H., 2015. ACTRIS ACSM intercomparison – Part 2: Intercomparison of ME-2 organic source apportionment results from 15 individual, co-located aerosol mass spectrometers. Atmos. Meas. Tech. 8, 2555–2576. https://doi.org/10.5194/amt-8-2555-2015.

Fröhlich, R., Cubison, M.J., Slowik, J.G., Bukowiecki, N., Prévôt, A.S.H., Baltensperger, U., Schneider, J., Kimmel, J.R., Gonin, M., Rohner, U., Worsnop, D.R., Jayne, J.T., 2013. The ToF-ACSM: a portable aerosol chemical speciation monitor with TOFMS detection. Atmos. Meas. Tech. 6, 3225–3241. https://doi.org/10.5194/amt-6-3225-2013.

Fuller, G.W., Tremper, A.H., Baker, T.D., Yttri, K.E., Butterfield, D., 2014. Contribution of wood burning to PM_{10} in London. Atmos. Environ. 87, 87–94. https://doi.org/10.1016/j.atmosenv.2013.12.037.

Grieshop, A.P., Donahue, N.M., Robinson, A.L., 2009. Laboratory investigation of photochemical oxidation of organic aerosol from wood fires 2: analysis of aerosol mass spectrometer data. Atmos. Chem. Phys. 9, 2227–2240. https://doi.org/10.5194/acp-9-2227-2009.

Heikkinen, L., Äijälä, M., Daellenbach, K.R., Chen, G., Garmash, O., Aliaga, D., Graeffe, F., Räty, M., Luoma, K., Aalto, P., Kulmala, M., Petäjä, T., Worsnop, D., Ehn, M., 2021. Eight years of sub-micrometre organic aerosol composition data from the boreal forest characterized using a machine-learning approach. Atmos. Chem. Phys. 21, 10081–10109. https://doi.org/10.5194/acp-21-10081-2021.

Heringa, M.F., DeCarlo, P.F., Chirico, R., Tritscher, T., Dommen, J., Weingartner, E., Richter, R., Wehrle, G., Prévôt, A.S.H., Baltensperger, U., 2011. Investigations of primary and secondary particulate matter of different wood combustion appliances with a high-resolution time-of-flight aerosol mass spectrometer. Atmos. Chem. Phys. 11, 5945–5957. https://doi.org/10.5194/acp-11-5945-2011.

Hinds, W.C., 1999. Aerosol Technology: Properties, Behavior, and Measurement of Airborne Particles, 2nd Edition, 2nd ed. A WILEY -INTERSCIENCE PUBLICATION. John Wiley & SONS, INC., NEW YORK/CHICHESTER/WEINHEIM/BRISBANE/SINGAPORE/TORONTO.

IPCC, 2021. AR6 Climate Change 2021: The Physical Science Basis. Cambridge University Press.

Jayne, J.T., Leard, D.C., Zhang, X., Davidovits, P., Smith, K.A., Kolb, C.E., Worsnop, D.R., 2000. Development of an aerosol mass spectrometer for size and composition analysis of submicron particles. Aerosol Sci. Technol. 33, 49–70. https://doi.org/10.1080/027868200410840.

Jimenez, J.L., Canagaratna, M.R., Donahue, N.M., Prevot, A.S.H., Zhang, Q., Kroll, J.H., DeCarlo, P.F., Allan, J.D., Coe, H., Ng, N.L., Aiken, A.C., Docherty, K.S., Ulbrich, I. M., Grieshop, A.P., Robinson, A.L., Duplissy, J., Smith, J.D., Wilson, K.R., Lanz, V.A., Hueglin, C., Sun, Y.L., Tian, J., Laaksonen, A., Raatikainen, T., Rautiainen, J., Vaattovaara, P., Ehn, M., Kulmala, M., Tomlinson, J.M., Collins, D.R., Cubison, M.J., Dunlea, J., Huffman, J.A., Onasch, T.B., Alfarra, M.R., Williams, P.I., Bower, K., Kondo, Y., Schneider, J., Drewnick, F., Borrmann, S., Weimer, S., Demerjian, K., Salcedo, D., Cottrell, L., Griffin, R., Takami, A., Miyoshi, T., Hatakeyama, S., Shimono, A., Sun, J.Y., Zhang, Y.M., Dzepina, K., Kimmel, J.R., Sueper, D., Jayne, J. T., Herndon, S.C., Trimborn, A.M., Williams, L.R., Wood, E.C., Middlebrook, A.M., Kolb, C.E., Baltensperger, U., Worsnop, D.R., 2009. Evolution of organic aerosols in the atmosphere. Science (80-.) 326 (5959), 1525–1529. https://doi.org/10.1126/science.1180353.

Kodros, J.K., Papanastasiou, D.K., Paglione, M., Masiol, M., Squizzato, S., Florou, K., Skyllakou, K., Kaltsonoudis, C., Nenes, A., Pandis, S.N., 2020. Rapid dark aging of biomass burning as an overlooked source of oxidized organic aerosol. Proc. Natl. Acad. Sci. 117, 33028–33033. https://doi.org/10.1073/pnas.2010365117.

Lanz, V.A., Alfarra, M.R., Baltensperger, U., Buchmann, B., Hueglin, C., Prévôt, A.S.H., 2007. Source apportionment of submicron organic aerosols at an urban site by factor analytical modelling of aerosol mass spectra. Atmos. Chem. Phys. 7, 1503–1522. https://doi.org/10.5194/acp-7-1503-2007.

Lanz, V.A., Prévôt, A.S.H., Alfarra, M.R., Weimer, S., Mohr, C., DeCarlo, P.F., Gianini, M. F.D., Hueglin, C., Schneider, J., Favez, O., D'Anna, B., George, C., Baltensperger, U., 2010. Characterization of aerosol chemical composition with aerosol mass spectrometry in Central Europe: an overview. Atmos. Chem. Phys. 10 (21), 10453–10471. https://doi.org/10.5194/acp-10-10453-2010.

Lee, C.P., Riva, M., Wang, D., Tomaz, S., Li, D., Perrier, S., Slowik, J.G., Bourgain, F., Schmale, J., Prevot, A.S.H., Baltensperger, U., George, C., El Haddad, I., 2020. Online aerosol chemical characterization by extractive electrospray ionization–ultrahigh-resolution mass spectrometry (EESI-Orbitrap). Environ. Sci. Technol. 54, 3871–3880. https://doi.org/10.1021/acs.est.9b07090.

Lin, C., Ceburnis, D., Huang, R.-J., Xu, W., Spohn, T., Martin, D., Buckley, P., Wenger, J., Hellebust, S., Rinaldi, M., Facchini, M.C., O'Dowd, C., Ovadnevaite, J., 2019. Wintertime aerosol dominated by solid-fuel-burning emissions across Ireland: insight into the spatial and chemical variation in submicron aerosol. Atmos. Chem. Phys. 19, 14091–14106. https://doi.org/10.5194/acp-19-14091-2019.

Lin, C., Huang, R.-J., Ceburnis, D., Buckley, P., Preissler, J., Wenger, J., Rinaldi, M., Facchini, M.C., O'Dowd, C., Ovadnevaite, J., 2018. Extreme air pollution from residential solid fuel burning. Nat. Sustain. 1, 512–517. https://doi.org/10.1038/s41893-018-0125-x.

Liu, C., Chen, R., Sera, F., Vicedo-Cabrera, A.M., Guo, Y., Tong, S., Coelho, M.S.Z.S., Saldiva, P.H.N., Lavigne, E., Matus, P., Valdes Ortega, N., Osorio Garcia, S., Pascal, M., Stafoggia, M., Scortichini, M., Hashizume, M., Honda, Y., Hurtado-Díaz, M., Cruz, J., Nunes, B., Teixeira, J.P., Kim, H., Tobias, A., Íñiguez, C., Forsberg, B., Åström, C., Ragettli, M.S., Guo, Y.-L., Chen, B.-Y., Bell, M.L., Wright, C. Y., Scovronick, N., Garland, R.M., Milojevic, A., Kyselý, J., Urban, A., Orru, H., Indermitte, E., Jaakkola, J.J.K., Ryti, N.R.I., Katsouyanni, K., Analitis, A., Zanobetti, A., Schwartz, J., Chen, J., Wu, T., Cohen, A., Gasparrini, A., Kan, H., 2019. Ambient particulate air pollution and daily mortality in 652 cities. N. Engl. J. Med. 381, 705–715. https://doi.org/10.1056/NEJMoa1817364.

Lopez-Hilfiker, F.D., Mohr, C., Ehn, M., Rubach, F., Kleist, E., Wildt, J., Mentel, T.F., Lutz, A., Hallquist, M., Worsnop, D., Thornton, J.A., 2014. A novel method for online analysis of gas and particle composition: description and evaluation of a Filter Inlet for Gases and AEROsols (FIGAERO). Atmos. Meas. Tech. 7, 983–1001. https://doi.org/10.5194/amt-7-983-2014.

Lopez-Hilfiker, F.D., Pospisilova, V., Huang, W., Kalberer, M., Mohr, C., Stefenelli, G., Thornton, J.A., Baltensperger, U., Prevot, A.S.H., Slowik, J.G., 2019. An Extractive Electrospray Ionization Time-of-Flight Mass Spectrometer (EESI-TOF) for online measurement of atmospheric aerosol particles. Atmos. Meas. Tech. 12, 4867–4886. https://doi.org/10.5194/amt-12-4867-2019.

Minguillón, M.C., Ripoll, A., Pérez, N., Prévôt, A.S.H., Canonaco, F., Querol, X., Alastuey, A., 2015. Chemical characterization of submicron regional background aerosols in the western Mediterranean using an Aerosol Chemical Speciation Monitor. Atmos. Chem. Phys. 15, 6379–6391. https://doi.org/10.5194/acp-15-6379-2015.

Mohr, C., DeCarlo, P.F., Heringa, M.F., Chirico, R., Slowik, J.G., Richter, R., Reche, C., Alastuey, A., Querol, X., Seco, R., Peñuelas, J., Jiménez, J.L., Crippa, M., Zimmermann, R., Baltensperger, U., Prévôt, A.S.H., 2012. Identification and quantification of organic aerosol from cooking and other sources in Barcelona using aerosol mass spectrometer data. Atmos. Chem. Phys. 12, 1649–1665. https://doi.org/10.5194/acp-12-1649-2012.

Ng, N.L., Canagaratna, M.R., Jimenez, J.L., Zhang, Q., Ulbrich, I.M., Worsnop, D.R., 2011a. Real-time methods for estimating organic component mass concentrations from aerosol mass spectrometer data. Environ. Sci. Technol. 45, 910–916. https://doi.org/10.1021/es102951k.

Ng, N.L., Canagaratna, M.R., Zhang, Q., Jimenez, J.L., Tian, J., Ulbrich, I.M., Kroll, J.H., Docherty, K.S., Chhabra, P.S., Bahreini, R., Murphy, S.M., Seinfeld, J.H., Hildebrandt, L., Donahue, N.M., DeCarlo, P.F., Lanz, V.A., Prévôt, A.S.H., Dinar, E., Rudich, Y., Worsnop, D.R., 2010. Organic aerosol components observed in Northern Hemispheric datasets from Aerosol Mass Spectrometry. Atmos. Chem. Phys. 10, 4625–4641. https://doi.org/10.5194/acp-10-4625-2010.

Ng, N.L., Herndon, S.C., Trimborn, A., Canagaratna, M.R., Croteau, P.L., Onasch, T.B., Sueper, D., Worsnop, D.R., Zhang, Q., Sun, Y.L., Jayne, J.T., 2011b. An Aerosol Chemical Speciation Monitor (ACSM) for routine monitoring of the composition and mass concentrations of ambient aerosol. Aerosol Sci. Technol. 45, 780–794. https://doi.org/10.1080/02786826.2011.560211.

Paatero, P., 1999. The multilinear engine—a table-driven, least squares program for solving multilinear problems, including the n -way parallel factor analysis model. J. Comput. Graph. Stat. 8, 854–888. https://doi.org/10.1080/10618600.1999.10474853.

Paatero, P., Eberly, S., Brown, S.G., Norris, G.A., 2014. Methods for estimating uncertainty in factor analytic solutions. Atmos. Meas. Tech. 7, 781–797. https://doi.org/10.5194/amt-7-781-2014.

Paatero, P., Hopke, P.K., 2009. Rotational tools for factor analytic models. J. Chemom. 23, 91–100. https://doi.org/10.1002/cem.1197.

Paatero, P., Hopke, P.K., Song, X.-H., Ramadan, Z., 2002. Understanding and controlling rotations in factor analytic models. Chemom. Intell. Lab. Syst. 60, 253–264. https://doi.org/10.1016/S0169-7439(01)00200-3.

Paatero, P., Tapper, U., 1994. Positive matrix factorization: a non-negative factor model with optimal utilization of error estimates of data values. Environmetrics 5, 111–126. https://doi.org/10.1002/env.3170050203.

Parworth, C., Fast, J., Mei, F., Shippert, T., Sivaraman, C., Tilp, A., Watson, T., Zhang, Q., 2015. Long-term measurements of submicrometer aerosol chemistry at the Southern Great Plains (SGP) using an Aerosol Chemical Speciation Monitor (ACSM). Atmos. Environ. 106, 43–55. https://doi.org/10.1016/j.atmosenv.2015.01.060.

Petit, J.-E., Dupont, J.-C., Favez, O., Gros, V., Zhang, Y., Sciare, J., Simon, L., Truong, F., Bonnaire, N., Amodeo, T., Vautard, R., Haeffelin, M., 2021. Response of atmospheric composition to COVID-19 lockdown measures during spring in the Paris region (France). Atmos. Chem. Phys. 21, 17167–17183. https://doi.org/10.5194/acp-21-17167-2021.

Pfaffenberger, L., Barmet, P., Slowik, J.G., Praplan, A.P., Dommen, J., Prévôt, A.S.H., Baltensperger, U., 2013. The link between organic aerosol mass loading and degree of oxygenation: an α-pinene photooxidation study. Atmos. Chem. Phys. 13, 6493–6506. https://doi.org/10.5194/acp-13-6493-2013.

Pieber, S.M., El Haddad, I., Slowik, J.G., Canagaratna, M.R., Jayne, J.T., Platt, S.M., Bozzetti, C., Daellenbach, K.R., Fröhlich, R., Vlachou, A., Klein, F., Dommen, J., Miljevic, B., Jiménez, J.L., Worsnop, D.R., Baltensperger, U., Prévôt, A.S.H., 2016. Inorganic salt interference on CO_2^+ in Aerodyne AMS and ACSM organic aerosol composition studies. Environ. Sci. Technol. 50, 10494–10503. https://doi.org/10.1021/acs.est.6b01035.

Poulain, L., Spindler, G., Grüner, A., Tuch, T., Stieger, B., van Pinxteren, D., Petit, J.-E., Favez, O., Herrmann, H., Wiedensohler, A., van Pinxteren, D., Herrmann, H., Wiedensohler, A., 2020. Multi-year ACSM measurements at the central European research station Melpitz (Germany) – Part 1: instrument robustness, quality assurance, and impact of upper size cutoff diameter. Atmos. Meas. Tech. 13, 4973–4994. https://doi.org/10.5194/amt-13-4973-2020.

Qi, L., Chen, M., Stefenelli, G., Pospisilova, V., Tong, Y., Bertrand, A., Hueglin, C., Ge, X., Baltensperger, U., Prévôt, A.S.H., Slowik, J.G., 2019. Organic aerosol source apportionment in Zurich using an extractive electrospray ionization time-of-flight mass spectrometer (EESI-TOF-MS) - Part 2: biomass burning influences in winter. Atmos. Chem. Phys. 19, 1–42. https://doi.org/10.5194/acp-19-8037-2019.

Sandradewi, J., Prévôt, A.S.H., Szidat, S., Perron, N., Alfarra, M.R., Lanz, V.A., Weingartner, E., Baltensperger, U., 2008. Using aerosol light absorption measurements for the quantitative determination of wood burning and traffic emission contributions to particulate matter. Environ. Sci. Technol. 42, 3316–3323. https://doi.org/10.1021/es702253m.

Stavroulas, I., Bougiatioti, A., Grivas, G., Paraskevopoulou, D., Tsagkaraki, M., Zarmpas, P., Liakakou, E., Gerasopoulos, E., Mihalopoulos, N., 2019. Sources and processes that control the submicron organic aerosol composition in an urban Mediterranean environment (Athens): a high temporal-resolution chemical composition measurement study. Atmos. Chem. Phys. 19, 901–919. https://doi.org/10.5194/acp-19-901-2019.

Stefenelli, G., Pospisilova, V., Lopez-Hilfiker, F.D., Daellenbach, K.R., Hüglin, C., Tong, Y., Baltensperger, U., Prevot, A.S.H., Slowik, J.G., 2019. Organic aerosol source apportionment in Zurich using an extractive electrospray ionization time-of-flight mass spectrometer (EESI-TOF-MS) - Part 1: biogenic influences and day-night chemistry in summer. Atmos. Chem. Phys. 19, 14825–14848. https://doi.org/10.5194/acp-19-14825-2019.

Stull, R.B., 1988. An Introduction to Boundary Layer Meteorology, 1st ed. Springer, Dordrecht Netherlands, Dordrecht. 10.1007/978-94-009-3027-8.

Sun, Y., Du, W., Fu, P., Wang, Q., Li, J., Ge, X., Zhang, Q., Zhu, C., Ren, L., Xu, W., Zhao, J., Han, T., Worsnop, D.R., Wang, Z., 2016. Primary and secondary aerosols in Beijing in winter: sources, variations and processes. Atmos. Chem. Phys. 16, 8309–8329. https://doi.org/10.5194/acp-16-8309-2016.

Tiitta, P., Leskinen, A., Hao, L., Yli-Pirilä, P., Kortelainen, M., Grigonyte, J., Tissari, J., Lamberg, H., Hartikainen, A., Kuuspalo, K., Kortelainen, A.-M., Virtanen, A., Lehtinen, K.E.J., Komppula, M., Pieber, S., Prévôt, A.S.H., Onasch, T.B., Worsnop, D.

R., Czech, H., Zimmermann, R., Jokiniemi, J., Sippula, O., 2016. Transformation of logwood combustion emissions in a smog chamber: formation of secondary organic aerosol and changes in the primary organic aerosol upon daytime and nighttime aging. Atmos. Chem. Phys. 16, 13251–13269. https://doi.org/10.5194/acp-16-13251-2016.

Tobler, A.K., Skiba, A., Canonaco, F., Močnik, G., Rai, P., Chen, G., Bartyzel, J., Zimnoch, M., Styszko, K., Nęcki, J., Furger, M., Różański, K., Baltensperger, U., Slowik, J.G., Prevot, A.S.H., 2021. Characterization of non-refractory (NR) PM_1 and source apportionment of organic aerosol in Kraków. Atmos. Chem. Phys. 21, 14893–14906. https://doi.org/10.5194/acp-21-14893-2021.

Ulbrich, I.M., Canagaratna, M.R., Zhang, Q., Worsnop, D.R., Jimenez, J.L., 2009. Interpretation of organic components from Positive Matrix Factorization of aerosol mass spectrometric data. Atmos. Chem. Phys. 9, 2891–2918. https://doi.org/10.5194/acp-9-2891-2009.

Via, M., Minguillón, M.C., Reche, C., Querol, X., Alastuey, A., 2021. Increase in secondary organic aerosol in an urban environment. Atmos. Chem. Phys. 21, 8323–8339. https://doi.org/10.5194/acp-21-8323-2021.

Weimer, S., Alfarra, M.R., Schreiber, D., Mohr, M., Prévôt, A.S.H., Baltensperger, U., 2008. Organic aerosol mass spectral signatures from wood-burning emissions: Influence of burning conditions and wood type. J. Geophys. Res. 113, D10304. https://doi.org/10.1029/2007JD009309.

World Health Organization, 2021. WHO global air quality guidelines. Particulate matter ($PM_{2.5}$ and PM_{10}), ozone, nitrogen dioxide, sulfur dioxide and carbon monoxide. Geneva.

Xie, M., Hannigan, M.P., Barsanti, K.C., 2014. Gas/Particle Partitioning of 2-Methyltetrols and Levoglucosan at an Urban Site in Denver. Environ. Sci. Technol. 48, 2835–2842. https://doi.org/10.1021/es405356n.

Xu, W., Croteau, P., Williams, L., Canagaratna, M., Onasch, T., Cross, E., Zhang, X., Robinson, W., Worsnop, D., Jayne, J., 2017. Laboratory characterization of an aerosol chemical speciation monitor with PM 2.5 measurement capability. Aerosol Sci. Technol. 51, 69–83. https://doi.org/10.1080/02786826.2016.1241859.

Yang, Y., Wang, H., Smith, S.J., Zhang, R., Lou, S., Yu, H., Li, C., Rasch, P.J., 2018. Source apportionments of aerosols and their direct radiative forcing and long-term trends over continental United States. Earth's Futur. 6, 793–808. https://doi.org/10.1029/2018EF000859.

Yang, Y., Ruan, Z., Wang, X., Yang, Y., Mason, T.G., Lin, H., Tian, L., 2019. Short-term and long-term exposures to fine particulate matter constituents and health: a systematic review and meta-analysis. Environ. Pollut. 247, 874–882. https://doi.org/10.1016/j.envpol.2018.12.060.

Yli-Juuti, T., Mielonen, T., Heikkinen, L., Arola, A., Ehn, M., Isokääntä, S., Keskinen, H.-M., Kulmala, M., Laakso, A., Lipponen, A., Luoma, K., Mikkonen, S., Nieminen, T., Paasonen, P., Petäjä, T., Romakkaniemi, S., Tonttila, J., Kokkola, H., Virtanen, A., 2021. Significance of the organic aerosol driven climate feedback in the boreal area. Nat. Commun. 12, 5637. https://doi.org/10.1038/s41467-021-25850-7.

Yttri, K.E., Canonaco, F., Eckhardt, S., Evangeliou, N., Fiebig, M., Gundersen, H., Hjellbrekke, A.-G., Lund Myhre, C., Platt, S.M., Prévôt, A.S.H., Simpson, D., Solberg, S., Surratt, J., Tørseth, K., Uggerud, H., Vadset, M., Wan, X., Aas, W., 2021. Trends, composition, and sources of carbonaceous aerosol at the Birkenes Observatory, northern Europe, 2001–2018. Atmos. Chem. Phys. 21, 7149–7170. https://doi.org/10.5194/acp-21-7149-2021.

Zhang, Q., Jimenez, J.L., Canagaratna, M.R., Allan, J.D., Coe, H., Ulbrich, I., Alfarra, M. R., Takami, A., Middlebrook, A.M., Sun, Y.L., Dzepina, K., Dunlea, E., Docherty, K., DeCarlo, P.F., Salcedo, D., Onasch, T., Jayne, J.T., Miyoshi, T., Shimono, A., Hatakeyama, S., Takegawa, N., Kondo, Y., Schneider, J., Drewnick, F., Borrmann, S., Weimer, S., Demerjian, K., Williams, P., Bower, K., Bahreini, R., Cottrell, L., Griffin, R.J., Rautiainen, J., Sun, J.Y., Zhang, Y.M., Worsnop, D.R., 2007. Ubiquity and dominance of oxygenated species in organic aerosols in anthropogenically-influenced Northern Hemisphere midlatitudes. Geophys. Res. Lett. 34 (13) https://doi.org/10.1029/2007GL029979.

Zhang, Q., Jimenez, J.L., Canagaratna, M.R., Ulbrich, I.M., Ng, N.L., Worsnop, D.R., Sun, Y., 2011. Understanding atmospheric organic aerosols via factor analysis of aerosol mass spectrometry: a review. Anal. Bioanal. Chem. 401, 3045–3067. https://doi.org/10.1007/s00216-011-5355-y.

Zhang, Y., Albinet, A., Petit, J.-E., Jacob, V., Chevrier, F., Gille, G., Pontet, S., Chrétien, E., Dominik-Sègue, M., Levigoureux, G., Močnik, G., Gros, V., Jaffrezo, J.-L., Favez, O., 2020. Substantial brown carbon emissions from wintertime residential wood burning over France. Sci. Total Environ. 743, 140752 https://doi.org/10.1016/j.scitotenv.2020.140752.

Zhang, Y., Favez, O., Petit, J.-E., Canonaco, F., Truong, F., Bonnaire, N., Crenn, V., Amodeo, T., Prévôt, A.S.H., Sciare, J., Gros, V., Albinet, A., 2019. Six-year source apportionment of submicron organic aerosols from near-continuous highly time-resolved measurements at SIRTA (Paris area, France). Atmos. Chem. Phys. 19, 14755–14776. https://doi.org/10.5194/acp-19-14755-2019.

Zotter, P., Herich, H., Gysel, M., El-Haddad, I., Zhang, Y., Močnik, G., Hüglin, C., Baltensperger, U., Szidat, S., Prévôt, A.S.H., 2017. Evaluation of the absorption Ångström exponents for traffic and wood burning in the Aethalometer-based source apportionment using radiocarbon measurements of ambient aerosol. Atmos. Chem. Phys. 17, 4229–4249. https://doi.org/10.5194/acp-17-4229-2017.

Annexe 5. *Rolling* vs. *seasonal* PMF: real-world multi-site and synthetic dataset comparison; Via et al. (2022)

Atmos. Meas. Tech., 15, 5479–5495, 2022
https://doi.org/10.5194/amt-15-5479-2022

Atmospheric Measurement Techniques
Open Access
EGU

Rolling vs. *seasonal* PMF: real-world multi-site and synthetic dataset comparison

Marta Via[1,2], Gang Chen[3,a], Francesco Canonaco[3,4], Kaspar R. Daellenbach[3], Benjamin Chazeau[5], Hasna Chebaicheb[6,7], Jianhui Jiang[8], Hannes Keernik[9,10], Chunshui Lin[11], Nicolas Marchand[5], Cristina Marin[12,13], Colin O'Dowd[11], Jurgita Ovadnevaite[11], Jean-Eudes Petit[14], Michael Pikridas[15], Véronique Riffault[6], Jean Sciare[15], Jay G. Slowik[3], Leïla Simon[7,13], Jeni Vasilescu[12], Yunjiang Zhang[7,13], Olivier Favez[7], André S. H. Prévôt[3], Andrés Alastuey[1], and María Cruz Minguillón[1]

[1]Institute of Environmental Assessment and Water Research, Barcelona, 08034, Spain
[2]Department of Applied Physics, University of Barcelona, Barcelona, 08028, Spain
[3]Laboratory of Atmospheric Chemistry, Paul Scherrer Institute, 5232 Villigen PSI, Switzerland
[4]Datalystica Ltd., Park innovAARE, 5234 Villigen, Switzerland
[5]Aix Marseille Univ., CNRS, LCE, Marseille, France
[6]IMT Nord Europe, Institut Mines-Télécom, Univ. Lille, Centre for Energy and Environment, 59000 Lille, France
[7]Institut National de l'Environnement Industriel et des Risques, Parc Technologique ALATA, 60550, Verneuil-en-Halatte, France
[8]Shanghai Key Lab for Urban Ecological Processes and Eco-Restoration, School of Ecological and Environmental Sciences, East China Normal University, 200241 Shanghai, China
[9]Air Quality and Climate Department, Estonian Environmental Research Centre, Marja 4d, 10617 Tallinn, Estonia
[10]Department of Software Science, Tallinn University of Technology, 19086 Tallinn, Estonia
[11]School of Physics and Centre for Climate and Air Pollution Studies, Ryan Institute, National University of Ireland Galway, University Road, H91CF50 Galway, Ireland
[12]National Institute of Research and Development for Optoelectronics INOE2000, Atomistilor 409, RO77125 Magurele, Romania
[13]Department of Physics, Politehnica University of Bucharest, 313 Spl. Independentei Str., Bucharest, Romania
[14]Laboratoire des Sciences du Climat et de l'Environnement, Orme des Merisiers, 91190 Gif-sur-Yvette, France
[15]Climate and Atmosphere Research Center, The Cyprus Institute, Nicosia, 2121, Cyprus
[a]now at: MRC Centre for Environment and Health, Environmental Research Group, Imperial College London, London, UK

Correspondence: Marta Via (marta.via@idaea.csic.es)

Received: 29 April 2022 – Discussion started: 30 May 2022
Revised: 30 August 2022 – Accepted: 31 August 2022 – Published: 27 September 2022

Abstract. Particulate matter (PM) has become a major concern in terms of human health and climate impact. In particular, the source apportionment (SA) of organic aerosols (OA) present in submicron particles (PM_1) has gained relevance as an atmospheric research field due to the diversity and complexity of its primary sources and secondary formation processes. Moreover, relatively simple but robust instruments such as the Aerosol Chemical Speciation Monitor (ACSM) are now widely available for the near-real-time online determination of the composition of the non-refractory PM_1. One of the most used tools for SA purposes is the source-receptor positive matrix factorisation (PMF) model. Even though the recently developed *rolling PMF* technique has already been used for OA SA on ACSM datasets, no study has assessed its added value compared to the more common *seasonal* PMF method using a practical approach yet. In this paper, both techniques were applied to a synthetic dataset and to nine European ACSM datasets in order to spot the main output discrepancies between methods. The main advantage of the synthetic dataset approach was that the meth-

ods' outputs could be compared to the expected "true" values, i.e. the original synthetic dataset values. This approach revealed similar apportionment results amongst methods, although the *rolling* PMF profile's adaptability feature proved to be advantageous, as it generated output profiles that moved nearer to the *truth* points. Nevertheless, these results highlighted the impact of the profile anchor on the solution, as the use of a different anchor with respect to the *truth* led to significantly different results in both methods. In the multi-site study, while differences were generally not significant when considering year-long periods, their importance grew towards shorter time spans, as in intra-month or intra-day cycles. As far as correlation with external measurements is concerned, *rolling* PMF performed better than *seasonal* PMF globally for the ambient datasets investigated here, especially in periods between seasons. The results of this multi-site comparison coincide with the synthetic dataset in terms of *rolling–seasonal* similarity and *rolling* PMF reporting moderate improvements. Altogether, the results of this study provide solid evidence of the robustness of both methods and of the overall efficiency of the recently proposed *rolling* PMF approach.

1 Introduction

Air pollution is one of the biggest current and future environmental threats to human health and climate change. Results from Chen and Hoek (2020) notably relate an increased risk for all-cause mortality due to fine aerosol ($PM_{2.5}$, particulate matter with an aerodynamic particle diameter below 2.5 mm) exposure. Also, even for concentrations below the WHO guidelines threshold (annual means of $5\,\mu g\,m^{-3}$ for $PM_{2.5}$ at the time that this article was published), the life expectancy of the population of Europe has been reduced by an average of about 8.6 months. In turn, fine atmospheric aerosols also play a role in climate change (IPCC, 2021) due to both their direct (through radiation) and indirect (through cloud interaction) effects.

Exposure to submicron particulate matter (PM_1, particulate matter with an aerodynamic particle diameter of less than 1 µm) is known to have severe impacts on the respiratory system (Yang et al., 2018) and even to pass the blood–brain barrier to act directly on the central nervous system (Shih et al., 2018; Yin et al., 2020). Impact mitigation strategies must be designed to both reduce emissions (primary aerosols) and prevent the formation of indirectly emitted (or secondary) aerosols as well as to target the most harmful components, especially since recent studies have demonstrated that the mitigation strategies might be more effective in tackling specific PM sources rather than the bulk PM (Daellenbach et al., 2020). With the purpose of identifying the most appropriate reduction strategies, source apportionment (SA) methodologies, designed for identifying pollutant sources, must be constantly improved. One of the most widely used receptor models for SA is the positive matrix factorisation (PMF) model (Paatero and Tapper, 1994) along with the ME-2 engine (Paatero, 1999). This model can handle various types of data, such as online and offline PM datasets (Amato et al., 2016; Crippa et al., 2014; Rai et al., 2020, respectively), VOCs (Yuan et al., 2012), multi-wavelength absorption of refractory carbon (Forello et al., 2019) etc.; assemble different types of pollutants (Ogulei et al., 2005); and also be coupled to machine learning techniques (Heikkinen et al., 2021; Rutherford et al., 2021).

Since organic species account for 20–90 % of the total submicron aerosol mass (Chen et al., 2022; Jimenez et al., 2009), scientific interest has been set on the characterisation of these pollutants by offline and online techniques. The use of ACSM (Aerosol Chemical Speciation Monitor, Aerodyne Research Inc., Billerica, MA, USA) for continuous monitoring and quantification of submicron non-refractory compounds has become a key approach for air quality (AQ) assessment. The application of PMF to long-term ACSM submicron organic aerosol (OA) datasets (Sun et al., 2018; Zhang et al., 2019) under the Source Finder (SoFi) Pro software package (Datalystica Ltd.) allows us to quantify and identify the contribution of major groups of organic compounds. The formerly recommended methodology for OA SA was *seasonal* PMF, which requires splitting the dataset into seasons to perform PMF independently, providing *seasonal* but not an intra-seasonal variation of factor profiles, as reported in Canonaco et al. (2015). The more recently developed *rolling* PMF (Canonaco et al., 2021; Parworth et al., 2015) applies the model on moving or rolling windows of a selected length, and therefore it accounts for the temporal evolution of the OA source fingerprints. The current state of the art supports that *rolling* PMF should be more accurate and/or suitable than *seasonal* PMF due to its profile-adaptation feature and its lower computational and evaluation time, which will be the base hypothesis of this study. Nevertheless, only a few individual studies (Chazeau et al., 2021; Chen et al., 2021; Tobler et al., 2021) and an intercomparison (Chen et al., 2022) using this technique have been published so far, and no thorough *seasonal vs. rolling* comparison has been conducted thus far to the best of our knowledge.

This research aims to contribute to a deeper understanding of the advantages and weaknesses of the *rolling* and *seasonal* methods, assessing the differences regarding site or dataset characteristics and evaluating the environmental reasonability of their outcomes. This task is of great importance, as the knowledge of the strengths of each method will come in handy when choosing the best one for each study necessity, e.g. the better SA method for specific OA source outbreaks. Furthermore, conclusions from this analysis will also impact the quality of health, climate and modelling studies by means of an improved description of the main OA pollution sources.

2 Methodology

2.1 Instrumentation and datasets

This study is one of the outcomes of the Chemical On-Line cOmpoSition and Source Apportionment of fine aerosoL (COLOSSAL) project (https://cost-colossal.eu/, last access: 14 September 2022) supported by the COST programme and based on measurements performed within the ACTRIS network. It is closely related to the overview study of Chen et al. (2022), in which 22 more-than-one-year-long PMF datasets were joined for a *rolling* PMF intercomparison. Participants of the WG2 of the COST COLOSSAL Action contributed to the preparation of a protocol for SA, with the purpose of homogenising the PMF application (Chen et al., 2022). A total of 9 of the 22 datasets from that study, whose main characteristics can be found in Table 1, were also provided for this *rolling–seasonal* comparison. Some of them contain site-specific sources related to instrument artefacts or proximity to pollution hotspots. The factors identified at all sites are hydrocarbon-like OA (HOA), biomass burning OA (BBOA, except for the Dublin site), less-oxidised oxygenated OA (LO-OOA), more-oxidised oxygenated OA (MO-OOA), and oxygenated OA (OOA), which represents the sum of LO-OOA and MO-OOA. Other factors are only present at one or two sites: cooking-like OA (COA; in Barcelona–Palau Reial and Marseille–Longchamp); 58-related OA (58-OA; in Magadino); shipping and industry OA (SHINDOA; in Marseille–Longchamp); wood combustion, coal combustion, and peat combustion OA (WCOA, CCOA, PCOA, respectively; in Dublin). The 58-related OA, as explained in Chen et al. (2021), is a factor dominated by nitrogen fragments (m/z 58, m/z 84, m/z 94) that appeared as an artefact after the filament replacement in that instrument.

All data presented in the multi-site intercomparison were obtained from ACSMs, which use a mass spectrometer to measure the composition of non-refractory submicron particulate matter (NR-PM_1) in near-real time. It works at a lower mass-to-charge resolution, but it is more robust compared to the aerosol mass spectrometer (AMS, Aerodyne Research Inc, Billerica, MA, USA), allowing for long-term deployment. Both quadrupole (Q-ACSM) and time-of-flight (ToF-ACSM) ACSMs were used, further described respectively in Fröhlich et al. (2013) and Ng et al. (2011a). The resolution of ToF-ACSM datasets (10 min) was averaged to 30 min (resolution of the Q-ACSM) to have harmonised timestamps. The analysis software (version 1.6.1.1 for Q-ACSM and version 2.3.9 for ToF-ACSM), implemented in Igor Pro (WaveMetrics, Inc.), was provided by Aerodyne Research Inc. The treatment of the multi-site ACSM data to generate PMF input matrices is summarised in Table S1 in the Supplement, and more details can be found in the publications cited therein.

Ancillary measurements consisted of (i) SO_4^{2-}, NO_3^-, NH_4^+, and Cl^- measurements from ACSM; (ii) black carbon (BC) from the filter-based absorption photometer AE33 from Magee Scientific (Drinovec et al., 2015), except for those from the Cyprus Atmospheric Observatory – Agia Marina Xyliatou and Magadino, in which the AE31 was used; BC concentrations were differentiated according to their main sources into fossil fuel (BC_{ff}) and wood burning (BC_{wb}) BC by applying the Sandradewi model (Sandradewi et al., 2008); (iii) NO_X concentrations; (iv) ultra-fine particles (range 20–1000 nm) at the Marseille–Longchamp site. Details on the complementary instrumentation at each site can be found in Table S2.

2.2 Synthetic dataset

Although the principal aim of this article is to inspect the differences in the methods amongst these European sites, a synthetic dataset comparison was first tackled. The main advantage of this procedure is that it allows the real-world environmental measurements already classified in OA sources to be mimicked so that PMF results can be compared with the incoming synthetic data. We created a synthetic dataset that mimics OA mass spectral analyses of a ToF-ACSM in Zurich. For that purpose, we used source-specific OA mass spectra retrieved from the AMS spectral database (Crippa et al., 2013; Ng et al., 2011b; Ulbrich et al., 2009) and OA source concentration time series generated by the air quality model CAMx (Comprehensive Air Quality Model with Extensions) previously published by Jiang et al. (2019). Details are described in Sect. S1. The dataset used to calculate the error matrix is that from the Zurich site, which ranges from February 2011 until December 2011. Hence, the same CAMx outcoming time series period was used to generate the concentration matrix. The represented OA sources are HOA, BBOA, SOA from biogenic emissions (SOA_{bio}), SOA from biomass burning (SOA_{bb}), and SOA from traffic and other anthropogenic sources (SOA_{tr}).

The first step for the synthetic dataset creation was to select p (number of factors), POA, and SOA spectral profiles from the high-resolution AMS spectral database (Crippa et al., 2013; Ng et al., 2010; Ulbrich et al., 2009) and to multiply them by the time series of the same sources from the model output. The error matrix was generated following the same steps as for real-world data, and real-world parameters were used as detailed in the Supplement. For this purpose, the dataset used is that from the Zurich site, which ranges from February 2011 until December 2011. Hence, the same CAMx outcoming time series period was used to generate the concentration matrix. Gaussian noise was subsequently added to the outcoming matrix. The resulting matrices were used as *rolling* and *seasonal* PMF input. Before the comparison to the original factors, several tests, as in the multi-site comparison, were performed to check the quality of the output; these tests included the mass closure test and the scaled residuals profile revision.

Table 1. Participant sites.

Site	Type	Latitude	Longitude	Height (m a.s.l.)	ACSM type	Network	Period
Barcelona – Palau Reial (BCN-PR)	Urban background	41°23′11.48″ N	02°07′05.00″ E	80	*Q*	ACTRIS, GAW	Sep 2017–Oct 2018
Cyprus Atm. Obs. – Agia Marina Xyliatou (CAO-AMX)	Remote	35°2′19.35″ N	33°3′27.95″ E	352	*Q*	ACTRIS, GAW	Mar 2015–Jan 2017
Dublin (DUB)	Urban background	53°18′19.08″ N	06°3′4.52″ W	35	*Q*	ACTRIS, AQ network in Ireland: http://www.macehead.org/ (last access: Sep 2022)	Sep 2015–Aug 2017
ATmospheric Observations in liLle (ATOLL)	Suburban	50°36′40.0 N	03°08′25.4″ E	70	*Q*	ACTRIS, CARA programme (French AQ network)	Oct 2016–Sep 2017
Magadino (MGD)	Rural	46°9′37″ N	8°56′2″ E	204	*Q*	GAW	Aug 2013–Oct 2014
Magurele – INOE (INO)	Peri-urban	44°20′52.98′, N	26°1′43.93″ E	93	*Q*	ACTRIS, GAW	Sep 2016–Sep 2017
Marseille–Longchamp (MRS-LCP)	Urban background	43°18′18.84″ N	5°23′40.89″ E	71	ToF	CARA programme (French AQ network)	Jan 2017–Apr 2018
SIRTA (SIR)	Suburban	48°42″36″ N	2°9″0″ E	163	*Q*	ACTRIS	Jan 2016–May 2017
Tartu (TAR)	Urban background	58°22′14.16″ N	26°44′5.64″ E	39	*Q*	National air monitoring station	Sep 2016–Jul 2017

2.3 Positive matrix factorisation

The positive matrix factorisation model (Paatero and Tapper, 1994) describes the measured matrix **X** of n timestamps and m variables as a product of two matrices, **G** and **F**, plus a residual matrix **E** for a given number of factors p:

$$x_{ij} = \sum_{i,j}^{n,m} g_{ik} \cdot f_{kj} + e_{ij}\,. \quad (1)$$

The matrices **G** and **F** can be randomly initialised with a priori information. The model then iterates until the quantity

$$Q = \sum_{i=1}^{n} \sum_{j=1}^{m} \left(\frac{e_{ij}}{\sigma_{ij}}\right)^2, \quad (2)$$

where σ_{ij} represents the uncertainties of the input matrix **X**, is minimised with respect to all model variables.

The use of a priori information reduces the rotational ambiguity of the model, consisting of a degeneration of solutions associated with a given Q value (Canonaco et al., 2013), and it is usually done from the a-value approach. This consists of initialising **F** (or **G**) with reference profiles (or time series) and multiplying them by the percentage of variation a, $a \in [0,1]$, where 0 and 1 would represent total constraint and freedom, respectively. The Source Finder (SoFi Pro, versions 6.8 and 8.04, Datalystica Ltd., Villigen, Switzerland) applies this algorithm through the multi-linear engine 2 (ME-2) (Paatero, 1999) within the Igor Pro software environment (Wavemetrics, Inc., Portland, OR, USA). SoFi is also a powerful software package for preparing the rolling conditions for the input matrices prior to the PMF algorithm and post-processing the outcomes afterwards.

2.3.1 *Seasonal* PMF

In order to apply *seasonal* PMF, the input matrix is divided into season-long submatrices, and PMF is applied independently, adjusting the number of necessary factors to the requirements of each subperiod. In order to reach an environmentally reasonable local Q minimum, the implemen-

tation of constraints on primary organic aerosol(POA) factors has been performed according to the COLOSSAL guidelines for source apportionment (COLOSSAL, COST Action CA16109, 2019) and the protocol from Chen et al. (2022). After unconstrained results exploration, which allowed for some marker identification, constraints based on the *a*-value approach were applied to primary OA factors. The systematic exploration of the *a*-value space has been performed for each season, with the aim of determining the combination of *a* values that maximises the correlations between factors and external correlations and represents an environmentally reasonable OA explanation, hereafter referred to as the base-case solution. The random *a*-value ranges and the reference profiles employed can be found in Tables S1 and S3a.

With respect to the synthetic dataset, the 11 months from 2011 data were split into three periods (and not four seasons to avoid running PMF over too short periods): February–May, June–August, and September–December. The real-world Marseille dataset also used the co-located SO_2 time series to force an industry + shipping factor to emerge, as reported in previous studies (Bozzetti et al., 2017; El Haddad et al., 2013). The seasonal averaging of the remaining runs were complemented by bootstrapping to estimate the statistical error of the solution.

Bootstrapping (Efron, 1979) the *seasonal* PMF input together with random *a*-value resampling allows for a statistical and rotational uncertainty assessment. The application of a criteria-based selection, which will be deeply explained in Sect. 2.3.2, was also used to discard those runs that did not comply with the user-defined standards. The outcome of this technique consists of *p* (number of factors) mass spectra and time series, including their uncertainty assessment, combined season-wise together to obtain period-long OA sources. This might lead to possible factor discontinuity. Moreover, from this approach, source fingerprints are static throughout a whole season and cannot adapt to the OA processes of lifetimes below a meteorological season (i.e. 90 d) but can nevertheless evolve from one season to another.

2.3.2 *Rolling* PMF

Rolling PMF runs the model on subsets of the input matrix with a user-defined (window) length in days. Then, the window is shifted by a number of days (also chosen by the user), and PMF is applied again (Parworth et al., 2015). Consequently, many PMF runs are performed in each window length period, so in the post-analysis, one can automatically discard the runs that do not meet certain user-defined criteria (Canonaco et al., 2015). To select the most environmentally reasonable runs, the remaining solutions are averaged to generate the final solution, which will be provided with statistical and rotational uncertainties based on random input resampling (bootstrap) and random *a*-value resampling, respectively.

A length of 14 d and a shift of 1 d were used in the current study for the synthetic dataset and for 7 out of the 9 datasets, which is a good compromise between Q/Q_{exp} values and the percentage of modelled points, as suggested in Canonaco et al. (2021). Window lengths of 28 d were also assessed, but the correlations to ancillary measurements deteriorated in most of the cases. Exceptions to this rule were the SIRTA and Tartu sites, for which the 28 d window offered better correlations. These window lengths are consistent with the life cycle lengths of atmospheric aerosols (Textor et al., 2006), and their outcomes do not differ significantly. The application of constraints in PMF, as advised in the protocols, consists of setting random *a* values within a reasonable range and accepting only the runs that comply with the criteria. This procedure will lead to the selection of *a* values that induce more environmentally reasonable solutions and whose average will provide the final number. In some cases, the reference profiles used in *rolling* PMF are those from the *seasonal* solution, as the protocol is flexible regarding this choice. However, this constraint can have an impact on the solution, and in order to identify its implications, the profiles used in each case are detailed in Tables S1 and S3a.

A criteria-based selection was developed to automatically inspect the large number of PMF runs provided by the *rolling* method (Canonaco et al., 2021). This consists of the application of certain criteria to be fulfilled by the PMF outcoming factors. The acceptance or rejection of a run can be dictated by the thresholds retrieved from bootstrapped *seasonal* solutions or, more advisably, from a double-tailed Welch's *t*-test hypothesis evaluation with *p* values (Chen et al., 2021) chosen by the user (not exceeding 0.05). This procedure allows for factor discontinuity, as one can run PMF for two consecutive numbers of factors and choose a certain criterion upon which to select one more (or less) factor depending on the outbreak or vanishing of a factor marker. The list of criteria is specified in Table S3b for the synthetic dataset and in the respective publications for each real-world site.

2.4 SA procedure and dataset homogenisation

A method to compare source apportionment performance, analogous to Belis et al. (2015) while adjusted for our specificities, was developed in this study. The first step consisted of preliminary checks, in which the minimum requirements for solution acceptance, such as the mass closure and reasonability of profiles, must be satisfied. Secondly, the characterisation of discrepancies between methods was addressed in order to confirm the presence or absence of significant differences between *rolling* and *seasonal* PMF. The decision of which method was more suitable for certain dataset particularities was a posteriori based on the quantification of the performance goodness of both methods by means of correlation to external measurements and residual analysis. This flow process was applied to both the multi-site analysis and the synthetic dataset.

All the participants of the multi-site comparison applied the SA protocol to their own datasets, benefiting from the expertise in the previous OA SA studies at their sites. The analysis of the differences between source contribution estimates by both methods was performed for each site individually and overall. The similarity of the time series from one method to the other was assessed not only for each whole dataset but also in a "rolling" fashion, that is to say, by calculating some metrics on the windows of a given number of days with 1 d shifts between windows. This approach allowed for the identification of significant discrepancies between both approaches for the set PMF window lengths (14 d for *rolling*, 90 d for *seasonal*), a feature that was not evident in the whole long-term time series. It also enabled the watching of intra-daily differences by setting period lengths of 1 d.

A detailed study of model residuals was also beneficial to quantify the accuracy of each technique's performance. Scaled residuals represent the model error (e_{ij}) normalised by the uncertainty matrix (σ_{ij}):

$$\text{Scaled residuals}_{ij} = \frac{e_{ij}}{\sigma_{ij}}. \quad (3)$$

Their i, j sum has been reported in Paatero and Hopke (2003) to describe a unimodal histogram within a ± 3 range under good model performance conditions. The output Q quantity has been compared in both a raw and normalised way. This normalisation aims to deprive the impact of the degrees of freedom that normally depend on the input size and on the number of factors, hence computing the quantity Q/Q_{exp}, where

$$Q_{\text{exp}} = m \cdot n - p \cdot (m + n). \quad (4)$$

Then, various PMF runs can be compared in a more fundamental way. The expressions used for the normalisation arrangement have to be adapted to the particular degrees of freedom of each method:

$$\left(\frac{Q}{Q\_\text{exp}}\right)_{\text{Rolling}} = \frac{Q}{m \cdot n - p \cdot (n + m \cdot n_{14})}, \quad (5)$$

$$\left(\frac{Q}{Q_{\text{exp}}}\right)_{\text{Seasonal}} = \frac{Q}{m \cdot n - \cdot p \cdot (n + m \cdot n_{90})}. \quad (6)$$

The parameters $n_{14\,\text{d}}$ and $n_{90\,\text{d}}$ refer to the number of periods throughout the dataset of 14 and 90 d, respectively.

For the synthetic dataset, the comparison between methods had to consider the error of each. For this purpose, the metric presented in Belis et al. (2015), the uncertainty-normalised root-mean-squared error (RMSE_u) was used:

$$\text{RMSE}_u = \frac{\sqrt{\frac{1}{n}\sum_{i=1}^{n}(m_i - r_i)^2}}{2u}. \quad (7)$$

In this expression, m represents the modelled values, r the reference values, and u the mean uncertainty of the model.

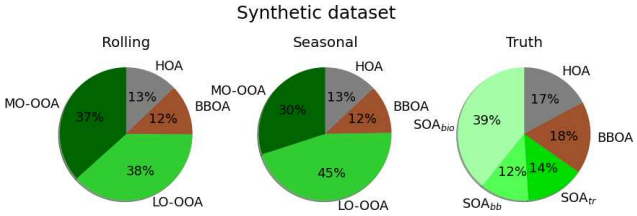

Figure 1. OA apportionment results for *rolling* and *seasonal* methods and *truth* output.

3 Results and discussion

3.1 Synthetic dataset

This section aims to assess the quality of the outcomes of the *rolling* and *seasonal* PMF methods. Relying on synthetic ToF-ACSM data offers the opportunity to compare the PMF outputs to the *truth*, which is not available for real-world measurements. We focus here on the OA sources' (factors') mean concentration and their temporal variability as well as the mean chemical composition and their temporal variability.

Regarding the OA apportionment vs. the input OA scatterplot, Table S4 presents the fitting coefficients for several resolutions, with no substantial difference between methods. Figure 1 shows the relative factor contributions to the apportioned OA for both methods. The POA factors do not differ substantially between the SA methods, but they are underestimated with respect to the *truth* (25 % of OA in *rolling* and *seasonal*, 35 % in *truth*). Also, whilst the LO-OOA-to-MO-OOA ratio is nearly 1 in the *rolling* case, it presents a much fresher secondary aerosol for the *seasonal* (1.5). Compared to the *truth*, PMF using a priori information on POA's chemical composition (HOA, BBOA) underestimates POA and overestimates SOA.

Figure 2 presents the time series, diel cycles of the *truth*, and *rolling* and *seasonal* methods as well as the scatter plots between the corresponding PMF time series. In time series and diel plots, it is noticeable that SOA is overestimated by PMF at the expense of POA (Fig. 2c). Squared Pearson correlation coefficients and slopes were similar for both *rolling* and *seasonal*, respectively, for HOA (0.89, 0.88) and OOA (0.95, 0.97) but not for BBOA, which *seasonal* resolves better (0.55, 0.72). Welch's t tests between *rolling* and *seasonal* time series rejected the similarity of all factors' concentrations. This test, applied to both methods against the *truth*, also rejected the hypothesis of significantly similar means, discarding a good method representation of *truth* results. This could be explained by the fact that *truth* profiles are static, and the methods were trying to adjust to moving fingerprints, and the anchor profiles might have influenced the results. For *rolling* and *seasonal* PMF results, the uncertainty-biased RMSE (RMSEu, Eq. 7) values are 1.10, 0.90 for HOA; 0.95, 1.98 for BBOA; and 0.05, 0.33 for

SOA, respectively. Values under 1 represent values within the range of PMF uncertainty and are therefore acceptable values, which is the case for all except the *rolling* HOA and *seasonal* BBOA. These exclusions could be explained by two, non-exclusive hypotheses: (i) the dissimilarity between methods and *truth* is large; and (ii) the uncertainties of the methods might be underestimated. In all cases except for HOA, *seasonal* presents higher RMSEu and therefore a worse fit to the *truth*. Besides, the statistical Welch's t test was performed on the synthetic dataset PMF results, testing the null hypothesis of statistically similar means with different variances.

The difference in the Pearson squared correlation coefficients between factors and their potential markers is shown as a histogram in Fig. S1 for each of the methods. The *truth* results show the worst correlation with ancillary measurements compared to modelled PMF. *Rolling* and *seasonal* results are very similar, although these correlations seem greater for *rolling* POA factors and for *seasonal* SOA factors. Slightly higher correlation coefficients were found for *rolling* in transition periods (i.e. ± 7 d before and after the change of seasons): 0.88 and 0.77 for HOA vs. BC; 0.74 and 0.65 for HOA vs. NO_X; 0.52 and 0.52 for OOA vs. NH_4; and 0.07 and 0.07 for MO-OOA vs. SO_4.

Profiles (Fig. 3a) did not show remarkable discrepancies between PMF methods, but nonetheless, these could be noticed when compared to the *truth* profiles. However, the cosine similarity method revealed high similarity of both methods to synthetic profiles (1.00 and 1.00 for HOA, 0.91 and 0.91 for BBOA, and 1.00 and 1.00 for SOA for *rolling* and *seasonal* PMF, respectively). However, it is noteworthy that both HOA's and BBOA's chemical compositions were constrained. Model HOA profiles were very similar to the *truth*, except for the lower m/z 44 and higher m/z 57 of the *truth*, and other HOA markers regarding models. Modelled BBOA presented significant differences between the *truth* and modelled profiles; the *truth* profiles contained a lower m/z 44-to-m/z 43 ratio, the lower influence of HOA markers, and much higher m/z 60 and m/z 73 BBOA tracers. Hence, modelled BBOA contained a higher proportion of other OA factor markers and lower of their own, meaning modelled profiles might have resulted in less cleanliness than the true ones. SOA PMF modelled profiles contained lower m/z 43 and m/z 44 than the *truth* profiles, although the rest remained very alike. In short, PMF results present a BBOA factor with more SOA and HOA influence as the main profile. The underestimation of POA is therefore understood to be due to a poorer modelisation of the key source identifiers, leading to a less pure profile and hence, a lower mass apportionment compared to *truth*.

The influence of reference profile constraints might have enhanced the misattribution of the profiles – for example, imposing m/z 44-to-m/z 43 ratios led to a significant difference in the degree of oxidation solution with respect to *truth*. Nevertheless, constraining profiles has provided more accurate solutions than unconstrained setups, as shown in Fig. S2. These plots show how *seasonal* constrained PMF launches always present higher similarity to *truth* in terms of key ions ratios. Moreover, OA sources of unanchored runs were less robust due to lower reproducibility along the accumulation of runs. By extension, rolling results are expected to reproduce the same results, as it has been proven that both techniques' outcomes converge sufficiently.

The adaptability of the models can be assessed from Fig. 3b, where the 60/55 vs. 44/43 (which are proxies for the BBOA–HOA differentiation and the SOA oxidation, respectively) is plotted for the *truth* and for both methods. Here we use m/z 55, since it is known to be a key marker for HOA. *Rolling* is shown to be a continuous time series, as the profiles for this method are time dependent, whilst the ratios for *seasonal* only vary from season to season. In HOA, the modelled points circle the actual *truth* and anchor profile points (which are similar or equal), but this is not the case for BBOA, in which the *rolling* and *seasonal* points are near the anchor profile but distant from the *truth*. This implies that the anchor profile, which was selected ignoring the *truth* profile characteristics, plays an important role in terms of adaptability to the actual solution. Overall, even for OA sources with nominally constant chemical composition (here HOA, BBOA), the factors resolved by PMF exhibit a varying chemical composition. Therefore, caution is required in interpreting the variability in sources of chemical variability resolved by *rolling* PMF. Oppositely, the SOA profiles, as they were unconstrained, can be compared more fairly. Both the *rolling* and *seasonal* dots are within the *truth* markers, except for some points of high 60/55, for which the highest disparity to *truth* is found for *seasonal*. This suggests a poorer PMF OOAs chemical composition profile apportionment, which in turn, might be influenced by the POA anchoring deficiencies.

The benefits of the continuity of the *rolling* profiles are reflected in time series, as can be seen in Fig. 3c, in which the behaviour of *seasonal* points is unrealistically drastic depending on the season. The profile adaptability of the *rolling* method represents a more resolute approach to positively representing the *truth*. Contrarily, the *seasonal* approach – although it can be plotted for each timestamp, as SOA is the sum of two OOAs – can only vary in lines of an equal 44/43 ratio, as the profiles are constant all through a season. In short, it can be stated that, as opposed to *seasonal* PMF or in general batch-wise PMF analysis, *rolling* PMF offers the potential to interpret changes (e.g. seasonal) in an OA sources' chemical composition, but the anchor profile selection has been shown to generate significant discrepancies when compared to the *truth* for both methods, requiring caution in interpreting such variability.

The SA method used has a severe impact on model-scaled residuals. Figure S3a shows the histogram of the scaled residuals for all the resolutions. In all cases, the *rolling* PMF histogram is significantly sharper, more centred to zero. Also,

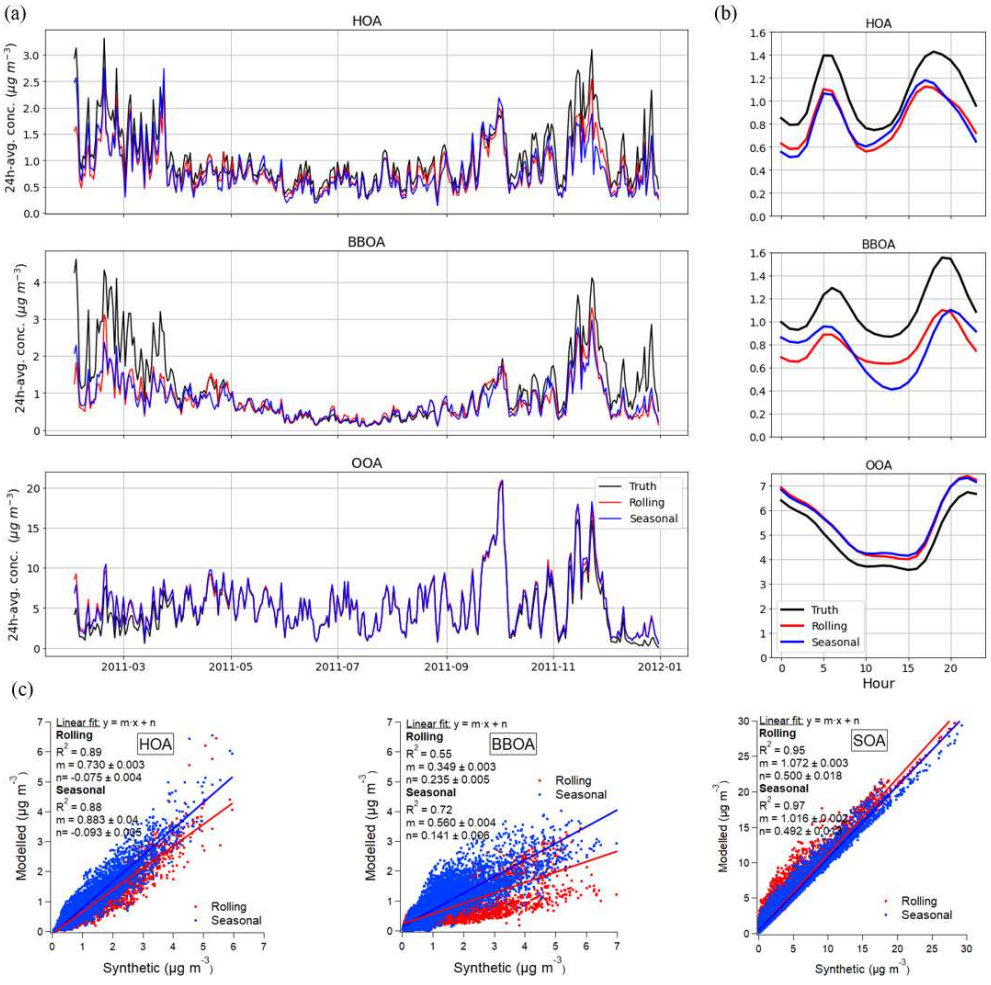

Figure 2. *Rolling*, *seasonal*, and *truth* (synthetic dataset original values) **(a)** time series (in hourly averages for the sake of clarity), **(b)** diel profiles, and **(c)** scatter plots.

the same effect is visible in the transition periods (Fig. S3b). Regarding Q values, the *rolling* value (3 838 356) is lower than the *seasonal* value (24 665 377), as expected, due to the higher extent of degrees of freedom of the former method. Q/Q_{exp} values, computed from Eqs. (5) and (6), are 7.08 and 37.58, respectively, for *rolling* and *seasonal* PMF. The fact that, when normalising by the model-specific degrees of freedom, the Q/Q_{exp} is lower for *rolling* than for *seasonal* leads to the conclusion that the minimisation of uncertainty-weighted errors is better achieved by the *rolling* method.

3.2 Multi-site comparison

3.2.1 Preliminary tests

Preliminary tests were performed to check the consistency of the reported results as well as the actual difference between the methods reported. An important performance metric is the closure of the OA mass – that is to say, the difference between the sum of all OA factor concentrations vs. the input mass. Table S4 provides the fit statistics of the input OA vs. the outcome OA for all the sites and four different time spans (the whole period, a season, a fortnight, and a day). All squared correlation coefficients are higher than 0.88, and slopes are within the 0.92–1.09 range. This ensures the quality of the PMF performance at all time resolutions and for both methods. A closer inspection of the table shows slightly higher correlation coefficients and slopes closer to 1 for *rolling*.

In order to confirm or reject the existence of systematic disparity between both methods, a two-tailed Welch's t test was performed under the null hypothesis of the time series having statistically similar expected values. In Table S5, all cells marked represent the runs that reject the null hypothesis, i.e. for which the factors retrieved from *rolling* and *seasonal* are not statistically equal (p values over 0.05). The row "all" refers to the concatenation of all the dataset time series. Apportioned OA presents the highest acceptance of the hypothesis rate, implying that the global apportionment

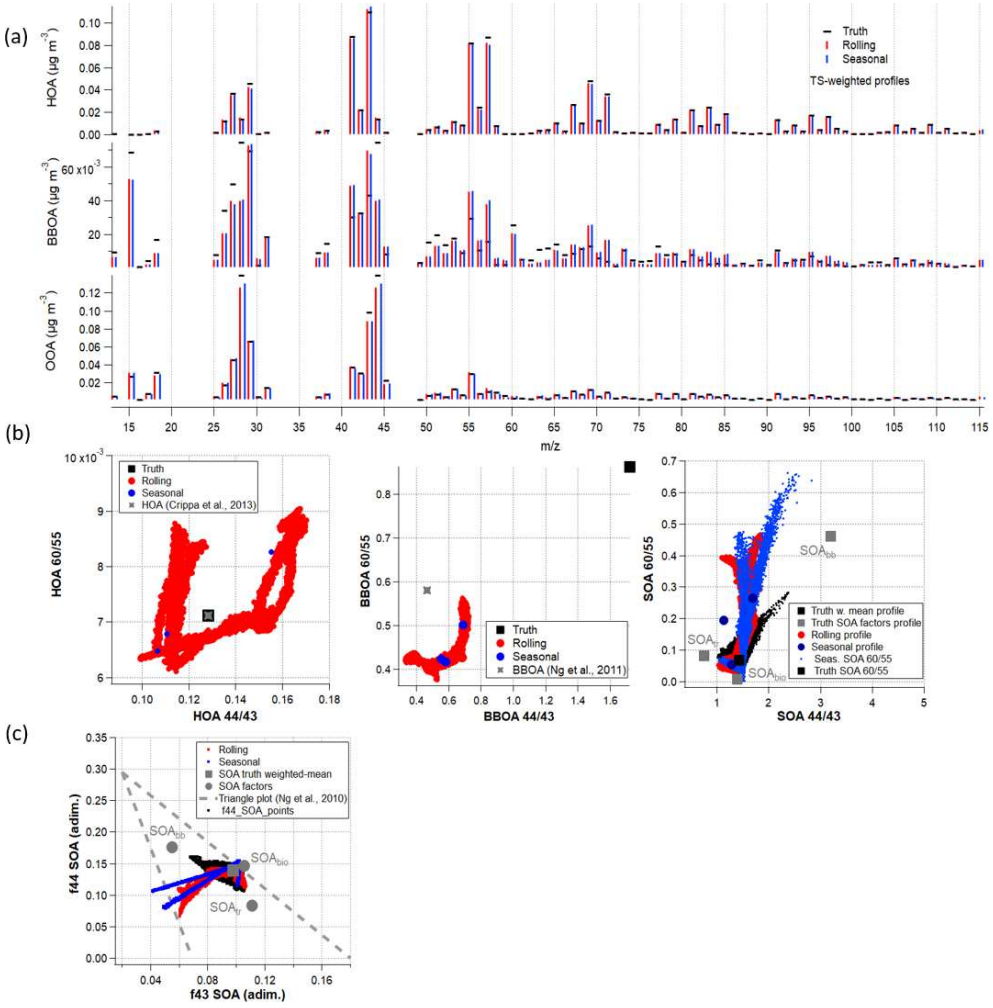

Figure 3. Synthetic dataset solution **(a)** profiles; **(b)** time-dependent profile variability of ratios 60/55 vs. 44/43; **(c)** triangle plot of f44 vs. f43 for *rolling* PMF (red), *seasonal* PMF (blue), and *truth* (black).

means are not significantly different. The factors with higher rejection rates are LO-OOA, MO-OOA, and HOA, in this order. OOA factors, as they are unconstrained, might be rather sensitive to source outbreaks or variations, which could have been caught or not by one model, although their sum (OOA) remains coherent. Period-long figures get the highest rejection rates, which decay rapidly from lower to higher resolutions, meaning the seasonal and fortnightly averages are still high despite their rapid resolution; on the other hand, for the daily resolution, this rate is very low. This fact highlights that the methods present significant differences with regard to means in intermediate resolutions.

Figure S4 compares the relative difference of the *rolling* minus *seasonal* concentrations for each factor in the all-sites ensemble. The factors with higher errors are MO-OOA and LO-OOA, tilted to positive values – that is, resulting in higher concentrations for *rolling*. This is probably related to the lack of anchors, which promotes higher freedom and hence, higher difference between methods. Also, BBOA presents significant positive whiskers, but as mean concentrations in Fig. 1 are equal, we suspect these are linked to sporadic high concentration outbreaks, which might only have been caught by the *rolling* method. Besides, the other factors are not significantly different from zero.

The pie charts in Fig. 4 show the amount of mass apportioned by the main OA sources in all datasets. These pies do not account for site-specific sources; they present the relative contribution of the all-sites ones scaled to account for the 360 degrees. OA is mainly driven by secondary organic aerosols in both cases, although the ratio of fresh-to-aged aerosol contributions – that is, LO-OOA over MO-OOA – is much higher for *rolling* (0.62) than for *seasonal* (0.54). The ratio of POA over SOA is higher for *seasonal* than for *rolling* (0.58 and 0.37, respectively), and the ratio of BBOA over HOA is considerably different (1.17 and 1.45, respectively). The fact that wood burning BC exceeds fossil fuel BC is consistent with the average ratio of 3.1 for BC_{wb} and BC_{ff}, implying that PMF reproduces this relation. Hence, *rolling*

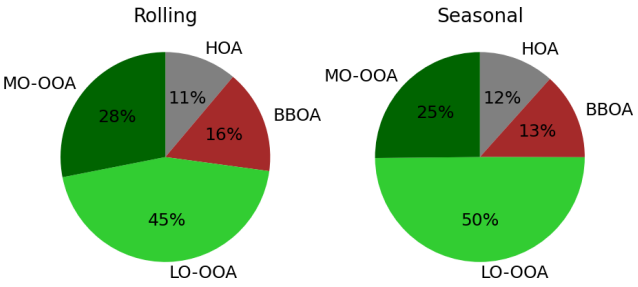

Figure 4. Pie charts of the mean concentrations of the main factors for the ensemble of all sites.

describes a more oxidised SOA, which is less prevailing than that of *seasonal*. In both, POA is governed by the biomass burning OA. Figure S5 shows the individual apportionment pies, in which the same trends can be generally recognised. In general terms, these results do not coincide with the ones from the synthetic dataset, in which the POA/SOA and LO-OOA/MO-OOA ratios were, respectively, equal and higher for *rolling*.

Figure 5 shows both the monthly and diel cycles of the *rolling* minus *seasonal* concentrations of the ensemble of sites for the main factors. In general terms, the intra-year variation is not remarkable, as all the boxes are mainly crossing the zero line. Besides, the differences between mean and median could indicate the adaptability to spiky events. The fact that HOA and BBOA are remarkably different throughout the whole period coincides with the aforementioned Welch's t tests. Moreover, the mean for HOA in January and December and for BBOA in July and August are positively set beyond the boxes, which could imply that the most extreme events are better captured by the *rolling*. This fact reinforces the hypothesis of a more precise capture of intra-month events. SOA factors present fewer clear trends, although an alternate sign between warm and cold months can be recognised. Figure S6 depicts the behaviour of the remaining factors, which are nearly zero except for 58-OA, which is significantly negative in summer, and SHINDOA, which alternates from positive to negative from summer to winter. In the case of 58-OA, this indicates a summertime under- or overestimation of one of the methods, and for the SHINDOA, a differing capturability of events along the year.

Regarding diel cycles (Fig. 5), the differences are evident in HOA and BBOA at night, implying that this is where the mixing between POA sources is aggravated. The SOA factors reveal that one of the methods overestimates the other throughout the daily cycle: *rolling* is greater for MO-OOA and OOA and lower for LO-OOA. Whilst these differences do not have an impact on the Welch's t test for LO-OOA, they do for the rest, even for HOA, for which they are not very uneven, probably due to the compensation of differences while averaging. Figure S6 shows similar behaviour for both methods in all the factors except for the WCOA, PCOA, and CCOA, which present higher differences at night. *Seasonal* concentrations, though, are remarkably higher for 58-OA throughout the period or daily cycle, somewhat superior in the COA 8h peak, and inferior in the SHINDOA afternoon. While these results do not have an impact on the p value for the Barcelona–Palau Reial and Magadino sites, it does for the Marseille–Longchamp site.

3.2.2 PMF goodness evaluation

Correlation with ancillary measurements

In order to assess the quality of each PMF method outcome, the correlation of factors with their potential markers was monitored from a single and global perspective. The pairs of variables compared were: HOA and BC_{ff}, HOA and NO_x, BBOA and BC_{wb}, MO-OOA and SO_4^{2-}, and OOA and NH_4^+. SHINDOA was compared to ultrafine particles with diameters of 10–20 nm coming from shipping or industry, differentiated according to Chazeau et al. (2021) and Rodríguez and Cuevas (2007). The correlation of LO-OOA vs. NO_3^- has been excluded in this study due to the plentiful sources of NO_3^-; besides, organonitrates would hamper the traceability of LO-OOA from this compound. This analysis has not been extended for the rest of the OA sources due to the lack of appropriate tracers available.

Figure 6 presents the Pearson squared correlation coefficient for all the pairs of markers and factors retrieved from *rolling* and *seasonal* PMF. Even though these marker time series are not deprived of errors, the hypothesis is that better agreement leads to better adaptation of the model to the OA source emitting these tracers. Overall, the *rolling* boxes are centred to higher correlation values than the *seasonal* ones, but their whiskers always reach the maximum value of 1 in both cases. The difference between methods is small, since medians do not differ by more than 0.05; however, the *seasonal* performance underscores these correlations slightly. This finding would support the hypothesis of the superior performance of the *rolling*, although HOA is evenly characterised in both methods, which is consistent with the great similarity in the apportionment of OA shown in Fig. 4. The histogram for the difference of Pearson squared correlation coefficients is plotted as a histogram for all sites in Fig. S7. Positivity in this graph reflects better *rolling* results matched with co-located measurements, and the histogram spreads the range of correlations. The amount of shoulders in the right half of these histograms is higher than those in the left, which implies systematic improvement of the *rolling* method with respect to *seasonal* in terms of correlation with ancillary measurements.

Periods of transition from one season to another are strategically relevant for this comparison, since the *seasonal* method, due to its profile staticity definition, could yield to discontinuities in the time series of the different components. The change of OA factors spectra for *rolling* is smooth; there-

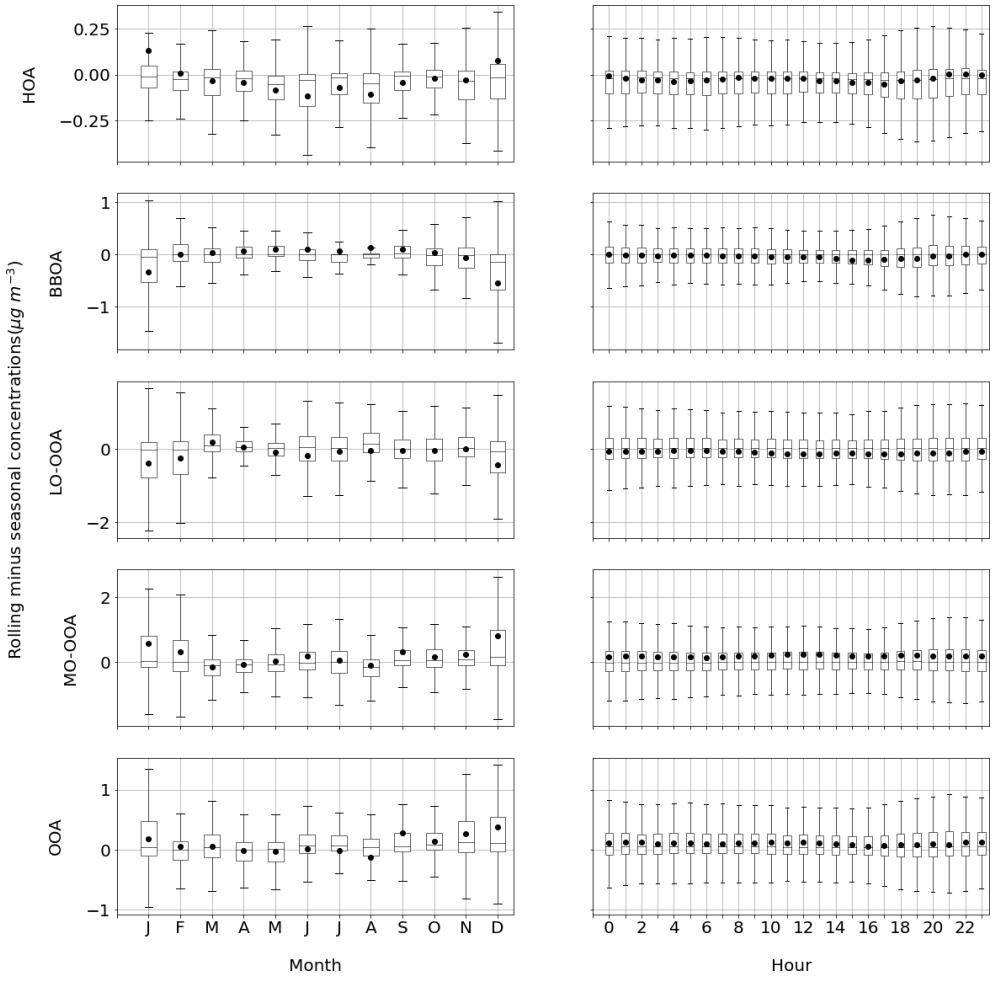

Figure 5. Boxplots of *rolling* minus *seasonal* factor absolute concentrations (in $\mu g\,m^{-3}$) per month and hour. Boxes show the Q1–Q3 range with the median (horizontal line) and the average (full circles); whiskers extend up to the range of the data.

fore, no abrupt changes should be expected in the season edges. Moreover, the *rolling* technique is capable of introducing factors depending on criteria compliance; therefore, their concentration edges are not as sharp as they would be for the *seasonal* PMF. This is the case for BBOA appearance in the cold months in Barcelona–Palau Reial and Marseille–Longchamp, and the 58-OA outbreak after the Q-ACSM filament replacement in Magadino. From these premises, one could expect to find better correlation coefficients relating to factors and their markers for the *rolling* method, which could better represent these periods. Table S6 shows the correlation of the OA factors and their markers for these periods only, both for the *rolling* and *seasonal* PMF. In all cases, the differences between methods are not extensive. However, it can be seen how the "whole" dataset figures are always greater for *rolling* than for *seasonal*. This finding supports the conjecture that the *seasonal* method presents greater difficulty in representing the edges of the seasons. The relevance of this conclusion is to be considered especially in the datasets in which the number of days near season changes is important due to data gaps.

Model residuals

Figure 7 shows the normalised scaled residuals distribution for both methods in a concatenated dataset including all the sites. Given that the uncertainty matrix was the same for both techniques, scaled residuals reflect the capacity of each technique to apportion the quantity of OA most similar to that which was entered as input. Boxplots show a tendency towards negative values for both methods, implying a systematic bias towards the overestimation of the input matrices. *Seasonal* errors present a higher spread and lower mean and medians; hence, *seasonal* results are less accurate and precise than those from *rolling*, overall. However, the span of both distributions does not exceed the $\pm 3\sigma$ threshold in any of the cases, meaning the results are acceptable for both techniques. Figure S8 shows the same plot for each of the participant sites. In general, the *rolling* histograms are more centred

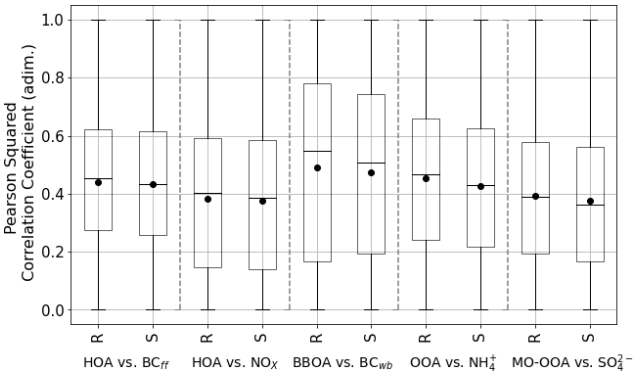

Figure 6. *Rolling* (R) and *seasonal* (S) boxplots of the Pearson squared correlation coefficient of each OA source with its respective markers for all sites.

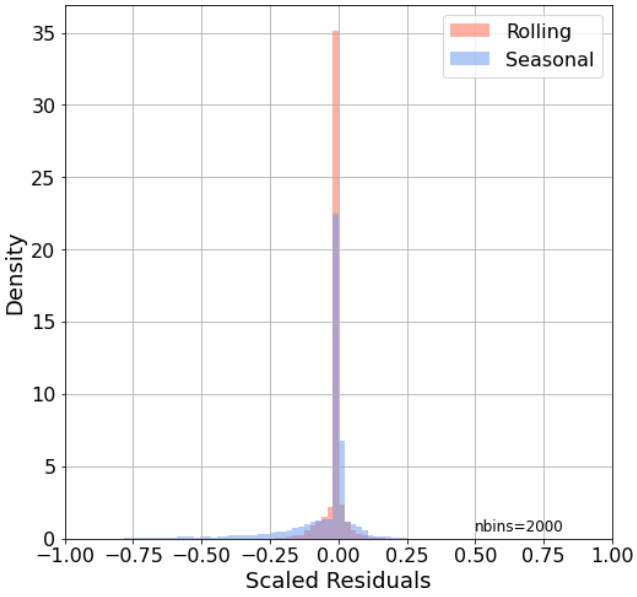

Figure 7. Normalised scaled residuals histogram for both PMF techniques.

to zero, and their sharpness is higher with respect to *seasonal* distributions. An exception to this behaviour is Marseille–Longchamp, which presents negatively shifted distributions probably related to the model's difficulty in differentiating between BBOA and LO-OOA.

Scaled residuals for the season transition periods are presented in Fig. S9. Both histograms extend largely beyond the (−3, 3) domain, implying that both methods struggle in this kind of period; however, the *seasonal* distribution of scaled residuals is much wider than that of *rolling*. Also, in the zoomed (−3, 3) range, *seasonal* results seem to present a wider distribution. Distribution shoulders are present in both – negative in *rolling* and positive in *seasonal* – indicating *rolling* overestimation and *seasonal* underestimation of input concentrations. These findings would imply that, even if the methods provide a substantial error in the transition periods, the *rolling* better captures the season change due to its profile adaptability.

Regarding Q values, the differences between techniques are presented in Table 2. Unweighted Q values show a clear pattern on lower values for *rolling* PMF, except for one site. The SIRTA datasets were treated by two different users, which might have led to different PMF steps and unreliable results. The generally greater minimisation of Q performed by the *rolling* PMF method can be explained by the major quantity of runs performed compared to *seasonal* PMF because of the proper definition of the method. By depriving the Q of the degrees of freedom effect, as shown in Eqs. (5), (6), the minimisation of both methods is signified. The trend generally points to lower figures for the *rolling* method, but whilst the minimisation of the unweighted Q was an expected fact, the implicit error reduction cannot be ensured within a theoretical frame. However, the majority of sites (excluding the aforementioned SIRTA) show lower Q/Q_{exp} values for the *rolling* method.

Table 2. Q/Q_{exp} values for *rolling* and *seasonal* solutions. Bold figures represent the lowest value in the *rolling–seasonal* comparison.

Q	Raw		Normalised	
	Rolling	Seasonal	Rolling	Seasonal
BCN – PR	**481 008**	1 766 588	**0.35**	1.14
CAO – AMX	**57 337**	5 101 949	**0.04**	2.87
DUB	**1 031 616**	1 261 451	**1.14**	1.19
ATOLL	**465 480**	477 145	0.84	**0.69**
MGD	**8 463 251**	3 117 660	**0.75**	2.46
INO	**6 138 684**	25 404 272	**4.58**	17.24
MRS – LCP	**57 337**	5 101 949	17.24	**2.87**
SIR	558 044	**44 965**	0.47	**0.10**
TAR	**82 742**	152 343	0.59	**0.34**

Adaptability tests

Adaptation tests were designed to inspect how much the methods comply with the input data. One of the main concerns to assess is the adaptability of the output profiles to short-lifetime events (order of magnitude of days), as it is the hypothesis onto which the *rolling* PMF is based. For this purpose, the check was based on the difference between main ion ratios, calculated from input values and the apportioned amounts of these ions by OOA factor profiles for both methods, e.g. $(m/z44/m/z43)_{\text{input}}$ – OOA $(m/z44/m/z43)$ Rolling or Seasonal. This can be seen in Fig. S10 in a time-series form for each site. Because $m/z44$ and $m/z43$ are also part of POA profiles, one should not expect to find a perfect match between the raw and the OOA profile ratios but rather a qualitative idea of how well the profiles adapt to the degree

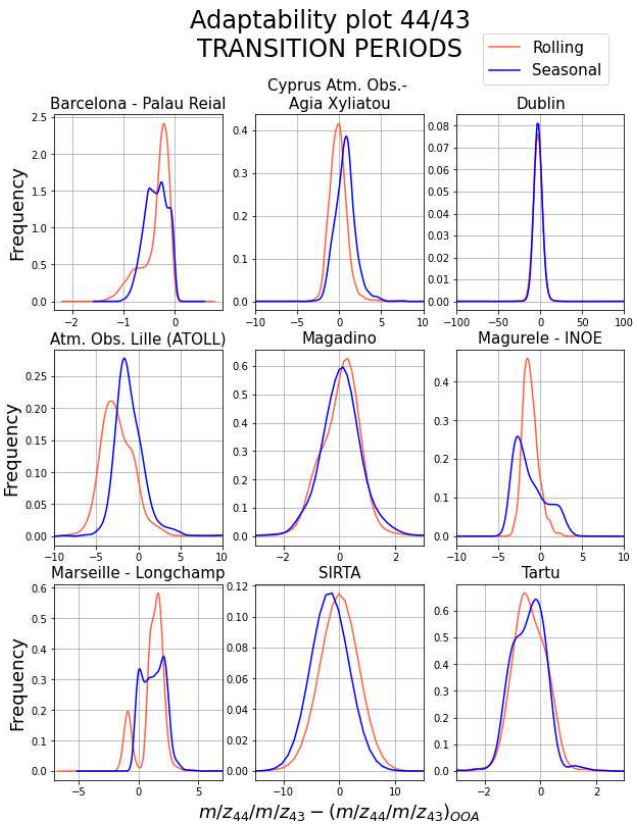

Figure 8. Kernel density estimation of the histograms of the subtraction of the m/z 44-to-43 ratio from the raw (from input matrices) time series data minus the apportioned quantity in profiles. These plots only contain those time lapses among the change of season (transition periods).

of aerosol ageing. In these plots, generally the *rolling* profile variation seems to adapt better than *seasonal*, which is a straight line along a season. Under the same logic, Fig. 8 shows the site histograms of the $(m/z44/m/z43)_{\text{input}} - \text{OOA}$ $(m/z44/m/z43)$ Rolling or Seasonal values only for periods around the change of season, which have been proven to be tricky for the PMF model.

Figure S9 shows, in general terms, how the *rolling* adapts to the main 44-to-43 trends, whilst *seasonal* can only present a single value for a whole season. Even though the *rolling* or *seasonal* SOA and the input time series are not expected to match perfectly, the main features of the variability are usually caught by the *rolling*. By taking a look only at the transition periods in Fig. 8, the tendency is that the difference between the input ratio and the *rolling* ratio is closer to zero or sharper around it than with *seasonal*. These qualitative appreciations bolster the aforementioned conclusion that *rolling* adapts the SOA profiles to specific singularities of the input time series, thus generating a more accurate solution.

4 Conclusions

The present study aimed at performing a comprehensive comparison between the two methodologies of fine organic aerosol (OA) source apportionment through the positive matrix factorisation (PMF) model: *rolling* and *seasonal* PMF.

The synthetic dataset *rolling* and *seasonal* outputs assessment has been rather fruitful for this comparison. The main highlight of this approach is that the modelled sources could be compared to the "*truth*" ones – that is, the OA sources chosen artificially during the dataset tailoring. Contrasting PMF results against the *truth* highlighted the model's overestimation of SOA and underestimation of POA (in the case of using a priori information on POA's chemical composition) for both *rolling* and *seasonal* and different degrees of SOA oxidation between methods. Nevertheless, the correlation of *rolling* and *seasonal* with the *truth* time series and profiles show very similar results in terms of concentrations. The temporal variability of OA sources' chemical composition has been shown to oscillate, even for POA components with temporally invariant chemical composition, and to be severely impacted by the selection of the profile anchors, as it differed significantly from the *truth* results when the anchor was significantly different to the *truth* profile. However, the use of profile constraints still provided solutions closer to the *truth* than unconstrained PMF. Besides, the *rolling* method has been proven to give a more sensitive representation of the continuous OA fingerprints variation. Scaled residuals minimisation also supported that the *rolling* solution was mathematically superior to *seasonal*.

The following multi-site comparison pretends to contrast both PMF methods in real-world datasets treated homogeneously under Chen et al.'s (2022) protocol to observe general performance trends. The *rolling* method generally presents a comparatively similar proportion of primary OA (POA) and a secondary OA (SOA) of a lower oxygenation degree, i.e. the ageing state. The double-tailed Welch's t test showed that the narrower the window of inspection, the higher the differences between factors retrieved from one method to the other. Moreover, towards weekly or daily periods, SOA factors differ more than POA factors. This fact is likely due to the absence of constraints for the SOA factors during PMF. Contrastingly, POA factors are more dissimilar period-wise. The ratio of BBOA to HOA differs considerably from *rolling* to *seasonal* (1.45 and 1.17, respectively) for the ensemble of sites, but in any case, it is over 1, as the ratio of BC_{wb} to BC_{ff} suggests.

In general terms, *rolling* results correlate better with ancillary measurements than those from *seasonal* for almost all of the considered external datasets at all sites. This is particularly true in the days surrounding the change of season, in which the *seasonal* profiles change drastically from one time point to the following. Model residuals also point to a better minimisation for the *rolling* PMF, although regarding scaled residuals, both methods comply with the $(-3, 3)$ range ad-

vised by the protocol. The time series of key ions also quantitatively pointed to a better adequation of the *rolling* SOA profiles to the oxygenated OA key ions. Finally, the errors also proved to be more stable for the *rolling* method, while it should be noted that the individual sites' discrepancies from the overall trends have not been discussed in this study.

Overall, these results confirm the hypothesis that the *rolling* PMF can be considered more accurate and precise, globally, than the *seasonal* one, although both meet the standards of quality required by the source apportionment protocol. Moreover, the *rolling* method was already recognised to involve less user subjectivity and computational time as well as being more suitable for long-term and evolving SA analysis, such as semi-automated online SA. This study, therefore, promotes the acceptance of this novel *rolling* method as an improved approach suitable for source apportionment studies. An additional conclusion stemming from this comparison is that the selection of anchor profiles strongly influence the OA factors, so local reference profiles are encouraged to minimise this impact.

Code availability. The codes used for this comparison can be found in https://doi.org/10.17632/nd79y8mpg3.1 (Via, 2022b).

Data availability. All data used in this study can be accessed at https://doi.org/10.17632/dsfty2rn7y.2 (Via, 2022a).

Author contributions. MV: conceptualisation, data curation, formal analysis, investigation, methodology, software, validation, visualisation, writing – original draft preparation, writing – review and editing. GC: conceptualisation, data curation, formal analysis, investigation, methodology, software, validation, writing – review and editing. FC: conceptualisation, investigation, methodology, software, supervision, validation, writing – review and editing. KRD: conceptualisation, data curation, formal analysis, funding, investigation, methodology, project administration, software, supervision, validation, writing – review and editing. BC: data curation, formal analysis, investigation, writing – review and editing. HC: data curation, formal analysis, investigation, writing – review and editing. JJ: methodology, software. HK: data curation, formal analysis, investigation, writing – review and editing. CL: data curation, formal analysis, investigation, writing – review and editing. NM: funding, project administration. CM: data curation, formal analysis, investigation, writing – review and editing. CO: conceptualisation, funding, project administration, supervision, writing – review and editing. JO: data curation, formal analysis, funding, project administration, supervision, writing – review and editing. J-EP: conceptualisation, funding, project administration, supervision, writing – review and editing. mp: data curation, formal analysis, investigation, writing – review and editing. VR: data curation, formal analysis, funding, methodology, project administration, writing – review and editing. JS: funding, project administration, writing – review and editing. JGS: conceptualisation, formal analysis, methodology, software, validation, writing – review and editing. LS: data curation, formal analysis, investigation, writing – review and editing. JV: data curation, formal analysis, funding, investigation, writing – review and editing. YZ: data curation, formal analysis, investigation, writing – review and editing. OF: conceptualisation, funding, project administration, supervision, writing – review and editing. ASHP: conceptualisation, funding, methodology, project administration, resources, supervision, writing – review and editing. AA: conceptualisation, funding, methodology, project administration, resources, supervision, validation, writing – review and editing. MCM: conceptualisation, data curation, formal analysis, funding, investigation, methodology, project administration, resources, supervision, validation, writing – review and editing.

Competing interests. The contact author has declared that none of the authors has any competing interests.

Disclaimer. Publisher's note: Copernicus Publications remains neutral with regard to jurisdictional claims in published maps and institutional affiliations.

Acknowledgements. IDAEA-CSIC is a Centre of Excellence Severo Ochoa (Spanish Ministry of Science and Innovation, Project CEX2018-000794-S). The authors gratefully acknowledge the Romanian National Air Quality Monitoring Network (NAQMN, https://www.calitateaer.ro/public/home-page/?__locale=ro, last access: September 2022) for providing NO_x data.

Financial support. This research has been supported by the Generalitat de Catalunya (grant no. AGAUR 2017 SGR41), the European Cooperation in Science and Technology (grant no. COST Action CA16109 COLOSSAL), the Ministerio de Ciencia, Innovación y Universidades (CAIAC, grant no. PID2019-108990RB-I00 and FEDER, grant no. EQC2018-004598-P.), the Horizon 2020, the Ministry of Education and Research, Romania (grant nos. PN-III-P1-1.1-TE-2019-0340 and 18PFE/30.12.2021, 18N/2019), the Agence Nationale de la Recherche (grant no. PIA, ANR-11_LABX-0005-01), the Conseil Régional Hauts-de-France (CLIMIBIO grant), the Ministère de l'Enseignement Supérieur et de la Recherche (CARA grant), the Environmental Protection Agency (AEROSOURCE, grant no. 2016-CCRP-MS-31), the Department of the Environment, Climate and Communications (AC3 network grant), and the Schweizerischer Nationalfonds zur Förderung der Wissenschaftlichen Forschung (SAMSAM, grant nos. IZCOZ9_177063 and PZPGP2_201992).

We acknowledge support of the publication fee by the CSIC Open Access Publication Support Initiative through its Unit of Information Resources for Research (URICI).

Review statement. This paper was edited by Mingjin Tang and reviewed by three anonymous referees.

References

Amato, F., Alastuey, A., Karanasiou, A., Lucarelli, F., Nava, S., Calzolai, G., Severi, M., Becagli, S., Gianelle, V. L., Colombi, C., Alves, C., Custódio, D., Nunes, T., Cerqueira, M., Pio, C., Eleftheriadis, K., Diapouli, E., Reche, C., Minguillón, M. C., Manousakas, M.-I., Maggos, T., Vratolis, S., Harrison, R. M., and Querol, X.: AIRUSE-LIFE+: a harmonized PM speciation and source apportionment in five southern European cities, Atmos. Chem. Phys., 16, 3289–3309, https://doi.org/10.5194/acp-16-3289-2016, 2016.

Belis, C. A., Pernigotti, D., Karagulian, F., Pirovano, G., Larsen, B. R., Gerboles, M., and Hopke, P. K.: A new methodology to assess the performance and uncertainty of source apportionment models in intercomparison exercises, Atmos. Environ., 119, 35–44, https://doi.org/10.1016/j.atmosenv.2015.08.002, 2015.

Bozzetti, C., El Haddad, I., Salameh, D., Daellenbach, K. R., Fermo, P., Gonzalez, R., Minguillón, M. C., Iinuma, Y., Poulain, L., Elser, M., Müller, E., Slowik, J. G., Jaffrezo, J.-L., Baltensperger, U., Marchand, N., and Prévôt, A. S. H.: Organic aerosol source apportionment by offline-AMS over a full year in Marseille, Atmos. Chem. Phys., 17, 8247–8268, https://doi.org/10.5194/acp-17-8247-2017, 2017.

Canonaco, F., Crippa, M., Slowik, J. G., Baltensperger, U., and Prévôt, A. S. H.: SoFi, an IGOR-based interface for the efficient use of the generalized multilinear engine (ME-2) for the source apportionment: ME-2 application to aerosol mass spectrometer data, Atmos. Meas. Tech., 6, 3649–3661, https://doi.org/10.5194/amt-6-3649-2013, 2013.

Canonaco, F., Slowik, J. G., Baltensperger, U., and Prévôt, A. S. H.: Seasonal differences in oxygenated organic aerosol composition: implications for emissions sources and factor analysis, Atmos. Chem. Phys., 15, 6993–7002, https://doi.org/10.5194/acp-15-6993-2015, 2015.

Canonaco, F., Tobler, A., Chen, G., Sosedova, Y., Slowik, J. G., Bozzetti, C., Daellenbach, K. R., El Haddad, I., Crippa, M., Huang, R.-J., Furger, M., Baltensperger, U., and Prévôt, A. S. H.: A new method for long-term source apportionment with time-dependent factor profiles and uncertainty assessment using SoFi Pro: application to 1 year of organic aerosol data, Atmos. Meas. Tech., 14, 923–943, https://doi.org/10.5194/amt-14-923-2021, 2021.

Chazeau, B., Temime-Roussel, B., Gille, G., Mesbah, B., D'Anna, B., Wortham, H., and Marchand, N.: Measurement report: Fourteen months of real-time characterisation of the submicronic aerosol and its atmospheric dynamics at the Marseille–Longchamp supersite, Atmos. Chem. Phys., 21, 7293–7319, https://doi.org/10.5194/acp-21-7293-2021, 2021.

Chen, G., Sosedova, Y., Canonaco, F., Fröhlich, R., Tobler, A., Vlachou, A., Daellenbach, K. R., Bozzetti, C., Hueglin, C., Graf, P., Baltensperger, U., Slowik, J. G., El Haddad, I., and Prévôt, A. S. H.: Time-dependent source apportionment of submicron organic aerosol for a rural site in an alpine valley using a rolling positive matrix factorisation (PMF) window, Atmos. Chem. Phys., 21, 15081–15101, https://doi.org/10.5194/acp-21-15081-2021, 2021.

Chen, G., Canonaco, F., Tobler, A., Aas, W., Alastuey, A., Allan, J., Atabakhsh, S., Aurela, M., Baltensperger, U., Bougiatioti, A., De Brito, J. F., Ceburnis, D., Chazeau, B., Chebaicheb, H., Daellenbach, K. R., Ehn, M., El Haddad, I., Eleftheriadis, K., Favez, O., Flentje, H., Font, A., Fossum, K., Freney, E., Gini, M., Green, D. C., Heikkinen, L., Herrmann, H., Kalogridis, A.-C., Keernik, H., Lhotka, R., Lin, C., Lunder, C., Maasikmets, M., Manousakas, M. I., Marchand, N., Marin, C., Marmureanu, L., Mihalopoulos, N., Močnik, G., Nęcki, J., O'Dowd, C., Ovadnevaite, J., Peter, T., Petit, J.-E., Pikridas, M., Platt, S. M., Pokorná, P., Poulain, L., Priestman, M., Riffault, V., Rinaldi, M., Różański, K., Schwarz, J., Sciare, J., Simon, L., Skiba, A., Slowik, J. G., Sosedova, Y., Stavroulas, I., Styszko, K., Teinemaa, E., Timonen, H., Tremper, A., Vasilescu, J., Via, M., Vodička, P., Wiedensohler, A., Zografou, O., Minguillón, M. C., and Prévôt, A. S. H.: European aerosol phenomenology – 8: Harmonised source apportionment of organic aerosol using 22 Year-long ACSM/AMS datasets, Environment International, ISSN 0160-4120, 166, https://doi.org/10.1016/j.envint.2022.107325, 2022.

Chen, J. and Hoek, G.: Long-term exposure to PM and all-cause and cause-specific mortality: A systematic review and meta-analysis, Environ. Int., 143, 105974, https://doi.org/10.1016/j.envint.2020.105974, 2020.

Crippa, M., DeCarlo, P. F., Slowik, J. G., Mohr, C., Heringa, M. F., Chirico, R., Poulain, L., Freutel, F., Sciare, J., Cozic, J., Di Marco, C. F., Elsasser, M., Nicolas, J. B., Marchand, N., Abidi, E., Wiedensohler, A., Drewnick, F., Schneider, J., Borrmann, S., Nemitz, E., Zimmermann, R., Jaffrezo, J.-L., Prévôt, A. S. H., and Baltensperger, U.: Wintertime aerosol chemical composition and source apportionment of the organic fraction in the metropolitan area of Paris, Atmos. Chem. Phys., 13, 961–981, https://doi.org/10.5194/acp-13-961-2013, 2013.

Crippa, M., Canonaco, F., Lanz, V. A., Äijälä, M., Allan, J. D., Carbone, S., Capes, G., Ceburnis, D., Dall'Osto, M., Day, D. A., DeCarlo, P. F., Ehn, M., Eriksson, A., Freney, E., Hildebrandt Ruiz, L., Hillamo, R., Jimenez, J. L., Junninen, H., Kiendler-Scharr, A., Kortelainen, A.-M., Kulmala, M., Laaksonen, A., Mensah, A. A., Mohr, C., Nemitz, E., O'Dowd, C., Ovadnevaite, J., Pandis, S. N., Petäjä, T., Poulain, L., Saarikoski, S., Sellegri, K., Swietlicki, E., Tiitta, P., Worsnop, D. R., Baltensperger, U., and Prévôt, A. S. H.: Organic aerosol components derived from 25 AMS data sets across Europe using a consistent ME-2 based source apportionment approach, Atmos. Chem. Phys., 14, 6159–6176, https://doi.org/10.5194/acp-14-6159-2014, 2014.

Daellenbach, K. R., Uzu, G., Jiang, J., Cassagnes, L. E., Leni, Z., Vlachou, A., Stefenelli, G., Canonaco, F., Weber, S., Segers, A., Kuenen, J. J. P., Schaap, M., Favez, O., Albinet, A., Aksoyoglu, S., Dommen, J., Baltensperger, U., Geiser, M., El Haddad, I., Jaffrezo, J. L., and Prévôt, A. S. H.: Sources of particulate-matter air pollution and its oxidative potential in Europe, Nature, 587, 414–419, https://doi.org/10.1038/s41586-020-2902-8, 2020.

Efron, B.: Bootstrap Methods: Another Look at the Jackknife, Ann. Stat., 7, 1–26, https://doi.org/10.1214/aos/1176344552, 1979.

El Haddad, I., D'Anna, B., Temime-Roussel, B., Nicolas, M., Boreave, A., Favez, O., Voisin, D., Sciare, J., George, C., Jaffrezo, J.-L., Wortham, H., and Marchand, N.: Towards a better understanding of the origins, chemical composition and aging of oxygenated organic aerosols: case study of a Mediterranean industrialized environment, Marseille, Atmos. Chem. Phys., 13, 7875–7894, https://doi.org/10.5194/acp-13-7875-2013, 2013.

Forello, A. C., Bernardoni, V., Calzolai, G., Lucarelli, F., Massabò, D., Nava, S., Pileci, R. E., Prati, P., Valentini, S., Valli, G., and Vecchi, R.: Exploiting multi-wavelength aerosol absorption coef-

ficients in a multi-time resolution source apportionment study to retrieve source-dependent absorption parameters, Atmos. Chem. Phys., 19, 11235–11252, https://doi.org/10.5194/acp-19-11235-2019, 2019.

Fröhlich, R., Cubison, M. J., Slowik, J. G., Bukowiecki, N., Prévôt, A. S. H., Baltensperger, U., Schneider, J., Kimmel, J. R., Gonin, M., Rohner, U., Worsnop, D. R., and Jayne, J. T.: The ToF-ACSM: a portable aerosol chemical speciation monitor with TOFMS detection, Atmos. Meas. Tech., 6, 3225–3241, https://doi.org/10.5194/amt-6-3225-2013, 2013.

Heikkinen, L., Äijälä, M., Daellenbach, K. R., Chen, G., Garmash, O., Aliaga, D., Graeffe, F., Räty, M., Luoma, K., Aalto, P., Kulmala, M., Petäjä, T., Worsnop, D., and Ehn, M.: Eight years of sub-micrometre organic aerosol composition data from the boreal forest characterized using a machine-learning approach, Atmos. Chem. Phys., 21, 10081–10109, https://doi.org/10.5194/acp-21-10081-2021, 2021.

IPCC: Climate Change 2021: The Physical Science Basis. Contribution of Working Group I to the Sixth Assessment Report of the Intergovernmental Panel on Climate Change, edited by: Masson-Delmotte, V., Zhai, P., Pirani, A., Connors, S. L., Péan, C., Berger, S., Caud, N., and Chen, Y., Cambridge Univ. Press, 3949, https://www.ipcc.ch/report/ar6/wg1/downloads/report/IPCC_AR6_WGI_Full_Report.pdf (last access: September 2022), 2021 (in press).

Jiang, J., Aksoyoglu, S., El-Haddad, I., Ciarelli, G., Denier van der Gon, H. A. C., Canonaco, F., Gilardoni, S., Paglione, M., Minguillón, M. C., Favez, O., Zhang, Y., Marchand, N., Hao, L., Virtanen, A., Florou, K., O'Dowd, C., Ovadnevaite, J., Baltensperger, U., and Prévôt, A. S. H.: Sources of organic aerosols in Europe: a modeling study using CAMx with modified volatility basis set scheme, Atmos. Chem. Phys., 19, 15247–15270, https://doi.org/10.5194/acp-19-15247-2019, 2019.

Jimenez, J. L., Canagaratna, M. R., Donahue, N. M., Prevot, A. S. H., Zhang, Q., Kroll, J. H., DeCarlo, P. F., Allan, J. D., Coe, H., Ng, N. L., Aiken, A. C., Docherty, K. S., Ulbrich, I. M., Grieshop, A. P., Robinson, A. L., Duplissy, J., Smith, J. D., Wilson, K. R., Lanz, V. A., Hueglin, C., Sun, Y. L., Tian, J., Laaksonen, A., Raatikainen, T., Rautiainen, J., Vaattovaara, P., Ehn, M., Kulmala, M., Tomlinson, J. M., Collins, D. R., Cubison, M. J., Dunlea, E. J., Huffman, J. A., Onasch, T. B., Alfarra, M. R., Williams, P. I., Bower, K., Kondo, Y., Schneider, J., Drewnick, F., Borrmann, S., Weimer, S., Demerjian, K., Salcedo, D., Cottrell, L., Griffin, R., Takami, A., Miyoshi, T., Hatakeyama, S., Shimono, A., Sun, J. Y., Zhang, Y. M., Dzepina, K., Kimmel, J. R., Sueper, D., Jayne, J. T., Herndon, S. C., Trimborn, A. M., Williams, L. R., Wood, E. C., Middlebrook, A. M., Kolb, C. E., Baltensperger, U., and Worsnop, D. R.: Evolution of organic aerosols in the atmosphere, Science, 80, 1525–1529, https://doi.org/10.1126/science.1180353, 2009.

Ng, N. L., Herndon, S. C., Trimborn, A., Canagaratna, M. R., Croteau, P. L., Onasch, T. B., Sueper, D., Worsnop, D. R., Zhang, Q., Sun, Y. L., and Jayne, J. T.: An Aerosol Chemical Speciation Monitor (ACSM) for routine monitoring of the composition and mass concentrations of ambient aerosol, Aerosol Sci. Technol., 45, 770–784, https://doi.org/10.1080/02786826.2011.560211, 2011a.

Ng, N. L., Canagaratna, M. R., Jimenez, J. L., Chhabra, P. S., Seinfeld, J. H., and Worsnop, D. R.: Changes in organic aerosol composition with aging inferred from aerosol mass spectra, Atmos. Chem. Phys., 11, 6465–6474, https://doi.org/10.5194/acp-11-6465-2011, 2011b.

Ogulei, D., Hopke, P. K., Zhou, L., Paatero, P., Park, S. S., and Ondov, J. M.: Receptor modeling for multiple time resolved species: The Baltimore supersite, Atmos. Environ., 39, 3751–3762, https://doi.org/10.1016/j.atmosenv.2005.03.012, 2005.

Paatero, P.: The Multilinear Engine – A Table-Driven, Least Squares Program for Solving Multilinear Problems, Including the n-Way Parallel Factor Analysis Model, J. Comput. Graph. Stat., 8, 854–888, https://doi.org/10.1080/10618600.1999.10474853, 1999.

Paatero, P. and Hopke, P. K.: Discarding or downweighting high-noise variables in factor analytic models, Anal. Chim. Acta, 490, 277–289, https://doi.org/10.1016/S0003-2670(02)01643-4, 2003.

Paatero, P. and Tapper, U.: Positive matrix factorization: A non-negative factor model with optimal utilization of error estimates of data values, Environmetrics, 5, 111–126, https://doi.org/10.1002/env.3170050203, 1994.

Parworth, C., Fast, J., Mei, F., Shippert, T., Sivaraman, C., Tilp, A., Watson, T., and Zhang, Q.: Long-term measurements of submicrometer aerosol chemistry at the Southern Great Plains (SGP) using an Aerosol Chemical Speciation Monitor (ACSM), Atmos. Environ., 106, 43–55, https://doi.org/10.1016/j.atmosenv.2015.01.060, 2015.

Rai, P., Furger, M., El Haddad, I., Kumar, V., Wang, L., Singh, A., Dixit, K., Bhattu, D., Petit, J. E., Ganguly, D., Rastogi, N., Baltensperger, U., Tripathi, S. N., Slowik, J. G., and Prévôt, A. S. H.: Real-time measurement and source apportionment of elements in Delhi's atmosphere, Sci. Total Environ., 742, 140332, https://doi.org/10.1016/j.scitotenv.2020.140332, 2020.

Rodríguez, S. and Cuevas, E.: The contributions of "minimum primary emissions" and "new particle formation enhancements" to the particle number concentration in urban air, J. Aerosol Sci., 38, 1207–1219, https://doi.org/10.1016/j.jaerosci.2007.09.001, 2007.

Rutherford, J. W., Larson, T. V., Gould, T., Seto, E., Novosselov, I. V., and Posner, J. D.: Source apportionment of environmental combustion sources using excitation emission matrix fluorescence spectroscopy and machine learning, Atmos. Environ., 259, 118501, https://doi.org/10.1016/j.atmosenv.2021.118501, 2021.

Shih, C.-H., Chen, J.-K., Kuo, L.-W., Cho, K.-H., Hsiao, T.-C., Lin, Z.-W., Lin, Y.-S., Kang, J.-H., Lo, Y.-C., Chuang, K.-J., Cheng, T.-J., and Chuang, H.-C.: Chronic pulmonary exposure to traffic-related fine particulate matter causes brain impairment in adult rats, Part. Fibre Toxicol., 15, 1–17, https://doi.org/10.1186/s12989-018-0281-1, 2018.

Sun, Y., Xu, W., Zhang, Q., Jiang, Q., Canonaco, F., Prévôt, A. S. H., Fu, P., Li, J., Jayne, J., Worsnop, D. R., and Wang, Z.: Source apportionment of organic aerosol from 2-year highly time-resolved measurements by an aerosol chemical speciation monitor in Beijing, China, Atmos. Chem. Phys., 18, 8469–8489, https://doi.org/10.5194/acp-18-8469-2018, 2018.

Textor, C., Schulz, M., Guibert, S., Kinne, S., Balkanski, Y., Bauer, S., Berntsen, T., Berglen, T., Boucher, O., Chin, M., Dentener, F., Diehl, T., Easter, R., Feichter, H., Fillmore, D., Ghan, S., Ginoux, P., Gong, S., Grini, A., Hendricks, J., Horowitz, L., Huang, P., Isaksen, I., Iversen, I., Kloster, S., Koch, D., Kirkevåg, A., Krist-

jansson, J. E., Krol, M., Lauer, A., Lamarque, J. F., Liu, X., Montanaro, V., Myhre, G., Penner, J., Pitari, G., Reddy, S., Seland, Ø., Stier, P., Takemura, T., and Tie, X.: Analysis and quantification of the diversities of aerosol life cycles within AeroCom, Atmos. Chem. Phys., 6, 1777–1813, https://doi.org/10.5194/acp-6-1777-2006, 2006.

Tobler, A. K., Canonaco, F., Skiba, A., Styszko, K., Nęcki, J., Slowik, J. G., and Baltensperger, U.: Characterization and source apportionment of PM 1 organic aerosol in Krakow, Poland, (April), 8299, 2021.

Ulbrich, I. M., Canagaratna, M. R., Zhang, Q., Worsnop, D. R., and Jimenez, J. L.: Interpretation of organic components from Positive Matrix Factorization of aerosol mass spectrometric data, Atmos. Chem. Phys., 9, 2891–2918, https://doi.org/10.5194/acp-9-2891-2009, 2009.

Via, M.: Rolling vs. Seasonal comparison, Mendeley Data [data set], V1, https://doi.org/10.17632/dsfty2rn7y.1, 2022.

Via, M.: "Rolling vs. Seasonal comparison", Mendeley Data [data set], V2, https://doi.org/10.17632/dsfty2rn7y.2, 2022a.

Via, M.: "Rolling vs. Seasonal PMF coding", Mendeley Data [code], v1 https://doi.org/10.17632/nd79y8mpg3.1, 2022b.

Yang, M., Chu, C., Bloom, M. S., Li, S., Chen, G., Heinrich, J., Markevych, I., Knibbs, L. D., Bowatte, G., Dharmage, S. C., Komppula, M., Leskinen, A., Hirvonen, M. R., Roponen, M., Jalava, P., Wang, S. Q., Lin, S., Zeng, X. W., Hu, L. W., Liu, K. K., Yang, B. Y., Chen, W., Guo, Y., and Dong, G. H.: Is smaller worse? New insights about associations of PM1 and respiratory health in children and adolescents, Environ. Int., 120, 516–524, https://doi.org/10.1016/j.envint.2018.08.027, 2018.

Yin, P., Guo, J., Wang, L., Fan, W., Lu, F., Guo, M., Moreno, S. B. R., Wang, Y., Wang, H., Zhou, M., and Dong, Z.: Higher Risk of Cardiovascular Disease Associated with Smaller Size-Fractioned Particulate Matter, Environ. Sci. Technol. Lett., 7, 95–101, https://doi.org/10.1021/acs.estlett.9b00735, 2020.

Yuan, B., Shao, M., De Gouw, J., Parrish, D. D., Lu, S., Wang, M., Zeng, L., Zhang, Q., Song, Y., Zhang, J., and Hu, M.: Volatile organic compounds (VOCs) in urban air: How chemistry affects the interpretation of positive matrix factorization (PMF) analysis, J. Geophys. Res.-Atmos., 117, 1–17, https://doi.org/10.1029/2012JD018236, 2012.

Zhang, Y., Favez, O., Petit, J.-E., Canonaco, F., Truong, F., Bonnaire, N., Crenn, V., Amodeo, T., Prévôt, A. S. H., Sciare, J., Gros, V., and Albinet, A.: Six-year source apportionment of submicron organic aerosols from near-continuous highly time-resolved measurements at SIRTA (Paris area, France), Atmos. Chem. Phys., 19, 14755–14776, https://doi.org/10.5194/acp-19-14755-2019, 2019.

Résumé

Considérant les impacts climatiques et sanitaires majeurs des particules fines, ce travail a étudié leur composition chimique sur 13 sites français de 2015 à 2021. L'aérosol organique (AO) prédomine, avec des augmentations en hiver (chauffage résidentiel), et en été (formation d'aérosols organiques secondaires). Le nitrate d'ammonium, polluant secondaire lui aussi issu des combustions et de l'agriculture, domine en particulier dans le nord lors des épisodes de pollution printaniers.

Les sources principales de l'AO sont liées principalement aux émissions du trafic et de la combustion de biomasse. D'autres sont spécifiques à certains sites (activités de cuisson, industrie, émissions des navires). Les facteurs oxygénés dominent l'AO, suggérant des processus de vieillissement et de formation secondaire. Ces résultats peuvent orienter les politiques visant à améliorer la qualité de l'air, contribuer à améliorer la précision des modèles et servir à de futures études épidémiologiques.

Abstract

Considering the major climatic and health impacts of fine particulate matter, this work studied their chemical composition at 13 French sites from 2015 to 2021. Organic aerosols (OA) predominate, with increases in winter (residential heating emissions) and summer (formation of secondary organic aerosols). Ammonium nitrate, also a secondary pollutant from combustion and agriculture, dominates during springtime pollution episodes, particularly in the north.

The main sources of OA are traffic emissions and biomass combustion. Others are site-specific (cooking activities, industry, ship emissions). Oxygenated factors dominate OA, suggesting aging and secondary formation processes. These results can guide policies aimed at improving air quality, help improve the model accuracy and inform future epidemiological studies.